

New approach methods in immunology

Edited by

Jeffrey John Bajramovic, Susan Gibbs, Emanuela Corsini
and Thomas Hartung

Published in

Frontiers in Immunology
Frontiers in Nutrition



FRONTIERS EBOOK COPYRIGHT STATEMENT

The copyright in the text of individual articles in this ebook is the property of their respective authors or their respective institutions or funders. The copyright in graphics and images within each article may be subject to copyright of other parties. In both cases this is subject to a license granted to Frontiers.

The compilation of articles constituting this ebook is the property of Frontiers.

Each article within this ebook, and the ebook itself, are published under the most recent version of the Creative Commons CC-BY licence. The version current at the date of publication of this ebook is CC-BY 4.0. If the CC-BY licence is updated, the licence granted by Frontiers is automatically updated to the new version.

When exercising any right under the CC-BY licence, Frontiers must be attributed as the original publisher of the article or ebook, as applicable.

Authors have the responsibility of ensuring that any graphics or other materials which are the property of others may be included in the CC-BY licence, but this should be checked before relying on the CC-BY licence to reproduce those materials. Any copyright notices relating to those materials must be complied with.

Copyright and source acknowledgement notices may not be removed and must be displayed in any copy, derivative work or partial copy which includes the elements in question.

All copyright, and all rights therein, are protected by national and international copyright laws. The above represents a summary only. For further information please read Frontiers' Conditions for Website Use and Copyright Statement, and the applicable CC-BY licence.

ISSN 1664-8714
ISBN 978-2-8325-5498-2
DOI 10.3389/978-2-8325-5498-2

About Frontiers

Frontiers is more than just an open access publisher of scholarly articles: it is a pioneering approach to the world of academia, radically improving the way scholarly research is managed. The grand vision of Frontiers is a world where all people have an equal opportunity to seek, share and generate knowledge. Frontiers provides immediate and permanent online open access to all its publications, but this alone is not enough to realize our grand goals.

Frontiers journal series

The Frontiers journal series is a multi-tier and interdisciplinary set of open-access, online journals, promising a paradigm shift from the current review, selection and dissemination processes in academic publishing. All Frontiers journals are driven by researchers for researchers; therefore, they constitute a service to the scholarly community. At the same time, the *Frontiers journal series* operates on a revolutionary invention, the tiered publishing system, initially addressing specific communities of scholars, and gradually climbing up to broader public understanding, thus serving the interests of the lay society, too.

Dedication to quality

Each Frontiers article is a landmark of the highest quality, thanks to genuinely collaborative interactions between authors and review editors, who include some of the world's best academicians. Research must be certified by peers before entering a stream of knowledge that may eventually reach the public - and shape society; therefore, Frontiers only applies the most rigorous and unbiased reviews. Frontiers revolutionizes research publishing by freely delivering the most outstanding research, evaluated with no bias from both the academic and social point of view. By applying the most advanced information technologies, Frontiers is catapulting scholarly publishing into a new generation.

What are Frontiers Research Topics?

Frontiers Research Topics are very popular trademarks of the *Frontiers journals series*: they are collections of at least ten articles, all centered on a particular subject. With their unique mix of varied contributions from Original Research to Review Articles, Frontiers Research Topics unify the most influential researchers, the latest key findings and historical advances in a hot research area.

Find out more on how to host your own Frontiers Research Topic or contribute to one as an author by contacting the Frontiers editorial office: frontiersin.org/about/contact

New approach methods in immunology

Topic editors

Jeffrey John Bajramovic — Utrecht University, Netherlands
Susan Gibbs — Amsterdam University Medical Center, Netherlands
Emanuela Corsini — University of Milan, Italy
Thomas Hartung — Johns Hopkins University, United States

Citation

Bajramovic, J. J., Gibbs, S., Corsini, E., Hartung, T., eds. (2024). *New approach methods in immunology*. Lausanne: Frontiers Media SA.
doi: 10.3389/978-2-8325-5498-2

Table of contents

06 **Editorial: New approach methods in immunology**
Thomas Hartung, Jeffrey John Bajramovic, Susan Gibbs and Emanuela Corsini

10 **Vascular inflammation on a chip: A scalable platform for trans-endothelial electrical resistance and immune cell migration**
Haley Ehlers, Arnaud Nicolas, Frederik Schavemaker, Jeroen P. M. Heijmans, Martin Bulst, Sebastiaan J. Trietsch and Lenie J. van den Broek

21 **Integration: Gospel for immune bioinformatician on epitope-based therapy**
Baozeng Sun, Junqi Zhang, Zhikui Li, Mingyang Xie, Cheng Luo, Yongkai Wang, Longyu Chen, Yueyue Wang, Dongbo Jiang and Kun Yang

28 **Corrigendum: Integration: gospel for immune bioinformatician on epitope-based therapy**
Baozeng Sun, Junqi Zhang, Zhikui Li, Mingyang Xie, Cheng Luo, Yongkai Wang, Longyu Chen, Yueyue Wang, Dongbo Jiang and Kun Yang

30 **Advances in phage display based nano immunosensors for cholera toxin**
Yang Li, Kai-di Yang, De-cai Kong and Jun-feng Ye

49 **Monocytes and T cells incorporated in full skin equivalents to study innate or adaptive immune reactions after burn injury**
Patrick P.G. Mulder, Marcel Vlijg, Anouk Elgersma, Lotte Rozemeijer, Leonore S. Mastenbroek, Esther Middelkoop, Irma Joosten, Hans J.P.M. Koenen and Bouke K.H.L. Boekema

62 **A bibliometric analysis: Ca^{2+} fluxes and inflammatory phenotyping by flow cytometry in peripheral blood mononuclear cells**
Camille Brun, Lucie Chalet, Florentin Moulin, Thomas Bochaton, Sylvie Ducreux, Melanie Paillard and Claire Crola Da Silva

75 **An optimized cocktail of small molecule inhibitors promotes the maturation of dendritic cells in GM-CSF mouse bone marrow culture**
Shintaro Matsuba, Hiroki Ura, Fumiji Saito, Chie Ogasawara, Shigetaka Shimodaira, Yo Niida and Nobuyuki Onai

90 **Omicron subvariants illustrate reduced respiratory tissue penetration, cell damage and inflammatory responses in human airway epithelia**
Viktoria Zaderer, Hussam Abd El Halim, Anna-Lena Wyremblewsky, Gaia Lupoli, Christopher Dächert, Maximilian Muenchhoff, Alexander Graf, Helmut Blum, Cornelia Lass-Flörl, Oliver T. Keppler, Lukas A. Huber, Wilfried Posch and Doris Wilflingseder

99 **A human 3D immune competent full-thickness skin model mimicking dermal dendritic cell activation**
Johanna Maria Hölken, Katja Friedrich, Marion Merkel, Nelli Blasius, Ursula Engels, Timo Buhl, Karsten Rüdiger Mewes, Lars Vierkotten and Nicole Elisabeth Teusch

113 **Feasibility and acceptability of undertaking postmortem studies for tuberculosis medical research in a low income country**
Gift Ahimbisibwe, Marjorie Nakibuule, Marvin Martin Ssejoba, David Oyamo, Rose Mulwana, Josephine Nabulime, Febronius Babirye, Musana Abdusalaamu Kizito, Hervé Monka Lekuya, Akello Suzan Adakun, Daisy Nalumansi, Stella Muryasingura, Robert Lukande, Andrew Kyazze, Joseph Baruch Baluku, Irene Andia Biraro and Stephen Cose

123 **A comprehensive battery of flow cytometric immunoassays for the *in vitro* testing of chemical effects in human blood cells**
Arkadiusz Pierzchalski, Ana C. Zenclussen and Gunda Herberth

139 **Transcriptional profile of human thymus reveals IGFBP5 is correlated with age-related thymic involution**
Xiaojing Yang, Xichan Chen, Wei Wang, Siming Qu, Binbin Lai, Ji Zhang, Jian Chen, Chao Han, Yi Tian, Yingbin Xiao, Weiwu Gao and Yuzhang Wu

153 **An in silico modeling approach to understanding the dynamics of the post-burn immune response**
H. Ibrahim Korkmaz, Vivek M. Sheraton, Roland V. Bumbuc, Meifang Li, Anouk Pijpe, Patrick P. G. Mulder, Bouke K. H. L. Boekema, Evelien de Jong, Stephan G. F. Papendorp, Ruud Brands, Esther Middelkoop, Peter M. A. Sloot and Paul P. M. van Zuijlen

167 **A novel IgE epitope-specific antibodies-based sandwich ELISA for sensitive measurement of immunoreactivity changes of peanut allergen Ara h 2 in processed foods**
Yan Yan, Liming Li, Caiyun Long, Yaping Dong, Jinyu Li, Caiyi Shen, Yiqian Zhao, Jiangqiang Zhao, Jianbin Wang, Anqi Xiong, Xin Li, Hongbing Chen and Shengfa He

181 **Utilizing murine dendritic cell line DC2.4 to evaluate the immunogenicity of subunit vaccines *in vitro***
Lantian Lu, Wei Yang Kong, Jiahui Zhang, Farrhana Firdaus, James W. Wells, Rachel J. Stephenson, Istvan Toth, Mariusz Skwarczynski and Jazmina L. Gonzalez Cruz

194 **Mathematical modeling in autoimmune diseases: from theory to clinical application**
Yaroslav Ugolkov, Antonina Nikitich, Cristina Leon, Gabriel Helmlinger, Kirill Peskov, Victor Sokolov and Alina Volkova

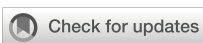
214 **An *in vitro* assay for toxicity testing of *Clostridium perfringens* type C β -toxin**
Marieke Hoonakker, Afshin Zariri, Lisette de Brouwer, Dionne David, Anouska Borgman and Arjen Sloots

225 *In vitro* immunity: an overview of immunocompetent organ-on-chip models

Andrew I. Morrison, Mirthe J. Sjoerds, Leander A. Vonk, Susan Gibbs and Jasper J. Koning

241 Generation of functionally active resident macrophages from adipose tissue by 3D cultures

Adèle Arlat, Marie-Laure Renoud, Jean Nakhle, Miguel Thomas, Jessica Fontaine, Emmanuelle Arnaud, Cédric Dray, Hélène Authier, Paul Monserrat, Agnès Coste, Louis Casteilla, Marielle Ousset and Béatrice Cousin



OPEN ACCESS

EDITED AND REVIEWED BY

Simon Mitchell,
Brighton and Sussex Medical School,
United Kingdom

*CORRESPONDENCE

Thomas Hartung
THartun1@jhu.edu

RECEIVED 30 August 2024

ACCEPTED 05 September 2024

PUBLISHED 18 September 2024

CITATION

Hartung T, Bajramovic JJ, Gibbs S and Corsini E (2024) Editorial: New approach methods in immunology.

Front. Immunol. 15:1488534.

doi: 10.3389/fimmu.2024.1488534

COPYRIGHT

© 2024 Hartung, Bajramovic, Gibbs and Corsini. This is an open-access article distributed under the terms of the [Creative Commons Attribution License \(CC BY\)](#). The use, distribution or reproduction in other forums is permitted, provided the original author(s) and the copyright owner(s) are credited and that the original publication in this journal is cited, in accordance with accepted academic practice. No use, distribution or reproduction is permitted which does not comply with these terms.

Editorial: New approach methods in immunology

Thomas Hartung^{1,2*}, Jeffrey John Bajramovic³, Susan Gibbs^{4,5} and Emanuela Corsini⁶

¹Center for Alternatives to Animal Testing (CAAT), Doerenkamp-Zbinden-Chair for Evidence-based Toxicology, Johns Hopkins Bloomberg School of Public Health, Baltimore, MD, United States,

²Center for Alternatives to Animal Testing (CAAT)-Europe, University of Konstanz, Konstanz, Germany,

³3Rs Centre Utrecht, Utrecht University, Utrecht, Netherlands, ⁴Department of Molecular Cell Biology and Immunology, Amsterdam University Medical Center (UMC), Infection & Immunity Institute, Vrije Universiteit Amsterdam, Amsterdam, Netherlands, ⁵Department of Oral Cell Biology, Academic Centre for Dentistry Amsterdam (ACTA), University of Amsterdam and Vrije Universiteit, Amsterdam, Netherlands, ⁶Department of Pharmacological and Biomolecular Sciences 'Rodolfo Paoletti', Università degli Studi di Milano, Milan, Italy

KEYWORDS

alternatives to animal testing, new approach methods (NAM), microphysiological system (MPS), artificial intelligence, cell culture

Editorial on the Research Topic

New approach methods in immunology

The field of immunology is undergoing a significant transformation with the advent of new approach methods (NAM) as alternatives to traditional animal models. These advancements are driven by economic, ethical, and scientific motivations, particularly the need to bridge the translational gap between animal studies and human clinical trials, often referred to as the 'valley of death.'

Immunology is uniquely positioned compared to other fields with respect to NAMs due to the intricate complexity and dynamic nature of the immune system. Unlike other biological systems, the immune system involves a vast array of cell types, signaling molecules, and interactions that span different tissues and organs. Key aspects that make immunology special in the context of NAMs include:

1. Complexity of Interactions: Immunological responses involve a highly coordinated interplay between innate and adaptive immune cells, which must be accurately replicated to understand mechanisms of disease and therapeutic interventions.

2. Spatial and Temporal Dynamics: Immune responses are characterized by precise spatial and temporal dynamics, requiring advanced modeling techniques to simulate processes such as cell migration, tissue infiltration, and the sequential activation of immune pathways.

3. Genetic and Functional Variability: The immune system exhibits significant genetic and functional variability among individuals, necessitating NAMs that can capture this diversity to provide more personalized insights into immune responses and disease susceptibilities.

4. Involvement of Multiple Organs and Systems: Immunological studies must consider the interconnectedness of various organs and systems, such as the lymph nodes, spleen, bone marrow, and mucosal surfaces, making the development of comprehensive NAMs particularly challenging and crucial.

5. Impact of Environmental Factors: The immune system is highly responsive to environmental factors, including pathogens, toxins, and lifestyle influences. NAMs must incorporate these variables to fully understand their impact on immune function and disease progression.

Traditional animal models often fail to replicate the human immune system's complexity accurately, leading to translational gaps. 90 million years of evolution under enormous selective pressure since rodents split from humans have left their mark. NAMs offer a more ethical and potentially more accurate alternative, enhancing the relevance of immunological research to human health. Especially animal studies involving infections to challenge the immune system are often involving very severe suffering.

Overall, the special requirements and challenges of immunology drive the need for sophisticated and innovative NAMs that can capture the multifaceted nature of immune responses, offering more relevant and humane alternatives to traditional animal-based research. This editorial summarizes the state-of-the-art developments in NAM for immunology, highlighting the efforts to mimic *in vivo* biology accurately and overcome specific challenges inherent to immunological research.

The 18 accepted contributions showcase advances in immunological non-animal methods:

Ahimbisibwe et al. examine the feasibility of conducting postmortem studies for tuberculosis research in Uganda. The researchers found good acceptance from next-of-kin for tissue donation, and demonstrated that postmortem procedures and tissue processing could be completed within 8 hours of death while maintaining cell viability for up to 14 hours. This work establishes the feasibility of using postmortem tissues for immunological studies, providing a valuable resource for understanding tissue-specific immune responses in humans as a valuable tool for understanding tissue-specific immune responses in tuberculosis and other diseases.

Arlat et al. present a method for generating functional adipose tissue-resident macrophages using 3D culture of stromal vascular cells from adipose tissue. The researchers show that these macrophages have distinct characteristics from bone marrow-derived macrophages, including metabolic activity and polarization responses. Importantly, single-cell analysis indicates the cultured macrophages mirror phenotypic and functional traits of *in vivo* adipose tissue-resident macrophages. This technique provides a valuable tool for studying adipose tissue macrophage biology without the need for cell sorting.

Brun et al. detail a 24-color flow cytometry panel that allows comprehensive immunophenotyping of human peripheral blood cells, facilitating high-throughput screening of chemicals and identifying affected cell types and signaling pathways. This review examines research on Ca^{2+} signaling and inflammation in peripheral blood mononuclear cells (PBMCs) through bibliometric analysis. The authors found that while Ca^{2+} signaling is crucial for immune cell function, flow cytometry-based analysis of Ca^{2+} in PBMCs is still underdeveloped. They highlight knowledge gaps regarding intracellular Ca^{2+} players in PBMCs and propose

flow cytometry as a complementary method to microscopy for studying Ca^{2+} dynamics in these cells.

Ehlers et al. developed a scalable microfluidic platform for modeling vascular inflammation using human endothelial cells. The system enables real-time measurement of endothelial barrier function via transendothelial electrical resistance (TEER) in 64 parallel microfluidic channels. The authors demonstrated the platform can detect inflammatory responses to cytokines and immune cells, including changes in barrier function, adhesion molecule expression, and immune cell migration. They propose it as a powerful tool for studying vascular inflammation and screening anti-inflammatory drugs.

Hölken et al. introduce a 3D full-thickness skin model with dermal dendritic cell surrogates derived from THP-1 cells, this model effectively mimics immune responses to sensitizers and serves as a valuable tool for studying skin sensitization and inflammatory responses. The integrated dendritic cells remained functional and responded to sensitizers by upregulating maturation markers. The model could detect suppression of dendritic cell activation by dexamethasone treatment. This immune-competent skin model may be useful for testing potential sensitizers and anti-inflammatory compounds.

Hoonakker et al. examine the *in vitro* toxicity testing of *Clostridium perfringens* type C beta-toxin using a cell-based assay with THP-1 cells. The researchers developed and validated the assay as an alternative to mouse-based tests for toxicity assessment of veterinary vaccines. They show the assay can detect toxin activity at high dilutions and is suitable for testing at multiple stages of vaccine production. The authors suggest this approach could reduce animal use in toxicity testing for *C. perfringens* vaccines.

Korkmaz et al. describe an *in silico* mechanistic modeling approach used to investigate the dynamics of the immune response following burn injuries. The model uses agent-based techniques to simulate the behavior of inflammatory agents, providing insights into post-burn inflammation and potential therapeutic interventions. The model incorporates various immune cells and cytokines to capture the complex dynamics of inflammation. Simulations identified key factors influencing inflammation intensity, including endothelial cell count. This computational approach could help predict inflammatory responses and test potential interventions for burn injuries.

Li et al. review recent developments in phage display-based nano immunosensors for detecting cholera toxin. The authors discuss how engineered bacteriophages with specific antibody fragments or mimotopes can enable sensitive and precise toxin detection. This approach offers an ethical alternative to animal-derived methods and has the potential to significantly improve cholera toxin detection capabilities. The authors highlight how engineered bacteriophages with specific antibody fragments or mimotopes can enable precise and sensitive detection of cholera toxin. This approach offers a promising alternative to animal-derived methods, potentially transforming cholera toxin detection with improved safety, sensitivity and ethics.

Lu et al. developed an *in vitro* assay using the DC2.4 dendritic cell line to evaluate the immunogenicity of peptide-based vaccines.

The assay measures dendritic cell uptake, maturation, and cytokine production in response to vaccine candidates. It showed good correlation with previously reported *in vivo* results for various peptide constructs. This assay could serve as a useful tool for screening vaccine candidates before animal testing.

Matsuba et al. developed a method to generate dendritic cells (DCs) from mouse bone marrow using small molecule inhibitors. The cocktail of inhibitors called YPPP enhanced DC maturation, increased IL-12 production, and improved T cell activation compared to conventional methods. In tumor models, YPPP-derived DCs showed enhanced anti-tumor effects, especially when combined with anti-PD-1 therapy. The authors propose this as a useful method for generating DCs with improved immunostimulatory functions for cancer immunotherapy.

Morrison et al. review multi-organ-on-chip (multi-OoC) systems for studying immunotoxicity. These systems replicate systemic immunological processes by integrating various immune cells and tissues in a controlled *in vitro* environment to study autoimmune diseases and immune responses. The authors describe various models for organs like lung, skin, intestine, and lymphoid tissues, highlighting how they recapitulate key aspects of organ-specific immunity. While progress has been made, especially for innate immunity, the authors note that incorporating adaptive immunity remains challenging. They suggest organ-on-chip models will be valuable for studying disease mechanisms and drug effects, but further development is needed to fully replicate systemic immune responses.

Mulder et al. developed a human full skin equivalent burn wound model based on the collagen-elastin matrix MatriDerm® incorporating peripheral blood-derived monocytes and T cells to study thermal injuries and the post-burn inflammatory processes. This study marks a significant step forward in creating an immunocompetent human skin model for investigating burn-induced immune responses, examining alterations in marker expression on immune cells and the secretion of cytokines in the culture medium.

Pierzchalski et al. present a suite of flow cytometry-based assays utilizing primary human blood cells to test the immunotoxic effects of chemicals. These assays target various immune cells, including T cells, NK cells, and B cells, offering a robust alternative to traditional cell line-based assays. The assays cover activation of various immune cell types including T cells, NK cells, B cells, basophils, and innate-like T cells. The authors demonstrate the assays can detect immunomodulatory effects of chemicals and propose them as a valuable tool for *in vitro* toxicity and immunomodulatory testing. The assays use primary human cells and provide high-throughput, multiparametric analysis. This test battery provides a standardized approach for evaluating chemical impacts on human immune cell function that could support toxicity testing and drug development.

Sun et al. proposed a novel train of thought, “integration”, to augment the breadth and depth of bioinformatics in peptide-based therapeutics. The advancement of epitope-based vaccines is a significant breakthrough in bioinformatics research, making the exploration of pathogen epitopes more convenient and cost-effective.

Ugolkov et al. review mathematical models of autoimmune diseases that focus on mechanistic descriptions of the immune

system. The authors identified 38 models covering 13 autoimmune conditions, with most using systems of ordinary differential equations to model immune components and interactions. While the models provide insights into autoimmune processes, many lack rigorous validation against clinical data or incorporation of pharmacokinetic elements. The authors suggest a need for more robust quantitative systems pharmacology models to support drug development for autoimmune diseases.

Yan et al. developed a novel sandwich ELISA method to detect the peanut allergen Ara h 2 and measure changes in its immunoreactivity in processed foods. The assay uses antibodies specific to IgE epitopes of Ara h 2 and shows high sensitivity and specificity. It was able to detect Ara h 2 in various food samples and measure changes in immunoreactivity after processing. This method could be useful for monitoring allergen levels and potential allergenicity of peanut proteins in foods.

Yang et al. analyze single-cell RNA sequencing data to create a cell atlas of the human thymus and investigate changes during aging. The researchers identified key signaling pathways and transcriptional regulators involved in early thymocyte development. They found that IGFBP5 expression increases with age in thymic epithelial cells and may play a role in thymic involution. The findings provide new insights into thymus biology and age-related changes.

Zaderer et al. This study compares the pathogenicity of Delta and Omicron SARS-CoV-2 subvariants using a human 3D respiratory model. Findings show that Delta penetrates deep into respiratory tissues causing significant damage and inflammation, while Omicron subvariants remain superficial, causing less tissue damage and lower inflammatory responses. These findings provide insights into the different clinical presentations of Delta and Omicron infections and highlight the importance of early virus-tissue interactions in shaping disease severity.

The collective efforts reflected in these articles demonstrate significant progress in the development and application of NAM in immunology. By continuing to refine these methods and overcome existing challenges, the scientific community can advance towards more ethical, cost-effective, and human-relevant research methodologies.

Author contributions

TH: Writing – original draft. JB: Writing – review & editing. SG: Writing – review & editing. EC: Writing – review & editing.

Conflict of interest

The authors declare that the research was conducted in the absence of any commercial or financial relationships that could be construed as a potential conflict of interest.

The author(s) declared that they were an editorial board member of Frontiers, at the time of submission. This had no impact on the peer review process and the final decision.

Publisher's note

All claims expressed in this article are solely those of the authors and do not necessarily represent those of their affiliated

organizations, or those of the publisher, the editors and the reviewers. Any product that may be evaluated in this article, or claim that may be made by its manufacturer, is not guaranteed or endorsed by the publisher.



OPEN ACCESS

EDITED BY

Wilfried Le Goff,
Institut National de la Santé et de la
Recherche Médicale (INSERM), France

REVIEWED BY

Jonathan Michael Flanagan,
Baylor College of Medicine, United States
Matthias Clauss,
Indiana University Bloomington,
United States

*CORRESPONDENCE

Lenie J. van den Broek
✉ lvandenbroek@mimetas.com

[†]These authors have contributed
equally to this work and share
first authorship

SPECIALTY SECTION

This article was submitted to
Inflammation,
a section of the journal
Frontiers in Immunology

RECEIVED 07 December 2022

ACCEPTED 11 January 2023

PUBLISHED 24 January 2023

CITATION

Ehlers H, Nicolas A, Schavemaker F, Heijmans JPM, Bulst M, Trietsch SJ and van den Broek LJ (2023) Vascular inflammation on a chip: A scalable platform for trans-endothelial electrical resistance and immune cell migration. *Front. Immunol.* 14:1118624. doi: 10.3389/fimmu.2023.1118624

COPYRIGHT

© 2023 Ehlers, Nicolas, Schavemaker, Heijmans, Bulst, Trietsch and van den Broek. This is an open-access article distributed under the terms of the [Creative Commons Attribution License \(CC BY\)](#). The use, distribution or reproduction in other forums is permitted, provided the original author(s) and the copyright owner(s) are credited and that the original publication in this journal is cited, in accordance with accepted academic practice. No use, distribution or reproduction is permitted which does not comply with these terms.

Vascular inflammation on a chip: A scalable platform for trans- endothelial electrical resistance and immune cell migration

Haley Ehlers^{1,2†}, Arnaud Nicolas^{1,2†}, Frederik Schavemaker¹,
Jeroen P. M. Heijmans¹, Martin Bulst³, Sebastiaan J. Trietsch¹
and Lenie J. van den Broek^{1*}

¹Mimetas B.V., Leiden, Netherlands, ²Leiden Academic Centre for Drug Research, Leiden University, Leiden, Netherlands, ³Sciospec GmbH, Bennewitz, Germany

The vasculature system plays a critical role in inflammation processes in the body. Vascular inflammatory mechanisms are characterized by disruption of blood vessel wall permeability together with increased immune cell recruitment and migration. There is a critical need to develop models that fully recapitulate changes in vascular barrier permeability in response to inflammatory conditions. We developed a scalable platform for parallel measurements of trans epithelial electrical resistance (TEER) in 64 perfused microfluidic HUVEC tubules under inflammatory conditions. Over 250 tubules were exposed to Tumor necrosis factor alpha (TNF α) and interferon gamma (INF- γ) or human peripheral blood mononuclear cells. The inflammatory response was quantified based on changes TEER and expression of ICAM and VE-cadherin. We observed changes in barrier function in the presence of both inflammatory cytokines and human peripheral blood mononuclear cells, characterized by decreased TEER values, increase in ICAM expression as well as changes in endothelial morphology. OrganoPlate 3-lane64 based HUVEC tubules provide a valuable tool for inflammatory studies in an automation compatible manner. Continuous TEER measurements enable long term, sensitive assays for barrier studies. We propose the use of our platform as a powerful tool for modelling endothelial inflammation in combination with immune cell interaction that can be used to screen targets and drugs to treat chronic vascular inflammation.

KEYWORDS

vascular inflammation, immune cell migration, TEER, organ-on-a-chip, endothelium, TNF α , INF- γ and OrganoPlate

1 Introduction

Acute inflammation is an essential mechanism to ward off infection and support healing of injuries. Autoimmune disorder or repeated injuries can impair the immune system's ability to regulate the inflammatory response, increasing the risks of inflammation becoming chronic and detrimental (1). Vasculature plays a crucial role in inflammatory processes by

transporting immune cells, cytokines and chemokines throughout the body (2). Chronic inflammation can affect the vasculature and is associated with increased risk of cardiovascular diseases like endothelial dysfunction and atherosclerosis (3). Unfortunately, cardiovascular diseases are one of the leading causes of deaths worldwide, taking approximately 17.9 million lives a year (4).

The endothelium is responsible for many functions like vascular tone, barrier function, injury repair, and metabolism (5). Endothelial dysfunction is characterized by an increase in permeability of the vessels and endothelial activation (6). In acute inflammation, barrier leakage is brief, but in chronic inflammation this leakage is sustained and the vasculature remodels to an activated leaky phenotype (7). In order to maintain healthy barriers, endothelial barrier comprise adherent junctions, tight junctions and gap junctions. VE-Cadherin is an adherent junction that is the main component in endothelial junctions and is essential for regulation of endothelial barrier (8). Pro-Inflammatory cytokines like tumor necrosis factor alpha (TNF α) and Interferon gamma (INF- γ) are known to cause endothelial cell activation (9, 10) and can lead to VE-Cadherin destabilization (11, 12). This endothelial activation leads to increased expression of various adhesion proteins like ICAM (5, 6, 13). Phosphorylation of VE-Cadherin (14, 15) allows for the migration of immune cells out of the vessel into the surrounding arterial tissue. While VE-Cadherin plays a critical role in vascular permeability and immune cell migration (16), the exact relationship between immune cell migration and vascular leakage is not fully understood (13, 17).

Therefore, there is a need of *in vitro* models that properly recapitulate the vascular barrier and methods that quantify the barrier integrity of these models.

The development of *in vitro* models of vascular barrier function has been facilitated by the development of 3D culture and microfluidic organ-on-a-chip technologies (18, 19). Vasculature-on-a-chip models have several benefits over conventional *in vivo* and cell culture methods, allowing for research on vessel formation and creation of *in vitro* models for changes in barrier (20–22). When modeling vasculature *in vitro*, important parameters to take into account include mechanical, chemical and biological factors that can be incorporated in the microfluidic models (23). Organ-on-a-chip models have previously been developed to study specific vascular diseases including atherosclerosis, radiation injury, and thrombosis (24).

We previously reported the capability of organ-on-a-chip assays for the formation of vascular models (25), including T cell migration (26) and monocyte adhesion (27) in the OrganoPlate. This platform integrates dozens independently addressable microfluidic circuits integrated into a laboratory standard 384 well microtiter plate (Figures 1A, B). By guiding extracellular matrix (ECM) gels into a microfluidic channel using capillary barriers called phaseguides (29), we could create independently accessible microfluidic channels on either side of an ECM scaffold. Once the endothelial cells have grown to form a tubule in the microfluidic channel and against the ECM gel, assays such as barrier analysis or the addition of PBMCs to the endothelial tubule can be performed (30–32).

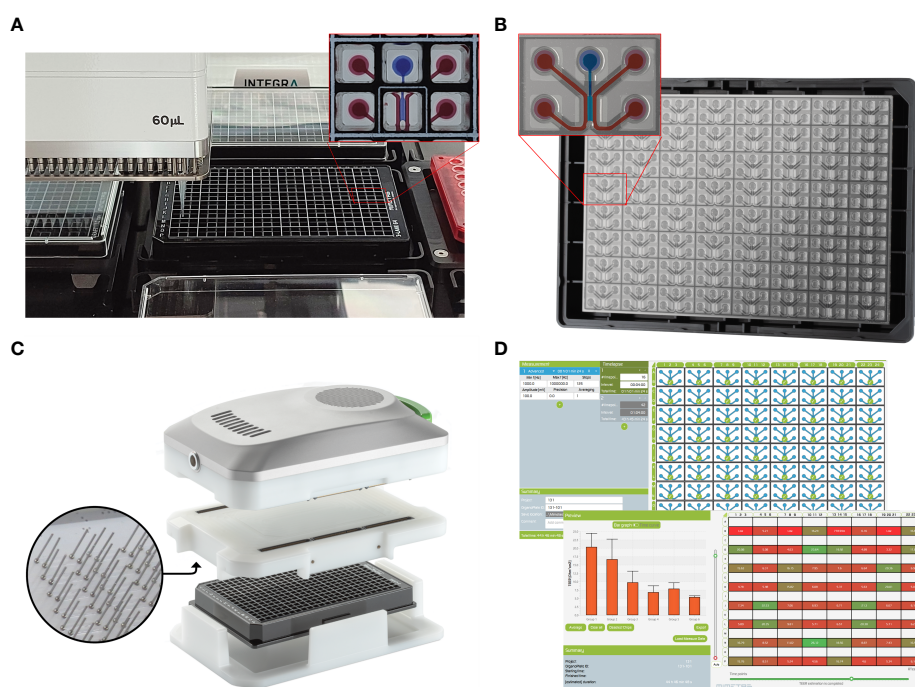


FIGURE 1

A screening platform for automated seeding of an organ-on-a-chip endothelial model combined with high throughput TEER measurements. (A) A OrganoPlate 3-lane 64 tissues in a standardized 384-titerplate format. Here, the OrganoPlate 3-lane 64 seeded on a Biomek i5 automated liquid handling platform. The expanded portion of the plate highlights the top view of one individual chip covering six microtiter wells. One microfluidic chip is enlarged to show the 3 individual microchannels. The perfusion channels used for vessel formation are filled with red dye and the gel channel is filled with blue dye. (B) The bottom view of the OrganoPlate 3-lane 64 highlighting the microfluidic channels, making up 64 individual chips attached to the bottom of the microtiter plate, allowing for high content imaging of each individual chip. One microfluidic chip is enlarged to highlight the 3 individual microchannels. The perfusion channels used for vessel formation are highlighted in red and the gel channel is highlighted in blue. (C) The OrganoTEER, a commercially available automated TEER measurement system compatible with previous OrganoPlate 3-lane 40 based tubular models (28). (D) OrganoTEER software used to perform TEER measurements and perform automated analysis of the results on an OrganoPlate 3-lane 64.

Changes in vascular barriers were measured using a fluorescent dextran assay (25). However, trans endothelial/epithelial electrical resistance (TEER) is used as the gold standard for assessing barrier function *in vitro* and has the potential to avoid the use of an added fluorescent probe and offer increase time resolution. Electrical impedance is correlated with biological aspects such as cell layer confluence, morphology and paracellular junction composition. TEER measurements are typically used in the context of 2D cell cultures, either in an insert-based culture device (33, 34) or directly onto a patterned electrode substrate (35). Such measurements have been used to interrogate epithelial and endothelial tissues (36, 37). We previously reported a method and instrument for rapidly and automatically measuring the TEER values of 40 independent chips in the OrganoPlate 3-lane 40 to study disease processes in gut on a chip models comprising immortalized cell lines or iPSC derived cells (28, 38, 39). However, *in vitro* models of endothelial barriers typically show much lower TEER values than other epithelial models (33) and thus require a significant increase in the sensitivity of instruments used for TEER measurements.

In this paper, we developed a scalable and real time method to study vascular barrier function by combining the speed and sensitivity of TEER based measurements with an automation friendly organ-on-a-chip platform. Due to its standard 384 well titer plate format, optically clear glass and a fixed microfluidic height of 220 μ m, the OrganoPlate is readily compatible with high content microscopy, confocal microscopy and is suitable for performing multiple high throughput assays on a single chip (40). We previously reported methods for the formation of endothelial tubules in the for angiogenic sprouting (41) and the use of the platform to study T cell migration (26) in Organoplate based 3D microfluidic channels. Here we used the OrganoPlate 3-lane 64 (Figure 1B), which allows for extracellular matrix (ECM) seeding in the middle channel and growth of endothelial tubules against the gel. Thanks to its two by three wells pitch, it is well suited for automation workflows (Figure 1A). We developed a 3-lane 64 OrganoPlate based TEER measurements apparatus that can be used inside an incubator for long term permeability studies of 64 separate tubules (Figures 1C, D). This combination of TEER and the OrganoPlate 3-lane 64 offers real time interrogation of up to 64 perfused endothelial models exposed to targeted apical and basal cues in a membrane free, ECM supported microenvironment. This paper shows the use of scalable, automatable OrganoPlate based model of vascular inflammation comprised of up to 64 HUVEC endothelial tubules per plate including cytokine treatment and/or to human Peripheral Blood Mononuclear Cells (PBMC) in combination with continuous TEER measurements. We demonstrate the capability for multiplexing readouts, such as barrier, phase contrast imaging and immunofluorescence, for recapitulating vascular inflammatory processes that can be used in drug development or drug delivery studies.

2 Methods

2.1 Cell culture

HUVECs (Lonza, C2519AS) were thawed and cultured in EGM-2 medium (Lonza, CC-3162). HUVECs were frozen at passage number

5 in EGM-2 + 10% FBS + 10% DMSO and stored at -150°C for further use. Peripheral blood mononuclear cells (PBMCs) were isolated from a Buffy Coat (Sanquin) as previously described by de Haan et al. (26) PBMCs were banked in 90% FBS + 10% DMSO and stored at -150°C for further use.

2.2 PBMC stimulation and labeling

PBMCs were thawed and cultured in AIM-V medium (Gibco, 12055-091). T cell population in the PBMCs were stimulated for 48 hours by Dynabeads® Human T-Activator CD3/CD28 (ThermoFisher Scientific, 11131D) according to the manufacturer's instructions. Unstimulated PBMCs were cultured in AIM-V for 48 hours. Prior to adding PBMCs to endothelial tubules in an OrganoPlate, PBMCs (both unstimulated and stimulated) were labeled with CellTracker Orange CMRA (Invitrogen, C34551), as previously described in de Haan et al. (26) In short, CMRA stock of 5 mM in dimethylsulfoxide (DMSO, Sigma, D8418) was diluted to a working concentration of 2.5 μ M in AIM-V medium. PBMCs were harvested and pelleted (300g for 5 min) before being resuspended in 2 ml of CMRA working solution. Cells were then placed in a humidified incubator at 37°C, 5% CO₂ for 30 minutes. After the incubation period, 10 mL of AIM-V medium was added, cells were counted, and cells were pelleted (300g for 5 min). The appropriate volume was added to the PBMCs to have a final concentration of 400,000 cells/ml.

2.3 OrganoPlate culture

OrganoReady Blood Vessel HUVEC 3-lane 64 plates (Mimetas B.V, MI-OR-BV-02) were cultured according to manufacturer's instructions. Medium was changed on day of receiving to OrganoMedium HUVEC-BM (Mimetas B.V.). OrganoReady Blood Vessel HUVEC 3-lane 64 are ready to use HUVEC tubes in OrganoPlates, that follow a similar process for ECM seeding (rat tail collagen 1 at 4mg/ml), endothelial cell seeding and establishment of perfusion through the tubules as described by Duinen et al. for the OrganoPlate 3-lane 40 (41). Perfusion flow was maintained by placing the plate on OrganoFlow rocker (Mimetas B.V., MI-OFPR-L) set at 14 degrees with 8-minute intervals optimized for the 3-lane 64. This allows the perfusion of medium through the endothelial tube. On the second day after receiving, cultures were exposed to cytokines or PBMCs. Prior to TEER timelapse set up, the OrganoPlate was transferred to the ImageXpress Micro XLS microscope (Molecular devices) and every individual chip on the OrganoPlate 3-lane 64 was imaged for 4x magnification phase contrast images. OrganoPlate was placed back to 37°C incubator. TEER timelapse were started directly after addition of medium.

2.4 Electrode board interface for the 3-lane 64 OrganoPlate

New electrode boards matching the layout of the 3-lane 64 (Figure 1), comprising 512 stainless steel electrodes were designed

and manufactured as previously reported (28). Prior to measurements, the electrode board was connected to the OrganoTEER measurement unit using mezzanine connectors and inserted into the inlet and access wells of the OrganoPlate to provide one current-carrying loop and one voltage-sensing loop for each of the 64 chips through a total of 512 electrodes.

2.5 Cytokine/PBMC exposure and TEER timelapse

Prior to all experiments, the OrganoTEER electrode boards were disinfected by spraying the electrodes surface with 70% ethanol and allowed to dry in a sterile flow cabinet. Before the start of timelapse measurements, a single electrode board and measurement unit were assembled and inserted into a sterile single well plate. The stack was then placed in an incubator at 37°C for at least two hours to allow the OrganoTEER temperature to equilibrate.

The left channel inlet and outlet of each chip were filled with 50 μ L of HBSS (for the cytokine exposure study) or basal medium (for the PBMC study) 1 hour prior to starting timelapse. For the PBMC study, the left 4 columns of chips had basal medium added to the left perfusion lane and the right 4 columns of chips had basal medium with 800 ng/ml of CLCX12 to the left perfusion lane. The incubated OrganoTEER was placed into the flow cabinet and the single well plate was replaced with the OrganoPlate. The OrganoTEER was placed back into the incubator and onto the OrganoFlow rocker for 30 minutes prior to the timelapse. The OrganoFlow rocker was set to a static horizontal position for 6 minutes to let the liquid levels within the wells equilibrate, after which the T_{-1} TEER measurement was taken.

For the cytokine exposure, TNF α (R&D Systems, 210-TA-020) and INF- γ (R&D systems, 285-IF-100) were diluted in OrganoMedium HUVEC-BM to the appropriate concentrations (0.1, 1, 10 and 100 ng/ml). The medium was equilibrated to 37°C for at least 30 minutes before addition of 50 μ l medium to inlets and outlets of each chip in the OrganoPlate.

For the experiments with PBMCs, PBMCs were harvested and prepared as mentioned above, for the addition of 20,000 cells/chip. For conditions with cytokines (10 ng/ml of TNF α and INF- γ), 2x concentration (20 ng/ml) of cytokines were added to medium. To ensure swift media change, the different medium conditions were pipetted in a 384 well plate according to the inlet and outlet layout of the OrganoPlate, and allowed to incubate for 15 minutes at 37°C. The conditions were arranged such that 50 μ l of medium containing 20,000 PBMCs were added to the corresponding OrganoPlate inlets and 50 μ l medium with or without cytokines were added to the corresponding OrganoPlate outlets.

To expose the tubules to their respective condition, the medium was aspirated from all inlet and outlet wells of the OrganoPlate. A multi-channel pipette was used to transfer 50 μ L of medium containing cytokines or PBMCs from the 384 well plate to the corresponding wells of the OrganoPlate. To minimize temperature fluctuation, the OrganoTEER assembly was placed on the static rocker platform. The first TEER measurement was taken immediately after the medium change. The OrganoFlow was started 30 seconds after the completion of the first timepoint measurement

(14 degrees changes every 8 minutes). To ensure synchronicity with the rocker cycle, TEER measurements were taken every subsequent 4 minutes for the first 44 minutes (16 points), then every 64 minutes for 43 hours. An endpoint measurement was taken between 44 to 48 hours. After the completion of the TEER timelapse, the OrganoPlate was removed from the TEER device and transferred to the microscope and phase contrast images of each chip were taken. After phase contrast imaging, the plates were fixed in 3.7% formaldehyde (Sigma, 252549) and stored at 4°C.

2.6 Data acquisition and extraction

All measurements were composed of 121 frequency dependent impedance points equally distributed in a logarithmic scale from 1000 Hz to 1 MHz. Using a controlled voltage source linked to an operational amplifier, the OrganoTEER imposed a sinusoidal AC voltage of 100 mV across the current carrying electrodes. The resulting current was measured across voltage sensing electrodes *via* a transimpedance amplifier. Within the measurement unit, a set of 12 separate digital impedance analyzer units linked to multiplexing units was used to acquire impedance values of 12 chips at a time.

2.7 Data compensation and fitting

To minimize the impact of parasitic capacitance (See [Supplementary Information 1](#)), we built three compensation boards by replacing the electrodes of each chip connection by a resistor of defined value per board (24 k Ω , 30 k Ω and 36 k Ω respectively, E24 standard). Each compensation board was measured once in the incubator where measurements were performed. The compensation spectra and associated resistor values were used by the OrganoTEER software to compensate the loss of high frequency signal induced by parasitic capacitances. All compensated measurement spectra were then automatically fitted against an analog model using the OrganoTEER fitting algorithm (28). The extracted barrier resistance parameter, measured in Ω , was multiplied by an approximative value of the ECM-cell interface area (0.0057 cm^2) to produce a TEER value per chip in $\Omega \cdot \text{cm}^2$.

2.8 Immunocytochemistry

After fixation, cultures in the OrganoPlate were stained for immunofluorescent markers. As described previously, in short, cells were permeabilized using a Triton X-100 solution for 10 min and blocked using a buffer containing FBS, bovine serum albumin, and Tween-20 for 45 min (42). Primary antibody was incubated for 1–2 hours or overnight, after which secondary antibody was incubated for 1 hour. The following primary antibodies were used to stain fixed cultures: Anti-VE-Cadherin 1:500 (Abcam, ab33168), anti-ICAM-1 1:50 (R&D systems, BBA3), anti-human CD45 (R&D systems, MAB1430). The following secondary antibodies were used to stain fixed cultures: Goat anti-rabbit IgG (H+L) Alexa Fluor 488 1:250 (Thermo Fischer Scientific, A11008), Goat anti-mouse IgG (H+L) Alexa Fluor 647 1:250 (Thermo Fischer Scientific, A21428) and

CF647 Goat anti-mouse IgG (H+L) Alexa Fluor 647 1:250 (Biotium, 20040). Nuclei were stained using Hoechst (ThermoFisher, H3570). After staining, the OrganoPlate was transferred to a confocal high content imaging microscope for automated imaging (Micro XLS-C, Molecular Devices). Images were acquired at 10x magnification at 3 μ m increments along the height of the microfluidic channel. Analysis was based on Sum Projection (ICAM expression) or Max projection (VE cadherin) images of the top and bottom 10 z-slices.

2.9 Image analysis

Quantification of PBMC dynamics and ICAM immunofluorescent staining was performed as previously reported by de Haan et al. in 2021 (26). Quantification of VE-Cadherin immunofluorescent staining was performed using machine learning based segmentation software Cellpose2 (43) and image processing software Fiji (44). The cell perimeter was segmented based on VE-Cadherin expression, using the built in livecell LC4 model. The segmented cell outlines were loaded into Fiji and roundness value for each outline was extracted using the built in Particle analysis tool.

2.10 Statistical analysis

Means of two or more groups were assessed using Brown-Forsythe and Welch ANOVA (Gaussian, heterogeneity of variance) or Kruskal-Wallis tests (non-Gaussian) for statistically significant differences. In the case of two or more factors, two-way ANOVA tests or three-way ANOVA tests were formed depending on the number of factors. Multiple comparisons were accounted for using Tukey's or Dunnett's tests. All data set were tested for normality using QQ-plots and residuals for normality. Statistical analyses were performed using GraphPad Prism v9.4 (GraphPad Software). Differences were considered significant when $p < 0.05$. For the number of replicates, each independent experiment is represented by a "N" and the individual chip is represented by a "n". Total number of replicates is $N \times n$.

3 Results

3.1 Enabling TEER measurements in the OrganoPlate 3-lane 64

The OrganoTEER platform was optimized for compatibility with the automation friendly OrganoPlate 3-lane 64 and sensitivity was improved to increase its dynamic range around typical TEER values of endothelial culture. We redesigned the OrganoTEER system for the measurement of single tubules in the OrganoPlate 3-lane 64. We built an Electrode board compatible with both the OrganoPlate 3-lane 64 and the OrganoTEER measurement unit (Figure 1B). The OrganoTEER software was rewritten to accommodate the setup and measurement of each 64 chips (Figures 1C, D). The system allowed 512 stainless steel electrodes to be inserted into each chip perfusion channels access wells. For each chip, one current-carrying one voltage-sensing loop was created from the inlet and outlet of one

perfusion channel to the outlet of the opposite perfusion channel (Figure 2C). For both the current carrying and voltage sensing loop, each point of the 4-terminal setup was shorted to a pair of electrodes inserted in both inlet and outlet of the same perfusion channel. A typical measurement takes under 2 minutes for an entire plate. The Software allows timelapse measurements to be configured to accommodate long term exposure over several days.

The configuration of our TEER measurement setup increased the chip electrical resistance over the 3-lane 40 due to longer current path. The electrode pairs on the basolateral side were inserted in the perfusion inlet and outlet in the 3-lane 64. This induced a higher impact from parallel parasitic elements. To compensate for this, we built three separate electrical compensation boards using the PCB layout the 3-lane 64 electrode board. In place of the electrodes, we soldered surface mounted resistors electrically connecting the reference and counter side to the work and working sense side. The boards resistances were 24 k Ω , 30 k Ω and 36 k Ω . Prior to the exposure experiment, we measured the impedance spectra of each of the 3 compensation boards, which we then used to perform a multiple load compensation on all measured data prior to fitting using the OrganoTEER software (Supplementary Information Figures 1, 2).

3.2 Evaluation of HUVEC tubule in 3-lane 64

OrganoReady Blood Vessel HUVEC 3-lane 64 contained 60 tubular structures were purchased. The endothelial cells in these tubules had a cobblestone like appearance that can be observed using phase contrast microscopy throughout the duration of the culture (Supplemental Figure 3A). These endothelial cells expressed VE-cadherin at the junctions between cells (Figure 2A). Using confocal microscopy, a 3D representative image was created showing that the endothelial cells formed a confluent 3-dimensional endothelial tubule (Figure 2B). Using the new TEER board set up described above, the lower resistance endothelial tubule was measured and disruptions in barrier due to Staurosporine could be detected (Figure 2D).

3.3 Cytokine induced vascular inflammation

To model vascular inflammation, the endothelial vessels were exposed to different inflammatory cytokines for 48 hours. Phase contrast images showed that the vessels exposed to INF- γ had minimal changes in morphology. However, as the concentration of TNF α increased, the endothelial cells showed a less rounded and aligned phenotype (Figure 3A). These changes in morphology were more pronounced in the combination of cytokines compared to TNF α alone.

The effect of inflammatory cytokines on TEER was monitor over 44 hours. INF- γ showed a dose dependent slow decrease in barrier integrity over time (Figure 3B). TNF α induced a sharp decline in barrier integrity around 2 hours which recovered towards the end of the exposure (Figure 3C). The higher concentrations of TNF α at 10 and 100 ng/ml induced the same amplitude of barrier leakage with no significant difference, indicating that the increasing concentration of TNF α did not cause increased disruption beyond 10 ng/ml. The lower

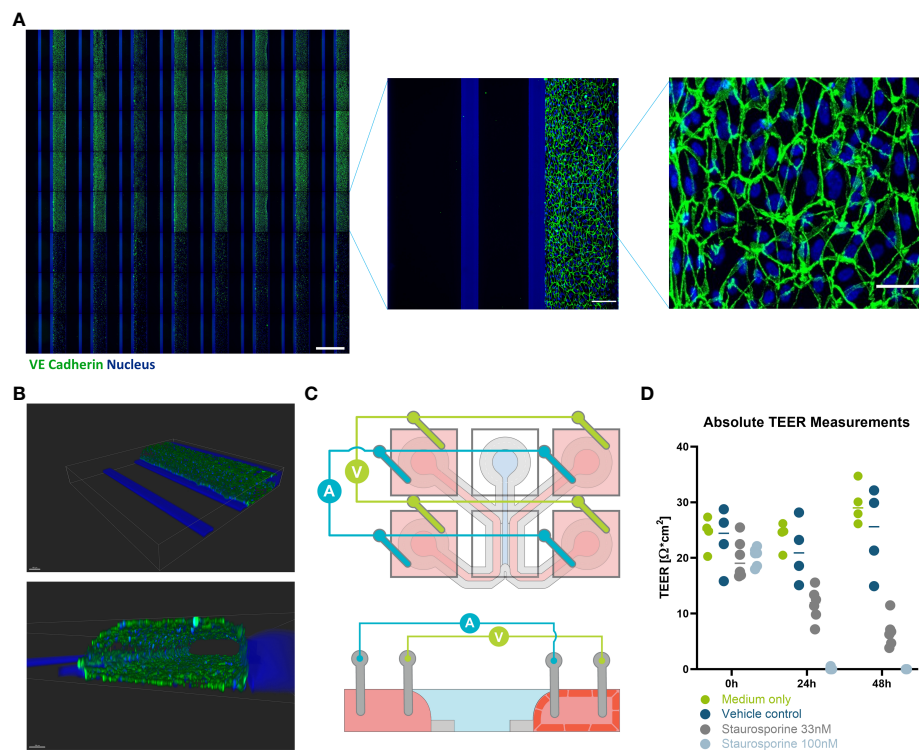


FIGURE 2

Immunofluorescent staining and TEER measurements of HUVEC endothelial tubules in OrganoPlate 3-lane 64. (A) Montage of Immunofluorescent images (VE-cadherin (green) and nucleus (blue)) of 64 HUVEC endothelial tubes (right perfusion channel) cultured against a collagen I ECM layer (center channel) in the OrganoPlate 3-lane 64 (scale bar 1000 μ m). Bottom three rows were Staurosporine treated. One chip from the montage is blown up to illustrate how the chip looks (scale bar 150 μ m). Another zoom of the endothelial tube is shown to demonstrate the cell morphology (scale bar 50 μ m). (B) Confocal reconstruction of a HUVEC tubule using VE-Cadherin (green) and DAPI (blue) staining. (C) Schematic illustration of how a microfluidic chip and the positioning of the TEER electrodes. Both current carrying and voltage sensing loops are formed across the gel and perfusion channel via four pairs of electrodes, shorted pairwise in the inlets and outlets of their perfusion channels. The bottom schematic depicts a side view of the chip in the X-Z plane showing how the endothelial cells will grow to form a tubule against the gel, while the left channel remains empty. (D) values of the HUVEC tube at 0, 24, and 48 hours with the addition of Staurosporine to interrupt the barrier ($n=4-6$). Scale bars are 100 μ m.

concentrations of TNF α (0.1 and 1 ng/ml) showed more dose dependent disruption. However endothelial barriers were fully recovered by the end of the exposure at which point their TEER was not statistically significantly different compared to medium control (Supplementary Figure 2B). The combination of INF- γ and TNF α had the largest effect on the barrier integrity of the endothelial vessel (Figure 3D). The combination of cytokines induced a dose dependent decrease in barrier integrity around 2 hours, similar to the changes in barrier due to TNF α only. However, the barrier did not recover for the remainder of the exposure as seen for the TNF α alone, except for the lowest concentration (0.1 ng/ml) which was not significantly different than the medium control at the final timepoint (Supplemental Figure 4C).

The two inflammatory cytokines also had a different effect on ICAM-1 expression. TNF α and combination of TNF α and INF- γ caused a significant dose dependent increase in ICAM-1 expression (Figures 4A, B). INF- γ only did not cause a significant increase in ICAM-1 expression. In addition to changing the ICAM-1 expression, TNF α and INF- γ affected the VE-cadherin expression differently. In the control conditions, the HUVEC cells showed a rounder and more cobblestone like appearance (Figure 4C). INF- γ did not have a strong effect on cell morphology and VE-cadherin expression. As the concentration of TNF α increased, the endothelial cell morphology

was less rounded and slightly more aligned (Figures 4C, D). At the higher concentrations with TNF α and both cytokines, the endothelial tubes are not only less round, but the consistency of the VE-cadherin staining is reduced (Supplemental Figure 3B). The combination of cytokines increased these changes in VE-cadherin expression with decreased roundness of cells and less consistent VE-cadherin expression in a dose dependent manner.

3.4 Effect of immune cells on vascular inflammation

To determine whether we could also study the effect of immune cells directly on vascular inflammation non stimulated and stimulated PBMCs were added in the lumen of the endothelial tubules. The addition of immune cells to the endothelial tubule did not interfere with the addition of the TEER electrodes as observed in the schematic (Figure 5A). Addition of unstimulated PBMCs did not influence the endothelial barrier when compared to the control conditions (Figure 5B). However, stimulated PBMCs had similar effect on the barrier as the 10 ng/ml of TNF α and INF- γ condition. In both conditions, there was a sharp decrease in the first 2 hours that remained for the rest of the exposure. Stimulated PBMCs adhered

to the vessel wall in greater number than unstimulated PBMCs (Figure 5C).

The chemoattractant, CLCX12, was added to the empty channel to create a chemotactic gradient to induce immune cell migration (Figure 5D). The addition of CXCL12 did not result in a significant change in barrier integrity of the vessels that were perfused with stimulated or unstimulated PBMCs (Figure 5E). Addition of only CXCL12 did not result in significant increase in adhesion (Supplemental Figure 5B) or extravasation of PBMCs (Figure 5F). The combination of CLCX12, TNF α and INF- γ resulted in a significant increase in migration of both unstimulated and stimulated PBMCs out of the vessel into the ECM (Figure 5F). PBMC migration into the gel channel was confirmed by the overlapping of CD45 and CellTrackerTM Orange (Figures 5G, H).

Adding stimulated PBMCs to the endothelial tubule caused a significant increase in ICAM-1 expression in the endothelial tubule when compared to the medium only or unstimulated PBMCs ($p<0.00001$) (Figure 5I and Supplemental Figure 5E). However when cytokines were added all conditions showed even higher ICAM-1 expression compared to stimulated PBMCs (Figure 5I). A significant effect on cell roundness by VE-cadherin expression was found by the addition of stimulated PBMCs (Figure 5J). The addition of cytokines did not have an added effect on cell roundness when compared to stimulated PBMC condition (Figure 5J and Supplemental Figure 5D). When both stimulated PBMCs and cytokines were added the VE-cadherin expression was almost gone (Supplemental Figure 5D).

4 Conclusion and discussion

Endothelial dysfunction induced by chronic inflammation is a precursor to atherosclerosis and is characterized by increased barrier permeability and immune cell migration. We have demonstrated an organ-on-a-chip platform capable for modeling and quantifying endothelial response to inflammation. We adapted the commercially available OrganoTEER system to enable simultaneous TEER measurement of 64 perfused endothelial tubules. Using our compensated TEER measurement assay, we showed significant dose dependent effect on endothelial barrier of different inflammatory cytokines triggers over a 48-hour time period. INF- γ , TNF α and their combination showed a significant decrease in endothelial barrier within four hours for all tested concentrations. We showed the effect of perfused immune cells on the endothelial barrier. In addition to following the endothelial barrier function over time, we multiplexed our assay with immunostaining-based assays to show immune typical expression of ICAM-1 and changes in cell morphology using VE-Cadherin. These findings demonstrate the capability to study how different compound or cytokines affect endothelial barriers and how they influence the immune endothelium interaction.

We adapted the OrganoTEER electrode board and data compensation method for the precise measurement of 64 endothelial tubules. With a total of 9940 TEER measurements in our monoculture cytokine exposure (160 chips over 44 hours) and 5580 measurements in our immune migration experiment (98 measured chips over 44 hours), this paper represents, to our

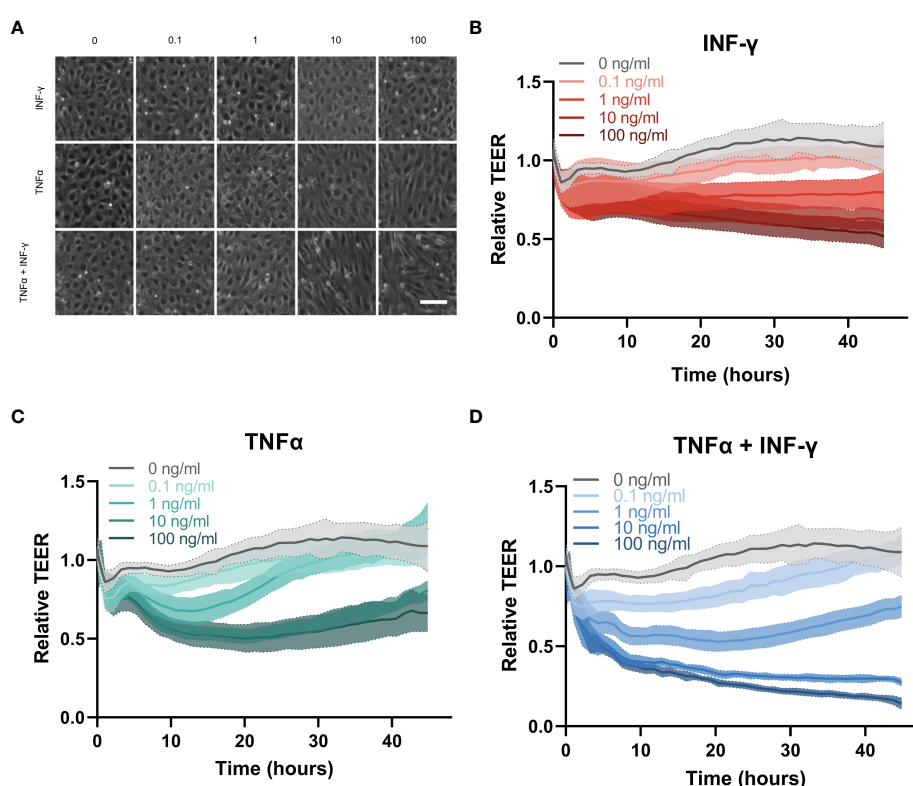


FIGURE 3

Cytokine response of HUVEC endothelial tubes in the OrganoPlate 3-lane 64. (A) Representative phase contrast images of zoom in of endothelial vessel exposed to inflammatory triggers for 44hrs. Concentration of TNF α and INF- γ in ng/ml. Scale bar is 100 μ m. (B–D) Relative TEER timelapse of 44 hours of exposure to increasing concentrations of (B) INF- γ , (C) TNF α and (D) combination of TNF α and INF γ (N=3, n=3–5 per experiment).

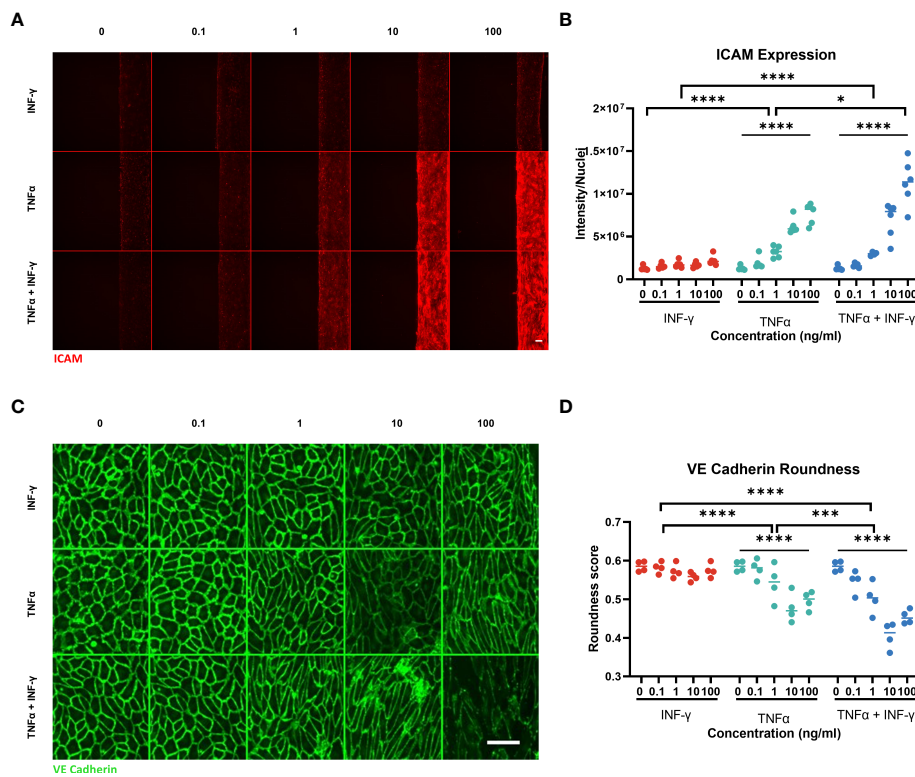


FIGURE 4
 ICAM-1 and VE-Cadherin staining of endothelial vessel. **(A)** ICAM-1 expression staining of endothelial vessel exposed to TNF α or/and INF- γ in ng/ml for 44hrs. Scale bar is 100 μ m. **(B)** Quantification of ICAM-1 staining. Significant difference between cytokine conditions (*p<0.05, ***p < 0.0001) as well as dose dependent effect for TNF α and TNF α + INF- γ (****p < 0.0001) Data was analyzed using Two-way ANOVA tests, followed by a Dunnet's multiple comparison tests and Tukey's multiple comparison test. **(C)** Montage of the max projection image of VE-Cadherin staining of the bottom 10 z-steps (3 μ m step size). Scale bar 100 μ m. **(D)** Quantification of cell roundness determined from VE-Cadherin staining. Significant difference between cytokine conditions (**p=0.0002, ***p < 0.0001) as well as a dose dependent effect for TNF α and TNF α + INF- γ (****p < 0.0001). Data was analyzed using Two-way ANOVA tests, Dunnet's multiple comparison tests and Tukey's multiple comparison tests. (N=2, n=3-6) Scale bars are 100 μ m.

present knowledge, the largest published TEER dataset on an organ-on-a-chip model. The ability to continuously assess the permeability of each individual tubule provided insight in the dynamics of the tested inflammation triggers. With such data density, we were able to observe concentration dependent transient effects, such as recovery of our TNF α exposed monocultures, which might not have been seen with larger measurement time intervals. The scalability of the system allowed us to use high numbers of replicates (between 7 and 14 depending on conditions) increasing the confidence in our results. This throughput could also be leveraged for large scale screening studies on an organ-on-a-chip platform. The small footprint of OrganoTEER system make it fast and easy to use in a manual, medium throughput setting, but could also be beneficial for integration in a robotic environment.

Due to the high background electrical resistance associated with the microscopic channels of microfluidic cell culture devices, it is necessary to adopt an approach which bypasses the need for baseline subtraction typically seen with single (12.5 Hz) frequency-based impedance measurements. Using a compensation method capable of correcting high frequency parasitics, we demonstrated the suitability of frequency sweep impedance measurements and analog fitting for on-a-Chip TEER applications. Finally, the absence of any membranes, filters or other barriers supporting the cells avoids the potential bias caused by pore size

and geometry. These properties combined with excellent imaging and automation compatibility make this platform the ideal candidate for transport and barrier integrity studies.

Helper T cells, specifically Th1 cells, are often found in atherosclerotic lesions and secrete INF- γ and TNF α , which both promote inflammation in endothelial cells (45–47). INF- γ showed a slow dose dependent decrease in endothelial barrier over the 48 hours but did not have a significant change in VE-Cadherin. Minagar et al. and Oshima et al. found that INF- γ caused a significant decrease in endothelial barrier and a small decrease in VE-Cadherin expression (48, 49). Interestingly, we did not observe a statistically significant increase in ICAM-1 expression after INF- γ exposure. In literature, it has been shown that INF- γ can cause an increase in ICAM-1 expression in some endothelial cell lines (50). However, this difference was observed using a monolayer of endothelial cells whereas the OrganoPlate is an organ-on-a-chip platform with perfusion which could lead to the difference in ICAM-1 expression.

TNF α had a significant dose dependent decrease in barrier but seemed to recover by the end of 48 hours. Using this platform, we were able to see the dynamic response TNF α had on the barrier that would have been missed with single timepoint measurements. It is interesting that the barrier appeared to recover at later time points

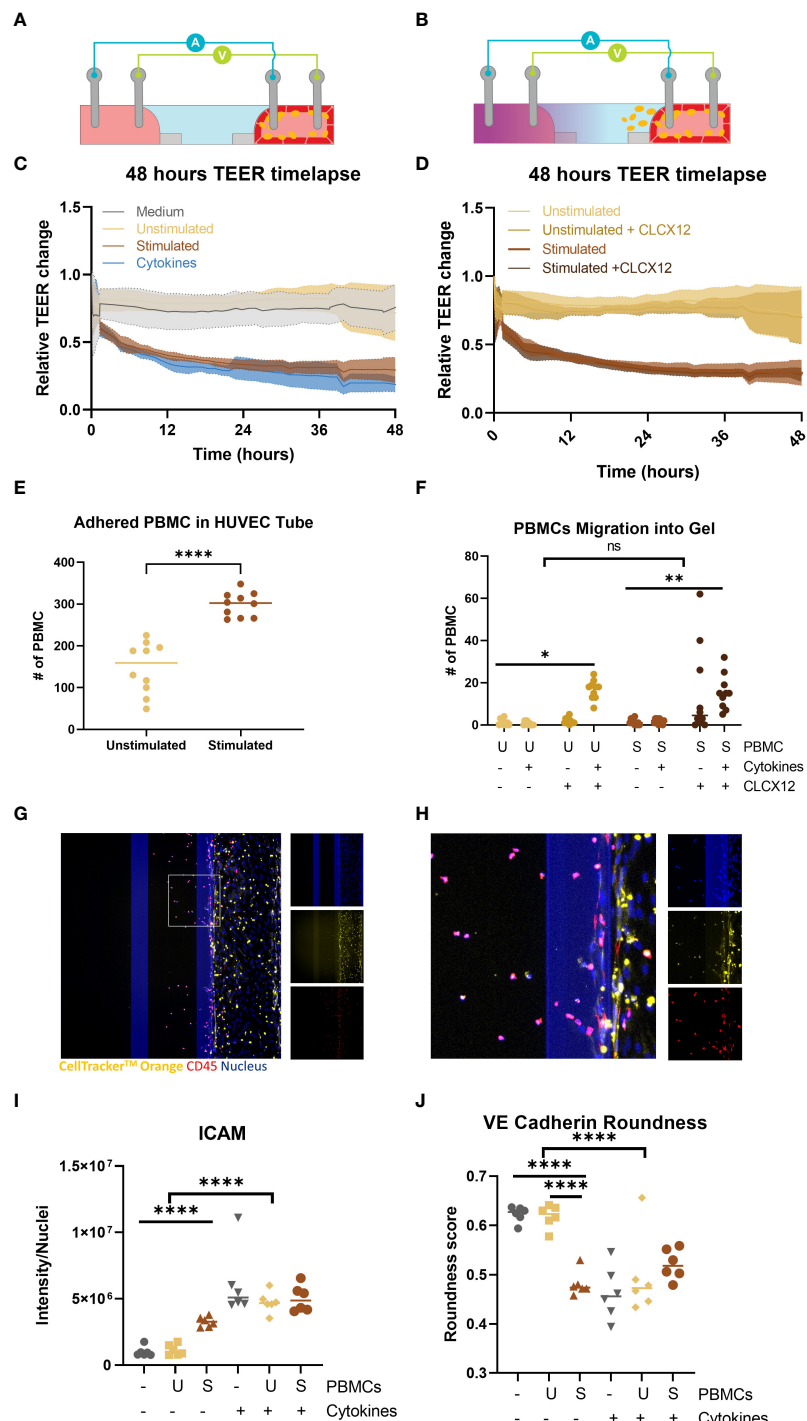


FIGURE 5

Perfusion and extravasation of peripheral blood mononuclear cells (PBMCs) through a HUVEC tubule into an ECM gel in an OrganoPlate 64. (A) Schematic of TEER electrodes with endothelial tube and PBMCs adhered to the endothelial tube (B) Schematic of TEER electrodes with endothelial tube and PBMCs migrating from the endothelial tube into gel channel due to addition of chemokine (purple) in basal lateral channel. (C) Relative change in barrier of PBMCs or 10 ng/ml of TNF α + INF- γ can be observed in the 48h timelapse. (D) TEER timelapse comparing conditions with and without CLCX12. No difference was observed between comparable conditions with +/- CLCX12. (E) Number of PBMCs adhered to the HUVEC tubules 48 hour after addition. Significant difference unstimulated and stimulated PBMCs (****p < 0.0001) was analyzed using Welch's T tests. (F) PBMC migration out of endothelial vessel into gel channel. Significant difference between PBMC and PBMCs with cytokines and CLCX12 (* p=0.04, ** p < 0.0018) was analyzed using Brown-Forsythe and Welch ANOVA tests and Dunnett's T3 multiple comparison test. 3way ANOVA showed no significant (ns) difference between unstimulated and stimulated PBMCs in migration of PBMCs into the ECM. (G) Fluorescent based image of immune cells perfused through a HUVEC tubule and migrated into ECM. (H) Area of interest from (G) to highlight PBMC migration and staining. Shown are nucleus (blue), CellTrackerTM Orange stain (yellow) and CD45 (red). (I) ICAM-1 quantification after exposure and addition of PBMCs. Significant difference due to addition of cytokines (****p < 0.0001) as well an effect of addition of stimulated PBMCs without cytokines (****p < 0.0001) Data was analyzed using Two-way ANOVA tests with Šidák's multiple comparisons test. (J) Quantification of cell roundness determined from VE-Cadherin staining. Significant difference due to addition of cytokines (****p < 0.0001) as well a significant different between medium and stimulated PBMC and unstimulated PBMCs and stimulated PBMCs (****p < 0.0001). Data was analyzed using Two-way ANOVA tests with Tukey's multiple comparisons test. (N=2, n=3-6).

because there was a significant change in cell morphology and appearance of VE-Cadherin expression. Similarly, Colas-Algora et al. show that TNF α causes a decrease TEER and VE-Cadherin reorganizing in HUVECs (51). TNF α did cause a significant increase in ICAM expression, which is consistent with literature (52, 53). Exposure to both cytokines together did appear to have an additive effect which greater changes in VE-Cadherin and ICAM expression. The change in barrier function showed both the sharp decrease in TEER associated with TNF α , and the slow constant decrease associated with INF- γ . These additive effects are in line with the exquisite control of inflammatory response achieved by complex mixtures of cytokines in physiological processes. Interestingly, the stimulated T cells had similar changes in barrier, ICAM expression and changes endothelial cell morphologies to the TNF α and INF- γ condition. Therefore, this data shows that vascular inflammation can be recapitulated using either inflammatory cytokines or activated immune cells.

Previously, we have reported the transendothelial migration of T cells from the endothelial tube into the collagen gel in the OrganoPlate (26). As with the results previously shown, both cytokines and a chemoattractant must be present for the migration of unstimulated immune cells, which is similar to *in vivo* settings (54). The unstimulated immune cells alone had no effect on the barrier, ICAM expression or migration but the addition of both 10 ng/ml of INF- γ and TNF α with CLCX12, there was significant migration into the ECM. Interestingly, the conditions with and without CLCX12 did not have any significant changes in barrier. Indicating that the migrating immune cells most likely have minimal effect on endothelial barrier, and/or that our TEER measurements were not sensitive enough to detect the slight changes in barrier. The unstimulated PBMCs did not have an effect on endothelial cell roundness but the stimulated PBMCs did have a significant decrease in roundness of the endothelial cells. The addition of cytokines to all conditions had the greatest effect on cell roundness, which indicates that cytokines could be a relevant trigger to model vascular inflammation in a simplistic model. This platform allows for the study of the effects of cytokines and chemoattractants on both immune cells and endothelial cells individually and in combination.

Here we used the addition of inflammatory cytokines and immune cells to model vascular inflammation looking at changes in barrier permeability over time, different inflammatory markers and adherent junctions and quantification of immune cell adhesion and migration. In addition to modeling vascular inflammation, the TEER timelapse could potentially be used to improve the blood brain barrier models (30, 55), immune-oncology (26), and many other diseases. Overall, the OrganoPlate 3-lane 64 is a scalable, automation compatible tool that allows for multiplexing of assays to be able to do complex disease modeling for drug development.

References

1. Pahwa R, Goyal A, Jialal I. Chronic inflammation. In: *Pathobiol hum dis a dyn encycl dis mech* (2022). [Book StatPearls: StatPearls Publishing, Treasure Island (FL)] Available at: <https://www.ncbi.nlm.nih.gov/books/NBK493173/>.
2. Zanolli L, Briet M, Empana JP, Guimarães Cunha P, Mäki-Petäjä M, Protogerou AD, et al. Vascular consequences of inflammation: A position statement from the ESH working group on vascular structure and function and the ARTERY society. *J Hypertens* (2020) 38(9):1682–98. doi: 10.1097/HJH.0000000000002508
3. Castellon X, Bogdanova V. Chronic inflammatory diseases and endothelial dysfunction. *Aging Dis* (2016) 7(1):1–89. doi: 10.14336/AD.2015.0803
4. Cardiovascular diseases . Available at: https://www.who.int/health-topics/cardiovascular-diseases#tab=tab_1.
5. Xu S, Ilyas I, Little PJ, Li H, Kamato D, Zheng X, et al. Endothelial dysfunction in atherosclerotic cardiovascular diseases and beyond: From mechanism to pharmacotherapies. *Pharmacol Rev* (2021) 73(3):924–67. doi: 10.1124/pharmrev.120.000096

Data availability statement

The raw data supporting the conclusions of this article will be made available by the authors, without undue reservation.

Author contributions

HE and AN contributed equally in preparation of the manuscript. AN and ST invented the OrganoTEER concept. AN, FS, MB, and ST contributed to the design and engineering of the instrument and software. HE, JH, AN, and LB planned, performed, and analyzed experiments. ST and LB supervised the work and edited the manuscript. All authors contributed to the article and approved the submitted version.

Funding

This project has received funding from the European Union's Horizon 2020 research and innovation program under the Marie Skłodowska-Curie grant agreement No 813920.

Conflict of interest

HE, AN, FS, ST, and LB are employees of Mimetas B.V., which markets the OrganoPlate, OrganoTEER and OrganoFlow, and holds the registered trademarks OrganoPlate, OrganoTEER and OrganoFlow. ST is shareholder of Mimetas B.V. MB is employed by Sciospec GmbH.

Publisher's note

All claims expressed in this article are solely those of the authors and do not necessarily represent those of their affiliated organizations, or those of the publisher, the editors and the reviewers. Any product that may be evaluated in this article, or claim that may be made by its manufacturer, is not guaranteed or endorsed by the publisher.

Supplementary material

The Supplementary Material for this article can be found online at: <https://www.frontiersin.org/articles/10.3389/fimmu.2023.1118624/full#supplementary-material>

6. Rafieian-Kopaei M, Setorki M, Doudi M, Baradarani A, Nasri H. Atherosclerosis: Process, indicators, risk factors and new hopes. *Int J Prev Med* (2014) 5(8):927–946.
7. McDonald DM. Angiogenesis and remodeling of airway vasculature in chronic inflammation. *Am J Respir Crit Care Med* (2001) 164(10 Pt 2):S39–S45. doi: 10.1164/ajrccm.164.supplement_2.2106065
8. Claesson-Welsh L, Dejana E, McDonald DM. Permeability of the endothelial barrier: Identifying and reconciling controversies. *Trends Mol Med* (2021) 27(4):314–31. doi: 10.1016/j.molmed.2020.11.006
9. Junaid A, Schoeman J, Yang W, Stam W, Mashaghi A, Van Zonneveld AJ, et al. Metabolic response of blood vessels to TNF α . *eLife* (2020) 9:1–17. doi: 10.7554/eLife.54754
10. Rajan S, Ye J, Bai S, Huang F, Guo YL. NF- κ B, but not p38 MAP kinase, is required for TNF- α -induced expression of cell adhesion molecules in endothelial cells. *J Cell Biochem* (2008) 105(2):477. doi: 10.1002/jcb.21845
11. Gavard J. Endothelial permeability and VE-cadherin. *Cell Adh Migr* (2013) 7(6):465–71. doi: 10.4161/cam.27330
12. Harris ES, Nelson J. *VE-cadherin: at the front, center, and sides of endothelial cell organization and function* (2022). Available at: www.sciencedirect.com.
13. Sluiter TJ, van Buul JD, Huvemeers S, Quax PHA, de Vries MR. Endothelial barrier function and leukocyte transmigration in atherosclerosis. *Biomedicines* (2021) 9(4):328. doi: 10.3390/biomedicines9040328
14. Allingham MJ, Van Buul JD, Burridge K. Transendothelial migration phosphorylation is required for leukocyte vascular endothelial cadherin tyrosine ICAM-1-Mediated, src- and Pyk2-dependent. *J Immunol Ref* (2007) 179:4053–64. doi: 10.4049/jimmunol.179.6.4053
15. Turowski P, Martinelli R, Crawford R, Wateridge D, Papageorgiou AP, Lampugnani MG, et al. Phosphorylation of vascular endothelial cadherin controls lymphocyte emigration. *J Cell Sci* (2008) 121(1):29–37. doi: 10.1242/jcs.022681
16. Broermann A, Winderlich M, Block H, Frye M, Rossant J, Zarbock A, et al. Dissociation of VE-PTP from ve-cadherin is required for leukocyte extravasation and for VEGF-induced vascular permeability in vivo. *J Exp Med* (2011) 208(12):2393–401. doi: 10.1084/jem.20110525
17. Heemskerk N, Schimmel L, Oort C, Van Rijssel J, Yin T, Ma B, et al. F-actin-rich contractile endothelial pores prevent vascular leakage during leukocyte diapedesis through local RhoA signalling. *Nat Commun* (2016) 7:10493. doi: 10.1038/ncomms10493
18. Sun W, Chen YQ, Luo GA, Zhang M, Zhang HY, Wang YR, et al. Organs-on-chips and its applications. *Chin J Anal Chem* (2016) 44(4):533–41. doi: 10.1016/S1872-2040(16)60920-9
19. Huh D, Hamilton GA, Ingber DE. From 3D cell culture to organs-on-chips. *Trends Cell Biol* (2011) 21(12):745–54. doi: 10.1016/j.tcb.2011.09.005
20. Doherty EL, Aw WY, Hickey AJ, Polacheck WJ. Microfluidic and organ-on-a-Chip approaches to investigate cellular and microenvironmental contributions to cardiovascular function and pathology. *Front Bioeng Biotechnol* (2021) 9(February):1–14. doi: 10.3389/fbioe.2021.624435
21. Partyka PP, Godsey GA, Galis JR, Kosciuk MC, Acharya NK, Nagel RG, et al. Mechanical stress regulates transport in a compliant 3D model of the blood–brain barrier. *Biomaterials* (2017) 115:30–9. doi: 10.1016/j.biomaterials.2016.11.012
22. Polacheck WJ, Kutys ML, Tefft JB, Chen CS. *Microfabricated blood vessels for modeling the vascular transport barrier* Vol. 14. Springer US: Nature Protocols (2019) p. 1425–54. doi: 10.1038/s41596-019-0144-8
23. Kim S, Kim W, Lim S, Jeon JS. Vasculature-on-a-chip for in vitro disease models. *Bioengineering* (2017) 4(4):8. doi: 10.3390/bioengineering4010008
24. Ingber DE. Human organs-on-chips for disease modelling, drug development and personalized medicine. *Nat Rev Genet* (2022) 23(August):467–91. doi: 10.1038/s41576-022-00466-9
25. Van Duinen V, Van Den Heuvel A, Trietsch SJ, Lanz HL, Van Gils JM, Van Zonneveld AJ, et al. 96 perfusable blood vessels to study vascular permeability in vitro. *Sci Rep* (2017) 7(1):1–11. doi: 10.1038/s41598-017-14716-y
26. de Haan L, Suijker J, van Roey R, Berges N, Petrova E, Queiroz K, et al. A microfluidic 3D endothelium-on-a-chip model to study transendothelial migration of T cells in health and disease. *Int J Mol Sci* (2021) 22(15):8234. Available at: <https://doi.org/10.3390/ijms22158234>
27. Poussin C, Kramer B, Lanz HL, van den Heuvel A, Laurent A, Olivier T, et al. 3D human microvessel-on-a-chip model for studying monocyte-to-endothelium adhesion under flow – application in systems toxicology. ALTEX - altern to anim exp (2020). Available at: <https://www.alTEX.org/index.php/alTEX/article/view/1212>.
28. Nicolas A, Schavemaker F, Kosim K, Kurek D, Haarmans M, Bulst M, et al. High throughput transepithelial electrical resistance (TEER) measurements on perfused membrane-free epithelia. *Lab Chip* (2021) 21(9):1676–85. doi: 10.1039/DOLC00770F
29. Vulto P, Podszun S, Meyer P, Hermann C, Manz A, Urban GA. Phagoseguides: A paradigm shift in microfluidic priming and emptying. *Lab Chip* (2011) 11(9):1596–602. doi: 10.1039/c0lc00643b
30. Wevers NR, Kasi DG, Gray T, Wilschut KJ, Smith B, Vugt R, et al. A perfused human blood–brain barrier on-a-chip for high-throughput assessment of barrier function and antibody transport. *Fluids Bar. CNS* (2018) 15(1):1–12. doi: 10.1186/s12987-018-0108-3
31. Riddle RB, Jennbacken K, Hansson KM, Harper MT. Endothelial inflammation and neutrophil transmigration are modulated by extracellular matrix composition in an inflammation-on-a-chip model. *Sci Rep* (2022) 12(1):1–14. doi: 10.1038/s41598-022-10849-x
32. Kramer B, Corallo C, van den Heuvel A, Crawford J, Olivier T, Elstak E, et al. High-throughput 3D microvessel-on-a-chip model to study defective angiogenesis in systemic sclerosis. *Sci Rep* (2022) 12(1):1–12. doi: 10.1038/s41598-022-21468-x
33. Eigenmann DE, Xue G, Kim KS, Moses AV, Hamburger M, Oufir M. Comparative study of four immortalized human brain capillary endothelial cell lines, hCMEC/D3, hBMEC, TY10, and BB19, and optimization of culture conditions, for an *in vitro* blood–brain barrier model for drug permeability studies. *Fluids Bar. CNS* (2013) 10(1):1–17. doi: 10.1186/2045-8118-10-33
34. Von Wedel-Parlow M, Wölte P, Galla HJ. Regulation of major efflux transporters under inflammatory conditions at the blood–brain barrier *in vitro*. *J Neurochem* (2009) 111(1):111–8. doi: 10.1111/j.1471-4159.2009.06305.x
35. Tiruppathi C, Malik AB, Del Vecchio PJ, Keese CR, Glaever I. Electrical method for detection of endothelial cell shape change in real time: assessment of endothelial barrier function. *Proc Natl Acad Sci* (1992) 89(17):7919–23. doi: 10.1073/pnas.89.17.7919
36. Benson K, Cramer S, Galla HJ. Impedance-based cell monitoring: Barrier properties and beyond. *Fluids Bar. CNS* (2013) 10(1):1–11. doi: 10.1186/2045-8118-10-5
37. Srinivasan B, Kolli AR, Esch MB, Abaci HE, Shuler ML, Hickman JJ. TEER measurement techniques for *In vitro* barrier model systems. *SLAS Technol* (2015) 20(2):107–26. doi: 10.1177/2211068214561025
38. Naumovska E, Aalderink G, Valencia CW, Kosim K, Nicolas A, Brown S, et al. Direct on-chip differentiation of intestinal tubules from induced pluripotent stem cells. *Int J Mol Sci* (2020) 21:4964. doi: 10.3390/ijms21144964
39. Beaurivage C, Naumovska E, Chang YX, Elstak ED, Nicolas A, Wouters H, et al. Development of a gut-on-a-Chip model for high throughput disease modeling and drug discovery. *Int J Mol Sci* (2019) 20:5661. doi: 10.3390/ijms20225661
40. Birsak KM, DeBiasio R, Miedel M, Alsebahi A, Reddinger R, Saleh A, et al. A 3D microfluidic liver model for high throughput compound toxicity screening in the OrganoPlate®. *Toxicology* (2021) 450:152667. doi: 10.1016/j.tox.2020.152667
41. van Duinen V, Zhu D, Ramakers C, van Zonneveld AJ, Vulto P, Hankemeier T. Perfused 3D angiogenic sprouting in a high-throughput *in vitro* platform.. *Angiogenesis* (2019) 22(1):157–65. doi: 10.1007/s10456-018-9647-0
42. Wevers NR, Van Vugt R, Wilschut KJ, Nicolas A, Chiang C, Lanz HL, et al. High-throughput compound evaluation on 3D networks of neurons and glia in a microfluidic platform. *Sci Rep* (2016) 6(November):1–10. doi: 10.1038/srep38856
43. Stringer C, Pachitariu M. Cellpose 2.0: how to train your own model. *Nat Methods* 19:1634–1641 (2022) doi: 10.1101/2022.04.01.486764
44. Schindelin J, Arganda-Carreras I, Frise E, Kaynig V, Longair M, Pietzsch T, et al. Fiji - an open source platform for biological image analysis. *Nat Methods* (2012) 9(7):676–82. doi: 10.1038/nmeth.2019
45. Moriya J. Critical roles of inflammation in atherosclerosis. *J Cardiol* (2019) 73(1):22–7. doi: 10.1016/j.jcc.2018.05.010
46. Nakiboneka R, Mugaba S, Auma BO, Kintu C, Lindan C, Nanteza MB, et al. Interferon gamma (IFN- γ) negative CD4+ and CD8+ T-cells can produce immune mediators in response to viral antigens. *Vaccine* (2019) 37(1):113. doi: 10.1016/j.vaccine.2018.11.024
47. Rodrigues LS, Barreto AS, Bomfim LGS, Gomes MC, Ferreira NLC, da Cruz GS, et al. Multifunctional, TNF- α and IFN- γ -Secreting CD4 and CD8 T cells and CD8High T cells are associated with the cure of human visceral leishmaniasis. *Front Immunol* (2021) 12(October):1–20. doi: 10.3389/fimmu.2021.773983
48. Minagar A, Long A, Ma T, Jackson TH, Kelley RE, Ostanin DV, et al. Interferon (IFN)- β 1a and IFN- β 1b block IFN- γ -Induced disintegration of endothelial junction integrity and barrier. *Endothelium* (2009) 10(6):299–307. doi: 10.1080/1062332090272299
49. Oshima T, Laroux FS, Coe LL, Morise Z, Kawachi S, Bauer P, et al. Interferon- γ and interleukin-10 reciprocally regulate endothelial junction integrity and barrier function. *Microvasc Res* (2001) 61(1):130–43. doi: 10.1006/mvre.2000.2288
50. Thornhill MH, Li J, Haskard DO. Leucocyte endothelial cell adhesion: a study comparing human umbilical vein endothelial cells and the endothelial cell line EA-hy926. *Scand J Immunol* (1993) 38(3):279–86. doi: 10.1111/j.1365-3083.1993.tb01726.x
51. Colás-Algora N, García-Weber D, Cacho-Navas C, Barroso S, Caballero A, Ribas C, et al. Compensatory increase of VE-cadherin expression through ETS1 regulates endothelial barrier function in response to TNF α . *Cellular and Molecular Life Sciences* (2020) 77:2125–40. doi: 10.1007/s00018-019-03260-9
52. Yang L, Froio RM, Sciuto TE, Dvorak AM, Alon R, Luscinskas FW. *ICAM-1 regulates neutrophil adhesion and transcellular migration of TNF-activated vascular endothelium under flow* (2005). Available at: <http://ashpublications.org/blood/article-pdf/106/2/584/1711514/zh801405000584.pdf>.
53. Jiang Y, Jiang LLI, Maimaitirexiati XMZY, Zhang Y, Wu L, Irbesartan attenuates TNF- α -induced ICAM-1, VCAM-1, and e-selectin expression through suppression of NF- κ b pathway in HUVECs. *Eur Rev Med Pharmacol Sci* (2015) 19(17):3295–302.
54. Reiss Y, Engelhardt B. T Cell interaction with ICAM-1-deficient endothelium *in vitro*: transendothelial migration of different T cell populations is mediated by endothelial ICAM-1 and ICAM-2. *Int Immunol* (1999) 11(9):1527–39. doi: 10.1093/intimm/11.9.1527
55. Wevers NR, Nair AL, Fowke TM, Pontier M, Kasi DG, Spijkers XM, et al. Modeling ischemic stroke in a triculture neurovascular unit on-a-chip. *Fluids Bar. CNS* (2021) 18(1):1–18. doi: 10.1186/s12987-021-00294-9



OPEN ACCESS

EDITED BY

Shisong Jiang,
University of Oxford, United Kingdom

REVIEWED BY

Ali Namvar,
Iranian Comprehensive Hemophilia Care
Center, Iran

*CORRESPONDENCE

Dongbo Jiang
✉ superjames1991@foxmail.com
Kun Yang
✉ yangkunkun@fmmu.edu.cn

[†]These authors share first authorship

SPECIALTY SECTION

This article was submitted to
Viral Immunology,
a section of the journal
Frontiers in Immunology

RECEIVED 20 October 2022

ACCEPTED 17 January 2023

PUBLISHED 31 January 2023

CITATION

Sun B, Zhang J, Li Z, Xie M, Luo C, Wang Y, Chen L, Wang Y, Jiang D and Yang K (2023) Integration: Gospel for immune bioinformatician on epitope-based therapy. *Front. Immunol.* 14:1075419. doi: 10.3389/fimmu.2023.1075419

COPYRIGHT

© 2023 Sun, Zhang, Li, Xie, Luo, Wang, Chen, Wang, Jiang and Yang. This is an open-access article distributed under the terms of the [Creative Commons Attribution License \(CC BY\)](#). The use, distribution or reproduction in other forums is permitted, provided the original author(s) and the copyright owner(s) are credited and that the original publication in this journal is cited, in accordance with accepted academic practice. No use, distribution or reproduction is permitted which does not comply with these terms.

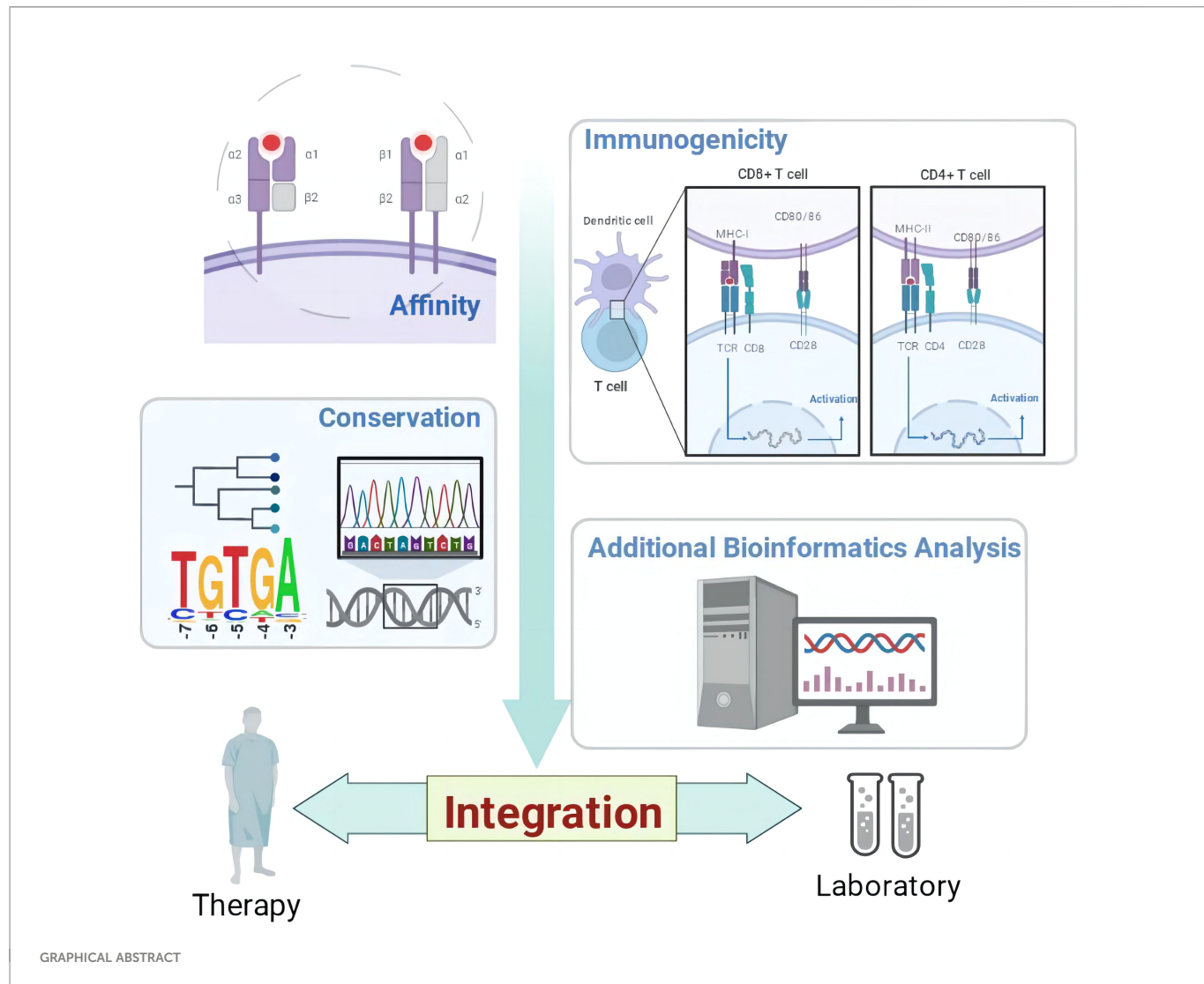
Integration: Gospel for immune bioinformatician on epitope-based therapy

Baozeng Sun^{1†}, Junqi Zhang^{1†}, Zhikui Li^{1†}, Mingyang Xie^{1†}, Cheng Luo¹, Yongkai Wang¹, Longyu Chen¹, Yueyue Wang¹, Dongbo Jiang^{1,2,3*} and Kun Yang^{1,2,4*}

¹Department of Immunology, Basic Medicine School, Air-Force Medical University (the Fourth Military Medical University), Xi'an, Shaanxi, China, ²The Key Laboratory of Bio-hazard Damage and Prevention Medicine, Basic Medicine School, Air-Force Medical University (the Fourth Military Medical University), Xi'an, Shaanxi, China, ³Department of Microbiology, Basic Medicine School, Air-Force Medical University (the Fourth Military Medical University), Xi'an, Shaanxi, China, ⁴Department of Rheumatology, Tangdu Hospital, Air-Force Medical University (the Fourth Military Medical University), Xi'an, Shaanxi, China

KEYWORDS

integration, epitope, immunotherapy, *in silico*, bioinformatics, immune response



1 Introduction

Peptide-based vaccines are attracting considerable attention due to the potential to precisely tune the immune response using antigen fragments or peptides, as well as the relative ease of production (1). So far, peptide vaccines against viral infectious diseases have been widely developed and entered phase I/II clinical trials (2), which include COVID-19, HIV, influenza, hepatitis B, and hepatitis C, meaning the mature technology in research and development. Also, NeuVax, a peptide vaccine against breast cancer, completed phase III clinical trial and declared safety *in vivo* (3). This is the furthest step in the quest for epitope vaccines for use in humans to date (4, 5), suggesting the effectiveness of strategies and the bright application prospect to design peptide-based vaccines (6, 7).

Effective epitopes play a major therapeutic role in synthetic peptide vaccines. Identifying and screening epitopes, however, is usually an endless and complex process (8). Fortunately, researchers have developed *in silico* prediction methods that dramatically reduce the burden associated with epitope mapping by minimizing the list of potential epitope candidates for experimental testing (9). These tools allow investigators to analyze antigenic properties at multiple levels and

multiple dimensions, such as affinity, immunogenicity, toxicity, and sensitization, which greatly promotes the further comprehension of pathogens and has a great role in promoting the research and development of drugs to benefit disease prevention and control (9–11).

However, the accuracy of single prediction analysis is often only 50%–70% (12–16). This is probably because of the inherent defects in computer algorithms based on epitope databases for fitting functions (8, 11). In view of above deficiencies, we propose a novel train of thought, “integration”, to augment the breadth and depth of bioinformatics in peptide-based therapeutics. At the same time, we call on researchers to excavate connotations with the characteristics of antigens behind the credit tool and to make breakthrough in the prevention and control of diseases such as infection and cancer.

1.1 “Integration”: Improving the accuracy of the analysis

Accuracy has always been the goal pursued by various bioinformatics algorithms. Therefore, researchers have relied on a variety of algorithms, such as artificial neural networks (ANNs) (17–19), the stabilized matrix method (SMM) (20), and the consensus method (21), and tested them in

tens of thousands of epitopes in multiple databases (17, 18). However, fully accurate algorithmic toolkits have not been developed to date. Meanwhile, *in silico* studies usually reveal their results with limited or even single predictive tools in respective orientations, which greatly hinders the application in general. Therefore, the concept of “integration” is advocated, which is the use of multiple analysis algorithms for an identical antigen, selecting the dominant epitopes predicted by each tool or adopting higher criteria. Considering this strategy in a purpose-oriented way, alternative methods output epitopes by different algorithms, collateral with false positives due to inherent defects of each toolkit. Theoretically, dominant epitopes should be defined through the intersection of multiple tools, which greatly reduces the probability of nondominant epitope output, thereby improving the accuracy of prediction.

Affinity analyses have been widely used in the study of infectious diseases (22–24), neoplasms (25) and autoimmune diseases (26). Table 1 lists the current international mainstream epitope analysis algorithms. There are multiple algorithms and platforms to analyze affinity, and the IEDB analysis resource (MHC-I binding and MHC-II binding) and DTU HEALTH TECH (NetMHCpan and NetMHCIIpan) platforms have taken over the absolute principal position. The functionality of affinity analysis provided by the IEDB Analytical Resources integrates multiple analytical methods (27),

including Artificial neural network (ANN) (19), Stabilized matrix method (SMM) (20), SMM with a Peptide: major histocompatibility complex(MHC) Binding Energy Covariance matrix (SMMPPMBEC) (28), and so on. Why not make full use of these algorithms to sharpen the accuracy of affinity analysis? Recently, immunologists followed this thought in glycoprotein epitope studies of Hantaan virus and Ebola virus, in which five or four affinity algorithms predicted MHC-I and MHC-II restricted epitopes, respectively, selecting epitopes with Rank \leq 2% 3 or 2 times among toolkits. Strong cellular responses in enzyme-linked immunospot assays with corresponding epitopes validated the effectiveness of this strategy in infectious diseases such as viral hemorrhagic fever virus (29–31).

1.2 “Integration”: Linking multiple assays and testifying each other

Most studies on bioinformatics exploration of peptide-based therapeutics lacked validation of relevant results (32–34). This may be related to the time- and resource-consuming experimental conditions. For example, considering the risk of Ebola virus and the harsh nature of the required test conditions, Alizadeh et al. resigned the evaluation after designing a multiepitope vaccine against Ebola

TABLE 1 The various tools involved in the article and their functions, websites.

function	platform	site
MHC-I restricted epitopes analysis	IEDB	https://www.iedb.org/
	NetMHCpan 4.1	https://services.healthtech.dtu.dk/service.php.NetMHCpan-4.1
	SYFPEITHI	http://www.syfpeithi.de/bin/MHCServer.dll/EpitopePrediction.htm
	Rankpep	http://imed.med.ucm.es/Tools/rankpep.html
	SMMPPMBEC	https://github.com/ykimbiology/smmppmbec
MHC-II restricted epitopes analysis	IEDB	https://www.iedb.org/
	NetMHCIIpan3.2	https://services.healthtech.dtu.dk/service.php.NetMHCIIpan-3.2
	SYFPEITHI	http://www.syfpeithi.de/bin/MHCServer.dll/EpitopePrediction.html
	Rankpep	http://imed.med.ucm.es/Tools/rankpep.html
B-cell epitopes analysis	BepiPred-2.0	https://services.healthtech.dtu.dk/service.php.BepiPred-2.0
	IEDB B-cell epitope analysis ¹	http://tools.iedb.org/bcell/
Immunogenicity Analysis	VaxiJen v2.0	http://www.ddg-pharmfac.net/vaxijen/VaxiJen/VaxiJen.html
	IEDB Immunogenicity Analysis	http://tools.iedb.org/immunogenicity/
Conservancy Analysis	IEDB conservancy Analysis	http://tools.iedb.org/conservancy/
	Blastp	https://blast.ncbi.nlm.nih.gov/Blast.cgi
Molecular docking of 9-mer peptide epitopes	HPEPDOCK 2.0	http://huanglab.phys.hust.edu.cn/hpepdock/
Molecular docking of 15-mer peptide epitopes	EpiDOCK server	http://www.ddg-pharmfac.net/epidock/EpiDockPage.html
Molecular Structure Model Query	RCSB PDB	https://www.rcsb.org/
Tertiary structure predict	I-TASSER	https://zhanglab.ccmb.med.umich.edu/I-TASSER/
Tertiary structures refinement	GalaxyRefine server	http://galaxy.seoklab.org/cgi-bin/submit.cgi?type=REFINE
Allergen analysis	AlgPred 2.0	https://webs.iiitd.edu.in/raghava/algpred2/
Toxicity analysis	ToxinPred2	https://webs.iiitd.edu.in/raghava/toxinpred2/index.html

¹IEDB B-cell epitope analysis tool includes six methods: Bepipred Linear Epitope Prediction, Parker Hydrophilicity Prediction, Kolaskar & Tongaonkar Antigenicity, Karplus & Schulz FlexTurn Prediction, Emini Surface Accessibility Prediction, and Chou & Fasman Beta-ability Prediction.

virus (35). However, we found a connection between different types of epitope analysis, so the results of multiple analyses can be compared to validate the results at the bioinformatics level.

Take an example of the depth implication in affinity analysis and molecular docking (8). Peptide-MHC interactions are crucial in immune functions. Therefore, determining the structure of Peptide-MHC complexes is important for understanding the molecular mechanism of related biological processes and developing peptide-based immunotherapy. Typically, the RCSB PDB (<https://www.rcsb.org/>) is used to obtain models of MHC molecules and then HEPEDOCK 2.0 is used to predict the possibility of MHC-peptide complexes and provide multiple docking models (36). EpiDOCK toolkit can be also used in MHC-II-peptide docking and predicting binding energy (37). Binding affinity and molecular docking share a similar connotation, indicating the binding ability of MHC molecules and epitopes (38, 39). Therefore, the results of both analyses can mutually validate each other *in silico*. However, if there is a gap in the above comparison, it may be derived from the defects in algorithms' intrinsic variety. More importantly, by simulating the docking between epitopes and MHC, the location and tightness of the docking can be directly figured out, so that the affinity data can be more intuitively reflected.

1.3 “Integration”: unveiling principles in comparative immunology, intriguingly

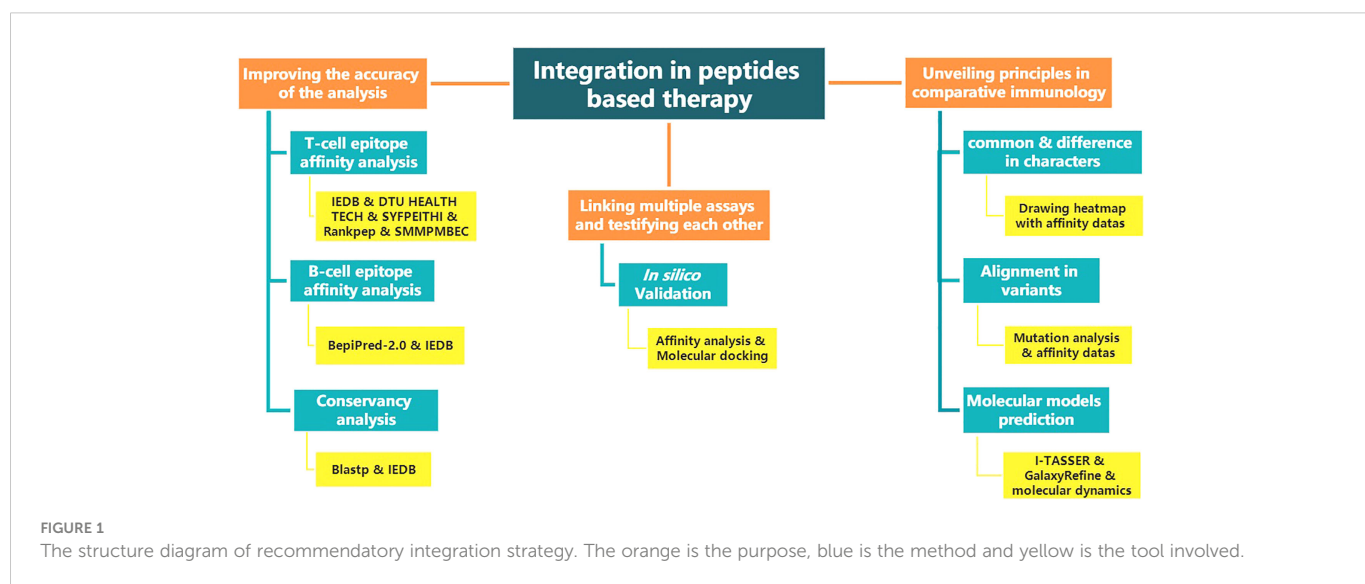
Most algorithms give only a large number of “cold” numbers in processing antigens. How to convert these numbers into meaningful models or illustrations related to the body's immunologic nature is an aporia faced by every bioinformatics researcher. Here are three approaches to delineate the above issues.

A large amount of data will be generated in the affinity analysis of multiple epitopes together with multi-MHC genotypes. It would not be state-of-art to present the whole things directly in the main text. By looking at these data using a holistic view, that is, using a heatmap form, which can show three dimensions: the epitopes, MHC genotypes and affinity ranks (40, 41). It is intuitive to exhibit the epitopes that are dominant in MHC genotypes. At the same time,

bihierarchical clustering would reveal the cross-reactivity between different genotypes based on affinity analysis data (42, 43). This intuitively reflects genotype proximity according to pathogen specificity, further understanding of susceptibility and resistance against pathogens in different races, geographies, populations, and even species. Using these forms to present data not only makes the expression more intuitive and concise but also fully interprets the deep-seated meaning of the data.

Alignment of variants has been implicated in many studies but is limited to the step of multiple sequence alignment, finding mutation sites, and exploring evolutionary clades (42, 44, 45). On this basis, another direction — further research on the impact of mutation sites — should also be taken into consideration. That is, the mutation site is brought into the original sequence to explore the impact of the mutation site on the affinity and immunogenicity of the specific epitopes (29, 31). This analysis of the mutated sequences *in silico* predicts the approximate direction of evolutionary impacts on immunogenetic variation and deepens the understanding of pathogen conservation.

Epitope studies always aim to design drugs or vaccines for clinical use. Therefore, building of molecular model will be a complex and important work. At present, there are two channels to obtain molecular structure models: one is based on the existing RCSB PDB database to retrieve the discovered molecular structures, and the other is *ab initio* prediction method based on molecular dynamic (MD). That is, 3D atomic models were building from different stringing arrangements and iterative structural assembly simulations according to amino acid sequences, and then the models are optimized by MD. MD is a computer simulation method which is employed in various engineering and science disciplines to calculate motion and equilibrium of each individual atom or molecule. It can be used to explore conformational space, and is often the method of choice for large molecules such as proteins. Recently, due to the continuous development of MD, molecular models and docking are closer to the real response (46). Here, we recommend a method, the integration of I-TASSER and GalaxyRefine server. I-TASSER integrates inter-residue contact maps from deep neural-network learning with the cutting-edge fragment assembly simulations (47). GalaxyRefine performs repeated structure perturbation and subsequent overall structural relaxation by molecular dynamics simulation (48). The



integration of I-TASSER and GalaxyRefine server allows the molecular structure to be rebuilt and optimized, providing an overall intuitive molecular structure (8, 49).

1.4 “Integration”: Adjusting cognition according to antigenic characteristics and contradiction

In recent years, bioinformatics has been widely used on epitope studies of pathogenic microorganisms. However, *in silico* analysis is not static and needs to be adjusted according to the characteristics of antigens and the purposes of the research. The contradictions investigated in tumor immunity and autoimmune diseases are distinguishing. Also, the “elegance” of integration should be noted.

Tumor antigens are usually cancer-specific peptides (neoepitopes) (50) generated by somatic mutations or genomic aberrations, posttranslational modifications (PTMs) (51), and translation from noncoding regions (52). The aim of tumor immunity is to circumvent immune suppressive evasion mechanisms used by cancer cells through modulation of T cell responses (2). Therefore, *in silico* analysis of tumor antigens mainly focuses on interrogating cytotoxic T (CTL) cell epitopes and promoting cytotoxicity (53). On the other hand, autoimmune diseases arise from immune responses to self-antigens and reflect a breakdown in immunological tolerance (54). Most classical autoimmune diseases have associations with genes in the MHC-II region (55), leading to the production of autoantibodies (56) or the activation of CTL cells (57) to autoantigens. Therefore, pathognomonic autoimmune diseases need to be specifically designed according to the disease mechanism and site of immunoreaction.

T-cell (CD8+ and CD4+ T-cell) epitopes and B-cell epitopes are the material basis of adaptive immune responses as allure to most of studies. However, few has addressed the association among them so far. It is well known that CD4+ T cells, as helper cells, promote both killer T cells and B cells and then strengthen humoral and cellular immunity (58). Obeying this immune principle, following routine can be considered: epitopes should be validated, and the links between genuine MHC-I and MHC-II dominance, perhaps MHC-II and B-cell antigenic determinants can be found to mine the substantial bases of cellular and humoral immunity.

The above renders multiple “integration” ideas. Figure 1 shows the structure diagram of recommendatory integration strategy. However, attentions should be paid in the practice: an epitope could be jointly selected with affinity, immunogenicity, conservation, toxicity, allergen analysis, etc. It would be interesting but challenging to figure out what impacts the different orders will have on the results and what particular connotations the epitopes will be endowed with. Additionally, for each operation, the results will be tested once. It is intractable to face false positives, false negatives or overfitting of the integrated results due to multiple testing. Finally, toolkits of the algorithms and datasets do not update in a timely manner, which directly affects the tool selection, priority of use, and settings of various parameters.

2 Discussion

The evolution of epitope-based vaccines is one of the most promising developments arising from bioinformatics-based research

(8), and the development of bioinformatics has also made pathogen epitope exploration convenient and cost-effective (11). We put forward a point of view, “Integration”, aiming to improve the accuracy and fit-in the body’s immune response. It says the opinion that integration manners are advances in bioinformatics rather than just a single algorithmic innovation. The acquisition of analytical results is by no means the terminus of epitopes studies. How to apply the toolkits *in silico* under the precondition for immunology principles will be critical issues to be addressed. In this opinion, the “integration” tenet was first put forward, dedicated to compensating for inherent deficiencies in current algorithms and simulating the realistic immune response model. It provided a novel train of thought for peptide-based immunotherapy *in silico* against infection, neoplasms and autoimmune diseases, and would by all odds promote the development and progress of the bioinformatics discipline.

Author contributions

Conceptualization: DJ, BS, and KY. Methodology: DJ, BS, and JZ. Formal analysis: SB and DJ. Investigation: BS, DJ, and YoW. Resources, DJ, and KY. Writing—original draft preparation: BS and JZ. Writing—review and editing: DJ, JZ, ZL, MX, and YoW. Peer discussion: YoW, CL, LC, and YuW. Visualization, BS, JZ, ZL, and MX. Supervision, DJ and KY. Project administration, DJ and KY. Funding acquisition: DJ and KY. All authors contributed to the article and approved the submitted version.

Funding

This study was supported by the General Program of National Nature Science Foundation of China (No. 82073154 to KY), the Youth Program of National Nature Science Foundation of China (No. 82203510 to DJ), the Key Research and Development Program of Shaanxi Province (2023-YBSF-198 to DJ), and the Promotion Program of Air Force Medical University (2020SWAQ03 to KY).

Conflict of interest

The authors declare that the research was conducted in the absence of any commercial or financial relationships that could be construed as a potential conflict of interest.

Publisher’s note

All claims expressed in this article are solely those of the authors and do not necessarily represent those of their affiliated organizations, or those of the publisher, the editors and the reviewers. Any product that may be evaluated in this article, or claim that may be made by its manufacturer, is not guaranteed or endorsed by the publisher.

References

1. Malonis RJ, Lai JR, Vergnolle O. Peptide-based vaccines: Current progress and future challenges. *Chem Rev* (2020) 120(6):3210–29. doi: 10.1021/acs.chemrev.9b00472
2. Hamley IW. Peptides for vaccine development. *ACS Appl Bio Mater* (2022) 5(3):905–44. doi: 10.1021/acsabm.1c01238
3. Mittendorf EA, Lu B, Melisko M, Price Hiller J, Bondarenko I, Brunt AM, et al. Efficacy and safety analysis of nelipepimut-s vaccine to prevent breast cancer recurrence: A randomized, multicenter, phase III clinical trial. *Clin Cancer Res* (2019) 25(14):4248–54. doi: 10.1158/1078-0432.CCR-18-2867
4. Nicolás-Morales MI, Luisa-Sanjuan A, Gutiérrez-Torres M, Vences-Velázquez A, Ortúño-Pineda C, Espinoza-Rojo M, et al. Peptide-based vaccines in clinical phases and new potential therapeutic targets as a new approach for breast cancer: A review. *Vaccines (Basel)* (2022) 10(8). doi: 10.3390/vaccines10081249
5. Davodabadi F, Sarhadi M, Arabpour J, Sargazi S, Rahdar A, Diez-Pascual AM. Breast cancer vaccines: New insights into immunomodulatory and nano-therapeutic approaches. *J Control Release* (2022) 349:844–75. doi: 10.1016/j.jconrel.2022.07.036
6. Mittendorf EA, Clifton GT, Holmes JP, Schneible E, van Echo D, Ponniah S, et al. Final report of the phase I/II clinical trial of the E75 (nelipepimut-s) vaccine with booster inoculations to prevent disease recurrence in high-risk breast cancer patients. *Ann Oncol* (2014) 25(9):1735–42. doi: 10.1093/annonc/mdu211
7. Errico A. Breast cancer: E75-a safe and effective vaccine for the prevention of disease recurrence. *Nat Rev Clin Oncol* (2014) 11(8):440. doi: 10.1038/nrclinonc.2014.11
8. Yurina V, Adianingsih OR. Predicting epitopes for vaccine development using bioinformatics tools. *Ther Adv Vaccines Immunother* (2022) 10:25151355221100218. doi: 10.1177/25151355221100218
9. Sanchez-Trincado JL, Gomez-Perez M, Reche PA. Fundamentals and methods for T- and b-cell epitope prediction. *J Immunol Res* (2017) 2017:2680160. doi: 10.1155/2017/2680160
10. Bahrami AA, Payandeh Z, Khalili S, Zakeri A, Bandehpour M. Immunoinformatics: In silico approaches and computational design of a multi-epitope, immunogenic protein. *Int Rev Immunol* (2019) 38(6):307–22. doi: 10.1080/08830185.2019.1657426
11. Kazi A, Chuah C, Majeed ABA, Leow CH, Lim BH, Leow CY. Current progress of immunoinformatics approach harnessed for cellular- and antibody-dependent vaccine design. *Pathog Glob Health* (2018) 112(3):123–31. doi: 10.1080/2047724.2018.1446773
12. Jurtz V, Paul S, Andreatta M, Marcatili P, Peters B, Nielsen M. NetMHCpan-4.0: Improved peptide-MHC class I interaction predictions integrating eluted ligand and peptide binding affinity data. *J Immunol* (2017) 199(9):3360–8. doi: 10.4049/jimmunol.1700893
13. Nielsen M, Lundsgaard C, Lund O. Prediction of MHC class II binding affinity using SMM-align, a novel stabilization matrix alignment method. *BMC Bioinf* (2007) 8:238. doi: 10.1186/1471-2105-8-238
14. Jensen KK, Andreatta M, Marcatili P, Buus S, Greenbaum JA, Yan Z, et al. Improved methods for predicting peptide binding affinity to MHC class II molecules. *Immunol* (2018) 154(3):394–406. doi: 10.1111/imm.12889
15. Wang P, Sidney J, Dow C, Mothé B, Sette A, Peters B. A systematic assessment of MHC class II peptide binding predictions and evaluation of a consensus approach. *Plos Comput Biol* (2008) 4(4):e1000048. doi: 10.1371/journal.pcbi.1000048
16. The problem with neopeptidogen prediction. *Nat Biotechnol* (2017) 35(2):97. doi: 10.1038/nbt.3800
17. Reynisson B, Barra C, Kaabinejad S, Hildebrand WH, Peters B, Nielsen M. Improved prediction of MHC II antigen presentation through integration and motif deconvolution of mass spectrometry MHC eluted ligand data. *J Proteome Res* (2020) 19(6):2304–15. doi: 10.1021/acs.jproteome.9b00874
18. Alvarez B, Reynisson B, Barra C, Buus S, Ternette N, Connelley T, et al. NNAlign_MA: MHC peptidome deconvolution for accurate MHC binding motif characterization and improved T-cell epitope predictions. *Mol Cell Proteomics* (2019) 18(12):2459–77. doi: 10.1074/mcp.TIR119.001658
19. Andreatta M, Nielsen M. Gapped sequence alignment using artificial neural networks: application to the MHC class I system. *Bioinformatics* (2016) 32(4):511–7. doi: 10.1093/bioinformatics/btv639
20. Peters B, Sette A. Generating quantitative models describing the sequence specificity of biological processes with the stabilized matrix method. *BMC Bioinf* (2005) 6:132. doi: 10.1186/1471-2105-6-132
21. Moutaftsi M, Peters B, Pasquetto V, Tscharke DC, Sidney J, Bui HH, et al. A consensus epitope prediction approach identifies the breadth of murine T(CD8+)-cell responses to vaccinia virus. *Nat Biotechnol* (2006) 24(7):817–9. doi: 10.1038/nbt1215
22. Cheng P, Wang L, Gong W. In silico analysis of peptide-based biomarkers for the diagnosis and prevention of latent tuberculosis infection. *Front Microbiol* (2022) 13:947852. doi: 10.3389/fmicb.2022.947852
23. Jiang S, Wu S, Zhao G, He Y, Guo X, Zhang Z, et al. Identification of a promiscuous conserved CTL epitope within the SARS-CoV-2 spike protein. *Emerg Microbes Infect* (2022) 11(1):730–40. doi: 10.1080/22221751.2022.2043727
24. Ullah A, Shahid FA, Haq MU, Tahir Ul Qamar M, Irfan M, Shaker B, et al. An integrative reverse vaccinology, immunoinformatic, docking and simulation approaches towards designing of multi-epitopes based vaccine against monkeypox virus. *J Biomol Struct Dyn* (2022), 1–14. doi: 10.1080/07391102.2022.2125441
25. Ragone C, Manolio C, Mauriello A, Cavalluzzo B, Buonaguro FM, Tornesello ML, et al. Molecular mimicry between tumor associated antigens and microbiota-derived epitopes. *J Transl Med* (2022) 20(1):316. doi: 10.1186/s12967-022-03512-6
26. Repac J, Mandić M, Lunić T, Božić B, Božić Nedeljković B. Mining the capacity of human-associated microorganisms to trigger rheumatoid arthritis-a systematic immunoinformatics analysis of T cell epitopes. *PLoS One* (2021) 16(6):e0253918. doi: 10.1371/journal.pone.0253918
27. Vita R, Mahajan S, Overton JA, Dhanda SK, Martini S, Cantrell JR, et al. The immune epitope database (IEDB): 2018 update. *Nucleic Acids Res* (2019) 47(D1):D339–d43. doi: 10.1093/nar/gky1006
28. Kim Y, Sidney J, Pinilla C, Sette A, Peters B. Derivation of an amino acid similarity matrix for peptide: MHC binding and its application as a Bayesian prior. *BMC Bioinf* (2009) 10:394. doi: 10.1186/1471-2105-10-394
29. Sun B, Zhang J, Wang J, Liu Y, Sun H, Lu Z, et al. Comparative immunoreactivity analyses of hantavirus glycoprotein-derived MHC-I epitopes in vaccination. *Vaccines (Basel)* (2022) 10(4):564. doi: 10.3390/vaccines10040564
30. Sun H, Lu Z, Xuan G, Liu N, Wang T, Liu Y, et al. Integrative analysis of HTNV glycoprotein derived MHC II epitopes by in silico prediction and experimental validation. *Front Cell Infect Microbiol* (2021) 11:671694. doi: 10.3389/fcimb.2021.671694
31. Liu Y, Sun B, Wang J, Sun H, Lu Z, Chen L, et al. In silico analyses and experimental validation of the MHC class-I restricted epitopes of ebolavirus GP. *Int Immunol* (2022) 34(6):313–25. doi: 10.1093/intimm/dxac006
32. Fereshteh S, Noori Goodarzi N, Sepehr A, Shafiei M, Ajdary S, Badmasti F. In silico analyses of extracellular proteins of acinetobacter baumannii as immunogenic candidates. *Iran J Pharm Res* (2022) 21(1):e126559. doi: 10.5812/ijpr.126559
33. Mia MM, Hasan M, Ahmed S, Rahman MN. Insight into the first multi-epitope-based peptide subunit vaccine against avian influenza a virus (H5N6): An immunoinformatics approach. *Infect Genet Evol* (2022) 104:105355. doi: 10.1016/j.meegid.2022.105355
34. Shantier SW, Mustafa MI, Abdelmoneim AH, Fadil HA, Elbager SG, Makhawi AM. Novel multi epitope-based vaccine against monkeypox virus: vaccinomic approach. *Sci Rep* (2022) 12(1):15983. doi: 10.1038/s41598-022-20397-z
35. Alizadeh M, Amini-Khoei H, Tahmasebian S, Ghatrehsamani M, Ghatrehsamani K, Edalatpanah Y, et al. Designing a novel multi-epitope vaccine against Ebola virus using reverse vaccinology approach. *Sci Rep* (2022) 12(1):7757. doi: 10.1038/s41598-022-11851-z
36. Tao H, Zhao X, Zhang K, Lin P, Huang SY. Docking cyclic peptides formed by a disulfide bond through a hierarchical strategy. *Bioinformatics* (2022) 38(17):4109–16. doi: 10.1093/bioinformatics/btac486
37. Atanasova M, Patronov A, Dimitrov I, Flower DR, Doytchinova I. EpiDOCK: a molecular docking-based tool for MHC class II binding prediction. *Protein Eng Des Sel* (2013) 26(10):631–4. doi: 10.1093/protein/gzt018
38. Reynisson B, Alvarez B, Paul S, Peters B, Nielsen M. NetMHCpan-4.1 and NetMHCIIpan-4.0: Improved predictions of MHC antigen presentation by concurrent motif deconvolution and integration of MS MHC eluted ligand data. *Nucleic Acids Res* (2020) 48(W1):W449–w54. doi: 10.1093/nar/gkaa379
39. Nielsen M, Andreatta M. NetMHCpan-3.0; improved prediction of binding to MHC class I molecules integrating information from multiple receptor and peptide length datasets. *Genome Med* (2016) 8(1):33. doi: 10.1186/s13073-016-0288-x
40. Sankaranarayanan S, Mohkhedkar M, Janakiraman V. Mutations in spike protein T cell epitopes of SARS-CoV-2 variants: Plausible influence on vaccine efficacy. *Biochim Biophys Acta Mol Basis Dis* (2022) 1868(9):166432. doi: 10.1016/j.bbadi.2022.166432
41. Salaiukumar MR, Kasamuthu PS, Aathmanathan VS, Burra V. An in silico approach to study the role of epitope order in the multi-epitope-based peptide (MEBP) vaccine design. *Sci Rep* (2022) 12(1):12584. doi: 10.1038/s41598-022-16445-3
42. Wu M, Chen Y, Lang W, Qin X, Ruan L, Su M, et al. Genetic variation analysis of porcine circovirus type 4 in south China in 2019 to 2021. *Viruses* (2022) 14(8):1736. doi: 10.3390/v14081736
43. Sami SA, Marma KKS, Mahmud S, Khan MAN, Albogami S, El-Shehawi AM, et al. Designing of a multi-epitope vaccine against the structural proteins of marburg virus exploiting the immunoinformatics approach. *ACS Omega* (2021) 6(47):32043–71. doi: 10.1021/acsomega.1c04817
44. Agarwal A, Beck KL, Capponi S, Kunitomi M, Nayar G, Seabolt E, et al. Predicting epitope candidates for SARS-CoV-2. *Viruses* (2022) 14(8):1837. doi: 10.3390/v14081837
45. Vale FF, Vitor JMB, Marques AT, Azevedo-Pereira JM, Anes E, Goncalves J. Origin, phylogeny, variability and epitope conservation of SARS-CoV-2 worldwide. *Virus Res* (2021) 304:198526. doi: 10.1016/j.virusres.2021.198526
46. Hu X, Zeng Z, Zhang J, Wu D, Li H, Geng F. Molecular dynamics simulation of the interaction of food proteins with small molecules. *Food Chem* (2023) 405(Pt A):134824. doi: 10.1016/j.foodchem.2022.134824
47. Zheng W, Zhang C, Li Y, Pearce R, Bell EW, Zhang Y. Folding non-homologous proteins by coupling deep-learning contact maps with I-TASSER assembly simulations. *Cell Rep Methods* (2021) 1(3):100014. doi: 10.1016/j.crmeth.2021.100014

48. Heo L, Park H, Seok C. GalaxyRefine: Protein structure refinement driven by side-chain repacking. *Nucleic Acids Res* (2013) 41(Web Server issue):W384–8. doi: 10.1093/nar/gkt458

49. Prawiningrum AF, Paramita RI, Panigoro SS. Immunoinformatics approach for epitope-based vaccine design: Key steps for breast cancer vaccine. *Diagnostics (Basel)* (2022) 12(12):2981. doi: 10.3390/diagnostics12122981

50. Schaap-Johansen AL, Vujošić M, Borch A, Hadrup SR, Marcatili P. T Cell epitope prediction and its application to immunotherapy. *Front Immunol* (2021) 12:712488. doi: 10.3389/fimmu.2021.712488

51. Malaker SA, Penny SA, Steadman LG, Myers PT, Loke JC, Raghavan M, et al. Identification of glycopeptides as posttranslationally modified neoantigens in leukemia. *Cancer Immunol Res* (2017) 5(5):376–84. doi: 10.1158/2326-6066.CIR-16-0280

52. Laumont CM, Vincent K, Hesnard L, Audemard É, Bonneil É, Laverdure JP, et al. Noncoding regions are the main source of targetable tumor-specific antigens. *Sci Transl Med* (2018) 10(470):eaau5516. doi: 10.1126/scitranslmed.aau5516

53. Duan F, Duitama J, Al Seesi S, Ayres CM, Corcelli SA, Pawashe AP, et al. Genomic and bioinformatic profiling of mutational neoepitopes reveals new rules to predict anticancer immunogenicity. *J Exp Med* (2014) 211(11):2231–48. doi: 10.1084/jem.20141308

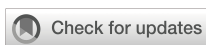
54. Streeter HB, Wraith DC. Manipulating antigen presentation for antigen-specific immunotherapy of autoimmune diseases. *Curr Opin Immunol* (2021) 70:75–81. doi: 10.1016/j.co.2021.03.019

55. Libert C, Dejager L, Pinheiro I. The X chromosome in immune functions: when a chromosome makes the difference. *Nat Rev Immunol* (2010) 10(8):594–604. doi: 10.1038/nri2815

56. Smith EL, Peakman M. Peptide immunotherapy for type 1 diabetes-clinical advances. *Front Immunol* (2018) 9:392. doi: 10.3389/fimmu.2018.00392

57. Matsoukas JM, Ligielli I, Chasapis CT, Kelaidonis K, Apostolopoulos V, Mavromoustakos T. Novel approaches in the immunotherapy of multiple sclerosis: Cyclization of myelin epitope peptides and conjugation with mannose. *Brain Sci* (2021) 11(12):1583. doi: 10.3390/brainsci11121583

58. Hesnard L, Legoux F, Gautreau L, Moyon M, Baron O, Devilder MC, et al. Role of the MHC restriction during maturation of antigen-specific human T cells in the thymus. *Eur J Immunol* (2016) 46(3):560–9. doi: 10.1002/eji.201545951



OPEN ACCESS

APPROVED BY
Frontiers Editorial Office,
Frontiers Media SA, Switzerland

*CORRESPONDENCE
Dongbo Jiang
✉ superjames1991@foxmail.com
Kun Yang
✉ yangkunkun@fmmu.edu.cn

[†]These authors share first authorship

RECEIVED 30 April 2023
ACCEPTED 18 May 2023
PUBLISHED 24 May 2023

CITATION
Sun B, Zhang J, Li Z, Xie M, Luo C, Wang Y, Chen L, Wang Y, Jiang D and Yang K (2023) Corrigendum: Integration: gospel for immune bioinformatician on epitope-based therapy. *Front. Immunol.* 14:1214876. doi: 10.3389/fimmu.2023.1214876

COPYRIGHT
© 2023 Sun, Zhang, Li, Xie, Luo, Wang, Chen, Wang, Jiang and Yang. This is an open-access article distributed under the terms of the [Creative Commons Attribution License \(CC BY\)](#). The use, distribution or reproduction in other forums is permitted, provided the original author(s) and the copyright owner(s) are credited and that the original publication in this journal is cited, in accordance with accepted academic practice. No use, distribution or reproduction is permitted which does not comply with these terms.

Corrigendum: Integration: gospel for immune bioinformatician on epitope-based therapy

Baozeng Sun^{1†}, Junqi Zhang^{1†}, Zhikui Li^{1†}, Mingyang Xie^{1†}, Cheng Luo¹, Yongkai Wang¹, Longyu Chen¹, Yueyue Wang¹, Dongbo Jiang^{1,2,3*} and Kun Yang^{1,2,4*}

¹Department of Immunology, Basic Medicine School, Air-Force Medical University (the Fourth Military Medical University), Xi'an, Shaanxi, China, ²The Key Laboratory of Bio-hazard Damage and Prevention Medicine, Basic Medicine School, Air-Force Medical University (the Fourth Military Medical University), Xi'an, Shaanxi, China, ³Department of Microbiology, Basic Medicine School, Air-Force Medical University (the Fourth Military Medical University), Xi'an, Shaanxi, China, ⁴Department of Rheumatology, Tangdu Hospital, Air-Force Medical University (the Fourth Military Medical University), Xi'an, Shaanxi, China

KEYWORDS

integration, epitope, immunotherapy, *in silico*, bioinformatics, immune response

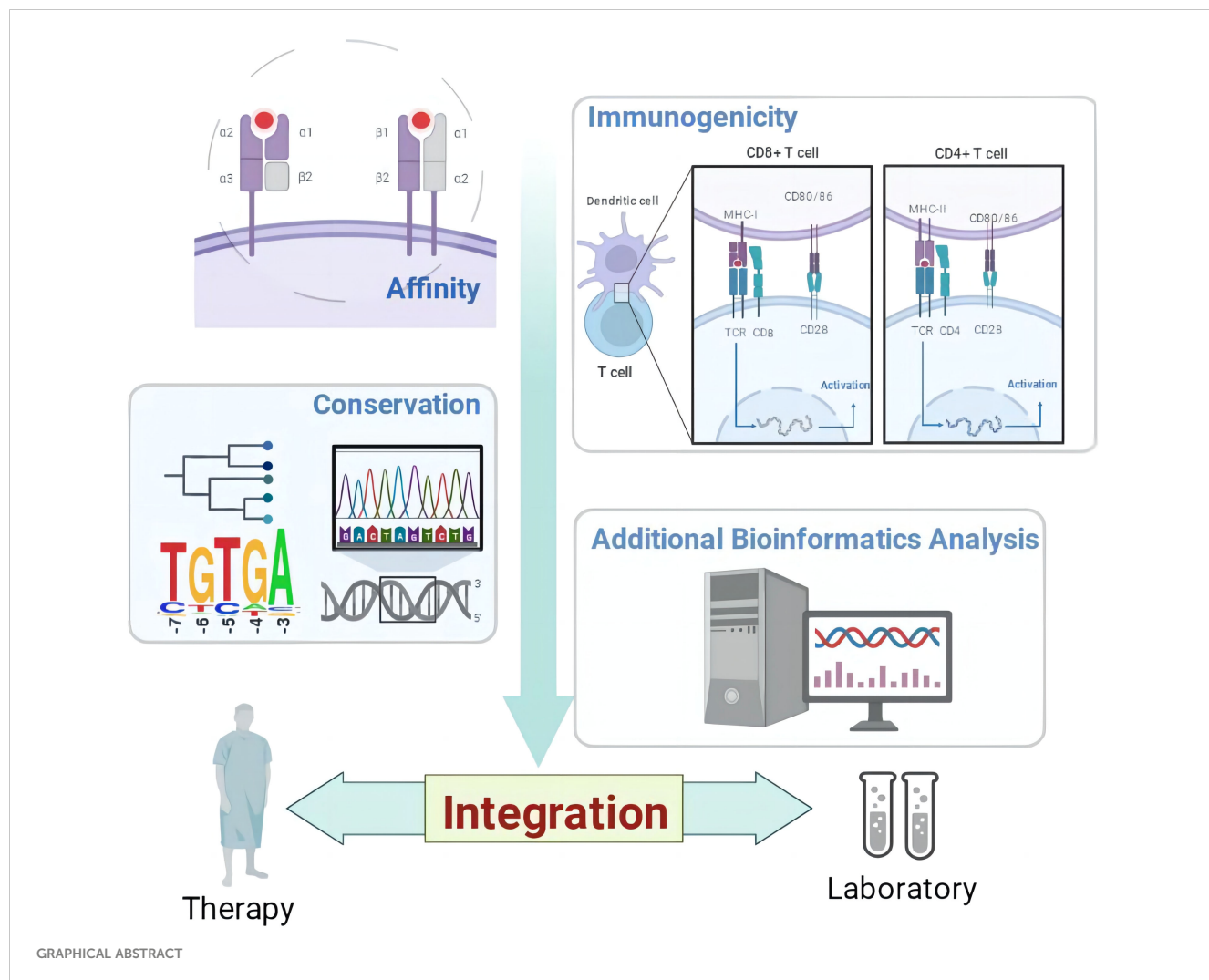
A Corrigendum on

[Integration: gospel for immune bioinformatician on epitope-based therapy](#)

by Sun B, Zhang J, Li Z, Xie M, Luo C, Wang Y, Chen L, Wang Y, Jiang D and Yang K (2023). *Front. Immunol.* 14:1075419. doi: 10.3389/fimmu.2023.1075419

In the published article, there were two errors in the Graphical Abstract as published. In the top right-hand corner of the image, under the “CD8 + T cell” section, “CD4” should read “CD8” and on the left-hand side of the image, “Conversation” should read “Conservation”. The corrected Graphical Abstract appears below.

The authors apologize for this error and state that this does not change the scientific conclusions of the article in any way. The original article has been updated.



Publisher's note

All claims expressed in this article are solely those of the authors and do not necessarily represent those of their affiliated

organizations, or those of the publisher, the editors and the reviewers. Any product that may be evaluated in this article, or claim that may be made by its manufacturer, is not guaranteed or endorsed by the publisher.



OPEN ACCESS

EDITED BY

Jeffrey John Bajramovic,
Utrecht University, Netherlands

REVIEWED BY

Oscar Medina-Contreras,
Mexico Children's Hospital, Mexico
Ariadna Cruz-Córdova,
Federico Gómez Children's Hospital,
Mexico

*CORRESPONDENCE

Jun-feng Ye
✉ yejunfeng@jlu.edu.cn

[†]These authors share first authorship

RECEIVED 17 May 2023

ACCEPTED 23 August 2023

PUBLISHED 13 September 2023

CITATION

Li Y, Yang K-d, Kong D-c and Ye J-f (2023) Advances in phage display based nano immunosensors for cholera toxin. *Front. Immunol.* 14:1224397. doi: 10.3389/fimmu.2023.1224397

COPYRIGHT

© 2023 Li, Yang, Kong and Ye. This is an open-access article distributed under the terms of the [Creative Commons Attribution License \(CC BY\)](#). The use, distribution or reproduction in other forums is permitted, provided the original author(s) and the copyright owner(s) are credited and that the original publication in this journal is cited, in accordance with accepted academic practice. No use, distribution or reproduction is permitted which does not comply with these terms.

Advances in phage display based nano immunosensors for cholera toxin

Yang Li^{1,2†}, Kai-di Yang^{2†}, De-cai Kong¹ and Jun-feng Ye^{1*}

¹General Surgery Center, First Hospital of Jilin University, Changchun, Jilin, China, ²School of Nursing, Jilin University, Changchun, China

Cholera, a persistent global public health concern, continues to cause outbreaks in approximately 30 countries and territories this year. The imperative to safeguard water sources and food from *Vibrio cholerae*, the causative pathogen, remains urgent. The bacterium is mainly disseminated via ingestion of contaminated water or food. Despite the plate method's gold standard status for detection, its time-consuming nature, taking several days to provide results, remains a challenge. The emergence of novel virulence serotypes raises public health concerns, potentially compromising existing detection methods. Hence, exploiting *Vibrio cholerae* toxin testing holds promise due to its inherent stability. Immunobiosensors, leveraging antibody specificity and sensitivity, present formidable tools for detecting diverse small molecules, encompassing drugs, hormones, toxins, and environmental pollutants. This review explores cholera toxin detection, highlighting phage display-based nano immunosensors' potential. Engineered bacteriophages exhibit exceptional cholera toxin affinity, through specific antibody fragments or mimotopes, enabling precise quantification. This innovative approach promises to reshape cholera toxin detection, offering an alternative to animal-derived methods. Harnessing engineered bacteriophages aligns with ethical detection and emphasizes sensitivity and accuracy, a pivotal stride in the evolution of detection strategies. This review primarily introduces recent advancements in phage display-based nano immunosensors for cholera toxin, encompassing technical aspects, current challenges, and future prospects.

KEYWORDS

immunosensors, phage display, cholera toxin, diagnostic approach, nano biosensors

Introduction

Cholera, a malady triggered by *Vibrio cholerae*, induces grave diarrhea and dehydration owing to its toxin production. Prevalent in areas with inadequate sanitation and restricted clean water access, this ailment poses a substantial threat to children under five, underscoring the significance of timely treatment to avert fatal consequences (1–3). Cholera's profound influence on global health is evident in its annual toll of millions of

cases and thousands of fatalities. Moreover, the economic ramifications are substantial, encompassing expenses for treatment, lost productivity, and public health interventions in affected nations (4–6). Cholera diagnosis entails laboratory testing, utilizing phage display-based nano immunosensors for cholera toxin detection. Early identification and treatment are vital for effective disease management. To combat cholera's global impact, prevention measures like enhanced sanitation and clean water access are crucial. *Vibrio cholerae*, the causative bacterium, encompasses various strains, with serotypes O1 and O139 commonly associated with outbreaks. These strains produce a potent cholera toxin, inducing severe diarrhea and dehydration in infected individuals, hallmarking characteristic symptoms like watery diarrhea and vomiting.

Vibrio cholerae secretes various toxins, intricately involved in cholera's pathogenesis (7, 8) (Figure 1A). These encompass: 1. Cholera toxin (CT): A protein complex responsible for hallmark cholera symptoms - watery diarrhea and vomiting. The toxin binds to intestinal cell surfaces, triggering a signaling cascade that induces chloride and water secretion into the intestinal lumen. 2. Toxin-coregulated pilus (TCP): An indispensable surface protein for *Vibrio cholerae* colonization in the human intestine. Facilitating bacterial biofilm formation and adherence to intestinal cells. 3. Zonula occludens toxin (ZOT): A protein toxin disrupting tight junctions between intestinal cells, causing increased permeability of the intestinal epithelium and loss of water and electrolytes. 4. Repeat in toxin (RTX): RTX, a protein toxin, lyses host cells, liberating

nutrients to fuel *Vibrio cholerae* growth and replication. 5. Accessory cholera enterotoxin (ACE): A protein toxin that potentiates cholera toxin activity, elevating water and electrolyte secretion into the intestinal lumen. 6. Cholerae-sensitive enterotoxin (Sta): A protein toxin intensifying cholera toxin activity and directly impacting the intestinal epithelium, heightening water and electrolyte secretion.

Vibrio cholerae primarily spreads via the fecal-oral route, stemming from direct contact with contaminated individuals or indirectly through fluids, food, or materials tainted by the pathogen (11). Widespread cholera outbreaks often correlate with natural or human-induced disasters that disrupt water and sanitation systems, facilitating disease transmission. The aquatic environment also acts as a key player in cholera spread, with the bacteria flourishing in waterways conducive to their proliferation (12, 13). The paramount importance of precise and dependable detection methods for monitoring and curtailing cholera transmission cannot be overstated (14). Thus, the imperative to devise effective, accurate, and reliable techniques for detecting pathogenic *Vibrio cholerae* in water sources becomes indispensable in mitigating the disease's propagation (15, 16). Although the gold standard for cholera diagnosis remains isolating *Vibrio cholerae* O1 serotype from fecal samples, novel virulent serotypes demand alternative detection approaches (17). Given the stable nature of cholera toxin's structure, detecting *Vibrio cholerae* toxin could offer significant advantages (18, 19). Cholera toxin (CT), a virulent protein produced by *Vibrio cholerae*, underpins disease

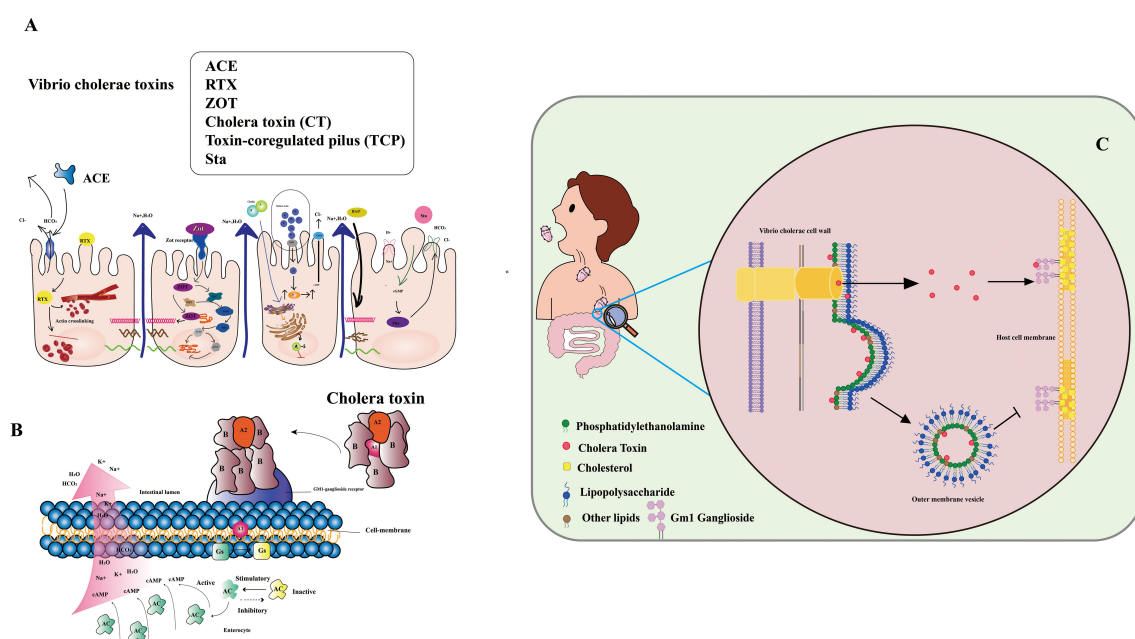


FIGURE 1

(A) Infection with *Vibrio cholerae*. The Cholera Toxin (CT) binds to the Ganglioside GM1 and increases cAMP by increasing adenylate cyclase (AC) activity. Zonula occludens toxin (Zot) affects the structure of intestinal mucosal epithelial cells. Accessory cholera enterotoxin (ACE) stimulates Cl⁻/HCO₃⁻-secretion in enterocytes. Heat-stable enterotoxin (Sta) increases cGMP while inhibiting the Na⁺/Cl⁻ regulation. (Adapted from [8]) (B) Mechanism of action of *V. cholerae* toxin. The complete toxin is shown to bind to the cell membrane's GM1-ganglioside receptor. The A1 catalyzes the GS regulatory protein, "locking" it in active. Accumulation of cAMP along the cell membrane is caused by increased adenylate cyclase (AC) activity. (Adapted from [9]) (C) CT secretion via OMVs and through the T2S (type II secretion) system are complementary mechanisms for CT delivery, ensuring that the toxin can effectively penetrate and damage host cells (Adapted from [10]).

symptoms. CT comprises CTA and CTB subunits, with CTA driving the disease phenotype and CTB serving as the vehicle transporting CTA to target cells. CTA consists of two major domains, CTA1 (the active toxin) and CTA2 (anchoring CTB). Conversely, CTB, a homotrimeric and non-toxic protein, exhibits robust binding to GM1 gangliosides on mammalian cells, displaying high affinity (20) (Figure 1B). CT lacks affinity for LPS, a major component of the outer membrane's outer leaflet (OM). Nonetheless, certain CT molecules enter the periplasm and integrate into OMVs (outer membrane vesicles), small spherical structures budding from the OM. Unlike soluble CT, OMV-incorporated CT fails to bind to the GM1 receptor on host cell lipid rafts due to its location within the OMV. Thus, CT secretion via OMVs and the T2S (type II secretion) system synergize as complementary mechanisms for effective toxin delivery, enabling penetration and damage to host cells (Figure 1C).

State-of-the-art approaches for cholera toxin analysis, like high-performance liquid chromatography (HPLC) (21), liquid chromatography-mass spectrometry (22), gas chromatography (23), and thin-layer chromatography (TLC) (24), boast sensitivity and precision. However, their practicality for field testing or extensive screening can pose challenges. Nano immunosensors offer a promising avenue for toxin rapid identification, boasting simplicity, cost-effectiveness, high specificity, and field monitoring prowess. Several immunoassay techniques, encompassing enzyme-linked immunosorbent assay (ELISA) (25), fluorescence polarization immunoassays (26), fluorescent immunoassays (27), and side-flow immunochromatographic assays (IFA) (28), have been documented for cholera toxin detection. In these assays, antibodies, including monoclonal, polyclonal, and recombinant variants, serve as primary immune reagents. Competition-based formats are common due to the toxin's small size, precluding simultaneous binding by both antibodies. A diverse range of antibodies targeting various cholera toxins, such as monoclonal antibodies (29), polyclonal antibodies (30), and recombinant antibodies (31), have been prepared. Currently, antibodies remain pivotal immune reagents and their preparation continues to evolve (32, 33). However, traditional antibody production can be intricate, time-consuming, and costly, hindering broad application (34). Specific antibody fragments or mimotopes present a compelling alternative for cholera toxin detection, as they exhibit precise binding to antibodies, competing with analytes for binding sites (35, 36). Mimotopes, peptides imitating protein, carbohydrate, or lipid epitopes, hold immense potential for diagnosis, immunotherapy, and vaccine development (37). With their vital roles in these fields, mimotopes emerge as a crucial asset (38–40). Nano immunosensors offer a promising departure from traditional immunoassays in toxin detection. By emulating toxin epitopes and mirroring their properties, nano immunosensors replace toxins or toxin-derived reagents in non-toxic analysis (41, 42). Notably, simulated peptides and anti-idiotype antibodies currently underpin toxin immunoassay development (43, 44). Incorporating a wide array of applications, phage display technology spans epitope mapping (45), enzymatic functions (46), targeted drug delivery (47, 48), and protein interaction definition (49, 50).

Recent research has centered on phage display-based nano immunosensors for cholera toxin detection. Utilizing phage-displayed peptides to mimic cholera toxin epitopes, these immunosensors enable rapid, sensitive, and specific detection in water samples. Nevertheless, challenges remain, necessitating improved stability and sensitivity, optimized detection conditions, and reduced production costs. Notwithstanding, phage display-based nano immunosensors exhibit promising potential, offering a new, safe, and swift detection technology for ensuring environmental water safety. Future research should focus on addressing these challenges, further enhancing performance, and expanding the applicability of phage display-based nano immunosensors in cholera toxin detection.

Preparation and functionalization of nano immunosensors

The production and functionalization of nano immunosensors, encompassing mimotope peptides and anti-idiotype antibodies (51), assume pivotal roles in enabling effective cholera toxin detection. Figure 2 illustrates the production and functionalization of these mimotope peptides and anti-idiotype antibodies. Utilizing phage display technology, simulated peptides are generated via biological panning, targeting primary antibodies of corresponding antigens (52). Anti-idiotype antibodies, encompassing monoclonal, polyclonal, and nano variants, can be obtained through immunizing animals with primary antibodies (53). To facilitate green immunoassays, functionalization of nano immunosensor mimotopes necessitates the use of carrier proteins or signaling probes as coated antigens or tracers (54, 55). Achieving functionalization is possible via chemical synthesis or molecular fusion techniques, with the latter showing greater potential for enhanced performance and specificity (56). Precise and efficient preparation and functionalization of nano immunosensors are paramount, ensuring their sensitivity, specificity, and accuracy in detecting cholera toxin in water sources.

Phage display technology

Phage display technology (Figure 3) emerges as the primary method for preparing mimicking peptides, vital in toxin detection. These polypeptides mimic antigen epitopes and entail genetic modification of phage DNA. By binding to a phage coat protein, peptides, proteins, and antibody fragments are expressed on the phage surface. Additionally, the introduction of exogenous DNA sequences permits the display of related genes and their products on the phage surface (58, 59). Moreover, the protein or peptide maintains its ability to recognize molecular targeted binding sites (60). In 1985, Smith pioneered the phage display technique, fusing the restriction endonuclease EcoR I with the PIII protein as a recombinant small coat protein (61). Subsequently, the shell proteins PVIII and PVI were also employed for phage display (62–64), with the innovative proposal of a dual display system (65). The M13 phages utilized in phage display can be classified into

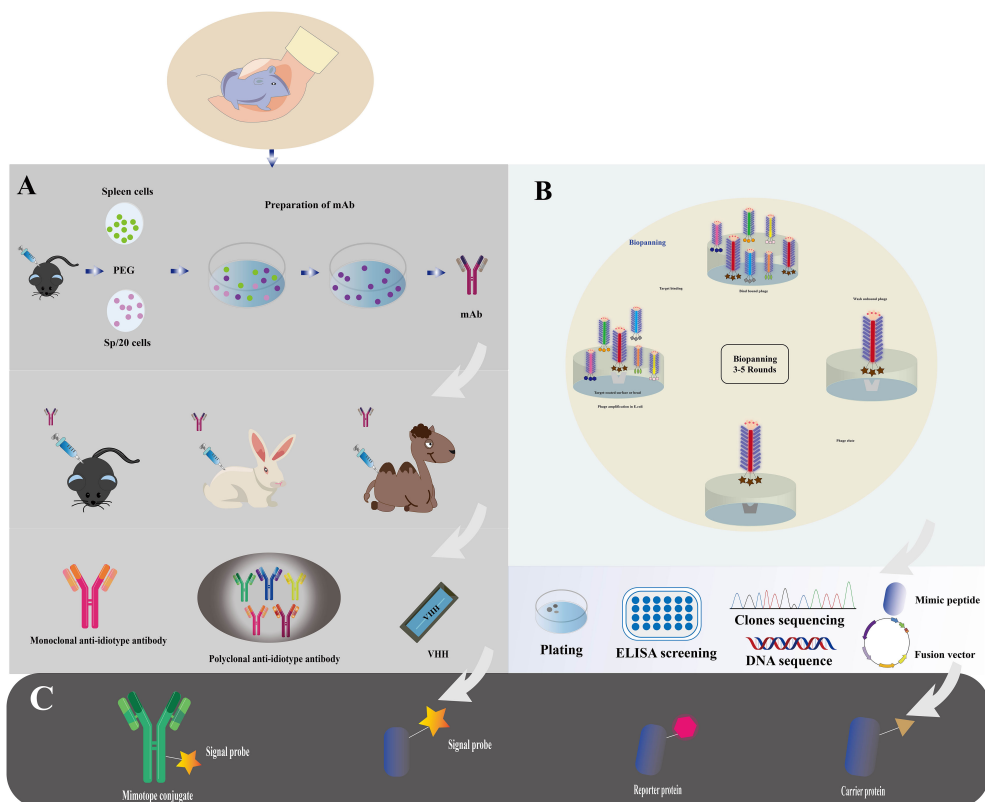


FIGURE 2

Immunosensor mimotope preparation schematic diagram. The preparation of mimotopes for use in immunosensors typically involves immunization or biopanning to obtain the mimotopes. Anti-idiotype antibodies can be prepared through immunization (A), while mimotope peptides can be obtained through phage biopanning (B). To expand their applications, mimotopes can be conjugated with signal probes or fused with reporter proteins and carrier proteins (C). This can enhance the sensitivity and specificity of the immunosensor. The schematic diagram for the preparation of mimotopes includes the steps of selection, amplification, and preparation of single-strand DNA (Adapted from [44]).

different carriers, including 3 + 3, 6 + 6, and 8 + 8 types. Phage vectors are primarily categorized into type 3/8 and type 33/88 vectors based on the number of displayed exogenous peptides (66). Phage display technology, renowned for its remarkable specificity and sensitivity, finds extensive application in nano immunosensor development for toxin detection. This versatile tool excels in epitope mapping and identifying mimotopes for diverse antigens. In essence, phage display technology stands as a potent approach for crafting highly specific and sensitive nano immunosensors, revolutionizing cholera toxin detection in water sources.

Phage display technology has revolutionized protein engineering and drug discovery. Among the most common type are random peptide libraries, showcasing millions of epitopes that aid in identifying specific binding peptides for various targets, including microorganisms, organ tissues, and nanoparticles (67). Biopanning enables the selection of peptides with high affinity and selectivity towards their targets (68). The advancement of cyclic peptides has further bolstered the technology, yielding peptides with enhanced stability and bioactivity. Notably, commercial libraries like the Ph.D-12 and Ph.D-7 phage display peptide libraries have been established, while chemical modifications can augment their

abundance (69). The construction of diverse phage libraries has provided a cornerstone for biological panning of targeted binding peptides, holding tremendous potential in disease diagnosis and treatment. Additionally, chemical modification of commercial libraries facilitates the creation of phage libraries with desired abundance without genetic recombination (70). The vast repertoire of random peptide libraries, with tens of millions of epitopes, plays a vital role in disease diagnosis and treatment (71). Biopanning allows for the selection of specific binding peptides against a myriad of targets, including microorganisms like cancer cells (72–74), bacteria, viruses (75, 76), organ tissues (77), and even nanoparticles (78). Balmforth et al. (79) harnessed phage display to identify two antibody mimics, anti-cholera toxins Affimer (ACTA)-A2 and ACTA-C6, demonstrating their non-covalent binding to the unbound plane of the B subunit of cholera toxin. This discovery showcased the selective *in vivo* delivery of Affimers to motor neurons, paving the way for the development of non-viral motor neuron drug delivery vectors. Furthermore, the establishment of various phage libraries, including random peptide libraries, antibody phage libraries, cDNA phage libraries, among others, underpins the biological panning of targeted binding peptides (80).

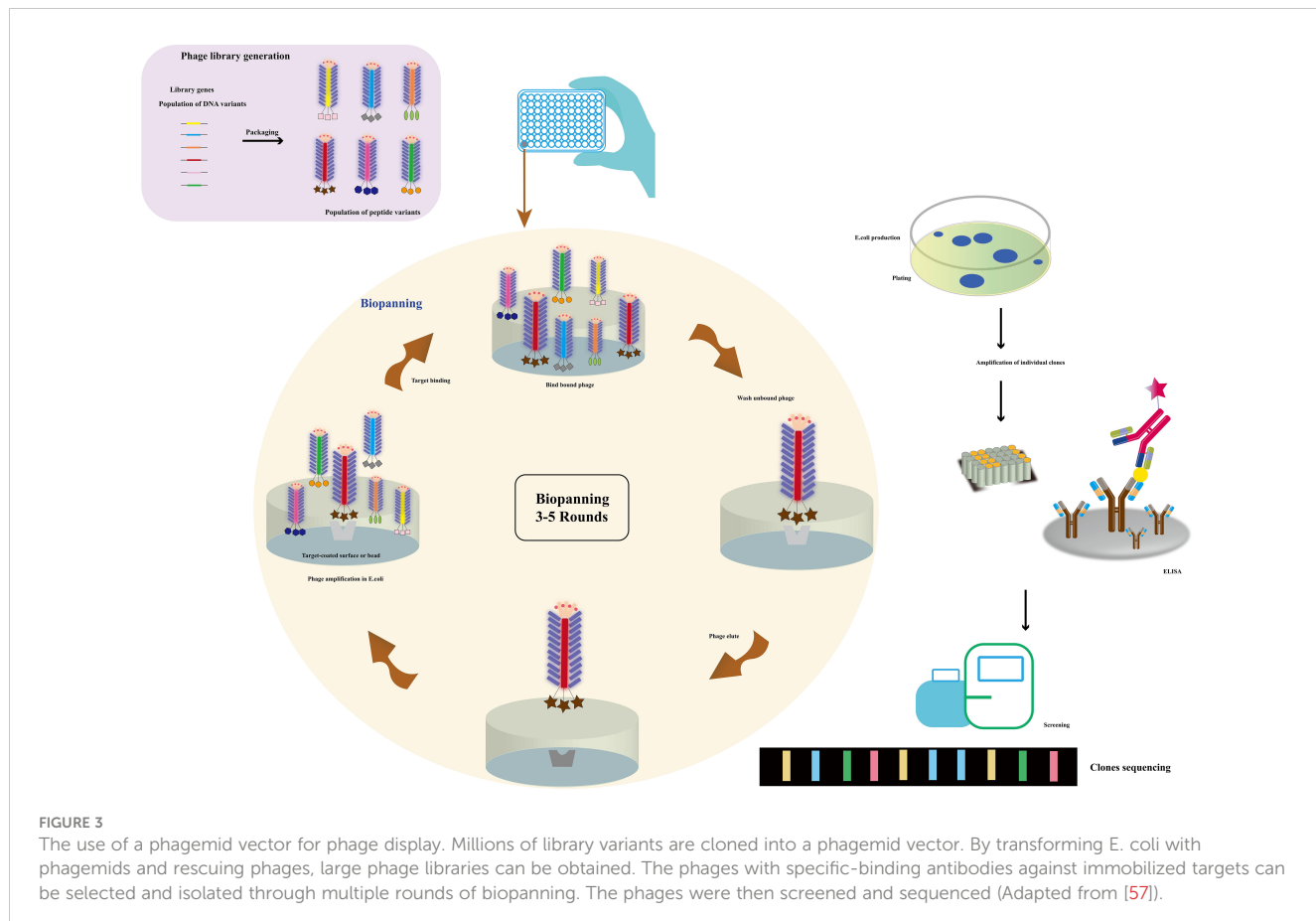


FIGURE 3

The use of a phagemid vector for phage display. Millions of library variants are cloned into a phagemid vector. By transforming *E. coli* with phagemids and rescuing phages, large phage libraries can be obtained. The phages with specific-binding antibodies against immobilized targets can be selected and isolated through multiple rounds of biopanning. The phages were then screened and sequenced (Adapted from [57]).

Structure and life cycle of phage M13

Phage M13, a filamentous bacteriophage, exhibits a diameter of 6.5 nm and a length of approximately 1000 nm (81). Its structure encompasses a single-stranded DNA genome enclosed in a protein tube comprising about 2700 copies of the PVIII molecule. Additionally, four minor coat proteins, each with 5 copies, namely PIII, PVI, PVII, and PIX, are present (82) (Figure 4A). Diverging from other phages, filamentous phages do not cause bacterial host lysis and primarily rely on F pili to infect *Escherichia coli* (84, 85) (Figure 4B). During infection, major coat proteins detach from the phage particles and are deposited in the host, while the single-stranded DNA (ssDNA) enters the cells and undergoes conversion into a double-stranded replication form. The progeny DNA replicates via a rolling cycle mechanism and assembles into a cell core protein complex with the viral replication assembly protein gp5. With the aid of host proteins, the virions are extruded through the membrane. Subsequently, the replication assembly proteins, which cover and protect viral DNA inside the cell, are replaced by coat proteins in the cell membrane to cover and protect viral DNA outside the cell. Ultimately, the virions are extruded through the membrane with the assistance of host proteins (86). The targeted proteins play a crucial role in expressing five structural coat proteins, where each of them has one side inserted into the bacterial inner membrane, facilitating the assembly of progeny particles. Notably, on a phage particle, units comprising five

proteins form a banded arrangement that encases the DNA (87). Among these coat proteins, g3p and g8p are of particular significance in the cloning and detection of recombinant phage antibodies and peptides. Typically, both g3p fusion proteins are expressed on the tip of phage M13 (88).

Phage display to prepare simulated peptides

Phage display technology enables the cost-effective screening of novel mimicking peptides through phage peptide libraries (Figure 3). Using the primary antibody corresponding to the antigen as the ligand for phage display biopanning, specific phage peptides can be obtained after several cycles of affinity biopanning. These peptides simulate the amino acid epitopes and physical and chemical properties of the corresponding antigens. Through multiple rounds of biopanning, unbound phages are washed out, and the specific phage is eluted for further amplification. After 3–5 cycles of affinity biopanning, the specific phage peptides are obtained, followed by DNA sequencing and analysis for further characterization (89). The specific phages obtained through panning can simulate not only the amino acid epitopes but also the physical and chemical properties of the corresponding antigens (90). Utilizing the ph.D-12/ph.D-7 phage display peptide library kits, novel peptides that bind to the anthrax toxin receptor (ATR)

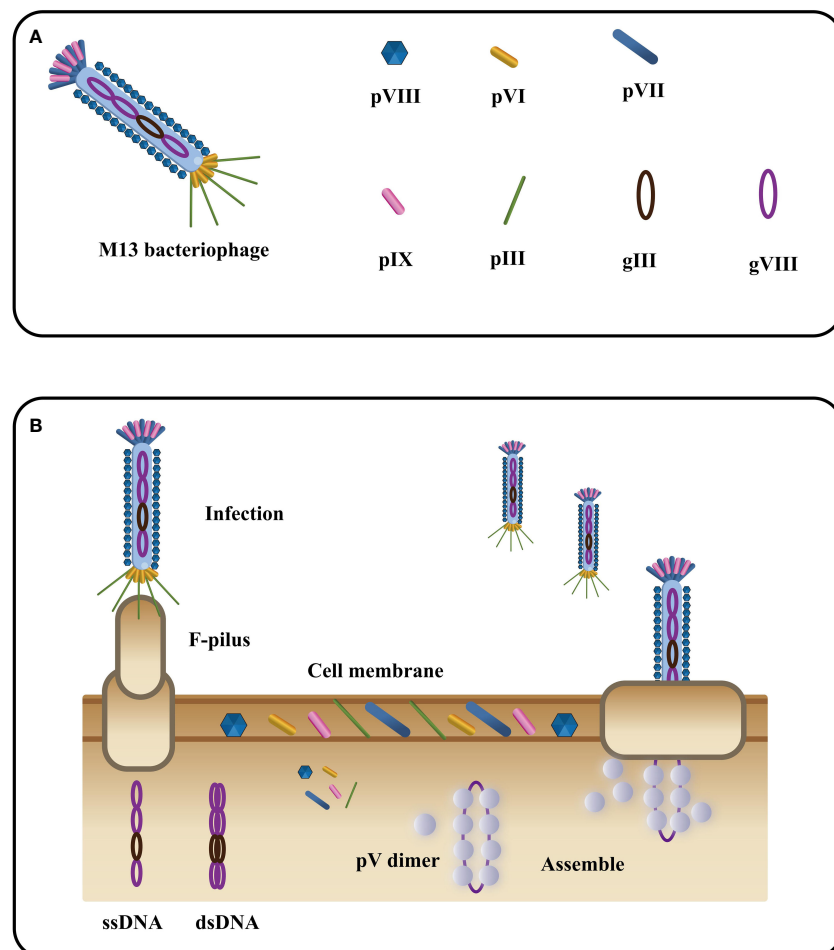


FIGURE 4
The filamentous bacteriophage's basic structure (A) and life cycle (B) (Adapted from [83]).

with high affinity and specificity have been identified, showing potential for neutralizing anthrax toxicity in cells. Lee, Sang-Choon and colleagues (91) used phage display to select ATR-binding peptides, resulting in the discovery of two novel peptides with high affinity and specificity that could neutralize anthrax toxicity in cells. Phage display technology is widely employed for the production of recombinant antibodies (RABs), where a specific peptide is displayed on the surface of a filamentous phage particle through fusion between the gene encoding the antibody and the coat protein (pIII or pVIII). The process involves exposing the antigen-coated surface to a phage library, followed by rigorous washing to remove antibody-bound phages, which are then re-amplified by infecting *E. coli*. This amplification and washing cycle is repeated, with an increase in specifically bound phages expected after each round. After several rounds of washing and amplification with *E. coli*, antigen-specific antibody phages can be examined using various methods (92). The substitution of mimotopes for toxins offers significant advantages in enhancing laboratory and environmental safety. Phage display technology enables rapid and cost-effective amplification and purification of mimotopes, making it a practical alternative to complete antigen synthesis. Moreover, the use of self-made phage display peptide libraries provides a cost-

effective approach to generate mimotopes specifically targeting the desired antigen (93, 94). This method holds immense potential for a wide range of applications, including disease diagnosis and treatment, drug discovery, and the development of toxin-free immunoassays. By leveraging phage display technology for mimotope production, researchers can explore novel avenues for safer and more efficient research and application in various scientific fields.

Preparation of anti-idiotype antibody

The concept of anti-idiotype antibodies, initially proposed by Jerne in 1974 as part of his “immune network theory” (95), has opened new possibilities for antigen detection. These antibodies mimic the spatial structure and biological activity of an antigen, allowing them to specifically bind to idiotypic antibodies (96). The preparation of anti-idiotype antibodies includes monoclonal, polyclonal, and nanobodies, offering a more stable conformation and enhanced environmental resistance compared to mimotope peptides. This promising attribute positions them as an attractive antigen alternative for the development of harmless immunoassays.

(97, 98). With their unique characteristics, anti-idiotype antibodies represent a significant advancement in immunosensor technology for safer and more reliable detection methodologies. The use of polyclonal antibodies (PABs) and monoclonal antibodies (Mabs) has been limited in simulating small haptens due to their large flat recognition surface (99). However, recent advancements have led to the emergence of nanobodies, derived from camels without light chains, offering immense potential for generating anti-idiotype antibodies. These nanobodies exhibit a smaller size, high solubility, thermostability, chemical stability, and suitability for genetic manipulation, making them a remarkable substitute in immune sensing. Notably, their variable domains can bind to antigens without domain pairing (100–103). Nanobodies, such as single-chain fragment variable antibodies (scFv) and variable domain of the heavy chain of the heavy-chain antibody (VHH), offer distinct advantages over conventional antibodies due to their smaller size (Figure 5). These compact nanobodies exhibit remarkable properties, including high solubility, thermostability, and chemical stability, making them exceptionally well-suited for genetic manipulation (104). As a result of these favorable characteristics, nanobodies have gained widespread recognition and have been extensively utilized in the development of toxin-free immunoassays (105). In a study conducted by Caixia Zhang et al. (106), two distinct anti-idiotypic nanobodies were isolated against OTA-specific monoclonal antibodies (mAb). Through careful examination of the primary structure, the researchers identified alterations in the complementary determining regions (CDRs). Notably, modifications were observed in CDR1, CDR2, and CDR3. The findings revealed that these anti-idiotypic nanobodies exhibited the potential to enhance the sensitivity of immunoassays. Leveraging these nanobodies as a safe substitute for conventional synthetic toxic antigens, the researchers successfully established an ELISA method that ensures both safety and efficacy.

Functionalization of nano immunosensors

In most cases, immunosensor mimotopes are strategically labeled or fused with signal probes and reporter proteins to achieve signal amplification or serve as effective tracers (Figure 6).

To further enhance the detection sensitivity, these immunosensor mimotopes can be labeled with biotin or composite probes. In a noteworthy study by Tong, Weipeng, et al. (107), a simulated peptide was obtained from a commercial phage display library, and to bolster sensitivity, biotin was introduced as a competitive antigen by modifying the main protein. The proposed method exhibited excellent linear detection within the range of 4.8 to 625 pg/mL, boasting an impressive detection limit (LOD) of 5.39 pg/mL. Remarkably, this LOD was approximately 26-fold lower than that of the conventional horseradish peroxidase (HRP)-based ELISA. Lu, Xin, et al. (108) have developed a remarkably sensitive electrochemical immunosensor utilizing phage display peptide derived from *Bacillus thuringiensis* protein. The targeted phage display peptide, obtained from the Ph.D.-12 phage display library, exhibited exceptional specificity, stability, and affinity. By integrating this selected peptide into the electrochemical immunosensor with a gold nanoparticle-modified electrode, they achieved impressive performance. The peptide-based immunosensor demonstrated a wide operating range of 0.01 to 100 ng/mL and an impressively low detection limit of 7 pg/mL. This innovative approach holds great promise for the ultra-sensitive detection of various proteins, opening up new possibilities for a range of applications. In a subsequent breakthrough, Mingyang Wang and their research team (109) introduced a screening strategy for VEGF members with a structural resemblance to VEGF165, considering its potential as a therapeutic target for various malignancies. Their aim was to significantly enhance the specificity of the selected phage monoclonal. Their efforts yielded a phage monoclonal expressing the peptide SPFLRLM, which displayed excellent affinity and specificity for VEGF165. Leveraging this specific phage-modified electrode, they successfully constructed a VEGF165 electrochemical impedance spectroscopy (EIS) immunosensor. Through meticulous optimization of experimental conditions, they achieved a linear range of 0.5–1000 pg/mL and a detection limit of 0.15 pg/mL. This phage-based EIS sensor holds promising prospects for applications in diagnostics and therapies, presenting a significant advancement in the field.

Nano immunosensors have emerged as a cutting-edge technology with tremendous potential for diverse applications,

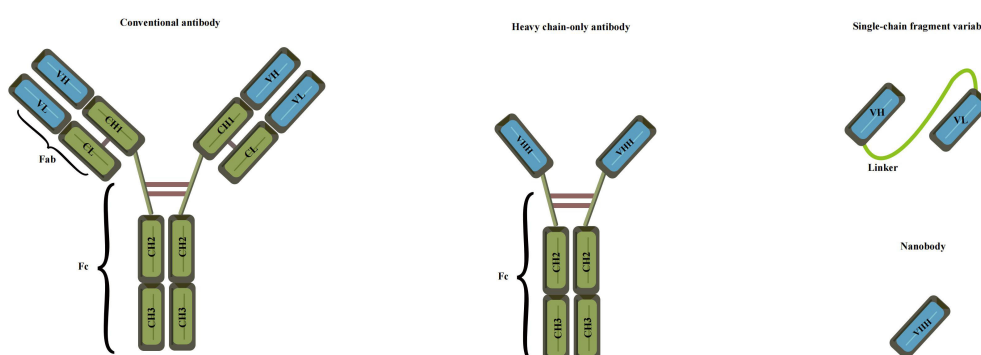


FIGURE 5
Various recombinant antibodies were compared to conventional antibodies (Adapted from [83]).

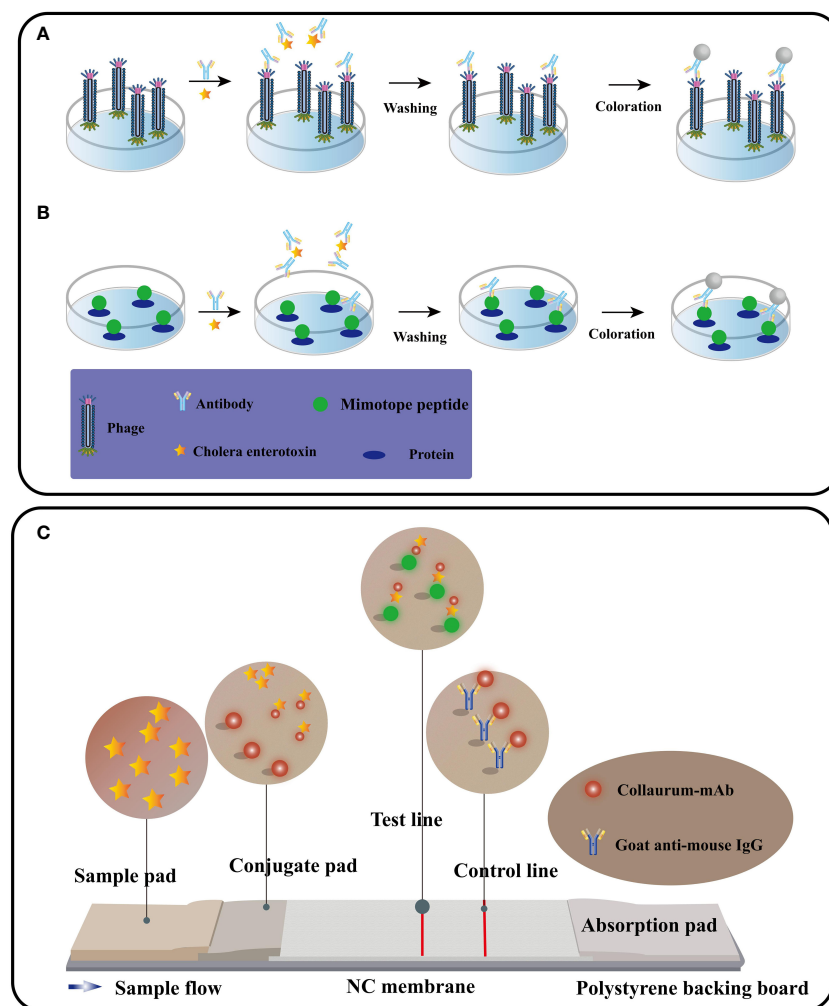


FIGURE 6

The procedure for performing competitive immunoassays using phage form (A) or peptide fusion protein (B). Immunochromatography schematic diagram (C) (Adapted from [83]).

including disease diagnosis, drug discovery, and environmental monitoring. Beyond the conventional methods of labeling or fusing with signal probes and reporter proteins, researchers have explored innovative ways to further enhance the performance of these sensors by functionalizing them with various nanomaterials. Gold nanoparticles (AuNPs), for instance, have proven to be valuable in modifying the electrode surface or serving as labels for the mimotope. Such modifications lead to improved sensitivity and stability of the immunosensor. Similarly, carbon nanotubes (CNTs) have been employed to enhance the electrode surface area and facilitate electron transfer, elevating the overall performance of the nano immunosensor. Additionally, other nanomaterials, including graphene oxide (GO), quantum dots (QDs), and magnetic nanoparticles (MNPs), have also been utilized for the surface modification of electrodes or labeling of mimotopes. By doing so, researchers have achieved heightened detection sensitivity and selectivity in these advanced immunosensors. The functionalization of nano immunosensors with diverse nanomaterials showcases a promising avenue to further enhance their capabilities and widen their scope of applications.

Application of nano immunosensors in the detection of cholera toxin

Nano immunosensors have gained widespread recognition as a valuable tool for cholera toxin detection, primarily due to their ability to obviate the need for competing antigens and tracers, streamlining the assay process and enhancing efficiency.

Cholera toxin detection based on immunosensor mimotopes

Cholera toxin, an AB5 toxin comprising A (CTA) and B subunits (CTB) (110), shares structural similarities with other toxins, such as *Escherichia coli* thermal instability toxin (111) or Shiga-like toxin (112). Consequently, when developing mimotopes for cholera toxin detection, meticulous attention must be given to ensuring their specificity. This crucial aspect safeguards against potential false-positive results arising from cross-reactivity with

similar toxins. Thus, stringent validation of the mimotopes is essential before practical implementation in the field (113). As delineated above, cholera toxin (CT) is a sophisticated protein complex consisting of A and B subunits. The B-subunit adeptly enters host cells by binding to ganglioside GM1, subsequently embarking on a journey to the endoplasmic reticulum. On the other hand, the A-subunit plays the role of an ADP-ribosyltransferase, catalyzing the transfer of ADP-ribose from NAD⁺ to specific target proteins. This enzymatic activity, orchestrated by the A1 chain of the A subunit, precipitates a cascade of events, culminating in the manifestation of watery diarrhea. Upon successful translocation of the A1 chain into the cytoplasm via the unfolded endoplasmic reticulum, a remarkable evasion from proteasomal degradation ensues. Swiftly, the A1 chain finds its equilibrium, resuming its role as a potent ADP-ribosyltransferase. Herein lies the crux of its toxicity, as the ADP-ribosylation of the heterotrimeric G protein G_sα ensues. This relentless activation of adenylate cyclase fuels an unprecedented surge in intracellular levels of cyclic AMP (cAMP). Within intestinal cells, the expeditious surge in cAMP production orchestrates chloride secretion, inevitably triggering substantial water loss. The profound consequence manifests as the hallmark symptom of cholera: relentless, watery diarrhea (114).

The use of immunosensor mimotopes as recognition components has gained significant traction owing to their ability to overcome limitations while seamlessly integrating into pharmaceutical processes (115). These unique components possess the capacity to spontaneously self-assemble into specific nanostructures through non-covalent interactions, rendering them ideal molecular elements for constructing cutting-edge detection platforms (116). For instance, a remarkable breakthrough came from the research team led by Jong Min Lim (117), who harnessed the power of M13 phage display to develop an affinity peptide specifically targeting the B subunit of *Vibrio cholerae*. Rigorous evaluations employing ELISA confirmed the robust binding affinity, while local surface plasmon resonance (LSPR) and surface-enhanced Raman spectroscopy (SERS) were employed to meticulously assess the performance of the prepared biosensors. Impressively, the LODs achieved by LSPR and SERS were recorded as 1.89 ng/mL and 3.51 pg/mL, respectively. The sensor stands as a non-labeling, non-interference solution for the sensitive detection of cholera toxin, presenting a solid foundation for cholera monitoring and control. In a similar vein, Alejandro D. Montaner's research team made noteworthy strides by identifying small peptides capable of binding to GM1 through the phage display of random peptides, with a focus on exploring their immunogenicity through chemical coupling (118).

Cholera toxin detection based on phage-ELISA

An exemplar application of immunosensor mimotopes in toxin detection lies in the novel cholera toxin (CT) assay, accomplished through phage-ELISA. Traditionally, competitive antigens are indispensable for immunoassays targeting small molecules,

necessitating the laborious synthesis of substantial quantities of these toxic small-molecular toxins. Leveraging mimotopes in immunoassays can circumvent the utilization of such hazardous compounds. In comparison to alternative analytical methods, immunoassays offer numerous advantages for rapid detection, boasting heightened sensitivity, augmented specificity, and simplified sample preparation (119). The inherent diminutive size of specific toxin mimotopes presents a challenge in their direct fixation to solid surfaces for immunoassays. Instead, these simulated peptides are ingeniously conjugated with specific proteins to generate fusion proteins amenable for immunoassays (120). A direct and effective approach involves utilizing M13 phages as coated antigens, in conjunction with the specific mimotope. Among the diverse immunoassay techniques, ELISA stands as a widely employed method for toxin detection. Consequently, employing specific mimotopes as antigen-coated phages within ELISA (phage-ELISA) presents a feasible and promising avenue (121). The mimotope, initially selected from a phage display library, underwent biotinylation for subsequent use as a competing antigen in the ELISA assay. To ensure specific recognition by the anti-CT monoclonal antibody, the mimotope was ingeniously fused to the p3 protein of the M13 phage. Detection of the biotinylated mimotope was achieved through the application of streptavidin-labeled polymeric horseradish peroxidase (HRP). Remarkably, this phage-ELISA approach exhibited remarkable sensitivity, boasting a detection limit of 0.05 ng/mL, surpassing traditional ELISA methods by 200-fold. By employing mimotopes in phage-ELISA assays, this method not only ensures enhanced sensitivity but also offers a safer and more efficient alternative, obviating the necessity for toxic small-molecule toxins.

Mimotopes have ushered in a revolutionary era in toxin detection, introducing a safer and more efficient alternative to conventional methods. Leveraging mimotopes within phage-ELISA assays has been scientifically demonstrated to augment sensitivity while concurrently reducing the reliance on toxic small-molecule toxins. Zhuolin Song and his accomplished team have engineered a groundbreaking ochratoxin A (OTA) assay using phage-ELISA, boasting an exceptional detection limit of 2.0 pg/mL (122). The pivotal element of this assay involves a simulated peptide meticulously screened from the M13 phage library, meticulously biotinylated, and subsequently employed as a competing antigen. Additionally, a heptapeptide simulated epitope, ingeniously fused to the p3 protein of M13, provided targeted recognition of the anti-OTA monoclonal antibody. By modifying the capsid p8 protein with biotin molecules, the team aptly loaded streptavidin-labeled polymeric horseradish peroxidase (HRP). Exhibiting remarkable sensitivity, this approach impressively outperforms traditional ELISA methods with an OTA detection limit 250 times lower. Furthermore, the integration of mimotopes has opened doors to the use of colloidal gold test strips, a rapid and cost-effective toxin detection method. Furthermore, Weihua Lai and colleagues have spearheaded the development of colloidal gold test strips tailored for OTA detection, culminating in an impressive detection limit of 10 ng/mL (123). Through meticulous panning from a random pool of seven-peptide phages, a transformative test paper was fashioned, ingeniously circumventing the problem of toxicity arising from

direct toxin usage. By harnessing the potential of mimotopes within multi-immunoassay systems, efficiency, cost-effectiveness, and sensitivity in toxin detection can be markedly enhanced. Indeed, the incorporation of mimotopes in toxin detection presents a promising pathway towards elevating the safety and efficacy of toxin detection methodologies.

Cholera toxin detection based on single-strand fragment variable antibody

In the realm of cholera toxin detection, the utilization of single-strand fragment variable (ScFv) antibodies emerges as a beacon of promise. ScFv epitomizes a recombinant protein formed by the fusion of the variable heavy chain region (VH) and variable light chain region (VL) of the antibody through a short peptide linker (124) (Figure 5). This strategic design imbues ScFv with a trifecta of virtues: a petite structure, enhanced permeability, and remarkable affinity. Owing to its diminutive molecular weight, formidable permeability, and exceptional affinity, scFv has garnered extensive usage in diverse domains, spanning tumor treatment (125), infectious disease prevention (126), and the detection of food safety residues (127). The advent of phage display as a remarkably efficient *in vitro* selection technique has positioned scFv as a compelling alternative to conventional antibodies. Through judicious mutation strategies, the affinity of scFv can be substantially augmented (128). This enhancement was vividly elucidated by the meticulous investigation of Lakzaei et al. (129), wherein they judiciously compared three distinct strategies: soluble antibody capture, PH step elution, and conventional panning, ultimately enriching specific antibody clones targeting diphtheria toxin. Fifteen phage ScFV-positive clones against diphtheria toxin were successfully isolated using the soluble antibody capture method. Conventional panning and PH step elution techniques yielded 9 and 5 positive phage ScFV clones, respectively. The soluble scFv fragments exhibited neutralizing activity ranging from 0.15 to 0.6 µg against the cytotoxic dose of diphtheria toxin, underscoring the effectiveness of soluble antibody capture in isolating specific scFv fragments. Embracing ScFv antibodies holds promise in enhancing the sensitivity and specificity of cholera toxin detection. Subsequently, Maryam Alibeiki et al. (130) employed a phage display library to select numerous antibody clones targeting clostridium perfringens toxin ETX. The enrichment of anti-ETX-specific clones was achieved through binding to immobilized antigens, followed by elution and phage proliferation. After multiple rounds of binding selection, ELISA analysis confirmed the high affinity and specificity of the isolated clones for ETX. In a recent study, Shadman et al. (131) successfully identified novel single-chain fragment variable (scFv) antibodies against the *Pseudomonas aeruginosa* exotoxin A domain I (ExoA-DI) from a human scFv phage library. To achieve this, the recombinant ExoA-DI of *Pseudomonas aeruginosa* was expressed in *Escherichia coli* and subsequently purified using a Ni-NTA column for the screening process of the human antibody phage library.

The development of recombinant antibodies against toxins through phage display technology presents a promising avenue for diagnosing and treating infections. The screening of human antibody phage libraries allows for the discovery of antibodies from naive antibody gene banks, which in turn can be utilized to create novel therapeutic agents targeting toxin-related diseases. A new screening procedure has been devised to prevent the elimination of rare specific clones, enabling the identification of highly reactive phage clones. In the case of exotoxin A from *Pseudomonas aeruginosa*, the purified scFv antibodies demonstrated remarkable specificity and reactivity with both the recombinant domain I and the full-length natural exotoxin A. This exciting finding lays the foundation for the potential development of new therapeutic agents to combat *Pseudomonas aeruginosa* infections. Altogether, phage display technology represents a powerful tool for the development of recombinant antibodies against toxins, revolutionizing the diagnosis and treatment of infectious diseases (132, 133).

Cholera toxin detection based on immunosensor anti-idiotype antibody

The anti-idiotype antibody, located in the variable region of the immunoglobulin with specific antigenic determinants, serves as a secondary antibody targeting a particular type of primary antibody (134, 135). Numerous anti-idiotypic antibodies have been developed, effectively targeting both large and small molecules, and have found applications in diagnosis and immunoassays (136–138). A captivating discovery was made in 1993 when camelidae antibodies were found to possess no light chains, comprising solely heavy chain antibodies. These unique antibodies feature a single variable domain (VHH) forming the variable domain (VH), giving rise to what is known as a nanobody. Notably, camel immune VHH libraries can be cloned using the M13 phage display vector. The M13 phage display vector, commonly employed for cloning such libraries, facilitates the generation of heavy chain-only antibodies lacking light chains. The V-domains from these antibodies are amplified from cDNA derived from lymphocytes found in peripheral blood, lymph nodes, or spleen of an immunized animal, subsequently cloned into the phage vector. Following transfection into *Escherichia coli* and infection with a helper phage, a library of recombinant phage particles can be harvested from the supernatant (Figure 7). Given their small size and ease of manipulation, anti-specific nanobodies have emerged as valuable tools for diagnostic and therapeutic purposes (140–143). Moreover, anti-idiotypic antibodies have found utility beyond their traditional applications, extending to immunoassays targeting small molecules. An illustrative example is the anti-idiotypic nanobody-phage display-mediated immuno-polymerase chain reaction method, enabling simultaneous quantitative detection of multiple toxins. In a recent investigation conducted by Dong, Sa et al. (144), anti-Cry1A polyclonal antibodies were employed as antigens to screen for anti-variant antibodies capable of mimicking the Cry1A toxin, using a phage display human domain antibody library. Following four rounds of biopanning, five positive clones

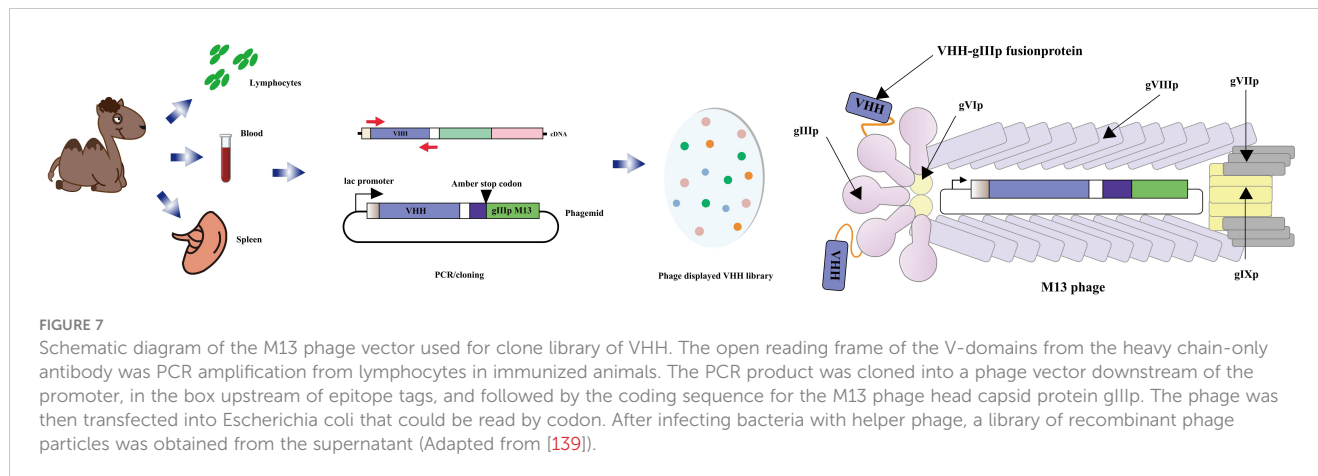


FIGURE 7

Schematic diagram of the M13 phage vector used for clone library of VHH. The open reading frame of the V-domains from the heavy chain-only antibody was PCR amplification from lymphocytes in immunized animals. The PCR product was cloned into a phage vector downstream of the promoter, in the box upstream of epitope tags, and followed by the coding sequence for the M13 phage head capsid protein gIIIp. The phage was then transfected into *Escherichia coli* that could be read by codon. After infecting bacteria with helper phage, a library of recombinant phage particles was obtained from the supernatant (Adapted from [139]).

exhibiting binding activity were identified, with clone D6 displaying a remarkable inhibitory effect on the binding of Cry1A toxin and anti-Cry1A polyclonal antibodies. D6 was characterized as a subtype anti-idiotypic antibody, proficient in mimicking Cry1A toxin and competitively binding to anti-Cry1A polyclonal antibodies. Intriguingly, bioassay results demonstrated that D6 possessed discernible insecticidal activity. The study lays a foundation for the development of toxin simulators, offering promising applications in the domains of agriculture and environmental protection.

Notably, Xu, Chongxin, et al. (145) have achieved a significant breakthrough in the field of toxin monitoring by developing a highly sensitive anti-microcystin single-chain variable fragment (scFv). The application of this scFv in an established ELISA showcased promising prospects for ultra-sensitive detection in water samples. Besides competitive immunoassays, innovative nanobody-based methods have also emerged, among which the phage display mediated immunopolymerase chain reaction (PD-IPCR) technique deserves special mention. PD-IPCR harnesses recombinant phage particles as readily available reagents for IPCR, obviating the need for conventional monoclonal antibodies (146), as shown in Figure 8. This technique exhibits tremendous potential as an ultra-sensitive assay for small molecules, rendering it a valuable tool for monitoring toxins in both environmental and clinical samples. Furthermore, Rezaei, Zahra S. et al. (147) have made strides in the detection of vascular endothelial growth factor (VEGF) by developing a precise PCR-conjugated phage display system using VHH nanobodies. This innovative approach, known as PD-IPCR, presents new avenues for VEGF detection, highlighting the versatility and potential of nanobody-based methods in diagnostics and therapeutics. In a remarkable development, a novel system has been devised utilizing anti-VEGF monoclonal antibodies as specific binding agents within a sandwich immunosorbent assay platform. Strikingly, the same anti-VEGF phage particles that serve as anti-VEGF reagents in the PD-IPCR method also function as DNA templates simultaneously. During validation, the anti-VEGF phage ELISA exhibited an impressive linear range of 3–250 ng/ml, setting a new standard with a remarkable detection limit (LOD) of 1.1 ng/ml. By leveraging the PD-IPCR method, the linear range for VEGF expanded to an

unprecedented 0.06–700 ng/ml, with an astonishingly low detection limit of 3 pg/ml. Such an advanced method displayed commendable sensitivity, yielding a serum recovery rate of 83–99% and a relative standard deviation of 1.2–4.9%, thus rendering it highly suitable for clinical analysis. The method's practicality and efficacy were evident as it was successfully applied to the clinical determination of VEGF in human serum samples. Impressively, the results obtained showed a strong correlation with conventional ELISA findings. These significant findings underscore the immense potential of the PD-IPCR method, positioning it as a valuable tool for clinical diagnosis and other multifaceted applications in the realm of VEGF detection.

A groundbreaking study by Ren et al. has unveiled an innovative approach utilizing anti-idiotype nanobody-phage display mediated immunopolymerase chain reaction for the simultaneous and quantitative detection of total aflatoxin and zearalenone in cereals (148). Impressively, this method exhibited exceptional sensitivity and specificity, boasting a linear range of 0.01–100 ng/mL for zearalenone (ZEN). Similarly, Xianxian Wang et al. have made substantial strides by developing a highly sensitive and specific immunoassay for the quantitative determination of ZEN, employing the anti-idiotype variable domain of heavy-chain antibodies (VHH) PD-IPCR (149). Through four cycles of refinement, a remarkable anti-idiotype VHH phage clone was isolated, and the LOD of PD-IPCR based on the VHH phage stood at an astonishing 6.5 pg/mL, surpassing phage ELISA by approximately 12-fold. The promise of high throughput analysis in practical applications became evident with the successful application of this method in ZEN detection of grain samples using liquid chromatography-tandem mass spectrometry (LC-MS/MS). These groundbreaking studies collectively underscore the immense potential of anti-idiotype PD-IPCR methods, offering a gateway to ultra-sensitive mycotoxin detection in cereals. The utilization of PD-IPCR not only enhances sensitivity and expands the linear range compared to phage ELISA but has also been verified for ZEN detection in grain samples through LC-MS/MS validation. In addition to PCR-based analysis, loop-mediated isothermal amplification (LAMP) represents another cutting-edge technique for the rapid and simple detection of target nucleic acids (150). The impact of this groundbreaking method is evident in a myriad of diagnostic fields, including bacterial, viral, and parasitic pathogen

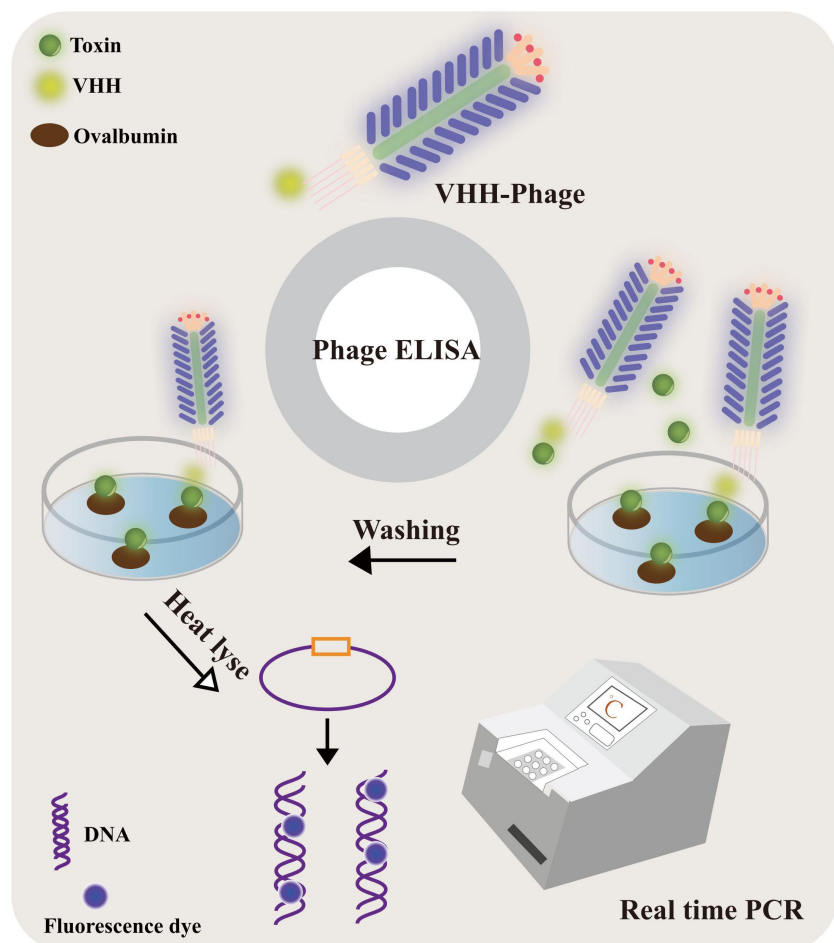


FIGURE 8

The VHH-phage-based PD-IPCR process. VHH-phages and toxin were mixed and incubated with ovalbumin-conjugated toxin precoated on a solid surface. The VHH-phage with toxin was washed out and the excess VHH-phage was fixed. The VHH-phage DNA was released by heat lysis as a template for real-time PCR.

detection (151, 152), as well as disease diagnosis (153). Among the innovative adaptations of the loop-mediated isothermal amplification technique, the immunolamp (iLAMP) assay has emerged as a particularly promising tool for toxin detection. Renowned for its specificity, visual identification capabilities, and isothermal amplification, the iLAMP assay follows a well-defined procedure. It involves applying antitoxin monoclonal antibodies to the base of a glutaraldehyde-treated PCR tube, followed by the addition of the sample extract and anti-idiotype nanobody phage to the tube. Following the reaction, unbound phage is meticulously removed, and the LAMP solution is introduced to the test tube for the amplification process. With encouraging results in toxin detection, the iLAMP assay holds significant potential as a rapid and straightforward detection tool across diverse fields of application.

In a groundbreaking study led by Chen Dailing et al. (154), the rapid detection of virulence-related genes in *Vibrio cholerae* (ace, zot, cri, and nanH) was achieved using the highly efficient Loop-mediated Isothermal Amplification (LAMP) visualization method. To accomplish this, the researchers designed and synthesized three

pairs of molecular probes for each gene. Positive results were readily identified by the development of a vibrant green color under visible light or green fluorescence under ultraviolet light (302nm). Remarkably, the LAMP method exhibited detection limits ranging from 1.85 to 2.06 pg per genomic DNA response, surpassing the sensitivity of standard PCR. These results highlight the potential of LAMP as an effective and sensitive tool for the rapid detection of *Vibrio cholerae* and its associated virulence factors. Another notable adaptation of LAMP, the immunolamp (iLAMP) assay, has emerged as a powerful approach for toxin detection, owing to its specificity, visual identification capability, and isothermal amplification. The fundamental procedure involves coating the bottom of a glutaraldehyde-treated PCR tube with antitoxin monoclonal antibodies (mAb), followed by the addition of sample extract and anti-idiotype nanobody phage to the test tube. These nanobody phages effectively mimic antigens (toxins) in the immune response, resulting in competition between phages and toxins for binding to mAb. After the reaction, unbound phages are meticulously removed through a washing step, and the LAMP solution is introduced to the test tube for the subsequent

amplification process. As a consequence, if the sample contains toxins, the mixture in the tube retains a distinctive purple color (indicating a positive result); otherwise, it turns sky blue (indicating a negative result) (155) (Figure 9). This approach holds remarkable potential for the rapid and straightforward detection of toxins, making it a valuable tool in various fields, including food safety and environmental monitoring.

Simultaneous determination of multiple cholera toxins

Currently, a diverse array of technologies is available for the detection of biotoxins, encompassing chromatography, immunochemical determination, and electrochemical methods (156–158). Notably, multiple immunochromatography (mICA) strips have been devised to enable simultaneous monitoring of multiple toxins (159). These innovative strips utilize various small molecular toxins or antibody-conjugated fluorescent nanoparticles, such as colloidal gold particles (160), fluorescent microbeads (161), and carbon nanoparticles (162). In light of the importance of efficient surveillance of freshwater sources, the electrospray ionization (ESI) liquid chromatography-mass spectrometry (LC-MS) technique has emerged as a formidable tool for biotoxin detection. In parallel, the development of a multiplex lateral flow immunoassay (LFA) has proved instrumental in the detection of primary marine biotoxin groups, including amnesic shellfish poisoning. Lastly, notable strides have been made in the development of multiple immunoassays targeting diverse biotoxins through the implementation of immunosensor mimotopes. This approach holds tremendous promise for the creation of more efficient and accurate detection methods specifically tailored for cholera toxin detection. These advancements signify significant progress in the field of biotoxin detection, paving the way for enhanced diagnostic capabilities and improved safety measures.

Immunoassay flow chromatography based on immunosensors

An immunoassay flow chromatography utilizing immunosensor mimotopes has emerged as a powerful method for the concurrent detection of multiple cholera toxins. Among the various screening platforms, immunochromatography (ICA) stands out as the most widely employed and well-established technique, offering advantages of simplicity, rapidity, stability, high throughput, ease of use, and cost-effectiveness (163) (Figure 6C). Central to ICA's functionality is the liquid test sample's flow, which interacts with the analyte through a strip containing antibodies, leading to the accumulation of a chromogenic substance that generates a readable signal (164). Presently, researchers are actively working on developing both single and multiple assays with conventional antibodies using ICA (Figure 10). The integration of immunosensor mimotopes in this approach holds tremendous promise to enhance the accuracy and sensitivity of the ICA method, positioning it as an invaluable tool for the detection of biotoxins across diverse fields, such as food safety and environmental monitoring. A series of recent studies conducted by Tong and his esteemed research team have been devoted to the development of innovative immunochromatography sensors for detecting zearalenone (ZEN), exhibiting excellent reproducibility and employing a bio-safe approach (166–168). Additionally, Yan, Jia-Xiang, and colleagues have made significant strides in creating a cost-effective and highly sensitive multiplex immunochromatographic assay (mICA) that allows for the rapid detection of fumonisins B-1 (FB1), zearalenone (ZEN), and ochratoxin A (OTA) (169). This groundbreaking mICA harnesses mimotopes of FB1, ZEN, and OTA from phage display technology, skillfully integrated with maltose binding protein (MBP) as simulated coated antigens applied to the mICA test line. Impressively, the visual detection limits achieved by this novel method are an astonishing 0.25 ng/mL for FB1, 3.0 ng/mL for ZEN, and 0.5 ng/mL for OTA, all within an impressive timeframe of merely 10 minutes. Subsequent testing using real-life samples has affirmed the method's accuracy, reproducibility, and practicality.

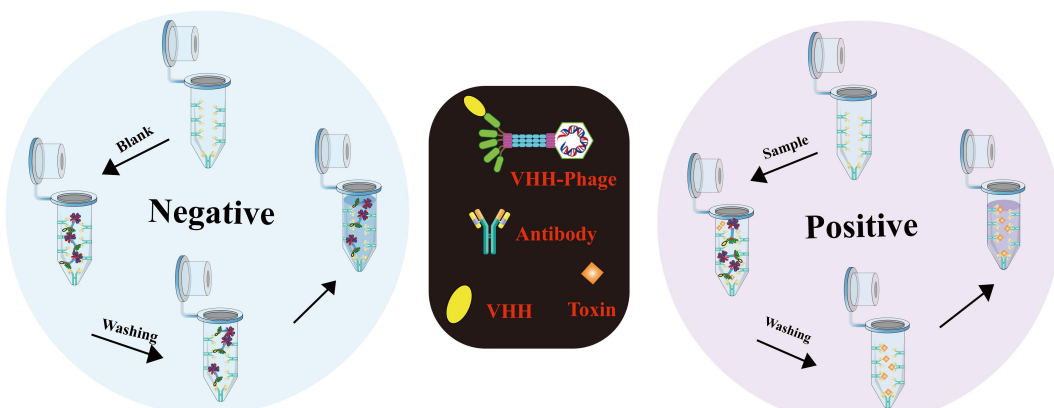


FIGURE 9
Detailed procedure for iLAMP detection (Adapted from [155]).

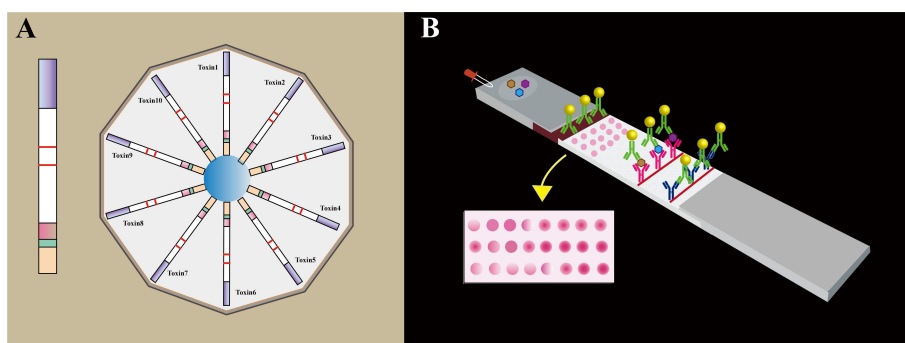


FIGURE 10

(A) The individual test strip for a single toxin by means of an antibody linked to a phosphorous probe. The 10 channels phosphorous probe-based lateral flow disc holds 10 detection channels (Toxin1 to Toxin10), each consisting of a single strip for the target toxin. (B) The schematic representation of the lateral flow microarray strip. Each of the 32 dots represents a distinct capturing agent (Adapted from [165]).

Notably, the proposed mICA technique has been demonstrated to yield results on par with those obtained from the widely regarded ultra-high-performance liquid chromatography combined with tandem mass spectrometry (UPLC-MS/MS) in detecting FB1, ZEN, and OTA using natural samples.

Multiple cholera toxins detection based on PD-IPCR

As discussed earlier, PD-IPCR represents an ultra-sensitive immunoassay for small-molecule biotoxin detection. Its remarkable sensitivity and specificity make it a highly promising solution for toxin detection across various domains, including food safety, environmental monitoring, and public health. Ren et al. (170) devised an innovative detection platform that integrates PD-IPCR and RT-PCR, enabling simultaneous detection of multiple toxins in stored corn. PD-IPCR, an ultra-sensitive immunoassay for small-molecule biotoxins, was combined with real-time PCR assays capable of detecting various genes, including the cholera toxin gene. This platform facilitated the concurrent detection of multiple toxins, while establishing a quantitative standard curve for comprehensive analysis. The detection limits were 0.02 ng/mL for aflatoxins and 8×10^2 spores/g for Aspergillus section Flavi, respectively. This method holds promise for simultaneous detection of small molecular pollutants and microorganisms, introducing novel perspectives in diagnostic and public health applications. The development of this detection platform has significant potential in simultaneously detecting small molecular pollutants and microorganisms, offering fresh insights for detection technology advancements. The capability to detect multiple toxins in one sample enhances detection efficiency, accuracy, and cost-effectiveness. This has profound implications in food safety, environmental monitoring, and public health. Continued progress in biosensors, chemosensors, and assays opens doors to innovative methods for screening and identifying other biotoxins.

Summary

Immunoassays play a crucial role in rapidly screening biotoxin residues in the environment for human health protection. However, their traditional approach involving large quantities of toxic biotoxins or complex chemical synthesis of coated antigens and tracers presents challenges. The chemical synthesis process suffers from drawbacks like intricate procedures, batch errors, low binding efficiency, and the use of organic solvents. As an innovative substitute, immunosensor mimotopes, such as simulated peptides and anti-idiotype antibodies, offer a safer option for these immunoassays. Utilizing phage display or monoclonal/polyclonal antibody technology, immunosensor mimotopes serve as competing antigens, tracers, or standard substitutes. They eliminate the need for toxic compounds and provide an eco-friendly analytical tool for biotoxin detection, addressing issues of batch errors, low binding efficiency, and organic solvent usage. Immunosensor mimotopes hold immense promise as reagents in the detection of cholera toxins.

Phage M13, widely used in mimotope biopanning, offers a versatile approach for detecting small analytes, including biotoxins, via M13 phage display technology. Construction of random peptide or recombinant antibody libraries facilitates the selection of alternative antigens or antibodies. The choice between libraries should consider specific application requirements, as each possesses distinct advantages and limitations. Random peptide libraries, simpler to construct, exhibit a broad epitope recognition range, including continuous and discontinuous sequences, allowing specific binding to various proteins or ligands. Conversely, recombinant antibody libraries offer higher affinity and specificity for the target analyte. In cholera toxin detection, the use of phage M13 in mimotope screening presents a powerful tool for alternative antigen or antibody development. Random peptide libraries demonstrate particular utility in detecting small antigens without bias. However, they may exhibit lower affinity, limiting certain applications. In such cases, recombinant antibody libraries become

a preferred choice, yielding antibodies with superior affinity. Thus, selection between random peptide and recombinant antibody libraries hinges on the specific needs of the intended application, ensuring optimal results for cholera toxin detection.

In practical applications, the detection of cholera toxins often involves using fusion proteins formed by coupling random peptides with other proteins, rather than single peptides or phages alone. Multifunctional phage display technology has enabled the development of versatile biosensors based on M13 phage for detection and analysis. Through surface modifications, M13 phage gains new characteristics, such as targeted binding ability, optical properties of quantum dots, and the accumulation of magnetic nanoparticles (171). These modifications make M13 phage an ideal platform for highly sensitive and selective biosensor development in cholera toxins detection, offering improved accuracy and efficiency. In contrast to random peptides, recombinant antibodies possess the advantage of direct fixation on both solid surfaces and antigens. Isolated from libraries, recombinant antibodies like scFvs and anti-idiotype antibodies find applications in sensitive diagnosis techniques such as ELISA, PD-IPCR, and iLAMP. Additionally, recombinant antibodies expand the scope of immunoassay agents, allowing for the detection of diverse biotoxins within the same group. The use of recombinant antibodies has led to simultaneous biotoxin detection based on phage display, showcasing their advantages, including enhanced specificity, increased sensitivity, shorter detection time, and improved safety. Recombinant antibodies represent a potent tool for the sensitive and specific detection of cholera toxins. In the quest for cholera toxin screening, researchers harnessed diverse resources, including antigens for antibody preparation, proteins, and antibody samples for immunomolecular sieving. Antigens, derived from animals, triggered immune responses, resulting in specific antibodies. To enhance affinity, an animal immune repository was utilized, spotlighting antibodies finely tuned to the toxin. Nanobodies, from animals like camels, featured compact size, stability, and genetic manipulability, becoming potent alternatives to conventional antibodies. Nanobodies played crucial roles, particularly in targeted antibody selection, mimicking toxin epitopes for precise immune analyses, thus serving as high-affinity substitutes. This integrated approach supported effective cholera toxin detection and analysis (172).

Despite the significant benefits offered by Immunosensor mimotopes in cholera toxins immunoassays, certain limitations persist. The preparation of mimicking peptides and anti-idiotype antibodies can be challenging, and the selection of mimotopes from phage display peptide libraries may encounter failure probabilities. Likewise, obtaining anti-idiotype antibodies from immune animals can also pose challenges. Overcoming these limitations requires expanding the diversity of peptide libraries and enhancing screening techniques for positive clones. Ongoing research to optimize conditions for mimotope selection and screening holds the potential to further improve their utility in cholera toxins detection. Despite the challenges, mimotopes present a promising avenue for the development of safe and effective immunoassays. While immunosensor mimotopes have shown promise in cholera toxins immunoassays, some reported mimotopes have demonstrated

only marginal improvements in assay performance. The use of phage display peptides can lead to complex procedures, and laboratory-synthesized mimotopes may lose binding activity in certain cases. To address these issues, further investigation into the structure of mimotopes and their interaction with receptors is essential. Site mutagenesis could be introduced to enhance the characteristics of mimotopes and optimize immunoassay performance.

This review delves into a pioneering avenue in the realm of cholera toxin detection: phage display-based nano immunoassays. Engineered bacteriophages, uniquely tailored with specific antibody fragments or mimotopes, exhibit an exceptional affinity for cholera toxin. This dynamic interplay orchestrates the generation of quantifiable signals, enabling remarkably sensitive detection and precise quantification. In the current landscape of cholera screening and detection, animals and animal-derived products play a significant role. Monoclonal antibody (mAb) based rapid diagnostic tests (RDTs) are employed, although their sensitivity is hindered by the presence of the common virulent bacteriophage ICP1 (172). A study explores phage-displayed mimotopes for a cholera vaccine, overcoming challenges posed by the toxic nature of lipopolysaccharide (LPS) (173). In contrast, phage display-based nano immunoassays emerge as an ethical and effective alternative (174). This innovative method demonstrates heightened affinity for cholera toxin, potentially transforming detection approaches, and reflecting the evolving landscape of efficient methodologies. This paradigm shift not only showcases the potential to revolutionize cholera toxin detection but also underscores its promise in advancing precision and efficacy in analytical methodologies (113, 173, 174).

Author contributions

YL: Conceptualization, Methodology. K-DY: Writing-Original Draft, Investigation. J-FY: Resources, Methodology. D-CK: Writing Review and Editing. All authors contributed to the article and approved the submitted version.

Funding

This study was supported by Scientific research project of Education Department of Jilin Province (No.JJKH20231194KJ); Scientific Research Project of Jilin Provincial Department of Finance (No.JLSWSRCZX2020-0030; No.JLSWSRCZX2021-074); Research Project of Undergraduate Teaching Reform in Jilin University(No.2021XZC087); Research Projects of Higher Education in Jilin Province(No.JGJX2021D53).

Conflict of interest

The authors declare that the research was conducted in the absence of any commercial or financial relationships that could be construed as a potential conflict of interest.

Publisher's note

All claims expressed in this article are solely those of the authors and do not necessarily represent those of their affiliated

organizations, or those of the publisher, the editors and the reviewers. Any product that may be evaluated in this article, or claim that may be made by its manufacturer, is not guaranteed or endorsed by the publisher.

References

1. Bina J, Zhu J, Dziejman M, Faruque S, Calderwood S, Mekalanos J. ToxR regulon of *Vibrio cholerae* and its expression in vibrios shed by cholera patients. *Proc Natl Acad Sci USA* (2003) 100(5):2801–6. doi: 10.1073/pnas.2628026100
2. Harris JB, LaRocque RC, Qadri F, Ryan ET, Calderwood SB. Cholera. *Lancet* (2012) 379(9835):2466–76. doi: 10.1016/s0140-6736(12)60436-x
3. Ali M, Lopez AL, You YA, Kim YF, Sab B, Maskery B, et al. The global burden of cholera. *Bull World Health Organization* (2012) 90(3):209–18. doi: 10.2471/blt.11.093427
4. Davis W, Narra R, Mintz ED. Cholera. *Curr Epidemiol Rep* (2018) 5(3):303–15. doi: 10.1007/s40471-018-0162-z
5. Mogasale V, Mogasale VV, Hsiao A. Economic burden of cholera in Asia. *Vaccine* (2020) 38:A160–6. doi: 10.1016/j.vaccine.2019.09.099
6. Mogasale V, Ngogoy SM, Mogasale VV. Model-based estimation of the economic burden of cholera in Africa. *BMJ Open* (2021) 11(3):e044615. doi: 10.1136/bmjjopen-2020-044615
7. Zingl FG, Thapa HB, Scharf M, Kohl P, Muller AM, Schild S. Outer Membrane Vesicles of *Vibrio cholerae* Protect and Deliver Active Cholera Toxin to Host Cells via Porin-Dependent Uptake. *Mbio* (2021) 12(3):e0053421. doi: 10.1128/mBio.00534-21
8. Perez-Reytor D, Jana V, Pavez L, Navarrete P, Garcia K. Accessory toxins of vibrio pathogens and their role in epithelial disruption during infection. *Front Microbiol* (2018) 9:2248. doi: 10.3389/fmicb.2018.02248
9. Philip CW, Cheung. A historical review of the benefits and hypothetical risks of disinfecting drinking water by chlorination. *J Environ Ecol* (2017) 8(1). doi: 10.5296/jee.v8i1.11338
10. Justin BN, Nataliya VB, Scott CK, Evan K, Eric K, Edward TL, et al. Aggregatibacter actinomycetemcomitans leukotoxin is delivered to host cells in an LFA-1-Independent manner when associated with outer membrane vesicles. *Toxins (Basel)* (2018) 10(10):414. doi: 10.3390/toxins10100414
11. Sack DA, Sack RB, Nair GB, Siddique AK. Cholera. *Lancet* (2004) 363(9404):223–33. doi: 10.1016/s0140-6736(03)15328-7
12. Usmani M, Brumfield KD, Jamal Y, Huq A, Colwell RR, Jutla A. A review of the environmental trigger and transmission components for prediction of cholera. *Trop Med Infect Disease* (2021) 6(3):147. doi: 10.3390/tropicalmed6030147
13. Deen J, Mengel MA, Clemens JD. Epidemiology of cholera. *Vaccine* (2020) 38: A31–40. doi: 10.1016/j.vaccine.2019.07.078
14. Baker-Austin C, Oliver JD, Alamo M, Ali A, Waldor MK, Qadri F, et al. Vibrio spp infections. *Nat Rev Dis Primers* (2018) 4(1):8. doi: 10.1038/s41572-018-0005-8
15. Bozdogan A, Seherler S, Ildeniz TAO, Anac I, Kok FN. Ieee. Surface plasmon fluorescence spectroscopy based biosensor for cholera toxin detection. *21st Natl Biomed Eng Meeting (BIYOMUT)* (2017) 18162107. doi: 10.1109/BIYOMUT.2017.8479292
16. Goel AK, Ponmariappan S, Kamboj DV, Singh L. Single multiplex polymerase chain reaction for environmental surveillance of toxigenic-pathogenic O1 and non-O1 *Vibrio cholerae*. *Folia Microbiologica* (2007) 52(1):81–5. doi: 10.1007/bf02932143
17. Keddy KH, Sooka A, Parsons MB, Njanpop-Lafourcade B-M, Fitchet K, Smith AM. Diagnosis of vibrio cholerae O1 infection in africa. *J Infect Diseases* (2013) 208: S23–31. doi: 10.1093/infdis/jit196
18. Dano EK, Asare P, Otchere ID, Akyeh LM, Asante-Poku A, Aboagye SY, et al. A molecular and epidemiological study of *Vibrio cholerae* isolates from cholera outbreaks in southern Ghana. *PLoS One* (2020) 15(7):e0236016. doi: 10.1371/journal.pone.0236016
19. Kumar V, Turnbull WB. Carbohydrate inhibitors of cholera toxin. *Beilstein J Organic Chem* (2018) 14:484–98. doi: 10.3762/bjoc.14.34
20. Baldauf KJ, Royal JM, Hamorsky KT, Matoba N. Cholera toxin B: one subunit with many pharmaceutical applications. *Toxins* (2015) 7(3):974–96. doi: 10.3390/toxins7030974
21. Lin W, Zheng X, Wang H, Yu L, Zhou X, Sun Y, et al. Purification and characterization of a novel cell-penetrating carrier similar to cholera toxin chimeric protein. *Protein Expression Purification* (2017) 129:128–34. doi: 10.1016/j.pep.2016.03.007
22. Carol J, Gorseling M, de Jong CF, Lingeman H, Kientz CE, van Baar BLM, et al. Determination of denatured proteins and biotoxins by on-line size-exclusion chromatography-digestion-liquid chromatography-electro spray mass spectrometry. *Analytical Biochem* (2005) 346(1):150–7. doi: 10.1016/j.ab.2005.08.023
23. Izzo AA, Capasso F, Costagliola A, Bisogno T, Marsicano G, Ligresti A, et al. An endogenous cannabinoid tone attenuates cholera toxin-induced fluid accumulation in mice. *Gastroenterology* (2003) 125(3):765–74. doi: 10.1016/s0016-5085(03)00892-8
24. Davidsson P, Fredman P, Mansson JE, Svennerholm L. Determination of gangliosides and sulfate in human cerebrospinal fluid with a microimmunoaffinity technique [; Research Support, Non-U.S. Gov't]. *Clinica chimica acta; Int J Clin Chem* (1991) 197(2):105–15. doi: 10.1016/0009-8981(91)90272-e
25. Edwards KA, March JC. GM(1)-functionalized liposomes in a microtiter plate assay for cholera toxin in *Vibrio cholerae* culture samples. *Analytical Biochem* (2007) 368(1):39–48. doi: 10.1016/j.ab.2007.04.019
26. Lippolis V, Maragos C. Fluorescence polarisation immunoassays for rapid, accurate and sensitive determination of mycotoxins. *World Mycotoxin J* (2014) 7(4):479–89. doi: 10.3920/wmj2013.1681
27. Goel AK, Tamrakar AK, Kamboj DV, Singh L. Direct immunofluorescence assay for rapid environmental detection of *Vibrio cholerae* O1. *Folia Microbiologica* (2005) 50(5):448–52. doi: 10.1007/bf02931428
28. Dick MH, Guillerm M, Moussy F, Chaignat C-L. Review of two decades of cholera diagnostics - how far have we really come? *PLoS Negl Trop Diseases* (2012) 6(10):e1845. doi: 10.1371/journal.pntd.0001845
29. Petrova EE, Komaleva RL, Lakhtina OE, Samokhvalova LV, Kalinina NA, Shoshina NS, et al. Preparation and characterization of monoclonal antibodies to the cholera toxin. *Russian J Bioorganic Chem* (2009) 35(3):326–34. doi: 10.1134/s1068162009030078
30. Kendall EA, Tarique AA, Hossain A, Alam MM, Arifuzzaman M, Akhtar N, et al. Development of Immunoglobulin M Memory to Both a T-Cell-Independent and a T-Cell-Dependent Antigen following Infection with *Vibrio cholerae* O1 in Bangladesh. *Infection Immunity* (2010) 78(1):253–9. doi: 10.1128/iai.00868-09
31. Zareitaher T, Ahmadi TS, Gargari SLM. Immunogenic efficacy of DNA and protein-based vaccine from a chimeric gene consisting OmpW, TcpA and CtxB, of *Vibrio cholerae*. *Immunobiology* (2022) 227(2):152190. doi: 10.1016/j.imbio.2022.152190
32. Li X, Rawal B, Rivera S, Letarte S, Richardson DD. Improvements on sample preparation and peptide separation for reduced peptide mapping based multi-attribute method analysis of therapeutic monoclonal antibodies using lysyl endopeptidase digestion. *J Chromatogr A* (2022) 1675:463161. doi: 10.1016/j.chroma.2022.463161
33. Tang Y, Li Y, Zhang S, Li J, Hu Y, Yang W, et al. Preparation of the luciferase-labeled antibody for improving the detection sensitivity of viral antigen. *Virol J* (2022) 19(1):126. doi: 10.1186/s12985-022-01855-6
34. Dou L, Zhang Y, Bai Y, Li Y, Liu M, Shao S, et al. Advances in chicken IgY-based immunoassays for the detection of chemical and biological hazards in food samples. *J Agric Food Chem* (2022) 70(4):976–91. doi: 10.1021/acs.jafc.1c06750
35. Zhao Z, Zhang Z, Zhang H, Liang Z. Small peptides in the detection of mycotoxins and their potential applications in mycotoxin removal. *Toxins* (2022) 14(11):795. doi: 10.3390/toxins14110795
36. Cheng S, Lin Z, Liu X, Zheng W, Lu G, Tu Z, et al. The epitope analysis of an antibody specifically against *Vibrio cholerae* O1 Ogawa by phage library study. *J Microbiological Methods* (2015) 117:22–7. doi: 10.1016/j.mimet.2015.07.006
37. Knittelfelder R, Riemer AB, Jensen-Jarolim E. Mimotope vaccination—from allergy to cancer. *Expert Opin Biol Ther* (2009) 9(4):493–506. doi: 10.1517/14712590902870386
38. Partidos CD, Steward MW. Mimotopes of viral antigens and biologically important molecules as candidate vaccines and potential immunotherapeutics. *Combinatorial Chem High Throughput Screening* (2002) 5(1):15–27. doi: 10.2174/138620702330589
39. Chen LP. Mimotopes of cytolytic T lymphocytes in cancer immunotherapy. *Curr Opin Immunol* (1999) 11(2):219–22. doi: 10.1016/s0952-7915(99)80037-5
40. Sharav T, Wiesmueller K-H, Walden P. Mimotope vaccines for cancer immunotherapy [Article; Proceedings Paper]. *Vaccine* (2007) 25(16):3032–7. doi: 10.1016/j.vaccine.2007.01.033
41. Zhou J, Li Y, Liu Z, Qian W, Chen Y, Qi Y, et al. Induction of anti-Zearalenone immune response with mimotopes identified from a phage display peptide library. *Toxicon* (2021) 199:1–6. doi: 10.1016/j.toxicon.2021.05.010
42. Zhao F, Tian Y, Shen Q, Liu R, Shi R, Wang H, et al. A novel nanobody and mimotope based immunoassay for rapid analysis of aflatoxin B1. *Talanta* (2019) 195:55–61. doi: 10.1016/j.talanta.2018.11.013
43. Peltonmaa R, Agudo-Maestro I, Mas V, Barderas R, Benito-Pena E, Moreno-Bondi MC. Development and comparison of mimotope-based immunoassays for the analysis of fumonisin B-1. *Analytical Bioanalytical Chem* (2019) 411(26):6801–11. doi: 10.1007/s00216-019-02068-7

44. Huang D-T, Fu H-J, Huang J-J, Luo L, Lei H-T, Shen Y-D, et al. Mimotope-based immunoassays for the rapid analysis of mycotoxin: A review. *J Agric Food Chem* (2021) 69(10):11743–52. doi: 10.1021/acs.jafc.1c04169

45. Huang J, Gutteridge A, Honda W, Kanehisa M. MIMOX: a web tool for phage display based epitope mapping. *BMC Bioinf* (2006) 7:451. doi: 10.1186/1471-2105-7-451

46. Hekim C, Leinonen J, Narvanen A, Koistinen H, Zhu L, Koivunen E, et al. Novel peptide inhibitors of human kallikrein 2. *J Biol Chem* (2006) 281(18):12555–60. doi: 10.1074/jbc.M600014200

47. DePorter SM, McNaughton BR. Engineered M13 bacteriophage nanocarriers for intracellular delivery of exogenous proteins to human prostate cancer cells. *Bioconjugate Chem* (2014) 25(9):1620–5. doi: 10.1021/bc500339k

48. Ju Z, Sun W. Drug delivery vectors based on filamentous bacteriophages and phage-mimetic nanoparticles. *Drug Delivery* (2017) 24(1):1898–908. doi: 10.1080/10717544.2017.1410259

49. Russel M. Protein-protein interactions during filamentous phage assembly [; Research Support, U.S. Gov't, Non-P.H.S.]. *J Mol Biol* (1993) 231(3):689–97. doi: 10.1006/jmbi.1993.1320

50. Caberoy NB, Zhou Y, Jiang X, Alvarado G, Li W. Efficient identification of tubby-binding proteins by an improved system of T7 phage display. *J Mol Recognit* (2010) 23(1):74–83. doi: 10.1002/jmr.983

51. Meloen RH, Puijk WC, Slootstra JW. Mimotopes: realization of an unlikely concept. *J Mol Recognit* (2000) 13(6):352–9. doi: 10.1002/1099-1352(200011/12)13:6<352::Aid-jmr509>3.0.co;2-c

52. Liu C, Pan Y, Chen J, Liu J, Hou Y, Shan Y. Quantitative detection of Ganoderma lucidum immunomodulatory protein-8 by a peptide-antigen-antibody sandwich ELISA. *J Microbiological Methods* (2022) 199:106518. doi: 10.1016/j.mimet.2022.106518

53. Kohler H, Pashov A, Kieber-Emmons T. The promise of anti-idiotype revisited. *Front Immunol* (2019) 10:808. doi: 10.3389/fimmu.2019.00808

54. Mu X, Tong Z, Huang Q, Liu B, Liu Z, Hao L, et al. An electrochemiluminescence immunosensor based on gold-magnetic nanoparticles and phage displayed antibodies. *Sensors* (2016) 16(3):308. doi: 10.3390/s16030308

55. Di Tocco A, Valeria Porcal G, Lassabe G, Gonzalez-Techera A, Alicia Zon M, Fernandez H, et al. Development of an electrochemical immunosensor for the determination of molinate by using phages labeled with CdS nanocrystals as a novel strategy to signal amplification. *Sensors Actuators B-Chemical* (2022) 367:132126. doi: 10.1016/j.snb.2022.132126

56. Zhan S, Fang H, Chen Q, Xiong S, Guo Y, Huang T, et al. M13 bacteriophage as biometric component for orderly assembly of dynamic light scattering immunosensor. *Biosensors Bioelectronics* (2022) 217:114693. doi: 10.1016/j.bios.2022.114693

57. Tafarel Andrade de S, Ana Paula C, Andreia SN, Cristina PB, Douglas Alexander A, Luciane BM, et al. Eosinophilic esophagitis auxiliary diagnosis based on a peptide ligand to eosinophil cationic protein in esophageal mucus of pediatric patients. *Sci Rep* (2022) 12(1):12226. doi: 10.1038/s41598-022-16293-1

58. Sioud M. Phage display libraries: from binders to targeted drug delivery and human therapeutics. *Mol Biotechnol* (2019) 61(4):286–303. doi: 10.1007/s12033-019-00156-8

59. Arap MA. Phage display technology - Applications and innovations. *Genet Mol Biol* (2005) 28(1):1–9. doi: 10.1590/s1415-47572005000100001

60. Bratkovic T. Progress in phage display: evolution of the technique and its application. *Cell Mol Life Sci* (2010) 67(5):749–67. doi: 10.1007/s0018-009-0192-2

61. Smith GP. Filamentous fusion phage: novel expression vectors that display cloned antigens on the virion surface [; Research Support, Non-U.S. Gov't; Research Support, U.S. Gov't, P.H.S.]. *Sci (New York NY)* (1985) 228(4705):1315–7. doi: 10.1126/science.4001944

62. Fagerlund A, Myrset AH, Kulseth MA. Construction of a filamentous phage display peptide library [; Research Support, Non-U.S. Gov't]. *Methods Mol Biol* (Clifton NJ) (2014) 2014:1088:19–33. doi: 10.1007/978-1-62703-673-3_2

63. Smith GP, Fernandez AM. Effect of DNA copy number on genetic stability of phage-displayed peptides. *Biotechniques* (2004) 36(4):610–+. doi: 10.2144/04364st01

64. Hufton SE, Moerkirk PT, Meulemans EV, de Bruine A, Arends JW, Hoogenboom HR. Phage display of cDNA repertoires: the PVI display system and its applications for the selection of immunogenic ligands. *J Immunol Methods* (1999) 231(1-2):39–51. doi: 10.1016/s0022-1759(99)00139-8

65. Mohan K, Weiss GA. Dual genetically encoded phage-displayed ligands [Article]. *Analytical Biochem* (2014) 453:1–3. doi: 10.1016/j.ab.2014.02.025

66. Jaroszewicz W, Morcinek-Orlowska J, Pierzynowska K, Gaffke L, Wegrzyn G. Phage display and other peptide display technologies. *FEMS Microbiol Rev* (2022) 46(2):fuab052. doi: 10.1093/femsre/fuab052

67. Pande J, Szewczyk MM, Grover AK. Phage display: concept, innovations, applications and future. *Biotechnol Adv* (2010) 28(6):849–58. doi: 10.1016/j.biotechadv.2010.07.004

68. Deyle K, Kong X-D, Heinis C. Phage selection of cyclic peptides for application in research and drug development. *Accounts Chem Res* (2017) 50(8):1866–74. doi: 10.1021/acs.accounts.7b00184

69. Xu P, Ghosh S, Gul AR, Bhamore JR, Park JP, Park TJ. Screening of specific binding peptides using phage-display techniques and their biosensing applications. *Trac-Trends Analytical Chem* (2021) 137:116229. doi: 10.1016/j.trac.2021.116229

70. Ng S, Jafari MR, Matochko WL, Derda R. Quantitative synthesis of genetically encoded glycopeptide libraries displayed on M13 phage. *ACS Chem Biol* (2012) 7(9):1482–7. doi: 10.1021/cb300187t

71. Bakhshinejad B, Sadeghizadeh M. Bacteriophages and their applications in the diagnosis and treatment of hepatitis B virus infection. *World J Gastroenterology* (2014) 20(33):11671–83. doi: 10.3748/wjg.v20.i33.11671

72. Li C, Gao N, Xue Q, Ma N, Hu Y, Zhang J, et al. Screening and identification of a specific peptide binding to cervical cancer cells from a phage-displayed peptide library. *Biotechnol Letters* (2017) 39(10):1463–9. doi: 10.1007/s10529-017-2381-7

73. Wang J-J, Liu Y, Zheng Y, Liao K-X, Lin F, Wu C-T, et al. Screening peptides binding specifically to colorectal cancer cells from a phage random peptide library. *Asian Pacific J Cancer Prev* (2012) 13(1):377–81. doi: 10.7314/apjcp.2012.13.1.377

74. Liao K-X, Yao X-Q, Wu C-T, Lin F, Wu W-L, Zeng S-d, et al. Screening peptides binding specifically to large intestinal cancer LoVo cells from phage random peptide library. *J South Med University* (2008) 28(6):986–90.

75. Morton J, Karounthaisiri N, Stewart LD, Oplatowska M, Elliott CT, Grant IR. Production and evaluation of the utility of novel phage display-derived peptide ligands to *Salmonella* spp. for magnetic separation. *J Appl Microbiol* (2013) 115(1):271–81. doi: 10.1111/jam.12207

76. Wang X, Li G, Ren Y, Ren X. Phages bearing affinity peptides to bovine rotavirus differentiate the virus from other viruses. *PLoS One* (2011) 6(12):e28667. doi: 10.1371/journal.pone.0028667

77. Trepel M, Pasqualini R, Arap W. Chapter 4. Screening phage-display Peptide libraries for vascular targeted peptides. *Meth Enzymol* (2008) 445:83–106. doi: 10.1016/S0076-6879(08)03004-8

78. Kodama T, Yoshihara A, Goel I, Sekino M, Kuwahata A, Yoshimori A, et al. Identification of metal-binding peptides and their conjugation onto nanoparticles of superparamagnetic iron oxides and liposomes. *ACS Appl Materials Interfaces* (2020) 12(22):24623–34. doi: 10.1021/acsami.0c06138

79. Balmforth MR, Haigh J, Kumar V, Dai W, Tiede C, Tomlinson DC, et al. Piggybacking on the cholera toxin: identification of a CTB-binding protein as an approach for targeted delivery of proteins to motor neurons. *Bioconjugate Chem* (2021) 32(10):2205–12. doi: 10.1021/acs.bioconjchem.1c00373

80. Kuegler J, Zantow J, Meyer T, Hust M. Oligopeptide M13 phage display in pathogen research [Review]. *Viruses-Basel* (2013) 5(10):2531–45. doi: 10.3390/v5102531

81. Vos WL, Nazarov PV, Koehorst RBM, Spruijt RB, Hemminga MA. From 'T' to 'L' and back again: the odyssey of membrane-bound M13 protein. *Trends Biochem Sci* (2009) 34(5):249–55. doi: 10.1016/j.tibs.2009.01.007

82. Smeal SW, Schmitt MA, Pereira RR, Prasad A, Fisk JD. Simulation of the M13 life cycle I: Assembly of a genetically-structured deterministic chemical kinetic simulation. *Virology* (2017) 500:259–74. doi: 10.1016/j.virol.2016.08.017

83. Wei S, Yan Z, Zhigang J. Mimotopes for mycotoxins diagnosis based on random peptides or recombinant antibodies from phage library. *Molecules* (2021) 26(24):7652. doi: 10.3390/molecules26247652

84. Askora A, Abdel-Halim MEF, Yamada T. Site-specific recombination systems in filamentous phages [Review]. *Mol Genet Genomics* (2012) 287(7):525–30. doi: 10.1007/s00438-012-0700-1

85. Bernard JM, Francis MB. Chemical strategies for the covalent modification of filamentous phage. *Front Microbiol* (2014) 5:734. doi: 10.3389/fmicb.2014.00734

86. Hemminga MA, Vos WL, Nazarov PV, Koehorst RBM, Wolfs CJAM, Spruijt RB, et al. Viruses: incredible nanomachines. New advances with filamentous phages. *Eur Biophysics J Biophysics Letters* (2010) 39(4):541–50. doi: 10.1007/s00249-009-0523-0

87. Nagler C, Nagler G, Kuhn A. Cysteine residues in the transmembrane regions of M13 procoat protein suggest that oligomeric coat proteins assemble onto phage progeny. *J Bacteriology* (2007) 189(7):2897–905. doi: 10.1128/jb.01551-06

88. Azzazy HM, Highsmith WE Jr. Phage display technology: clinical applications and recent innovations. *Clin Biochem* (2002) 35(6):425–45. doi: 10.1016/s0009-9120(02)00343-0

89. Tang ZM, Jiang WC, Chang PP, Fang M, Rong Y, Hu LH. Mimotope selection of blood group A antigen from a phage display 15-mer peptide library. *Transplant Immunol* (2013) 29(1-4):39–42. doi: 10.1016/j.trim.2013.06.001

90. Rami A, Behdani M, Yardehnavi N, Habibi-Anbouhi M, Kazemi-Lomedasht F. An overview on application of phage display technique in immunological studies. *Asian Pacific J Trop Biomedicine* (2017) 7(7):599–602. doi: 10.1016/j.apjtb.2017.06.001

91. Lee S-C, Yoon M-Y. Development of a receptor-based inhibitory penta-unit-conjugated peptide to enhance anthrax toxin neutralization. *Int J Biol Macromolecules* (2020) 163:327–35. doi: 10.1016/j.ijbiomac.2020.06.264

92. Raeisi H, Azimirad M, Asadzadeh Aghdaei H, Yadegar A, Zali MR. Rapid-format recombinant antibody-based methods for the diagnosis of *Clostridioides difficile* infection: Recent advances and perspectives [Review]. *Front Microbiol* (2022) 13:1043214. doi: 10.3389/fmicb.2022.1043214

93. Thirumala-Devi K, Miller JS, Reddy G, Reddy DVR, Mayo MA. Phage-displayed peptides that mimic aflatoxin B1 in serological reactivity. *J Appl Microbiol* (2001) 90(3):330–6. doi: 10.1046/j.1365-2672.2001.01249.x

94. Bracci L, Lozzi L, Lelli B, Pini A, Neri P. Mimotopes of the nicotinic receptor binding site selected by a combinatorial peptide library. *Biochemistry* (2001) 40(22):6611–9. doi: 10.1021/bi0023201

95. Jerne NK. The immune system: a web of V-domains. *Harvey lectures* (1974) 70 (Series):93–110.

96. Yu FY, Chu FS. Production and characterization of a monoclonal anti-anti-idiotypic antibody against fumonisin B(1). *J Agric Food Chem* (1999) 47(11):4815–20. doi: 10.1021/jf990185x

97. Maragos CM. Production of anti-idiotype antibodies for deoxynivalenol and their evaluation with three immunoassay platforms. *Mycotoxin Res* (2014) 30(2):103–11. doi: 10.1007/s12550-014-0190-6

98. Mills C, Campbell K. A new chapter for anti-idiotypes in low molecular weight compound immunoassays [Review]. *Trends Biotechnol* (2022) 40(9):1102–20. doi: 10.1016/j.tibtech.2022.02.008

99. Wang D, Xu Y, Tu Z, Fu Jin H, Xiong Yong H, Feng F, et al. Isolation and characterization of recombinant variable domain of heavy chain anti-idiotypic antibodies specific to aflatoxin B-1 [Letter]. *Biomed Environ Sci* (2014) 27(2):118–21. doi: 10.3967/bes2014.025

100. Walter G, Bussow K, Lueking A, Glöckler J. High-throughput protein arrays: prospects for molecular diagnostics [Editorial Material]. *Trends Mol Med* (2002) 8(6):250–3. doi: 10.1016/s1471-4914(02)02352-3

101. Li Q, Zhang F, Lu Y, Hu H, Wang J, Guo C, et al. Highly potent multivalent VHH antibodies against Chikungunya isolated from an alpaca naïve phage display library. *J Nanobiotechnology* (2022) 20(1):231. doi: 10.1186/s12951-022-01417-6

102. Ferrara F, Erasmus MF, D'Angelo S, Leal-Lopes C, Teixeira AA, Choudhary A, et al. A pandemic-enabled comparison of discovery platforms demonstrates a naïve antibody library can match the best immune-sourced antibodies. *Nat Commun* (2022) 13(1):462. doi: 10.1038/s41467-021-27799-z

103. Zhu K, Dietrich R, Didier A, Doyscher D, Maertlbauer E. Recent developments in antibody-based assays for the detection of bacterial toxins. *Toxins* (2014) 6(4):1325–48. doi: 10.3390/toxins6041325

104. Gonzalez-Sapienza G, Rossotti MA, Tabares-da Rosa S. Single-domain antibodies as versatile affinity reagents for analytical and diagnostic applications. *Front Immunol* (2017) 8:977. doi: 10.3389/fimmu.2017.00977

105. Fleming BD, Ho M. Generation of single-domain antibody-based recombinant immuno toxins [; research support, N.I.H., intramural]. *Methods Mol Biol* (Clifton NJ) (2022) 2022:2446:489–512. doi: 10.1007/978-1-0716-2075-5_25

106. Zhang C, Zhang W, Tang X, Zhang Q, Zhang W, Li P. Change of amino acid residues in idiotypic nanobodies enhanced the sensitivity of competitive enzyme immunoassay for mycotoxin ochratoxin A in cereals. *Toxins* (2020) 12(4):273. doi: 10.3390/toxins12040273

107. Tong W, Fang H, Xiong H, Wei D, Leng Y, Hu X, et al. Eco-friendly fluorescent ELISA based on bifunctional phage for ultrasensitive detection of ochratoxin A in corn. *Foods* (2021) 10(10):2429. doi: 10.3390/foods10102429

108. Lu X, Jiang D-j, Yan J-x, Ma Z-e, Luo X-e, Wei T-l, et al. An ultrasensitive electrochemical immuno sensor for Cry1Ab based on phage displayed peptides. *Talanta* (2018) 179:646–51. doi: 10.1016/j.talanta.2017.11.032

109. Wang M, Zheng Z, Zhang Y, Wang G, Liu J, Yu H, et al. An ultrasensitive label-free electrochemical impedimetric immuno sensor for vascular endothelial growth factor based on specific phage via negative pre-screening. *Analytica Chimica Acta* (2022) 1225:340250. doi: 10.1016/j.aca.2022.340250

110. Wernick NLB, Chinnapen DJF, Cho JA, Lencer WI. Cholera toxin: an intracellular journey into the cytosol by way of the endoplasmic reticulum. *Toxins* (2010) 2(3):310–25. doi: 10.3390/toxins2010310

111. Lencer WI, Hirst TR, Holmes RK. Membrane traffic and the cellular uptake of cholera toxin. *Biochim Et Biophys Acta-Molecular Cell Res* (1999) 1450(3):177–90. doi: 10.1016/s0167-4889(99)00070-1

112. Lin C-F, Chen C-L, Huang W-C, Cheng Y-L, Hsieh C-Y, Wang C-Y, et al. Different types of cell death induced by enterotoxins. *Toxins* (2010) 2(8):2158–76. doi: 10.3390/toxins2012158

113. Ligler FS, Taitt CR, Shriver-Lake LC, Sapsford KE, Shubin Y, Golden JP. Array biosensor for detection of toxins [Review]. *Analytical Bioanalytical Chem* (2003) 377 (3):469–77. doi: 10.1007/s00216-003-1992-0

114. Cho JA, Chinnapen DJF, Aamar E, te Welscher YM, Lencer WI, Massol R. Insights on the trafficking and retro-translocation of glycosphingolipid-binding bacterial toxin. *Front Cell Infect Microbiol* (2012) 2:51. doi: 10.3389/fcimb.2012.00051

115. Saw PE, Xu X, Kim S, Jon S. Biomedical applications of a novel class of high-affinity peptides. *Accounts Chem Res* (2021) 54(18):3576–92. doi: 10.1021/acs.accounts.1c00239

116. Wang M, Li L, Zhang L, Zhao J, Jiang Z, Wang W. Peptide-derived biosensors and their applications in tumor immunology-related detection. *Analytical Chem* (2022) 94(1):431–41. doi: 10.1021/acs.analchem.1c04461

117. Lim JM, Heo NS, Oh SY, Ryu MY, Seo JH, Park TJ, et al. Selection of affinity peptides for interference-free detection of cholera toxin. *Biosensors Bioelectronics* (2018) 99:289–95. doi: 10.1016/j.bios.2017.07.075

118. Montaner AD, De Nichilo A, Elias F, Rodriguez JM, Flo JM, Lopez RA, et al. Ganglioside GM1-binding peptides as adjuvants of antigens inoculated by the intranasal route. *Vaccine* (2006) 24(11):1889–96. doi: 10.1016/j.vaccine.2005.10.037

119. Adunphatcharaphon S, Elliott CT, Sooksimuang T, Charlermroj R, Petchkongkaew A, Karoonuthaisiri N. The evolution of multiplex detection of mycotoxins using immunoassay platform technologies. *J Hazard Mater* (2022) 432:128706. doi: 10.1016/j.jhazmat.2022.128706

120. Shu M, Xu Y, Wang D, Liu X, Li Y, He Q, et al. Anti-idiotypic nanobody: A strategy for development of sensitive and green immunoassay for Fumonisin B-1. *Talanta* (2015) 143:388–93. doi: 10.1016/j.talanta.2015.05.010

121. Zou X, Chen C, Huang X, Chen X, Wang L, Xiong Y. Phage-free peptide ELISA for ochratoxin A detection based on biotinylated mimotope as a competing antigen. *Talanta* (2016) 146:394–400. doi: 10.1016/j.talanta.2015.08.049

122. Song Z, Feng L, Leng Y, Huang M, Fang H, Tong W, et al. Dramatically enhancing the sensitivity of immunoassay for ochratoxin A detection by cascade-amplifying enzyme loading. *Toxins* (2021) 13(11):781. doi: 10.3390/toxins13110781

123. Lai W, Fung DYC, Xu Y, Liu R, Xiong Y. Development of a colloidal gold strip for rapid detection of ochratoxin A with mimotope peptide [Article]. *Food Control* (2009) 20(9):791–5. doi: 10.1016/j.foodcont.2008.10.007

124. Sain A, Sen P, Venkataraman K, Vijayalakshmi MA. Expression of a tagless single-chain variable fragment (scFv) of anti-TNF-alpha by a salt inducible system and its purification and characterization. *Protein Pept Letters* (2021) 28(11):1272–80. doi: 10.2174/092986652866210922141402

125. Liu C, Liu M, Huang Y, Chu F, Li Y, Li Z. Preparation and cytotoxic effects of scFv targeting human c-Met protein on lung adenocarcinoma A549 cells. *Chin J Cell Mol Immunol* (2018) 34(5):401–7.

126. Peng S, Yu L, He Y, Chen D, Wang L, Zhou X, et al. Recombinant scFv inhibit Newcastle disease virus *in vitro* infection [Article]. *Thail J Veterinary Med* (2022) 52 (2):293–301. doi: 10.14456/tjvm.2022.33

127. Wang F, Li N, Zhang Y, Sun X, Hu M, Zhao Y, et al. Preparation and directed evolution of anti-ciprofloxacin scFv for immunoassay in animal-derived food. *Foods* (2021) 10(8):1933. doi: 10.3390/foods10081933

128. Li L, Wu S, Si Y, Li H, Yin X, Peng D. Single-chain fragment variable produced by phage display technology: Construction, selection, mutation, expression, and recent applications in food safety. *Compr Rev Food Sci Food Safety* (2022) 21(5):4354–77. doi: 10.1111/1541-4337.13018

129. Lakzaei M, Rasaee MJ, Fazaeli AA, Aminian M. A comparison of three strategies for biopanning of phage-scFv library against diphtheria toxin. *J Cell Physiol* (2019) 234(6):9486–94. doi: 10.1002/jcp.27636

130. Alibeiki M, Golchin M, Tabatabaei M. Development of a double-recombinant antibody sandwich ELISA for quantitative detection of epsilon toxin concentration in inactivated Clostridium perfringens vaccines. *BMC Veterinary Res* (2020) 16(1):361. doi: 10.1186/s12917-020-02572-4

131. Shadman Z, Farajinia S, Pazhang M, Tohidkia M, Rahbarnia L, Najavand S, et al. Isolation and characterizations of a novel recombinant scFv antibody against exotoxin A of *Pseudomonas aeruginosa*. *BMC Infect Diseases* (2021) 21(1):300. doi: 10.1186/s12879-021-05969-0

132. Kuhn P, Fuehner V, Unkauf T, Moreira GMSG, Frenzel A, Miethe S, et al. Recombinant antibodies for diagnostics and therapy against pathogens and toxins generated by phage display. *Proteomics Clin Applications* (2016) 10(9–10):922–48. doi: 10.1002/prca.201600002

133. Unkauf T, Miethe S, Fuehner V, Schirrmann T, Frenzel A, Hust M. Generation of recombinant antibodies against toxins and viruses by phage display for diagnostics and therapy. *Adv Exp Med Biol* (2016) 917:55–76. Protein Targeting Compounds: Prediction, Selection and Activity of Specific Inhibitors. doi: 10.1007/978-3-319-32805-8_4

134. Greiner JW, Guadagni F, Hand PH, Pestka S, Noguchi P, Fisher PB, et al. Augmentation of tumor antigen expression by recombinant human interferons: enhanced targeting of monoclonal antibodies to carcinomas. *Cancer Treat Res* (1990) 1990:51:413–32. doi: 10.1007/978-1-4613-1497-4_21

135. Damen CWN, de Groot ER, Heij M, Boss DS, Schellens JHM, Rosing H, et al. Development and validation of an enzyme-linked immunosorbent assay for the quantification of trastuzumab in human serum and plasma. *Analytical Biochem* (2009) 391(2):114–20. doi: 10.1016/j.ab.2009.05.030

136. Zhao Q, Wong P-F, Lee SST, Leung S-O, Cheung W-T, Wang J-Z. Generation of anti-idiotype scFv for pharmacokinetic measurement in lymphoma patients treated with chimeric anti-CD22 antibody SM03. *PLoS One* (2014) 9(5):e96697. doi: 10.1371/journal.pone.0096697

137. Kobayashi N, Oiwa H, Kubota K, Sakoda S, Goto J. Monoclonal antibodies generated against an affinity-labeled immune complex of an anti-bile acid metabolite antibody: an approach to noncompetitive hapten immunoassays based on anti-idiotype or anti-metatype antibodies. *J Immunol Methods* (2000) 245(1–2):95–108. doi: 10.1016/s0022-1759(00)00291-x

138. Xia Y, Huang W, Huang B, Jin X, Li B. Production and detection of monoclonal anti-idiotype antibodies against *Vibrio anguillarum*. *Acta microbiologica Sinica* (2001) 41(4):447–51.

139. Janusz W, Vanina A, Jan R, Mandy U, Karla J, Mariela U, et al. Single domain antibodies: promising experimental and therapeutic tools in infection and immunity. *Med Microbiol Immunol* (2009) 198(3):157–74. doi: 10.1007/s00430-009-0116-7

140. Romao E, Morales-Yanez F, Hu Y, Crauwels M, De Pauw P, Hassanzadeh GG, et al. Identification of useful nanobodies by phage display of immune single domain libraries derived from camelid heavy chain antibodies. *Curr Pharm Design* (2016) 22 (43):6500–18. doi: 10.2174/138161282266160923114417

141. Barakat S, Berksoz M, Zahedimaram P, Piepoli S, Erman B. Nanobodies as molecular imaging probes [Article]. *Free Radical Biol Med* (2022) 182:260–75. doi: 10.1016/j.freeradbiomed.2022.02.031

142. Sun S, Tan X, Pang X, Li M, Hao X. Recent advances in the application of nanobody technology: a review [Review]. *Sheng wu gong cheng xue bao = Chin J Biotechnol* (2022) 38(3):855–67. doi: 10.13345/j.cjb.210464

143. Verhaar ER, Woodham AW, Ploegh HL. Nanobodies in cancer. *Semin Immunol* (2021) 52:101425. doi: 10.1016/j.smim.2020.101425

144. Dong S, Guan L, He K, Yang W, Deng W, Yuan S, et al. Screening of anti-idiotypic domain antibody from phage library for development of Bt Cry1A simulants. *Int J Biol Macromolecules* (2021) 183:1346–51. doi: 10.1016/j.ijbiomac.2021.05.093

145. Xu C, Liu X, Liu Y, Zhang X, Zhang C, Li J, et al. High sensitive single chain variable fragment screening from a microcystin-LR immunized mouse phage antibody library and its application in immunoassay. *Talanta* (2019) 197:397–405. doi: 10.1016/j.talanta.2019.01.064

146. Guo Y-C, Zhou Y-F, Zhang X-E, Zhang Z-P, Qiao Y-M, Bi L-J, et al. Phage display mediated immuno-PCR. *Nucleic Acids Res* (2006) 34(8):e62. doi: 10.1093/nar/gkl260

147. Rezaei ZS, Shahangian SS, Hasannia S, Sajedi RH. Development of a phage display-mediated immunoassay for the detection of vascular endothelial growth factor. *Analytical Bioanalytical Chem* (2020) 412(27):7639–48. doi: 10.1007/s00216-020-02901-4

148. Ren X, Zhang Q, Wu W, Yan T, Tang X, Zhang W, et al. Anti-idiotypic nanobody-phage display-mediated real-time immuno-PCR for sensitive, simultaneous and quantitative detection of total aflatoxins and zearalenone in grains. *Food Chem* (2019) 297:124912. doi: 10.1016/j.foodchem.2019.05.186

149. Wang X, He Q, Xu Y, Liu X, Shu M, Tu Z, et al. Anti-idiotypic VHH phage display-mediated immuno-PCR for ultrasensitive determination of mycotoxin zearalenone in cereals. *Talanta* (2016) 147:410–5. doi: 10.1016/j.talanta.2015.09.072

150. Alp A. Recent advances in molecular point of care tests. *Mikrobiyoloji Bulteni* (2022) 56(3):580–91. doi: 10.5578/mb.20229717

151. Atceken N, Alseed MM, Dabbagh SR, Yetisen AK, Tasoglu S. Point-of-care diagnostic platforms for loop-mediated isothermal amplification. *Adv Eng Mater* (2022) 25:2201174. doi: 10.1002/adem.202201174

152. Garg N, Ahmad FJ, Kar S. Recent advances in loop-mediated isothermal amplification (LAMP) for rapid and efficient detection of pathogens. *Curr Res Microbial Sci* (2022) 3:100120–0. doi: 10.1016/j.crmicr.2022.100120

153. Erber AC, Sandler PJ, de Avelar DM, Swoboda I, Cota G, Walochnik J. Diagnosis of visceral and cutaneous leishmaniasis using loop-mediated isothermal amplification (LAMP) protocols: a systematic review and meta-analysis. *Parasites Vectors* (2022) 15(1):34. doi: 10.1186/s13071-021-05133-2

154. Chen D, Liang Z, Ren S, Alali W, Chen L. Rapid and visualized detection of virulence-related genes of vibrio cholerae in water and aquatic products by loop-mediated isothermal amplification. *J Food Protection* (2022) 85(1):44–53. doi: 10.4315/jfp-21-182

155. Lei J, Han X, Tang X, Wang H, Zhang Q. Development of anti-idiotypic nanobody-phage based immuno-loop-mediated isothermal amplification assay for aflatoxins in peanuts. *Toxins* (2020) 12(9):565. doi: 10.3390/toxins12090565

156. Bosch-Orea C, Sanchis J, Farre M, Barcelo D. Analysis of lipophilic marine biotoxins by liquid chromatography coupled with high-resolution mass spectrometry in seawater from the Catalan Coast. *Analytical Bioanalytical Chem* (2017) 409(23):5451–62. doi: 10.1007/s00216-017-0536-y

157. Stewart LD, Elliott CT, Walker AD, Curran RM, Connolly L. Development of a monoclonal antibody binding okadaic acid and dinophysistoxins-1,2 in proportion to their toxicity equivalence factors. *Toxicon* (2009) 54(4):491–8. doi: 10.1016/j.toxicon.2009.05.015

158. Song S-H, Gao Z-F, Guo X, Chen G-H. Aptamer-based detection methodology studies in food safety [Review]. *Food Analytical Methods* (2019) 12(4):966–90. doi: 10.1007/s12161-019-01437-3

159. Lu Y-N, Shan Y, Huang H, Zhu L, Li B, Wang S, et al. Quantum dot microsphere-based immunochromatography test strip enabled sensitive and quantitative on-site detections for multiple mycotoxins in grains. *Food Chem* (2022) 376:131868. doi: 10.1016/j.foodchem.2021.131868

160. Lyubavina IA, Valyakina TI, Grishin EV. Monoclonal antibodies labeled with colloidal gold for immunochromatographic express analysis of diphtheria toxin. *Russian J Bioorganic Chem* (2011) 37(3):326–32. doi: 10.1134/s1068162011030113

161. Liu D, Huang Y, Chen M, Wang S, Liu K, Lai W. Rapid detection method for aflatoxin B-1 in soybean sauce based on fluorescent microspheres probe. *Food Control* (2015) 50:659–62. doi: 10.1016/j.foodcont.2014.10.011

162. Xu L-D, Zhu J, Ding S-N. Highly-fluorescent carbon dots grown onto dendritic silica nanospheres for anthrax protective antigen detection. *Analytical Methods* (2022) 14(19):1836–40. doi: 10.1039/d2ay00623e

163. Li H, Wang D, Tang X, Zhang W, Zhang Q, Li P. Time-resolved fluorescence immunochromatography assay (TRFICA) for aflatoxin: aiming at increasing strip method sensitivity. *Front Microbiol* (2020) 11:676. doi: 10.3389/fmicb.2020.00676

164. Xing G, Sun X, Li N, Li X, Wu T, Wang F. New advances in lateral flow immunoassay (LFI) technology for food safety detection. *Molecules* (2022) 27(19):6596. doi: 10.3390/molecules27196596

165. Anfossi L, Di Nardo F, Cavalera S, Giovannoli C, Baggiani C. Multiplex lateral flow immunoassay: An overview of strategies towards high-throughput point-of-Need testing. *Biosensors-Basel* (2018) 9(1):2. doi: 10.3390/bios9010002

166. Bu T, Zhao S, Bai F, Sun X, He K, Wang Q, et al. Diverse dyes-embedded staphylococcus aureus as potential biocarriers for enhancing sensitivity in biosensing. *Analytical Chem* (2021) 93(17):6731–8. doi: 10.1021/acs.analchem.1c00346

167. Bu T, Bai F, Zhao S, Cao Y, He K, Sun X, et al. Multifunctional bacteria-derived tags for advancing immunoassay analytical performance with dual-channel switching and antibodies bioactivity sustaining. *Biosensors Bioelectronics* (2021) 192:5546–54. doi: 10.1016/j.bios.2021.113538

168. Bu T, Bai F, Zhao S, Sun X, Jia P, He K, et al. Dual-modal immunochromatographic test for sensitive detection of zearalenone in food samples based on biosynthetic staphylococcus aureus-mediated polymer dot nanocomposites. *Analytical Chem* (2022) 94(14):5546–54. doi: 10.1021/acs.analchem.1c04721

169. Yan J-x, Hu W-j, You K-h, Ma Z-e, Xu Y, Li Y-p, et al. Biosynthetic mycotoxin conjugate mimetics-mediated green strategy for multiplex mycotoxin immunochromatographic assay. *J Agric Food Chem* (2020) 68(7):2193–200. doi: 10.1021/acs.jafc.9b06383

170. Ren X, Yue X, Mwakinyali SE, Zhang W, Zhang Q, Li P. Small molecular contaminant and microorganism can be simultaneously detected based on nanobody-phage: using carcinogen aflatoxin and its main fungal aspergillus section flavi spp. in stored maize for demonstration. *Front Microbiol* (2020) 10:3023. doi: 10.3389/fmicb.2019.03023

171. Sawada T, Serizawa T. Filamentous viruses as building blocks for hierarchical self-assembly toward functional soft materials. *Bull Chem Soc Japan* (2018) 91(3):455–66. doi: 10.1246/bcsj.20170428

172. Abu Sayeed M, Paisie T, Alam MT, Ali A, Camilli A, Wrammert J, et al. Development of a monoclonal antibody to a vibriophage as a proxy for vibrio cholerae detection. *Infection Immunity* (2022) 90(8):682–8. doi: 10.1128/iai.00161-22

173. Ghazi FMP, Gargari SLM. Development of lipopolysaccharide-mimicking peptides and their immunoprotectivity against Vibrio cholerae serogroup O1. *J Pept Science* (2016) 22(11–12):682–8. doi: 10.1002/psc.2930

174. Ebrahimizadeh W, Gargari SM, Rajabibazl M, Ardekani LS, Zare H, Bakherad H. Isolation and characterization of protective anti-LPS nanobody against V. cholerae O1 recognizing Inaba and Ogawa serotypes [Article]. *Appl Microbiol Biotechnol* (2013) 97(10):4457–66. doi: 10.1007/s00253-012-4518-x



OPEN ACCESS

EDITED BY

Emanuela Corsini,
University of Milan, Italy

REVIEWED BY

Leon Coleman Jr.,
University of North Carolina at Chapel Hill,
United States
David Burmeister,
Uniformed Services University of the
Health Sciences, United States

*CORRESPONDENCE

Patrick P.G. Mulder
✉ pmulder@burns.nl
Bouke K.H.L. Boekema
✉ bboekema@burns.nl

RECEIVED 21 July 2023

ACCEPTED 03 October 2023

PUBLISHED 13 October 2023

CITATION

Mulder PPG, Vlij M, Elgersma A,
Rozemeijer L, Mastenbroek LS,
Middelkoop E, Joosten I, Koenen HJPM
and Boekema BKHL (2023) Monocytes and
T cells incorporated in full skin equivalents
to study innate or adaptive immune
reactions after burn injury.
Front. Immunol. 14:1264716.
doi: 10.3389/fimmu.2023.1264716

COPYRIGHT

© 2023 Mulder, Vlij, Elgersma, Rozemeijer,
Mastenbroek, Middelkoop, Joosten, Koenen
and Boekema. This is an open-access article
distributed under the terms of the [Creative
Commons Attribution License \(CC BY\)](#). The
use, distribution or reproduction in other
forums is permitted, provided the original
author(s) and the copyright owner(s) are
credited and that the original publication in
this journal is cited, in accordance with
accepted academic practice. No use,
distribution or reproduction is permitted
which does not comply with these terms.

Monocytes and T cells incorporated in full skin equivalents to study innate or adaptive immune reactions after burn injury

Patrick P.G. Mulder ^{1,2*}, Marcel Vlij ¹, Anouk Elgersma¹,
Lotte Rozemeijer¹, Leonore S. Mastenbroek¹,
Esther Middelkoop ^{1,3,4}, Irma Joosten ²,
Hans J.P.M. Koenen ² and Bouke K.H.L. Boekema ^{1,3*}

¹Preclinical Research, Association of Dutch Burn Centres (ADBC), Beverwijk, Netherlands,
²Laboratory of Medical Immunology, Department of Laboratory Medicine, Radboud University
Medical Center, Nijmegen, Netherlands, ³Department of Plastic, Reconstructive and Hand Surgery,
Amsterdam UMC, VU University Amsterdam, Amsterdam, Netherlands, ⁴Tissue Function and
Regeneration, Amsterdam Movement Sciences, Amsterdam, Netherlands

Introduction: Thermal injury often leads to prolonged and excessive inflammation, which hinders the recovery of patients. There is a notable absence of suitable animal-free models for investigating the inflammatory processes following burn injuries, thereby impeding the development of more effective therapies to improve burn wound healing in patients.

Methods: In this study, we established a human full skin equivalent (FSE) burn wound model and incorporated human peripheral blood-derived monocytes and T cells.

Results: Upon infiltration into the FSEs, the monocytes differentiated into macrophages within a span of 7 days. Burn-injured FSEs exhibited macrophages with increased expression of HLA-DR⁺ and elevated production of IL-8 (CXCL8), in comparison to uninjured FSEs. Among the T cells that actively migrated into the FSEs, the majority were CD4⁺ and CD25⁺. These T cells demonstrated augmented expression of markers associated with regulatory T cell, Th1, or Th17 activity, which coincided with significant heightened cytokine production, including IFN-γ, IL-4, IL-6, IL-8, IL-10, IL-12p70, IL-17A, IP-10 (CXCL10), and TGF-β1. Burn injury did not impact the studied effector T cell subsets or cytokine levels.

Discussion: Collectively, this study represents a significant advancement in the development of an immunocompetent human skin model, specifically tailored for investigating burn-induced innate or adaptive immune reactions at the site of burn injury.

KEYWORDS

immune response, cytokines, flow cytometry, immunohistochemistry, macrophages

1 Introduction

Burn injuries often trigger an excessive and uncontrolled immune response, resulting in various secondary complications such as systemic inflammation, delayed healing, wound deepening, and severe scarring (1–4). Gaining a better understanding of the underlying reactions responsible for burn-induced inflammation is crucial for effectively managing the inflammatory processes in burn wound healing. Detailed knowledge on the role and impact of specific immune cells and cytokines that are involved in the inflammatory response is, however, still limited. Most studies in this field rely on animal models, primarily rodents, which may not directly translate to the human context. To advance our understanding without relying on experimental animals, it is imperative to develop appropriate human 3D skin models that can study immune dysfunction at the site of burn injury.

Immediately after burn injury, pro-inflammatory neutrophils and macrophages accumulate at the wound site (5–7). These phagocytic cells play a critical role in eliminating cell debris and pathogens from the injured area (8). However, high numbers of hyperactive innate immune cells can damage healthy tissues and hamper the wound healing process (9–11). Initially, pro-inflammatory macrophages (referred to as M1) dominate, followed by anti-inflammatory macrophages (known as M2) in later stages, which suppress inflammatory responses and support wound healing (8, 12). Later in the inflammation process, T cells migrate to the wound area to coordinate targeted anti-pathogen responses and regulate ongoing inflammation to advance wound healing (13, 14). Different subsets of effector T cells, such as Th1 and Th17, are known to enhance inflammation, whereas Th2 and regulatory T cells (Tregs) are involved in the resolution of inflammation (15, 16). Achieving a proper immune balance between pro- and anti-inflammatory responses is critical for an uncomplicated and timely transition from inflammation to wound healing. Yet the exact mechanisms underlying distorted immune reactions after burn injury and the methods to restore proper immune function remain unclear.

Studying the immune response in burn patients faces limitations due to the absence of baseline measurements, inter-individual variability, differences in injuries, and constraints on collecting patient samples (6, 17). Consequently, most knowledge about the immune response following burn trauma is obtained from animal experiments (6, 17, 18) and has provided essential data for the advancement of human therapeutics. However, the use of experimental animals presents ethical concerns and translation challenges (19). Although valuable insights can be derived from animal studies, animals do not accurately reflect the human situation due to differences in skin architecture and wound healing processes (18, 20–22). It is therefore challenging to extrapolate relevant findings to burn patients. Thus, alternative approaches for research on burn wound healing need to be developed (23). *In vitro* human skin models are promising alternative experimental tools for studying various aspects of skin injury based on the behavior of keratinocytes and fibroblasts (23–25). Currently, many existing skin models fail to capture the

complex processes of skin inflammation because they lack essential immune components (26, 27). In order to make *in vitro* skin models more useful and appropriate, it is necessary to incorporate immune cells and inflammatory mediators.

In this study, we aimed to develop a human full skin equivalent (FSE) based on the collagen-elastin matrix MatriDerm® (28, 29), as we described previously (30). MatriDerm is a clinically applied matrix that provides a robust extracellular matrix architecture supporting skin regeneration in cutaneous defects (31–34). Our objective was to investigate the effect of burn injury on immune cells within the FSEs (1.13 cm² with a burned surface of 19%). With a 19% burn, the effect of the injury is clearly present, while there is enough material and cells that is not destroyed so that cells can enter. We hypothesized that burn injury alters the inflammatory state of immune cells in these FSEs, which can be detected by changes in cell phenotype and cytokine expression. Cells from the innate and the adaptive immune system, namely monocytes and T cells, were isolated from human buffy coats and cultured in the FSE. We examined alterations in marker expression on immune cells and the secretion of cytokines in the culture medium.

2 Materials and methods

2.1 Human skin samples

Skin samples were obtained from adult patients who underwent abdominoplasty at the Red Cross Hospital in Beverwijk, Medical Clinic in Velsen or Spaarne Gasthuis in Haarlem. Samples from 17 different donors were used (donor age: 48 ± 13 years; sex: 93% female). Consent for the use of these anonymized, post-operative residual tissue samples was received through an informed opt-out protocol, in accordance with the national guidelines (<https://www.coreon.org/>) and approved by the institutional privacy officers. Subjects were actively informed of this procedure and were able to easily withdraw at any point. Split-thickness samples of 0.3 mm were harvested using a dermatome (Aesculap AG & Co. KG, Tuttlingen, Germany).

2.2 Isolation of human keratinocytes and fibroblasts

See **Supplementary Table 1** for the contents of culture media. Harvested skin was incubated in 0.25% dispase (Gibco, ThermoFisher Scientific, Paisley, UK) at 37°C for 45 min. The epidermis was separated from the dermis using forceps. For fibroblast isolation, the dermal part of the split skin was cut into small pieces and submerged into a 0.25% collagenase A (Roche, Basel, Switzerland) solution at 37°C for 2 h. After addition of 1 mM EDTA (Life Technologies, Paisley, UK) + PBS (Gibco) to inhibit enzyme activity, the cell suspension was poured through a 500 µm cell strainer (PluriSelect, Leipzich, Germany) and centrifuged for 10 min at 360 × g. The cell pellet was resuspended in culture medium and poured through a 70 µm cell strainer (Starstedt AG &

Co. KG, Nümbrecht, Germany) and cultured at 37°C with 5% CO₂. For keratinocyte isolation, the epidermis was transferred into 0.05% trypsin (Gibco) and incubated for 20 min at 37°C. The cell suspension was poured through a 70 µm cell strainer and centrifuged for 10 min at 110 × g. Next, the cell pellet was washed in culture medium and centrifuged for 10 min at 160 × g. The cell pellet was then resuspended in CnT-07 medium (CELLnTEC Advanced Cell Systems AG, Bern, Switzerland) and keratinocytes were transferred onto a 1 µg/cm² collagen type IV (Sigma-Aldrich, Saint Louis, MO, USA)-coated culturing flasks (Starstedt) at 37°C with 5% CO₂.

2.3 Human full skin equivalents

Our FSE development protocol was based on previous experiments (30). MatriDerm® (MedSkin Solutions Dr. Suwelack AG, Billerbeck, Germany) with a thickness of 3 mm was cut into circular pieces of 1.13 cm². At day one, 2 × 10⁵ fibroblasts were seeded onto the matrix and the matrix was submerged in culture medium containing 65 µg/mL ascorbic acid for 4 days at 37°C with 5% CO₂ (Figure 1A). Subsequently, 1 × 10⁵ keratinocytes were seeded on the opposite side and the model was cultured submerged in FSE I medium containing 2 ng/ml KGF (ImmunoTools GmbH, Friesoythe, Germany) and 0.5 ng/ml EGF (R&D Systems, Inc., Minneapolis, MN, USA) for 4 days at 37°C with 5% CO₂. Next, the FSE was transferred to a transwell (Starstedt) and cultured air-exposed in deep well plates (Greiner Bio-One BV, Alphen aan den Rijn, the Netherlands) with FSE II medium containing 4 ng/ml KGF and 1 ng/ml EGF. From day 11 onward the FSE was cultured in FSE III medium containing 4 ng/ml KGF and 1 ng/ml EGF and from day 15 onward in FSE III medium that was refreshed twice weekly. At day 22, the FSE was ready to use for immune cell culture. Cell numbers and culture conditions are based on preceding experiments (30).

2.4 Induction of burn injury

Our burn injury procedure was based on previous experiments (30). A copper plate (2 × 10 mm) attached to a PACE intelliHeat ST50 soldering iron (Vass, USA) was heated to 80–90°C and stably applied to the epidermal side of the FSE for 20 sec to make contact without exerting pressure or indenting the FSE samples (Figure 1A). The temperature of the copper device was measured by an external digital thermometer (Farnell InOne, Utrecht, the Netherlands). Using this procedure, we created a burn injury that covered about 19% of the surface area of the model.

2.5 PBMC isolation from human buffy coat

PBMCs were isolated from buffy coats obtained from healthy donors (Sanquin, Amsterdam, the Netherlands) by density gradient centrifugation using Lymphoprep (Stemcell Technologies, Vancouver, Canada). The buffy coat was diluted in 0.5% Bovine serum albumin in PBS and layered over the density gradient medium. After centrifugation at 1000 × g for 15 min (without brakes), the PBMCs were collected in FSE I medium. Cells were resuspended in 50% fetal bovine serum (Gibco) + 40% FSE I medium + 10% dimethyl sulfoxide. After 24 h storage in Mr. Frosty (ThermoFisher scientific) with isopropanol at -80°C, cells were stored in liquid nitrogen until use.

2.6 Incorporating monocytes into the FSE

PBMCs were incubated with anti-CD14 beads (Invitrogen, Waltham, MA, USA) at a bead/cell ratio of 2.5:1 at 2–8°C for 20 min on a tube roller. Monocytes were isolated from the PBMCs using a magnet (Invitrogen Dynal AS, Oslo, Norway). Monocytes were resuspended in FSE I medium and 2.5 × 10⁵ cells were added

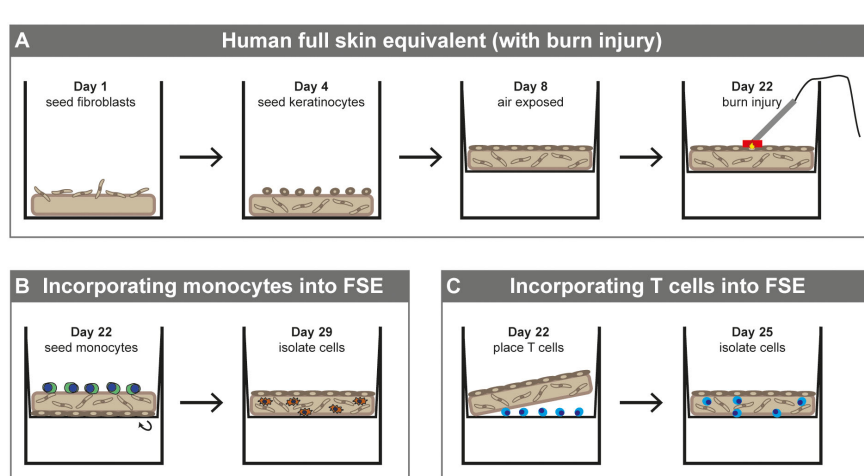


FIGURE 1

Development of human full skin equivalent (burn wound) model with monocytes or T cells. (A) Development of FSE. (B) Incorporating monocytes into FSE (directly after burn injury). (C) Incorporating T cells into FSE (directly after burn injury).

to the dermal side of the FSE. For burn-injured FSEs, the cells were added directly after burn injury was inflicted. Inverted FSE with monocytes was incubated at 37°C for 2 h and subsequently placed back into the transwell (Figure 1B). The FSE with monocytes was cultured for 7 more days with a medium change at day 3.

2.7 Incorporating T cells into the FSE

Lymphocytes were isolated by culturing PBMCs in a culture flask. After 24 h, adherent cells were removed. T cells were activated by adding anti-CD3/CD28 Dynabeads (Gibco) at a bead/cell ratio of 5:1 at 37°C for 4 h. After the activation, cells were resuspended in FSE I medium and 2.5×10^5 cells were placed between the transwell membrane and the dermal side of the FSE (Figure 1C), based on previous findings (35). Of these cells, $71 \pm 14\%$ was CD3⁺. For burn-injured FSEs, the cells were added directly after burn injury was inflicted. The FSE with T cells was cultured for 3 more days.

2.8 Dissociation of FSE for flow cytometry analysis

The FSE dissociation procedure was based on a protocol from He et al. (36). Macrophage FSEs were incubated with 0.25 U/ml collagenase A (Roche) at 37°C in a shaking water bath for 20 min. Because enzymes affect the expression chemokine receptors (37), T cell models were not dissociated using collagenase A. FSEs were then put in C-tubes (Miltenyi Biotec GmbH, Bergisch Gladbach, Germany) with 5 mL of PBS containing 1 mM EDTA and (further) dissociated by running program “B” twice on a tissue dissociator (gentleMACS, Miltenyi Biotec GmbH). Samples were passed through a 500 µm cell-strainer (PluriSelect) and then a 40 µm cell strainer (Sarstedt) to obtain a single cell suspension.

2.9 Flow cytometry

Single cell suspensions were stained using the macrophage or T cell panel (Supplementary Table 2). Zombie Aqua (BioLegend, San Diego, CA, USA) was used in the macrophage panel and propidium iodide (Miltenyi Biotec GmbH) was used in the T cell panel to determine viability of cells. Stained cell samples were acquired on the flow cytometer (MACS Quant Analyzer 10, Miltenyi Biotec GmbH) and gating (Supplementary Figure 1) was performed in FlowLogic (Inivai Technologies, Victoria, Australia).

2.10 Immunohistochemistry

See Supplementary Table 3 for antigen retrieval and primary antibodies. Kryofix (50% ethanol + 7% PEG300 in demineralized water)-fixed paraffin-embedded samples were cut into sections with a thickness of 5 µm and rehydrated followed by hematoxylin and eosin staining or blocking of endogenous peroxidase using 1% hydrogen peroxide at room temperature for 15 min. After antigen

retrieval was performed, sections were pre-incubated with 5% normal goat serum (Sigma-Aldrich) diluted in PBS + 1% bovine serum albumin (ThermoFisher). Sections were then incubated with primary antibodies at room temperature for 1 h followed by incubation with a poly-HRP-goat-anti-mouse or rabbit secondary antibody (BrightVision, VWR, Amsterdam, the Netherlands) at room temperature for 30 min. After washing, detection was established using 3,3'-diaminobenzidine (DAB). After DAB staining was completed, sections were counterstained with hematoxylin, dehydrated and mounted with Eukit Mounting Medium (Sigma-Aldrich).

2.11 Lactate dehydrogenase staining

Snap-frozen FSEs from -80°C were thawed and fixated in 1% paraformaldehyde (Sigma) for 2 h at 4°C. The FSEs were then put in 20% sucrose (Sigma) in PBS solution overnight at 4°C. FSEs were embedded in Tissue Tek OCT (Sakura Finetek Europe B.V., Alphen aan de Rijn, Netherlands) and sections of 10 µm were cut using a cryotome (Slee MNT, Adamas Instruments B.V., Rhenen, Netherlands). Dried sections were washed in PBS and incubated with LDH solution (2 mM Gly-Gly (Sigma); 0.75% NaCl (Sigma); 5% polypep (Sigma); 1.75 mg/ml β-nicotinamide adenine dinucleotide (Sigma); 3 mg/ml nitroblue tetrazolium (Sigma) in demineralized water of pH 8) for 3 h at 37°C. Sections were washed in tap water at 50°C and in PBS and then stained with Eosin Y for 4 min. Sections were then put in PBS for 1 sec, acetone for 30 sec, acetone/xylene (1:1) for 1 min and xylene for 1 min, before embedding with Eukit Mounting Medium.

2.12 Microscopy

Microscopic visualization was performed with a Zeiss Axioskop40FL microscope (Zeiss, Breda, The Netherlands). Images were acquired using a Nikon Eclipse TS2 camera and the NIS-Elements software version 4.4 (Nikon Instruments, Amsterdam, The Netherlands).

2.13 Re-epithelialization rate

Length of re-epithelialization in the FSEs was measured in microscopic images of H&E-stained sections by two assessors using NIS-Elements software. The mean of the two wound sides was used for analysis.

2.14 Immunoassay

Cytokines, chemokines and growth factors were analyzed in samples of medium. Neat samples were measured using the Human Essential Immune Response LegendPlex Multi-analyte Flow Assay kit (cat. 740929, BioLegend), according to the manufacturer's instructions and were acquired on the flow cytometer. This 13-

plex immunoassay included: IFN- γ , IL-1 β , IL-2, IL-4, IL-6, IL-8 (CXCL8), IL-10, IL-12p70, IL-17A, IP-10 (CXCL10), MCP-1 (CCL2), TNF- α and TGF- β 1. Concentrations were determined using FlowLogic software. When cytokine levels were lower than the standard range, the lowest level of quantification was used. When cytokine levels were higher than the standard range, the levels were estimated based on the fluorescent signal in the assay.

2.15 Statistical analysis and data visualization

We used the Shapiro-Wilk test in R (ggpubr and ggplot2 packages, open source) to determine distribution of data and found that the majority of data were not normally distributed. Therefore, differences in cell number/percentages and cytokines levels between different modeling conditions were explored using Mann-Whitney U test in R (ggpubr and ggplot2 packages, open source). Data was visualized using R (ggplot2 package, open source) and significant (p value of < 0.05) differences were indicated by asterisks.

3 Results

3.1 Human FSEs facilitate the study of burn injury *in vitro*

FSEs were generated by seeding human keratinocytes and fibroblasts into a collagen-elastin containing matrix from MatriDerm

(see Figure 1A for procedure), as we described previously (30). After 3 weeks of culture, the FSEs presented a well-established epidermis and dermis (Figures 2A, B). Burn injury inflicted on the FSE was visualized by microscopy. Three days post injury the burn wound was visible, characterized by detachment of the epidermis from the affected region of the dermis (Figure 2C). Staining for lactate dehydrogenase (LDH) (38) showed viable cells in the dermis (fibroblasts) and epidermis (keratinocytes) up to the wound edge but not in the wound, confirming that the injury resulted in cell damage (Figure 2D).

3.2 Monocytes differentiated into macrophages in the FSEs and showed upregulated M1 marker expression upon burn injury

Unstimulated monocytes were introduced to full-established (burn-injured) FSEs to simulate an innate immune response. To prevent the cells from adhering to the transwell membrane, monocytes (about 2.5×10^5) were administered directly to the dermal side of the FSEs (see Figure 1B for procedure). Monocytes cultured in suspension or in matrix without skin cells served as controls. Through microscopy analysis, we confirmed the presence of monocytes within the FSE in both uninjured and burn-injured models (Figure 3A). Monocytes seemed to downregulate or lose monocyte marker CD14 (data not shown) and upregulate the expression of macrophage marker CD68 in the cultured FSEs, regardless of burn injury (Figure 3A). This showed that the monocytes differentiated into macrophages within a span of 7

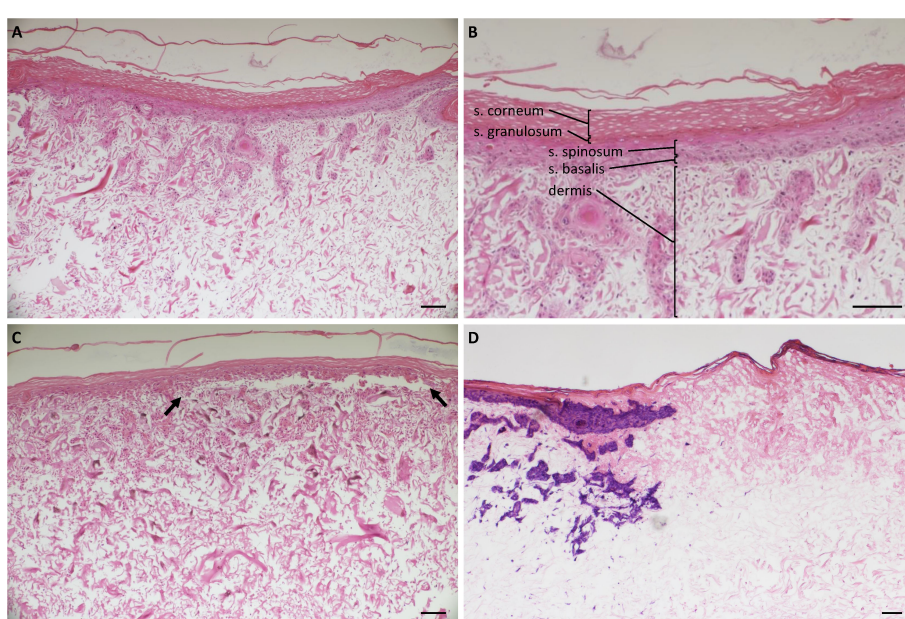


FIGURE 2

Histology of uninjured and burn-injured FSEs. H&E staining of (A) Uninjured FSE after 3 weeks of culture; (B) Uninjured FSE after 3 weeks of culture at a higher magnification. Dermis and the different epidermal layers are indicated: stratum corneum, s. granulosum, s. spinosum and s. basalis; (C) FSE after 3 weeks of culture and 3 days after burn injury. The detached epidermis caused by the burn is clearly visible between black arrows. (D) Immunohistochemical LDH staining of an FSE after 3 weeks of culture and 3 days after burn injury. Blue-purple staining indicates viable cells present in the epidermis (keratinocytes) and dermis (fibroblasts) up until the wound edge. Experiments were performed in duplicate using keratinocytes and fibroblasts from 6 different donors. Black scale bar = 100 μ m; black arrows indicate burn injured area.

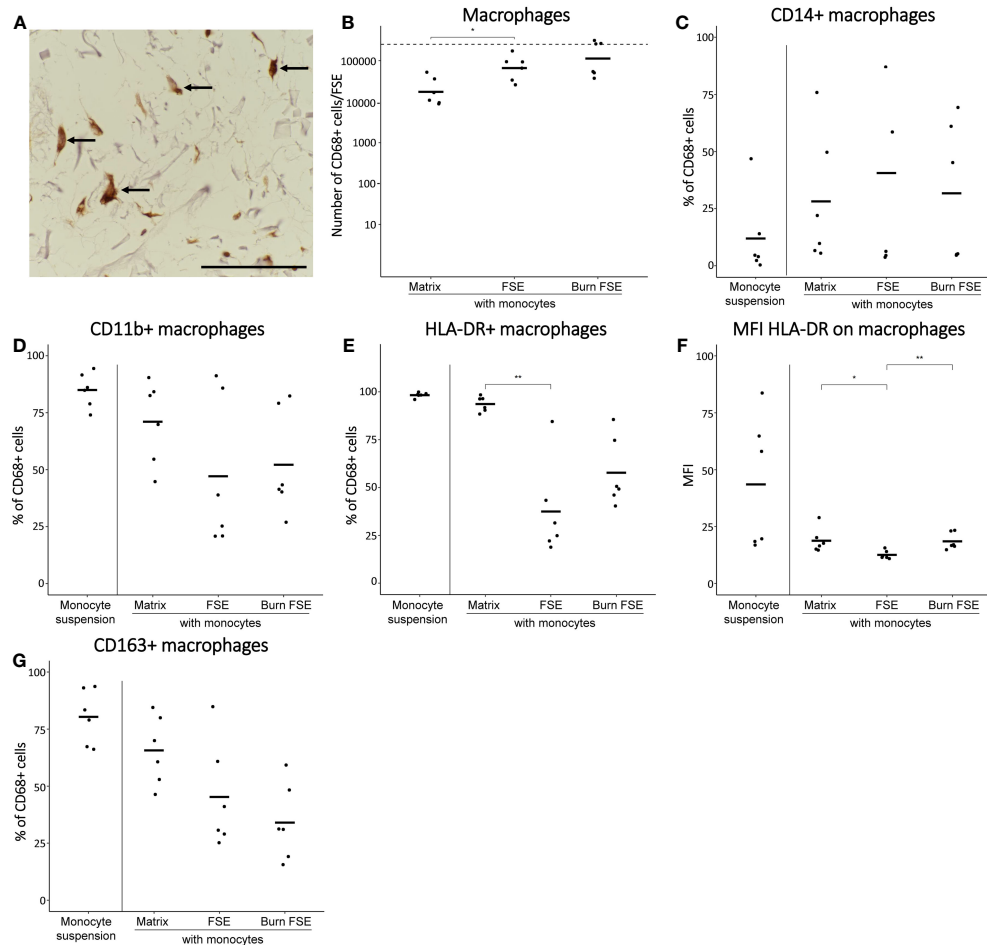


FIGURE 3

Monocytes after 7 days of culture in (burn-injured) FSEs. (A) Immunohistochemical CD68 staining of an injured FSE. Black arrows point to positive cells in the FSE. (B) Number of CD68⁺ cells (macrophages) per FSE after isolation based on flow cytometry; dashed line indicates the number of monocytes added to the dermal side of the FSE. Percentage of CD68⁺ cells (macrophages) that were (C) CD14⁺; (D) CD11b⁺; (E) HLA-DR⁺. (F) Mean fluorescence intensity (MFI) of HLA-DR on CD68⁺ cells macrophages. (G) Percentage of CD68⁺ cells (macrophages) that were CD163⁺. Experiments were performed in duplicate using 6 different keratinocyte donors, 6 fibroblast donors and 4 monocytes donors. Only comparisons between monocytes in matrix, in uninjured FSEs and in burn-injured FSEs are shown. Statistically significant differences were calculated using Mann-Whitney U test. Significant differences are indicated by asterisks: *p < 0.05; **p < 0.01.

days. Rate of re-epithelialization in the FSEs after 7 days was $347 \pm 16 \mu\text{m}$. The re-epithelialization rate was slightly higher in FSEs with monocytes ($439 \pm 126 \mu\text{m}$), but did not reach significance.

To study the effect of burn injury on these monocyte-derived macrophages in more detail, FSEs were dissociated after 7 days of culturing the full-established FSEs. Using flow cytometry, we identified the macrophages based on their expression of CD68 (macrophage marker), CD14 (monocyte marker), CD11b (activation marker), HLA-DR (M1 differentiation marker) and CD163 (M2 differentiation marker). In uninjured FSEs, an average of 8.0×10^4 CD68⁺ macrophages were present (Figure 3B). There was high variability in the fraction of CD68⁺ macrophages that expressed CD14 or CD11b (Figures 3C, D), irrespective of burn injury. This variation in macrophage differentiation and activation within the FSEs, was presumably dependent on the donor (buffy coat, fibroblast or keratinocyte donor). Comparing the FSEs to macrophages cultured in the matrix without skin cells, we observed a smaller proportion of HLA-DR⁺ or CD163⁺ (Figures 3E, G) macrophages in the FSEs. Burn injury

appeared to increase the average number of CD68⁺ macrophages in the FSE (1.6×10^5 ; Figure 3B), although not significantly. Interestingly, the percentage of CD14⁺ macrophages was significantly decreased after burn injury (Figure 3C). Furthermore, burn injury significantly increased the expression of HLA-DR on macrophages (Figure 3F) and appeared to decrease the percentage of CD163⁺ macrophages within the FSEs (Figure 3G). Thus, we generated a human FSE model incorporating monocytes capable of actively differentiating into macrophages during culture and observed that burn injury appeared to enhance M1 differentiation of macrophages.

3.3 Inclusion of monocytes in FSEs slightly increased production of inflammatory cytokines, regardless of burn injury

At day 7 (when FSEs were terminated), the levels of 13 inflammatory cytokines in the culture media were analyzed

(Figure 4). In the absence of monocytes, FSEs secreted high levels of IL-6, IL-8 and MCP-1 (Figure 4D, E; Supplementary Figure 2). Burn injury significantly increased the level of IL-8 and IL-12p70 (Figures 4E, G). Because of the high MCP-1 levels in the FSEs, the cytokine assay reached maximum signals, making it impossible to detect differences in MCP-1 levels between burn-injured and uninjured models. When monocytes were incorporated into the FSEs, there was a slight increase in the levels of IL-4, IL-6, IL-8, IP-10 and TGF- β 1 (Figures 4C-E, H, I). Burn injury on the monocyte incorporated FSEs led to a further increase of IL-8. Cytokines IL-2, IL-17A and TNF- α were not detected in any of the experimental conditions (Supplementary Figure 2).

3.4 T cells that migrated into FSEs expressed Th1 and Th17 chemokine receptors, irrespective of burn injury

To simulate an adaptive immune response, we introduced CD3/CD28 bead pre-activated T cells into fully-established (burn-

injured) FSEs. Approximately 2.5×10^5 T cells were placed between the transwell membrane and the dermal side of the FSEs, and they were cultured for a duration of 3 days (see Figure 1C for procedure), following a previously established protocol (35). Pre-activated T cells cultured in suspension or in matrix without skin cells served as controls. Using microscopy, we could detect CD3 $^+$ T cells that had actively migrated into the FSEs (Figure 5A). As 3 days was too soon after burn injury, the re-epithelialization rate in these FSEs could not be measured.

Following a 3-day culture period, FSEs were dissociated to perform flow cytometric analysis of T cells. T cell differentiation was examined based on their expression of CD3 (T cell marker), CD4 (effector T cell marker), CD25/CD127 (activation marker and regulatory T cell marker), CXCR3 (Th1 differentiation marker) and CCR4/CCR6 (Th17 differentiation marker). Only a small portion (2.8×10^3) of T cells had migrated into the FSEs (Figure 5B). Among these migrated T cells, the majority (approximately 86.7%) were CD4 $^+$ T cells (Figure 5C). Most of these CD4 $^+$ T cells expressed CD25, indicating their activation and suggesting a correlation between T cell activation and migration (Figure 5D).

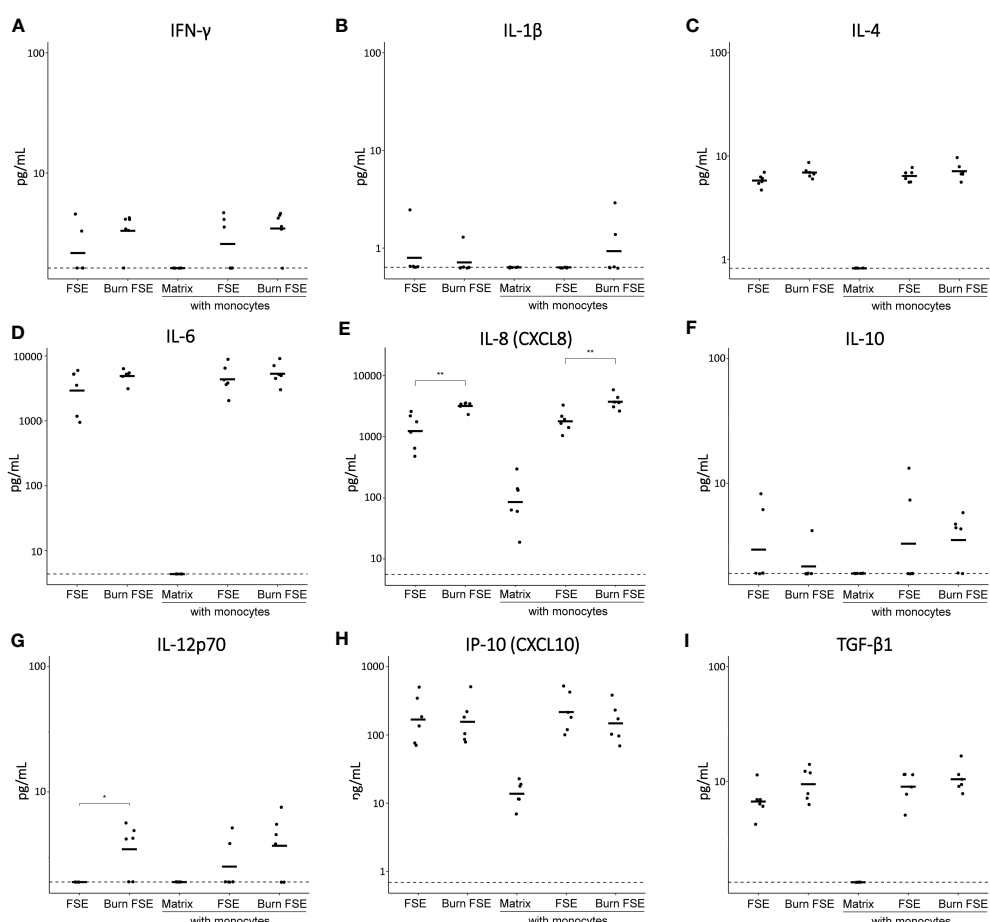


FIGURE 4

Cytokine levels in medium of (burn-injured) FSEs after 7 days of culture with monocytes. (A) IFN- γ ; (B) IL-1 β ; (C) IL-4; (D) IL-6; (E) IL-8; (F) IL-10; (G) IL-12p70; (H) IP-10; (I) TGF- β 1. Samples from biological duplicates were averaged per donor. Concentrations are reported in pg/mL medium. Experiments were performed in duplicate using 6 different keratinocyte donors, 6 fibroblast donors and 4 monocytes donors. The dashed line indicates the lowest level of quantification. Statistically significant differences were calculated using Mann-Whitney U test. Only comparisons between uninjured and burn-injured models or between models without and with monocytes are shown. Significant differences are indicated by asterisks: * $p < 0.05$; ** $p < 0.01$.

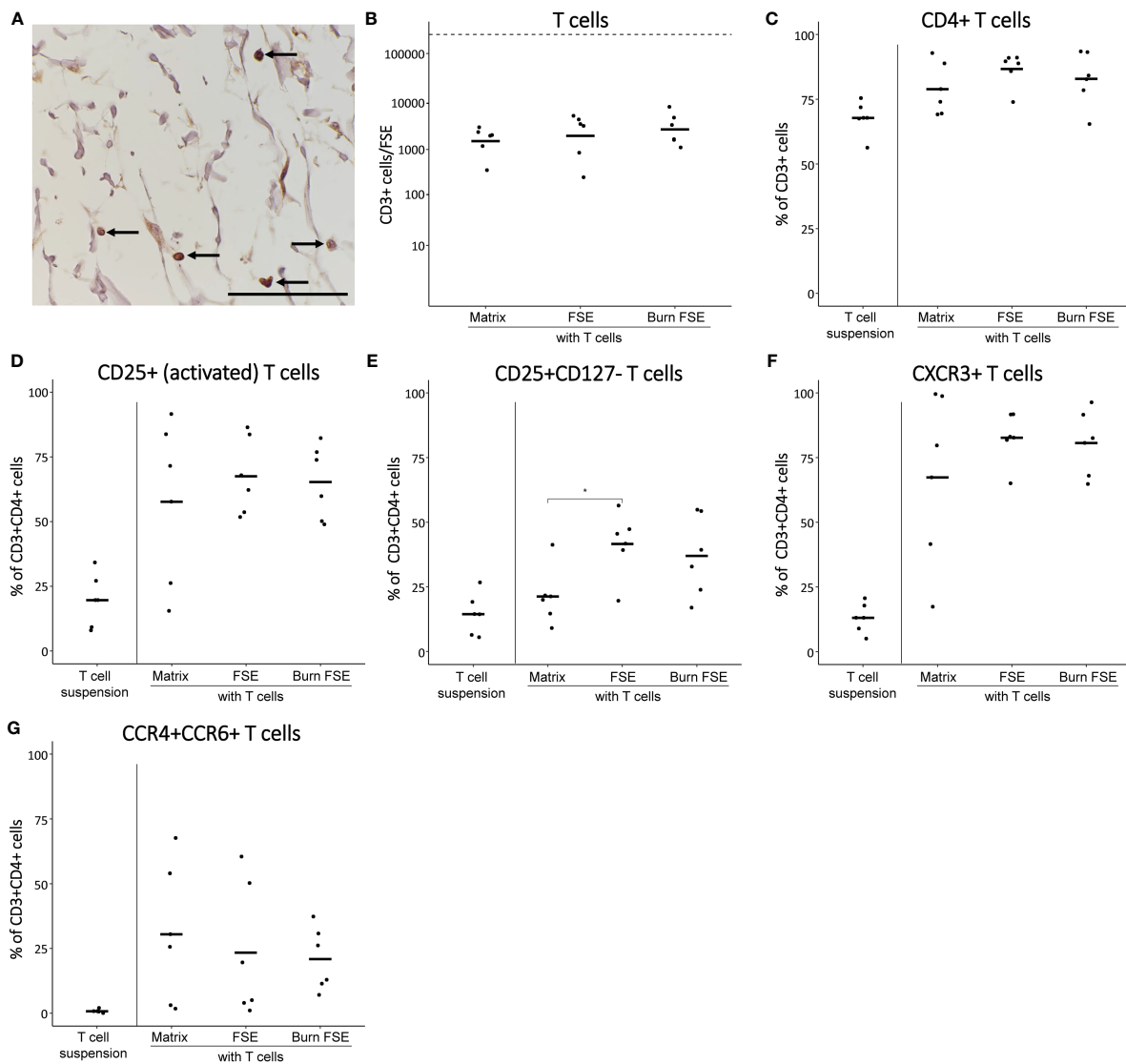


FIGURE 5

Pre-activated T cells after 3 days of culture in (burn-injured) FSEs. **(A)** Immunohistochemical CD3 staining of an injured FSE. Black arrows point to positive cells in the FSE. **(B)** Number of T cells (CD3⁺ cells) per FSE after isolation using flow cytometry; dashed line indicates the number of T cells added to the transwell. **(C)** Percentage of CD3⁺ (T cells) that are CD4⁺. Percentage of CD3⁺CD4⁺ T cells that were **(D)** CD25⁺; **(E)** CD25⁺CD127⁻; **(F)** CXCR3⁺; **(G)** CCR4⁺CCR6⁺. Experiments were performed in duplicate using 6 different keratinocyte donors, 6 fibroblast donors and 5 T cell donors. Only comparisons between T cells in matrix, in uninjured FSEs and in burn-injured FSEs are shown. Statistically significant differences were calculated using Mann-Whitney U test. Significant differences are indicated by asterisks: *p < 0.05.

The percentage of CD25⁺CD127⁻ T cells, potentially indicating Treg differentiation, was higher in the FSEs compared to T cells cultured in the matrix alone (Figure 5E). Furthermore, the FSEs contained a higher percentage of CXCR3⁺ T cells, indicating enhanced Th1 activity (Figure 5F). Similarly, an increase in the percentage of CCR4⁺CCR6⁺ T cells was observed in the FSEs, suggesting augmented Th17 activity (Figure 5G). The average number of T cells in burn-injured FSEs was comparable to that in the uninjured FSEs (Figure 5B) and burn injury did significantly not affect the investigated T cell markers (Figures 5D-G). Together, our findings demonstrate that particularly activated T cells migrated into the FSEs, and there is a potential enhancement of Treg and Th1/Th17 activation, regardless of burn injury.

3.5 Inclusion of T cells in uninjured or burn-injured FSEs increased the levels of inflammatory cytokines

To investigate cytokine secretion in the T cell-incorporated FSEs, we analyzed the culture medium at day 3. FSEs without T cells produced high levels of IL-6, IL-8 and MCP-1 (Figures 6C, D; Supplementary Figure 3), consistent with the expression observed after 7 days of culture (Figures 4C, D; Supplementary Figure 2). In FSEs cultured without T cells, burn injury significantly increased the levels of IL-4, IL-6, IL-8, IL-12p70 and TGF- β 1 (Figures 6B-D, F, I).

Introducing T cells into uninjured FSEs resulted in elevated levels of IFN- γ , IL-2, IL-4, IL-6, IL-8, IL-10, IL-12p70, IL-17A, IP-10

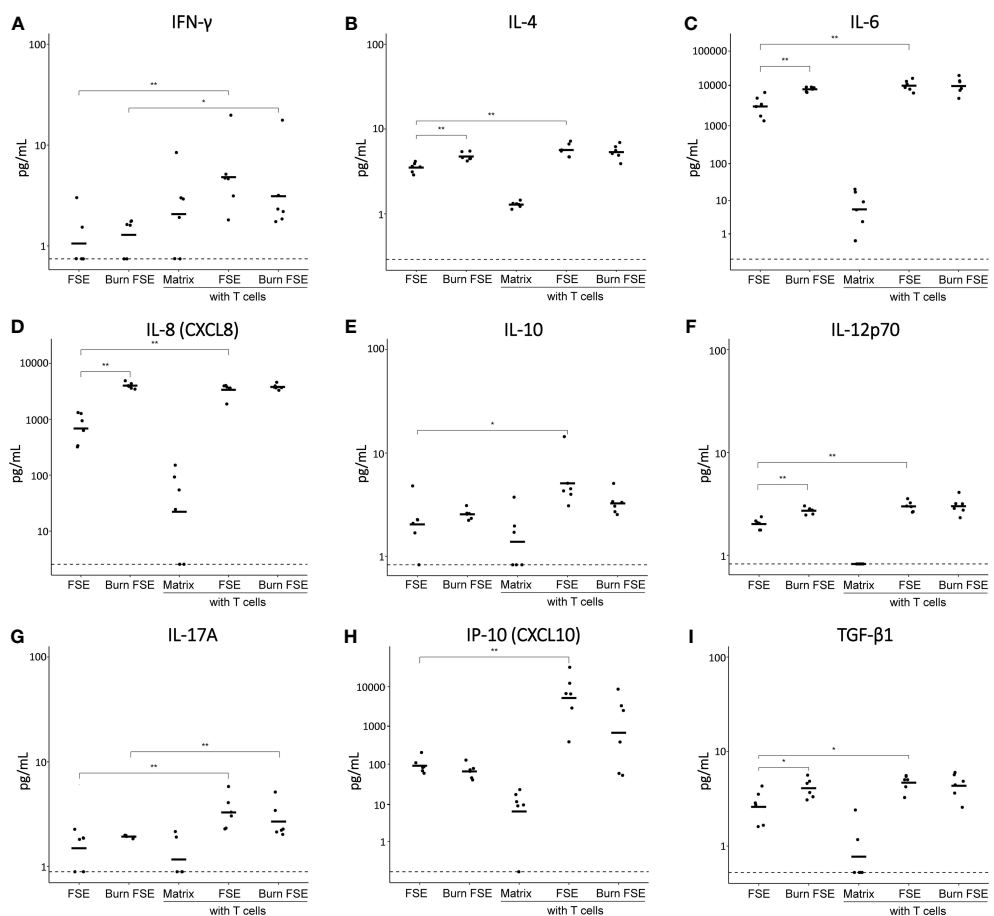


FIGURE 6

Cytokine levels in medium of (burn-injured) FSEs after 3 days of culture with pre-activated T cells. (A) IFN- γ ; (B) IL-4; (C) IL-6; (D) IL-8; (E) IL-10; (F) IL-12p70; (G) IL-17A; (H) IP-10; (I) TGF- β 1. Samples from biological duplicates were averaged per donor. Concentrations are reported in pg/mL medium. Experiments were performed in duplicate using 6 different keratinocyte donors, 6 fibroblast donors and 5 T cell donors. The dashed line indicates the lowest level of quantification. Statistically significant differences were calculated using Mann-Whitney U test. Only comparisons between uninjured and burn-injured models or models without and with T cells are shown. Significant differences are indicated by asterisks: *p < 0.05; **p < 0.01.

and TGF- β 1 (Figures 6A–I; Supplementary Figure 3). While burn injury did not further increase the levels of these cytokines, it slightly decreased the levels of IL-10 and IP-10 in the presence of T cells. IL-2 was only detected in the presence of T cells and no significant differences were observed for the levels of IL-1 β and TNF- α (Supplementary Figure 3). Overall, the inclusion of T cells in the FSEs appeared to further increase both pro- and anti-inflammatory cytokines, while burn injury specifically reduced the T cell induced levels of IL-10 and IP-10.

4 Discussion

There is a pressing need for appropriate, animal-free models to investigate immune reactions following burn injury. Conventional FSEs cannot capture the complex immune responses associated with burn injury because they lack crucial immune components such as monocytes and T cells (5, 26, 27, 30, 39–43). As monocytes are actively involved in the acute inflammatory phase and T cells are

crucial for regulation of ongoing inflammation, these cells are essential to model the burn immune response more accurately (44, 45). In this study, we developed an FSE and incorporated monocytes or T cells to simulate innate and adaptive immune reactions to burn injury, respectively. Flow cytometry analysis of human primary monocytes or T cells cultured in the FSEs allowed us to examine changes in immune cell phenotype and cytokine expression between 3 to 7 days.

Certain cytokines, namely IL-6, IL-8 and MCP-1, were expressed by the FSEs even in the absence of immune cells. This secretion of cytokines was also seen by others (40) and likely originates from stress responses in fibroblasts and keratinocytes induced by *in vitro* culturing and skin morphogenesis. This cell stress response should not be overlooked; however, information regarding its cause or methods to reduce it is very limited. Interestingly, burn injury further increased the levels of IL-4, IL-6, IL-8, IL-12p70 and TGF- β 1, significantly at day 3. By day 7, only IL-8 and IL-12p70 remained significantly increased compared to uninjured FSEs, suggesting a reaction of the fibroblasts and/or

keratinocytes to the burn injury. This indicates that these cytokines are likely involved in the initiation of an inflammatory response. Previous studies utilizing fibroblasts and keratinocytes in similar collagen matrices have also reported increased levels of pro-inflammatory cytokines, such as IL-6, IL-8, and MCP-1, in response to burn injury (30, 40, 46).

We demonstrated the differentiation of monocytes into macrophages in these FSE within 7 days. This was shown by upregulation of CD68 expression in monocytes, consistent with previous findings by Smith et al. and Safi et al. (47, 48). Burn-injured FSEs contained macrophages with enhanced expression of HLA-DR compared to uninjured FSEs, indicating an M1-like response of macrophages to burn injury. HLA-DR expression on macrophages is an MHC class II molecule associated with inflammatory stimuli and M1 activity (49). The high percentage of HLA-DR⁺ macrophages that we found when they were cultured in suspension could be attributed to the culture conditions such as the media or the cell repellent surface (50). Although CD163 expression, indicative of M2 activation, showed a slight decrease in burn-injured FSEs, it was not statistically significant. Variation in the number of cells expressing CD14 and CD11b markers among different PBMC donors suggests distinct (donor-dependent) activation or differentiation rates. Although the increase of M1 macrophages is advantageous early during wound healing, it might slow down wound healing when M1 macrophages persist in the wound area. In this study, we did not observe a significant difference in re-epithelialization rate between FSEs with or without macrophages. It would be interesting to see how these macrophages behave over a longer period of time and if they can be manipulated towards M1 or M2 to either delay or accelerate wound healing, as is suggested to happen *in vivo* (20). Despite the increased expression of HLA-DR on macrophages, there was a minimal effect on cytokine expression. In order to observe an effect on cytokine expression, the model might need to include higher numbers of monocytes or specific macrophage subtypes.

Several studies have developed skin models with macrophages to investigate skin diseases such as inflammatory skin disorders and carcinoma. For instance, Chung et al. co-cultured FSEs with RAW264.7 cells to simulate inflammatory skin responses, highlighting interactions between skin cells and macrophages that affect cytokine production and the degree of inflammation (51). In this model, the FSE was placed on a transwell membrane while RAW264.7 cells were cultured underneath the transwell. Linde et al. developed a human skin squamous cell carcinoma model incorporating PBMC-derived macrophages to study macrophage polarization and identified M2 activation in their tumor model (52). In another study, Bechettoille et al. produced a dermal construct with fibroblasts and investigated the effect of introducing dermal-type macrophages on cytokine production and macrophage phagocytic potential (53). Our study uniquely focused on the effect of burn injury on primary monocytes within a 3D skin model, allowing flow cytometry and cytokine production analysis.

When pre-activated T cells were introduced to the FSEs, a fraction of these cells actively migrated into the FSEs. The population of migrated T cells showed increased numbers of both

Th1 receptor CXCR3 expressing cells (54) and Th17 receptors CCR4/CCR6 expressing cells (55), regardless of burn injury. This coincided with elevated levels of pro-inflammatory cytokines such as IFN- γ , IL-6, IL-8, IL-12p70, IL-17A, and IP-10. The production of chemokines like IP-10, induced by IFN- γ , is known to occur in inflamed tissue (56, 57). IP-10 is a chemoattractant for T cells and binds to chemokine receptor CXCR3 (58). The decrease in IP-10 production in burn-injured FSEs may be attributed to the loss of keratinocytes caused by the burn injury, as about 19% of the surface area of the model was burned. Moreover, the percentage of CD25⁺CD127⁻ T cells, possibly Tregs, was increased, accompanied by elevated levels of IL-4, IL-10, and TGF- β 1. However, IL-10 production was slightly reduced in burn-injured FSEs, which could be related to keratinocyte destruction or impaired regulatory activity caused by burn injury. Nevertheless, more research is needed to elucidate the role of different T cells during wound healing.

Our approach to incorporate T cells into the FSEs was inspired by previous studies in which T cells were cultured in an epidermal construct to examine their interactions with keratinocytes (35, 59). Similar skin models have been utilized to understand the pathophysiology of skin diseases such as psoriasis or atopic dermatitis (35, 60, 61). In these studies, T cells were stimulated to favor Th1/Th17 responses to explore their role in psoriatic skin models (60, 61). Shin et al. established a T cell model that showed a psoriatic epidermal phenotype and characteristic cytokine profiles and responded to various classes of psoriasis drugs (60). After infiltration of activated T cells, the psoriatic skin model from Lorthois et al. displayed a strong psoriasis-like activated inflammatory phenotype, including altered differentiation of keratinocytes and increased secretion of pro-inflammatory cytokines (61).

In our study, only a small fraction of pre-activated T cells migrated into the FSEs. Several factors may have contributed to this limited migration, including incomplete activation or overactivation of T cells, T cell death, insufficient migratory activity, or suboptimal isolation of the cells from the FSEs. To preserve the presence of chemokine receptors, we performed the isolation of T cells from FSEs without the use of collagenase, which is known to affect these receptors. However, this approach might have led to a lower yield of T cells compared to monocytes/macrophages obtained from the FSEs. The migratory activity of T cells can be enhanced by introducing additional chemotactic stimuli, such as T cell chemokines MIP-1 α (CCL3), MIP-1 β (CCL4), and RANTES (CCL5) (44). Exploring the effects of prolonged culture on the migratory activity as well as the phenotype and cytokine production of T cells would also be of interest. Furthermore, the technique used to prepare T cells can be improved by using magnetic or fluorescence cell sorting to establish an enriched population of T cells prior to their introduction into the model.

Our FSE model offers distinct advantages over other models by utilizing primary cells rather than cell lines, thereby making these models more representative for the *in vivo* situation. Furthermore, unlike microscopy-based studies, our research employed flow

cytometry for quantification and analysis of macrophages and T cells. Although our flow cytometry panel did not include markers specific to keratinocytes and fibroblasts, investigating their expression of markers such as elafin, CK10, CK17, CD10, Ki67, FAP, or α -SMA, could provide more detailed insights into the effect of monocytes or T cells on burn wound healing processes. Although the effect of burn injury on the studied monocyte and T cell markers appeared limited in our current set-up, further investigations involving other time points, longer culture periods, distinct immune cell activation methods or different burn techniques (i.e. burn temperature or duration) are warranted. In addition, our model can be used to study the effect of burn injury on specific immune cell subsets, or a combination thereof. This can be achieved by differentiating monocytes into M1 or M2 macrophages or skewing T cells towards Tregs, Th1, Th2, or Th17 cells before introducing them into the FSEs. Including neutrophils in the model, despite the challenges involved, would also contribute to a better understanding of the burn-induced immune response and their role in wound healing (5, 62). However, culturing neutrophils in FSEs is difficult due to their short lifespan and the inability to cryopreserve them (63). Integrating a combination of certain immune cell subsets in the FSE will create an even more realistic environment to simulate burn wound healing and it would be interesting to study cell interactions (64) and the effect on wound parameters.

In conclusion, our developed FSE incorporating monocytes and T cells represents a significant step towards the development of a more realistic skin model that allows the study of innate and adaptive immune reactions related to burn injury, while avoiding the use of experimental animals. Ultimately, our immunocompetent model has the potential to advance the study of therapeutics modulating inflammatory reactions in burned skin to improve wound healing.

Data availability statement

The raw data supporting the conclusions of this article will be made available by the authors, without undue reservation.

Ethics statement

Ethical approval was not required for the studies involving humans because in this study, tissue samples were obtained from planned elective plastic surgeries (healthy skin) that were part of routine patient treatment. Therefore, these tissues are residual materials and no evaluation by the medical ethical committee was required for the collection of these samples. As described in the Materials and Methods section, we used an opt-out protocol to receive tissue samples. Subjects were informed of this procedure and were able to withdraw at any point. This procedure is in accordance with the national guidelines (<https://www.coreon.org/>) and institutional guidelines of the local hospitals in Beverwijk. Buffy coats from healthy donors were purchased at the Dutch Blood bank (Sanquin, Amsterdam, the Netherlands), in accordance with the national and institutional guidelines. The studies were conducted in

accordance with the local legislation and institutional requirements. Written informed consent for participation was not required from the participants or the participants' legal guardians/next of kin in accordance with the national legislation and institutional requirements because in this study, tissue samples were obtained from planned elective plastic surgeries (healthy skin) that were part of routine patient treatment. Therefore, these tissues are residual materials and no evaluation by the medical ethical committee was required for the collection of these samples. As described in the Materials and Methods section, we used an opt-out protocol to receive tissue samples. Subjects were informed of this procedure and were able to withdraw at any point. This procedure is in accordance with the national guidelines (<https://www.coreon.org/>) and institutional guidelines of the local hospitals in Beverwijk. Buffy coats from healthy donors were purchased at the Dutch Blood bank (Sanquin, Amsterdam, the Netherlands), in accordance with the national and institutional guidelines.

Author contributions

PM: Conceptualization, Data curation, Formal Analysis, Funding acquisition, Investigation, Methodology, Project administration, Software, Supervision, Visualization, Writing – original draft. MV: Conceptualization, Formal Analysis, Investigation, Methodology, Software, Validation, Visualization, Writing – review & editing. AE: Formal Analysis, Investigation, Methodology, Validation, Writing – review & editing. LR: Formal Analysis, Investigation, Software, Visualization, Writing – review & editing. LM: Formal Analysis, Investigation, Visualization, Writing – review & editing. EM: Conceptualization, Formal Analysis, Funding acquisition, Methodology, Project administration, Resources, Supervision, Writing – review & editing. IJ: Conceptualization, Formal Analysis, Funding acquisition, Methodology, Supervision, Writing – review & editing. HK: Conceptualization, Formal Analysis, Funding acquisition, Methodology, Supervision, Writing – review & editing. BB: Conceptualization, Formal Analysis, Funding acquisition, Methodology, Project administration, Resources, Supervision, Writing – review & editing.

Funding

The author(s) declare financial support was received for the research, authorship, and/or publication of this article. This research was funded by the Dutch Burns Foundation under grant numbers WO/17.108 (BB) and WO/22.106 (PM).

Acknowledgments

MatriDerm® was kindly provided as research material by MedSkin Solutions, Dr. Suwelack AG, Billerbeck, Germany. We thank Chloë Gans for technical assistance.

Conflict of interest

The authors declare that the research was conducted in the absence of any commercial or financial relationships that could be construed as a potential conflict of interest.

Publisher's note

All claims expressed in this article are solely those of the authors and do not necessarily represent those of their affiliated organizations, or those of the publisher, the editors and the reviewers. Any product that may be evaluated in this article, or claim that may be made by its manufacturer, is not guaranteed or endorsed by the publisher.

Supplementary material

The Supplementary Material for this article can be found online at: <https://www.frontiersin.org/articles/10.3389/fimmu.2023.1264716/full#supplementary-material>

References

1. Comish PB, Carlson D, Kang R, Tang D. Damage-associated molecular patterns and the systemic immune consequences of severe thermal injury. *J Immunol* (2020) 205:1189–97. doi: 10.4049/jimmunol.2000439
2. Jeschke MG, Chinkes DL, Finnerty CC, Kulp G, Suman OE, Norbury WB, et al. Pathophysiology response to severe burn injury. *Ann Surg* (2008) 248:387–400. doi: 10.1097/SLA.0b013e3181856241
3. Jeschke MG, van Baar ME, Choudhry MA, Chung KK, Gibran NS, Logsetty S. Burn injury. *Nat Rev Dis Prim* (2020) 6:1–25. doi: 10.1038/s41572-020-0145-5
4. Eming SA, Wynn TA, Martin P. Inflammation and metabolism in tissue repair and regeneration. *Science* (2017) 356:1026–30. doi: 10.1126/science.aam7928
5. Mulder PPG, Vlij M, Fasse E, Stoop MM, Pijpe A, van Zuijlen PPM, et al. Burn-injured skin is marked by a prolonged local acute inflammatory response of innate immune cells and pro-inflammatory cytokines. *Front Immunol* (2022) 13:1034420. doi: 10.3389/fimmu.2022.1034420
6. Mulder PPG, Koenen HJPM, Vlij M, Joosten I, de Vries RBM, Boekema BKHL. Burn-induced local and systemic immune response: systematic review and meta-analysis of animal studies. *J Invest Dermatol* (2022) 142:3093–3109.e15. doi: 10.1016/j.jid.2022.05.004
7. Velnar T, Bailey T, Smrkolj V. The wound healing process: An overview of the cellular and molecular mechanisms. *J Int Med Res* (2009) 37:1528–42. doi: 10.1177/147323000903700531
8. Rodrigues M, Kosaric N, Bonham CA, Gurtner GC. Wound healing: A cellular perspective. *Physiol Rev* (2019) 99:665–706. doi: 10.1152/physrev.00067.2017
9. Koh TJ, DiPietro LA. Inflammation and wound healing: the role of the macrophage. *Expert Rev Mol Med* (2011) 13:e23. doi: 10.1017/S1462399411001943
10. Wilgus TA, Roy S, McDaniel JC. Neutrophils and wound repair: positive actions and negative reactions. *Adv Wound Care* (2013) 2:379–88. doi: 10.1089/wound.2012.0383
11. Bergquist M, Hästbacka J, Glaumann C, Freden F, Huss F, Lipcsey M. The time-course of the inflammatory response to major burn injury and its relation to organ failure and outcome. *Burns* (2019) 45:354–63. doi: 10.1016/j.burns.2018.09.001
12. Lucas T, Waisman A, Ranjan R, Roes J, Krieg T, Muller W, et al. Differential roles of macrophages in diverse phases of skin repair. *J Immunol* (2010) 184:3964–77. doi: 10.4049/jimmunol.0903356
13. Mai T, Saunders M, Jett B. T Cell Development, Activation and Effector Functions. In: *Primer to the Immune Response*. Amsterdam, Netherlands: Elsevier (2014) p. 197–226. doi: 10.1016/B978-0-12-385245-8.00009-1
14. Ho AW, Kupper TS. T cells and the skin: from protective immunity to inflammatory skin disorders. *Nat Rev Immunol* (2019) 19:490–502. doi: 10.1038/s41577-019-0162-3
15. Rendon JL, Choudhry MA. Th17 cells: critical mediators of host responses to burn injury and sepsis. *J Leukoc Biol* (2012) 92:529–38. doi: 10.1189/jlb.0212083
16. Sasaki JR, Zhang Q, Schwacha MG, Manuscript A. Burn induces a Th-17 inflammatory response at the injury site. *Burns* (2011) 37:646–51. doi: 10.1016/j.burns.2011.01.028
17. Hao D, Nourbakhsh M. Recent advances in experimental burn models. *Biol (Basel)* (2021) 10:526. doi: 10.3390/biology10060526
18. Abdullahe A, Amini-Nik S, Jeschke MG. Animal models in burn research. *Cell Mol Life Sci* (2014) 71:3241–55. doi: 10.1007/s00018-014-1612-5
19. Hubrecht RC, Carter E. The 3Rs and humane experimental technique: implementing change. *Animals* (2019) 9:754. doi: 10.3390/ani9100754
20. Zomer HD, Trentin AG. Skin wound healing in humans and mice: Challenges in translational research. *J Dermatol Sci* (2018) 90:3–12. doi: 10.1016/j.jdermsci.2017.12.009
21. Seok J, Warren HS, Alex GC, Michael NM, Henry VB, Xu W, et al. Genomic responses in mouse models poorly mimic human inflammatory diseases. *Proc Natl Acad Sci U.S.A.* (2013) 110:3507–12. doi: 10.1073/pnas.1222878110
22. Mestas J, Hughes CCW. Of mice and not men: differences between mouse and human immunology. *J Immunol* (2004) 172:2731–8. doi: 10.4049/jimmunol.172.5.2731
23. Mathes SH, Ruffner H, Graf-Hausner U. The use of skin models in drug development. *Adv Drug Delivery Rev* (2014) 69–70:81–102. doi: 10.1016/j.addr.2013.12.006
24. Liu C, Rinderknecht H, Histing T, Kolbenschlag J, Nussler AK, Ehnert S. Establishment of an *in vitro* scab model for investigating different phases of wound healing. *Bioengineering* (2022) 9:191. doi: 10.3390/bioengineering9050191
25. Coolen NA, Verkerk M, Reijnen L, Vlij M, Van Den Bogaerd AJ, Breetveld M, et al. Culture of keratinocytes for transplantation without the need of feeder layer cells. *Cell Transplant* (2007) 16:649–61. doi: 10.3727/000000007783465046
26. Bergers LJJC, Reijnders CMA, van den Broek LJ, Spijkstra SW, de Gruyij TD, Weijers EM, et al. Immune-competent human skin disease models. *Drug Discovery Today* (2016) 21:1479–88. doi: 10.1016/j.drudis.2016.05.008
27. Pupovac A, Senturk B, Griffoni C, Maniura-Weber K, Rottmar M, McArthur SL. Toward immunocompetent 3D skin models. *Adv Health Mater* (2018) 7:1–11. doi: 10.1002/adhm.201701405
28. Min JH, Yun IS, Lew DH, Roh TS, Lee WJ. The use of Matriderm and autologous skin graft in the treatment of full thickness skin defects. *Arch Plast Surg* (2014) 41:330–6. doi: 10.5999/aps.2014.41.4.330
29. Maitz J, Wang Y, Fathi A, Ximena Escobar F, Parungao R, van Zuijlen P, et al. The effects of cross-linking a collagen-elastin dermal template on scaffold bio-stability and degradation. *J Tissue Eng Regener Med* (2020) 14:1189–200. doi: 10.1002/term.3082

SUPPLEMENTARY FIGURE 1

Gating strategy. Gating strategy is shown for (A) monocyte-derived macrophage panel and (B) T cell panel.

SUPPLEMENTARY FIGURE 2

Cytokine levels (IL-2, IL-17A, MCP-1, TNF- α) in medium of (burn-injured) FSEs after 7 days of culture with monocytes. Samples from biological duplicates were averaged per donor. Concentrations are reported in pg/mL medium. Experiments were performed in duplicate using 6 different keratinocyte donors, 6 fibroblast donors and 4 monocytes donors. The dashed line indicates the lowest level of quantification and the highest limit of quantification (for MCP-1). Statistically significant differences were calculated using Mann-Whitney U test. Only comparisons between uninjured and burn-injured models or between models without and with monocytes are shown. Significant differences are indicated by asterisks: *: $p < 0.05$.

SUPPLEMENTARY FIGURE 3

Cytokine levels (IL-1 β , IL-2, MCP-1, TNF- α) in medium of (burn-injured) FSEs after 7 days of culture with pre-activated T cells. Samples from biological duplicates were averaged per donor. Concentrations are reported in pg/mL medium. Experiments were performed in duplicate using 6 different keratinocyte donors, 6 fibroblast donors and 5 T cell donors. The dashed line indicates the lowest level of quantification and the highest limit of quantification (for MCP-1). Statistically significant differences were calculated using Mann-Whitney U test. Only comparisons between uninjured and burn-injured models or models without and with T cells are shown. Significant differences are indicated by asterisks: *: $p < 0.05$.

30. Mulder PPG, Raktoe RS, Vlijg M, Elgersma A, Middelkoop E, Boekema BKHL. Full skin equivalent models for simulation of burn wound healing, exploring skin regeneration and cytokine response. *J Funct Biomater* (2023) 14:29. doi: 10.3390/jfb14010029

31. Jordan SW, Turin SY, Zielinski ER, Galiano RD. Matrices and dermal substitutes for wound treatment. In: *Interventional Treatment of Wounds: A Modern Approach for Better Outcomes*. Midtown Manhattan, New York City, USA: Springer International Publishing AG (2018) p. 215–50. doi: 10.1007/978-3-319-66990-8_13

32. Corrêa FB, Castro JCD, Almeida IR, Farina-Junior JA, Coltro PS. Evaluation of contraction of the split-thickness skin graft using three dermal matrices in the treatment of burn contractures: A randomised clinical trial. *Wound Repair Regener* (2022) 30:222–31. doi: 10.1111/wrr.13002

33. Shahrokh S, Arno A, Jeschke MG. The use of dermal substitutes in burn surgery: Acute phase. *Wound Repair Regener* (2014) 22:14–22. doi: 10.1111/wrr.12119

34. Udeabor SE, Herrera-Vizcaíno C, Sader R, Kirkpatrick CJ, Al-Maawi S, Ghanaati S. Characterization of the cellular reaction to a collagen-based matrix: An *in vivo* histological and histomorphometrical analysis. *Materials (Basel)* (2020) 13:1–16. doi: 10.3390/ma13122730

35. Van Den Bogaard EH, Tjabringa GS, Joosten I, Vonk-Bergers M, Van Rijssen E, Tijssen HJ, et al. Crosstalk between keratinocytes and T cells in a 3D microenvironment: A model to study inflammatory skin diseases. *J Invest Dermatol* (2014) 134:719–27. doi: 10.1038/jid.2013.417

36. He X, de Oliveira VL, Keijsers R, Joosten I, Koenen HJ. Lymphocyte isolation from human skin for phenotypic analysis and ex vivo cell culture. *J Vis Exp* (2016), 7–13. doi: 10.3791/52564

37. Reichard A, Asosingh K. Best practices for preparing a single cell suspension from solid tissues for flow cytometry. *Cytom Part A* (2019) 95:219–26. doi: 10.1002/cyt.a.23690

38. Karim AS, Yan A, Ocotl E, Bennett DD, Wang Z, Kendziora C, et al. Discordance between histologic and visual assessment of tissue viability in excised burn wound tissue. *Wound Repair Regener* (2019) 27:150–61. doi: 10.1111/wrr.12692

39. Iljas JD, Röhl J, McGovern JA, Moromizato KH, Parker TJ, Cuttle L. A human skin equivalent burn model to study the effect of a nanocrystalline silver dressing on wound healing. *Burns* (2021) 47:417–29. doi: 10.1016/j.burns.2020.07.007

40. Breetveld M, Richters CD, Rustemeyer T, Schepers RJ, Gibbs S. Comparison of wound closure after burn and cold injury in human skin equivalents. *J Invest Dermatol* (2006) 126:1918–21. doi: 10.1038/sj.jid.5700330

41. Lee D-Y, Cho K-H. The effects of epidermal keratinocytes and dermal fibroblasts on the formation of cutaneous basement membrane in three-dimensional culture systems. *Arch Dermatol Res* (2005) 296:296–302. doi: 10.1007/s00403-004-0529-5

42. Mulder PPG, Vlijg M, Boekema BKHL, Stoop MM, Pijpe A, van Zuijlen PPM, et al. Persistent systemic inflammation in patients with severe burn injury is accompanied by influx of immature neutrophils and shifts in T cell subsets and cytokine profiles. *Front Immunol* (2021) 11:621222. doi: 10.3389/fimmu.2020.621222

43. Moon S, Kim DH, Shin JU. *In vitro* models mimicking immune response in the skin. *Yonsei Med J* (2021) 62:969–80. doi: 10.3349/ymj.2021.62.11.969

44. Short WD, Wang X, Keswani SG. The role of T lymphocytes in cutaneous scarring. *Adv Wound Care* (2022) 11:121–31. doi: 10.1089/wound.2021.0059

45. Kotwal GJ, Chien S. Macrophage differentiation in normal and accelerated wound healing. *Macrophages Orig Funct Biointerven* (2017) 62:353–64. doi: 10.1007/978-3-319-54090-0_14

46. Schneider V, Kruse D, de Mattos IB, Zöpfl S, Tiltmann KK, Reigl A, et al. A 3D *in vitro* model for burn wounds: Monitoring of regeneration on the epidermal level. *Biomedicines* (2021) 9:1–18. doi: 10.3390/biomedicines9091153

47. Smith SR, Schaaf K, Rajabalee N, Wagner F, Duverger A, Kutsch O, et al. The phosphatase PPM1A controls monocyte-to-macrophage differentiation. *Sci Rep* (2018) 8:1–14. doi: 10.1038/s41598-017-18832-7

48. Safi W, Kuehnl A, Nüssler A, Eckstein HH, Pelisek J. Differentiation of human CD14+ monocytes: an experimental investigation of the optimal culture medium and evidence of a lack of differentiation along the endothelial line. *Exp Mol Med* (2016) 48:1–9. doi: 10.1038/EMM.2016.11

49. Ma J, Liu L, Che G, Yu N, Dai F, You Z. The M1 form of tumor-associated macrophages in non-small cell lung cancer is positively associated with survival time. *BMC Cancer* (2010) 10:1–9. doi: 10.1186/1471-2407-10-112

50. Griffoni C, Neidhart B, Yang K, Groeber-Becker F, Maniura-Weber K, Dandekar T, et al. *In vitro* skin culture media influence the viability and inflammatory response of primary macrophages. *Sci Rep* (2021) 11:1–11. doi: 10.1038/s41598-021-86486-7

51. Chung E, Choi H, Lim JE, Son Y. Development of skin inflammation test model by co-culture of reconstituted 3D skin and RAW264.7 cells. *Tissue Eng Regener Med* (2014) 11:87–92. doi: 10.1007/s13770-013-1113-x

52. Linde N, Gutschalk CM, Hoffmann C, Yilmaz D, Mueller MM. Integrating macrophages into organotypic co-cultures: A 3D *in vitro* model to study tumor-associated macrophages. *PLoS One* (2012) 7:e40058. doi: 10.1371/journal.pone.0040058

53. Bechetoile N, Vachon H, Gaydon A, Boher A, Fontaine T, Schaeffer E, et al. A new organotypic model containing dermal-type macrophages. *Exp Dermatol* (2011) 20:1035–7. doi: 10.1111/j.1600-0625.2011.01383.x

54. Manicone AM, Burkhardt KM, Lu B, Clark JG. CXCR3 ligands contribute to Th1-induced inflammation but not to homing of Th1 cells into the lung. *Exp Lung Res* (2008) 34:391–407. doi: 10.1080/01902140802221987

55. Zhao F, Hoechst B, Gamrekelashvili J, Ormandy LA, Voigtlander T, Wedemeyer H, et al. Human CCR4+CCR6+Th17 cells suppress autologous CD8+ T cell responses. *J Immunol* (2012) 188:6055–62. doi: 10.4049/jimmunol.1102918

56. Peperzak V, Veraar EAM, Xiao Y, Bajbala N, Thiadens K, Brugmans M, et al. CD8+ T cells produce the chemokine CXCL10 in response to CD27/CD70 costimulation to promote generation of the CD8+ Effector T cell pool. *J Immunol* (2013) 191:3025–36. doi: 10.4049/jimmunol.1202222

57. Peters JH, Tjabringa GS, Fasse E, de Oliveira VL, Schalkwijk J, Koenen HJPM, et al. Co-culture of healthy human keratinocytes and T-cells promotes keratinocyte chemokine production and ROR γ t positive IL-17 producing T-cell populations. *J Dermatol Sci* (2013) 69:44–53. doi: 10.1016/j.jdermsci.2012.10.004

58. Kuo PT, Zeng Z, Salim N, Mattarollo S, Wells JW, Leggatt GR. The role of CXCR3 and its chemokine ligands in skin disease and cancer. *Front Med* (2018) 5:271. doi: 10.3389/fmed.2018.00271

59. Tjabringa G, Bergers M, Van Rens D, De Boer R, Lamme E, Schalkwijk J. Development and validation of human psoriatic skin equivalents. *Am J Pathol* (2008) 173:815–23. doi: 10.2353/ajpath.2008.080173

60. Shin JU, Abaci HE, Herron L, Guo Z, Sallee B, Pappalardo A, et al. Recapitulating T cell infiltration in 3D psoriatic skin models for patient-specific drug testing. *Sci Rep* (2020) 10:1–12. doi: 10.1038/s41598-020-60275-0

61. Lorthois I, Simard M, Morin S, Pouliot R. Infiltration of T cells into a three-dimensional psoriatic skin model mimics pathological key features. *Int J Mol Sci* (2019) 20:1670. doi: 10.3390/ijms20071670

62. Laggner M, Lingitz M-T, Copic D, Direder M, Klas K, Bormann D, et al. Severity of thermal burn injury is associated with systemic neutrophil activation. *Sci Rep* (2022) 12:1654. doi: 10.1038/s41598-022-05768-w

63. Li R, Wang Z, Huang J, He S, Peng Y, Wan Y, et al. Neutrophils culture in collagen gel system. *Front Immunol* (2022) 13:816037. doi: 10.3389/fimmu.2022.816037

64. Roth S, Cao J, Singh V, Tiedt S, Hundeshagen G, Li T, et al. Post-injury immunosuppression and secondary infections are caused by an AIM2 inflammasome-driven signaling cascade. *Immunity* (2021) 54:648–659.e8. doi: 10.1016/j.jimmuni.2021.02.004



OPEN ACCESS

EDITED BY

Jeffrey John Bajramovic,
Utrecht University, Netherlands

REVIEWED BY

Luiz Henrique Agra Cavalcante-Silva,
Federal University of Paraíba, Brazil
Katherina Psarra,
Evaggelismos General Hospital, Greece

*CORRESPONDENCE

Claire Crola Da Silva
✉ claire.crola-da-silva@univ-lyon1.fr
Melanie Paillard
✉ melanie.paillard@univ-lyon1.fr
Sylvie Ducreux
✉ sylvie.ducreux@univ-lyon1.fr

[†]These authors have contributed
equally to this work and share
last authorship

RECEIVED 04 August 2023

ACCEPTED 02 October 2023

PUBLISHED 13 October 2023

CITATION

Brun C, Chalet L, Moulin F, Bochaton T, Ducreux S, Paillard M and Crola Da Silva C (2023) A bibliometric analysis: Ca^{2+} fluxes and inflammatory phenotyping by flow cytometry in peripheral blood mononuclear cells. *Front. Immunol.* 14:1272809. doi: 10.3389/fimmu.2023.1272809

COPYRIGHT

© 2023 Brun, Chalet, Moulin, Bochaton, Ducreux, Paillard and Crola Da Silva. This is an open-access article distributed under the terms of the [Creative Commons Attribution License \(CC BY\)](#). The use, distribution or reproduction in other forums is permitted, provided the original author(s) and the copyright owner(s) are credited and that the original publication in this journal is cited, in accordance with accepted academic practice. No use, distribution or reproduction is permitted which does not comply with these terms.

A bibliometric analysis: Ca^{2+} fluxes and inflammatory phenotyping by flow cytometry in peripheral blood mononuclear cells

Camille Brun¹, Lucie Chalet^{1,2}, Florentin Moulin¹,
Thomas Bochaton^{1,3}, Sylvie Ducreux^{1*†}, Melanie Paillard^{1*†}
and Claire Crola Da Silva^{1*†}

¹Univ Lyon, CarMeN Laboratory, INSERM, INRA, INSA Lyon, Université Claude Bernard Lyon 1, Bron, France, ²Olea Medical, La Ciotat, France, ³Hospices Civils de Lyon, Hôpital Louis Pradel, Services D'explorations Fonctionnelles Cardiovasculaires et CIC de Lyon, Lyon, France

Background: The immune system, composed of organs, tissues, cells, and proteins, is the key to protecting the body from external biological attacks and inflammation. The latter occurs in several pathologies, such as cancers, type 1 diabetes, and human immunodeficiency virus infection. Immunophenotyping by flow cytometry is the method of choice for diagnosing these pathologies. Under inflammatory conditions, the peripheral blood mononuclear cells (PBMCs) are partially activated and generate intracellular pathways involving Ca^{2+} -dependent signaling cascades leading to transcription factor expression. Ca^{2+} signaling is typically studied by microscopy in cell lines but can present some limitations to explore human PBMCs, where flow cytometry can be a good alternative.

Objective: In this review, we dived into the research field of inflammation and Ca^{2+} signaling in PBMCs. We aimed to investigate the structure and evolution of this field in a physio-pathological context, and then we focused our review on flow cytometry analysis of Ca^{2+} fluxes in PBMCs.

Methods: From 1984 to 2022, 3865 articles on inflammation and Ca^{2+} signaling in PBMCs were published, according to The Clarivate Web of Science (WOS) database used in this review. A bibliometric study was designed for this collection and consisted of a co-citation and bibliographic coupling analysis.

Results: The co-citation analysis was performed on 133 articles: 4 clusters highlighted the global context of Ca^{2+} homeostasis, including chemical probe development, identification of the leading players in Ca^{2+} signaling, and the link with chemokine production in immune cell function. Next, the bibliographic coupling analysis combined 998 articles in 8 clusters. This analysis outlined the mechanisms of PBMC activation, from signal integration to cellular response. Further explorations of the bibliographic coupling network, focusing on flow cytometry, revealed 21 articles measuring cytosolic Ca^{2+} in PBMCs, with only 5 since 2016. This final query showed that Ca^{2+} signaling analysis in human PBMCs using flow cytometry is still underdeveloped and investigates mainly the cytosolic Ca^{2+} compartment.

Conclusion: Our review uncovers remaining knowledge gaps of intracellular players involved in Ca^{2+} signaling in PBMCs, such as reticulum and mitochondria, and presents flow cytometry as a solid option to supplement gold-standard microscopy studies.

KEYWORDS

flow cytometry, B cells, T cells, Ca^{2+} signaling, kinetics, immune cells, inflammation

1 Introduction

Blood samples are routinely used in clinics for disease diagnosis or prognosis. The main components of blood are plasma and leukocytes. The immunophenotyping of leukocytes, notably the peripheral blood mononuclear cells (PBMCs), has emerged as an essential tool for medical research. This diagnostic tool is widespread in hematology, cancerology, and neurology fields.

For clinical diagnosis, multiparametric phenotyping is typically achieved using flow cytometry. This method achieves 10000 to 40000 cell reads per second on average with the most recent cytometers, enabling statistical robustness compared to microscopy imaging, high sensitivity and specificity to detect the most under-represented subpopulations, and fast diagnosis (usually under 48 hours) (1, 2). Diagnosis is based on detecting PBMC-specific membrane glycoproteins called “cluster of differentiation” (CD), commonly associated with their immune function and cell subpopulation (3). The simultaneous expression of multiple CD markers serves as a cellular signature comparable to an “identity card.” PBMCs can easily be isolated from blood sampling followed by centrifugation. Therefore, PBMCs have recently emerged as complementary biomarkers to stratify patients in several pathologies by characterizing their immunophenotypes. For instance, monitoring the level of CD4^+ T cells in Human Immunodeficiency Virus (HIV) infections is crucial to monitoring disease progression (4). Flow cytometry has also become essential to study the activation of basophilic cells in the presence of a given allergen (5) and can even be used to diagnose acute leukemia (6). In fact, flow cytometry is extensively used in several clinical applications notably in clinical practice. Indeed, flow cytometry is largely used to characterize diseases such as malignancies (leukemia, lymphoma (7, 8)), infectious diseases (9) and degenerative diseases (10, 11) through immunophenotyping. More recently, Obasanmi et al. studied PBMC cytokine production levels in patients with type 1 diabetes and diabetic retinopathy. Their work revealed that PBMCs from diabetic patients have a specifically enhanced interleukin-10 (IL-10) and interleukin-6 (IL-6) releases, associated with increased interleukin-17A (IL-17A) production from myeloid cells and impaired CD3^+ T cell-induced interferon-gamma (IFN- γ) production (12). Flow cytometry is recognized as the method of choice for immunophenotyping based on this non-exhaustive list of examples.

Under inflammatory conditions, PBMCs are partially activated by T or B cell membrane receptors (TCR or BCR, respectively) and Fc receptors for monocytes and macrophages. Their activation through these receptors involves a Ca^{2+} -dependent signaling cascade, starting from the ligand binding on the receptor through intracellular pathways up to the regulation of gene expression. More precisely, membrane receptor activation triggers a transitory Ca^{2+} release from internal stores, further leading to a store-operated Ca^{2+} entry (SOCE), raising the intracellular Ca^{2+} concentration (13, 14), which in turn, regulates several processes such as proliferation, phagocytosis, chemotaxis, and cytokine secretion (15). Thus, Ca^{2+} is considered as a key regulator of the immune cell. In 1994, Partisetti et al. reported an altered Ca^{2+} influx following TCR aggregation in native T cells in immunodeficient patients, visualized with microscopy and electrophysiological recordings (16). So far, microscopy is the most common method to identify and analyze Ca^{2+} fluxes in cell line models. It offers the advantage of visualizing the intracellular architecture of the cell. However, the statistical power brought by the number of events analyzed, the high acquisition rate, and the possibility of exploring a more significant number of parameters simultaneously on the same sample all favor the use of flow cytometry. Consequently, it represents a powerful alternative to assess Ca^{2+} fluxes, but still remains underused. It has been shown that alteration or modulation of calcium signaling can impact immune cell function in some pathologies (17, 18). To identify existing protocols for analyzing calcium signaling, we proposed this bibliometric review questioning the role of flow cytometry in studying Ca^{2+} signaling, specifically in peripheral blood mononuclear cells. To this end, we first outlined the inflammatory and Ca^{2+} research field and then focused on Ca^{2+} homeostasis studies performed by flow cytometry on PBMCs.

2 Materials and methods

2.1 Bibliometric analysis

The bibliometric analysis is suited when the scope of the review is broad and the dataset is too large for manual review. This analysis presents the intellectual structure and emerging trends of a research topic. The study was designed following the guidelines of Donthu et al. and the methodology of Chalet et al. (19, 20). The flowchart

depicted in **Figure 1** summarizes the methodology used to highlight the literature selection.

2.2 Scope and aim of the analysis

We aimed to determine the research structure and evolution of inflammatory and Ca^{2+} signaling in PBMCs in a physio-pathological context. Based on these first results, we further explored the development of Ca^{2+} analysis by flow cytometry.

2.3 Definition and selection of bibliometric analysis techniques

The structure and dynamics of the scholar knowledge were assessed and represented using science maps. To provide an overview of our research topic and to explore the emerging trends, co-citation analysis and bibliographic coupling were carried out.

- The co-citation analysis determines the relationships among cited publications, highlighting the most influential themes.
- The bibliographic coupling forms thematic clusters.

2.4 Collecting scientific literature data

Clarivate Web of Science[®] was used to collect data (Copyright Clarivate 2022WoS). It is a selective, structured, and balanced database with complete citation links and enhanced metadata. It can inform about citation indexes representing the connections between scholarly research articles in globally significant journals, books, and proceedings chapters. Exported data included the complete set of references enabling in-depth analysis of the intellectual structure.

We applied the following query to article titles and abstracts:

[pbmc OR "peripheral blood mononuclear cells" OR lymphocyte* OR monocyte* OR macrophage*] AND [“ Ca^{2+} ” OR calcium] AND [physiological OR inflammat* OR ischem*]

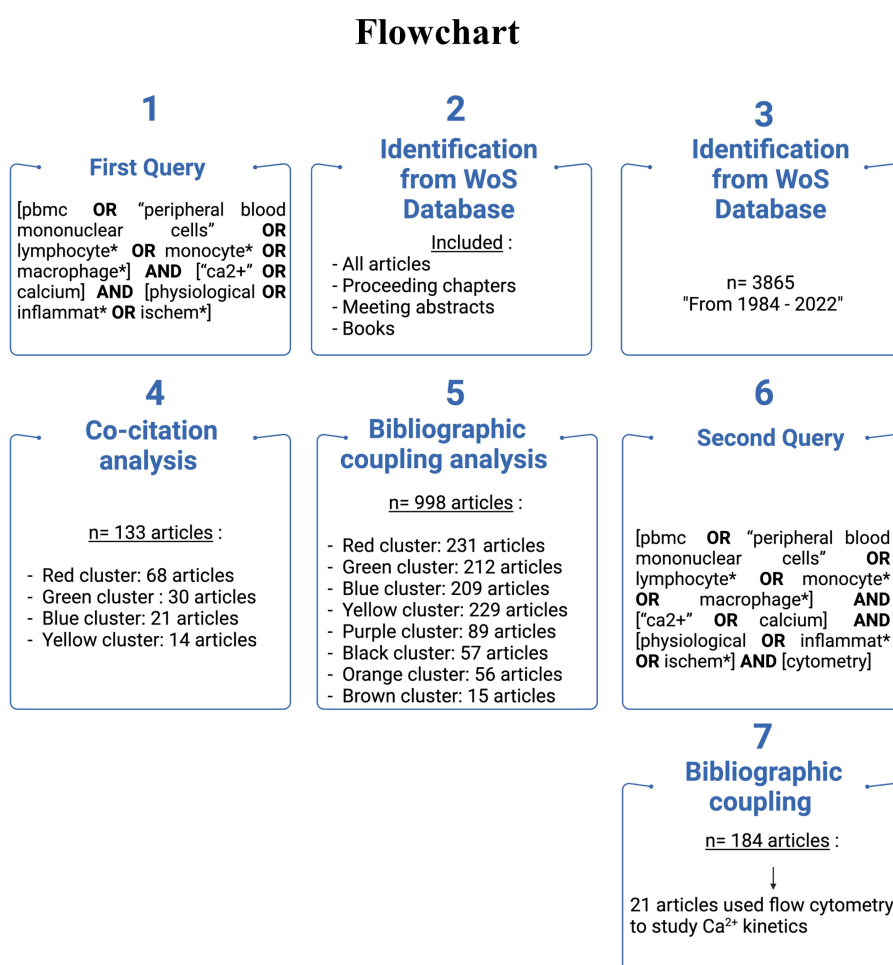


FIGURE 1
Flowchart showing the methodology to identify, filter and analyze papers.

We included all articles, proceeding chapters, meeting abstracts, and books. The query ranged from 1984 to 2022, and 3865 articles were collected. All data were exported from the WoS database on July 22, 2022.

Further analysis of the field, focusing on the evolution of Ca^{2+} analysis by flow cytometry, was carried out based on the following query applied to abstracts and titles:

[pbmc OR “peripheral blood mononuclear cells” OR lymphocyte* OR monocyte* OR macrophage*] AND [“ Ca^{2+} ” OR calcium] AND [physiological OR inflammat* OR ischem*] AND [cytometry]

We included all articles, book chapters, and meeting abstracts. The query ranged from 1993 to 2022, and 185 articles were obtained.

2.5 Network generation and display

VOS viewer was used to display bibliometric networks represented through mapping and clustering (21) to perform the analysis.

2.6 Co-citation method

Two articles are co-cited when they appear together in the reference list of another publication. Frequently co-cited documents in a corpus represent its knowledge foundations. This technique highlights influential publications and unveils the structure of the research field. The co-citation was conducted in VOS viewer using reference analysis. The results were displayed as network visualization. The minimum number of co-cited references was fixed to 20 to obtain the most influential articles. 133 co-cited documents were included in our analysis and mapping, and were clustered and displayed on the VOS viewer. Included references grouped by clusters are displayed in [Supplementary Figure S1](#). To determine the main subject of each cluster, we focused our analysis on the most significant publications in each cluster, i.e., in the 3rd quartile.

2.7 Bibliographic coupling method

The bibliographic coupling method considers publications that share common references as an indication of similarities in content. This analysis provides a clustered visualization of the field in themes and includes recent and niche publications. The bibliographic coupling analysis was obtained with VOS viewer, with coupling analysis of references. The results were displayed as network visualization. This bibliographic coupling was carried out to determine the knowledge in the field of Ca^{2+} and inflammation in PBMCs. Articles from 1990 to 2022 were included, and 998 were grouped in clusters. Cluster constituents are detailed in [Supplementary Figure S2](#).

The exploration of the clusters was performed on the highest total link strength articles, corresponding to the link of an item with

other items in a network. To get an overview of the dominant theme of each cluster, the references with a total link strength equal to or higher than the 3rd quartile of the full scores in their cluster were selected for a thorough analysis.

2.8 Limitations of bibliographic coupling analysis

The term “inflammat*” covers a large field of research, including several pathologies. Thus, the most influential articles in our “inflammatory” cluster discuss chemokines in HIV. The abbreviation T cells or B cells were not included in the query.

3 Results

3.1 General information: Trend of publication

The first query aimed to overview Ca^{2+} and inflammation research in immune cells in the current literature. In total, 3865 articles were published between 1984 and 2022. An average of 90 publications per year between 1990 and 2010 were reported. Over the next ten years, publications increased strongly, up to 2-fold from 2010 to 2021. Analysis was done until July 2022, which explains the lowest number of publications for this year ([Figure 2](#)). Most of them were published in the United States of America and China and, to a lesser extent, in Europe, Canada, and South America ([Figure 3](#)). However, the number of collaborations between all these countries was important. Collaborations for these articles were made mainly between the USA, European countries, and China, indicating a worldwide interest in the Ca^{2+} and inflammation topic in immune cells ([Figure 4](#)).

3.2 Co-citation analysis

The co-citation analysis provides an overview of the most substantial contributions to the field by measuring the frequency of two articles being cited together in a scientific literature corpus (19). The analysis was done on the 133 most co-cited documents grouped into 4 clusters. This threshold highlights the most influential articles. The cluster denomination was based on articles from the previously described selection method. The co-citation network is displayed in [Figure 5](#). The cluster position provides information about the relationship between topics. We observed the closeness of the red and yellow clusters and their remote connection to the blue and green clusters. The content of each cluster will be further developed to provide interpretation resources on the relations between these groups.

In the red cluster, we observed two groups; one has a central position and is related to all the other clusters, i.e., yellow, green, and blue clusters. In the red cluster, 17 out of 68 publications were in the 3rd quartile, ranging from 1976 to 2012. The red cluster

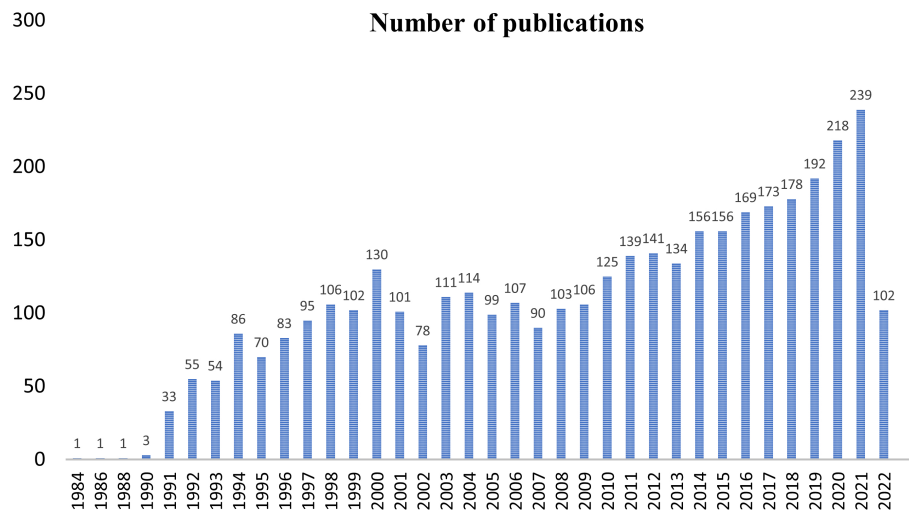


FIGURE 2
Annual number of publications worldwide from 1984 to 2022.

relates to Ca^{2+} signaling and channels in the plasma membrane. Most publications are focused on the Stromal Interaction Molecule (STIM), a Ca^{2+} sensor essential for the SOCE through its binding to ORAI1 (Calcium Release-Activated Calcium Modulator 1). ORAI proteins are STIM-binding partners that form the channel pore in the plasma membrane (22, 23). These channels represent the main pathway of Ca^{2+} influx in T- and B-cells and promote the immune response by partly activating the transcription factor nuclear factor of activated T-cells (NFAT) (14, 24, 25). The study by Gryniewicz et al., published in 1985 (26), appears in a central position. This article deals with a new generation of highly fluorescent indicators to study the physiological role of cytosolic free Ca^{2+} concentration, with greatly improved fluorescence properties. Most articles in the second part of the red cluster use the probes described in Gryniewicz's article, notably Fura2-AM (27–29). Therefore, this cluster highlights the fundamental knowledge of Ca^{2+} signaling in PBMCs.

Near the red cluster, the yellow cluster includes 3 out of 14 publications in the 3rd quartile ranging from 1987 to 1991. They refer to calcium-binding proteins (CaBPs), such as the S100 protein. S100 was reported to be associated with specific stages of monocyte differentiation (30, 31). S100 function is still unclear, but some evidence suggests that macrophages infiltrated during inflammation express the myeloid-related protein 8 (MRP8) and the myeloid-related protein 14 (MRP-14) members of the S100 protein family in rheumatoid arthritis pathology (32). These two clusters related to the Ca^{2+} topic support the critical role of Ca^{2+} signaling in immune cell function.

The last two clusters, green and blue, are located on the opposite side of the maps and share close positions and content. No temporal evolution was observed in these two clusters, since all the articles were published in the 90s (33–36). The green cluster contains 7 out of 30 articles in the 3rd quartile, ranging from 1991 to 1995, which refer to chemokine receptors involved in inflammation. In its

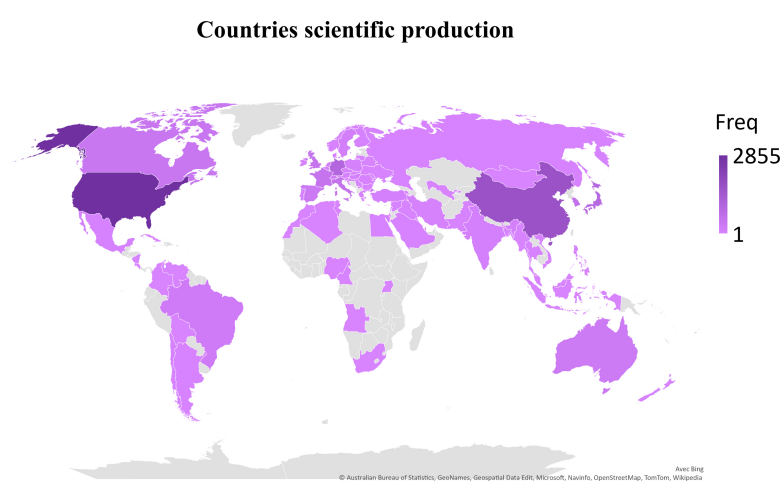


FIGURE 3
Scientific production by country, displayed by the total number of publications over the query time (Freq).

International collaborations map



FIGURE 4

International collaborations map, represented by the number of collaborative studies between countries.

vicinity, the blue cluster with 5 out of 21 articles in the 3rd quartile, from 1995 to 1996, focuses on chemokines, especially the regulated-on activation, normal T cell expressed and secreted (RANTES) or chemokine ligand 5 (CCL5) axis in HIV infections. Indeed, RANTES research was achieved at the time of the outbreak emergence of HIV at the beginning of the 1980s, instigating extensive research on this chemokine.

To conclude, the co-citation analysis supports the crucial role of Ca^{2+} and chemokine signaling in the immune cell function, which depends on signal integration, stress, chemical environment, and inflammation, key features of several pathologies. More precisely, all these parameters lead to modulation and cell activation by intracellular pathways, activating CaBPs and partially leading to their translocation to the nucleus. The latter activates Ca^{2+} -dependent transcription factors that control PBMC functions such as proliferation, differentiation, and cytokine production.

3.3 Bibliographic coupling analysis

Bibliographic coupling is based on the idea that two publications sharing common references have similar content. This analysis enables the formation of thematic clusters in the literature corpus obtained with our query. Consequently, recent niche publications may appear in our analysis. This section aimed to determine what drove the calcium and inflammation research field on PBMCs over the last three decades. The analysis was done on 998 articles, and 8 clusters were identified (Figure 6). The large number of articles and the link between them make the interpretation complex; a preliminary exploration of the clusters showed a large representation of pathologies involving an immune response, and the in-depth analysis of the clusters provided further knowledge on the field structure.

The red cluster contains 57 out of 232 articles in the 3rd quartile and refers to the SOCE. This cluster can be further divided into subgroups related to lymphocytes and macrophages, respectively.

We identified articles about the calcium release-activated channel (CRAC) components in the lymphocyte cluster. In 2005 – 2006, both STIM1 Ca^{2+} sensor and ORAI1 channel-forming protein were determined by Feske et al. The CRAC composition depends on cell type, localization, and activation state, but ORAI1 is the dominant channel member in several immune cells, mainly in neutrophils and mast cells (37–39). In physiological conditions, the CRAC channel is activated by inositol 1,4,5 phosphate (IP_3) binding to IP_3 receptors (IP_3R) in the endoplasmic reticulum (ER) membrane following TCR or BCR activation. IP_3 leads to IP_3R opening, resulting in Ca^{2+} release from the ER into the cytosol. The resulting ER Ca^{2+} decrease induces a conformational change of STIM1, which binds to ORAI1 channels to open its pore in the plasma membrane. The importance of Ca^{2+} influx through plasma membrane channels in T cells was

Co-citation analysis



VOSviewer

FIGURE 5

Co-citation network providing an overview of the most contributing publications in the Ca^{2+} and inflammation context. Red cluster [1976 - 2006]: Development of Ca^{2+} probes, Ca^{2+} signaling, and channels identified in the plasma membrane. Yellow cluster [1987 - 1997]: intracellular pathways & calcium-binding proteins; Green cluster [1991 - 1995]: chemokine receptors; Blue cluster [1995 - 2006]: RANTES chemokines in HIV.

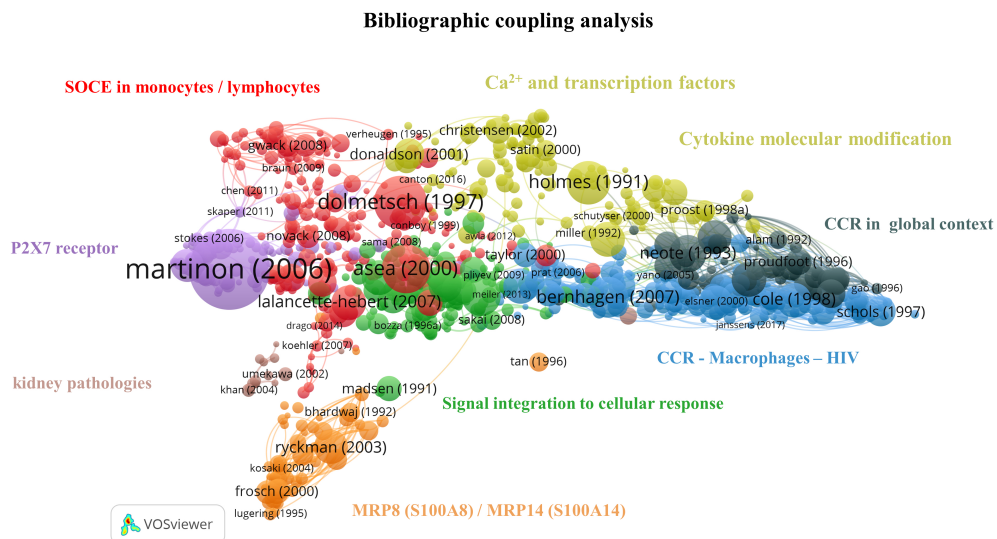


FIGURE 6

Bibliographic coupling network: Ca^{2+} and inflammation in PBMCs [1990-2023]. The red cluster represents the CRAC channel in lymphocytes and monocytes. The purple cluster focuses on the P2X7 purinergic receptor in macrophages. The orange cluster refers to the specific calcium-binding protein MRP8 (S100A8)/MRP14 (S100A14). The green cluster covers the cascade from signal integration to cellular response. The yellow cluster relates to Ca^{2+} signaling, transcription factors and cytokine molecular modifications. The black cluster targets chemokine receptors, the blue cluster accounts for chemokine receptors in HIV infections, and the brown cluster focuses on kidney pathologies.

characterized by studying the Ca^{2+} conductance triggered by the TCR. An absence of this current was demonstrated in human T cells from patients with immunodeficiency diseases (16). Missense mutations in ORAI1 affect the channel function and the subsequent T-cell function leading to severe immunodeficient phenotypes (40, 41).

In non-excitable cells such as lymphocytes, potassium (K^+) channels were identified in 1983 by Matteson and Deutschand in 1984 by DeCoursey et al. The latter publication shows their implication in functional processes such as mitogenesis (42). In T-lymphocytes, the engagement of the TCR/CD3 complex upon antigen binding leads to the increase of intracellular Ca^{2+} . This Ca^{2+} influx is maintained by K^+ channels through K^+ release outside the cells, preserving the electrochemical potential gradient. Panyi et al. reported that the interleukin-2 (IL-2) production and cell proliferation in T cells are partly mediated by K^+ channels (43). The inhibition of the K^+ channel, named Kv1.3, inhibits T-cell activation, calcium signaling, cytokine production, and cell proliferation (44).

STIM1 and ORAI proteins were also identified in phagocytic immune cells, notably in macrophages, as demonstrated in papers in the related sub-clusters (38). There are several phenotypes of macrophages: the pro-inflammatory one, also known as classical monocytes (M1), with an important phagocytosis function; and the anti-inflammatory one as non-classical monocytes (M2). Macrophage plasticity is essential for innate immunity since macrophages can switch their phenotype according to their chemical environment. Chauban et al. showed that ORAI1 significantly contributes to Ca^{2+} entry *in vitro* using non-differentiated macrophages (M0). In contrast, *in vitro* M1 polarization induced by IFN_γ is associated with the recruitment of the transient receptor potential cation channel 1 (TRPC1) to

enhance Ca^{2+} entry, leading to high expression of inflammatory genes (45).

Additionally, this subcluster references the monovalent cation channel transient receptor potential melastatin (TRPM), involved in the physiological response in some immune cells, i.e., monocytes and macrophages, through intracellular Ca^{2+} level regulation. High intracellular Ca^{2+} concentration leads to TRPM4 opening, regulating Na^+ entry and Ca^{2+} efflux. Indeed, TRPM4 works in concert with the CRAC channel to achieve this regulation. Serafini et al. studied TRPM4 deletion in a sepsis mouse model. They observed an altered function in the absence of TRPM4 through a decrease in phagocytosis and an increased pro-inflammatory cytokine production, leading to an alteration of macrophage function affecting the mouse survival (46).

In summary, the red cluster highlights the central role of Ca^{2+} signaling in the immune function of macrophages and lymphocytes. It therefore represents the largest cluster in our query, gathering around 23% of the articles in the bibliographic coupling map.

Close to the red cluster, the main topic of the purple cluster is centered on purinergic receptors, such as P2X7, and includes 22/89 articles in the 3rd quartile, from 2003 to 2016. It is well known that Ca^{2+} signaling enhances mitochondrial adenosine triphosphate (ATP) production in activated T cells (14). ATP is then exported outside T cells through the Pannexin 1 channel and activates P2X7, which causes further Ca^{2+} entry (14). P2X7 receptors are expressed on mast cells, lymphocytes, erythrocytes, fibroblasts, and peripheral macrophages. In monocytes/macrophages, P2X7 receptor activation leads to interleukin production, notably interleukin 1- β (IL-1 β) as a pro-inflammatory factor (47).

The orange cluster contains 14/57 publications in the 3rd quartile and is localized in the network periphery. It refers to the specific CaBP S100 (48), an inflammatory marker, thus explaining

its remote connection to the other inflammation-themed clusters (49).

In the green cluster, 27 articles cover the role of intracellular pathways in immune cells, including Ca^{2+} fluxes, receptors, and transcription factors such as nuclear factor kappa B (NF- κ B) (50–52). The remaining 7 publications focus on cytokines, key soluble elements of signal integration in cellular stress (53–59). Therefore, this cluster gives an overview of immune cell signal integration from the cytokine binding to its receptor up to the gene expression, explaining its central position on this bibliographic coupling map.

The yellow cluster is widely extended and includes 32/129 articles in the 3rd quartile. A part of it is located close to the red cluster and covers articles related to Ca^{2+} signaling and transcription factors (60, 61). In contrast, the other part contains those related to cytokine molecular modification (62–64). This latter part is close to the black cluster that contains 14/58 publications in the 3rd quartile and focuses on chemokine receptors (CCR) and their ligand. Chemokine receptors are G-protein-coupled-receptors serpentine receptors. Chemokines, a particular type of small cytokines, are known to contribute to the trafficking of leukocytes to the inflammation site through a signaling cascade. Depending on the environment, chemokines activate neutrophils to attract and activate monocytes, basophils, eosinophils, or lymphocytes (65). Several subclasses of chemokine receptors exist and are expressed constitutively or induced by inflammation (66). Moreover, some receptors can bind specific ligands or several chemokines. Thus, chemoattractants possess a crucial regulatory role in immunity and are involved in viral infection (67).

The blue cluster, with 53/210 articles in the 3rd quartile, includes articles from 1997 to 2004, correlating with the HIV epidemic starting in 1981, and completes the preceding cluster by specifying the role of chemokine receptors in HIV infection. The HIV virion targets the cellular plasma membrane, and the fusion reaction occurs thanks to the viral envelope glycoprotein, which binds the CD4 surface marker (68). The virus uses the CXCR4 and CCR5 receptors for T cells and macrophages, respectively. The CXCR4 ligand is a natural ligand identified as stromal cell-derived factor 1 (SDF-1), also known as chemokine-12 (CXCL-12), and has the properties of a selective inhibitor of T cell tropism (69). Moreover, in 1995, Lusso et al. indicated that the CCL5 or RANTES cytokine, the macrophage inflammatory proteins 1 α (MIP-1 α /CCL3) and 1 β (MIP-1 β /CCL4) were all HIV-suppressive factors released by CD8 $^{+}$ T cells (70, 71).

The brown cluster focuses on kidney pathologies, especially on calcium oxalate crystal formation and on the role of monocytes-macrophages and the chemokine ligand 2 (CCL2), also known as monocyte chemoattractant protein 1 (MCP-1), in this pathology. This cluster contains 2/15 publications in the 3rd quartile with two different topics. The first one investigates macrophage capacity to suppress renal crystal formation (72). At the same time, the second one refers to the CCL2 role in tubulointerstitial inflammation during kidney failure by inducing cytokine and adhesion molecule production (73). Of note, this cluster does not appear as the most relevant for the bibliometric coupling map analysis due to

its low article number and its remote location and topic from other clusters mainly focused on Ca^{2+} signaling.

Altogether, this bibliographic coupling showed that Ca^{2+} signaling is widely studied in physiological conditions and several pathologies involving an immune response. Since intracellular Ca^{2+} signaling partly controls cytokine production, it was expected to see such a coupling between the Ca^{2+} signaling clusters and the inflammatory ones. Therefore, the resulting map aligns with our current field knowledge.

3.4 Ca^{2+} analysis by flow cytometry

Immunophenotyping using flow cytometry has become the gold standard method used in clinical (74) and fundamental research laboratories to characterize immune cells derived from patient blood samples. As the bibliographic coupling reveals, Ca^{2+} signaling is crucial in controlling immune cell functions. We next wanted to determine the evolution of flow cytometry-based studies to evaluate the Ca^{2+} kinetics in PBMCs over the last three decades. To perform this analysis, another query was defined to focus on flow cytometry, as specified in the “Materials and Methods” section. Ranging from 1993 to 2022, we obtained 184 articles. These articles were split into two flow cytometry usage categories: (1) for the phenotyping of immune cell profiles and (2) to analyze Ca^{2+} kinetics in PBMCs. We reported and focused our review on the 21 publications falling in the latter category (Table 1).

Regarding the cell compartment analyzed, all the publications obtained by this query referred to the cytosolic Ca^{2+} pool. Among them, 13 articles focused on cytosolic Ca^{2+} levels using the non-ratiometric probes Fluo3 or Fluo4, thus not allowing any resting Ca^{2+} level measurement. The other 8 articles performed ratiometric measurements, mainly through the association of Fluo3 and FuraRed probes: the ratio between the green fluorescence of Fluo3 over the red fluorescence of FuraRed, respectively increasing and decreasing when bound to Ca^{2+} , was used as a ratiometric measurement of cytosolic Ca^{2+} level (93, 94). Indeed, ratiometric fluorescent Ca^{2+} indicators minimize the effects of photobleaching, leakage, and uneven loading delivery, allowing more robust and reproducible results. Over the last decades, the combination of Fluo3 and FuraRed has been performed in flow cytometry, displaying a greater response magnitude than the ratiometric probe Indo1 requiring ultraviolet excitation, which is often unavailable on flow cytometers (94). It has been adapted to other cell types, such as platelets (78). Importantly, as FuraRed is a stand-alone ratiometric probe, its single-use showed similar efficiency in ratiometric measurements of cytosolic Ca^{2+} level in PBMCs (95). The single-use of FuraRed, compared to its combination with Fluo3, enables additional cell subtype labeling through additional channels with a faster, cheaper, and more accurate preparation (loading of only one dye).

Regarding the stimulation employed for the Ca^{2+} signaling pathways, the authors focused mainly on extracellular stimulation through the plasma membrane modulation of TCR/BCR or K^{+} channels. Notably, Toldi et al. used flow cytometry to understand how potassium channel inhibition impacts calcium influx in human

TABLE 1 Summary of the 21 articles using flow cytometry to analyze Ca^{2+} kinetics in PBMCs.

Articles	Cell type	Drugs	Ca^{2+} sensing probe	Date
Non-ratiometric probes				
Gauduchon et al. (75)	Human polymorphonuclear neutrophils	Panton-Valentine Leucocidin-derived protein	Fluo-3	2001
Kirchhoff et al. (76)	Human dendritic cells	Anaphylatoxins C5a and C3a	Fluo-3	2001
Princen et al. (77)	Lymphocyte and monocyte cell lines/Fresh PBMC	SDF-1	Fluo-3	2002
Heinemann et al. (78)	Human basophil cells	Anti-IgE, MCP-1, Eotaxin, MIP-1 α , C5a and NGF	Fluo-3	2003
Nishizaki et al. (79)	Rat thymic lymphocytes	PbCl2 and Ca^{2+} -dependant K^+ channel activator (A23187)	Fluo-3	2003
Lamoureux et al. (80)	Human B lymphocytes	Cysteinyl-leukotrienes	Fluo-3	2006
Ceballos et al. (81)	Human immature dendritic cells	SPC	Fluo-3	2007
Chen et al. (82)	Human PBMC	Flagellin	Fluo-3	2013
Orbán et al. (83)	Human T lymphocytes	Phytohemagglutinin (PHA)	Fluo-3	2014
Gutzmer et al. (84)	Human monocytes derived dendritic cells	Histamine	Fluo-4	2002
Sun et al. (85)	BALB/c mice T lymphocytes	Concanavalin A	Fluo-4	2017
Tran et al. (86)	Human PBMC	Goitrin	Fluo-4	2018
Kushnir et al. (17)	Human B lymphocytes	Caffeine/4-CmC	Fluo-4	2018
Ratiometric probes				
Boltz et al. (87)	Human T lymphocytes	Margatoxin/Anti-CD3	Indo-1 and Fura-2	1994
Bates et al. (88)	Rabbit alveolar macrophages	Tannin	Indo-1	1995
Tárnok et al. (89)	Bovin alveolar macrophages	4 bromo - A23187	Indo-1 and Fluo-3	2001
Si et al. (90)	Human T lymphocytes	Phytohemagglutinin (PHA)	Fluo-4 and FuraRed	2005
Toldi et al. (91)	Human T lymphocytes	Margatoxin/triaryl methane/Phytohemagglutinin	Fluo-3 and FuraRed	2011
Toldi et al. (44)	Human T lymphocytes	Margatoxin/triaryl methane/Phytohemagglutinin	Fluo-3 and FuraRed	2013
Orbán et al. (92)	Human T lymphocytes	Margatoxin/triaryl methane/Phytohemagglutinin	Fluo-3 and FuraRed	2016
Toldi et al. (93)	Human T lymphocytes	Margatoxin/triaryl methane/Phytohemagglutinin	Fluo-3 and FuraRed	2020

SPC, Sphingosylphosphorylcholine.

T lymphocytes of patients with autoimmune disorders, using triaryl methane as a specific inhibitor of IKCa1 channel (44). Flow cytometry also enabled multiparametric analyses to study Ca^{2+} fluxes in T cell subpopulations even in low abundance, i.e., CD4 $^{+}$ /CD8 $^{+}$ /CD4 $^{+}$ /CXCR3 $^{+}$ or CD4/CCR4 $^{+}$ (91, 93).

Overall, this query highlights that the study of Ca^{2+} signaling could rely more on flow cytometry. However, the trend is increasing over the last decade (8 out of 21 publications published after 2013). As for the techniques employed, both non-ratiometric and ratiometric probes are used, mainly to assess cytosolic Ca^{2+} levels,

therefore putting aside several actors of Ca^{2+} signaling in other cell compartments. From this particular query, only one paper performed intracellular stimulations on a reticular player: Kushnir et al. (17) focused on the major ER Ca^{2+} release channel, ryanodine receptor (RyR), using caffeine as an agonist. They specifically looked at the cytosolic Ca^{2+} level with Fluo4 in human B lymphocytes targeted with an anti-CD19 antibody in PBMCs. The Ca^{2+} response amplitudes obtained by a 50 mM caffeine stimulation were recorded in normal or congestive heart failure lymphocytes and revealed an ER Ca^{2+} leakage as a signature of the pathology.

4 Discussion & perspectives

Our literature review query on inflammation and Ca^{2+} signaling revealed 3865 articles published between 1984 and 2022, which supported the design of a bibliometric analysis. We reported that conventional flow cytometry is extensively used in clinical routine as a tool for diagnosis and monitoring of inflammatory diseases. A significant advantage of this method lies in the compensation process to correct fluorescent spillovers, increasing the number of parameters studied and enabling target analysis of specific cell populations. Clinical biomarkers of inflammatory pathologies were identified with this quantitative multi-parametric analysis. More recently, spectral flow cytometry collecting the full light spectrum has enabled the distinction of unique fluorophores with overlapping emission spectra (96, 97). Alongside with technological improvements, ratiometric chemical probes have steadily evolved since the 1980s (26, 95).

Regarding Ca^{2+} signaling, we highlighted that Ca^{2+} players involved in human PBMC models were studied and described in physiological settings. Indeed, Ca^{2+} ions are ubiquitous intracellular second messengers with a crucial role in the immune cell function: from the cell-specific membrane receptor activation to the SOCE, all contributing to the transcription of immune response genes (Figure 7). Therefore, flow cytometry represents a powerful tool compatible with immunophenotyping, allowing the analyses of Ca^{2+}

fluxes in immune cell subtypes, even when underrepresented. So far, we have reported only 21 articles using flow cytometry to study Ca^{2+} signaling focused on cytosolic Ca^{2+} level variations bypassing the contribution of organelles, notably the ER as the main Ca^{2+} store and mitochondria whose function depends, in part, on Ca^{2+} signaling. Interestingly, a Ca^{2+} coupling exists between ER and mitochondria to control mitochondrial functions. In this regard, Assis et al. suggested that the width of ER-mitochondria coupling was associated with the macrophage activation status (98). However, whether this structural modification translates into functional consequences on the Ca^{2+} transfer from the ER to mitochondria requires further investigation. Additionally, a recent study demonstrated a reduced mitochondrial Ca^{2+} uptake via the mitochondrial Ca^{2+} uniporter during aging in macrophages as a potential contributor to inflammation in humans (99). The Ryanodine receptor is expressed in immune cells and regulates intracellular Ca^{2+} homeostasis. Osipchuk et al. reported that pharmacological inhibition of RyR leads to intracellular Ca^{2+} alteration and alters immune cell functions *in vitro* and *in vivo* (100). In PBMCs from heart failure patients, Kushnir et al. (17) reported an ER Ca^{2+} leakage in B cells as a biomarker of this pathology. Regarding the SERCA pump, its role is yet to be described in PBMCs. Therefore, the contribution of the different organelles, notably ER, mitochondria, and their coupling, in regulating the immune cell function remains to be deciphered. Albeit combining two Ca^{2+} chemical probes to study two cellular

Visual summary abstract

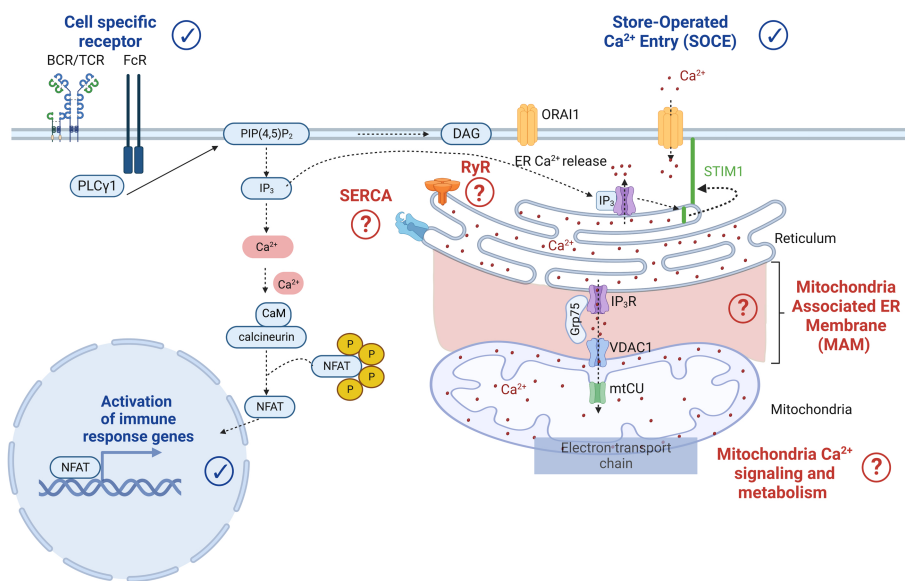


FIGURE 7

Cell-specific receptor activation through antigens induces protein kinase phosphorylation and phospholipase C gamma 1 activation. The latter leads to the production of the second messenger inositol-1,4,5-triphosphate (IP_3), which binds to the IP_3 receptor (IP_3R) in the endoplasmic reticulum (ER) membrane. IP_3R activation induces Ca^{2+} efflux from the ER to the cytosol. As a result, an increase of the cytosolic Ca^{2+} concentration and a decrease of the ER Ca^{2+} concentration occur. Sensors in the ER called Stromal Interaction Molecule 1 (STIM1) detect the ER Ca^{2+} decrease, leading to STIM1 oligomerization and translocation to the plasma membrane where it binds to the ORAI1 protein. STIM1-ORAI1 interactions contribute to Ca^{2+} influx which elevates the intracellular Ca^{2+} concentration leading to the restoration of the ER Ca^{2+} stocks via repumping through the Sarco-Endoplasmic Reticulum Calcium ATPase (SERCA). In parallel, the increase in cytosolic Ca^{2+} concentration also triggers the calcineurin- NFAT pathways. More recently, Ca^{2+} players such as ryanodine receptors (RyR), SarcoEndoplasmic Reticulum Calcium ATPase (SERCA), the IP_3R -Grp75-VDAC complex, and the mitochondrial Ca^{2+} uniporter (mtCU) have emerged as potential contributors to the Ca^{2+} signaling pathway, requiring further dedicated research.

compartments simultaneously remains unexplored. However, with the increasing development of new ratiometric sensors targeting several cell compartments, multiparametric analyses of Ca^{2+} fluxes by flow cytometry may become a promising alternative for human immune cell research in the coming decades.

Author contributions

CB: Conceptualization, Data curation, Formal Analysis, Investigation, Methodology, Resources, Software, Visualization, Writing – original draft, Writing – review & editing. LC: Conceptualization, Data curation, Formal Analysis, Investigation, Methodology, Software, Writing – review & editing. FM: Conceptualization, Formal Analysis, Investigation, Writing – review & editing. TB: Funding acquisition, Project administration, Supervision, Validation, Writing – review & editing. SD: Conceptualization, Supervision, Validation, Writing – review & editing. MP: Conceptualization, Funding acquisition, Project administration, Supervision, Validation, Writing – review & editing. CCDS: Conceptualization, Funding acquisition, Project administration, Supervision, Validation, Writing – review & editing.

Funding

The author(s) declare financial support was received for the research, authorship, and/or publication of this article. This project was funded by grants from the Fondation de l'Avenir (n° AP-RM-20-008), from the French National League of Basketball, from the Agence Nationale de la Recherche (ANR- 20-CE14-0013-01) and Fédération Française de Cardiologie (FFC-BOCHATON-Dotation

References

2020). The Ph.D. salary of LC (Cifre, Olea Medical) is co-funded by the French Ministry of Higher Education and Research (ANRT).

Acknowledgments

We would like to thank the members of IRIS team for their fruitful discussions.

Conflict of interest

LC was employed by Olea Medical.

The remaining authors declare that the research was conducted in the absence of any commercial or financial relationships that could be construed as a potential conflict of interest.

Publisher's note

All claims expressed in this article are solely those of the authors and do not necessarily represent those of their affiliated organizations, or those of the publisher, the editors and the reviewers. Any product that may be evaluated in this article, or claim that may be made by its manufacturer, is not guaranteed or endorsed by the publisher.

Supplementary material

The Supplementary Material for this article can be found online at <https://www.frontiersin.org/articles/10.3389/fimmu.2023.1272809/full#supplementary-material>

1. Finak G, Langweiler M, Jaimes M, Malek M, Taghiyar J, Korin Y, et al. Standardizing flow cytometry immunophenotyping analysis from the human immunoPhenotyping consortium. *Sci Rep* (2016) 6:20686. doi: 10.1038/sep20686
2. Baumgarth N, Roederer M. A practical approach to multicolor flow cytometry for immunophenotyping. *J Immunol Methods* (2000) 243:77–97. doi: 10.1016/S0022-1759(00)00229-5
3. McKinnon KM. Flow cytometry: an overview. *Curr Protoc Immunol* (2018) 120:5.1.5. doi: 10.1002/cpim.40
4. Barnett D, Walker B, Landay A, Denny TN. CD4 immunophenotyping in HIV infection. *Nat Rev Microbiol* (2008) 6:S7–15. doi: 10.1038/nrmicro1998
5. Bridts CH, Sabato V, Mertens C, Hagendorens MM, De Clerck LS, Ebo DG. Flow cytometric allergy diagnosis: basophil activation techniques. In: Gibbs BF, Falcone FH, editors. *Basophils and Mast Cells: Methods and Protocols*. New York, NY: Springer (2014). p. 147–59.
6. Li W. Flow cytometry in the diagnosis of leukemias, in: *Leukemia* (2022). Brisbane (AU): Exon Publications. Available at: <http://www.ncbi.nlm.nih.gov/books/NBK586209/> (Accessed 7 May 2023).
7. Coppola L, Smaldone G, D'aiuto M, D'aiuto G, Mossetti G, Rinaldo M, et al. Identification of immune cell components in breast tissues by a multiparametric flow cytometry approach. *Cancers* (2022) 14:3869. doi: 10.3390/cancers14163869
8. Lopresti A, Malergue F, Bertucci F, Liberatoscioli ML, Garnier S, DaCosta Q, et al. Sensitive and easy screening for circulating tumor cells by flow cytometry. *JCI Insight* (2019) 5:e128180, 128180. doi: 10.1172/jci.insight.128180
9. Bourgoin P, Soliverez T, Ahriz D, Arnoux I, Meisel C, Unterwalder N, et al. Clinical research assessment by flow cytometry of biomarkers for infectious stratification in an Emergency Department. *Biomark Med* (2019) 13:1373–86. doi: 10.2217/bmm-2019-0214
10. Amin J, Boche D, Clough Z, Teeling J, Williams A, Gao Y, et al. Peripheral immunophenotype in dementia with Lewy bodies and Alzheimer's disease: an observational clinical study. *J Neurol Neurosurg Psychiatry* (2020) 91:1219–26. doi: 10.1136/jnnp-2020-323603
11. Pellicanò M, Larbi A, Goldeck D, Colonna-Romano G, Buffa S, Bulati M, et al. Immune profiling of Alzheimer patients. *J Neuroimmunol* (2012) 242:52–9. doi: 10.1016/j.jneuroim.2011.11.005
12. Obasanmi G, Lois N, Armstrong D, Hombrebueno JMR, Lynch A, Chen M, et al. Peripheral blood mononuclear cells from patients with type 1 diabetes and diabetic retinopathy produce higher levels of IL-17A, IL-10 and IL-6 and lower levels of IFN- γ —A pilot study. *Cells* (2023) 12:467. doi: 10.3390/cells12030467
13. Feske S. Calcium signaling in lymphocyte activation and disease. *Nat Rev Immunol* (2007) 7:690–702. doi: 10.1038/nri2152
14. Trebak M, Kinet J-P. Calcium signalling in T cells. *Nat Rev Immunol* (2019) 19:154–69. doi: 10.1038/s41577-018-0110-7
15. Nunes P, Demaurex N. The role of calcium signaling in phagocytosis. *J Leukoc Biol* (2010) 88:57–68. doi: 10.1189/jlb.0110028
16. Partisetti M, Le Deist F, Hivroz C, Fischer A, Korn H, Choquet D. The calcium current activated by T cell receptor and store depletion in human lymphocytes is absent

in a primary immunodeficiency. *J Biol Chem* (1994) 269:32327–35. doi: 10.1016/S0021-9258(18)31639-9

17. Kushnir A, Santulli G, Reiken SR, Coromilas E, Godfrey SJ, Brunjes DL, et al. Ryanodine receptor calcium leak in circulating B-lymphocytes as a biomarker in heart failure. *Circulation* (2018) 138:1144–54. doi: 10.1161/CIRCULATIONAHA.117.032703

18. Bajnok A, Serény-Litvai T, Temesföi V, Nörenberg J, Herczeg R, Kaposi A, et al. An optimized flow cytometric method to demonstrate the differentiation stage-dependent Ca^{2+} Flux responses of peripheral human B cells. *Int J Mol Sci* (2023) 24:9107. doi: 10.3390/ijms24109107

19. Donthu N, Kumar S, Mukherjee D, Pandey N, Lim WM. How to conduct a bibliometric analysis: An overview and guidelines. *J Bus Res* (2021) 133:285–96. doi: 10.1016/j.jbusres.2021.04.070

20. Chalet L, Boutelier T, Christen T, Raguenes D, Debatissé J, Eker OF, et al. Clinical imaging of the penumbra in ischemic stroke: from the concept to the era of mechanical thrombectomy. *Front Cardiovasc Med* (2022) 9:861913. doi: 10.3389/fcvm.2022.861913

21. van Eck NJ, Waltman L. *VOSviewer Manual*, Netherlands: University of Leiden. (2022) 54.

22. Liou J, Kim ML, Heo WD, Jones JT, Myers JW, Ferrell JE, et al. STIM is a Ca^{2+} sensor essential for Ca^{2+} -store-depletion-triggered Ca^{2+} influx. *Curr Biol CB* (2005) 15:1235–41. doi: 10.1016/j.cub.2005.05.055

23. Feske S, Gwack Y, Prakriya M, Srikanth S, Puppel S-H, Tanasa B, et al. A mutation in Orai1 causes immune deficiency by abrogating CRAC channel function. *Nature* (2006) 441:179–85. doi: 10.1038/nature04702

24. Vig M, Kinet J-P. Calcium signaling in immune cells. *Nat Immunol* (2009) 10:21–7. doi: 10.1038/ni.f.220

25. Oh-hora M, Rao A. Calcium signaling in lymphocytes. *Curr Opin Immunol* (2008) 20:250–8. doi: 10.1016/j.coim.2008.04.004

26. Grynkiewicz G, Poenie M, Tsien RY. A new generation of Ca^{2+} indicators with greatly improved fluorescence properties. *J Biol Chem* (1985) 260:3440–50. doi: 10.1016/S0021-9258(19)83641-4

27. Zweifach A, Lewis RS. Mitogen-regulated Ca^{2+} current of T lymphocytes is activated by depletion of intracellular Ca^{2+} stores. *Proc Natl Acad Sci* (1993) 90:6295–9. doi: 10.1073/pnas.90.13.6295

28. Dolmetsch RE, Lewis RS, Goodnow CC, Healy JI. Differential activation of transcription factors induced by Ca^{2+} response amplitude and duration. *Nature* (1997) 386:855–8. doi: 10.1038/386855a0

29. Parekh AB, Putney JW. Store-operated calcium channels. *Physiol Rev* (2005) 85:757–810. doi: 10.1152/physrev.00057.2003

30. Teigkamp S, Bhardwaj RS, Roth J, Meinardus-Hager G, Karas M, Sorg C. Calcium-dependent complex assembly of the myeloid differentiation proteins MRP-8 and MRP-14. *J Biol Chem* (1991) 266:13462–7. doi: 10.1016/S0021-9258(18)98862-9

31. Edgeworth J, Gorman M, Bennett R, Freemont P, Hogg N. Identification of p8,14 as a highly abundant heterodimeric calcium binding protein complex of myeloid cells. *J Biol Chem* (1991) 266:7706–13. doi: 10.1016/S0021-9258(20)89506-4

32. Odink K, Cerletti N, Brüggen J, Clerc RG, Tarczay L, Zwadlo G, et al. Two calcium-binding proteins in infiltrate macrophages of rheumatoid arthritis. *Nature* (1987) 330:80–2. doi: 10.1038/330080a0

33. Choe H, Farzan M, Sun Y, Sullivan N, Rollins B, Ponath PD, et al. The beta-chemokine receptors CCR3 and CCR5 facilitate infection by primary HIV-1 isolates. *Cell* (1996) 85:1135–48. doi: 10.1016/s0092-8674(00)81313-6

34. Doranz BJ, Rucker J, Yi Y, Smyth RJ, Samson M, Peiper SC, et al. A dual-tropic primary HIV-1 isolate that uses fusin and the β -chemokine receptors CCR-5, CCR-3, and CCR-2b as fusion cofactors. *Cell* (1996) 85:1149–58. doi: 10.1016/S0092-8674(00)81314-8

35. Deng H, Liu R, Ellmeier W, Choe S, Unutmaz D, Burkhardt M, et al. Identification of a major co-receptor for primary isolates of HIV-1. *Nature* (1996) 381:661–6. doi: 10.1038/381661a0

36. Dragic T, Litwin V, Allaway GP, Martin SR, Huang Y, Nagashima KA, et al. HIV-1 entry into CD4+ cells is mediated by the chemokine receptor CC-CKR-5. *Nature* (1996) 381:667–73. doi: 10.1038/381667a0

37. Bogeski I, Kummerow C, Al-Ansary D, Schwarz EC, Koehler R, Kozai D, et al. Differential redox regulation of ORAI ion channels: A mechanism to tune cellular calcium signaling. *Sci Signal* (2010) 3:ra24–4. doi: 10.1126/scisignal.2000672

38. Demaurex N, Nunes P. The role of STIM and ORAI proteins in phagocytic immune cells. *Am J Physiol-Cell Physiol* (2016) 310:C496–508. doi: 10.1152/ajpcell.00360.2015

39. Ambudkar IS, de Souza LB, Ong HL, TRPC1, Orai1, and STIM1 in SOCE: Friends in tight spaces. *Cell Calcium* (2017) 63:33–9. doi: 10.1016/j.ceca.2016.12.009

40. Wenning AS, Neblung K, Strauß B, Wolfs M-J, Sappok A, Roth M, et al. TRP expression pattern and the functional importance of TRPC3 in primary human T-cells. *Biochim Biophys Acta BBA - Mol Cell Res* (2011) 1813:412–23. doi: 10.1016/j.bbamcr.2010.12.022

41. Feske S. Immunodeficiency due to defects in store-operated calcium entry. *Ann NY Acad Sci* (2011) 1238:74–90. doi: 10.1111/j.1749-6632.2011.06240.x

42. DeCoursey TE, Chandy KG, Gupta S, Cahalan MD. Voltage-gated K+ channels in human T lymphocytes: a role in mitogenesis? *Nature* (1984) 307:465–8. doi: 10.1038/307465a0

43. Panyi G, Possani L, de la Vega RC, Gaspar R, Varga Z. K+ Channel blockers: novel tools to inhibit T cell activation leading to specific immunosuppression. *Curr Pharm Des* (2006) 12:2199–220. doi: 10.2174/13816120677585120

44. Toldi G, Bajnok A, Dobi D, Kaposi A, Kovács L, Vásárhelyi B, et al. The effects of Kv1.3 and IKCa1 potassium channel inhibition on calcium influx of human peripheral T lymphocytes in rheumatoid arthritis. *Immunobiology* (2013) 218:311–6. doi: 10.1016/j.imbio.2012.05.013

45. Chauhan A, Sun Y, Sukumaran P, Zangbede FOQ, Jondle CN, Sharma A, et al. M1 macrophage polarization is dependent on TRPC1-mediated calcium entry. *iScience* (2018) 8:85–102. doi: 10.1016/j.isci.2018.09.014

46. Serafini N, Dahdah A, Barbet G, Demion M, Attout T, Gautier G, et al. The TRPM4 channel controls monocyte and macrophage, but not neutrophil, function for survival in sepsis. *J Immunol* (2012) 189:3689–99. doi: 10.4049/jimmunol.1102969

47. Honore P, Donnelly-Roberts D, Namovic M, Zhong C, Wade C, Chandran P, et al. The antihyperalgesic activity of a selective P2X7 receptor antagonist, A-839977, is lost in IL-1 α β knockout mice. *Behav Brain Res* (2009) 204:77–81. doi: 10.1016/j.bbbr.2009.05.018

48. Bhardwaj RS, Zotz C, Roth J, Goebeler M, Mahnke K, Falk M, et al. The calcium-binding proteins MRP8 and MRP14 form a membrane-associated heterodimer in a subset of monocytes/macrophages present in acute but absent in chronic inflammatory lesions. *Eur J Immunol* (1992) 22:1891–7. doi: 10.1002/eji.1830220732

49. Jinquan T, Vorum H, Larsen CG, Madsen P, Rasmussen HH, Gesser B, et al. Psoriasin: A novel chemoattractant protein. *J Invest Dermatol* (1996) 107:5–10. doi: 10.1111/1523-1747.ep12294284

50. Lötzter K, Spanbroek R, Hildner M, Urbach A, Heller R, Bretschneider E, et al. Differential leukotriene receptor expression and calcium responses in endothelial cells and macrophages indicate 5-lipoxygenase-dependent circuits of inflammation and atherogenesis. *Arterioscler Thromb Vasc Biol* (2003) 23:e32–6. doi: 10.1161/01.ATV.0000082690.23131.CB

51. Mikulski Z, Hartmann P, Jositsch G, Zasłona Z, Lips KS, Pfeil U, et al. Nicotinic receptors on rat alveolar macrophages dampen ATP-induced increase in cytosolic calcium concentration. *Respir Res* (2010) 11:133. doi: 10.1186/1465-9921-11-133

52. Hsuan SL, Kannan MS, Jeyaseelan S, Prakash YS, Malazdrewich C, Abrahamsen MS, et al. Pasteurella hemolytica leukotoxin and endotoxin induced cytokine gene expression in bovine alveolar macrophages requires NF- κ B activation and calcium elevation. *Microb Pathog* (1999) 26:263–73. doi: 10.1006/mpat.1998.0271

53. Dewin DR, Catusse J, Gompels UA. Identification and characterization of U83A viral chemokine, a broad and potent β -chemokine agonist for human CCRs with unique selectivity and inhibition by spliced isoform. *J Immunol* (2006) 176:544–56. doi: 10.4049/jimmunol.176.1.544

54. Sakai A, Sugawara Y, Kuroishi T, Sasano T, Sugawara S. Identification of IL-18 and Th17 cells in salivary glands of patients with Sjögren's syndrome, and amplification of IL-17-mediated secretion of inflammatory cytokines from salivary gland cells by IL-18. *J Immunol* (2008) 181:2898–906. doi: 10.4049/jimmunol.181.4.2898

55. Martin L, Pingle SC, Hallam DM, Rybak LP, Ramkumar V. Activation of the adenosine A3 receptor in RAW 264.7 cells inhibits lipopolysaccharide-stimulated tumor necrosis factor- α Release by reducing calcium-dependent activation of nuclear factor- κ B and extracellular signal-regulated kinase 1/2. *J Pharmacol Exp Ther* (2006) 316:71–8. doi: 10.1124/jpet.105.091868

56. Triggiani M, Gentile M, Secondo A, Granata F, Oriente A, Tagliatela M, et al. Histamine induces exocytosis and IL-6 production from human lung macrophages through interaction with H1 receptors. *J Immunol* (2001) 166:4083–91. doi: 10.4049/jimmunol.166.6.4083

57. Shinkai A, Yoshisue H, Koike M, Shoji E, Nakagawa S, Saito A, et al. A novel human CC chemokine, eotaxin-3, which is expressed in IL-4-stimulated vascular endothelial cells, exhibits potent activity toward eosinophils. *J Immunol Baltim Md 1950* (1999) 163:1602–10. doi: 10.4049/jimmunol.163.3.1602

58. Schuerer-Maly CC, Eckmann L, Kagnoff MF, Falco MT, Maly FE. Colonic epithelial cell lines as a source of interleukin-8: stimulation by inflammatory cytokines and bacterial lipopolysaccharide. *Immunology* (1994) 81:85–91.

59. Thivierge M, Parent JL, Stankova J, Rola-Pleszczynski M. Modulation of formyl peptide receptor expression by IL-10 in human monocytes and neutrophils. *J Immunol Baltim Md 1950* (1999) 162:3590–5. doi: 10.4049/jimmunol.162.6.3590

60. Locati M, Zhou D, Luini W, Evangelista V, Mantovani A, Sozzani S. Rapid induction of arachidonic acid release by monocyte chemoattractant protein-1 and related chemokines. Role of Ca^{2+} influx, synergism with platelet-activating factor and significance for chemotaxis. *J Biol Chem* (1994) 269:4746–53. doi: 10.1016/S0021-9258(17)37607-X

61. Al-Aouky A, Rolstad B, Gaiad A, Maghazachi AA. MIP-3alpha, MIP-3beta and fractalkine induce the locomotion and the mobilization of intracellular calcium, and activate the heterotrimeric G proteins in human natural killer cells. *Immunology* (1998) 95:618–24. doi: 10.1046/j.1365-2567.1998.00603.x

62. Proost P, Meester JD, Schols D, Struyf S, Lambeir A-M, Wuyts A, et al. Amino-terminal truncation of chemokines by CD26/dipeptidyl-peptidase IV: CONVERSION OF RANTES INTO A POTENT INHIBITOR OF MONOCYTE CHEMOTAXIS AND HIV-1-INFECTION *. *J Biol Chem* (1998) 273:7222–7. doi: 10.1074/jbc.273.13.7222

63. Struyf S, De Meester I, Scharpé S, Lenaerts J-P, Menten P, Wang JM, et al. Natural truncation of RANTES abolishes signaling through the CC chemokine receptors CCR1 and CCR3, impairs its chemotactic potency and generates a CC

chemokine inhibitor. *Eur J Immunol* (1998) 28:1262–71. doi: 10.1002/(SICI)1521-4141(199804)28:04<1262::AID-IMMU1262>3.0.CO;2-G

64. Wuyls A, D'Haese A, Cremers V, Menten P, Lenaerts JP, De Loof A, et al. NH2- and COOH-terminal truncations of murine granulocyte chemotactic protein-2 augment the *in vitro* and *in vivo* neutrophil chemotactic potency. *J Immunol Baltim Md* 1950 (1999) 163:6155–63.

65. Imai T, Baba M, Nishimura M, Kakizaki M, Takagi S, Yoshie O. The T cell-directed CC chemokine TARC is a highly specific biological ligand for CC chemokine receptor 4*. *J Biol Chem* (1997) 272:15036–42. doi: 10.1074/jbc.272.23.15036

66. Proudfoot AEI. Chemokine receptors: multifaceted therapeutic targets. *Nat Rev Immunol* (2002) 2:106–15. doi: 10.1038/nri722

67. Salentin R, Gemsa D, Sprenger H, Kaufmann A. Chemokine receptor expression and chemotactic responsiveness of human monocytes after influenza A virus infection. *J Leukoc Biol* (2003) 74:252–9. doi: 10.1189/jlb.1102565

68. Berger EA, Murphy PM, Farber JM. CHEMOKINE RECEPTORS AS HIV-1 CORECEPTORS: roles in viral entry, tropism, and disease. *Annu Rev Immunol* (1999) 17:657–700. doi: 10.1146/annurev.immunol.17.1.657

69. Schols D, Struyf S, Damme JV, Esté JA, Henson G, Clercq ED. Inhibition of T-tropic HIV strains by selective antagonization of the chemokine receptor CXCR4. *J Exp Med* (1997) 186:1383–8. doi: 10.1084/jem.186.8.1383

70. Lusso P. HIV and the chemokine system: 10 years later. *EMBO J* (2006) 25:447–56. doi: 10.1038/sj.emboj.7600947

71. Cocchi F, DeVico AL, Garzino-Demo A, Arya SK, Gallo RC, Lusso P. Identification of RANTES, MIP-1 alpha, and MIP-1 beta as the major HIV-suppressive factors produced by CD8+ T cells. *Science* (1995) 270:1811–5. doi: 10.1126/science.270.5243.1811

72. Taguchi K, Okada A, Kitamura H, Yasui T, Naiki T, Hamamoto S, et al. Colony-stimulating factor-1 signaling suppresses renal crystal formation. *J Am Soc Nephrol* (2014) 25:1680. doi: 10.1681/ASN.2013060675

73. Viedt C, Dechend R, Fei J, Hänsch GM, Kreuzer J, Orth SR. MCP-1 induces inflammatory activation of human tubular epithelial cells: involvement of the transcription factors, nuclear factor- κ B and activating protein-1. *J Am Soc Nephrol* (2002) 13:1534. doi: 10.1097/01.ASN.0000015609.31253.7F

74. Betters P, RN DM. Use of flow cytometry in clinical practice. *J Adv Pract Oncol* (2015) 6:437. doi: 10.6004/jadpro.2015.6.5.4

75. Gauduchon V, Werner S, Prévost G, Monteil H, Colin DA. Flow cytometric determination of pantom-valentine leucocidin S component binding. *Infect Immun* (2001) 69:2390–5. doi: 10.1128/IAI.69.4.2390-2395.2001

76. Kirchhoff K, Weinmann O, Zwirner J, Begemann G, Gotze O, Kapp A, et al. Detection of anaphylatoxin receptors on CD83+ dendritic cells derived from human skin. *Immunology* (2001) 103:210–7. doi: 10.1046/j.1365-2567.2001.01197.x

77. Princen K, Hatse S, Vermeire K, De Clercq E, Schols D. Evaluation of SDF-1/CXCR4-induced Ca^{2+} signaling by fluorometric imaging plate reader (FLIPR) and flow cytometry. *Cytometry* (2003) 51A:35–45. doi: 10.1002/cyto.a.10008

78. Heinemann A, Ofner M, Amann R, Peskar BA. A novel assay to measure the calcium flux in human basophils: effects of chemokines and nerve growth factor. *Pharmacology* (2003) 67:49–54. doi: 10.1159/000066786

79. Nishizaki Y, Oyama Y, Sakai Y, Hirama S, Tomita K, Nakao H, et al. PbCl2-induced hyperpolarization of rat thymocytes: Involvement of charybdotoxin-sensitive K+ channels. *Environ Toxicol* (2003) 18:321–6. doi: 10.1002/tox.10132

80. Lamoureux J, Stankova J, Rolapleszczynski M. Leukotriene D4 enhances immunoglobulin production in CD40-activated human B lymphocytes. *J Allergy Clin Immunol* (2006) 117:924–30. doi: 10.1016/j.jaci.2005.12.1329

81. Ceballos A, Sabaté J, Nahmod K, Martínez D, Salamone G, Vermeulen M, et al. Sphingosylphosphorylcholine activates dendritic cells, stimulating the production of interleukin-12. *Immunology* (2007) 121:328–36. doi: 10.1111/j.1365-2567.2007.02578.x

82. Chen Y-L, Chen Y-S, Lin H-H, Chan C-W, Chen S-C, Chen C-H. Immunostimulatory flagellin from *Burkholderia pseudomallei* effects on an increase in the intracellular calcium concentration and up-regulation of TNF- α by mononuclear cells. *Microbiol Immunol* (2007) 51:81–6. doi: 10.1111/j.1348-0421.2007.tb03893.x

83. Orbán C, Bajnok A, Vásárhelyi B, Tulassay T, Toldi G. Different calcium influx characteristics upon Kv1.3 and IKCa1 potassium channel inhibition in T helper subsets: Calcium Influx Kinetics in T Helper Subsets. *Cytometry A* (2014) 85:636–41. doi: 10.1002/cyto.a.22479

84. Gutzmer R, Langer K, Lisewski M, Mommert S, Rieckborn D, Kapp A, et al. Expression and function of histamine receptors 1 and 2 on human monocyte-derived dendritic cells. *J Allergy Clin Immunol* (2002) 109:524–31. doi: 10.1067/mai.2002.121944

85. Sun C, Jiang M, Zhang L, Yang J, Zhang G, Du B, et al. Cycloastragenol mediates activation and proliferation suppression in concanavalin A-induced mouse lymphocyte pan-activation model. *Immunopharmacol Immunotoxicol* (2017) 39:131–9. doi: 10.1080/08923973.2017.1300170

86. Tran HTT, Herz C, Ruf P, Stetter R, Lamy E. Human T2R38 bitter taste receptor expression in resting and activated lymphocytes. *Front Immunol* (2018) 9:2949. doi: 10.3389/fimmu.2018.02949

87. Boltz RC“Dutch”, Sirotina A, Blake T, Kath G, Uhrig B, McKeel J, et al. A disposable-chamber temperature-regulation system for the study of intracellular calcium levels in single live T cells using fluorescence digital-imaging microscopy. *Cytometry* (1994) 17:128–34. doi: 10.1002/cyto.990170204

88. Bates PJ, Ralston NV, Vuk-Pavlovic Z, Rohrbach MS. Calcium influx is required for tannin-mediated arachidonic acid release from alveolar macrophages. *Am J Physiol Lung Cell Mol Physiol* (1995) 268:L33–40. doi: 10.1152/ajplung.1995.268.1.L33

89. Tárnok A, Dörger M, Berg I, Gercken G, Schlüter T. Rapid screening of possible cytotoxic effects of particulate air pollutants by measurement of changes in cytoplasmic free calcium, cytosolic pH, and plasma membrane potential in alveolar macrophages by flow cytometry. *Cytometry* (2001) 43:204–10. doi: 10.1002/1097-0320(20010301)43:3<204::AID-CYTO1051>3.0.CO;2-Z

90. Si M-S, Reitz BA, Borie DC. Effects of the kinase inhibitor CGP41251 (PKC 412) on lymphocyte activation and TNF- α production. *Int Immunopharmacol* (2005) 5:1141–9. doi: 10.1016/j.intimp.2005.02.012

91. Toldi G, Folyovich A, Simon Z, Zsiga K, Kaposi A, Mészáros G, et al. Lymphocyte calcium influx kinetics in multiple sclerosis treated without or with interferon beta. *J Neuroimmunol* (2011) 237:80–6. doi: 10.1016/j.jneuroim.2011.06.008

92. Orbán C, Szabó D, Bajnok A, Vásárhelyi B, Tulassay T, Arató A, et al. Altered calcium influx of peripheral Th2 cells in pediatric Crohn's disease: infliximab may normalize activation patterns. *Oncotarget* (2016) 7:44966–74. doi: 10.18632/oncotarget.10036

93. Toldi G, Legány N, Ocsovszki I, Balog A. Calcium influx kinetics and the characteristics of potassium channels in peripheral T lymphocytes in systemic sclerosis. *Pathobiology* (2020) 87:311–6. doi: 10.1159/000509674

94. Novak EJ, Rabinovitch PS. Improved sensitivity in flow cytometric intracellular ionized calcium measurement using fluo-3/Fura Red fluorescence ratios. *Cytometry* (1994) 17:135–41. doi: 10.1002/cyto.990170205

95. Wendl ER, Ferry H, Greaves DR, Keshav S. Ratiometric analysis of fura red by flow cytometry: a technique for monitoring intracellular calcium flux in primary cell subsets. *PLoS One* (2015) 10:e0119532. doi: 10.1371/journal.pone.0119532

96. *The evolution of spectral flow cytometry - Nolan - 2022 - Cytometry Part A - Wiley Online Library* (Accessed 8 September 2023).

97. *Panel Design and Optimization for High-Dimensional Immunophenotyping Assays Using Spectral Flow Cytometry - Ferrer-Font - 2020 - Current Protocols in Cytometry - Wiley Online Library* (Accessed 8 September 2023).

98. Assis LH de P, Dorighello G de G, de Oliveira HCF. Pro-inflammatory polarization of macrophages is associated with reduced endoplasmic reticulum-mitochondria interaction. *Biochem Biophys Res Commun* (2022) 606:61–7. doi: 10.1016/j.bbrc.2022.03.086

99. Seegren PV, Harper LR, Downs TK, Zhao X-Y, Viswanathan SB, Strembska ME, et al. Reduced mitochondrial calcium uptake in macrophages is a major driver of inflamming. *Nat Aging* (2023) 3:796–812. doi: 10.1038/s43587-023-00436-8

100. Osipchuk NC, Soulika AM, Fomina AF. Modulation of ryanodine receptors activity alters the course of experimental autoimmune encephalomyelitis in mice. *Front Physiol* (2021) 12. doi: 10.3389/fphys.2021.770820



OPEN ACCESS

EDITED BY

Thomas Hartung,
Johns Hopkins University, United States

REVIEWED BY

Kenichi Asano,
Tokyo University of Pharmacy and Life
Sciences, Japan
Izumi Sasaki,
Wakayama Medical University, Japan

*CORRESPONDENCE

Nobuyuki Onai
✉ onai@kanazawa-med.ac.jp

RECEIVED 21 July 2023

ACCEPTED 21 September 2023

PUBLISHED 13 October 2023

CITATION

Matsuba S, Ura H, Saito F, Ogasawara C,
Shimodaira S, Niida Y and Onai N (2023)
An optimized cocktail of small molecule
inhibitors promotes the maturation of
dendritic cells in GM-CSF mouse
bone marrow culture.

Front. Immunol. 14:1264609.
doi: 10.3389/fimmu.2023.1264609

COPYRIGHT

© 2023 Matsuba, Ura, Saito, Ogasawara,
Shimodaira, Niida and Onai. This is an open-
access article distributed under the terms of
the [Creative Commons Attribution License
\(CC BY\)](#). The use, distribution or
reproduction in other forums is permitted,
provided the original author(s) and the
copyright owner(s) are credited and that
the original publication in this journal is
cited, in accordance with accepted
academic practice. No use, distribution or
reproduction is permitted which does not
comply with these terms.

An optimized cocktail of small molecule inhibitors promotes the maturation of dendritic cells in GM-CSF mouse bone marrow culture

Shintaro Matsuba¹, Hiroki Ura^{2,3}, Fumiji Saito¹,
Chie Ogasawara¹, Shigetaka Shimodaira^{4,5}, Yo Niida^{2,3}
and Nobuyuki Onai^{1*}

¹Department of Immunology, Kanazawa Medical University, Uchinada, Ishikawa, Japan, ²Center for Clinical Genomics, Kanazawa Medical University Hospital, Uchinada, Ishikawa, Japan, ³Division of Genomic Medicine, Department of Advanced Medicine, Medical Research Institute, Kanazawa Medical University, Uchinada, Ishikawa, Japan, ⁴Department of Regenerative Medicine, Kanazawa Medical University, Uchinada, Ishikawa, Japan, ⁵Center for Regenerative Medicine, Kanazawa Medical University Hospital, Uchinada, Ishikawa, Japan

Dendritic cells (DCs) are the most potent antigen-presenting cells, playing an essential role in the pathogen and tumor recognition, and anti-tumor immunity, and linking both the innate and adaptive immunity. The monocyte-derived DCs generated by ex vivo culture, have been used for cancer immunotherapy to eliminate tumor; however, the clinical efficacies are not sufficient, and further improvement is essential. In this study, we established a method to generate DCs using small molecule compounds for cancer immunotherapy. We observed an increase in the percentage of CD11c⁺I-A/I-E^{high} cells, representing DCs, by adding four small molecular inhibitors: Y27632, PD0325901, PD173074, and PD98059 (abbreviated as YPPP), in mouse bone marrow (BM) culture with granulocyte-macrophage colony stimulating factor (GM-CSF). BM-derived DCs cultured with YPPP (YPPP-DCs) showed high responsiveness to lipopolysaccharide stimulation, resulting in increased interleukin (IL) -12 production and enhanced proliferation activity when co-cultured with naïve T cells compared with the vehicle control. RNA-seq analysis revealed an upregulation of peroxisome proliferator - activated receptor (PPAR) γ associated genes increased in YPPP-DCs. In tumor models treated with anti-programmed death (PD) -1 therapies, mice injected intratumorally with YPPP-DCs as a DCs vaccine exhibited reduced tumor growth and increased survival. These findings suggested that our method would be useful for the induction of DCs that efficiently activate effector T cells for cancer immunotherapy.

KEYWORDS

dendritic cells, small molecule inhibitor, cytokine production, mixed lymphoid reaction, immunotherapy

Introduction

Dendritic cells (DCs) initiate the acquired immunity to eliminate cancer and pathogens through antigen presentation and cytokine production in lymphoid and nonlymphoid tissues (1). In the peripheral tissue, DCs capture the debris from tumor, pathogen-infected cells, or dead cells, process them and presents to T cells as antigen. This is important for initiating adaptive immune responses against a variety of antigens, including pathogens, tumors, and self-antigens.

DCs originate from hematopoietic stem cells (HSCs) through several stages of DC progenitors, known as common DC progenitors (CDPs) (2–4). Specific transcription factors for DC polarization have been identified for each type, including conventional DCs (cDCs) and plasmacytoid DCs (pDCs) (2, 5). The cDCs are further subdivided into conventional DC1 (cDC1) and conventional DC2 (cDC2), spread in the lymphoid and non-lymphoid tissues. The cDC1 have excellent cross-presentation activity, therefore, these cells are an attractive target for vaccination against intracellular pathogens and tumors, unfortunately, very few of these cells can be isolated from tissue (6, 7).

Large numbers of DC can be generated from the BM cells as BM-derived DCs using an *in vitro* culture with granulocyte-macrophage colony stimulating factor (GM-CSF) or Fms like tyrosine kinase 3 ligand (Flt3L) (8–10). *In vitro* cultures with GM-CSF mainly produce DCs that are similar to monocyte-derived DCs (8). In contrast, cultures with Flt3L best reflects physiological DC development, but results in a mixture of pDC and cDC, in which cDCs correspond to cDC1 and cDC2 (10). Recently, an efficiently induction culture system for CD103⁺ DCs derived from mouse BM using a combination of GM-CSF and Flt3L has been reported (11). Taking advantage of these features of cDCs, priming tumor antigens to DCs and returning them to the body to induce cancer-specific immune responses is a typical immune-cell therapy (12, 13). However, current methods often fail to obtain the necessary number of DCs from cancer patients for cancer immunotherapy. Previous studies have attempted to induce DCs derived from human embryonic stem (hES) cells or induced pluripotent stem (iPS) cells, but issues such as a long culture time for DC induction, high costs, and the risk of cancerous transformation still persist (14–16).

Recently, it has been reported that a cocktail of low molecular weight compounds can reprogram hepatocytes lacking the proliferative potential into liver progenitor cells with proliferative and differentiation potential (17). While DCs can be induced from the BM or peripheral blood using GM-CSF or Flt3L in an *in vitro* culture system (8, 10), the induction of DCs using by small molecule cocktails has not been reported. Previous studies have shown that inhibition of Rho-associated kinase (ROCK) by the small molecule compound Y27632 can overcome the massive cell death associated with hES cell dissociation (18). Additionally, the mitogen-activated protein kinase (MEK) inhibitors PD98059 and PD0325901 (19–21) has been found to help hES cells survive in culture and maintain their proliferation over time. PD173074, an inhibitor of the fibroblast growth factor (FGF) receptor, has been implicated in

hES cell self-renewal (19). Therefore, we hypothesized that these small molecules could efficiently induce high-quality DCs.

This study is the first time to report that a small molecule cocktail, comprising Y27632, PD0325901, PD173074, and PD98059 (YPPP), promotes DC maturation in mouse BM culture with GM-CSF. BM-derived DCs culturing with YPPP (YPPP-DCs) showed heightened responsiveness to lipopolysaccharide (LPS) stimulation, resulting in increased interleukin (IL)-12 production and enhanced proliferation activity of effector T cells. YPPP-DCs showed increased PPAR γ -associated gene transcriptions in steady state. These results indicate that YPPP can effectively be used as a DC differentiation and maturation reagent.

Materials and methods

Mice and reagents

C57BL/6 mice (6–9 weeks old) and BALB/c mice (6–9 weeks old) were purchased from Japan SLC (Shizuoka, Japan). Rag2^{-/-}OT-I and Rag2^{-/-}OT-II T cell receptor (TCR) transgenic mice (6–9 weeks old) were purchased from Taconic Biosciences. These mice were kept and bred in the animal unit at Kanazawa Medical University, an environmentally controlled and specific pathogen-free facility, in accordance with the guidelines for experimental animals defined by the facilities. Animal experimental protocols were approved by the Animal Research Committee at Kanazawa Medical University (Approval No.:2020-30, 2022-17). The procedures were carried out in accordance with the approved guidelines. Ovalbumin (OVA) ₂₅₇₋₂₆₄ peptide SIINFEKL and OVA₃₂₃₋₃₃₉ peptide were purchased from Anaspec.

Cell lines and culture

E.G7 tumor cell line was purchased from the American Type Culture Collection (ATCC) and B16 melanoma cell line was kindly gifted by Dr. Nobuo Yamaguchi (Kanazawa Medical University). E.G7 cells were cultured in Roswell Park Memorial Institute (RPMI)-1640 medium modified to contain 2mM L-glutamine, 10mM HEPES, 1mM sodium pyruvate, 4500mg/l glucose, and 1500mg/l sodium bicarbonate (Sigma-Aldrich) supplemented with 10% fetal calf serum (FCS), B16 cells were cultured in Dulbecco's modified eagle medium (DMEM)supplemented with 10% FCS.

Preparation of small molecule cocktails

The four small molecule inhibitors (YPPP) were first reconstituted into stock solutions; 10 mM Y27632 (Fujifilm Wako) was prepared in sterilized phosphate buffered saline (PBS), and 40 mM PD0325901 (Fujifilm Wako), 10 mM PD173074 (Fujifilm Wako) and 10 mM PD98059 (Fujifilm Wako) were prepared in dimethyl sulfoxide (DMSO, Nakarai tesque). Stock solutions were stored at -20°C until use. Y27632, PD0325901,

PD173074 and PD98059 were used at final concentrations of 50, 0.04, 0.01, 6.3 μ M.

Generation of murine BM-derived dendritic cells

BM cells were prepared from C57BL/6 mice and these cells were cultured with GM-CSF as we described previously (8). Briefly, BM cells were cultured in RPMI-1640 supplemented with 10% FCS, 5 \times 10⁻⁵M 2-mercaptoethanol, 100 U/ml penicillin, 100 μ g/ml streptomycin and 25 ng/ml GM-CSF (Biolegend) and with DMSO or YPPP for 6 days. On day 6, CD11c⁺ cells were isolated using the magnetic-activated cell sorting (MACS) system with magnetic microbead-conjugated anti-CD11c antibody (Miltenyi Biotec). The purities of the sorted CD11c⁺ fractions by using CD11c microbeads were consistently \geq 90% (Supplementary Figure 2). In E.G7 tumor model, CD11c⁺ cells were stimulated with 10 ng/ml lipopolysaccharide (LPS) for 12 h and loaded with 10 μ M OVA₂₅₇₋₂₆₄ peptide SIINFEKL for 2h prior to injection. In B16 melanoma model, CD11c⁺ cells were stimulated with 10 ng/ml lipopolysaccharide (LPS) for 12 h prior to injection.

Flow cytometry and cell sorting

Flow cytometry was conducted using the following antibodies (All purchased from Biolegend unless stated otherwise): anti-CD11c (N418), anti-I-A/I-E (M5/114.15.2), anti-CCR7 (4B12), anti-CD40 (3/23), anti-CD11b (M1/70), anti-CD80 (16-10A1), anti-CD86 (GL-1), anti-CD4 (GK1.5), anti-CD8 (53-6.7), anti-CD25 (PC61), anti-CD62L (MEL14), anti-CD69(H1.2F3) and anti-PD-L2 (TY25). Fc-mediated nonspecific staining was blocked with anti-CD16/32 (2.4G2 hybridoma culture supernatant). Events were acquired using a FACSCanto II (BD Biosciences), and the data of 10,000-100,000 events were analyzed using the FACSDiva (BD Biosciences) or FlowJo software programs (FlowJo). The surface molecule expressions were calculated by defining the delta mean fluorescence intensity between the specific antibody stain and the isotype-matched control antibody. CD11c⁺I-A/I-E^{high} cells and CD11c⁺I-A/I-E^{int} cells were isolated by using a cell sorting system (SH800; Sony Biotechnology) or FACS Aria fusion (BD Biosciences). Separation of these cells were shown in Supplementary Figures 5A, B. Briefly, BM lineage negative (Lin (-)) cells were immunomagnetically pre-enriched using PE-Cy5-conjugated antibodies against lineage antigens, including CD3e (145-2C11), CD4 (GK1.5), CD8 α (53-6.7), B220 (RA3-6B2), CD19 (MB19-1), CD11c (N418), CD11b (M1/70), Gr-1 (RB6-8C5), NK1.1 (PK136), anti-Cy5 microbeads and autoMACSpro (Miltenyi Biotec). BM- Lin (-) cells were cultured with 25 ng/ml GM-CSF (Biolegend) for 6 days. On day 3, BM-Lin (-) derived CD11c⁺ cells were isolated using the MACS system with magnetic microbead-conjugated anti-CD11c antibody (Miltenyi Biotec). BM-Lin (-) cells were then stained with FITC-anti-I-A/I-E (M5/114.15.2) and PE-Cy7-anti-CD11c (N418) (all from

BioLegend). CD11c⁺I-A/I-E^{high} cells and CD11c⁺I-A/I-E^{int} cells were sorted by gating on indicated cells from CD11c⁺ cells. The purity of the sorted populations was consistently \geq 90%.

In vitro T cell proliferation assays

OT-I T cells

Thy1.2⁺ T cells from spleen of OT-I or OT-I x Rag2^{-/-} mice were enriched using the MACS system with magnetic microbead-conjugated anti-CD90.2 antibody (Miltenyi Biotec), according to manufacturer's instructions. Enriched Thy1.2⁺ T cells were then labeled with celltracker Cytotell green (AAT Bioquest) at 37 °C for 10 min, washed, and counted before culture with antigen presenting cells (APCs).

OT-II T cells

Thy1.2⁺ T cells from spleen of OT-II x Rag2^{-/-} mice were enriched using the MACS system with magnetic microbead-conjugated anti-Thy1.2⁺ antibody (Miltenyi Biotec), according to manufacturer's instructions. Enriched Thy1.2⁺ T cells were then labeled with celltracker Cytotell green at 37 °C for 10 min, washed, and counted before culture with APCs.

BALB/c T cells

Thy1.2⁺ T cells from spleen of BALB/c mice were enriched using the MACS system with magnetic microbead-conjugated anti-CD90.2 antibody (Miltenyi Biotec), according to manufacturer's instructions. Enriched Thy1.2⁺ T cells were then labeled with celltracker Cytotell green at 37°C for 10 min, washed, and counted before culture with APCs.

Stimulation

Sorted CD11c⁺ cells in mouse bone marrow culture with GM-CSF and DMSO/YPPP for 6 days were incubated in 96-well round-bottom tissue culture plates. For OT-I T cells stimulation, CD11c⁺ cells were incubated with OVA₂₅₇₋₂₆₄ peptide (1 nM) in the presence of 100 ng/ml of LPS. For OT-II T cells stimulation, CD11c⁺ cells were incubated with OVA₃₂₃₋₃₃₉ peptide (10 μ M) in the presence of 100 ng/ml of LPS and co-cultured with naive Cytotell green-labeled OT-II T cell. For allogenic BALB/c T cells stimulation, CD11c⁺ cells were incubated with LPS (100 μ g/ml). Various number of CD11c⁺ cells (7.3 x, 22.0 x or 66.0 x 10² cells) were incubated with 2.0 x 10⁴ T cells. T cell proliferation and activation was assessed by flow cytometry after 3 days for OT-I T cells and after 5 days for OT-II and BALB/c T cells.

Cell counting kit-8 assay

Cells were grown into 24 well plates. At day 6, 10 μ l of CCK-8 solution (Dojindo) was added into each well and cultured for another 2 hours, and measured at 490 nm in a microplate reader

Multiscan JX (Thermo scientific). The ratios of proliferation were calculated as follows: the absorbance of culture supernatants at 490 nm/absorbance of the control cell supernatants at 490 nm.

ELISA

Cells were incubated with the indicated stimulators. The levels of cytokines in the culture supernatants were determined using ELISA kits, in accordance with the manufacturers' instructions. The mouse IL-12p70, IL-12p40, IL-6, TNF- α ELISA MAX Standard kits (Biologend) were used.

Immunoblotting

The cells for immunoblotting were prepared as we described previously (22). Briefly, Cells were solubilized in lysis buffer (1.0% NP-40, 50 mM HEPES, pH7.4, 150 mM NaCl), containing protease and phosphatase inhibitor (Thermo fisher scientific). Cell lysates were separated by sodium dodecyl sulfate (SDS)- polyacrylamide gel electrophoresis (PAGE), transferred to a Polyvinylidene difluoride (PVDF) membrane (Merck), and detected with the following antibodies using ECL substrate (Bio-Rad): rabbit anti-CCAAT enhancer binding protein (C/EBP) α anti-phospho-C/EBP α (Ser21), anti-phospho- C/EBP α (Thr221/226), anti-Erk1/2, anti-phospho- Erk1/2, anti-JNK, anti-phospho-JNK, anti-NF- κ B (p65), anti-phospho-NF- κ B(p65), mouse anti-I κ B α (Cell Signaling Technology), mouse anti-I κ B β (Santa Cruz Biotechnology), mouse anti- β actin (Sigma-aldrich), horseradish peroxidase (HRP)-conjugated mouse IgG (Cell Signaling Technology), or rabbit IgG antibodies (Cell Signaling Technology). Digital images were obtained using an ImageQuant LAS4000 mini instrument (GE Healthcare). Densitometry was performed on scanned blots using the ImageQuant TL software program (GE Healthcare).

Tumor model

The protocol by which E.G7 or B16 melanoma tumor model were previously described (23, 24). These tumor cells were established by intradermally injecting 2 x or 10 x 10⁵ tumor cells (in 50 μ l of DMEM) into the back flanks of 8-9 weeks old C57BL/6 mice (day 0). For dendritic cell vaccine (DCV) therapy, on days 7, 10, 13, 1.25 or 12.5 x 10⁴ syngeneic BM derived CD11c $^+$ cells (in 50 μ l DMEM/0.1% bovine serum albumin) were injected intratumorally with or without anti Programmed death (PD)-1 (Biologend, 20 μ g/mouse) in 200 μ l saline intraperitoneal injection. Tumor sizes were measured twice a week. Tumor volume was calculated by the following formula: tumor volume. 0.4 x length (mm) x [width (mm)]² (24). Mice were euthanized when they became moribund or when their tumors exceeded 20 mm in diameter.

Gene expression analysis

Total RNA extraction

Total RNA was extracted with AllPrep DNA/RNA kit (Qiagen) according to the manufacturer's instructions. Subsequently, the concentration and purity of isolated RNA molecules were measured spectrophotometrically by Nanodrop (Thermo scientific), after which the RNA integrity number was measured using TapeStation 4200 with a High Sensitivity RNA Screen Tape (Agilent Technologies).

RNA-seq library construction and library sequencing

The fragmented double-strand cDNA was synthesized using NEB Next Ultra II Directional RNA Library Prep Kit (New England BioLabs) according to manufacturer's instructions. After library quality was assessed using the TapeStation 4200 with High Sensitivity D1000 ScreenTape (Agilent Technologies). All libraries were quantified using the HS Qubit dsDNA assay (Thermo Fisher Scientific). All libraries were sequenced (2 x 75 bp) using Illumina NextSeq 500 (Illumina) according to the standard Illumina protocol. The FASTQ files were generated using the bcl2fastq software (Illumina).

Data analysis

FASTQ files were aligned to the reference mouse genome (mm10) using HISAT2 (version 2.1.0) (25). The StringTie algorithm (v.1.3.4d) (26) was then used with default parameter settings to assemble RNA-Seq alignments into annotated transcripts to estimate their expression using the UCSC annotated mouse genome (mm10) assembly file. Subsequently, the transcript expression was normalized using the transcripts per million (TPM) algorithms. For differential expression analysis, we used the R package (edger) (27), as described previously (28, 29). Gene ontology (GO) and Kyoto Encyclopedia of Genes and Genomes (KEGG) analyses were performed using Enrichr web server (<https://maayanlab.cloud/Enrichr/>) (30–32).

Statistical analysis

Statistical analysis was carried out by ANOVA using GraphPad Prism software. All experimental repetitions and numbers of specimens and mice are indicated in the figure legends. One-way and two-way ANOVA were used for the experiments with one variable and two variables, respectively. $p < 0.05$ was considered to be statistically significant. For survival analysis, p values were computed using the Log Rank test. p values < 0.05 was considered to be statistically significant.

Results

Establishment of the optimal combination of small molecules for DC differentiation

Previous study in mouse BM culture with GM-CSF have demonstrated the presence of primarily two subsets: CD11c⁺I-A/I-E^{high} cells (GM-DCs) and CD11c⁺I-A/I-E^{int} cells (GM-Macs) (33). To determine the optimal combination for DC differentiation in a mouse BM-derived DC culture system, we initially examined 16 different combinations of the four small molecule compounds (Figure 1A). The optimal concentration of Y27632, PD0325901 and PD173074 were determined through preliminary tests (Supplementary Figures 1A, B), while effective concentration of PD98059 was demonstrated in previous study (21, 34). In this culture system, the addition groups of the 6th, 13th, and 16th combination of the small molecule inhibitors significantly increased the percentages of CD11c⁺I-A/I-E^{high} cells in the 40.1 ± 25.0, 44.8 ± 16.5, and 53.4 ± 11.7% compared to 17.4 ± 10.5% for the control (Figures 1B, C). No effect was observed with the other additional groups. On the other hand, the addition groups of the 3th, 5th 15th, and 16th combination of the small molecule inhibitors significantly decreased the percentages of CD11c⁺I-A/I-E^{int} cells in the 25.8 ± 2.40, 25.2 ± 0.49, 24.5 ± 0.57, and 30.0 ± 1.77% compared to 45.4 ± 6.35% for the control (Figures 1B, E). The total cell number of CD11c⁺I-A/I-E^{high} cells shows no significant difference between control and 16th group (Figure 1D). However, the total cell number of CD11c⁺I-A/I-E^{int} cells of 16th group is markedly reduced when compared with control (Figure 1F). These results indicate that the addition of these small molecule inhibitor cocktails significantly altered the percentage of CD11c⁺I-A/I-E^{high} cell, representing DCs, with the 16th small molecule inhibitor cocktail YPPP, yielding cells of the highest purity (Figures 1B-F). It has been reported that GM-CSF induced differentiation of myeloid-derived suppressor cells (MDSCs) from BM cells, defined as Ly6G^{high}Ly6c^{int} cells (35). Therefore, we examined the effect of YPPP on GM-CSF induced MDSCs. The YPPP did not have a significant impact on MDSCs differentiation (Supplementary Figures 2A, B).

Enhanced IL-12 production in YPPP-CD11c⁺ cells after LPS stimulation

The anti-tumor activity of DCV used in cancer immunotherapy relies on the quality of the DC-containing cell fraction CD11c⁺ cells in the DCV. Therefore, we examined cytokine production in DMSO- and YPPP-treated BM-derived CD11c⁺ cells, as LPS is known to be a potent inducer of the Th1 cytokine IL-12 by using magnetically purified CD11c⁺ cells (Supplementary Figure 3). The level of proinflammatory cytokine IL-6 and IL-12 were measured after LPS stimulation. As shown in Figure 2A, YPPP-treated BM derived CD11c⁺ cells (YPPP- CD11c⁺ cells) produced high amount of IL-12p70 and IL-12p40 compared to DMSO-treated CD11c⁺ cells (DMSO- CD11c⁺ cells) after LPS stimulation, while no difference was observed in IL-6 and TNF- α levels between DMSO

and YPPP-CD11c⁺ cells. Next, we investigated the activation of key signaling molecules in the Toll like receptor (TLR) 4-mediated signaling pathway, which was activated by LPS stimulation. Previous studies have shown that CCAAT enhancer binding protein alpha (C/EBP α), whose activation is regulated by extracellular signal-regulated kinase 1/2 (Erk1/2), negatively regulates IL-12 production upon LPS stimulation (36). Therefore, we examined the phosphorylation of Erk1/2 and C/EBP α (murine Ser21 and Thr222/226) upon LPS stimulation. While NF- κ B and JNK phosphorylation were comparably increased in DMSO- and YPPP-CD11c⁺ cells, Erk1/2 phosphorylation was decreased in YPPP-CD11c⁺ cells (Figure 2B, lanes 4, 5, 6, 7, 8 and 9). Surprisingly, pSer21 C/EBP α was decreased in YPPP-CD11c⁺ cells, whereas C/EBP α (Ser21) was phosphorylated in DMSO-CD11c⁺ cells, even after LPS stimulation (Figure 2B, lanes 1 and 3, and Figure 2C). In contrast, Thr222/226 C/EBP α was equally phosphorylated in both DMSO- and YPPP-CD11c⁺ cells (Figure 2B, lane 2). I κ B α and I κ B β levels were equivalently decreased in DMSO- or YPPP-CD11c⁺ cells (Figure 2B, lanes 10 and 11). These results suggest that IL-12 production is enhanced by suppressing C/EBP α activation upon LPS stimulation in YPPP-CD11c⁺ cells.

YPPP-CD11c⁺ cells primed ovalbumin are more efficient in T cell activation and proliferation than DMSO-CD11c⁺ cells

The ability of DCV to promote T cell proliferation is a critical function for anti-tumor activity. Therefore, we examined the T cell proliferation activities of DMSO- or YPPP-CD11c⁺ cells in a mixed lymphocyte reaction (MLR). Cell tracker Cytotell green labeled Thy1⁺ splenic CD4⁺ or CD8⁺ T cells from OT-II or OT-I mice were co-cultured with DMSO- or YPPP-CD11c⁺ cells from B6-WT mice for 3 or 5 days *in vitro*. The proliferation was monitored using CCK-8 and flow cytometry. As shown in Figure 3A, we observed a significantly increased number of proliferating cells in the group in which YPPP-CD11c⁺ cells, as determined by the CCK-8 proliferation assay. Furthermore, flow cytometric (FCM) analysis revealed that a significant increase of the population of Cytotell green^{low}CD25⁺CD8⁺ T cells, Cytotell green^{low}CD69⁺CD8⁺ T cells, and Cytotell green^{low}CD62L^{low}CD8⁺ T cells at 1: 3 CD11c⁺/T cell ratio in the presence of YPPP-CD11c⁺ cells (Figures 3B-G).

Next, we examined whether YPPP-CD11c⁺ cells can efficiently expand splenic CD4⁺ T cells isolated from OT-II mice. As shown in Supplementary Figure 4A, we found a significantly increased number of proliferating cells in the group in which YPPP-CD11c⁺ cells, as determined by the CCK-8 assay. FCM analysis revealed that an increased population of Cytotell green^{low}CD25⁺CD4⁺ T cells and Cytotell green^{low}CD69⁺CD4⁺ T cells in co-culture groups with YPPP-CD11c⁺ cells (Supplementary Figures 4B-E). Consistent with previous results, the MLR assay using BALB/c T cells also demonstrated enhancement of T-cell proliferation and activation in the presence of YPPP-CD11c⁺ cells (Supplementary Figures 5A-E). These results indicate that the

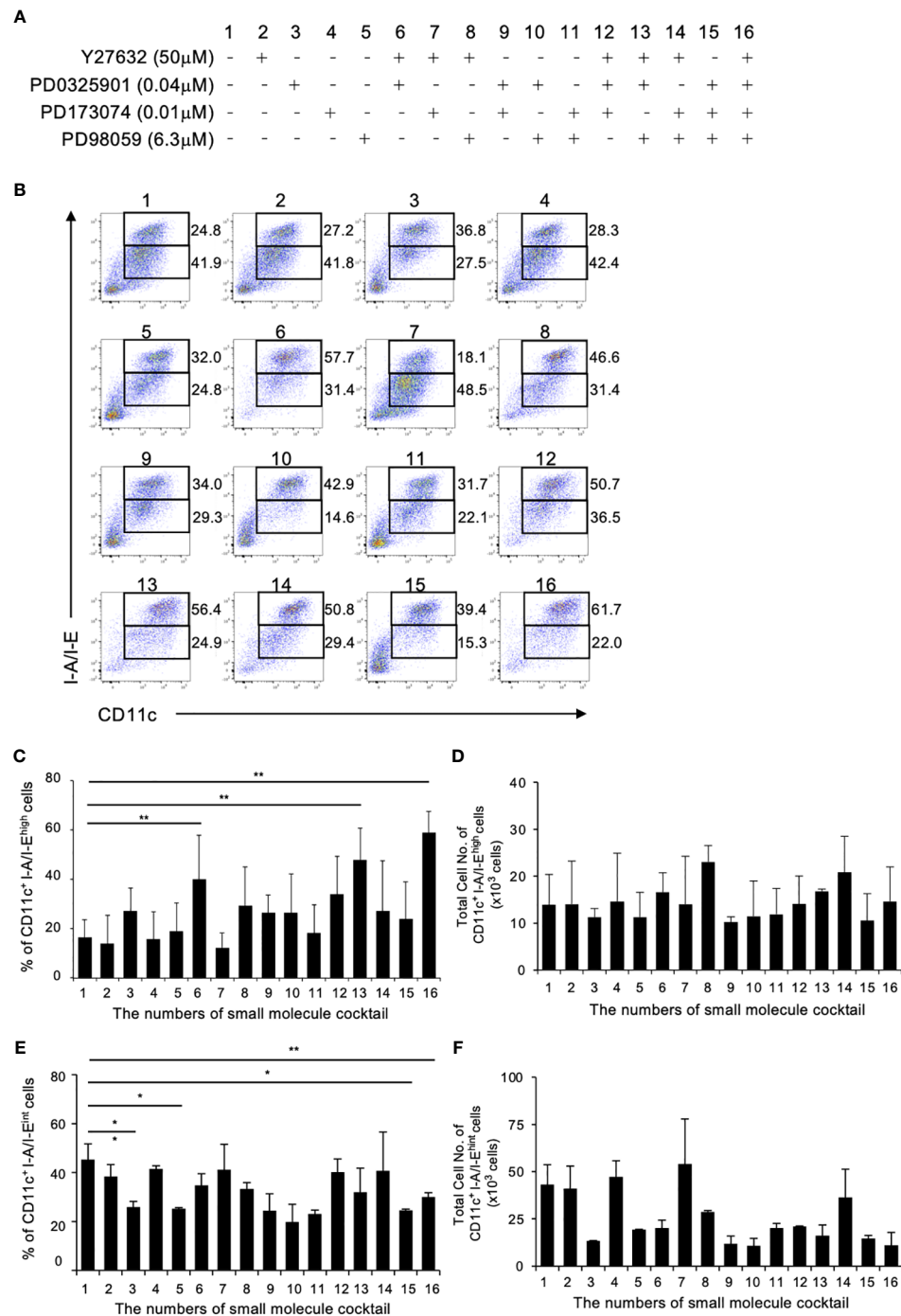


FIGURE 1

Initial combination trial of four small molecule inhibitors. Using single concentrations of each small molecule cocktail, a total of 16 unique combinations were tested in GM-CSF mouse BM culture. BM cells were cultured with GM-CSF and indicated small molecule cocktail for 6 days. On day 6, Cells were analyzed by flow cytometry. (A) The combinations of small molecule cocktail. (B) The percentages of CD11c+I-A/I-E^{high} cells (Upper fraction) and CD11c+I-A/I-E^{int} cells (Lower fraction) on day 6. Data are representative of three independent experiments. (C, D) Frequency (C) and total cell number (D) of the indicated CD11c+I-A/I-E^{high} cells (GM-DCs). (E, F) Frequency (E) and total cell number (F) of the indicated CD11c+I-A/I-E^{int} cells (GM-Macs). (C-F) Data are shown as the mean \pm SEM of three independent experiments. * p <0.05, ** p <0.01.

YPPP-CD11c⁺ cells are more efficient than DMSO-CD11c⁺ cells in priming and expanding T cells.

Finally, we compared IL-12p40 production and T cell activation ability between CD11c⁺I-A/I-E^{high} cells and CD11c⁺I-A/I-E^{int} cells treated with DMSO/YPPP. The YPPP-treated

CD11c⁺I-A/I-E^{high} cells produced more IL-12p40 than the other cells upon LPS or CpG stimulation (Figure 4A). Additionally, CD11c⁺I-A/I-E^{high} cells demonstrated the highest CD8⁺ T cell proliferation and IFN- γ ⁺ cell-inducing-abilities compared with other cells (Figures 4B-E).

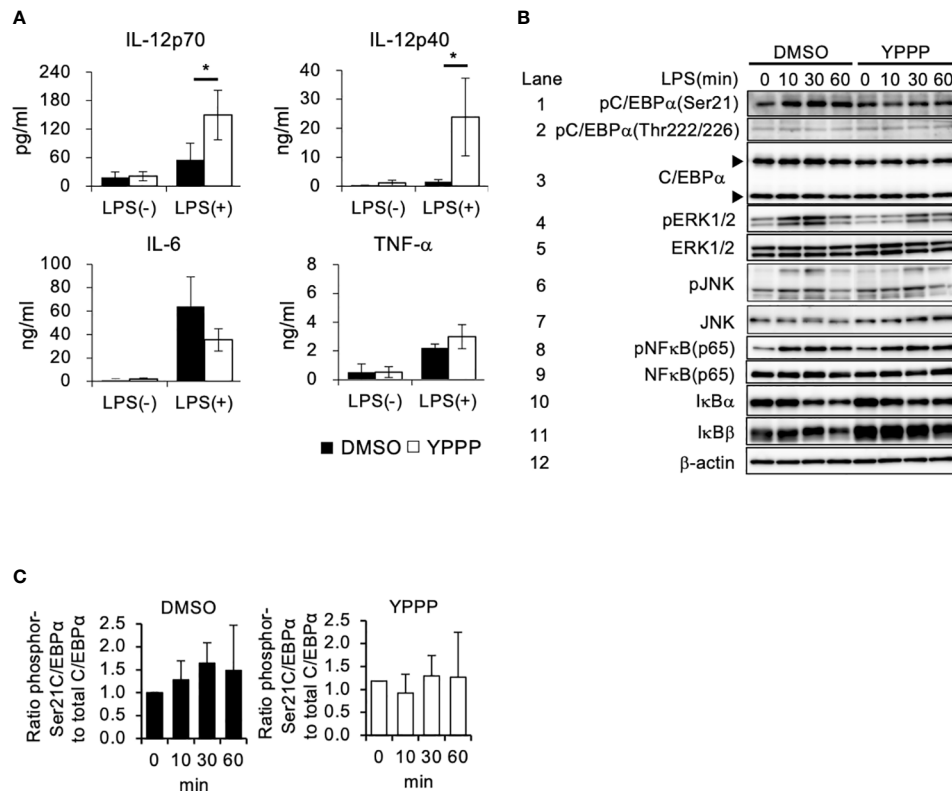


FIGURE 2

BM-derived CD11c⁺ cells induced by GM-CSF and YPPP increase interleukin (IL) -12 production via the negatively regulation of Toll-like receptor (TLR) 4-mediated C/EBP α activation. (A) The IL-12p70, IL-12p40, IL-6 and TNF- α levels in supernatants of DMSO- or YPPP-BM-derived CD11c⁺ cells after LPS stimulation for 48 h. The levels were measured by an ELISA. (B) BM-derived CD11c⁺ cells induced by DMSO and YPPP were stimulated with LPS (1 μ g/ml). Representative immunoblots of the indicated proteins are shown at the indicated time after LPS stimulation. The arrows indicate the 42kDa and 30kDa isoforms of C/EBP α . β -actin was used as loading and internal monitoring controls. (C) The relative intensities of phosphor-C/EBP α to total C/EBP α in BM-derived CD11c⁺ cells induced by DMSO and YPPP were estimated by densitometric scanning with normalization to β -actin (means \pm SD). Data are representative of two or three separate experiments. * p <0.05.

Characterization of YPPP-CD11c⁺ cells

To elucidate the mechanism of enhanced IL-12 production and T cell priming activity in YPPP-CD11c⁺ cells, we examined the effect of YPPP on the differentiation of DCs derived from mouse BM cells cultured with GM-CSF. We focused on the morphological analysis of CD11c⁺I-A/I-E^{high} cells. FCM analysis showed that an increased population of the CD11c⁺I-A/I-E^{high} cells in the YPPP treatment group and a decreased population of CD11c⁺I-A/I-E^{int} cells, representing macrophages (Figure 5A; Supplementary Figures 6A, B). Diff-Quick staining did show marked differences between DMSO- and YPPP-CD11c⁺I-A/I-E^{high} cells (Figure 5A). There were no significant differences in the number of terminally differentiated cells with or without YPPP, and responsiveness to LPS stimulation (Figure 5B). Furthermore, FCM analysis of these DC surface makers revealed up-regulation of CD11c, CCR7, and CD80, and down-regulation of CD11b in the YPPP-treated CD11c⁺I-A/I-E^{high} cells (Figure 5C). Additionally, both DMSO-treated and YPPP-treated DCs did not express cDC1 marker XCR1 (Supplementary Figure 7). These changes align with the general characteristics of GM-DCs (33).

Gene expression profiles of CD11c⁺I-A/I-E^{high} cells and CD11c⁺I-A/I-E^{int} cells in DC vaccines

To compare *in vitro* DC induced by YPPP, we performed RNA sequencing (RNA-Seq) of CD11c⁺I-A/I-E^{high} cells and CD11c⁺I-A/I-E^{int} cells differentiated under DMSO or YPPP conditions for 0, 3, and 6 days (Figure 6A). As a result, approximately 6,030, 5,620, 5,626 and 5,662 differentially expressed (DE) genes were identified between DMSO-CD11c⁺I-A/I-E^{high} cells and YPPP-CD11c⁺I-A/I-E^{high} cells on day 3, between DMSO-CD11c⁺I-A/I-E^{int} cells and YPPP-CD11c⁺I-A/I-E^{int} cells on day 3, between DMSO-CD11c⁺I-A/I-E^{high} cells and YPPP-CD11c⁺I-A/I-E^{high} cells on day 6, and between DMSO-CD11c⁺I-A/I-E^{int} cells and YPPP-CD11c⁺I-A/I-E^{int} cells on day 6 (Figure 6B; Supplementary Figures 8A-D). Principal component analysis (PCA) based on differentially expressed genes clearly separated CD11c⁺I-A/I-E^{high} cells cultured with or without YPPP based on both location and genotype (Figure 6C). The outcomes of ChIP Enrichment Analysis (ChEA) revealed a significant enrichment of different expressed gene set, and the top 15 enriched gene set up- or down- regulated by YPPP are shown in Supplementary Figure 8. And so some of

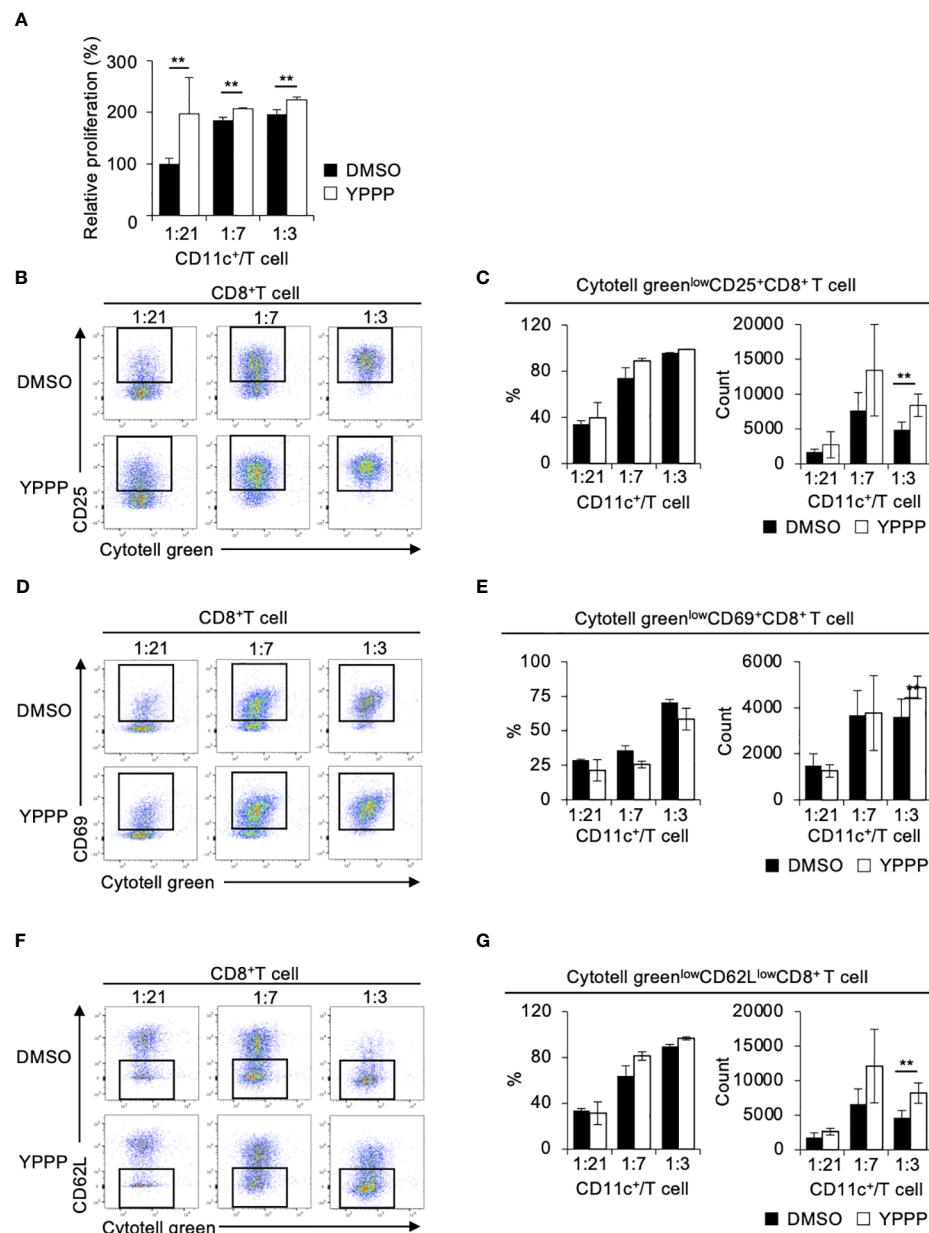


FIGURE 3

BM-derived CD11c⁺ cells induced by GM-CSF and YPPP augments the activation of OT-I T cells *in vitro*. DMSO- or YPPP-BM-derived CD11c⁺ cells were incubated with OVA₂₅₇₋₂₆₄ peptide and co-cultured with Cytotell green labeled naive splenic Thy1.2⁺ cells. T cell proliferation and expansion were assessed on 3 days after co-cultured. (A) T cell proliferation assay measured by Cell Counting Kit 8 (CCK-8). The relative proliferation of OT-I T cells in indicated BM derived CD11c⁺ cells and T cells ratios at day 3 were calculated as the ratio of proliferation to CD11c⁺/T cell (B, D, F). FCM analysis of Cytotell green^{low}CD25⁺CD8⁺ T cells (B), Cytotell green^{low}CD69⁺CD8⁺ T cells (D) and of Cytotell green^{low}CD62L^{low}CD8⁺ T cells (F). (C, E, G) Frequency (left) and number (right) of the indicated cells. Data in the bar graph are mean \pm SD of triplicate wells for the representative experiment shown. ** p <0.01.

genes known to be important for DC differentiation were shown (Supplementary Figure 8E). The outcomes of Kyoto Encyclopedia of Genes and Genomes (KEGG) pathway enrichment analysis revealed a significant enrichment of different expressed gene set, and the top 10 enriched gene set up-regulated by YPPP are shown in Figure 6D. Within this gene set, Peroxisome Proliferator-Activated Receptor (PPAR) signaling pathway genes exhibited statistically significant upregulation in YPPP-treated CD11c⁺I-A/I-E^{high} cells when compared to DMSO-treated CD11c⁺I-A/I-E^{high}

cells. The MA plot showed up-regulated several genes associated with PPAR γ , and transforming growth factor (TGF)- β (Figures 6E, F). Consistent with RNA-seq analysis, immunoblotting demonstrated higher expression level of fatty acid binding protein (FABP) 4, FABP5 and PPAR γ in YPPP-CD11c⁺ cells compared to DMSO-CD11c⁺ cells (Figure 6G). Previous reports have shown that FABP family plays an important role in DC function and T cell priming (37, 38). These results provide further insight in our data that the YPPP-

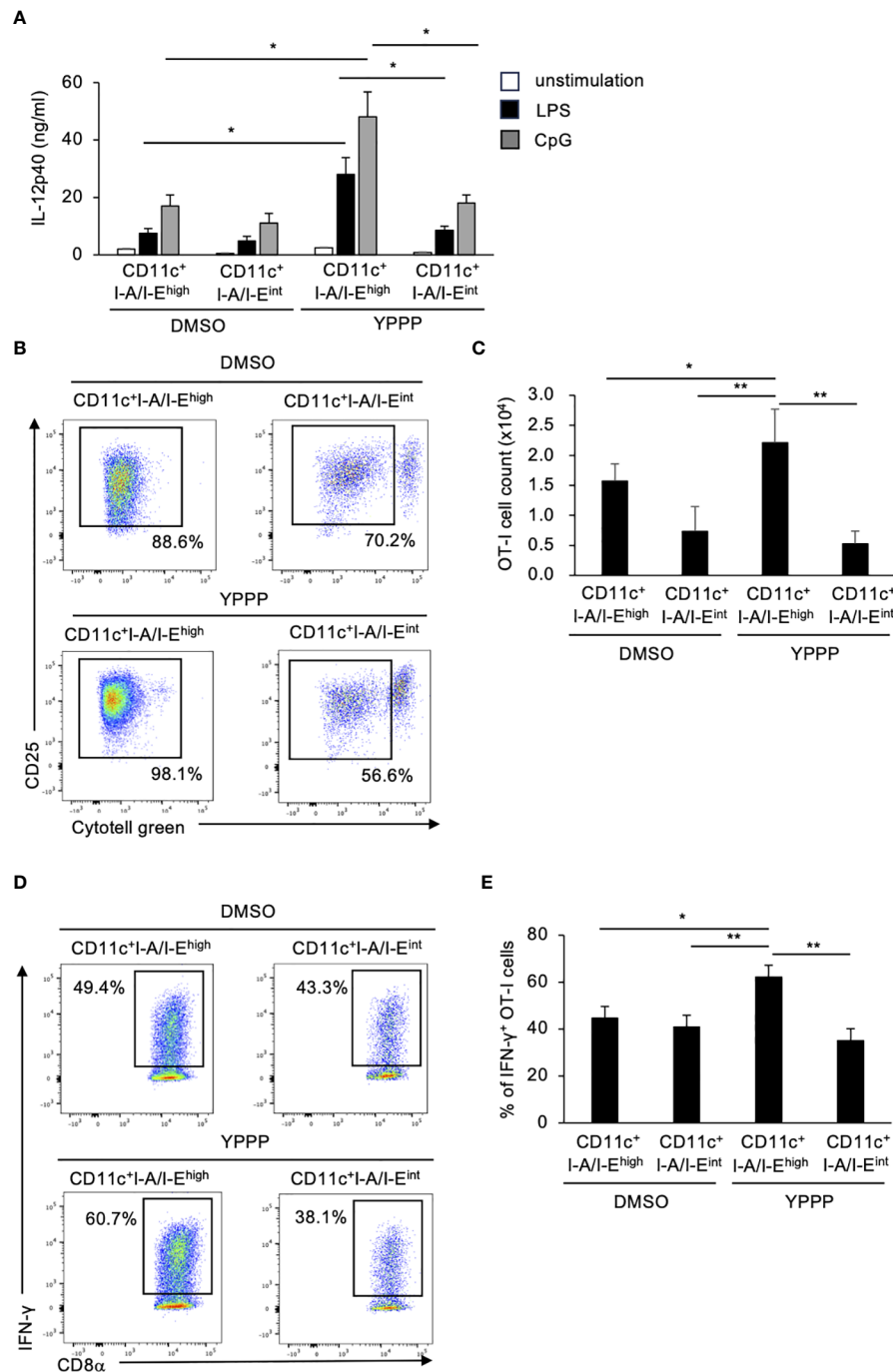


FIGURE 4

BM-derived CD11c⁺I-A/I-E^{high} cells induced by GM-CSF and YPPP augments IL-12p40 production and the activation of OT-I T cells *in vitro*. (A) IL-12p40 levels in supernatants of DMSO- or YPPP-BM-derived CD11c⁺I-A/I-E^{high} and CD11c⁺I-A/I-E^{int} cells after LPS (100 ng/ml) or CpG (1nM) stimulation for 48 h. The levels were measured by an ELISA. (B, C) DMSO- or YPPP-BM derived CD11c⁺I-A/I-E^{high} and CD11c⁺I-A/I-E^{int} cells were incubated with OVA₂₅₇₋₂₆₄ peptide and co-cultured with Cytotell green labeled naïve splenic Thy1.2⁺ cells. T cell proliferation and expansion were assessed on 3 days after co-culture. FCM analysis of Cytotell green^{low}CD25⁺CD8⁺ T cells (B) and total cell number of CD25⁺CD8⁺ T cells (C). (D, E) The percentage of IFN-γ⁺ cells differentiated from naïve OT-I cells cocultured with DMSO- or YPPP-BM-derived CD11c⁺I-A/I-E^{high} and CD11c⁺I-A/I-E^{int} cells. Data in the bar graph are mean ± SD of triplicate wells for the representative experiment shown. *p<0.05, **p<0.01.

treated CD11c⁺I-A/I-E^{high} cells produced more IL-12p40 than DMSO-treated CD11c⁺I-A/I-E^{high} cells upon LPS and CpG stimulation (Figure 4A). Additionally, no significant differences were observed in the expression of the major cDC1-related genes

(Xcr1, Irf8, and Batf3) between DMSO- and YPPP-treated cells (Supplementary Figure 8E). These results suggested that YPPP instructs the direction of DC differentiation via the activating of PPARγ and TGF-β associated genes.

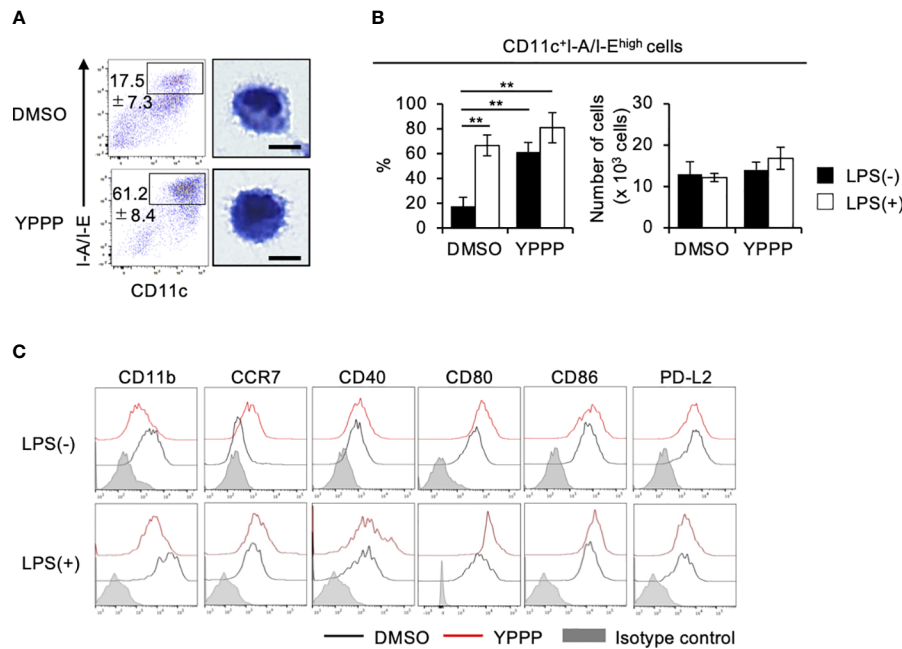


FIGURE 5

YPPP enhances the DC maturation in mouse BM culture with GM-CSF. **(A)** Representative flow cytometry profiles (left) and microscopic images (right) by Diff-Quick staining of sorted CD11c⁺I-A/I-E^{high} cells in GM-CSF mouse BM culture (Scale bar: 5μm). **(B)** Frequency (left) and number (right) of the indicated cells with or without LPS stimulation. **(C)** Representative histograms of the indicated surface antigens from BM-derived CD11c⁺I-A/I-E^{high} cultured with DMSO (black) or YPPP (red). The shaded area shows the isotype control. ** p <0.05.

The DCV produced by YPPP has an excellent anti-tumor activity

To investigate the *in vivo* anti-tumor potential of the DCV produced by adding YPPP, we evaluated its therapeutic efficacy against established E.G7 and B16 melanoma tumor models (Figure 7A). The mice were injected with E.G7 tumor cells (Day 0). On day 7, 10 and 13 post tumor inoculation, the mice were vaccinated with DMSO- or YPPP-CD11c⁺ cells cultured with GM-CSF. As shown in Figures 7B, C, a notable decrease in tumor growth and an improvement in survival is apparent within the DCV-administered group (both DMSO and YPPP treated-group), in comparison to the DCV-non-administered group. In addition, DMSO-CD11c⁺ cells (DMSO-DCV) were unable to suppress tumor growth completely, whereas YPPP-CD11c⁺ cells (YPPP-DCV) significantly reduced tumor growth, although they could not eradicate the tumor. These results indicated that YPPP-DCV has superior anti-tumor effects than DMSO-DCV (Figures 7B-E).

YPPP-DCV enhances the efficacy of anti-PD-1 based cancer therapy

The combination of anti-PD-1, an immune checkpoint inhibitor, and other therapies has shown remarkable efficacy (39). Thus, we examined the combined anti-tumor activities of DCV with anti-PD-1 in the same tumor model as mentioned above. As shown in Figures 8A-C, tumor growth and mortality of the group treated with YPPP-DCV significantly reduced in the E.G7 tumor model

(Log-rank test, p =0.0164), although these activities were not observed in the B16 melanoma model (Figures 8D, E). These results suggest that YPPP-DCV enhances the efficacy of anti-PD-1 therapy in some cancer models.

Discussion

In this study, we screened small molecule inhibitor cocktails and discovered that a particular cocktail, YPPP promoted DC differentiation in GM-CSF mouse BM cultures. DCs induced with YPPP produced more IL-12 upon LPS stimulation, leading to a strong promotion of cytotoxic T cell activation and proliferation. In addition, we found that DCs induced by YPPP had a synergistic effect with anti-PD-1 therapy, resulting in high anti-tumor activity.

Previous report has demonstrated that GM-CSF-induced BMDC consist of two subsets: CD11c⁺I-A/I-E^{high} cells (GM-DC) and CD11c⁺I-A/I-E^{int} cells (GM-Mac). The CD11c⁺I-A/I-E^{high} cells originate from CDP, while CD11c⁺I-A/I-E^{int} cells were derived from common monocyte progenitor (cMoP) and monocytes (33). As shown in Figure 1B, the predominant fraction form BM cultured with YPPP is CD11c⁺I-A/I-E^{high} cells when compared with DMSO-control. The total cell number of CD11c⁺I-A/I-E^{high} cells shows no significant difference between control and 16th group (Figure 1D). However, the total cell number of CD11c⁺I-A/I-E^{int} cells of 16th group is markedly reduced when compared with control (Figure 1F). Consequently, it is likely that YPPP suppresses the differentiation of cMoP and monocytes into CD11c⁺I-A/I-E^{int} cells, rather than promoting the differentiation from CDP into CD11c⁺I-A/I-E^{high} cells.

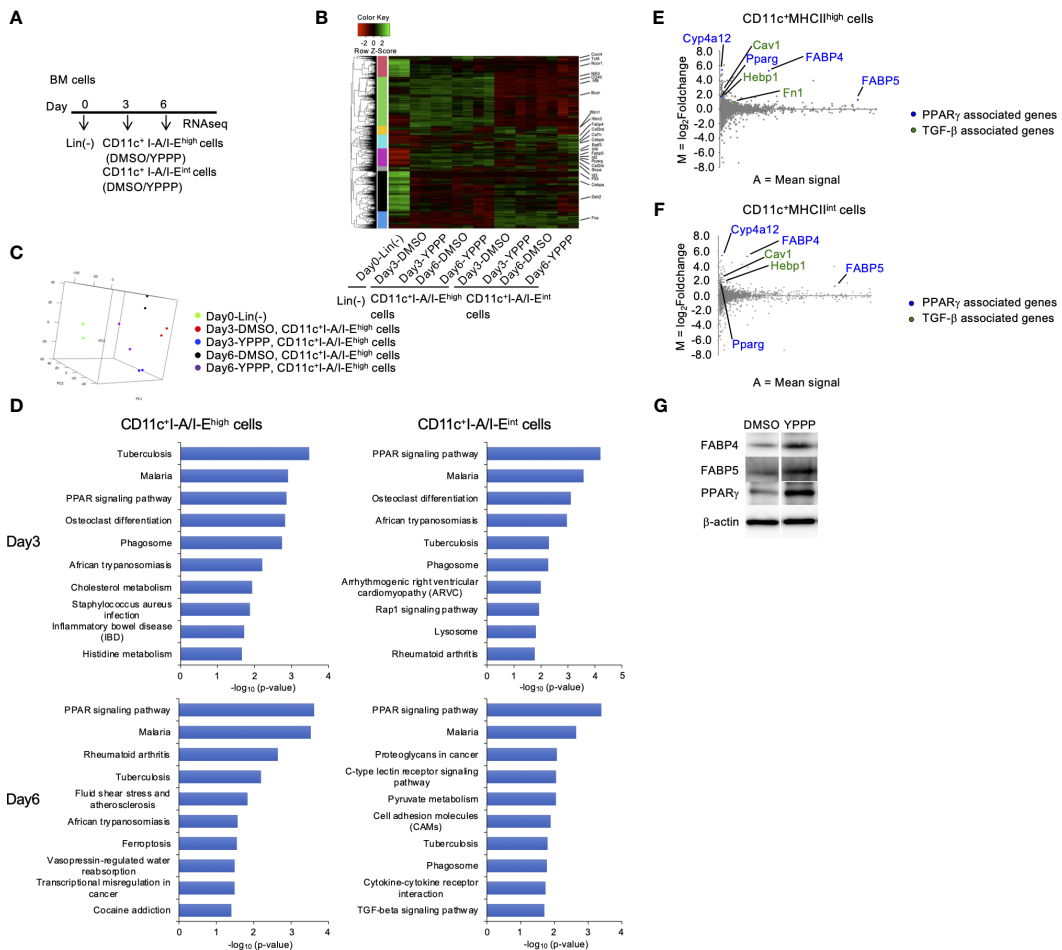


FIGURE 6
 PPAR γ -associated genes are increased in BM-derived CD11c $^{+}$ I-A/I-E $^{\text{high}}$ cells induced by GM-CSF and YPPP. **(A)** Experimental scheme of RNAseq analysis. RNA extracted on day 0, 3 and 6 in GM-CSF mouse BM culture. **(B)** Heatmap of differentially expressed genes of CD11c $^{+}$ I-A/I-E $^{\text{high}}$ cells and CD11c $^{+}$ I-A/I-E $^{\text{int}}$ cells in BM derived CD11c $^{+}$ cells. **(C)** PCA analysis of indicated cells. **(D)** Bar chart of top enriched terms from the KEGG_2019_Mouse gene set library. The top 10 enriched terms for the YPPP up-regulated gene set are displayed based on the $-\log_{10}(p\text{-value})$, with the actual p-value shown next to each term. The term at the top has the most significant overlap with the input query gene set. **(E, F)** MA plot showing differentially expressed genes in YPPP- versus DMSO-CD11c $^{+}$ I-A/I-E $^{\text{high}}$ cells **(E)** and CD11c $^{+}$ I-A/I-E $^{\text{int}}$ cells **(F)** on day 6. Up-regulated PPAR γ and TGF- β associated genes are highlighted in the indicated colors. **(G)** Representative immunoblots of the indicated proteins in BM-derived CD11c $^{+}$ cells induced by GM-CSF and DMSO/YPPP.

Previous reports have demonstrated that a specific ROCK inhibitor, Y27632, is protected from apoptosis in hES cells, and regulates morphology and function in human monocyte-derived DCs (40–42). Moreover, MEK mitogen-activated protein kinase inhibitors, such as PD0325901 and PD98059, are negatively regulates cytokine production in macrophages (43, 44). Furthermore, FGF receptor inhibitor, PD173074, plays an essential role in osteocyte differentiation (44). However, most of these studies focused on short-term administration of small molecule compounds, and the effects of their long-term administration are largely unknown. Additionally, it has been reported that high doses of PD98059 (25 μ M or 50 μ M) induce apoptosis in human monocyte derived DCs (45, 46). Conversely, low concentrations of PD98059 (6.3 μ M) contribute the CD11c⁺I-A/I-E^{high} cells differentiation in GM-CSF-induced BMDC with other small compounds. It is important to note that none of the compounds exhibit any toxicity for BMDCs in our experimental

condition. Our data provide novel insights for understanding DC differentiation and activation.

The role of PPAR γ in the differentiation and function of myeloid cells has yielded conflicted results (47, 48). The previous study has reported pharmacological inhibition of PPAR γ induces differentiation and immunogenic function of human monocyte-derived DCs (48). Our research demonstrated an up-regulation of PPAR γ and its-associated genes (FABP4 and FABP5) in the YPPP-treated DCs. These cells exhibited increased capacity for IL-12 production, CD8 $^+$ T cell proliferation, and induction of IFN- γ $^+$ CD8 $^+$ T cells. Moreover, previous study has reported that both FABP4 and FABP5 play a role in IL-12 production and T cell priming in human monocyte-derived DCs (37, 38). Therefore, the enhancement PPAR γ signaling contributes to the increased DC function in the YPPP-treated DC.

We observed strong suppression of phosphorylation of C/EBP α (Ser21) in YPPP-CD11c $^+$ cells after LPS stimulation, while pSer21

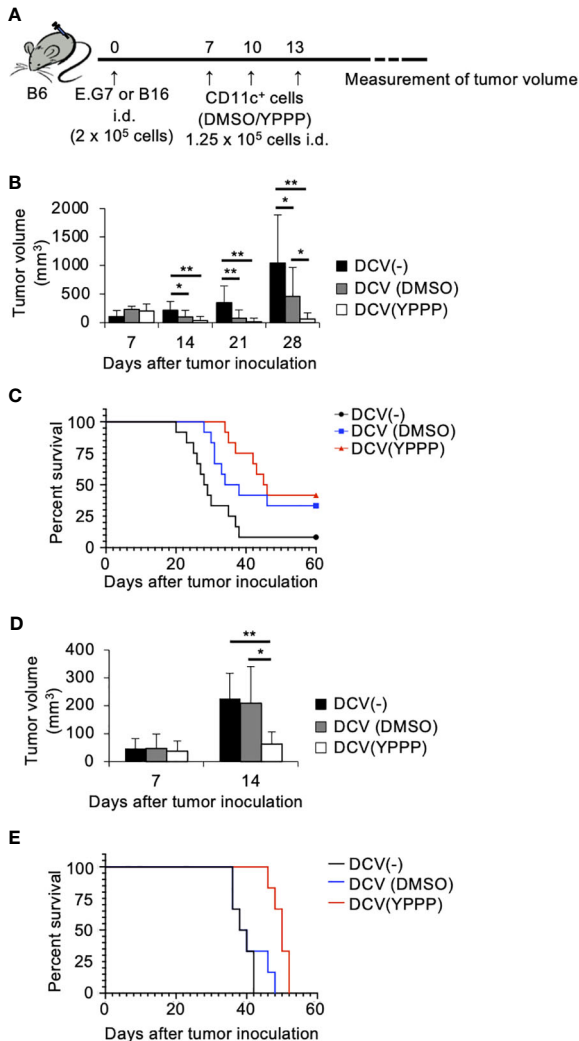


FIGURE 7
Small molecule cocktail YPPP enhances the anti-tumor activity of dendritic cells vaccine. **(A)** Schematic of tumor vaccine strategy. Mice were injected with 2×10^5 E.G7 or B16 melanoma tumor cells. On the 7, 10 and 13 days after tumor inoculation, mice were vaccinated with 1.25×10^5 BM-derived CD11c⁺ cells induced by GM-CSF and DMSO/YPPP. The growth or rejection of E.G7 or B16 melanoma tumor was monitored. E.G7 **(B)** or B16 melanoma **(D)** tumor volume in untreated (DCV(-)), DMSO-CD11c⁺ cells (DCV (DMSO)) or YPPP-CD11c⁺ cells (DCV(YPPP)) vaccinated mice at indicated days after tumor inoculation. Kaplan –Meier curves of E.G7 **(C)** or B16 melanoma **(E)** showing survival of mice. * $p < 0.05$, ** $p < 0.01$.

C/EBP α was remarkably increased in DMSO- CD11c⁺ cells. A previous study reported that the phosphorylated C/EBP α (Ser21) inhibits IL-12/IL-23 expression (36), suggesting that YPPP induces high IL-12 production by suppressing C/EBP α activation. Further studies are required to clarify the detailed mechanism how YPPP affects the C/EBP pathway upon LPS stimulation, as YPPP may prevent ERK1/2-dependent C/EBP α activation and impair Ser21 phosphorylation of C/EBP α .

It has been reported that GM-CSF-induced monocyte-derived DC exhibit a restricted ability to migrate during lymph nodes (49). Therefore, the limited effectiveness of the DC vaccine could be a

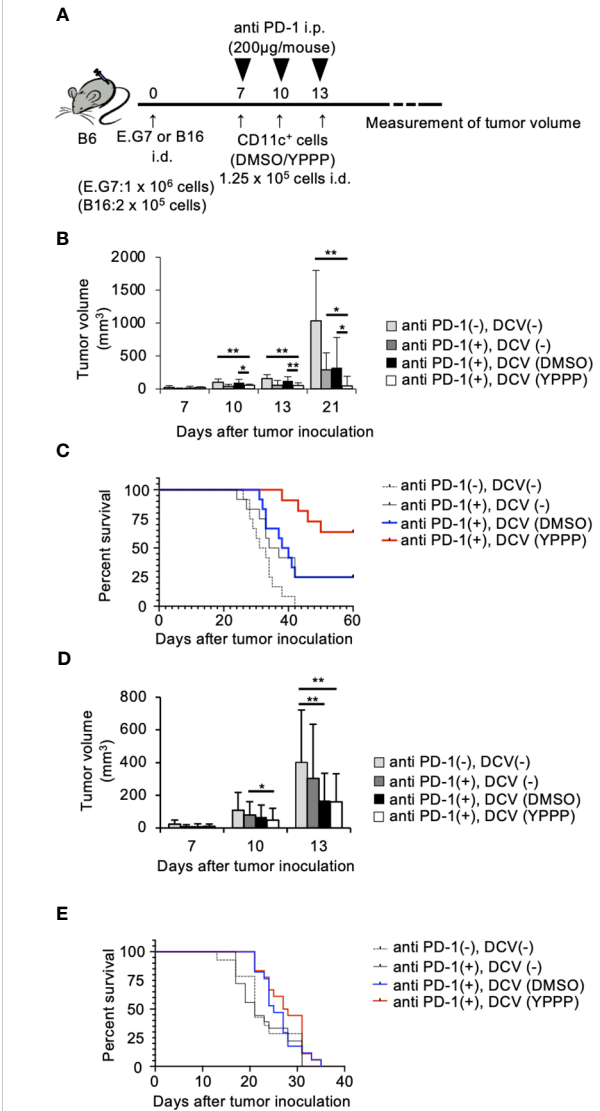


FIGURE 8
Small molecule cocktail YPPP enhances the anti-tumor activity of dendritic cells vaccine in anti PD-1 therapy. **(A)** Schematic of tumor vaccine strategy. Mice were injected with 1×10^6 E.G7 or 2×10^5 B16 melanoma tumor cells. On the 7, 10 and 13 days after tumor inoculation, mice were vaccinated with 1.25×10^4 BM-derived CD11c⁺ cells induced by GM-CSF and DMSO/YPPP. The growth or rejection of E.G7 or B16 melanoma tumor was monitored. E.G7 **(B)** or B16 melanoma **(D)** tumor volume in untreated (anti PD-1(-), DCV (-)), anti-PD-1 treatment only (anti PD-1(+), DCV(-)), anti-PD-1 and DMSO-CD11c⁺ cells (anti PD-1(+), DCV(DMSO)) or YPPP-CD11c⁺ cells (anti PD-1(+), DCV(YPPP)) vaccinated mice at indicated days after tumor inoculation. Kaplan –Meier curves of E.G7 **(C)** or B16 melanoma **(E)** showing survival of mice. * $p < 0.05$, ** $p < 0.01$.

result of protocols that fail to induce an optimal T cell priming. Endogenous DCs are required for T cell priming upon injection of antigen-loaded exogenous DCs (50, 51). In our study, we utilized ova peptide-loaded GM-CSF-induced BMDCs for DC vaccine in E.G7 tumor model. We demonstrated a significant reduction in tumor growth and an improvement in survival within the YPPP-treated DC-administered group. Furthermore, we confirmed that YPPP-treatment led to an up-regulation CCR7 in the DCs, a critical chemokine receptor facilitating the migration of DCs into the

lymph node. While both exogenous and endogenous DCs play a role in T cell priming, it is likely that YPPP-treated DCs efficiently migrate lymph node and act as a source of antigen.

The YPPP-treated CD11c⁺ cells were included the CD11c⁺I-A/I-E^{high} cells and CD11c⁺I-A/I-E^{int} cells. The YPPP-treated CD11c⁺I-A/I-E^{high} cells demonstrated more CD8⁺ T cell proliferation and IFN- γ cell-inducing abilities compare with the YPPP-treated CD11c⁺I-A/I-E^{int} cells. These data demonstrated that YPPP-treated CD11c⁺I-A/I-E^{high} cells possesses significantly superior dendritic cell capabilities. Consequently, it is suggested that YPPP-treated CD11c⁺I-A/I-E^{high} cells may exhibit and contribute anti-tumor effect *in vivo*. Our data showed that *in vivo* anti-tumor activity of YPPP-DCV was superior to that of DMSO-DCV in E.G7 or B16 melanoma-bearing mouse models. However, our results with YPPP-DCV are consistent with a previous report—the complete elimination of tumor growth was not achieved; therefore, further therapeutic modifications are required to address this issue. The efficacy of DCV in combination with anti-PD-1 therapy has been reported (23, 24). Moreover, the combination of antibodies that block these other inhibitory receptors is expected to enhance the anti-tumor effect of DCV. Our experiments focused in the E.G7 tumor cells, which have shown sensitivity to anti-PD-1 in previous studies (52), and B16 melanoma cells, in which little effect was observed (53). The combined effect of anti-PD-1 and DCV was more prominent for E.G7, especially for YPPP-DCV, showing strong tumor growth suppression and improved survival. However, the anti-tumor activity of YPPP-DCV was limited in the B16 melanoma model, suggesting that the combination therapy with YPPP-DCV and anti-PD-1 provides more effective anti-tumor immunity against anti-PD-1-sensitive cancer cells.

The potential of administration of GM-CSF based therapy to cancer patients has been suggested (54). Therefore, co-administration of YPPP and GM-CSF with anti-PD-1 to tumor-bearing mouse model is expected to be effective. However, the dose of GM-CSF was critical for anti- or pro-tumorigenic effect in human (54). Thus, the fine tuning of GM-CSF and YPPP concentrations will be necessary. On the other hand, the YPPP-DCV is a simpler approach. Therefore, we propose development of DCV with small molecule inhibitors, combined with anti-PD-1 therapy to enhance *in vivo* anti-tumor activity. To achieve successful cancer immunotherapy, a more detailed mechanistic understanding of YPPP-DCV and further strategies to overcome tumor immunosuppressive mechanisms will be essential.

Data availability statement

The datasets presented in this study can be found in online repositories. The names of the repository/repositories and accession number(s) can be found below: <https://www.ncbi.nlm.nih.gov>; GSE239334.

Ethics statement

The animal study was approved by the Animal Research Committee at Kanazawa Medical University (Approval No.:2020-30, 2022-17). The study was conducted in accordance with the local legislation and institutional requirements.

Author contributions

SM: Funding acquisition, Investigation, Formal Analysis, Writing – original draft. HU: Formal Analysis, Investigation, Methodology, Writing – review & editing. FS: Investigation, Writing – review & editing, Data curation. CO: Data curation, Investigation, Writing – review & editing. SS: Writing – review & editing. YN: Writing – review & editing, Formal Analysis, Methodology. NO: Supervision, Methodology, Writing – review & editing, Conceptualization, Funding acquisition, Investigation.

Funding

The author(s) declare financial support was received for the research, authorship, and/or publication of this article. This work was supported by Grants-in-aid for Scientific Research 19K17843 to SM, and 22H02855 to NO from the JSPS KAKEN grant and Kanazawa Medical University Research Project "Strategic Development and Innovation in Cell Therapy in the Hokuriku District of Japan" (RP2017-01 to NO and RP2020-04 to SM) through the Private University Research Branding Project of MEXT (Ministry of Education, Culture, Sports, Science and Technology), Japan, and by Promoted Research (S2018-4 to SM) from Kanazawa Medical University and by The Hokkoku Cancer Foundation and Takeda Science Foundation to NO.

Acknowledgments

We thank Ms. H. Nakamura for providing technical assistance.

Conflict of interest

The authors declare that the research was conducted in the absence of any commercial or financial relationships that could be construed as a potential conflict of interest.

The author(s) declared that they were an editorial board member of Frontiers, at the time of submission. This had no impact on the peer review process and the final decision.

Publisher's note

All claims expressed in this article are solely those of the authors and do not necessarily represent those of their affiliated organizations, or those of the publisher, the editors and the reviewers. Any product that may be evaluated in this article, or claim that may be made by its manufacturer, is not guaranteed or endorsed by the publisher.

Supplementary material

The Supplementary Material for this article can be found online at: <https://www.frontiersin.org/articles/10.3389/fimmu.2023.1264609/full#supplementary-material>

References

- Merad M, Sathe P, Helft J, Miller J, Mortha A. The dendritic cell lineage: ontogeny and function of dendritic cells and their subsets in the steady state and the inflamed setting. *Annu Rev Immunol* (2013) 31:563–604. doi: 10.1146/annurev-immunol-020711-074950
- Guilliams M, Ginhoux F, Jakubzick C, Naik SH, Onai N, Schraml BU, et al. Dendritic cells, monocytes and macrophages: a unified nomenclature based on ontogeny. *Nat Rev Immunol* (2014) 14(8):571–8. doi: 10.1038/nri3712
- Onai N, Obata-Onai A, Schmid MA, Ohteki T, Jarrossay D, Manz MG. Identification of clonogenic common Flt3⁺M-CSFR⁺ plasmacytoid and conventional dendritic cell progenitors in mouse bone marrow. *Nat Immunol* (2007) 8(11):1207–16. doi: 10.1038/ni1518
- Onai N, Kurabayashi K, Hosoi-Amaike M, Toyama-Sorimachi N, Matsushima K, Inaba K, et al. A clonogenic progenitor with prominent plasmacytoid dendritic cell developmental potential. *Immunity* (2013) 38(5):943–57. doi: 10.1016/j.immuni.2013.04.006
- Nutt SL, Chopin M. Transcriptional networks driving dendritic cell differentiation and function. *Immunity* (2020) 52(6):942–56. doi: 10.1016/j.immuni.2020.05.005
- Cabeza-Cabrerozo M, Cardoso A, Minutti CM, Pereira da Costa M, Reis e Sousa C. Dendritic cells revisited. *Annu Rev Immunol* (2021) 39:131–66. doi: 10.1146/annurev-immunol-061020-053707
- Ferris ST, Durai V, Wu R, Theisen DJ, Ward JP, Bern MD, et al. cDC1 prime and are licensed by CD4⁺ T cells to induce anti-tumour immunity. *Nature* (2020) 584(7822):624–9. doi: 10.1038/s41586-020-2611-3
- Inaba K, Inaba M, Romani N, Aya H, Deguchi M, Ikehara S, et al. Generation of large numbers of dendritic cells from mouse bone marrow cultures supplemented with granulocyte/macrophage colony-stimulating factor. *J Exp Med* (1992) 176(6):1693–702. doi: 10.1084/jem.176.6.1693
- Sallusto F, Lanzavecchia A. Efficient presentation of soluble antigen by cultured human dendritic cells is maintained by granulocyte:Macrophage colony-stimulating factor plus interleukin 4 and downregulated by tumor necrosis factor. *J Exp Med* (1994) 179:1109–18. doi: 10.1084/jem.179.4.1109
- Naik SH, Proietti AI, Wilson NS, Dakic A, Schnorrer P, Fuchsberger M, et al. Cutting edge: generation of splenic CD8⁺ and CD8⁻ dendritic cell equivalents in Fms-like tyrosine kinase 3 ligand bone marrow cultures. *J Immunol* (2005) 174(11):6592–7. doi: 10.4049/jimmunol.174.11.6592
- Mayer CT, Ghorbani P, Nandan A, Dudek M, Arnold-Schrauf C, Hesse C, et al. Selective and efficient generation of functional Batf3-dependent CD103⁺ dendritic cells from mouse bone marrow. *Blood* (2014) 124(20):3081–91. doi: 10.1182/blood-2013-12-545772
- Gardner A, de Mingo Pulido A, Ruffell B. Dendritic cells and their role in immunotherapy. *Front Immunol* (2020) 11:924. doi: 10.3389/fimmu.2020.00924
- Carreno BM, Magrini V, Becker-Hapak M, Kaabinejad S, Hundal J, Petti AA, et al. Cancer immunotherapy. A dendritic cell vaccine increases the breadth and diversity of melanoma neoantigen-specific T cells. *Science* (2015) 348(6236):803–8. doi: 10.1126/science.aaa3828
- Senju S, Haruta M, Matsunaga Y, Fukushima S, Ikeda T, Takahashi K, et al. Characterization of dendritic cells and macrophages generated by directed differentiation from mouse induced pluripotent stem cells. *Stem Cells* (2009) 27(5):1021–31. doi: 10.1002/stem.33
- Kitadani J, Ojima T, Iwamoto H, Tabata H, Nakamori M, Nakamura M, et al. Cancer Vaccine Therapy Using Carcinoembryonic Antigen - expressing Dendritic Cells generated from Induced Pluripotent Stem Cells. *Sci Rep* (2018) 8(1):4569. doi: 10.1038/s41598-018-23120-z
- Fukushima S, Hirata S, Motomura Y, Fukuma D, Matsunaga Y, Ikuta Y, et al. Multiple antigen-targeted immunotherapy with alpha-galactosylceramide-loaded and genetically engineered dendritic cells derived from embryonic stem cells. *J Immunother* (2009) 32(3):219–31. doi: 10.1097/CJI.0b013e318194b63b
- Katsuda T, Kawamata M, Hagiwara K, Takahashi RU, Yamamoto Y, Camargo FD, et al. Conversion of terminally committed hepatocytes to culturable bipotent progenitor cells with regenerative capacity. *Cell Stem Cell* (2017) 20(1):41–55. doi: 10.1016/j.stem.2016.10.007
- Silva J, Barrandon O, Nichols J, Kawaguchi J, Theunissen TW, Smith A. Promotion of reprogramming to ground state pluripotency by signal inhibition. *Plos Biol* (2008) 6(10):e253. doi: 10.1371/journal.pbio.0060253
- Ying QL, Wray J, Nichols J, Batlle-Morera L, Doble B, Woodgett J, et al. The ground state of embryonic stem cell self-renewal. *Nature* (2008) 453(7194):519–23. doi: 10.1038/nature06968
- Okita K, Yamanaka S. Intracellular signaling pathways regulating pluripotency of embryonic stem cells. *Curr Stem Cell Res Ther* (2006) 1(1):103–11. doi: 10.2174/157488806775269061
- Tsutsui H, Valamehr B, Hindoyan A, Qiao R, Ding X, Guo S, et al. An optimized small molecule inhibitor cocktail supports long-term maintenance of human embryonic stem cells. *Nat Commun* (2011) 2:167. doi: 10.1038/ncomms1165
- Matsuba S, Yabe-Wada T, Takeda K, Sato T, Suyama M, Takai T, et al. Identification of secretory leukoprotease inhibitor as an endogenous negative regulator in allergic effector cells. *Front Immunol* (2017) 8:1538. doi: 10.3389/fimmu.2017.01538
- Nagaoka K, Hosoi A, Iino T, Morishita Y, Matsushita H, Kakimi K. Dendritic cell vaccine induces antigen-specific CD8⁺ T cells that are metabolically distinct from those of peptide vaccine and is well-combined with PD-1 checkpoint blockade. *Oncoimmunology* (2018) 7(3):e1395124. doi: 10.1080/2162402X.2017.1395124
- Wakita D, Chamoto K, Zhang Y, Narita Y, Noguchi D, Ohnishi H, et al. An indispensable role of type-1 IFNs for inducing CTL-mediated complete eradication of established tumor tissue by CpG-liposome co-encapsulated with model tumor antigen. *Int Immunol* (2006) 18(3):425–34. doi: 10.1093/intimm/dxh381
- Kim D, Langmead B, Salzberg SL. HISAT: a fast spliced aligner with low memory requirements. *Nat Methods* (2015) 12(4):357–60. doi: 10.1038/nmeth.3317
- Perte M, Perte GM, Antonescu CM, Chang TC, Mendell JT, Salzberg SL. StringTie enables improved reconstruction of a transcriptome from RNA-seq reads. *Nat Biotechnol* (2015) 33(3):290–5. doi: 10.1038/nbt.3122
- Robinson MD, McCarthy DJ, Smyth GK. edgeR: a Bioconductor package for differential expression analysis of digital gene expression data. *Bioinformatics* (2010) 26(1):139–40. doi: 10.1093/bioinformatics/btp616
- Ura H, Togi S, Niida Y. Target-capture full-length double-strand cDNA sequencing for alternative splicing analysis. *RNA Biol* (2021) 18(11):1600–7. doi: 10.1080/15476286.2021.1872961
- Ura H, Togi S, Niida Y. Targeted double-stranded cDNA sequencing-based phase analysis to identify compound heterozygous mutations and differential allelic expression. *Biology (Basel)* (2021) 10(4):256. doi: 10.3390/biology10040256
- Chen EY, Tan CM, Kou Y, Duan Q, Wang Z, Meirelles GV, et al. Enrichr: interactive and collaborative HTML5 gene list enrichment analysis tool. *BMC Bioinf* (2013) 12(14):128. doi: 10.1186/1471-2105-14-128
- Kuleshov MV, Jones MR, Rouillard AD, Fernandez NF, Duan Q, Wang Z, et al. Enrichr: a comprehensive gene set enrichment analysis web server 2016 update. *Nucleic Acids Res* (2016) 44:W90–7. doi: 10.1093/nar/gkw377
- Xie Z, Bailey A, Kuleshov MV, Clarke DJB, Evangelista JE, Jenkins SL, et al. Gene set knowledge discovery with Enrichr. *Curr Protoc* (2021) 1:e90. doi: 10.1002/cp2.90
- Helft J, Bottcher J, Chakravarty P, Zelenay S, Huotari J, Schraml BU, et al. GM-CSF mouse bone marrow cultures comprise a heterogeneous population of CD11c⁺MHCII⁺ Macrophages and dendritic cells. *Immunity* (2015) 42(6):1197–211. doi: 10.1016/j.jimmuni.2015.05.018
- Simard FA, Cloutier A, * Ear T, Vardhan H, McDonald PP. MEK-independent ERK activation in human neutrophils and its impact on functional responses. *J Leukoc Biol* (2015) 98:565–73. doi: 10.1189/jlb.2MA1214-599R
- Zhou H, Xie Z, Morikawa N, Sakurai F, Mizuguchi H, Okizaki D, et al. Modified method for differentiation of myeloid-derived suppressor cells *in vitro* enhances immunosuppressive ability via glutathione metabolism. *Biochem Biophys Rep* (2023) 33:101616. doi: 10.1016/j.bbrep.2022.101416
- Zhang Y, Ma X. Triptolide inhibits IL-12/IL-23 expression in APCs via CCAAT/enhancer-binding protein alpha. *J Immunol* (2010) 184(7):3866–77. doi: 10.4049/jimmunol.0903417
- Furushashi M, Hotamisligil GS. Fatty acid-binding proteins: role in metabolic diseases and potential as drug targets. *Nat Rev Drug Discovery* (2008) 7(6):489–503. doi: 10.1038/nrd2589
- Zhu Y, Dun H, Ye L, Terada Y, Shriver LP, Patti GJ, et al. Targeting fatty acid beta-oxidation impairs monocyte differentiation and prolongs heart allograft survival. *JCI Insight* (2022) 7(7). doi: 10.1172/jci.insight.151596
- Zhang Y, Wakita D, Chamoto K, Narita Y, Matsubara N, Kitamura H, et al. Th1 cell adjuvant therapy combined with tumor vaccination: a novel strategy for promoting CTL responses while avoiding the accumulation of Tregs. *Int Immunol* (2007) 19(2):151–61. doi: 10.1093/intimm/dxl132
- Alspach E, Lussier DM, Miceli AP, Kizhvatov I, DuPage M, Luoma AM, et al. MHC-II neoglycan shape tumour immunity and response to immunotherapy. *Nature* (2019) 574(7780):696–701. doi: 10.1038/s41586-019-1671-8
- Watanaabe K, Ueno M, Kamiya D, Nishiyama A, Matsumura M, Wataya T, et al. A ROCK inhibitor permits survival of dissociated human embryonic stem cells. *Nat Biotechnol* (2007) 25(6):681–6. doi: 10.1038/nbt1310
- Kobayashi M, Azuma E, Ido M, Hirayama M, Jiang Q, Iwamoto S, et al. A pivotal role of Rho GTPase in the regulation of morphology and function of dendritic cells. *J Immunol* (2001) 167(7):3585–91. doi: 10.4049/jimmunol.167.7.3585
- Goodridge HS, Harnett W, Liew FY, Harnett MM. Differential regulation of interleukin-12 p40 and p35 induction via Erk mitogen-activated protein kinase e-dependent and -independent mechanisms and the implications for bioactive IL-12 and IL-23 responses. *Immunology* (2003) 109(3):415–25. doi: 10.1046/j.1365-2567.2003.01689.x
- Kyono A, Avishai N, Ouyang Z, Landreth GE, Murakami S. FGF and ERK signaling coordinately regulate mineralization-related genes and play essential roles in osteocyte differentiation. *J Bone Miner Metab* (2012) 30(1):19–30. doi: 10.1007/s00774-011-0288-2

45. Xie J, Qian J, Yang J, Wang S, Freeman III M, E, Yi Q. Critical roles of Raf/MEK/ERK and PI3K/AKT signaling and inactivation of p38 MAP kinase in the differentiation and survival of monocyte-derived immature dendritic cells. *Exp Hematol* (2005) 33(5):564–72. doi: 10.1016/j.exphem.2005.03.001

46. Woltman AM, Kooij SW, Coffer PJ, Offringa R, Daha MR, Kooten C. Rapamycin specifically interferes with GM-CSF signaling in human dendritic cells, leading to apoptosis via increased p27kip1 expression. *Blood* (2003) 101(4):1439–45. doi: 10.1182/blood-2002-06-1688

47. Heming M, Gran S, Jauch SL, Fischer-Riepe L, Russo A, Klotz L, et al. Peroxisome proliferator-activated receptor-gamma modulates the response of macrophages to lipopolysaccharide and glucocorticoids. *Front Immunol* (2018) 9:893. doi: 10.3389/fimmu.2018.00893

48. Erra Diaz F, Mazzitelli I, Bleichmar L, Melucci C, Thibodeau A, Dalotto Moreno T, et al. Concomitant inhibition of PPAR γ and mTORC1 induces the differentiation of human monocytes into highly immunogenic dendritic cell. *Cell Rep* (2023) 43(3):112156. doi: 10.1016/j.celrep.2023.112156

49. Josien R, Li HL, Ingulli E, Sarma S, Wong BR, Vologodskaia M, et al. TRANCE, a tumor necrosis factor family member, enhances the longevity and adjuvant properties of dendritic cells in vivo. *J Exp Med* (2000) 191:495–502. doi: 10.1084/jem.191.3.495

50. Kleindienst P, Brocker T. Endogenous dendritic cells are required for amplification of T cell responses induced by dendritic cell vaccines *in vivo*. *J Immunol* (2003) 170:2817–23. doi: 10.4049/jimmunol.170.6.2817

51. Yewdall AW, Drutman SB, Jinwala F, Bahjat KS, Bhardwaj N. CD8 $^{+}$ T cell priming by dendritic cell vaccines requires antigen transfer to endogenous antigen presenting cells. *PLoS One* (2010) 5:e11144. doi: 10.1371/journal.pone.0011144

52. Kataoka K, Shiraishi Y, Takeda Y, Sakata S, Matsumoto M, Nagano S, et al. Aberrant PD-L1 expression through 3'-UTR disruption in multiple cancers. *Nature* (2016) 534(7607):402–6. doi: 10.1038/nature18294

53. Kumar A, Chamoto K, Chowdhury PS, Honjo T. Tumors attenuating the mitochondrial activity in T cells escape from PD-1 blockade therapy. *eLife* (2020) 9:e52330. doi: 10.7554/eLife.52330

54. Kumar A, Taghi Khani A, Sanchez Ortiz A, Swaminathan S. GM-CSF: A double-edged sword in cancer immunotherapy. *Front Immunol* (2022) 13:901277. doi: 10.3389/fimmu.2022.901277



OPEN ACCESS

EDITED BY

Jeffrey John Bajramovic,
Utrecht University, Netherlands

REVIEWED BY

Dongbo Jiang,
Air Force Medical University, China
Zi Wei Chang,
A*STAR Infectious Disease Labs, Singapore

*CORRESPONDENCE

Doris Wilflingseder
✉ doris.wilflingseder@i-med.ac.at
Wilfried Posch
✉ wilfried.posch@i-med.ac.at

RECEIVED 13 July 2023

ACCEPTED 02 October 2023

PUBLISHED 17 October 2023

CITATION

Zaderer V, Abd El Halim H, Wyremblewsky A-L, Lupoli G, Dächert C, Muenchhoff M, Graf A, Blum H, Lass-Flörl C, Keppler OT, Huber LA, Posch W and Wilflingseder D (2023) Omicron subvariants illustrate reduced respiratory tissue penetration, cell damage and inflammatory responses in human airway epithelia. *Front. Immunol.* 14:1258268. doi: 10.3389/fimmu.2023.1258268

COPYRIGHT

© 2023 Zaderer, Abd El Halim, Wyremblewsky, Lupoli, Dächert, Muenchhoff, Graf, Blum, Lass-Flörl, Keppler, Huber, Posch and Wilflingseder. This is an open-access article distributed under the terms of the Creative Commons Attribution License (CC BY). The use, distribution or reproduction in other forums is permitted, provided the original author(s) and the copyright owner(s) are credited and that the original publication in this journal is cited, in accordance with accepted academic practice. No use, distribution or reproduction is permitted which does not comply with these terms.

Omicron subvariants illustrate reduced respiratory tissue penetration, cell damage and inflammatory responses in human airway epithelia

Viktoria Zaderer¹, Hussam Abd El Halim¹, Anna-Lena Wyremblewsky¹, Gaia Lupoli², Christopher Dächert², Maximilian Muenchhoff², Alexander Graf³, Helmut Blum³, Cornelia Lass-Flörl¹, Oliver T. Keppler², Lukas A. Huber^{4,5}, Wilfried Posch^{1*} and Doris Wilflingseder^{1*}

¹Institute of Hygiene and Medical Microbiology, Medical University of Innsbruck, Innsbruck, Austria

²Virology, Max von Pettenkofer Institute and Gene Center, Ludwig-Maximilians-Universität (LMU), München, Munich, Germany, ³Laboratory for Functional Genome Analysis, Gene Center, Ludwig-Maximilians-Universität (LMU), Munich, Germany, ⁴Institute of Cell Biology, Biocenter, Medical University of Innsbruck, Innsbruck, Austria, ⁵ADSI - Austrian Drug Screening Institute GmbH, Innsbruck, Austria

Introduction: To explore whether the reported lower pathogenicity in infected individuals of variant of concern (VoC) Omicron and its current subvariants compared to VoC Delta may be related to fundamental differences in the initial virus-tissue interaction, we assessed their ability to penetrate, replicate and cause damage in a human 3D respiratory model.

Methods: For this, we used TEER measurements, real-time PCR, LDH, cytokine and complex confocal imaging analyses.

Results and discussion: We observed that Delta readily penetrated deep into the respiratory epithelium and this was associated with major tissue destruction, high LDH activity, high viral loads and pronounced innate immune activation as observed by intrinsic C3 activation and IL-6 release at infection sites. In contrast, Omicron subvariants BA.5, BQ.1.1 and BF7 remained superficially in the mucosal layer resulting merely in outward-directed destruction of cells, maintenance of epithelial integrity, minimal LDH activity and low basolateral release of virus at infection sites, as well as significantly smaller areas of complement activation and lower IL-6 secretion. Interestingly, also within Omicron subvariants BQ.1.1 and BF.7 illustrating significantly reduced viral loads, IL-6 release and LDH activity compared to BA.5. Our data indicate that earliest interaction events after SARS-CoV-2 transmission may have a role in shaping disease severity.

KEYWORDS

SARS-CoV-2, VOCs, delta, omicron, epithelial barrier model

Highlights

- Delta penetrates deep into the respiratory epithelium and is associated with tissue destruction, cellular stress, innate immune activation and high viral loads.
- Omicron subvariants remain apically distributed in respiratory tissues and are associated with outward directed cell destruction, low cell stress and innate immune activation and low basolateral virus release.

Introduction

Novel SARS-CoV-2 variants of concern (VoC) rapidly emerge. With multiple mutations in its receptor-binding domain (RBD), Omicron (B.1.1.529 with subvariants BA.1, BA.2, BA.4, BA.5, BQ1.1, BF7, XBB.1.5) is entirely different from the former dominant Delta variant in terms of its contagiousness, evasion of pre-existing antibodies, and evidence of milder disease progression (1–5). Rapid increases in cases, reinfections as well as vaccine breakthrough infections with the Omicron variants have been reported. Nevertheless, there are several lines of evidence worldwide that Omicron causes a less severe form of COVID-19 with less hospitalizations of adults relative to previous variants such as Delta (B.1.617.2) (1, 6). In January 2022, the two Omicron lineages, BA.4 and BA.5, appeared in South Africa and over the last months several other Omicron subvariants (BQ.1, BQ.1.1, XBB.1.5, BF7) emerged (3). While BQ.1 and BQ.1.1 evolved from BA.5, recombination of two BA.2 lineages resulted in XBB subvariants (7). There is evidence from *in vitro* data with the Omicron variants that the virus itself showed similar replication for Omicron and Delta in human nasal epithelia, while in lung and gut cells the Omicron spike protein was less efficiently cleaved and illustrated lower replication (8). Significant replication defects of Omicron BA.1 were measured relative to Delta in cells where TMPRSS2, needed for cell-cell fusion, was present (8). The rapid displacement of Delta by the less pathogenic Omicron variant as well as the rapid evolution of Omicron subvariants with a broad array of mutations in the spike protein (7) call for a more detailed and comparative characterization of what happens in human target cells upon virus entry and host cell defense. Earlier, a robust engagement of complement concomitant with excessive pro-inflammatory cytokine induction was detected following SARS-CoV-2 infection of highly differentiated, pseudostratified human airway epithelia (HAE) from upper and lower respiratory tract (9). Here, we describe that the Omicron variants BA.1, BA.2, BA.5 and also the newer subvariants BQ.1.1 and BF7 are differently handled within highly differentiated, pseudostratified respiratory epithelia compared to Delta in terms of tissue penetration and cell destruction, intrinsic complement and IL-6 activation as well as LDH and virus release.

Materials and methods

Human airway epithelial cell culture

Normal human bronchial epithelial (NHBE, Lonza, cat# CC-2540 S, upper respiratory tract) are available in our laboratory and routinely cultured in air liquid interface (ALI) as described (9–11). Briefly, cells were cultured as a monolayer for 2–4 days until they reached 80% confluence. Cells were detached and seeded onto GrowDexT (UPM)-coated 0.33 cm² porous (0.4 µm) polyester membrane inserts with a seeding density of 1 × 10⁵ cells per Transwell (Costar, Corning, New York, NY, USA). The cells were grown to near confluence in submerged culture for 3 days in specific epithelial cell growth medium according to the manufacturer's instructions (StemcellTM). Cultures were maintained in a humidified atmosphere with 5% CO₂ at 37 °C and then transferred to ALI culture for another four weeks until cells were fully differentiated. The epithelium was expanded and differentiated using airway media from StemcellTM. The number of days in development was designated relative to initiation of ALI culture, corresponding to day 0.

Vero cells

VeroE6/TMPRSS2/ACE2 is an engineered VeroE6 cell line expressing high levels of TMPRSS2 and ACE2 and highly susceptible to SARS-CoV-2 infection. This cell line was used to expand characterized BA.1 and BA.4/5 viruses from patient isolates and to perform plaque assays to test infectivity. The cell line was obtained via the CFAR (NIBSC) and is described in (9).

Transepithelial electrical resistance measurement

TEER values were measured using EVOM volt-ohm-meter with STX-2 chopstick electrodes (World Precision Instruments, Stevenage, UK) as described (9). Briefly, for measurements, 100 µl and 700 µl of medium were added to the apical and basolateral chambers, respectively, and cells were allowed to equilibrate before TEER was measured. TEER values reported were corrected for the resistance and surface area of the Transwell filters.

Staining and high content screening

To visualize SARS-CoV-2 infection in monolayers and 3D tissue models, cells were infected with clinical specimen of SARS-CoV-2 Delta and Omicron variants and analyzed for characteristic markers in infection experiments on day 2 post infection (2 dpi). After SARS-CoV-2 exposure, 3D cell cultures were fixed with 4% paraformaldehyde. Intracellular staining was performed using 1x

Intracellular Staining Permeabilization Wash Buffer (10x; BioLegend, San Diego, CA, USA). Cells were stained using phalloidin-Alexa647 (Thermofisher Scientific, Waltham, MA, USA), nuclei using Hoechst (Cell Signaling Technologies, Danvers, MA, USA), and complement C3 using a C3-FITC antibody (Agilent Technologies, Santa Clara, CA, USA). Intracellular SARS-CoV-2 was detected using Alexa594-labeled SARS-CoV-2 antibodies against N (Sino Biological, Beijing, China). The Alexa594-labeling kit was purchased from Abcam, Cambridge, UK. After staining, 3D cultures were mounted in Mowiol. To study these complex models using primary cell cultured in 3D and to generate detailed phenotypic fingerprints for deeper biological insights in a high throughput manner, the Operetta CLS System (PerkinElmer, Waltham, MA, USA) was applied. Spot analyses and absolute quantification for SARS-CoV-2-containing cells, Harmony™ Software was performed in more than 2000 cells per condition, since in five independent experiments at least 400 cells defined by nuclear stain (Höchst) were analyzed.

Real-time RT-PCR for absolute quantification of SARS-CoV-2

SARS-CoV-2 RNA was extracted using FavorPrep Viral RNA Mini Kit, according to manufacturer's instructions (Favorgen Europe, cat# FAVRE 96004, Austria). Sequences specific to 2 distinct regions of the Nucleocapsid (N) gene, N1 and N2, and for the detection of a human housekeeping gene, Ribonuclease P, were used. Single target assays of all 3 targets were performed in combination with the Luna Universal Probe One-Step RT-qPCR Kit (New England Biolabs, cat# E3006, Germany). For absolute quantification using the standard curve method, SARS-CoV-2 RNA was obtained as a PCR standard control from the National Institute for Biological Standards and Control, UK. All runs were performed on a Bio-Rad CFX 96 instrument and analyzed by the Bio-Rad CFX Maestro 1.1 software (Bio-Rad, Germany).

Viruses

Clinical specimens for SARS-CoV-2 VoC Delta and Omicron subvariants (BA.1, BA.2, BA.5, BQ1.1, BF7) from sequenced COVID-19 positive swabs were propagated and subsequently used to infect cells at a MOI of 0.0025. All experiments, where we used live virus strains (infection, plaque assays) were performed under BSL3 conditions.

Plaque assay

VeroE6/ACE2/TMPRSS2 cells were inoculated with serial dilutions of 2 dpi subnatants from Omicron subvariant- or Delta-infected HAE cells for 1h at 37°C/5%CO₂. Inoculate was replaced with culture medium containing 1.5% carboxymethylcellulose and incubated for 3 days at 37°C/5% CO₂ before plaque visualization and counting as described (12).

Statistical analysis

Statistical analysis of differences in infection levels, TEER values, or cytokine production was performed utilizing the GraphPad prism software and using OneWay ANOVA with Tukey's posttest.

Ethics statement

Written informed consent was obtained from all donors of leftover nasopharyngeal/oropharyngeal specimens and EDTA blood by the participating clinics. The Ethics Committee of the Medical University of Innsbruck (ECS1166/2020) approved the use of anonymized leftover specimens of COVID-19 patients for scientific purposes.

Results

Delta penetrates deep into the pseudostratified, columnar tracheal epithelium, while Omicron variants remain superficial

First, we analyzed the localization of Delta and Omicron-infected epithelial cultures by immunofluorescence followed by 3D analysis. We noticed that Delta distributed over the entire width of the epithelium and localized very close to the basement membrane (Figure 1A, upper panel, Supplementary Figure 1, middle, right panel). In contrast, all Omicron subvariants tested in immunofluorescence analyses (BA.1, BA.2, BA.5, BQ1.1) remained apically distributed and did not dig that deep into the pseudostratified columnar epithelium (Figure 1A, lower panel, Supplementary Figure 1, Omicron (BA.5), right panel). Next, we analyzed the infected tissue models in more detail using phalloidin staining and performing XYZ analysis. The widespread dissemination of the Delta variant reaching the basement membrane became even more apparent, while Omicron only associated with the apical plasma membrane, but did not penetrate into the tissue (Figure 1B, left). When measuring the distance of viral particles from the apical site in multiple samples, a highly significant ($p<0.0001$) difference between Delta and Omicron subvariants BA.1, BA.2, BA.5 and BQ1.1 was illustrated, with Delta diving deep (mean 30 μ m) into the columnar, pseudostratified epithelium and Omicron remaining on the surface of the epithelium (mean 3.5 μ m) (Figure 1B, right). Our data indicate that Delta is more likely able to penetrate the tissue, while Omicron stays superficially.

Epithelial integrity of HAE cultures is retained upon Omicron infection, while interrupted by Delta

To monitor, if the observed differences in tissue penetration between Delta and Omicron are associated with differences in epithelial integrity, transepithelial electrical resistance (TEER) was

measured on 2 days post infection (2 dpi) using a low multiplicity of infection (MOI) of 0.0025 for the virus preparations to avoid too fast tissue destruction and cell death. From here on, only the more recent Omicron subvariants BA.5, BA1.1, BF.7 are illustrated, since results from BA.1 and BA.2-infected cultures were earlier published by our group (10, 13). Despite low MOI, analyses revealed that upon Delta infection, TEER values of HAE cells significantly dropped compared to mock-treated cells (UI, uninfected) and to cells infected with the Omicron subvariants BA1.1 and BF.7 (Figure 2A, TEER). Omicron BA1.1- and BF.7-infected cultures were similar in their TEER values relative to UI ones on 2 dpi, while BA.5 showed significantly lower TEER values (Figure 2A, TEER). From day 3 post infection on, tissue destruction was also observed using Omicron subvariants, since the Transwell is a closed system

and viruses cannot be cleared. Here, we found that epithelial integrity is more likely maintained in Omicron- versus Delta-infected HAE cultures.

Viral loads are significantly lower in Omicron- versus Delta-infected HAE cultures

In accordance to image analyses and TEER, absolute quantification of viral load from 2 dpi supernatants of differently treated cells revealed a significantly lower SARS-CoV-2-N1 RNA copy number in Omicron subvariant- compared to Delta-infected HAE cultures after infection at a MOI 0.0025 (Figure 2A, middle).

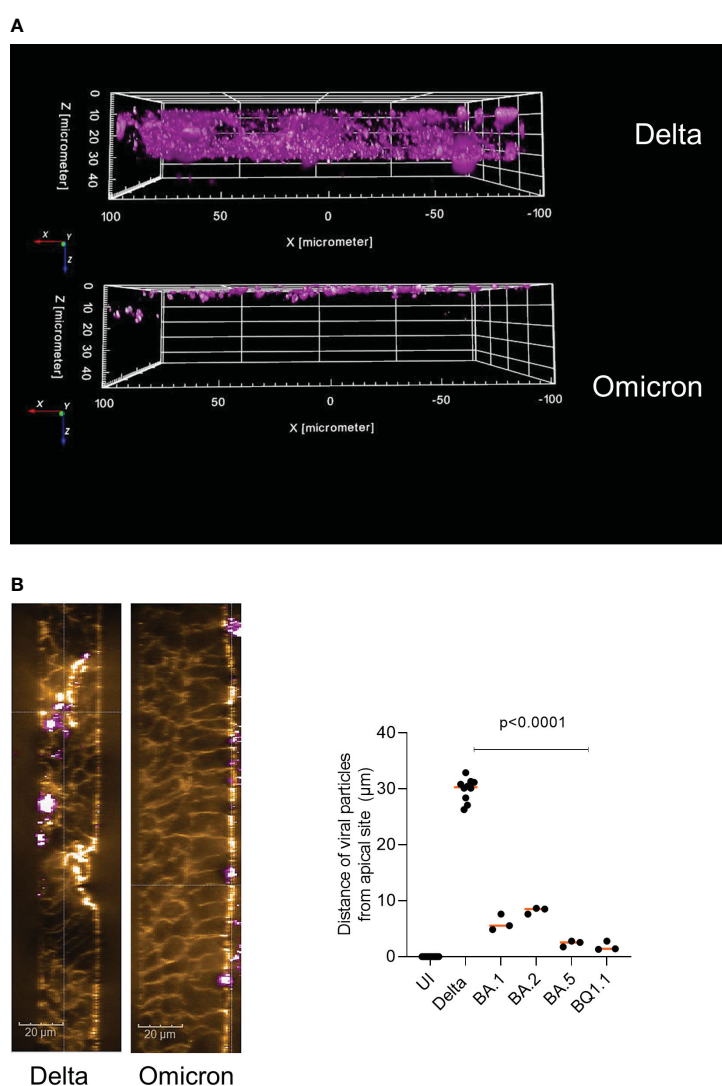


FIGURE 1

Delta penetrates deep into HAE cells compared to apical distribution of Omicron. Pseudostratified epithelia were infected by apical addition of SARS-CoV-2 Delta or Omicron subvariants BA.1, BA.2, BA.5 or BA1.1 for 48h and immunofluorescence analyses were performed to stain for virus (pink), actin (orange), C3 (green) and nuclei (blue). (A) 3D image analyses of virus penetration into the pseudostratified HAE model generated using the Harmony™ software (Perkin Elmer). In panel A, the virus signal in Delta vs. Omicron infected tissues is depicted, while in (B) an XYZ-analyses was performed, illustrating the ZY-axis and phalloidin (orange) and virus (pink) staining (left), scale bars 20μm. The experiment was repeated 8 to 10 times using Delta and various Omicron subvariants and distance was statistically determined by one-way ANOVA with Tukey's multiple comparisons test. Each dot represents an independent experiment and means are depicted in orange (right).

Here, all Omicron subvariants tested (BA.5, BQ1.1, BF.7) revealed significantly lower viral loads compared to Delta. This resulted in highly significant reduction of viral titers as analyzed by plaque assay of 2 dpi subnatants from infected HAE cells (Figure 2A, right). Mock-treated cultures (UI) served as controls. Defective replication and infectivity of Omicron variants compared to Delta within highly differentiated HAE cells were illustrated herein.

Cell viability is significantly higher in Omicron- versus Delta-infected HAE cultures

Next, we discriminated live and dead cells in cultures infected with either Delta or Omicron BA.5, BQ1.1 or BF7 by using amine-reactive dyes appropriate for fixed samples. Immunofluorescence analyses revealed significantly higher numbers of dead cells upon infection with the Delta variant compared to all Omicron subvariants tested (BA.5, BQ1.1, BF7) (Figure 2B, left and right). On 2 dpi, only isolated dead cells were detected in uninfected (UI), or Omicron BQ1.1 or BF7-infected cultures, while BA.5-infected cells demonstrated higher cell death (Figure 2B, left, dead cells – red, phalloidin – gray, nuclei – blue). Delta-infected cells showed the highest cell death rates (Figure 2B, left). When analyzing percentages of dead cells, between 20 to 50% were detected in Delta-infected cultures, and between 1 to 9% in cell cultures infected with Omicron BA.5, BQ1.1 or BF7 (Figure 2B, right). BA.5 illustrated a significantly higher cell death rate compared to the newer emerging subvariants BQ1.1 or BF7 (Figure 2B, right). Further image analyses revealed leaky tissue structures with big areas of cell detachment in Delta-infected tissues (Supplementary Figure 1, 2nd panel), while Omicron subvariants displayed only superficial cell destruction without porous structures (Supplementary Figure 1, 3rd panel). UI cultures served as controls (Supplementary Figure 1, 1st panel). An overview of UI, Delta, and Omicron-infected cells and nuclei counts of at least 2000 cells is depicted in Supplementary Figure 1, 4th panel. Thus, Delta displays considerably higher cell death of HAE cells compared to all Omicron subvariants tested, and cell death of BA.5-infected cultures is significantly higher compared to BQ1.1- and BF7-exposed cells.

Delta triggers significantly higher LDH release compared to Omicron

Moreover, we measured LDH activity of HAE cells exposed to Delta versus Omicron subvariants BA.5, BQ.1.1 and BF7. We found that upon infection with Delta, excessive LDH activation was measured that was significantly higher compared to UI, BA.5, BQ.1.1 and BF7 (Figure 2C). In accordance to the higher cell destruction observed, the Omicron BA.5 subvariant mediated significantly higher LDH activity compared to BQ.1.1 and BF7, and BF7 exerted lowest LDH activity levels (Figure 2C). Thus, the enhanced tissue damage observed with the Delta variant was accompanied by significantly higher LDH activity compared to all Omicron subvariants.

Intrinsic C3 activation and IL-6 production are induced to significantly lower levels in Omicron- vs. Delta-infected HAE cultures

Extensive intrinsic C3 linked to excessive secretion of the anaphylatoxin C3a at infection sites was reported in patient samples' bronchoalveolar lavages (BALs) and from HAE cells upon infection with previous variants of SARS-CoV-2 (9, 14, 15). Thus, we were interested, if the dissimilar processing of Delta and Omicron subvariants within HAE cells is linked to a difference in intracellular C3 and pro-inflammatory cytokine (IL-6) production. 3D analyses of Z-stacks over the entire width of mock-treated, Delta- and Omicron-BA.5-infected HAE cultures illustrated a greater area of C3-positive cells (green) in Delta-infected cultures in the epithelium compared to Omicron (Figure 3A; Supplementary Figure 1, 2nd and 3rd panel). Despite the significantly lower productive infection, tissue destruction and superficial localization, Omicron mediated a significantly higher intrinsic C3 generation (green) compared to mock-treated cells (Figure 3A, Omicron subvariants vs. UI). Nevertheless, intracellular (IC) C3 produced was still substantially reduced in Omicron- versus Delta-infected cultures, independent on the subvariant used. As shown earlier (9), IC C3 production and subsequent C3a release resulted in induction of pro-inflammatory cytokines IL-1 α , RANTES, MIP-1 β and IL-6 from highly differentiated HAE cells. Analyzing IL-6 following infection with Delta versus Omicron subvariants BA.5, BQ.1.1 and BF7 revealed a significantly higher cytokine secretion in Delta-infected cultures relative to UI or Omicron-infected cultures. Moreover, we found that the BA.5 VOC caused significantly higher IL-6 release compared to the newer subvariants BQ.1.1 or BF7 (Figure 3B), nicely correlating to the inflammatory response induced by the different subvariants. These data reveal that Omicron infection of differentiated HAE cells resulted in substantial C3 generation compared to UI, which is still significantly lower relative to Delta and not sufficient to effectively induce excessive pro-inflammatory responses.

Conclusions

Here, we analyzed in more detail entry and early events during the infection process of Delta versus Omicron subvariants (BA.1, BA.2, BA.5, BQ.1.1, BF7) in highly differentiated, primary human airway epithelial cells grown at an air-liquid-interface. These analyses revealed that Delta massively penetrates the pseudostratified human airway epithelium, thereby resulting in excessive tissue destruction, cell death, as well as high inflammatory responses. In contrast, all Omicron subvariants tested remained apically on the airway epithelium causing cell death only superficially, and stress-response and inflammatory signals to significantly lower levels up to two days after infection within the ALI system. From day 3 on, also Omicron subvariants caused enhanced tissue destruction, since the viruses remain in the closed Transwell system and cannot be cleared. Studies on the virological

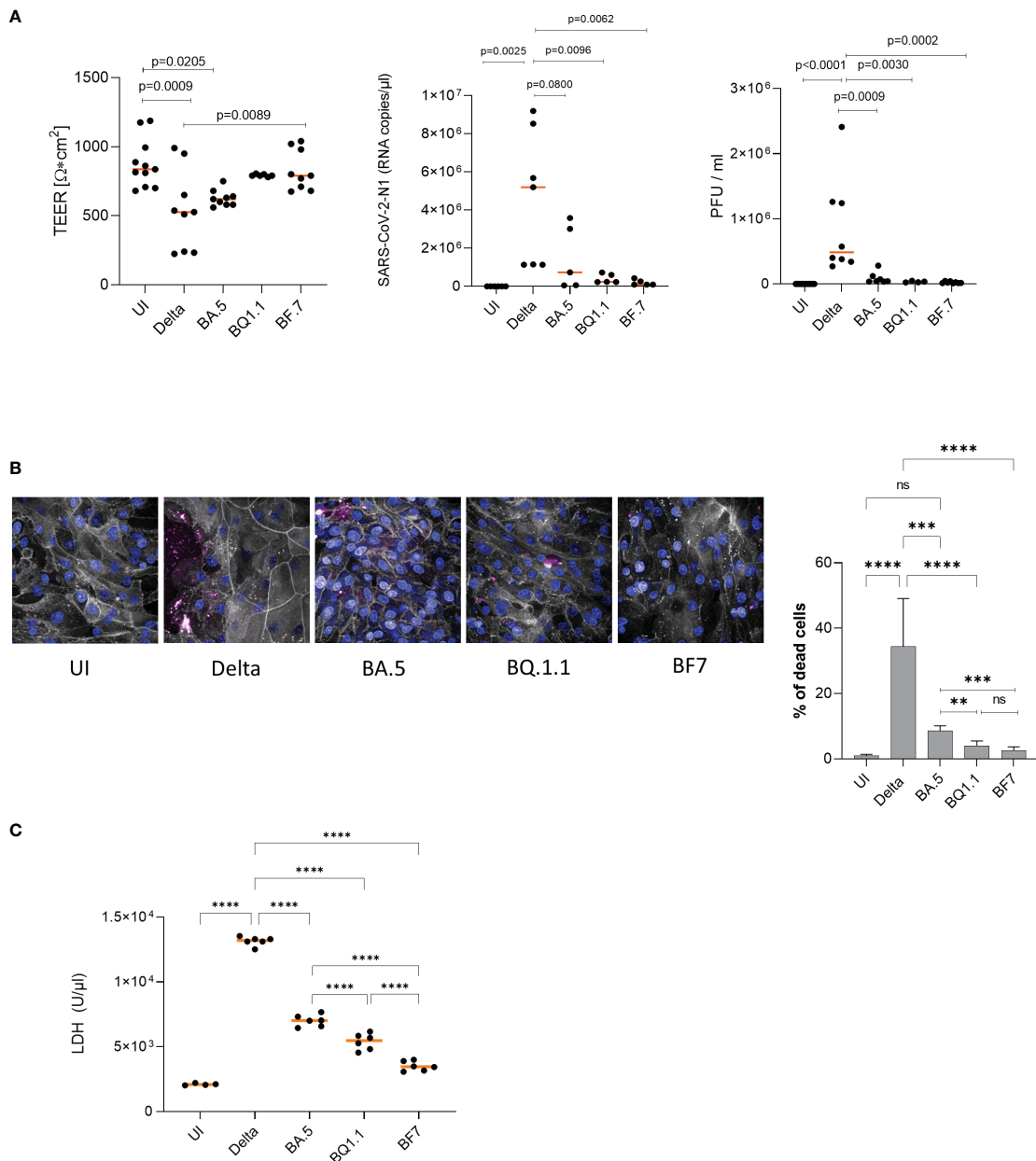


FIGURE 2

(A, left) Epithelial integrity is significantly disrupted in Delta versus Omicron. TEER was measured on 2 dpi (left) using a EVOM volt-ohm-meter. TEER in Ω/cm^2 was determined for all conditions (UI, Delta, Omicron subvariants BA.5, BQ1.1, BF.7) and plotted on a dot graph. Dots represent infection experiments of pseudostratified epithelia using Delta or Omicron subvariants BA.5, BQ1.1 or BF.7 measured in triplicates. Statistical significance was calculated using One-way ANOVA with Tukey's multiple comparisons test, means are depicted in orange. (A, middle, right) Viral load and infectivity are significantly higher in Delta versus Omicron. (A, middle) Viral load was determined by absolute quantification using real-time RT-PCR and a SARS-CoV-2 N standard. While Delta-infected epithelia depicted a high basolateral viral load, HAE infected with Omicron subvariants illustrated low-level infection, which corresponded to (A, right) the infectivity of released viruses as measured by plaque assay on VeroE6/ACE2/TMPRSS2-expressing cells. (B) Delta mediates higher cell death in HAE compared to Omicron subvariants BA.5, BQ1.1 and BF.7. Immunofluorescence staining of HAE cells infected for 2 days with Delta or the indicated Omicron subvariants was performed using phalloidin (orange), Hoechst (blue) and a live/dead cell staining kit (red) as described. % of dead cells were calculated using the Harmony™ software and one-way ANOVA with Tukey's multiple comparisons test. (C) LDH activity is significantly higher in Delta versus Omicron. Cytotoxicity was analyzed using the Cytotoxicity Detection Kit (LDH) from Roche according to the manufacturer's instructions (Merck, cat# 1164493001, Austria). This kit is based on measuring LDH activity released from damaged cells. Treatment of 3D human respiratory tissue models with Delta or Omicron subvariants BA.5, BQ1.1 or BF.7 revealed a significantly higher LDH activity in cells infected with Delta- versus all tested Omicron subvariants. The newest subvariants BQ1.1 and BF.7 were even significantly lower in their LDH activities compared to the BA.5 subvariant, indicating less cell stress and cytotoxicity. Statistical significance was calculated using One-way ANOVA with Tukey's multiple comparisons test, means are depicted in orange. **p<0.01; ***p<0.001; ****p<0.0001. ns not significant.

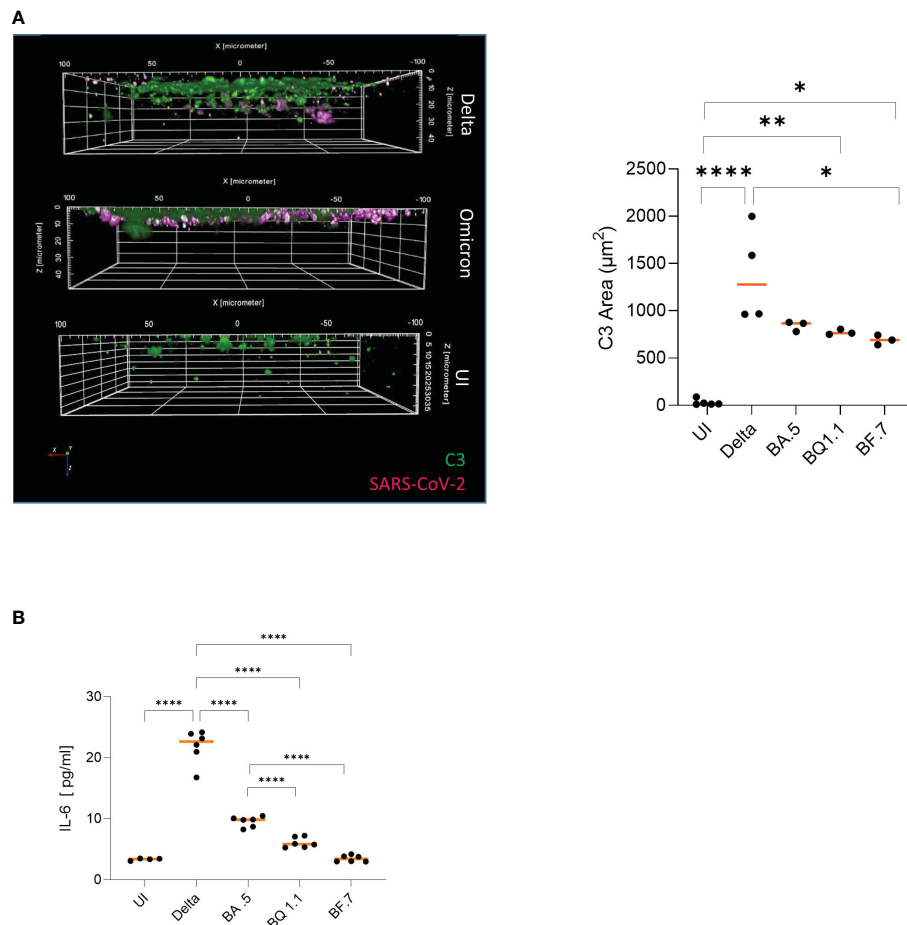


FIGURE 3

(A) Higher local complement C3 is induced in Delta versus Omicron-infected epithelia. Visualization of virus binding (SARS-CoV-2 N, pink) and complement (C3-FITC, green) in SARS-CoV-2 infected 3D pseudostratified epithelia. On 2 dpi, filters were fixed, stained for SARS-CoV-2 N (pink), and complement C3 (green) then analyzed by HCS. Higher IC C3 mobilization was monitored in Delta versus Omicron-infected cultures (right), while no virus and low C3 signals were detected in UI. Areas of C3 production were absolutely quantified from at least three different areas using the Harmony™ software (right). Statistical significances were analyzed with GraphPad Prism software using One-way ANOVA and Tukey's posttest. As representative image, infection with Omicron subvariant BA.5 is depicted. **(B)** Significantly higher IL-6 is induced in Delta versus Omicron-infected epithelia. Intracellular C3 mobilization was associated with pro-inflammatory cytokine induction like IL-6. Upon infection of HAE cells with in particular Delta or the Omicron subvariant BA.5, significantly higher IL-6 secretion was mediated in contrast to BQ1.1-, BF7- or uninfected cultures. Statistical significances were analyzed with GraphPad Prism software using One-way ANOVA and Tukey's posttest, means are depicted in orange. * $p<0.05$, ** $p<0.01$; *** $p<0.0001$.

properties of the Omicron variant, which rapidly replaced the former Delta variant in the beginning of 2022, revealed that despite its modest severity, it has a 3.3-fold higher transmissibility rate as well as an increased resistance to antiviral immunity (8, 16). These characteristics were explained by multiple amino acid substitutions in the S2 region of the Omicron spike protein that are associated with an enhanced ACE2 binding affinity (16), and an altered endocytic pathway utilizing mainly the cathepsin-dependent endocytic pathway in contrast to Delta using TMPRSS2-dependent fusion (17). In VeroE6/TMPRSS2 cells, larger syncytia formation was observed for Delta, while Omicron showed only weak syncytia formation (16). These data are in accordance with the data found here in highly differentiated, human airway epithelial cells, since infection with the Delta variant resulted in significantly higher penetration of the human airway epithelium going along with extensive tissue destruction and pore formation on 2 dpi, loss in epithelial integrity and cell death. In contrast, all Omicron subvariants tested remained apically distributed and exerted a significantly lower

destruction of the pseudostratified epithelium until 2 dpi. While Meng et al. (8) described similar replication kinetics and rates of Delta and Omicron in 3D primary human nasal epithelial cells, in our 3D primary upper respiratory tract model, we found significant differences in terms of viral load and infectivity of released viruses. Delta infection resulted in high productive infection of HAE cells, whereas the replication rates and infectivity of Omicron subvariants was significantly lower. These differences can be explained by infecting with diverse infectious units or by different sampling; Meng et al. collected from the apical, i.e. air, side, while here samples were acquired from the basolateral, i.e. systemic, side to associate systemic infection rate with other factors such as inflammation, cell death, cell stress. In addition to the higher tissue destruction and viral load observed during Delta infections, higher cell death and LDH activity were detected. Previous studies reported on the pro-apoptotic activities of SARS-CoV-2 ORF3a that triggers a range of host cellular immune responses, including cellular stress and pro-inflammatory cytokine responses and

induces cell death through apoptosis, necrosis and pyroptosis, thus contributing to tissue damage (12, 18). ORF3a is directly involved in activation of NLRP3 inflammasomes and pro-inflammatory cytokine induction. This in turn directly connects to the recently described ‘complement-metabolism-inflammasome’ axis (19) described in immune cells. Both anaphylatoxins, C3a and C5a, have been confirmed as important drivers of NLRP3 inflammasome activation (19), and recently, exacerbating intracellular C3 mobilization as well as anaphylatoxin secretion from non-immune HAE cells following infection with SARS-CoV-2 wild type, Beta and Delta variants were described (9, 10, 15, 20). Going along with the lower pathogenicity of the Omicron subvariants in our model, here we found significantly lower complement C3 mobilization that was rather superficially distributed. In contrast, Delta-infected tissues that illustrated a deeper penetration associated with higher tissue destruction, cell death and LHD activity, showed larger C3-containing areas and C3 activation up to 30 µm of depth within the tissue. The massive intracellular C3 activation was further associated with anaphylatoxin and pro-inflammatory cytokine production (9). While the Omicron subvariants only induced low-level IL-6 release from HAE cells, with the novel Omicron variants BQ1.1 and BF.7 even being less inflammatory, the Delta variant demonstrated significantly higher IL-6 levels. Limitations of this study include that cytokine and C3 expression as well as LDH release were not cross-validated by other methods. However, in earlier reports using SARS-infected tissue culture models, we extensively illustrated the association of these factors (C3, IL-6) with other proinflammatory responses (9, 20, 21). Although the main objective of our study was to compare the pathogenicity between Delta and Omicron variants, our data also revealed differences in viral loads, TEER, LDH and IL-6 expression within Omicron subvariants. While LDH and IL-6 expression were significantly higher in BA.5 compared to BQ1.1 and BF.7, viral loads and TEER were only slightly changed. In a previous study, we also demonstrated elevated viral loads in BA.5-infected HAE cultures compared to BF.7- or BQ1.1-infected tissue models (22). So far, human cohort studies investigated disease severity between Delta and Omicron waves, but only little is known about the pathogenicity between Omicron subvariants (23). Therefore, more results are needed to allow a clear statement on pathogenicity between Omicron subvariants. Recent studies on rhesus macaques and hamsters demonstrated reduced disease severity as well as cytokine and chemokine expression caused by Omicron subvariants compared to Delta (16, 24, 25). These findings are in accordance to our data using a primary human *in vitro* model. In summary, here we could shed new light on the initial pathomechanisms of human HAE cultures infected with Delta or Omicron variants, including novel subvariants such as BF.7 and BQ1.1. Additionally, our *in vitro* findings illustrated that Delta variant penetrates deep into the pseudostratified epithelial layer and thereby initiates not only higher rates of virus release, cell death and inflammation, which was assessed by significantly higher local complement C3 and IL-6 secretion. In contrast, all Omicron subvariants tested (BA.1, BA.2, BA.5, BQ1.1, BF7) remained apically distributed. Upon focus on the novel variants BA.5, BQ1.1 and BF7, we found that in particular BQ1.1 and BF7 were associated with superficial

cell death only, significantly lower systemic virus secretion and intracellular C3 mobilization and IL-6 release.

Data availability statement

The original contributions presented in the study are included in the article/[Supplementary Material](#), further inquiries can be directed to the corresponding author/s.

Ethics statement

Written informed consent was obtained from all donors of leftover nasopharyngeal/oropharyngeal specimens and EDTA blood by the participating clinics. The Ethics Committee of the Medical University of Innsbruck (ECS1166/2020) approved the use of anonymized leftover specimens of COVID-19 patients for scientific purposes. The studies were conducted in accordance with the local legislation and institutional requirements. The participants provided their written informed consent to participate in this study.

Author contributions

VZ: Visualization, Data curation, Investigation, Methodology, Writing – review & editing. HA: Methodology, Visualization, Writing – review & editing. A-LW: Methodology, Visualization, Writing – review & editing. GL: Investigation, Methodology, Writing – review & editing. CD: Resources, Methodology, Writing – review & editing. MM: Methodology, Resources, Writing – review & editing. AG: Methodology, Resources, Writing – review & editing. HB: Investigation, Methodology, Writing – review & editing. CL-F: Conceptualization, Supervision, Validation, Writing – review & editing. OK: Data curation, Project administration, Resources, Conceptualization, Validation, Writing – review & editing. LH: Conceptualization, Data curation, Project administration, Validation, Writing – review & editing. WP: Conceptualization, Data curation, Project administration, Writing – review & editing, Supervision, Writing – original draft, Investigation, Funding acquisition, Formal Analysis. DW: Conceptualization, Data curation, Funding acquisition, Investigation, Project administration, Supervision, Writing – original draft, Writing – review & editing, Validation, Resources, Methodology.

Funding

The author(s) declare financial support was received for the research, authorship, and/or publication of this article. The authors declare financial support was received for the research, authorship, and/or publication of this article. The authors were supported by the Austrian Science Fund (FWF; P 34070-B to WP and P33510-B to DW).

Acknowledgments

We thank our technicians Viktoria Kozubowski and Andrea Windisch, for their valuable help and support regarding this manuscript.

Conflict of interest

Author LH was a co-founder of ADSI GmbH and consults in cell biology.

The remaining authors declare that the research was conducted in the absence of any commercial or financial relationships that could be construed as a potential conflict of interest.

References

1. Sigal A. Milder disease with Omicron: is it the virus or the pre-existing immunity? *Nat Rev Immunol* (2022) 22(2):69–71. doi: 10.1038/s41577-022-00678-4
2. Liu L, Iketani S, Guo Y, Chan JF, Wang M, Liu L, et al. Striking antibody evasion manifested by the Omicron variant of SARS-CoV-2. *Nature* (2022) 602(7898):676–81. doi: 10.1038/s41586-021-04388-0
3. Tegally H, Moir M, Everett J, Giovanetti M, Scheepers C, Wilkinson E, et al. Emergence of SARS-CoV-2 Omicron lineages BA.4 and BA.5 in South Africa. *Nat Med* (2022) 28:1785–90. doi: 10.1038/s41591-022-01911-2
4. Thorne LG, Bouhaddou M, Reuschl AK, Zuliani-Alvarez L, Polacco B, Pelin A, et al. Evolution of enhanced innate immune evasion by SARS-CoV-2. *Nature* (2022) 602(7897):487–95. doi: 10.1038/s41586-021-04352-y
5. Tuckprakhon A, Nutalai R, Djokokaite-Guraliuc A, Zhou D, Ginn HM, Selvaraj M, et al. Antibody escape of SARS-CoV-2 Omicron BA.4 and BA.5 from vaccine and BA.1 serum. *Cell* (2022) 185(14):2422–2433 e2413. doi: 10.1016/j.cell.2022.06.005
6. Sigal A, Milo R, Jassat W. Estimating disease severity of Omicron and Delta SARS-CoV-2 infections. *Nat Rev Immunol* (2022) 22(5):267–9. doi: 10.1038/s41577-022-00720-5
7. Wang Q, Iketani S, Li Z, Liu L, Guo Y, Huang Y, et al. Alarming antibody evasion properties of rising SARS-CoV-2 BQ and XBB subvariants. *Cell* (2023) 186(2):279–286 e278. doi: 10.1016/j.cell.2022.12.018
8. Meng B, Abdullaah A, Ferreira I, Goonawardane N, Saito A, Kimura I, et al. Altered TMPRSS2 usage by SARS-CoV-2 Omicron impacts infectivity and fusogenicity. *Nature* (2022) 603(7902):706–14. doi: 10.1038/s41586-022-04474-x
9. Posch W, Vosper J, Noureen A, Zaderer V, Witting C, Bertacchi G, et al. C5aR inhibition of nonimmune cells suppresses inflammation and maintains epithelial integrity in SARS-CoV-2-infected primary human airway epithelia. *J Allergy Clin Immunol* (2021) 147(6):2083–2097 e2086. doi: 10.1016/j.jaci.2021.03.038
10. Dichtl S, Zaderer V, Kozubowsk V, Abd El Halim H, Lafon E, Langer L, et al. Cilgavimab/Tixagevimab as alternative therapeutic approach for BA.2 infections. *Front Med (Lausanne)* (2022) 9:1005589. doi: 10.3389/fmed.2022.1005589
11. Matsuyama S, Nao N, Shirato K, Kawase M, Saito S, Takayama I, et al. Enhanced isolation of SARS-CoV-2 by TMPRSS2-expressing cells. *Proc Natl Acad Sci USA* (2020) 117(13):7001–3. doi: 10.1073/pnas.2002589117
12. Ren Y, Shu T, Wu D, Mu C, Wang M, Huang Y, et al. The ORF3a protein of SARS-CoV-2 induces apoptosis in cells. *Cell Mol Immunol* (2020) 17(8):881–3. doi: 10.1038/s41423-020-0485-9
13. Zaderer V, Dichtl S, Posch W, Abiatiari I, Bonn KG, Jakschitz T, et al. GlyPerA effectively shields airway epithelia from SARS-CoV-2 infection and inflammatory events. *Respir Res* (2023) 24(1):88. doi: 10.1186/s12931-023-02397-3
14. Afzali B, Noris M, Lambrecht BN, Kemper C. The state of complement in COVID-19. *Nat Rev Immunol* (2022) 22(2):77–84. doi: 10.1038/s41577-021-00665-1
15. Yan B, Freiwald D, Chauss D, Wang L, West E, Mirabelli C, et al. SARS-CoV-2 drives JAK1/2-dependent local complement hyperactivation. *Sci Immunol* (2021) 6(58). doi: 10.1126/sciimmunol.abg0833
16. Suzuki R, Yamasoba D, Kimura I, Wang L, Kishimoto M, Ito J, et al. Attenuated fusogenicity and pathogenicity of SARS-CoV-2 Omicron variant. *Nature* (2022) 603(7902):700–5. doi: 10.1038/s41586-022-04462-1
17. Hui KPY, Ho JCW, Cheung MC, Ng KC, Ching RHH, Lai KL, et al. SARS-CoV-2 Omicron variant replication in human bronchus and lung *ex vivo*. *Nature* (2022) 603(7902):715–20. doi: 10.1038/s41586-022-04479-6
18. Zhang J, Ejikemeuwa A, Gerzanich V, Nasr M, Tang Q, Simard JM, et al. Understanding the role of SARS-CoV-2 ORF3a in viral pathogenesis and COVID-19. *Front Microbiol* (2022) 13:854567. doi: 10.3389/fmicb.2022.854567
19. Arbore G, Kemper C. A novel "complement-metabolism-inflammasome axis" as a key regulator of immune cell effector function. *Eur J Immunol* (2016) 46(7):1563–73. doi: 10.1002/eji.201546131
20. Posch W, Vosper J, Zaderer V, Noureen A, Constant S, Bellmann-Weiler R, et al. ColdZyme maintains integrity in SARS-CoV-2-infected airway epithelia. *mBio* (2021) 12(2). doi: 10.1128/mBio.00904-21
21. Zaderer V, Dichtl S, Bellmann Weiler R, Lass-Florl C, Posch W, Wilflingseder D. ColdZyme(R) protects airway epithelia from infection with BA.4/5. *Respir Res* (2022) 23(1):300. doi: 10.1186/s12931-022-02223-2
22. Diem G, Dichtl S, Zaderer V, Lass-Florl C, Reindl M, Lupoli G, et al. Salivary antibodies induced by BA.4/BA.5-convalescence or bivalent booster Immunoglobulin vaccination protect against novel SARS-CoV-2 variants of concern. *Microbiol Spectr* (2023):e0179323. doi: 10.1128/spectrum.01793-23
23. Menni C, Valdes AM, Polidori L, Antonelli M, Penamakuri S, Nogal A, et al. Symptom prevalence, duration, and risk of hospital admission in individuals infected with SARS-CoV-2 during periods of omicron and delta variant dominance: a prospective observational study from the ZOE COVID Study. *Lancet* (2022) 399(10335):1618–24. doi: 10.1016/S0140-6736(22)00327-0
24. van Doremalen N, Singh M, Saturday TA, Yinda CK, Perez-Perez L, Bohler WF, et al. SARS-CoV-2 Omicron BA.1 and BA.2 are attenuated in rhesus macaques as compared to Delta. *Sci Adv* (2022) 8(46):eade1860. doi: 10.1126/sciadv.ade1860
25. Tamura T, Ito J, Uriu K, Zahradnik J, Kida I, Anraku Y, et al. Virological characteristics of the SARS-CoV-2 XBB variant derived from recombination of two Omicron subvariants. *Nat Commun* (2023) 14(1):2800. doi: 10.1038/s41467-023-38435-3

Publisher's note

All claims expressed in this article are solely those of the authors and do not necessarily represent those of their affiliated organizations, or those of the publisher, the editors and the reviewers. Any product that may be evaluated in this article, or claim that may be made by its manufacturer, is not guaranteed or endorsed by the publisher.

Supplementary material

The Supplementary Material for this article can be found online at: <https://www.frontiersin.org/articles/10.3389/fimmu.2023.1258268/full#supplementary-material>



OPEN ACCESS

EDITED BY

Jeffrey John Bajramovic,
Utrecht University, Netherlands

REVIEWED BY

Shaikh Muhammad Atif,
University of Colorado Anschutz Medical
Campus, United States
Cosmin Mihai Vesa,
University of Oradea, Romania
Ahmet Eken,
Erciyes University, Türkiye

*CORRESPONDENCE

Nicole Elisabeth Teusch
✉ nicole.teusch@hhu.de

RECEIVED 11 August 2023

ACCEPTED 12 October 2023

PUBLISHED 06 November 2023

CITATION

Hölken JM, Friedrich K, Merkel M, Blasius N, Engels U, Buhl T, Mewes KR, Vierkotten L and Teusch NE (2023) A human 3D immune competent full-thickness skin model mimicking dermal dendritic cell activation. *Front. Immunol.* 14:1276151. doi: 10.3389/fimmu.2023.1276151

COPYRIGHT

© 2023 Hölken, Friedrich, Merkel, Blasius, Engels, Buhl, Mewes, Vierkotten and Teusch. This is an open-access article distributed under the terms of the [Creative Commons Attribution License \(CC BY\)](#). The use, distribution or reproduction in other forums is permitted, provided the original author(s) and the copyright owner(s) are credited and that the original publication in this journal is cited, in accordance with accepted academic practice. No use, distribution or reproduction is permitted which does not comply with these terms.

A human 3D immune competent full-thickness skin model mimicking dermal dendritic cell activation

Johanna Maria Hölken¹, Katja Friedrich¹, Marion Merkel^{1,2},
Nelli Blasius², Ursula Engels², Timo Buhl³,
Karsten Rüdiger Mewes², Lars Vierkotten²
and Nicole Elisabeth Teusch^{1*}

¹Institute of Pharmaceutical Biology and Biotechnology, Heinrich Heine University Düsseldorf, Düsseldorf, Germany, ²Alternative Methods and Tissue Engineering, Henkel AG & Co. KGaA, Düsseldorf, Germany, ³Department of Dermatology, Venereology and Allergology, University Medical Center Göttingen, Göttingen, Germany

We have integrated dermal dendritic cell surrogates originally generated from the cell line THP-1 as central mediators of the immune reaction in a human full-thickness skin model. Accordingly, sensitizer treatment of THP-1-derived CD14⁻, CD11c⁺ immature dendritic cells (iDCs) resulted in the phosphorylation of p38 MAPK in the presence of 1-chloro-2,4-dinitrobenzene (DNCB) (2.6-fold) as well as in degradation of the inhibitor protein kappa B alpha (IkB α) upon incubation with NiSO₄ (1.6-fold). Furthermore, NiSO₄ led to an increase in mRNA levels of IL-6 (2.4-fold), TNF- α (2-fold) and of IL-8 (15-fold). These results were confirmed on the protein level, with even stronger effects on cytokine release in the presence of NiSO₄: Cytokine secretion was significantly increased for IL-8 (147-fold), IL-6 (11.8-fold) and IL-1 β (28.8-fold). Notably, DNCB treatment revealed an increase for IL-8 (28.6-fold) and IL-1 β (5.6-fold). Importantly, NiSO₄ treatment of isolated iDCs as well as of iDCs integrated as dermal dendritic cell surrogates into our full-thickness skin model (SM) induced the upregulation of the adhesion molecule clusters of differentiation (CD)54 (iDCs: 1.2-fold; SM: 1.3-fold) and the co-stimulatory molecule and DC maturation marker CD86 (iDCs ~1.4-fold; SM: ~1.5-fold) surface marker expression. Noteworthy, the expression of CD54 and CD86 could be suppressed by dexamethasone treatment on isolated iDCs (CD54: 1.3-fold; CD86: 2.1-fold) as well as on the tissue-integrated iDCs (CD54: 1.4-fold; CD86: 1.6-fold). In conclusion, we were able to integrate THP-1-derived iDCs as functional dermal dendritic cell surrogates allowing the qualitative identification of potential sensitizers on the one hand, and drug candidates that potentially suppress sensitization on the other hand in a 3D human skin model corresponding to the 3R principles ("replace", "reduce" and "refine").

KEYWORDS

full-thickness skin model, dermal dendritic cell, nickel, DNCB, CD86, p38 MAPK, NF- κ B

Introduction

Immune responses in the skin are mediated by antigen-presenting cells (APCs) such as macrophages, monocytes and most importantly dendritic cells (1). Cutaneous dendritic cells include epidermal Langerhans cells (LCs) and dermal dendritic cells (DDCs), located beneath the epidermal-dermal junction and throughout the dermis (2). While Langerhans cells are characterized by the expression of Langerin (3), to date, no specific marker exclusively expressed on all dermal dendritic subsets has been reported. However, dermal dendritic cells can be identified and distinguished from dermal monocytes and macrophages by a low CD14 expression and a high CD11c expression (4, 5). Yet, the primary and common function of all cutaneous dendritic cell subsets includes endocytosis/phagocytosis, processing and presenting antigens to naïve T cells (6).

The activation of cutaneous dendritic cells can be divided into different central events (Figure 1): Upon exposure to inflammatory stimuli like interleukin (IL)-1 β , lipopolysaccharide (LPS) or sensitizing agents such as 1 chloro-2,4-dinitrobenzene (DNCB) or nickel sulfate (NiSO₄), keratinocytes start to secrete a variety of cytokines including IL-1, TNF- α or IL-18 (7–9). Consequently, cutaneous dendritic cells such as Langerhans cells and dermal dendritic cells become activated and start to phagocytose the hapten accompanied by cell maturation and the upregulation of adhesion molecules, such as clusters of differentiation (CD)54 and co-stimulatory molecules including CD80 and CD86 (10, 11). Upregulation of the intracellular adhesion molecule (ICAM-1)/CD54 is required to form a stable signaling structure, the so-called immunological synapse (IS) with the leukocyte function-associated antigen 1 (LFA-1) alpha (CD11a) and beta-2 (CD18) in naïve CD4 $^+$ T cells (12). High expressions of CD80 (B7-1) and CD86 (B7-2) finally ensure the co-stimulation of naïve CD4 $^+$ T cells via their CD28 and cytotoxic T-lymphocyte-associated protein 4 (CTLA-4)/(CD152) receptors (13).

Regarding the underlying intracellular signal transduction, different studies with cord blood derived DCs as well as PBMC derived DCs were able to prove the central role of the mitogen-activated protein kinases (MAPK) pathway and the nuclear factor (NF)- κ B pathway in skin sensitization and dendritic cell activation (14–16). Inhibition of the p38 MAPK pathway inhibited the upregulation of the DC maturation markers CD80, CD86 and CD83 in PBMC derived DCs (16). In addition, the up-regulation and secretion of IL-1, IL-8 and tumor necrosis factor (TNF)- α was suppressed (15, 16). Inhibition of the NF- κ B pathway resulted in a downregulation of CD86 and CD83 and abolished the secretion of IL-8, IL-6 and IL-12p40 in cord blood derived DCs (14). While IL-8 functions as a chemotactic for neutrophils and T cells (17, 18), IL-6 is considered as a pleiotropic cytokine involved in DC maturation, T cell differentiation and proliferation as well as in B cell activation (19). TNF- α induces the expression of adhesion molecules such as vascular endothelial cell adhesion molecule (VCAM)-1 and ICAM-1 as well as T cell infiltration into the skin (20). IL-1 induces the expression of adhesion molecules on endothelial cells, promotes T cell priming, causes vasodilatation and hypotension (21, 22). Finally, secretion of IL-12 leads to upregulation of the transcription factor T-

box expressed in T cells (T-bet) promoting T cell differentiation into interferon- γ producing T helper 1 cells (Th1) (23, 24).

In the past decades, dendritic cell activation, toxicological assessment studies, as well as studies investigating pathophysiological pathways of inflammatory skin diseases have been conducted almost exclusively in animal models, mostly in mice. However, when compared to the situation in humans, species-specific differences in the anatomy, immune cell populations, especially in DC subsets, and pathophysiology are tremendous (25). Furthermore, humans and mice have only ~ 30% of skin-associated genes in common (26), which impairs the translation from mouse models to human skin diseases. Admittedly, human *ex vivo* skin explants are a valuable tool for research; however, they are limited by ethical approval, logistics and high donor and anatomic site variation (27–29). Hence, there is an urgent need for alternative predictive human *in vitro* models.

Immune competent skin models reported to date focus mostly on the integration of Langerhans cell surrogates either derived from the human myeloid leukemia-derived cell line Mutz-3 (30–35), originated from cord-blood derived CD34 $^+$ hematopoietic progenitor (36, 37) or generated from CD14 $^+$ peripheral blood mononuclear cells (32). Notably, only one full-thickness skin equivalent has been described containing LC and DDC surrogates derived from CD14 $^+$ monocytes isolated from peripheral blood mononuclear cells aiming at analyzing the impact of ultraviolet (UV) stress on skin immune cells (38). However, no immune competent human full-thickness model with integrated functional dermal dendritic cells for sensitizer or drug analysis has been described so far. This is surprising as several studies have indicated the crucial role of DDC for antigen presentation in the skin. For instance, after sensitizer treatment dermal dendritic cells might migrate and activate T cells faster and outnumber LCs by 10:1 in draining lymph nodes (39, 40). Furthermore, DDCs might be able to induce a stronger T cell proliferation than LCs (39).

Our previously published results showed that the human monocytic cell line THP-1 can be differentiated into immature dendritic cells (iDCs), displaying a sufficient ability and sensitivity to robustly identify classified proficiency chemicals and model sensitizers such as DNCB and NiSO₄ *in vitro*. Furthermore, as expected from antigen presenting cells, THP-1-originated iDCs have proven to phagocytose membrane components derived from pathogens such as zymosan and, finally, iDCs might be able to induce T cell activation via upregulation of IL-12p40 upon sensitizer treatment (41). Since THP-1-derived iDCs fulfill all required *in vitro* criteria, we aim to demonstrate in this study the functionality of stably integrated iDCs as dermal dendritic cell surrogates within a human full-thickness skin model and their subsequent molecular characterization before and after sensitizer treatment.

Materials and methods

Generation of immature dendritic cells

Immature dendritic cells were generated according to the protocol described by Hölken and Teusch (41). In total, 1 x 10⁶

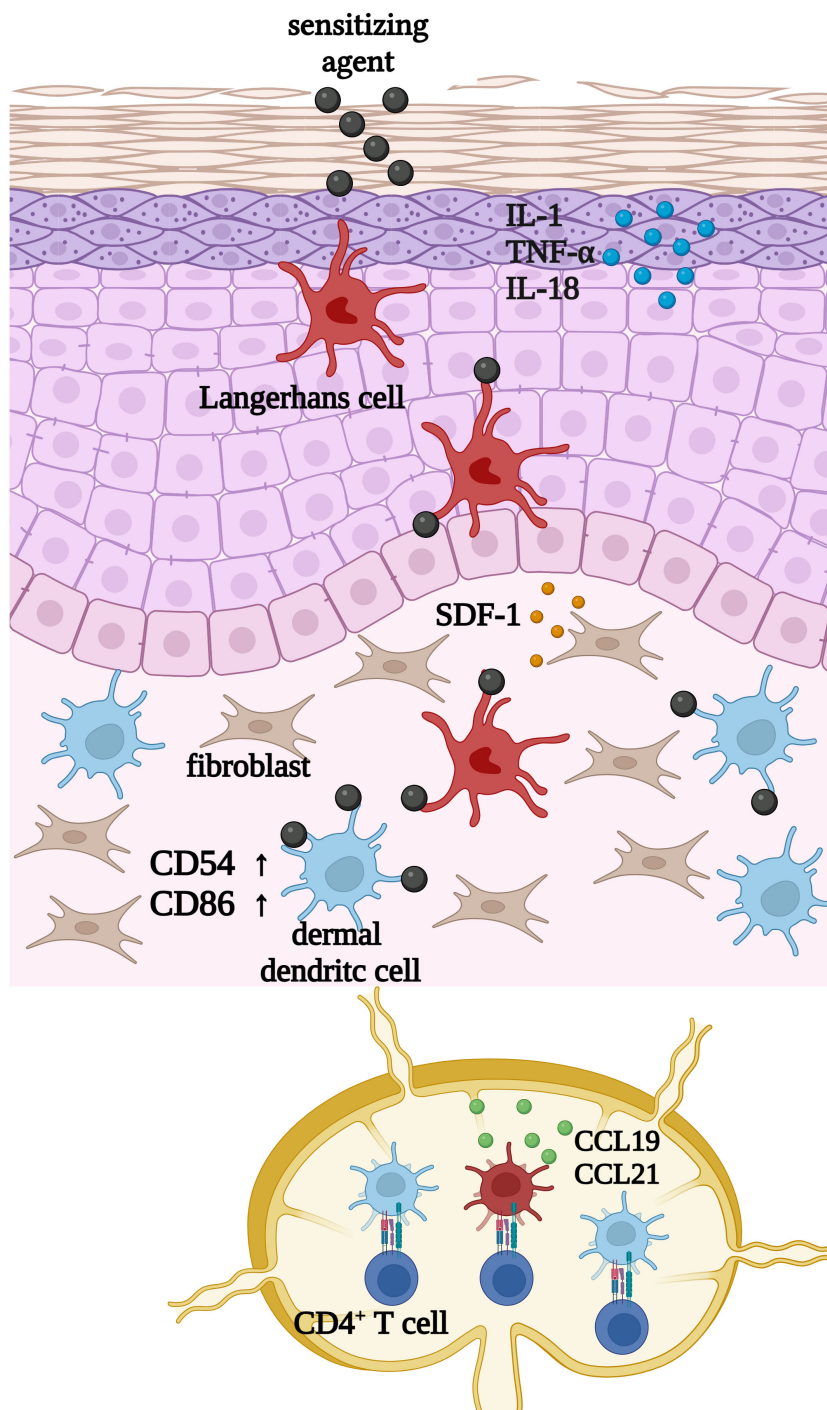


FIGURE 1

Upon exposure to inflammatory stimuli such as LPS, or sensitizing chemicals such as 1 chloro-2,4-dinitrobenzene (DNCB) or nickel sulfate (NiSO_4), keratinocytes start to secrete inflammatory cytokines such as IL-1, TNF- α and IL-18. Subsequently cutaneous dendritic cells such as Langerhans cells and dermal dendritic cells become activated and start to phagocytose haptens or exogenous particles, which is accompanied by cell maturation and the upregulation of CD54 and CD86. Finally, DCs migrate to draining lymph nodes to present the processed antigen in order to activate CD4 $^{+}$ T cells. Created with [BioRender.com](https://biorender.com).

THP-1 cells were seeded in 5 mL RPMI-1640 (Gibco, #22400089) containing 10% FBS (Gibco, #10270-106), 50 U/mL Pen-Strep (Gibco, #15140122) and 50 μ M 2-mercaptoethanol (Gibco, #21985023) into a T25 flask. For the differentiation 1500 IU/mL

rhGM-CSF (ImmunoTools, #11343125) and 1500 IU/ml rhIL-4 (ImmunoTools, #11340045) were added with a medium exchange on day 3. The cells were incubated in total for 5 days at 37°C, 5% CO₂.

Sensitization assays

1×10^6 THP-1-derived iDCs were seeded into a 24-well plate in 1 mL RPMI-1640 containing 10% FBS, 50 U/ml Pen-Strep, and 50 μ M 2-mercaptoethanol. Cells were pre-treated with 1 μ M dexamethasone (Peprotech, #5000222) for 1 h. Afterwards cells were treated with 1-chloro-2,4-dinitrobenzene (DNB) [20 μ M] (Sigma-Aldrich, #237329, Darmstadt, Germany), nickel sulfate (NiSO_4) [380 μ M] (Sigma-Aldrich, #227676) or their respective solvent control dimethyl sulfoxide (DMSO). After 24 h, the cells were harvested for the analysis of surface marker expression via flow cytometry.

Flow cytometry

The cells were harvested after differentiation, treatment or skin model dissociation and washed in Automacs Running Buffer (Miltenyi, #130-091-221). At least 2×10^5 cells for each antibody panel were transferred to 96-well u-bottom plates. For staining the cells were incubated in Automacs Running Buffer with the following antibodies (1:50): REA Control (S)-VioGreen (Miltenyi, #130-113-444), REA Control (S)-PE (Miltenyi, #130-113-438), REA Control (S)-APC (Miltenyi, #130-113-434); REA Control (S)-PE-Vio770, (Miltenyi, #130-113-440); CD54-APC (Miltenyi, #130-121-342); CD86-APC (Miltenyi, #130-116-161), CD14-VioGreen (Miltenyi, #130-110-525), CD11c-APC (Miltenyi, #130-113-584) for 10 minutes in the dark. For single cells from the dissociates skin models the following antibodies were used (1:50): CD45-VioBright R667 (Miltenyi, #130-110-779), CD54-PE-Vio770 (Miltenyi, #130-127-992), CD86-PE-Vio770 (Miltenyi, #130-116-265). The cells were washed twice with automacs running buffer. To determine the cell viability, cells were stained with DAPI (Sigma, #D9542). Flow cytometry analysis was performed using the CytoFlex (B5-R3-V5) from Beckman Coulter.

Western blot analysis

THP-1-derived iDCs were seeded with 1×10^6 cells into a 24-well plate in 1 mL RPMI-1640 containing 10% FBS, 50 U/ml Pen-Strep, and 50 μ M 2-mercaptoethanol. Cells were treated with DNB [25 μ M] (Sigma-Aldrich, #237329) and NiSO_4 [500 μ M] (Sigma-Aldrich, #227676) for 30 min or 1 h. Cells were harvested, washed once in 1x PBS and lysed with radioimmunoprecipitation assay (RIPA) buffer containing a protease inhibitor (Roche, #11836170001) and a phosphatase inhibitor (Roche, #04906845001). Protein concentration was determined using a BCA protein assay kit (Thermo Scientific, 23227). For western blot analysis, Laemmli buffer (Bio-Rad Laboratories, Inc., #1610747) was added to 20 μ g protein lysate. Proteins were denatured for 10 min at 95°C and separated on 10% SDS-Gels using a Biometra Eco-Mini Buffer Tank system (Analytik Jena, #846-017-103/017-170). Protein transfer to a PVDF membrane (BioRad Laboratories, Inc., #1620177) was performed with the Biometra Fastblot system (Analytik Jena, #846-015-299). The

membrane was blocked in 5% BSA (Roth, #8076.2) and then incubated with the respective primary antibodies, p38 MAPK (Cell Signaling Technology, #8690T), phospho-p38 MAPK (Thr180/Tyr182) (Cell Signaling Technology, #4511T), I κ B α (Cell Signaling Technology, #9242S) or vinculin (Cell Signaling Technology, #13901S) over night at 4°C. After washing with 1x TBS-T the membrane was incubated with the respective horseradish peroxidase-coupled secondary antibody (Goat anti-Rabbit (H+L), Thermo Fisher Scientific, #31460) for 1 h at room temperature. Antibody binding was detected with the SuperSignal West Pico Plus substrate kit (Thermo Fisher Scientific, #34577). For imaging we used a ChemStudio Imager (Analytik Jena, #849-97-0928-04).

qRT-PCR

THP-1-derived iDCs were seeded with 1×10^6 cells into a 24-well plate in 1 mL RPMI-1640 containing 10% FBS, 50 U/ml Pen-Strep, and 50 μ M 2-mercaptoethanol. Cells were treated with DNB [20 μ M] (Sigma-Aldrich, #237329) and NiSO_4 [380 μ M] (Sigma-Aldrich, #227676) or their respective solvent control dimethyl sulfoxide (DMSO) for 6 h. RNA-extraction was performed using the RNeasy MiniKit (Qiagen, #74104). Following, the RNA yield and concentration was determined via OD260/280 measurement using the Tecan Spark NanoQuant Plate. For reverse transcription the QuatiTect Reverse Transcription Kit (Qiagen, #205311) was used and a total of 1 μ g of RNA was transcribed. Quantitative real-time PCR (qPCR) reactions were performed in triplicates for 50 ng cDNA per sample using Luna Universal qPCR Master Mix (NEB, #M3003L) on a qTower3 G (Analytik Jena, #844-00556-2). The specific primers used were GAPDH (forward, 5'-TGCACCAACTGCTTAGC-3'; reverse, 5'-GGCATGGACTGTGGTCATGAG-3'), IL-6 (forward, 5'-GGCACTGGCAGAAAACAACC-3'; reverse, 5'-GCAAGTCTCC TCATTGAATCC-3'), IL-8 (forward, 5'-ACTGAGAGTGATT GAGAGTGGAC-3'; reverse, 5'-AACCTCTGCACCCAGTTTC-3'), TNF- α (forward, 5'-CCCTGCTGCACTTGGAGTG-3'; reverse, 5'-TCGGGGTCGAGAAGATGAT-3'). After amplification, a threshold was set for each gene and Ct values were calculated for all samples.

Cytokine secretion

THP-1-derived iDCs were seeded with 1×10^6 cells into a 24-well plate in 1 mL RPMI-1640 containing 10% FBS, 50 U/ml Pen-Strep, and 50 μ M 2-mercaptoethanol. Cells were treated with DNB [20 μ M] (Sigma-Aldrich, #237329) and NiSO_4 [380 μ M] (Sigma-Aldrich, #227676) or their respective solvent control dimethyl sulfoxide (DMSO). Supernatants were collected after 24 h for cytokine analysis. Secretion of the inflammatory cytokines was detected according to the manufacturer's instructions of the Cytometric Bead Array Human Inflammatory Cytokines Kit (BD, #551811) and the CytoFlex (B5-R3-V5) from Beckman Coulter. Analysis was performed using the CBA Analysis Software (BD Biosciences).

3D immune competent skin model generation

Feeder cells (Phenion, #hFeeder) were seeded with 5×10^5 cells in 23 mL keratinocyte medium (Phenion, #K CM-250) into a T175 flask. After three days 5×10^5 primary human foreskin keratinocytes from juvenile donors (Phenion, #hK P1) were seeded onto the feeder cells. After 6 days of cultivation, feeder cells were detached by incubation with 0.05% trypsin (Gibco, #25300054) for 2 min at 37°C, 5% CO₂ and keratinocytes were harvested using 0.05% trypsin for 6 min, 37°C, 5% CO₂. 5×10^5 Keratinocytes in P2 were seeded together with 1×10^6 THP-1-derived iDCs (ratio 1:2) in 1 mL keratinocyte medium (Phenion, #K CM-250) onto dermis models based on a solid and porous collagen matrix (42, 43) and primary human foreskin fibroblasts (kindly provided by Henkel AG & Co. KGaA, Düsseldorf, Germany). After 24 h of incubation at 37°C, 5% CO₂ the medium was exchanged. After 24 h submerge phase, the skin models were lifted into the Air-liquid Interface and cultivated with Air-liquid Interface Culture Medium (Phenion, #ALI CM HC-250, w/o hydrocortisone) for 10 to 14 days.

Cryosectioning and immunofluorescence staining

Skin models were embedded and frozen in Tissue-Tek (Sakura, #4583), cut into 7 μm slices and transferred to Microscope slides (expredia, #J1800AMNZ). The tissue slides were fixed in ice-cold acetone for 10 minutes and blocked in 10% normal goat serum (Invitrogen, #50062Z), for 1 h at room temperature. Primary antibodies were diluted in DAKO antibody diluent (Dako, #S0809) and Cytokeratin 5 (OriGene, DM361) (1:75) and CD45-VioBright R667 (Miltenyi, #130-110-779) (1:50) were applied for staining at 4°C overnight. Secondary antibody staining with Alexa Flour 488 (Invitrogen, #A11017) (1:200) combined with DAPI staining (10 μg/ml) (Sigma, ##D9542) was performed for 1 h at room temperature (RT). The stained tissue slides were imbedded with Tissue Fluorescence mounting medium (Agilent, S3023) to avoid bleaching and imaged using confocal spinning disc microscopy (CQ1, Yokogawa). For immunofluorescent staining of the isolated iDCs, cells were transferred into a 96 well plate and fixed with 4% paraformaldehyde (PFA) (Roth, #0964.1) for 10 min. The cells were blocked and permeabilized in 0.1% BSA (Roth, #8076.2), 0.01% Tween20 (Sigma, #P7949) and 0.1% Triton X100 (Sigma, #T9284) in 1x PBS for 30 min. The primary antibody CD45-VioBright R667 was diluted 1:50 in DAKO antibody diluent and applied over night at 4°C. DAPI staining (10 μg/ml) was performed the next day for 1 h at RT. Washing steps were performed each 3x with 1 x PBS at 200 xg for 3 min. Immunofluorescent staining of the cells was analyzed using fluorescence microscopy (Keyence, #BZ-X800L/BZ-X810).

Hematoxylin and eosin staining

Skin models were fixed in 4% formaldehyde solution (Roth, #P087.5) for at least 24 h before dehydration was

conducted in the automated tissue processor (Sakura Finetek USA, Inc., #Tissue-Tek VIP 5 Jr.). For paraffin embedding, samples were processed on Histo Core Arcadia C/H (Leica) and cut into 5 μm sections with the rotary microtome (Leica, #RM2145). Transferred sections on object slides were dried overnight at 37°C in a heating cabinet (Memmert) followed by automated hematoxylin and eosin staining procedure (Thermo Scientific, #Gemini AS). Images were taken with Olympus microscope (BX51, Camera Olympus DP7).

Skin model dissociation

The immune competent skin models were digested on ALI day 11, 24 h after sensitizer treatment. The tissue was minced via scalpel and tissue scissors and transferred to 1.5 ml tubes. For enzymatic dissociation 1 mL RPMI-1640 containing 10% FBS, 50 U/mL Pen-Strep, 50 μM 2-mercaptoethanol, 100 μg/mL liberase (Roche, #05401119001) and 40 μg/mL DNase (Roche, #10104159001) was added and the tissue was incubated for 90 min at 37°C, 400 RPM on a thermoshaker (Eppendorf, #PMCT). After 90 minutes, the dissociated cell suspension was filtered through a 70 μm cell strainer (VWR, #732-2758) to obtain single cell suspensions. The cells were washed with PBS and stained for flow cytometry analysis.

Statistical evaluation

Analysis of the data was conducted with GraphPad Prism version 8.4.3 (GraphPad Software, Inc., San Diego, CA, USA). Statistical significance was calculated using an unpaired t-test, one-way ANOVA or two-way ANOVA. Significance was defined and referred to as * = p ≤ 0.05; ** = p ≤ 0.01; *** = p ≤ 0.001; **** = p ≤ 0.0001.

Results

When compared to original THP-1 cells our recent study confirmed the expected pronounced ability of THP-1-derived iDCs to phagocytose pathogen membrane particles such as zymosan. Furthermore, iDCs, but not undifferentiated THP-1 cells, are able to induce T cell activation via upregulation of IL-12p40 upon sensitizer treatment (41). Thus, a logical subsequent step is to prove whether the iDCs might be suitable surrogates for dermal dendritic cells. Firstly, the expression of CD11c, which is known to be highly expressed on dermal dendritic cells, and the absence of CD14, a marker for monocytic cells and often used to distinguish DCs from monocytes and macrophages, was investigated. While undifferentiated THP-1 cells, as well as THP-1-derived iDCs express almost no CD14, both express CD11c. However, the expression of CD11c is significantly higher (~1.3-fold) on THP-1-derived iDCs compared to THP-1 cells (Figures 2A, C). Hence, our iDCs might be suitable CD14⁻, CD11c⁺ dermal dendritic cell surrogates for the integration into a full-thickness skin model.

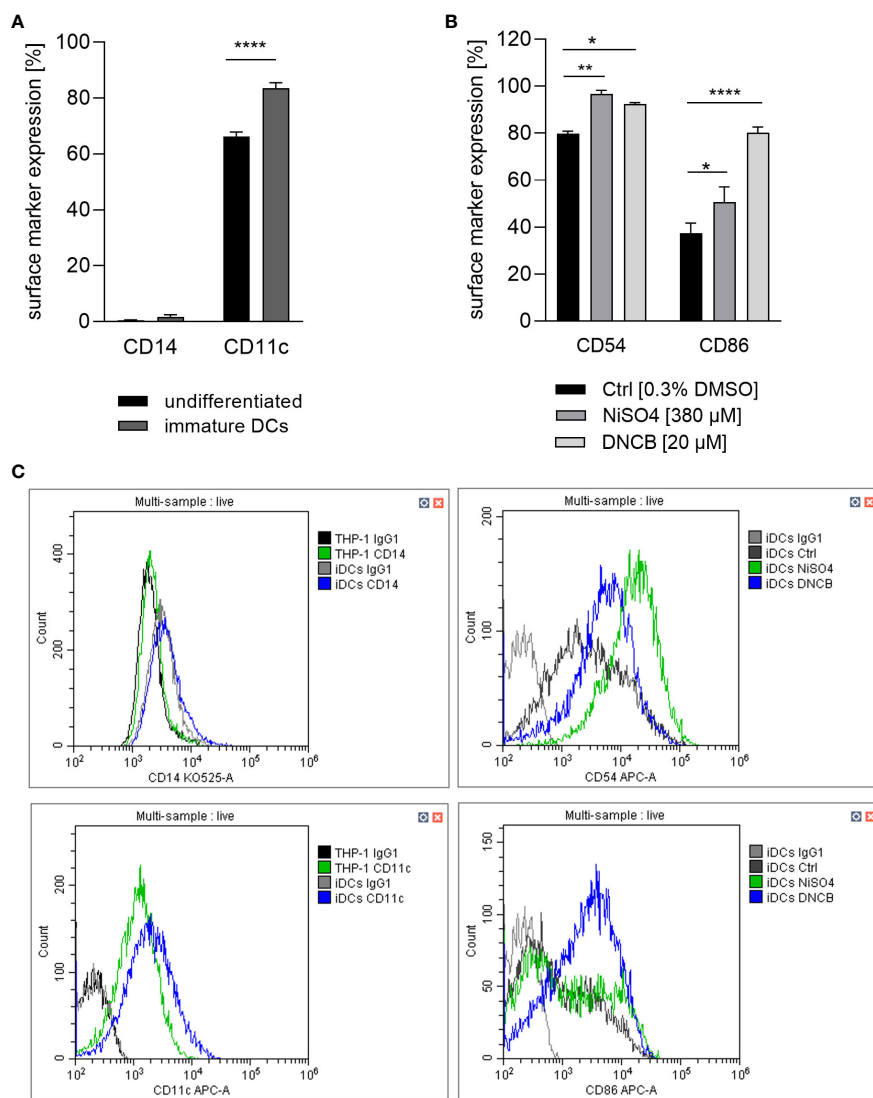


FIGURE 2

(A) CD14 and CD11c surface marker expression of the undifferentiated THP-1 cell line and THP-1-derived iDCs. THP-1 cells were differentiated with 1500 U/ml GM-CSF and 1500 U/ml IL-4 for 5 days, with medium exchange on day 3. (B) iDCs were treated with NiSO₄ [380 μM] and DNCB [20 μM] for 23 h. (C) Gating strategy. Surface marker expression (depicted as percentage of positive cells) of at least 10,000 viable cells was analyzed via flow cytometry. Error bars indicate the standard errors of the mean (n = 3 independent experiments with *p ≤ 0.05 and ****p ≤ 0.0001).

Dendritic cell activation and maturation is characterized by the upregulation of adhesion molecules like CD54 and co-stimulatory molecules and DC maturation markers such as CD86, which are both required for the stimulation of T cells. As expected, treatment of iDCs with NiSO₄ led to a significantly higher expression of CD54 (~97%) and CD86 (~51%) while DNCB also resulted in a significantly upregulation of CD54 (~93%) and an even higher expression of CD86 (~80%) compared to the solvent control (CD54: ~80%, CD86: ~37%) (Figures 2B, C). Furthermore, a few studies demonstrated the activation of the NF-κB pathway in the presence of nickel salts (14, 15). In contrast, for DNCB a phosphorylation of p38 MAPK in DC surrogates was shown (14–16). Moreover, it was proven that both pathways are required for the upregulation of DC activation markers and the subsequent secretion of inflammatory cytokines such as IL-8, IL-6, IL-1 or TNF-α (14–16). We therefore investigated the activation

of these pathways as well as the expression of inflammatory cytokines. Treatment of iDCs with 500 μM NiSO₄ led to significant reduction (1.6-fold) of the inhibitor protein kappa B alpha (IκBα) expression, but (according to previously reported studies) no significant phosphorylation of p38 MAPK could be detected. Contrary, DNCB [25 μM] treatment led to a significant phosphorylation of p38 MAPK (2.6-fold), but no degradation of IκBα (Figure 3).

In order to prove whether our iDCs are able to up-regulate the expression and to secrete inflammatory cytokines after sensitizer treatment similar to previously reported DC surrogates from various sources, mRNA levels of the inflammatory cytokines IL-8, IL-6 and TNF-α were analyzed. Treatment of iDCs with NiSO₄ [380 μM] for 6 h induced significant upregulation of mRNA levels for IL-8 (15-fold), IL-6 (2.4-fold) and TNF-α (2-fold). DNCB [20 μM] treatment led to significantly higher IL-8 mRNA levels (17-fold),

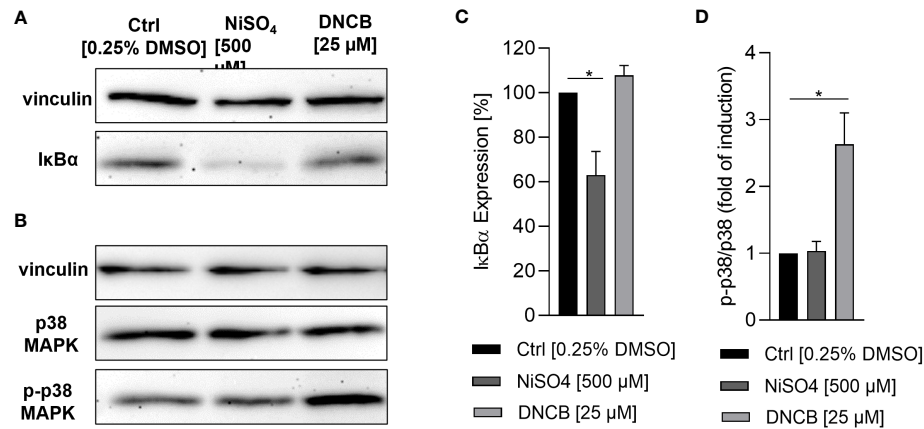


FIGURE 3

Activation of inflammatory pathways in iDCs after sensitizer treatment. **(A, C)** Degradation of IκBα after NiSO₄ [500 μM] and DNCB [25 μM] treatment for 1 h, respectively. **(B, D)** Phosphorylation of p38 MAPK after NiSO₄ [500 μM] and DNCB [25 μM] treatment for 30 min. **(A, B)** depict one representative blot of three independent experiments. The housekeeping gene vinculin serves as a loading control. **(C, D)** Show the quantification of image bands normalized to the solvent control. Error bars indicate the standard errors of the mean ($n = 3$ independent experiments with $*p \leq 0.05$).

but no significant upregulation of IL-6 and contrary to NiSO₄ treatment, significant reduction of TNF- α mRNA levels (0.2-fold) (Figure 4). To confirm the mRNA results on the protein level, iDCs were treated for 24 h with 380 μM NiSO₄ or 20 μM DNCB and the absolute cytokine concentration was determined via a Multiplexing Cytometric Bead Array Assay. Treatment of iDCs with NiSO₄ induced the secretion of ~17,000 pg/ml IL-8, ~20 pg/ml IL-6, ~30 pg/ml IL-1 β and ~7 pg/ml TNF- α , respectively, while DNCB treatment induced the secretion of ~3376 pg/ml IL-8 and ~5.8 pg/ml IL-1 β . Secretion of IL-6 and TNF- α could not be detected after DNCB treatment (Figure 5). Overall, upon sensitizer treatment THP1-derived iDCs are able to secrete inflammatory cytokines relevant for the activation and recruitment of T cells in the skin, although in different patterns depending on the applied sensitizers.

Next, we aimed to integrate the iDCs into a full-thickness skin model as potential dermal DC surrogates and to prove their functionality *in vitro*. Therefore, iDCs were integrated into the well-established and commercially available Phenion® Full-Thickness Skin Model (44–46). The Phenion® Full-Thickness Skin Model comprises a fully stratified epidermis including a

stratum basale, stratum spinosum, stratum granulosum and stratum corneum as well as a mechanically stable dermis. The rigid porous structure allows the fibroblasts to migrate into the scaffold and to synthesize and secrete extracellular matrix components such as elastin and fibrillin-1, mimicking the elastic network of native human skin (44, 47) and thereby potentially providing the organ-specific environment for DDCs.

To develop an immune competent skin model, iDCs, were seeded together with primary human keratinocytes onto matured dermis equivalents. After 10 days of air-liquid interphase (ALI) cultivation, allowing the complete differentiation of all epidermal layers, the skin models were either cryo-sectioned for histological analysis or treated with a sensitizer (NiSO₄ or DNCB) for 24 h and subsequently proceeded towards enzymatic dissociation and DC surface marker analysis (Figure 6A). On ALI day 10, the skin model is fully differentiated displaying all epidermal layers typical for native human skin including a stratum corneum, and a dermal compartment enriched with newly synthesized ECM proteins (Figures 6, 7A, C). Histological analysis of the full-thickness skin models reveals the integration of iDCs in the dermis, mostly located

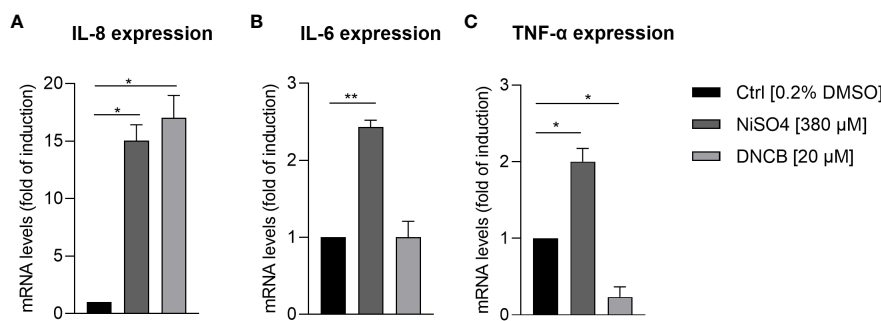


FIGURE 4

mRNA levels of inflammatory cytokine expression by iDCs: **(A)** IL-8, **(B)** IL-6, **(C)** TNF- α , after NiSO₄ [380 μM] and DNCB treatment [20 μM] for 6 h. Results are depicted as fold of induction compared to the solvent control [0.2% DMSO] and normalized to the expression of the housekeeping gene [GAPDH]. Error bars indicate the standard errors of the mean ($n = 3$ independent experiments with $*p \leq 0.05$, $**p \leq 0.01$).

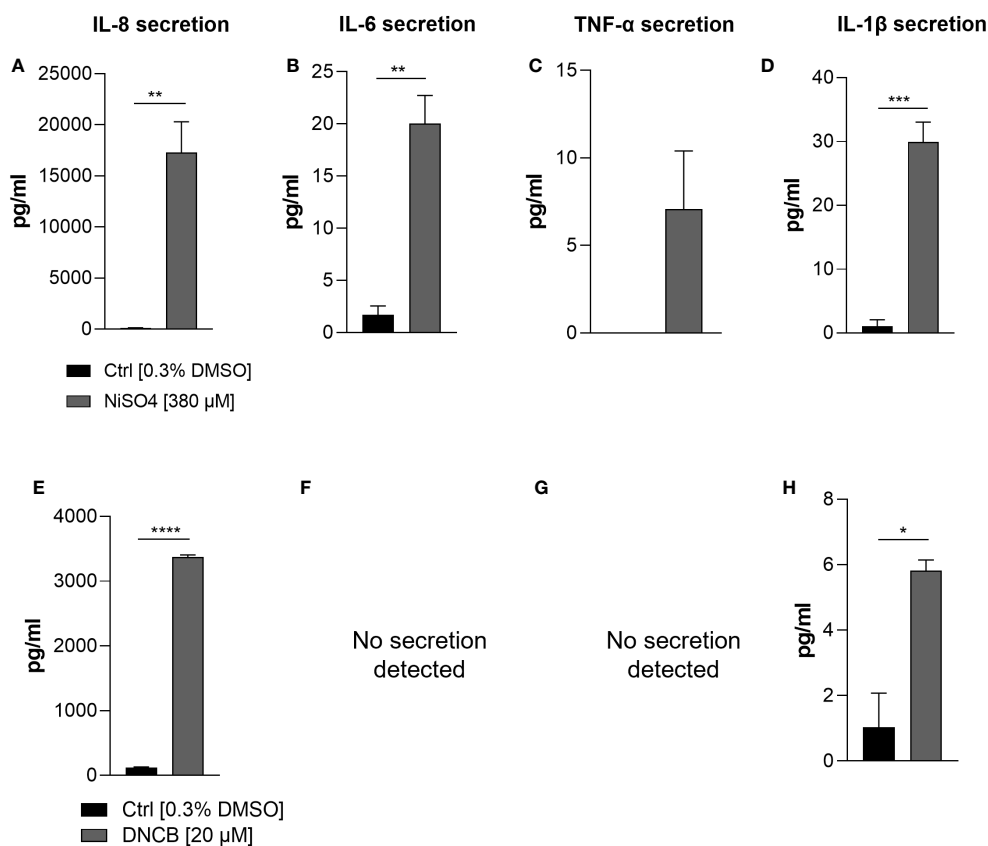


FIGURE 5

Secretion of inflammatory cytokines: IL-8 (A, E), IL-6 (B, F), TNF- α (C, G) IL-1 β (D, H) by iDCs after NiSO₄ [380 μ M] (A-D) and DNCB [20 μ M] (E-H) treatment. Supernatants were harvested after 24 h and cytokine concentrations were detected using a Cytometric Bead Array Assay. Error bars indicate the standard errors of the mean (n = 3 independent experiments with *p \leq 0.05, **p \leq 0.01, ***p \leq 0.001, and ****p \leq 0.0001).

underneath the epidermis, which proves the integration as dermal dendritic cells. Compared to the control model, the overall histology of the epidermis is not impaired by the integration of our iDCs and the epidermis remains fully stratified (Figure 7).

To prove whether iDCs are applicable to a qualitative characterization of sensitizers and perspectively of drug candidates, iDCs were pre-treated for 1 h with dexamethasone, an anti-inflammatory, anti-allergic synthetic glucocorticoid (48), before applying NiSO₄ [380 μ M] for 23 h. Treatment of isolated iDCs with NiSO₄ alone induced the upregulation of CD54 (~1.2-fold) and a significant upregulation of CD86 (~1.4-fold). The pre-treatment with dexamethasone led to the reduction of the NiSO₄ induced CD54 (~1.3-fold) expression and a significant reduction of the NiSO₄ induced CD86 expression (~2.1-fold) (Figure 8A) as well as a significant reduction of the IL-8 (23.5-fold), IL-6 (~20-fold) and IL-1 β (~30-fold) secretion (Figure 8C).

To validate the functionality and immune competence of the DDC surrogate skin model, a topical administration of dexamethasone [1 μ M] for 1 h was followed by a topical exposure of NiSO₄ [380 μ M] for 23 h. Afterwards, the skin models were dissociated enzymatically into single cell suspensions and CD45 positive cells were gated for the analysis of the CD54 and CD86 expression on the tissue-integrated iDCs. Topical treatment of the immune competent skin model with NiSO₄ alone induced a proven upregulation of CD54 (~1.3-fold) and

CD86 (~1.5-fold) on the iDCs dissociated from the dermal layer (Figure 8B), demonstrating the robust functionality of our dermal DC surrogates *in vitro*. Furthermore, pre-treatment with dexamethasone led to the reduction of the CD54 (~1.4-fold) and a significant reduction of the CD86 (~1.6-fold) expression on iDCs after topical treatment of the immune competent skin model (Figure 8B). In conclusion, we were able to engineer a skin model with fully functional dermal dendritic cell surrogates derived from the monocytic cell line THP-1. Furthermore, our immune competent skin model allows the qualitative identification of potential sensitizers and perspectively the evaluation of novel drug candidates potentially suppressing skin sensitization.

Discussion

The aim of this study was to explore and validate immature dendritic cells (iDCs) derived from the monocytic cell line THP-1 as suitable surrogates for dermal dendritic cells upon integration into a human full-thickness skin model. The ability of THP-1-derived iDCs to identify sensitizers such as NiSO₄ and DNCB and to upregulate the DC activation markers CD54 and CD86 has been recently shown (41). Furthermore, the capability to phagocytose pathogen-derived membrane components and to potentially induce

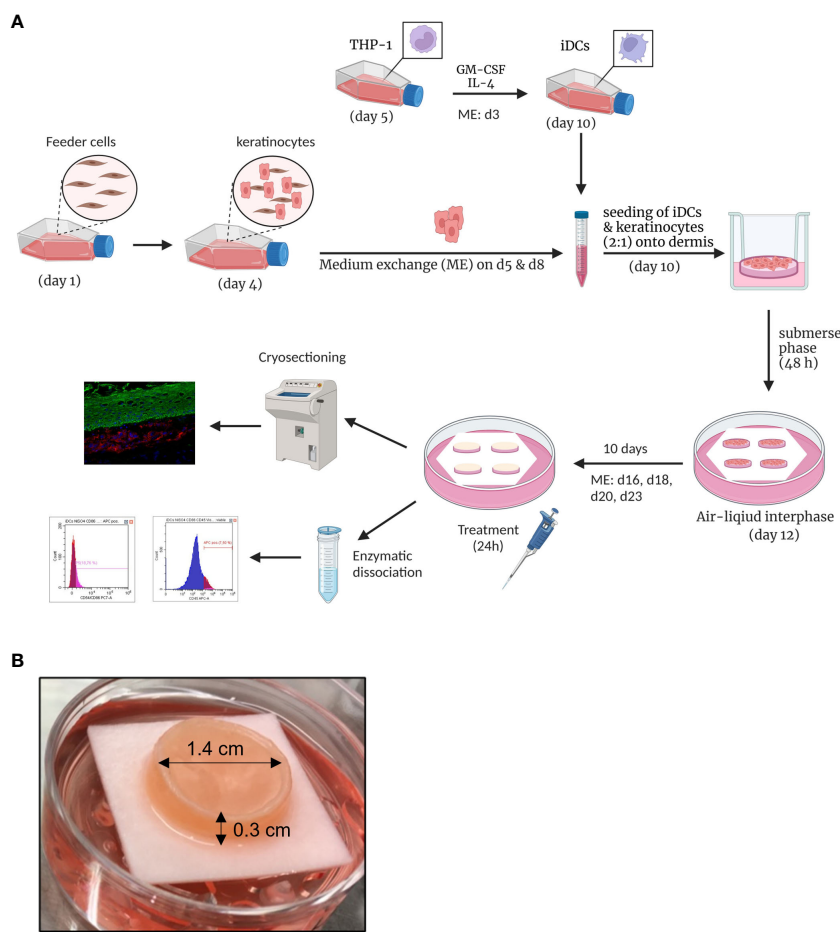


FIGURE 6

Engineering of human 3D immune competent full-thickness skin models. **(A)** Primary human foreskin keratinocytes are seeded onto feeder cells and harvested after six days of cultivation and seeded together with THP-1-derived iDCs (ratio 1:2) onto dermis models based on a solid collagen matrix and primary fibroblasts. After 48 h of cultivation in a submerge phase, the skin models are lifted into an air-liquid interphase. After 10 days, the skin models are cryo-sectioned for histological analysis or treated with sensitizers for 24 h and enzymatically dissociated. Created with [BioRender.com](https://biorender.com). **(B)** The full-thickness skin model is characterized by a diameter of 1.4 cm and a height of 0.3 cm. The photo was taken on ALI d10 and depicts our immune competent skin model with a fully differentiated epidermis.

T cell activation via upregulation of IL-12p40 upon sensitizer treatment has been proven (41). Subsequently, the next logically step was to prove whether our iDCs might be suitable surrogates for dermal dendritic cells.

Dermal dendritic cells can be identified and distinguished from dermal monocytes and macrophages by a low CD14 expression and a high CD11c expression (4, 5). However, in contrast to Langerhans cells, no exclusive cell-specific marker expressed on all dermal dendritic subsets has been reported so far. A commonly described low CD14 expression and a high CD11c expression could be confirmed on the THP-1-derived iDCs. In addition, the significant up-regulation of the DC activation markers CD54 and CD86 after NiSO₄ and DNCB treatment was verified, confirming the expected ability to respond to sensitizers as a required prerequisite for DC activation and subsequent maturation. Since several studies elucidated the necessity of the activation of the NF-κB pathway and the p38 MAPK pathway for the process of DC activation and maturation marker upregulation (14–16), we studied the impact of the two model sensitizers, NiSO₄ and DNCB on both

pathways in the THP-1-derived iDCs. In line with the published studies, we were able to confirm a significant degradation of IκBα after NiSO₄ treatment and an induction of phosphorylation of p38 MAPK after DNCB treatment. Treatment of DCs derived from human cord blood with NiSO₄ led to maximal degradation of IκBα after 1 h and recovery after 4 h, while treatment with DNCB could not induce the degradation of IκBα (14). Similarly, NiCl₂, but not DNCB treatment of PBMC-derived DCs for 1 h led to the phosphorylation and degradation of IκBα. In addition, the NiCl₂-induced activation of NF-κB could be proven via NF-κB p65 transcriptional factor assay kit (15). Conversely, DNCB treatment of human cord blood- derived DCs induced a strong phosphorylation of p38 MAPK after 30 min, while NiSO₄ treatment could only induce minor phosphorylation of p38 MAPK after 30 min (14). Furthermore, treatment of PBMC derived DCs with DNCB induced a strong dose-dependent phosphorylation of p38 MAPK (15). However, treatment of a fetal mouse skin-derived skin line with NiSO₄ induced only a weak phosphorylation of p38 MAPK after 2 h of treatment and

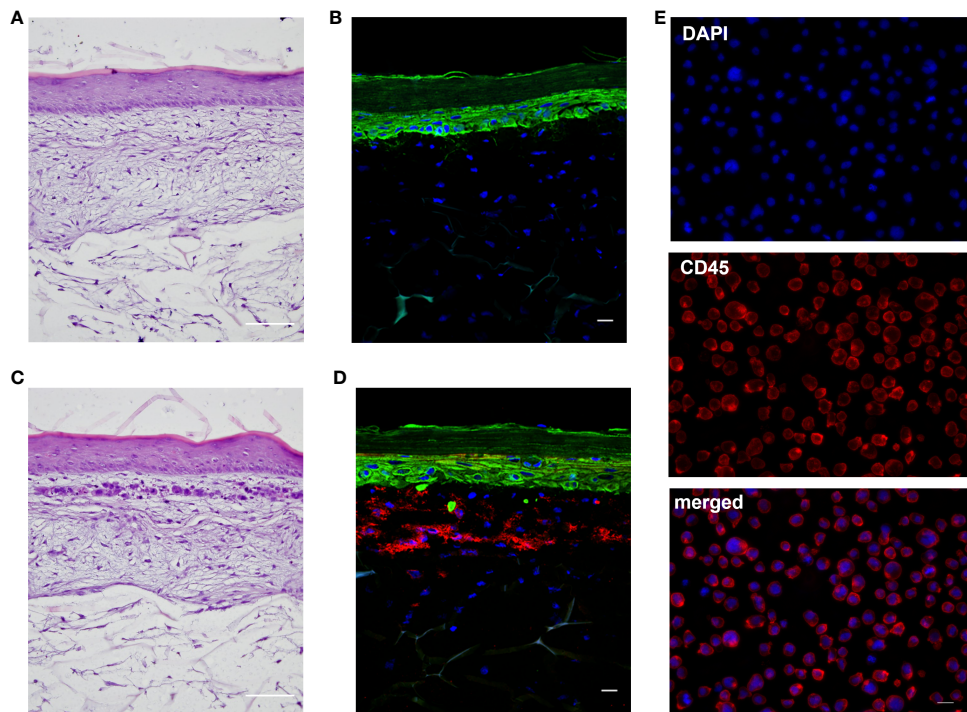


FIGURE 7

Histological analysis of the full-thickness skin models. (A, C): H&E staining of the regular model without immune cells (A) and the skin model including DDC surrogates (C). Scale bar = 100 μ m. (B, D): Immunofluorescent staining of the regular model without immune cells (B) and skin model including DDC surrogates (D). Keratinocytes were stained with cytokeratin 5 (green signal). DDC surrogates were stained with CD45 (red signal). Nuclei were stained with DAPI (blue signal). Scale bar = 20 μ m. (E) Immunofluorescent staining of DDC surrogates before integration into the skin models. DDC surrogates were stained with CD45 (red signal). Nuclei were stained with DAPI (blue signal). Scale bar = 20 μ m.

no degradation of $I\kappa B\alpha$ (49). In fact, sensitization to nickel in mice cannot be achieved without an additional adjuvant to induce the expansion of nickel reactive T cells, while in humans nickel functions as its own adjuvant via the Toll like receptor (TLR) 4, which was identified as receptor for Ni^{2+} in human, but not in mice (50). These results clearly underline the species-specific differences and the necessity to study the skin immunity in human-derived systems. Furthermore, it needs to be mentioned that the TLR4 mediated nickel skin sensitization is most likely guided by dermal dendritic cells, since TLR4 is not expressed on human LCs (51, 52).

Next to the sensitizer induced upregulation of DC activation and maturation markers such as CD54 and CD86 and the activation of the NF- κ B as well as the p38 MAPK pathways, the up-regulation and secretion of inflammatory cytokines such as IL-8, IL-6, IL-1 and TNF- α has been described for various DC surrogates (14–16, 53). Thus, we were intrigued to prove the sensitizer- induced expression and secretion of those interleukins in our iDCs as well. Treatment of iDCs with $NiSO_4$ resulted in a significant upregulation of mRNA levels for IL-8, IL-6 and TNF- α . These results were confirmed on the protein level, by significant higher cytokine secretion for IL-8, IL-6 and additionally IL-1 β . The secretion of IL-8 and IL-6 after $NiSO_4$ treatment has been shown for cord blood- derived iDCs as well (14). Furthermore, enhanced mRNA levels as well as cytokine secretion of IL-1 β , IL-6, IL-8, TNF- α could be detected after treatment of PBMC derived DCs with $NiCl_2$ (15, 53). Treatment of iDCs with DNCB led to a significant upregulation of mRNA

levels for IL-8 and IL-6 and significant cytokine secretion for IL-8 and IL-1 β . Treatment of PBMC derived iDCs with DNCB resulted in enhanced mRNA levels for IL-8, IL-1 β and TNF- α , but only in a significant increased secretion of IL-8 (15). However, treatment of PBMC derived DCs from a different study could prove in line with our results the DNCB induced secretion of IL-1 β and no secretion of IL-6 and TNF- α (53). Taken together, our results mirror the results published for other DC surrogates in regard of the p38 MAPK pathway, the NF- κ B pathway and inflammatory cytokine induction, suggesting distinct activation mechanisms, different targets and signaling pathways for DNCB compared to nickel salts. Investigating those differences, Ade et al. were able to show that the inhibition of NF- κ B with BAY 11-7085 suppressed the $NiSO_4$ induced increase of CD86 and CD83 and abolished the $NiSO_4$ induced secretion of IL-8, IL-6 and IL12-p40 in cord blood derived DCs (14). However, inhibition of p38 MAPK in PBMC derived DCs with PD98059 suppressed the $NiCl_2$ induced IL-1 β , IL-8, and TNF- α secretion (15). Inhibition of p38 MAPK in PBMC derived iDCs with SB203580 led to suppressed DNCB induced augmentation of CD86 as well as a suppressed secretion of IL-8 (15). Furthermore, it was shown that DNCB treatment inhibits TNF- α induced activation of the NF- κ B pathway in cord blood derived DCs (14). One hypothesis for the distinct mechanisms of action for $NiSO_4$ and DNCB could underly their lipophilicity. While DNCB as a lipophilic hapten is able to penetrate directly into the DCs, it can be processed endogenously and presented via MHC

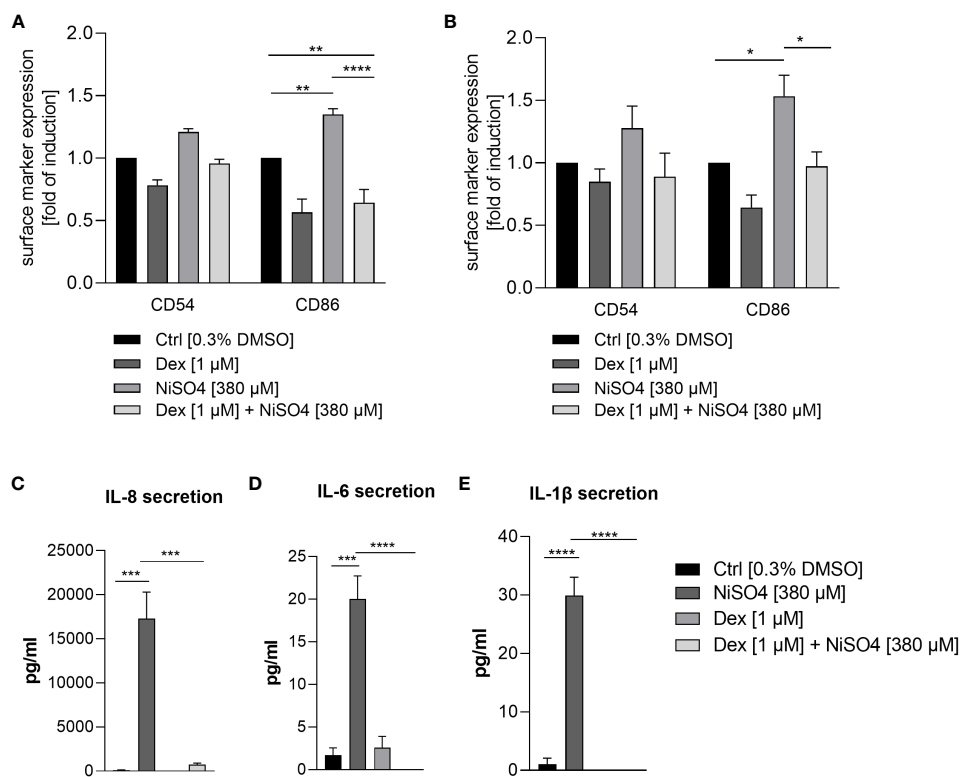


FIGURE 8

Surface marker expression of CD54 and CD86 (depicted as fold of induction of the percentage of all positive cells) after (A) pre-treatment of THP-1-derived iDCs and (B) topical treatment of the immune competent skin model with dexamethasone for 1 h, followed by NiSO₄ treatment for 23 h. Results were depicted as fold of induction compared to the solvent control [0.3% DMSO]. (C–E) Cytokine secretion of iDCs after 1 h dexamethasone pre-treatment, followed by 23 h of NiSO₄ exposure. Error bars indicate the standard errors of the mean (n = 3 independent experiments for (A, C) and n=4 independent experiments for (B) with *p ≤ 0.05, **p ≤ 0.01, ***p ≤ 0.001, and ****p ≤ 0.0001).

class I molecules, hydrophilic nickel ions are more likely processed exogenously and presented via the MHC class II molecules (54–56). In order to elucidate the distinct activation of iDCs upon sensitizer treatment, the molecular mechanism of the haptenization, including the (covalent) binding and modification of proteins followed by the individual, sensitizer or hapten specific DC activation, needs to be addressed in future studies. Although the binding capacity of migratory DCs in skin-draining lymph nodes was proven (57), unfortunately, to date, the precise mechanism of the DNCB and NiSO₄ DC activation has not been fully established. Furthermore, it has been reported that metal ions such as nickel are bound and presented via different ways to CD4⁺ T cells. While classic allergens such as DNCB tend to form covalent bonds with MHC-bound proteins, metal ions can interact via several molecular mechanisms with T cells (58).

By proving low CD14 and high CD11c expression, the activation of the p38 MAPK and the NF-κB pathway as well as the secretion of inflammatory cytokines after sensitizer treatment in addition to their capability to phagocytose pathogen-derived membrane particles, our THP-1-derived iDCs could be identified as potential dermal dendritic cell surrogates.

For compound characterization, a robust and relatively easily accessible human tissue platform would be desirable as an alternative to animal experiments or highly variable and time-

consuming transplants from human skin. Hence, the overall aim was to integrate the iDCs into a human skin model. For this the Phenion® Full-Thickness Skin Model was chosen due its unique porous matrix, which allows the fibroblasts to adhere to and migrate into the collagen and to secrete extracellular matrix components such as elastin and fibrillin-1 (44, 47), mimicking the elastic network of native human skin and thereby potentially providing the inevitable environment for DDCs. Histological analysis of the skin tissue revealed the integration iDCs in the dermis, predominantly underneath the epidermis. This location is in line with the observation for CD11c positive dendritic cells in normal human skin, which have been found to be located in the superior dermis (59). Contrary, cells expressing monocyte/macrophage markers such as CD14 or CD163 are largely located in the superior papillary and reticular dermis (59). Noteworthy, the integration of the iDCs as DDCs did not impair the stratification of the epidermis.

To prove the immune competence of the newly developed iDC containing full-thickness skin model, the skin models were treated topically with 380 μM NiSO₄ and 20 μM DNCB for 23 h and subsequently dissociated enzymatically into single cell suspensions for the analysis of the surface marker expression of CD54 and CD86 on the DDC surrogates (identified via CD45 expression). While treatment of iDCs with NiSO₄ only resulted in a 1.2-fold up-

regulation of CD54 and a 1.4-fold upregulation of CD86, topical sensitizer administration resulted in a 1.3-fold upregulation of CD54 and a 1.5-fold upregulation of CD86 on tissue-integrated iDCs. Thus, we were able to prove the functionality and thereby the immune competence of our DDC surrogate model 12 days after the integration of iDCs. Noteworthy, despite the vigorous enzymatic dissociation, the expression of both surface markers was still detectable on tissue-integrated iDCs and the upregulation could be detected in a similar manner (fold of induction) compared to the isolated iDCs. In fact, this is not self-evidently, as on one hand the protein expression pattern could change due to the complex three-dimensional co-cultivation with keratinocytes and fibroblasts and on the other hand the enzymatic tissue dissociation has been proven to alter or even diminish the cell surface antigen expression on distinct immune cell populations (60–63).

In order to initially assess the potential of our engineered skin tissue for drug discovery applications, we aimed to prove that our immune competent skin model is amenable for the qualitative characterization of putative anti-inflammatory compounds. Therefore, isolated iDCs as well as the immune competent skin model were treated with dexamethasone, an anti-inflammatory, anti-allergic synthetic glucocorticoid (48), for 1 h followed by 23 h of NiSO₄ exposure. Indeed, pre-treatment with dexamethasone significantly reduced the NiSO₄ induced secretion of IL-8, IL-6 and IL-1 β and could suppress the expression of CD54 and CD86 on isolated as well as on the tissue-integrated iDCs. In line with our results, the expression of CD54 and CD86 on murine bone marrow derived DC surrogates was downregulated by dexamethasone treatment in a dose-dependent manner and the secretion of IL-1 β was decreased significantly (64). Furthermore, the presence of dexamethasone during the differentiation of PBMC into DC surrogates decreased the basal expression of CD86 as well as the TNF- α induced upregulation of CD86 and the LPS-induced secretion of TNF- α and IL-1 β (65). By suppressing the expression of CD54 and CD86, as well as the secretion of IL-8, IL-6 and IL-1, which are required for the activation, stimulation and recruitment of T cells, dexamethasone might contribute to T cell inhibitory effects and thereby suppressing the immune response.

Altogether, the THP-1 derived iDCs are profoundly characterized by a low CD14 and high CD11c expression, the ability phagocytose membrane components derived from pathogens (41) and to identify sensitizers such as DNCB and NiSO₄, which is subsequently followed by the upregulation of adhesion molecules, such as CD54 and co-stimulatory molecules such as CD86 required for the co-stimulation of naïve CD4 $^+$ T cells. In addition, T cell activation might be supported via upregulation of IL-12p40 upon sensitizer treatment (41). Our findings may contribute to the understanding of the crucial role of DDC for antigen presentation in the skin and the potential to migrate and activate T cells faster and outnumber LCs by 10:1 in draining lymph nodes (39, 40). Furthermore, the sensitizer induced activation of the NF- κ B and the p38 MAPK pathway and the secretion of inflammatory cytokines such as IL-8, IL-6, IL-1 β and TNF- α as it was stated for other DC surrogates could be validated. Thus, our THP-1-derived iDCs fulfill all required *in vitro* criteria for dermal dendritic cell surrogates. By integrating those iDCs into a full-thickness skin model, we are the first to engineer a human immune

competent full-thickness skin model containing THP-1-derived iDCs as dermal dendritic cell surrogates, which serve as an easily accessible tool to identify sensitizers and to qualitatively analyze putative anti-inflammatory compounds according to the 3R principles. Prospectively, our immune competent DDC model might be suitable for the research and understanding of inflammatory skin conditions such as psoriasis or diabetic skin manifestations often accompanied with recurring fungal or bacterial infections (66, 67).

Data availability statement

The raw data supporting the conclusions of this article will be made available by the authors, without undue reservation.

Ethics statement

Ethical approval was not required for the studies on humans in accordance with the local legislation and institutional requirements because only commercially available established cell lines were used.

Author contributions

NT: Conceptualization, Funding acquisition, Project administration, Resources, Supervision, Writing – review & editing. JH: Data curation, Investigation, Methodology, Visualization, Writing – original draft. KF: Data curation, Investigation, Validation, Visualization, Writing – review & editing. MM: Validation, Data curation, Investigation, Visualization, Writing – review & editing. NB: Investigation, Data curation, Methodology, Validation, Visualization, Writing – review & editing. UE: Methodology, Validation, Investigation, Visualization, Writing – review & editing. TB: Conceptualization, Funding acquisition, Supervision, Project administration, Resources, Writing – review & editing. KM: Funding acquisition, Methodology, Project administration, Supervision, Resources, Investigation, Writing – review & editing. LV: Data curation, Methodology, Resources, Supervision, Validation, Investigation, Visualization, Writing – review & editing.

Funding

The author(s) declare financial support was received for the research, authorship, and/or publication of this article. This research was funded by a grant to NT, TB and KM by the Bundesministerium für Ernährung und Landwirtschaft (BMEL), funding number: 281A308C18.

Acknowledgments

We would like to thank Prof. Dr. Eckhard Lammert for his profound support throughout this work.

Conflict of interest

Authors MM, NB, UE, KM, LV are employed by the company Henkel AG & Co. KGaA.

The remaining authors declare that the research was conducted in the absence of any commercial or financial relationships that could be construed as a potential conflict of interest.

Publisher's note

All claims expressed in this article are solely those of the authors and do not necessarily represent those of their affiliated organizations, or those of the publisher, the editors and the reviewers. Any product that may be evaluated in this article, or claim that may be made by its manufacturer, is not guaranteed or endorsed by the publisher.

References

1. Kabashima K, Honda T, Ginhoux F, Egawa G. The immunological anatomy of the skin. *Nat Rev Immunol* (2019) 19(1):19–30. doi: 10.1038/s41577-018-0084-5
2. Matejuk A. Skin immunity. *Archivum Immunol Therapie Experimentalis*. (2018) 66(1):45–54. doi: 10.1007/s00005-017-0477-3
3. Valladeau J, Ravel O, Dezutter-Dambuyant C, Moore K, Kleijmeer M, Liu Y, et al. Langerin, a novel C-type lectin specific to Langerhans cells, is an endocytic receptor that induces the formation of Birbeck granules. *Immunity* (2000) 12(1):71–81. doi: 10.1016/S1074-7613(00)80160-0
4. Zaba LC, Fuentes-Duculan J, Steinman RM, Krueger JG, Lowes MA. Normal human dermis contains distinct populations of CD11c+BDCA-1+ dendritic cells and CD163+FXIIIA+ macrophages. *J Clin Invest.* (2007) 117(9):2517–25. doi: 10.1172/JCI32282
5. Zaba LC, Krueger JG, Lowes MA. Resident and “Inflammatory” Dendritic cells in human skin. *J Invest Dermatol* (2009) 129(2):302–8. doi: 10.1038/jid.2008.225
6. Sumpter TL, Balmert SC, Kaplan DH. Cutaneous immune responses mediated by dendritic cells and mast cells. *JCT Insight* (2019) 4(1).
7. Naik SM, Cannon G, Burbach GJ, Singh SR, Swerlick RA, Wilcox JN, et al. Human keratinocytes constitutively express interleukin-18 and secrete biologically active interleukin-18 after treatment with pro-inflammatory mediators and dinitrochlorobenzene. *J Invest Dermatol* (1999) 113(5):766–72. doi: 10.1046/j.1523-1747.1999.00750.x
8. Lisby S, Müller KM, Jongeneel CV, Saurat J-H, Hauser C. Nickel and skin irritants up-regulate tumor necrosis factor- α mRNA in keratinocytes by different but potentially synergistic mechanisms. *International Immunology* (1995) 7(3):343–52.
9. Gueniche A, Viac J, Lizard G, Charveron M, Schmitt D. Effect of nickel on the activation state of normal human keratinocytes through interleukin 1 and intercellular adhesion molecule 1 expression. *Br J Dermatol* (1994) 131(2):250–6. doi: 10.1111/j.1365-2133.1994.tb08500.x
10. Tuschl H, Kovac R. Langerhans cells and immature dendritic cells as model systems for screening of skin sensitizers. *Toxicol Vitro.* (2001) 15(4):327–31. doi: 10.1016/S0887-2333(01)00030-3
11. Xu H, Guan H, Zu G, Bullard D, Hanson J, Slater M, et al. The role of ICAM-1 molecule in the migration of Langerhans cells in the skin and regional lymph node. *Eur J Immunol* (2001) 31(10):3085–93. doi: 10.1002/1521-4141(200110)31:10<3085::AID-IMMU3085>3.0.CO;2-B
12. Dustin ML, Tseng S-Y, Varma R, Campi G. T cell-dendritic cell immunological synapses. *Curr Opin Immunol* (2006) 18(4):512–6. doi: 10.1016/j.co.2006.05.017
13. Sharpe AH, Freeman GJ. The B7-CD28 superfamily. *Nat Rev Immunol* (2002) 2(2):116–26. doi: 10.1038/nri727
14. Ade N, Antonios D, Kerdine-Romer S, Boislevre F, Rousset F, Pallardy M. NF- κ B plays a major role in the maturation of human dendritic cells induced by NiSO(4) but not by DNCB. *Toxicol Sci* (2007) 99(2):488–501. doi: 10.1093/toxsci/kfm178
15. Aiba S, Manome H, Nakagawa S, Mollah ZUA, Mizuashi M, Ohtani T, et al. p38 mitogen-activated protein kinase and extracellular signal-regulated kinases play distinct roles in the activation of dendritic cells by two representative haptens, nCl2 and 2,4-dinitrochlorobenzene. *J Invest Dermatol* (2003) 120(3):390–9. doi: 10.1046/j.1523-1747.2003.12065.x
16. Arrighi J-F, Rebsamen M, Rousset F, Kindler V, Hauser C. A critical role for p38 mitogen-activated protein kinase in the maturation of human blood-derived dendritic cells induced by lipopolysaccharide, TNF- α , and contact sensitizers. *J Immunol* (2001) 166(6):3837–45. doi: 10.4049/jimmunol.166.6.3837
17. Casilli F, Bianchini A, Gloaguen I, Biordi L, Alesse E, Festuccia C, et al. Inhibition of interleukin-8 (CXCL8/IL-8) responses by repertaxin, a new inhibitor of the chemokine receptors CXCR1 and CXCR2. *Biochem Pharmacol* (2005) 69(3):385–94. doi: 10.1016/j.bcp.2004.10.007
18. Harada A, Sekido N, Akahoshi T, Wada T, Mukaida N, Matsushima K. Essential involvement of interleukin-8 (IL-8) in acute inflammation. *J leukocyte Biol* (1994) 56(5):559–64. doi: 10.1002/jlb.56.5.559
19. Xu Y-D, Cheng M, Shang P-P, Yang Y-Q. Role of IL-6 in dendritic cell functions. *J Leukocyte Biol* (2022) 111(3):695–709. doi: 10.1002/jlb.3MR0621-616RR
20. Briscoe D, Cotran R, Pober J. Effects of tumor necrosis factor, lipopolysaccharide, and IL-4 on the expression of vascular cell adhesion molecule-1 in vivo. Correlation with CD3+ T cell infiltration. *J Immunol (Baltimore Md: 1950)* (1992) 149(9):2954–60.
21. Feldmeyer L, Werner S, French LE, Beer H-D. Interleukin-1, inflammasomes and the skin. *Eur J Cell Biol* (2010) 89(9):638–44. doi: 10.1016/j.ejcb.2010.04.008
22. Nakae S, Asano M, Horai R, Sakaguchi N, Iwakura Y. IL-1 enhances T cell-dependent antibody production through induction of CD40 ligand and OX40 on T cells. *J Immunol* (2001) 167(1):90–7. doi: 10.4049/jimmunol.167.1.90
23. Riemann H, Schwarz A, Grabbe S, Aragane Y, Luger TA, Wysocka M, et al. Neutralization of IL-12 in vivo prevents induction of contact hypersensitivity and induces hapten-specific tolerance. *J Immunol* (1996) 156(5):1799–803. doi: 10.4049/jimmunol.156.5.1799
24. Tait Wojno ED, Hunter CA, Stumhofer JS. The immunobiology of the interleukin-12 family: room for discovery. *Immunity* (2019) 50(4):851–70. doi: 10.1016/j.immuni.2019.03.011
25. Pasparakis M, Haase I, Nestle FO. Mechanisms regulating skin immunity and inflammation. *Nat Rev Immunol* (2014) 14(5):289–301. doi: 10.1038/nri3646
26. Gerber PA, Buhren BA, Schrumpf H, Homey B, Zlotnik A, Hevezi P. The top skin-associated genes: a comparative analysis of human and mouse skin transcriptomes. *Biol Chem* (2014) 395(6):577–91. doi: 10.1515/hsz-2013-0279
27. Rougier A, Lotte C, Maibach HI. *In vivo* percutaneous penetration of some organic compounds related to anatomic site in humans: predictive assessment by the stripping method. *J Pharm Sci* (1987) 76(6):451–4. doi: 10.1002/jps.2600760608
28. Abd E, Yousef SA, Pastore MN, Telaprolu K, Mohammed YH, Namjoshi S, et al. Skin models for the testing of transdermal drugs. *Clin Pharmacol* (2016) 8:163–76. doi: 10.2147/CPAA.S64788
29. Van Gele M, Geusens B, Brochez L, Speeckaert R, Lambert J. Three-dimensional skin models as tools for transdermal drug delivery: challenges and limitations. *Expert Opin Drug Delivery* (2011) 8(6):705–20. doi: 10.1517/17425247.2011.568937
30. Laubach V, Zöller N, Rossberg M, Görg K, Kippenberger S, Bereiter-Hahn J, et al. Integration of Langerhans-like cells into a human skin equivalent. *Arch Dermatol Res* (2011) 303(2):135–9. doi: 10.1007/s00403-010-1092-x
31. Ouwehand K, Spiekstra SW, Waaijman T, Schepers RJ, de Gruijl TD, Gibbs S. Technical advance: Langerhans cells derived from a human cell line in a full-thickness skin equivalent undergo allergen-induced maturation and migration. *J Leukoc Biol* (2011) 90(5):1027–33. doi: 10.1189/jlb.0610374
32. Bock S, Said A, Müller G, Schäfer-Korting M, Zoschke C, Weindl G. Characterization of reconstructed human skin containing Langerhans cells to monitor molecular events in skin sensitization. *Toxicol In Vitro.* (2018) 46:77–85. doi: 10.1016/j.tiv.2017.09.019
33. Kosten IJ, Spiekstra SW, de Gruijl TD, Gibbs S. MUTZ-3 derived Langerhans cells in human skin equivalents show differential migration and phenotypic plasticity after allergen or irritant exposure. *Toxicol Appl Pharmacol* (2015) 287(1):35–42. doi: 10.1016/j.taap.2015.05.017
34. Rodrigues Neves CT, Spiekstra SW, de Graaf NP, Rustemeyer T, Feilzer AJ, Kleverlaan CJ, et al. Titanium salts tested in reconstructed human skin with integrated MUTZ-3-derived Langerhans cells show an irritant rather than a sensitizing potential. *Contact Derm* (2020) 83(5):337–46. doi: 10.1111/cod.13666
35. Koning JJ, Rodrigues Neves CT, Schimek K, Thon M, Spiekstra SW, Waaijman T, et al. A multi-organ-on-chip approach to investigate how oral exposure to metals can cause systemic toxicity leading to Langerhans cell activation in skin. *Front toxicol* (2022) 3:824825. doi: 10.3389/itox.2021.824825
36. Régnier M, Staquet MJ, Schmitt D, Schmidt R. Integration of Langerhans cells into a pigmented reconstructed human epidermis. *J Invest Dermatol* (1997) 109(4):510–2. doi: 10.1111/1523-1747.ep12336627
37. Régnier M, Patwardhan A, Scheynius A, Schmidt R. Reconstructed human epidermis composed of keratinocytes, melanocytes and Langerhans cells. *Med Biol Eng Comput* (1998) 36(6):821–4. doi: 10.1007/BF02518889
38. Bechettoile N, Dezutter-Dambuyant C, Damour O, André V, Orly I, Perrier E. Effects of solar ultraviolet radiation on engineered human skin equivalent containing

both Langerhans cells and dermal dendritic cells. *Tissue Eng.* (2007) 13(11):2667–79. doi: 10.1089/ten.2006.0405

39. Fukunaga A, Khaskhely NM, Sreevidya CS, Byrne SN, Ullrich SE. Dermal dendritic cells, and not Langerhans cells, play an essential role in inducing an immune response. *J Immunol* (2008) 180(5):3057–64. doi: 10.4049/jimmunol.180.5.3057

40. Kissenkampf A, Henri S, Dubois B, Laplace-Builhé C, Perrin P, Romani N, et al. Dynamics and function of Langerhans cells *in vivo*: dermal dendritic cells colonize lymph node areas distinct from slower migrating Langerhans cells. *Immunity* (2005) 22(5):643–54. doi: 10.1016/j.jimmuni.2005.04.004

41. Hölken JM, Teusch N. The monocytic cell line THP-1 as a validated and robust surrogate model for human dendritic cells. *Int J Mol Sci* (2023) 24(2). doi: 10.3390/ijms24021452

42. Bernd A, Friess W, Mewes KR, Raus M, Bendz H, Kippenberger S. 2006/018147 A3. 23.02.2006:1452. Germany patent WO.

43. Escherich D, Graf R, Mewes RM, Raus M. . 10 2006 006 461. 23.08.2007. Germany patent DE.

44. Mewes KR, Raus M, Bernd A, Zöller NN, Sättler A, Graf R. Elastin expression in a newly developed full-thickness skin equivalent. *Skin Pharmacol Physiol* (2006) 20(2):85–95. doi: 10.1159/000097655

45. Vierkotten L, Petersohn D, Förster T, Mewes KR. The importance of being three-dimensional in biology.

46. Reisinger K, Pfuhler S. 3D skin comet assay. *Alternatives Dermal Toxic Test* (2017), 527–39. doi: 10.1007/978-3-319-50353-0_38

47. Mewes KR, Zöller NN, Bernd A, Prießner A, DeWever B, Graf R, et al. *Expression of Dermal Extracellular Matrix Proteins in a Newly Developed Full-Thickness Skin Model. Cells and Culture*. Dordrecht: Springer Netherlands (2010).

48. Cohen DE, Heidary N. Treatment of irritant and allergic contact dermatitis. *Dermatol Ther* (2004) 17(4):334–40. doi: 10.1111/j.1396-0296.2004.04031.x

49. Neves BM, Rosa SC, Martins JD, Silva A, Gonçalo M, Lopes MC, et al. Development of an *in vitro* dendritic cell-based test for skin sensitizer identification. *Chem Res Toxicol* (2013) 26(3):368–78. doi: 10.1021/tx300472d

50. Schmidt M, Raghavan B, Müller V, Vogl T, Fejer G, Tchaptchet S, et al. Crucial role for human Toll-like receptor 4 in the development of contact allergy to nickel. *Nat Immunol* (2010) 11(9):814–9. doi: 10.1038/ni.1919

51. van der Aar AMG, Sylva-Steenland RMR, Bos JD, Kapsenberg ML, de Jong EC, Teunissen MBM. Cutting edge: loss of TLR2, TLR4, and TLR5 on langerhans cells abolishes bacterial recognition1. *J Immunol* (2007) 178(4):1986–90. doi: 10.4049/jimmunol.178.4.1986

52. Takeuchi J, Watari E, Shinya E, Norose Y, Matsumoto M, Seya T, et al. Down-regulation of Toll-like receptor expression in monocyte-derived Langerhans cell-like cells: implications of low-responsiveness to bacterial components in the epidermal Langerhans cells. *Biochem Biophys Res Commun* (2003) 306(3):674–9. doi: 10.1016/S0006-291X(03)01022-2

53. Aiba S, Terunuma A, Manome H, Tagami H. Dendritic cells differently respond to haptens and irritants by their production of cytokines and expression of co-stimulatory molecules. *Eur J Immunol* (1997) 27(11):3031–8. doi: 10.1002/eji.1830271141

54. Czarnobilska E, Obtułowicz K, Wsólek K, Pietowska J, Spiewak R. Mechanisms of nickel allergy. *Przeglad Lekarski* (2007) 64(7-8):502–5.

55. Chipinda I, Hettick JM, Siegel PD. Haptens: chemical reactivity and protein binding. *J Allergy* (2011) 2011. doi: 10.1155/2011/839682

56. Rustemeyer T, Van Hoogstraten IM, Von Blomberg BME, Scheper RJ. Mechanisms of allergic contact dermatitis. *Kanerva's Occup Dermatol* (2020), 151–90. doi: 10.1007/978-3-319-68617-2_14

57. Kuroishi T, Bando K, Bakti RK, Ouchi G, Tanaka Y, Sugawara S. Migratory dendritic cells in skin-draining lymph nodes have nickel-binding capabilities. *Sci Rep* (2020) 10(1):5050. doi: 10.1038/s41598-020-61875-6

58. Thierse H-J, Gamerdinger K, Junkes C, Guerreiro N, Weltzien HU. T cell receptor (TCR) interaction with haptens: metal ions as non-classical haptens. *Toxicology* (2005) 209(2):101–7. doi: 10.1016/j.tox.2004.12.015

59. Ochoa MT, Loncaric A, Krutzik SR, Becker TC, Modlin RL. “Dermal dendritic cells” Comprise two distinct populations: CD1+ Dendritic cells and CD209+ Macrophages. *J Invest Dermatol* (2008) 128(9):2225–31. doi: 10.1038/jid.2008.56

60. Hagan DK, Kuzma JN, Larson I, Foster-Schubert KE, Kuan LY, Cignarella A, et al. Characterizing and quantifying leukocyte populations in human adipose tissue: impact of enzymatic tissue processing. *J Immunol Methods* (2012) 386(1-2):50–9. doi: 10.1016/j.jim.2012.08.018

61. Ford AL, Foulcher E, Goodsall AL, Sedgwick JD. Tissue digestion with dispase substantially reduces lymphocyte and macrophage cell-surface antigen expression. *J Immunol Methods* (1996) 194(1):71–5. doi: 10.1016/0022-1759(96)00067-1

62. Autengruber A, Gereke M, Hansen G, Hennig C, Bruder D. Impact of enzymatic tissue disintegration on the level of surface molecule expression and immune cell function. *Eur J Microbiol Immunol* (2012) 2(2):112–20. doi: 10.1556/EuJMI.2.2012.2.3

63. Abuzakouk M, Feighery C, O'Farrelly C. Collagenase and Dispase enzymes disrupt lymphocyte surface molecules. *J Immunol Methods* (1996) 194(2):211–6. doi: 10.1016/0022-1759(96)00038-5

64. Pan J, Ju D, Wang Q, Zhang M, Xia D, Zhang L, et al. Dexamethasone inhibits the antigen presentation of dendritic cells in MHC class II pathway. *Immunol Letters* (2001) 76(3):153–61. doi: 10.1016/S0165-2478(01)00183-3

65. Piemonti L, Monti P, Allavena P, Sironi M, Soldini L, Leone BE, et al. Glucocorticoids affect human dendritic cell differentiation and maturation1. *J Immunol* (1999) 162(11):6473–81. doi: 10.4049/jimmunol.162.11.6473

66. Popoviciu MS, Kaka N, Sethi Y, Patel N, Chopra H, Cavalu S. Type 1 diabetes mellitus and autoimmune diseases: A critical review of the association and the application of personalized medicine. *J Personal Med* (2023) 13(3):422. doi: 10.3390/jpm13030422

67. Kamata M, Tada Y. Dendritic cells and macrophages in the pathogenesis of psoriasis. *Front Immunol* (2022) 13. doi: 10.3389/fimmu.2022.941071



OPEN ACCESS

EDITED BY

Jeffrey John Bajramovic,
Utrecht University, Netherlands

REVIEWED BY

Charles Scanga,
University of Pittsburgh, United States
Yongbin Wang,
Xinxiang Medical University, China

*CORRESPONDENCE

Stephen Cose
✉ Stephen.Cose@mrcuganda.org
Gift Ahimbisibwe
✉ gift.ahimbisibwe@mrcuganda.org

RECEIVED 20 July 2023

ACCEPTED 01 November 2023

PUBLISHED 06 December 2023

CITATION

Ahimbisibwe G, Nakibuule M, Martin Ssejoba M, Oyamo D, Mulwana R, Nabulime J, Babirye F, Kizito MA, Lekuya HM, Adakun AS, Nalumansi D, Muryasingura S, Lukande R, Kyazze A, Baluku JB, Biraro IA and Cose S (2023) Feasibility and acceptability of undertaking postmortem studies for tuberculosis medical research in a low income country. *Front. Immunol.* 14:1264351. doi: 10.3389/fimmu.2023.1264351

COPYRIGHT

© 2023 Ahimbisibwe, Nakibuule, Martin Ssejoba, Oyamo, Mulwana, Nabulime, Babirye, Kizito, Lekuya, Adakun, Nalumansi, Muryasingura, Lukande, Kyazze, Baluku, Biraro and Cose. This is an open-access article distributed under the terms of the Creative Commons Attribution License (CC BY). The use, distribution or reproduction in other forums is permitted, provided the original author(s) and the copyright owner(s) are credited and that the original publication in this journal is cited, in accordance with accepted academic practice. No use, distribution or reproduction is permitted which does not comply with these terms.

Feasibility and acceptability of undertaking postmortem studies for tuberculosis medical research in a low income country

Gift Ahimbisibwe^{1*}, Marjorie Nakibuule¹, Marvin Martin Ssejoba¹, David Oyamo², Rose Mulwana², Josephine Nabulime², Febronius Babirye², Musana Abdusalaamu Kizito³, Hervé Monka Lekuya⁴, Akello Suzan Adakun², Daisy Nalumansi², Stella Muryasingura², Robert Lukande³, Andrew Kyazze⁵, Joseph Baruch Baluku⁵, Irene Andia Biraro^{5,6} and Stephen Cose^{1,7*}

¹Medical Research Council (MRC)/Uganda Virus Research Institute (UVRI) and London School of Hygiene and Tropical Medicine (LSHTM) Uganda Research Unit, Entebbe, Uganda, ²Mulago National Referral Hospital, Kampala, Uganda, ³Department of Pathology, Makerere University, Kampala, Uganda, ⁴Department of Surgery, Makerere University, Kampala, Uganda, ⁵Division of Pulmonology, Kiruddu National Referral Hospital, Kampala, Uganda, ⁶Department of Internal Medicine, Makerere University, Kampala, Uganda, ⁷Clinical Research Department, London School of Hygiene and Tropical Medicine, London, United Kingdom

Introduction: If we are to break new ground in difficult-to-treat or difficult-to-vaccinate diseases (such as HIV, malaria, or tuberculosis), we must have a better understanding of the immune system at the site of infection in humans. For tuberculosis (TB), the initial site of infection is the lungs, but obtaining lung tissues from subjects suffering from TB has been limited to bronchoalveolar lavage (BAL) or sputum sampling, or surgical resection of diseased lung tissue.

Methods: We examined the feasibility of undertaking a postmortem study for human tuberculosis research at Mulago National Referral Hospital in Kampala, Uganda.

Results: Postmortem studies give us an opportunity to compare TB-involved and -uninvolved sites, for both diseased and non-diseased individuals. We report good acceptability of the next-of-kin to consent for their relative's tissue to be used for medical research; that postmortem and tissue processing can be undertaken within 8 hours following death; and that immune cells remain viable and functional up to 14 hours after death.

Discussion: Postmortem procedures remain a valuable and essential tool both to establish cause of death, and to advance our medical and scientific understanding of infectious diseases.

KEYWORDS

postmortem studies, feasibility & acceptability, tuberculosis, tissues, T cells

Introduction

There is no question that the SARS-CoV-2 (COVID-19) pandemic has reversed many of the gains made in fighting the effort to control the infection and spread of *Mycobacterium tuberculosis* (*M.tb*), the causative agent of tuberculosis (TB), and has set back the fight against TB by years (1). Nevertheless, we cannot blame our lack of success in controlling TB on COVID-19 alone. We have lived with TB long enough not to have it as the leading cause of death from a single infectious disease prior to SARS-CoV-2, and by all accounts it is set to regain its number one spot again (2). The major challenges to realizing the global 2030 End TB reduction targets include the lack of efficient TB vaccines, diagnostic challenges, drug resistance, and inaccessibility to effective chemotherapy (2, 3).

The best intervention against TB, or in fact any infectious disease, is one that breaks the transmission cycle. Lessons from other infectious diseases that have now been eradicated, such as smallpox and rinderpest, have shown that vaccination is the best way to break transmission; polio is almost eradicated as well due to the WHO's determined vaccination strategy (4). TB vaccination has been extensively taken up by most TB-endemic countries. However, it is well-known that BCG, currently the only licensed TB vaccine, is not effective against adult pulmonary TB, the most transmissible form of the disease in endemic countries (5). We need to develop more effective TB vaccines and develop shorter drug regimens, amongst a plethora of other interventions (2). The last few years have witnessed a reawakening of novel TB vaccine approaches. There is hope in some current trial vaccines (M72, BCG REVAC, VPM1002, H56/IC31), but tertiary trial results will not be out for several years (6, 7). In the meantime, we need vaccine strategies based on deeper insights into the immunity underlying TB, and not just in blood, but most importantly, at the site of infection in humans.

This is not to say that we have little idea of tissue-specific cell subsets in human tissue; tissue-resident immune cells have been successfully isolated from the lungs of organ donors (8, 9), and include subsets such as tissue-resident memory (TRM) T cells (10), macrophages (11), NK and innate lymphoid cell (ILC) subsets (12–14), mucosal-associated invariant T (MAIT) cells (15, 16) and $\gamma\delta$ T cells (17). But only a few studies have looked at these subsets in the lungs of TB-diseased individuals (17–19), and none in otherwise healthy individuals with a latent TB infection (LTBI). Studies have been largely restricted to relatively accessible sites such as bronchoalveolar lavage (BAL) (20–22), the pleural fluid (23–25), or occasionally pleural or lymph node biopsies when clinically indicated (26). New techniques such as Positron Emission Tomography – Computed Tomography (PET-CT) can help us to understand the resolution or progression of disease (27–31), but cannot assess specific cellular functions. We therefore have only a superficial knowledge of how the immune system responds at the main site of TB infection and disease in humans – the lungs.

To address this, we conducted a postmortem study to determine whether we could use immune cells isolated from tissues taken postmortem for medical research. We show that we were able to get consent from the next of kin(s) (NoKs), perform a full postmortem,

and collect and process tissues with little loss in cell viability or function, up to 14 hours post-death.

Materials and methods

Ethics

This study obtained ethical approval from five ethics bodies: the Makerere University School of Biomedical Sciences Research & Ethics Committee (SBS-REC-721), the Mulago National Referral Hospital Ethics Committee (MHREC 1849), the Kiruddu National Referral Hospital School of Biochemical Research and Ethics Committee (CRD/ADMIN/120/1), the Uganda National Council of Science and Technology Ethics Committee (HS703ES), and the London School of Hygiene and Tropical Medicine Ethics Committee (22922).

Consent

Trained grief counselors were employed to sensitively obtain informed consent from the next-of-kin (NoK) as described by Uganda Law. The NoK gave consent for a full postmortem, for donation of tissues for medical research and future use, and for access to previous medical records. A case record form was used by the counselors to collect reasons for consent or decline from the NoK.

Participants

We recruited deceased subjects from Mulago National Referral Hospital in Kampala, Uganda, between January 2021 and June 2022. Only subjects above 18 years of age whose NoK consented to the study were recruited into the study. Active TB subjects were recruited from Wards 4, 5, and 6 of Mulago National Referral Hospital (MNRH), as well as the Infectious Diseases Ward. We used road traffic accident victims as our non-TB subjects, who were recruited from the Accident and Emergency Unit of MNRH (referred to as the Surgical Emergency Unit, SEU). Recruited subjects from this Unit were otherwise healthy at the time of death, with no obvious underlying morbidity or chest involvement at the time of death. Patient demographics are described in Table 1.

Tissues and sample collection

A full postmortem was performed by the study pathologist on all study subjects to establish the cause of death and identify any underlying conditions that may have been missed during routine clinical and laboratory examination. Tissue samples, including lung, lymph nodes draining the lung (Hilar Lymph Nodes - HLNs), spleen, distal lymph nodes (Iliac and inguinal lymph nodes - DLNs), and blood were collected. The solid tissues were placed in

TABLE 1 Patient demographics.

	SEU ^a	TB ^b
Gender		
Male	37	20
Female	10	13
Age Range		
18-35	26 (26.3) ^c	13 (28.6)
36-55	12 (41.7)	15 (43.8)
≥56	9 (69.4)	5 (67)
HIV status		
Positive	6	23
Negative	41	10
Cause of death		
Trauma		
Head trauma	35	
Abdominal	8	
Gunshot	1	
Non trauma		
Intestinal obstruction	2	
Duodenal ulcers	1	
TB Cases		
Pulmonary TB		12
Extrapulmonary TB		13
HIV associated		8
Total	47	33

Data shows collated patient demographics across the whole study.

^aSurgical Emergency Unit.

^bTuberculosis Wards.

^cParentheses represent average age.

50ml tubes with 20% FBS in RPMI medium. Bronchoalveolar lavage (BAL) washing of both the left and right lungs was performed with PBS. Arterial blood was collected from the carotid artery into heparin tubes; arteries were considered instead of veins due to regular venous collapse after death. Sample tubes were tightly capped, placed in a rack in a sealable cool box, and transported to the BSL3 laboratory at the MRC/UVRI and LSHTM Uganda Research Unit at room temperature. All sample processing was performed under BSL3 conditions.

PBMC isolation

Heparinized blood was diluted with RPMI media and layered manually on FicollPaque PLUS media. PBMCs were then isolated by density centrifugation. The buffy coat was harvested and centrifuged to obtain a cell pellet. Red blood cells in the pellet

were lysed, then the cells were washed and counted on an automated cell counter (TC20; Biorad).

Cell isolation from tissues

Lung

Cells were obtained from lung tissue by enzymatic digestion using collagenase D (1mg/ml) and DNase I (1g/ml) (hereafter referred to as “the enzyme mixture”) and physical disintegration using the gentleMACS Octo Dissociator (Milteyni Biotech) as described previously (8). Briefly, the lungs were cut into small pieces using fine scissors and forceps in a sterile petri dish, placed in gentleMACS purple C tubes with the enzyme mixture, loaded on the gentleMACS Octo Dissociator, and run using Lung Program 1. The tubes were then incubated in a CO₂ incubator for 25 minutes and then run using Lung Program 2. 1ml of smashed tissue was taken off to perform MGIT culture. The sample was then filtered through a 70 µm filter followed by a 40 µm filter and centrifuged at 600 rcf for 5 minutes to obtain a cell pellet. Residual red blood cells were lysed using ACK lysis buffer, leaving behind a pure black cell pellet. We assume the cell pellet from the draining lungs was black due to a lifetime of exposure to carbon residues as a result of inhalation of carbon fumes from vehicles, firewood, and charcoal smoke (32). The cells were washed in RPMI and counted using an automated TC20 cell counter (Biorad).

Lymph nodes

Lymph nodes were first cleaned by teasing the lymph node tissue from surrounding fat using forceps and scissors, cut into small pieces using fine scissors and forceps in a sterile petri dish, and mixed with RPMI media. The resultant mixture was then filtered through a 70 µm filter followed by a 40 µm filter, then centrifuged at 600 rcf for 5 minutes to obtain a cell pellet. Red blood cells were lysed using ACK lysis buffer. The resultant pellet was washed with RPMI and counted using an automated TC20 cell counter.

Spleen

Spleen sections were chopped into small pieces using fine scissors and forceps in a sterile petri dish and mixed with RPMI media. The resultant mixture was then filtered through a 70 µm filter and centrifuged at 600 rcf for 5 minutes to obtain a cell pellet. The pellet was then reconstituted with RPMI and layered manually onto FicollPaque PLUS media. Spleen mononuclear cells were then obtained by density centrifugation. The buffy coat was harvested and centrifuged to obtain a cell pellet. Residual red blood cells in the pellet were lysed using ACK lysis buffer, and the cells were then washed and counted using an automated TC20 cell counter.

Bronchoalveolar lavage fluid (BAL)

BAL was collected in 50ml PBS, using a standard BAL procedure, but washing both lungs and deeper airways than would normally be performed for a living subject. BAL fluid was filtered through a 70 µm filter followed by a 40 µm filter, then

centrifuged at 600 rcf for 5 minutes to obtain a cell pellet. Red blood cells were lysed using ACK lysis buffer. The resultant pellet was washed with RPMI and counted using an automated TC20 cell counter.

T-SPOT[®].TB assay

This assay was performed using the T-SPOT[®].TB kit (TB.300, Oxford Immunotec) to enumerate individual TB-specific activated effector T cells producing IFN γ . Samples were run in duplicate. The procedure was performed as per insert, except for incubation time (36 hrs) and media (RPMI plus 10% FBS). Extensive testing showed that this time and media yielded the best results from our deceased subjects, above that of the recommended protocol for live venous blood. Resultant spots were read using an ELISPOT reader (AID iSpot ELR08IFL), and were interpreted as per insert.

BACTEC MGIT 960 for recovery of *M.tb*

Tissue or BAL was processed as per the BD BBL MycoPrep decontamination kit (Cat. No. 240862, 240863), with minor modifications. Briefly, tissue or BAL was decontaminated with MycoPrep for 30 minutes while vortexing every 5 minutes. Positive and negative controls of known time to positivity and bacterial load were included to control for the decontamination process. Sterile Phosphate Buffered Saline (PBS) was then added to stop the reaction

followed by a 3500g spin for 15 minutes. The sediment was then inoculated into the MGIT tubes with BBLTM MGITTM PANTATM Antibiotic Mixture (245114) to minimize contamination and enhance *M.tb* growth. MGIT tubes were then incubated in the BD BACTECTM MGITTM Automated Mycobacterial Detection System for 42 days. Positive growths were confirmed by positive Ziehl-Neelsen (ZN) staining and the MPT64 antigen assay. For all of the samples included in this manuscript, no tissue or BAL sample was confirmed as *M.tb* positive amongst the non-TB subjects.

T cell phenotypic analysis by flow cytometry

A 29-color antibody T and B cell panel was used to phenotype cells isolated from each of the tissues. The gating strategy for PBMCs and tissues are shown in Figures 1, 2, respectively. Antibodies used were CD3 (PACIFIC BLUE HIT3a BioLegend), CD38 (BV510 HIT2 BioLegend), CCR7 (BV605 G043H7 BioLegend), PD-1 (BV650 NAT105 Biolegend), CD69 (BV711 FN50 Biolegend), CD28 (BV750 CD28.2 Biolegend), CD27 (BV785 O323 Biolegend) CD8 (SPARK BLUE 550SK1 Biolegend) FCLR4 (PE413D12 Biolegend), CD127 (SPARK YG581 A019B5 Biolegend) CD4 (PECY5 RPA-T4 Biolegend), CD57 (PECY7 HNK-1 Biolegend), IgG (APC M1310G05 Biolegend), KLRG1 (ALEXAFLUOR 647 SA231A2 Biolegend), CD21 (ALEXAFLUOR 700 Bu32 Biolegend) HLADR (APC-FIRE 810 I243 Biolegend), LIVE/DEAD (ZOMBIE UV Biolegend) CD103 (BUV395 Ber ACT8 BD), CD25 (BUV496 M-A251 BD), CD196 (BUV563 11A9

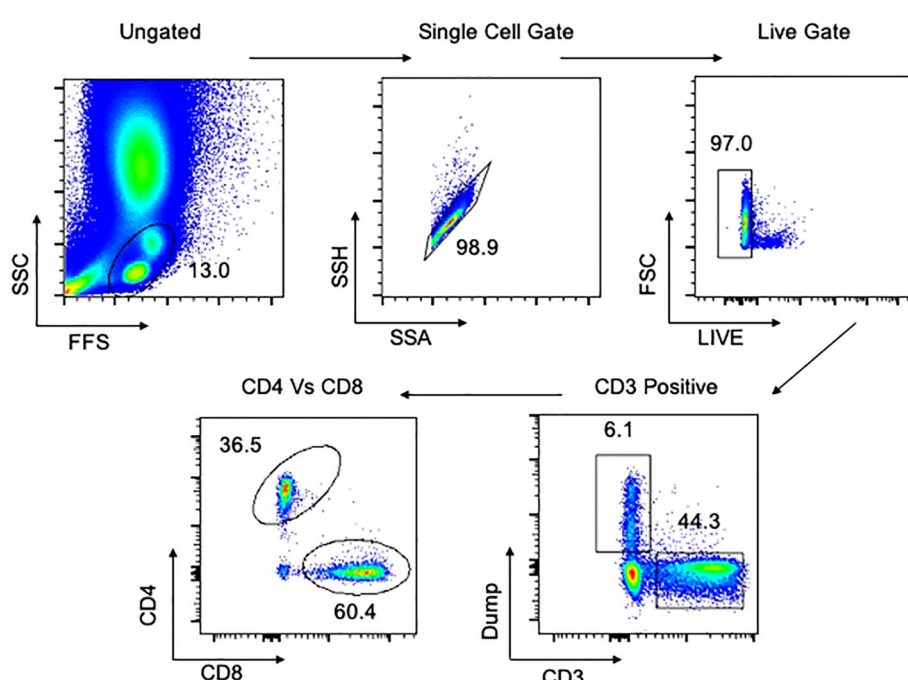


FIGURE 1

Gating strategy for flow cytometry in PBMCs. Representative plot of total cells from arterial PBMCs taken postmortem. Total cells are first gated by FSC/SSC, then singlets isolated, followed by selection of live cells and then CD3 positive cells. The dump gate, used to make the CD3 gate cleaner, consists of CD19/CD56/CD14. Finally, cells are separated based on CD4 and CD8, followed by specific staining as represented in the Results. Data comes from a 65-year-old male HIV-/TB- subject recruited from the SEU.

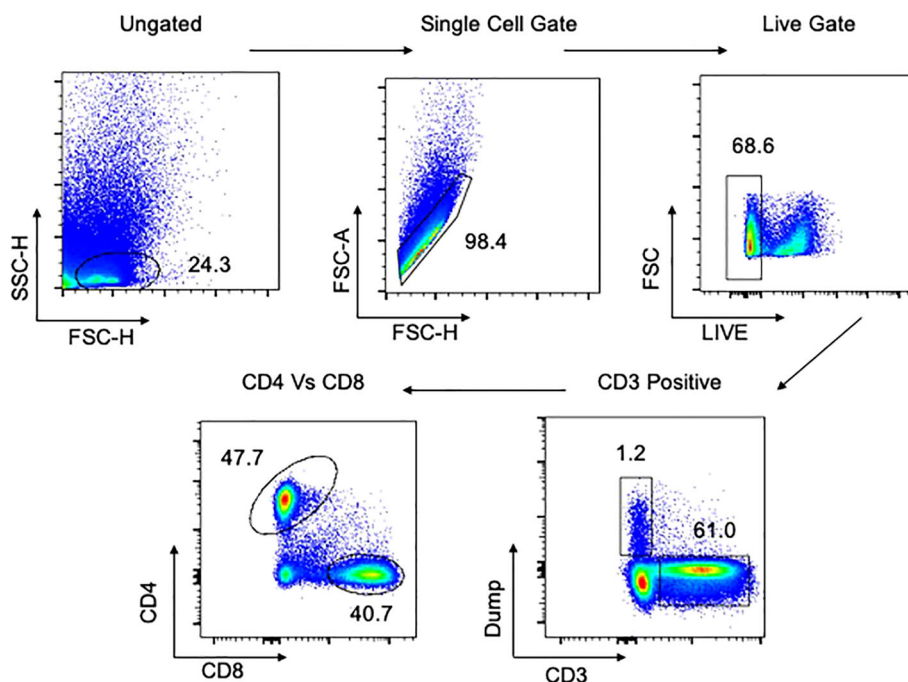


FIGURE 2

Gating strategy for flow cytometry in tissues. Representative plot of total cells from lung tissue taken postmortem. Total cells are first gated by FSC/SSC, then singlets isolated, followed by selection of live cells and then CD3 positive cells. The dump gate, used to make the CD3 gate cleaner, consists of CD19/CD56/CD14. Finally, cells are separated based on CD4 and CD8, followed by specific staining as represented in the Results. A similar gating strategy was employed for all other tissues. Data comes from a 65-year-old male HIV-/TB- subject recruited from the SEU.

BD), CD278 (BUV661 DX29 BD), IgM (BUV737 UCH-B1 BD), CD45RA (BUV805 HI100 BD), CD5 (BV421 UCHT2 BioLegend), CD24 (FITC eBioSN3 eBioscience), CD183 (BB700 1C6/CXCR3 BD), CD10 (PerCP eFluor710 SN5c Life Technologies), IgD (PE-Dazzle594 IA6-2 BD), CD19 (APC-H7 SJ25C1 BD).

Viability staining was performed first with the fixable viability dye, zombie UV, for 20 minutes in the dark at room temperature. Cells were washed and resuspended in 100 μ l of surface antibody cocktail for 20 minutes in the dark at 4°C, after which they were washed to remove excess antibody. Cells were acquired using a Cytek Aurora Spectral Analyser. All flow cytometry data was analysed using FlowJo version 10.8.1. Compensation controls to remove spectral overlap and Fluorescence Minus One (FMO) controls were used to establish gates. Representative gating strategies for PBMC and lung samples are shown in Figures 1, 2, respectively.

Statistical analysis

FlowJo and GraphPad Prism Version 9 software were used for graphical representation and statistical analysis.

Results

To determine whether tissue-specific immunology studies could be performed on tissues donated for medical research following

death, we assessed two essential elements: 1) could we get consent from the NoK, and if so, 2) how viable would cells be following death and the postmortem process.

We found that we could get consent from the NoK with very high acceptability rates at the SEU (94% of those approached; Table 2), and with more modest rates on the TB and ID Wards (35% of those approached; Table 2). The latter consent rate was in line with a previous study assessing consent across all Wards at MNRH (33). The high rate of consent at the SEU was a surprise, as we had assumed a sudden, unexpected death might mean that the NoK would be less willing to consent, whereas the consent rate on the TB and ID Wards might be higher because the patient and family have usually built a rapport with hospital staff, and may therefore be more keen to know the actual cause of death of their relative. Most NoKs believed that understanding the reason for a loved one's sudden death would help them to better come to terms with their loss; the low consent rate on the TB and ID Wards was mainly attributed to religious norms that do not allow a postmortem to be undertaken (Table 2).

After obtaining consent, the body was taken for a full postmortem. Tissues were taken to assess the viability of cells over time, from the time of death through sample processing to cell counting in the laboratory. We found that cells were viable up to 14 hours post-death, but that there was considerable variability in viability depending on the tissue sample (Figure 3). Arterial blood maintained a high level of viability out to 14 hours post-death, but other tissues examined were considerably lower; around 40% of the cells isolated were viable. A regression analysis showed no effect of

TABLE 2 Reasons for consent and decline.

Numbers	SEU ^a	TB ^b
Met study criteria	50	94
Consented	47	33
Declined	3	61
Consent rate	94%	35%
Reasons for Consent	SEU ^a	TB ^b
Gender		
Male	13	10
Female	34	23
Knowing the cause of death will help prevent more deaths	5	10
It is important in settling NSSF, deceased's bank payments	8	8
Understanding the reason for a loved one's death helps them come to terms with their loss	17	9
It sounds like the right thing to do	9	1
It is a way of saving future lives	4	5
Reasons for Decline	SEU ^a	TB ^b
Gender		
Male	1	27
Female	2	34
Reasons for decline		
Religious norms	1	16
Cultural norms	1	12
Fear of body disorientation	1	8
Process will delay funeral arrangements		10
PM not necessary		2
Lack of authority		3
Not sure deceased would approve		4
No reason		6

Whilst approaching families for consent to the study, we asked a short questionnaire on why they did or didn't accept for their deceased family member to be a part of the study, and for the use of their tissues for medical research. Data shows the responses given by the families that agreed to answer the questionnaire.

^aSurgical Emergency Unit.

^bTuberculosis Wards.

time from death on viability for any tissue, with the exception of PBMCs. For PBMCs, we found a significant decrease of 1.4% viability for every hour following death that the samples were processed. We did not see a difference in cell viability in any tissue between TB and non-TB groups.

Having shown that we could isolate viable cells from the organs of deceased subjects, we next tested whether the cells were functional using the T-SPOT[®].TB assay to assess exposure to *M.tb* antigens (ESAT-6 and CFP-10) (Figure 4). We found that PBMCs isolated postmortem were just as functional as PBMCs isolated from the venous blood of a living subject (Figure 4A). Furthermore, the T-SPOT[®].TB assay worked on spleen and

bronchoalveolar lavage (BAL) samples, showing that cells isolated from tissues are not just viable, but are functional as well. In undertaking the T-SPOT[®].TB assay, we were able to identify both T-SPOT[®].TB positive and negative subjects (Figure 4B). PBMCs isolated postmortem from HIV-positive blood did not give reliable responses, so HIV-positive participants were excluded from this analysis. We found that 61% (Figure 4B) of the subjects tested were T-SPOT[®].TB positive – a finding similar to other studies conducted in the same population (34, 35), and suggesting no overt bias in our non-TB postmortem population.

Lastly, we asked whether T cells isolated from different organs showed evidence of classical immunological naïve and memory T cell subsets (Figures 5A, B; representative data). In all organs analyzed, both CD4 (Figure 5A) and CD8 (Figure 5B) T cells had naïve (CCR7⁺CD45RA⁺; T_N), central memory (CCR7⁺CD45RA⁻; T_{CM}), effector memory (CCR7⁻CD45RA⁻; T_{EM}) and effector memory RA (CCR7⁻CD45RA⁺; T_{EMRA}) subsets, albeit at different frequencies. Additionally, we asked whether Tissue Resident Memory (TRM) T cells, defined by co-expression of CD69 and CD103, were present in the different organs, for both CD4 (Figure 5C) and CD8 (Figure 5D) T cells. As expected, TRM T cells (CD69⁺CD103⁺) could be identified in the lung tissue (LUNG), bronchoalveolar lavage (BAL), and the lung draining hilar lymph nodes (HLN), but were not found in the blood.

Discussion

Development of better TB vaccine strategies needs to be based on deeper insights into the immunity underlying TB, and not just in blood, which is commonly undertaken, but perhaps more importantly, at the site of infection. Our knowledge of TB immune responses at the main site of infection, the lungs, is largely derived from animal models and whilst clearly important, few animal models exist that recapitulate the complex natural history of disease progression and reactivation as it exists in humans. Non-human primate (NHP) models are our closest model to human infection and disease, but are limited by cost and exposure to concurrent (or prior) unrelated infections and vaccine responses. Current human lung studies are sampled from patients with severe lung complications at the extreme end of the TB disease spectrum, and often lack normal lung tissue from non-diseased individuals for comparison. Another approach to tackle the burden of disease is to undertake postmortem studies. Postmortem studies allow us to not only compare the immunology within the tissues of people who have died from TB disease from those who have died of other causes, but also allow us to study the immunology of disease at other, non-involved tissues within the same individual. Postmortem studies also allow us to sample the entire population, and study tissue-specific responses in otherwise healthy people at the time of death – road traffic accident victims, for example.

We report that hospital-driven postmortems are feasible in Uganda. Aligned with a previous study (36), we found that consent rates were highly dependent on whether death was sudden or not. The consent rate on the TB and ID Wards was more than two-fold lower than at the SEU, but comparable to what

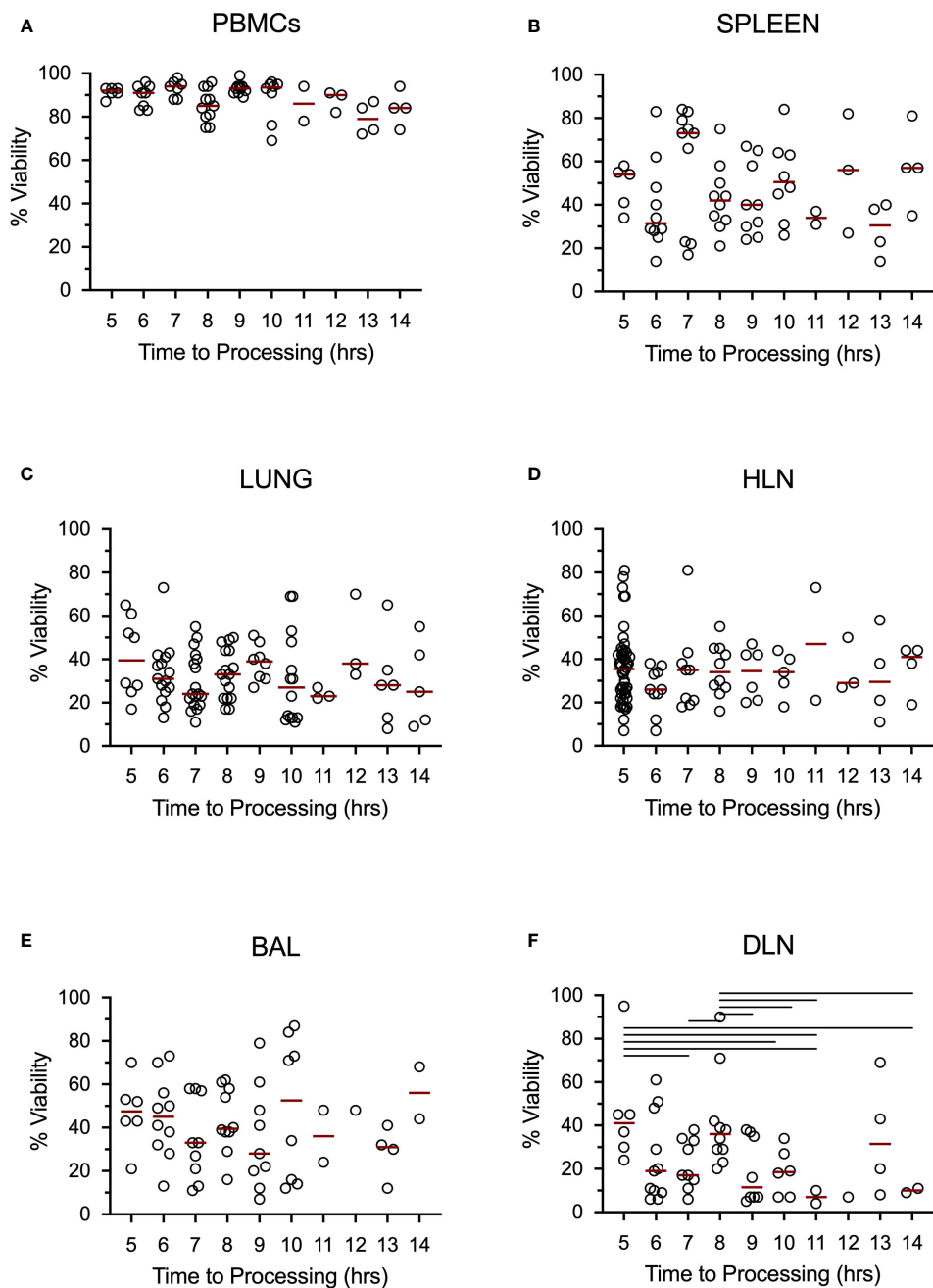


FIGURE 3

Tissue cells collected postmortem are viable up to 14 hours post-death. Data shows percent viability of isolated single cells from the Blood (A), Spleen (B), Lungs (C), Hilar lung draining lymph nodes (D), Bronchoalveolar lavage (E), and distal, non-draining lymph node (iliac lymph nodes) (F). Bars represent medians and lines above each graph represent a significant difference between the two groups at a significance level of $p < 0.05$. Data came from all subjects.

has previously been reported at Mulago National Referral Hospital (33). The reason for this may be that on Wards other than the SEU, patients are admitted and stay for longer periods of time, during which a clinical diagnosis is established, and relatives therefore have no need for a postmortem to be conducted to determine the cause of death. Indeed, the major reason for consent given by the NoKs at the SEU, where the average length of a hospital stay for RTA victims was 10 hours, was that knowing the cause of death helped in coming to terms with their relative's death.

In this paper, we show that lymphocytes remain viable and functional up to 14 hours post-death. Previous studies have reported good cell viability up to several days following death (37–39), far longer than the time frame of our study. However, few studies have looked at the functionality of cells isolated postmortem (8, 9), even fewer in tissues, and even fewer that are focussed on *M.tb* (17–19). Of note, the T-SPOT[®].TB test that we used for *M.tb*-specific functionality required a change of incubation time from the manufacturer's recommendation of 24 hours to 36 hours. In addition, changing the media to RPMI from

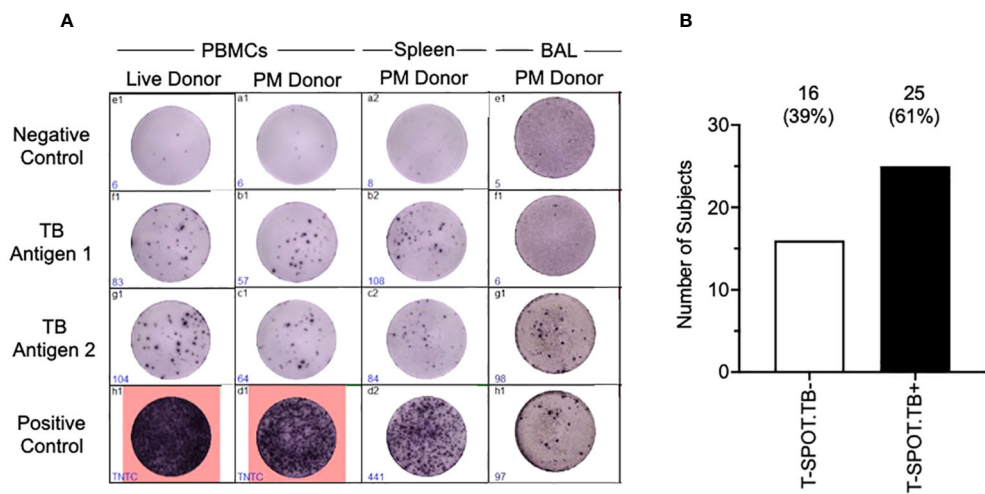


FIGURE 4

Tissue cells collected postmortem are functional in a T-SPOT®.TB Assay. T-SPOT®.TB data (A) shows that arterial PBMCs isolated and collected postmortem perform as well as venous blood from a live donor. In addition, the T-SPOT®.TB assay also works in tissues such as the spleen and BAL. Culture conditions were slightly altered to enable the assay to work, as described in the methods. (B) shows latent TB infection (LTBI) data collected from our non-TB arterial blood samples, assayed using the T-SPOT®.TB assay. Data are from HIV-/TB- people recruited from the SEU.

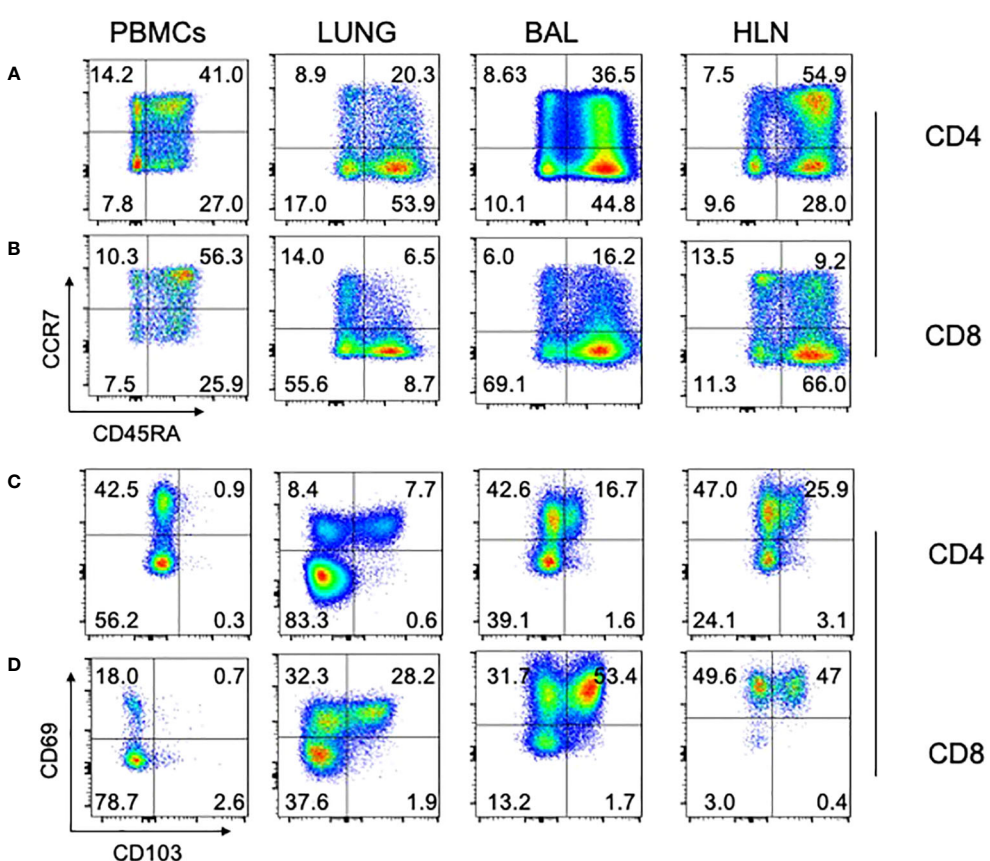


FIGURE 5

Naïve, memory, and TRM subsets in different human tissues. Standard phenotypical markers (CCR7/CD45RA) were used to differentiate memory subsets within the indicated tissues for CD4 (A) and CD8 (B) T cells. Tissue-specific memory T cell markers (CD69/CD103) were also used to identify cell subsets within human tissue, again for both CD4 (C) and CD8 (D). Note that lung tissue-specific memory T cells (CD69+/CD103+) cells are absent from PBMCs, but present in lung tissue, BAL, and HLN. Representative plots are shown, from a 74 year old HIV-/TB- person recruited from the SEU. BAL, Bronchoalveolar lavage; HLN, draining lung hilar lymph node.

the recommended media (AIMV) yielded more consistent results. It is unclear why these two changes improved the consistency of the T-SPOT[®].TB test in our case.

Finally, we presented a snapshot of T cell subsets in the blood and tissues of a subject from the SEU, showing that 1) classical naïve and memory T cell subsets were present in all organs, but at different frequencies, and 2) TRM T cells could be detected within the tissues and were absent from the blood, as would be expected. This work presents the platform under which we can undertake further research to understand the immune response to TB within different human tissues, and between those individuals who died from TB and those who were otherwise healthy at the time of death, but died from other causes, such as RTA victims.

Conclusion

This study presented the feasibility of undertaking postmortem studies for medical research. A clear limitation in this kind of hospital-based study is that patient demographics are skewed; this is particularly the case for TB subjects and is a well-recognized epidemiological quirk. In addition, our non-TB subjects were skewed in terms of gender, limiting the overall generalisability of this study; ongoing recruitment of further subjects may help resolve this issue.

These limitations notwithstanding, we have shown that postmortem studies are a feasible approach to studying tissue-specific immune responses to disease in humans. Lymphocytes can be isolated from tissues up to 14 hours after death with no loss of viability. These cells are functional and show tissue-specific surface markers. Different tissues show clear differences in classical T cell memory and TRM subsets. Human postmortem procedures remain a valuable and essential tool to advance our medical and scientific understanding, not just for understanding TB disease and its progression, but for any disease with a tissue-specific tropism. Although largely fallen out of favor in first-world settings, postmortem studies are clearly a valuable tool in our race to understand immune responses at the site of infection, and in the rational design of future tissue-specific vaccines.

Data availability statement

The raw data supporting the conclusions of this article will be made available by the authors, without undue reservation.

Ethics statement

The studies involving humans were approved by School of Biological Sciences Research Ethics Committee (SBS REC), Makerere University, Kampala, Uganda Mulago National Referral Hospital Research Ethics Committee (MNRH REC), MNRH, Kampala, Uganda Kiruddu National Referral Hospital Research Ethics Committee (KNRH REC), KNRH, Kampala, Uganda Uganda National Council for Science and Technology (UNCST),

Kampala, Uganda London School of Hygiene and Tropical Medicine Research Ethics Committee (LSHTM REC), London, UK. The studies were conducted in accordance with the local legislation and institutional requirements. The participants provided their written informed consent to participate in this study.

Author contributions

GA: Investigation, Methodology, Writing – original draft, Writing – review & editing, Data curation, Project administration. MN: Data curation, Investigation, Methodology, Writing – review & editing. MM: Investigation, Methodology, Writing – review & editing. DO: Investigation, Writing – review & editing. RM: Investigation, Writing – review & editing. JN: Investigation, Writing – review & editing. FB: Investigation, Writing – review & editing. MK: Investigation, Writing – review & editing. HL: Investigation, Writing – review & editing. AA: Investigation, Writing – review & editing. DN: Investigation, Writing – review & editing. SM: Investigation, Writing – review & editing. RL: Investigation, Writing – review & editing. AK: Investigation, Writing – review & editing. JB: Investigation, Writing – review & editing. IA: Investigation, Writing – review & editing, Conceptualization. SC: Conceptualization, Investigation, Writing – review & editing, Funding acquisition, Methodology, Resources, Supervision, Writing – original draft.

Funding

The author(s) declare financial support was received for the research, authorship, and/or publication of this article. This work was supported by NIH Contract 75N93019C00070 and was conducted at the MRC/UVRI and LSHTM Uganda Research Unit which is jointly funded by the UK Medical Research Council (MRC) part of UK Research and Innovation (UKRI) and the UK Foreign, Commonwealth and Development Office (FCDO) under the MRC/FCDO Concordat agreement and is also part of the EDCTP2 programme supported by the European Union.

Acknowledgments

We are grateful to the Administration of Mulago National Referral Hospital and Kiruddu National Referral Hospital for their enthusiasm and cooperation in this research. We extend our gratitude to the bereaved families who gave permission to enroll deceased relatives into the study.

Conflict of interest

The authors declare that the research was conducted in the absence of any commercial or financial relationships that could be construed as a potential conflict of interest.

Publisher's note

All claims expressed in this article are solely those of the authors and do not necessarily represent those of their affiliated

organizations, or those of the publisher, the editors and the reviewers. Any product that may be evaluated in this article, or claim that may be made by its manufacturer, is not guaranteed or endorsed by the publisher.

References

1. Jeremiah C, Eskild P, Rebecca N, Brenda NM, Giovanni Battista M, Farhana A, et al. The WHO Global Tuberculosis 2021 Report – not so good news and turning the tide back to End TB. *Int J Infect Dis* (2022) 124:S26–9. doi: 10.1016/j.ijid.2022.03.011
2. Who. *Global TB Report*. Geneva: World Health Organization (2022).
3. Dye C, Glaziou P, Floyd K, Ravaglione M. Prospects for tuberculosis elimination. *Annu Rev Public Health* (2013) 34:271–86. doi: 10.1146/annurev-publhealth-031912-114431
4. Who. *Polio Eradication Strategy 2022–2026: Delivering on a promise*. Geneva: World Health Organization (2021).
5. Martinez L, Cords O, Liu Q, Acuna-Villaorduna C, Bonnet M, Fox GJ, et al. Infant BCG vaccination and risk of pulmonary and extrapulmonary tuberculosis throughout the life course: a systematic review and individual participant data meta-analysis. *Lancet Global Health* (2022) 10:e1307–16. doi: 10.1016/S2214-109X(22)00283-2
6. Frick M. Tuberculosis Vaccines: Running a different race. In: *2021 Pipeline Report Tuberculosis Vaccines*. The Netherlands: TBVI (2021).
7. Atulomah NO, Pelzer PT, Seeley J, Sun FY, Tameris M, Tao L, et al. Potential implementation strategies, acceptability, and feasibility of new and repurposed TB vaccines. *PLoS Global Public Health* (2022) 2. doi: 10.1371/journal.pgph.0000076
8. Sathaliyawala T, Kubota M, Yudanin N, Turner D, Camp P, Thome JJ, et al. Distribution and compartmentalization of human circulating and tissue-resident memory T cell subsets. *Immunity* (2013) 38:187–97. doi: 10.1016/j.immuni.2012.09.020
9. Kumar BV, Ma W, Miron M, Granot T, Guyer RS, Carpenter DJ, et al. Human tissue-resident memory T cells are defined by core transcriptional and functional signatures in lymphoid and mucosal sites. *Cell Rep* (2017) 20:2921–34. doi: 10.1016/j.celrep.2017.08.078
10. Thome JJ, Farber DL. Emerging concepts in tissue-resident T cells: lessons from humans. *Trends Immunol* (2015) 36:428–35. doi: 10.1016/j.it.2015.05.003
11. Grassin-Delyle S, Abrial C, Salvator H, Brollo M, Naline E, Devillier P. The role of toll-like receptors in the production of cytokines by human lung macrophages. *J Innate Immun* (2018) 1–11. doi: 10.1159/000494463
12. Kloverpris HN, Kazer SW, Mjosberg J, Mabuka JM, Wellmann A, Ndhlovu Z, et al. Innate lymphoid cells are depleted irreversibly during acute HIV-1 infection in the absence of viral suppression. *Immunity* (2016) 44:391–405. doi: 10.1016/j.immuni.2016.01.006
13. Simoni Y, Fehlings M, Kloverpris HN, McGovern N, Koo SL, Loh CY, et al. Human innate lymphoid cell subsets possess tissue-type based heterogeneity in phenotype and frequency. *Immunity* (2017) 46:148–61. doi: 10.1016/j.immuni.2016.11.005
14. Ardain A, Domingo-Gonzalez R, Das S, Kazer SW, Howard NC, Singh A, et al. Group 3 innate lymphoid cells mediate early protective immunity against tuberculosis. *Nature* (2019) 570:528–32. doi: 10.1038/s41586-019-1276-2
15. Hinks TS. Mucosal-associated invariant T cells in autoimmunity, immune-mediated diseases and airways disease. *Immunology* (2016) 148:1–12. doi: 10.1111/imm.12582
16. Hinks TS, Wallington JC, Williams AP, Djukanovic R, Staples KJ, Wilkinson TM. Steroid-induced deficiency of mucosal-associated invariant T cells in the chronic obstructive pulmonary disease lung. Implications for nontypeable *haemophilus influenzae* infection. *Am J Respir Crit Care Med* (2016) 194:1208–18. doi: 10.1164/rccm.201601-0002OC
17. Ogongo P, Steyn AJ, Karim F, Dullabh KJ, Awala I, Madansein R, et al. Differential skewing of donor-unrestricted and $\gamma\delta$ T cell repertoires in tuberculosis-infected human lungs. *J Clin Invest* (2020) 130:214–30. doi: 10.1172/JCI130711
18. Ogongo P, Porterfield JZ, Leslie A. Lung tissue resident memory T-cells in the immune response to mycobacterium tuberculosis. *Front Immunol* (2019) 10:992. doi: 10.3389/fimmu.2019.00992
19. Ogongo P, Tezera LB, Ardain A, Nhamoyebonde S, Ramsuran D, Singh A, et al. Tissue-resident-like CD4+ T cells secreting IL-17 control Mycobacterium tuberculosis in the human lung. *J Clin Invest* (2021) 131. doi: 10.1172/JCI142014
20. Flieger FG, Tschernerg T, Pabst R. Comparison of lymphocyte subsets, monocytes, and NK cells in three different lung compartments and peripheral blood in the rat. *Exp Lung Res* (1996) 22:677–90. doi: 10.3109/01902149609070037
21. Klemm A, Tschernerg T, Krug N, Pabst R. Lymphocyte subsets in distinct lung compartments show a different ability to produce interferon-gamma (IFN-gamma) during a pulmonary immune response. *Clin Exp Immunol* (1998) 113:252–7. doi: 10.1046/j.1365-2249.1998.00657.x
22. Ekberg-Jansson A, Arva E, Nilsson O, Lofdahl CG, Andersson B. A comparison of the expression of lymphocyte activation markers in blood, bronchial biopsies and bronchoalveolar lavage: evidence for an enrichment of activated T lymphocytes in the bronchoalveolar space. *Respir Med* (1999) 93:563–70. doi: 10.1016/S0954-6111(99)90156-7
23. Nemeth J, Rumetshofer R, Winkler HM, Burghuber OC, Muller C, Winkler S. Active tuberculosis is characterized by an antigen specific and strictly localized expansion of effector T cells at the site of infection. *Eur J Immunol* (2012) 42:2844–50. doi: 10.1002/eji.201242678
24. Sutherland JS, Garba D, Fombah AE, Mandy-Gomez A, Mandy FS, Antonio M, et al. Highly accurate diagnosis of pleural tuberculosis by immunological analysis of the pleural effusion. *PLoS One* (2012) 7:e30324. doi: 10.1371/journal.pone.0030324
25. Fu X, Yu S, Yang B, Lao S, Li B, Wu C. Memory-like antigen-specific human NK cells from TB pleural fluids produced IL-22 in response to IL-15 or mycobacterium tuberculosis antigens. *PLoS One* (2016) 11:e0151721. doi: 10.1371/journal.pone.0151721
26. Diedrich CR, O'hern J, Gutierrez MG, Allie N, Papier P, Meintjes G, et al. Relationship between HIV coinfection, interleukin 10 production, and mycobacterium tuberculosis in human lymph node granulomas. *J Infect Dis* (2016) 214:1309–18. doi: 10.1093/infdis/jiw313
27. Chen RY, Dodd LE, Lee M, Paripati P, Hammoud DA, Mountz JM, et al. PET/CT imaging correlates with treatment outcome in patients with multidrug-resistant tuberculosis. *Sci Transl Med* (2014) 6:265ra166. doi: 10.1126/scitranslmed.3009501
28. Coleman MT, Chen RY, Lee M, Lin PL, Dodd LE, Maiello P, et al. PET/CT imaging reveals a therapeutic response to oxazolidinones in macaques and humans with tuberculosis. *Sci Transl Med* (2014) 6:265ra167. doi: 10.1126/scitranslmed.3009500
29. Lin PL, Maiello P, Gideon HP, Coleman MT, Cadena AM, Rodgers MA, et al. PET/CT identifies reactivation risk in cynomolgus macaques with latent M. tuberculosis. *PLoS Pathog* (2016) 12:e1005739. doi: 10.1371/journal.ppat.1005739
30. Maherbe ST, Shemai S, Ronacher K, Loxton AG, Dolganov G, Kriel M, et al. Persisting positron emission tomography lesion activity and Mycobacterium tuberculosis mRNA after tuberculosis cure. *Nat Med* (2016) 22:1094–100. doi: 10.1038/nm.4177
31. Marakala MJ, Raju RM, Sharma K, Zhang YJ, Eugenin EA, Prideaux B, et al. Inflammatory signaling in human tuberculosis granulomas is spatially organized. *Nat Med* (2016) 22:531–8. doi: 10.1038/nm.4073
32. Ural BB, Caron DP, Dogra P, Wells SB, Szabo PA, Granot T, et al. Inhaled particulate accumulation with age impairs immune function and architecture in human lung lymph nodes. *Nat Med* (2022) 28:2622–32. doi: 10.1038/s41591-022-02073-x
33. Cox JA, Lukande RL, Katerregga A, Mayanja-Kizza H, Manabe YC, Colebunders R. Autopsy acceptance rate and reasons for decline in Mulago Hospital, Kampala, Uganda. *Trop Med Int Health* (2011) 16:1015–8. doi: 10.1111/j.1365-3156.2011.02798.x
34. Biraro IA, Egesa M, Toulza F, Levin J, Cose S, Joloba M, et al. Impact of co-infections and BCG immunisation on immune responses among household contacts of tuberculosis patients in a Ugandan cohort. *PLoS One* (2014) 9:e111517. doi: 10.1371/journal.pone.0111517
35. Kizza FN, List J, Nkwata AK, Okwera A, Ezeamama AE, Whalen CC, et al. Prevalence of latent tuberculosis infection and associated risk factors in an urban African setting. *BMC Infect Dis* (2015) 15:165. doi: 10.1186/s12879-015-0904-1
36. Maixenchs M, Anselmo R, Zielinski-Gutierrez E, Odhiambo FO, Akello C, Ondire M, et al. Willingness to know the cause of death and hypothetical acceptability of the minimally invasive autopsy in six diverse African and Asian settings: A mixed methods socio-behavioural study. *PLoS Med* (2016) 13:e1002172. doi: 10.1371/journal.pmed.1002172
37. Laiho K, Penttila A. Autolytic changes in blood cells and other tissue cells of human cadavers. I. Viability and ion studies. *Forensic Sci Int* (1981) 17:109–20. doi: 10.1016/0379-0738(81)90003-7
38. Babapulle CJ, Jayasundera NP. Cellular changes and time since death. *Med Sci Law* (1993) 33:213–22. doi: 10.1177/002580249303300306
39. Dokgoz H, Arican N, Elmas I, Fincanci SK. Comparison of morphological changes in white blood cells after death and in vitro storage of blood for the estimation of postmortem interval. *Forensic Sci Int* (2001) 124:25–31. doi: 10.1016/S0379-0738(01)00559-X



OPEN ACCESS

EDITED BY

Emanuela Corsini,
University of Milan, Italy

REVIEWED BY

Vic Johnson,
Burleson Research Technologies,
United States
Domenico Mavilio,
University of Milan, Italy
Luigi Cari,
University of Perugia, Italy

*CORRESPONDENCE

Gunda Herberth
✉ gunda.herberth@ufz.de
Arkadiusz Pierzchalski
✉ arkadiusz.pierzchalski@ufz.de

RECEIVED 25 October 2023

ACCEPTED 05 December 2023

PUBLISHED 02 January 2024

CITATION

Pierzchalski A, Zenclussen AC and Herberth G (2024) A comprehensive battery of flow cytometric immunoassays for the *in vitro* testing of chemical effects in human blood cells. *Front. Immunol.* 14:1327960. doi: 10.3389/fimmu.2023.1327960

COPYRIGHT

© 2024 Pierzchalski, Zenclussen and Herberth. This is an open-access article distributed under the terms of the [Creative Commons Attribution License \(CC BY\)](#). The use, distribution or reproduction in other forums is permitted, provided the original author(s) and the copyright owner(s) are credited and that the original publication in this journal is cited, in accordance with accepted academic practice. No use, distribution or reproduction is permitted which does not comply with these terms.

A comprehensive battery of flow cytometric immunoassays for the *in vitro* testing of chemical effects in human blood cells

Arkadiusz Pierzchalski^{1*}, Ana C. Zenclussen^{1,2}
and Gunda Herberth^{1*}

¹Helmholtz Centre for Environmental Research - UFZ, Department of Environmental Immunology, Leipzig, Germany, ²Perinatal Immunology Research Group, Medical Faculty, Saxonian Incubator for Clinical Translation (SIKT), University of Leipzig, Leipzig, Germany

Background: There is a growing need for immunological assays to test toxic and modulatory effects of chemicals. The assays should be easy to use, reproducible and superior to cell line-based assays. We have therefore developed a comprehensive portfolio of assays based on primary human blood cells that are suitable for testing chemical effects.

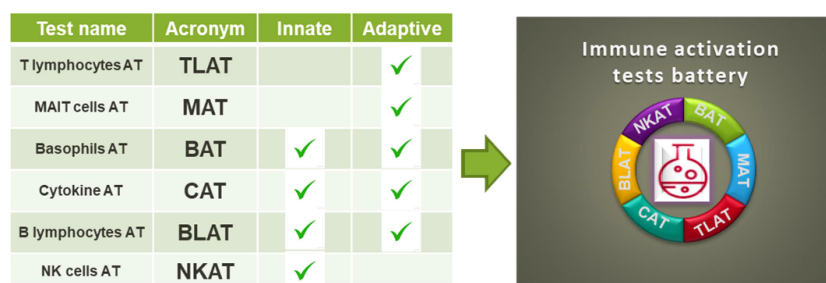
Methods: The flow cytometry-based assays were designed to target a wide range of human peripheral blood mononuclear cells and whole blood, including T cells, NK cells, B cells, basophils and innate-like T cells such as $\gamma\delta$ T, MAIT and NKT cells. We have selected a set of activation markers for each immune cell, e.g: CD154 (T cells), CD137, CD107a (NK cells), CD63 (basophils), CD69, CD83 (B cells), CD69, IFN- γ (MAIT cells) and we selected cell specific stimuli: aCD3 antibodies (T cells); *E. coli* and cytokines IL-12/15/18 (MAIT cells); CpG ODN2006, R848 or aCD40 antibodies (B cells), fMLP or aFc ϵ R1 (basophils) or K562 cells (NK cells).

Results: By selecting immune cell-specific markers and cell-specific stimuli, we were able to induce particular immune responses from the targeted immune cells. For example, the response to stimulation with anti-CD3 antibodies was in 36.8% of CD107a+CD8+ cells. Cytokine stimulation induced the production of IFN- γ in 30% of MAIT cells. After stimulation with *E. coli*, around 50% of MAIT cells produced TNF. About 40% of basophils responded to aFc ϵ R1 stimulation. Similar activation ranges were achieved in K562-stimulated NK cells.

Conclusion: Our test portfolio covers the most relevant immune cells present in human blood, providing a solid basis for *in vitro* toxicity and immunomodulatory testing of chemicals. By using human blood, the natural composition of cells found in the blood can be determined and the effects of chemicals can be detected at the cellular level.

KEYWORDS

immune assays, human blood, flow cytometry, chemical testing, activation marker, immune cells, immunomodulation, immunotox



GRAPHICAL ABSTRACT

Introduction

The classical assessment of the public health risk associated with a certain compound and new chemicals placed on the market includes among others acute toxicity, skin irritation, carcinogenicity, reproductive toxicity and toxicity to a specific organ. By now, immunotoxicity, immunosuppression or immunomodulation is not included in the safety test systems of manufacturers. However, exposure to chemicals can target immune cells and lead to health impairment likewise allergies, autoimmune diseases and even cancer (1–3). But, assessing the effects of chemicals on the human immune system is challenging. Assays to investigate the impact of a stressor at immune cell level should cover many different cell types from both, the innate and the adaptive immune system that respond to different stimuli, similar to the response to bacteria or viruses. Recently, immune assays that can validate the influence of specific chemicals on the activity of immune cells (i.e. modulatory effects) were reported (4). These assays include *in vitro* testing of chemicals on keratinocytes (5), dendritic cell lines (6) and lymphocyte cell lines (7). Further, assays for the analysis of immune relevant effects in peripheral blood mononuclear cells (PBMCs) (8) or in the whole blood (9) were developed. For established cell lines, gene activation in reporter assays is employed. However, very often the effects imply activation of a particular pathway in generic cells, and this gives little or no

information about its significance in living individuals. The analysis of immune effects in PBMCs focuses on general cell stimulation, such as PMA/ionomycin or LPS, by measuring cytokine secretion. The assays used today for chemical testing either lack the complexity of the cell composition in biological samples that is required to mount a proper immune response (as in the case of cell lines) or are too general in their induction of a cell response e.g. by a generalized readout such as cytokine secretion. To address the need for single cell analysis in the diversity of human peripheral blood cell types, flow cytometry is our method of choice. This technology allows simultaneous analysis of the majority of immune cell populations based on their precise determination of phenotype as well as response to stimuli, which is possible by careful selection of lineage and activation markers (10). The use of flow cytometry for single cell analysis allows high-throughput screening of chemicals (11), which promises to identify affected cells and determine which signaling pathway may have been affected (12). Here, we propose a battery of *in vitro* assays to address the diversity of immune responses in human peripheral blood. Our test portfolio covers the activation of T cells and their subtypes including T helper (Th) cell subtypes, $\gamma\delta$ T cells, MAIT and NKT cells. In addition, we have established assays for the activation of NK and B cells as well as basophils (Graphical Abstract). In addition to basophil testing, for which whole blood is used, we established tests for isolated human peripheral blood mononuclear

cells (PBMC). The advantage of the established tests is that they are fast, sensitive and easy to perform.

Methods

Supplementary Table 1 presents the summary of all activation tests including stimulus type, targeted cells, activation time needed to exert the effect, number of markers used for the antibody panel as well as activation markers selected for cell-type specific activation.

PBMC and whole blood collection

Pseudonymous buffy coat samples and heparin-collected whole blood from healthy adult volunteers were obtained from the blood bank at the University of Leipzig, after written informed consent. The study was approved by the Ethics Committees of the University of Leipzig (#079-15-09032015). PBMCs were isolated by density-gradient centrifugation using Ficoll Paque Plus (Cytiva Sweden AB, Uppsala, Sweden). Cells were then stored in 10% DMSO (Sigma-Aldrich, St. Louis, US) in fetal bovine serum (FBS) (Sigma-Aldrich, St. Louis, US) at -150 °C until use. Before treatment, PBMCs were thawed and cultured in IMDM (Gibco, Thermo Fisher Scientific, Waltham, US) supplemented with 10% fetal bovine serum (Sigma-Aldrich, St. Louis, US), 1X Penicillin-Streptomycin (Gibco, Thermo Fisher Scientific, Waltham, US), and 50 µM β-mercaptoethanol (Sigma-Aldrich, St. Louis, US) (complete IMDM medium). Assays were performed with PBMCs or whole blood from at least 4 different donors, results from one representative donor are shown.

T Lymphocyte activation test (TLAT)

PBMC treatment and staining

PBMCs were plated at 10⁶ cells/well in 100 µl complete IMDM medium in U-bottom 96-well microplates (Greiner Bio-One, Frickenhausen, Germany) for at least 2 h at 37°C in a 5% CO₂ incubator. PBMCs were stimulated in a total volume of 200 µl complete IMDM medium with anti-CD3 antibodies (0.5 ng/ml, Clone: OKT-3, BioLegend, San Diego, CA, USA) for 6 h to induce activation. For the last 4 h of incubation Brefeldin A (10 µg/ml) and monensin (1 µM) with anti-CD107a AlexaFluor 647 antibodies (1:1600) in additional 22.5 µl of complete IMDM medium were used.

Following 6 h stimulation, PBMCs were transferred to V-bottom 96-well microplates (Thermo Fisher Scientific Waltham, US). To discriminate between viable and dead cells, the samples were stained in 100 µl of with fixable viability dye-Zombie NIR™ (BioLegend) in PBS for 15 min at RT, thereafter cells were pre-stained with 40 µl anti-CXCR3, -CXCR5 and -TCRgd antibodies in staining buffer (1% FBS in PBS) for 10 min at RT which was followed up by anti-CD3, CD4, CD8, CD19, CD56, CD161, TCRVα7.2, TCRVα24, CD45RA, CD62L, CD27, CCR4, CCR6, CCR10 antibody surface staining in 60 µl of staining buffer for additional 20 min at RT (**Supplementary Table 2**). After surface staining PBMCs were fixed using FACS™ Lysing Solution (BD Biosciences, San Jose, US) for 10 min, and permeabilized with FACS™ Permeabilizing Solution 2 (BD Biosciences, San Jose, US) for further 10 min. Finally, PBMCs were stained for activation and intracellular markers (CD69, CD154, TNF-α, and IFN-γ) in 100 µl staining buffer for 20 min at RT (**Supplementary Table 2**). A representative gating strategy for TLAT is shown in **Figure 1** (FlowJo® v10 software). To present the expression of all activation markers on all T cell subtypes, tSNE analysis (FCS Express 7, *De Novo* Software) was performed (**Figure 2**).

Biosciences, San Jose, US) for 10 min, and permeabilized with FACS™ Permeabilizing Solution 2 (BD Biosciences, San Jose, US) for further 10 min. Finally, PBMCs were stained for activation and intracellular markers (CD69, CD154, TNF-α, and IFN-γ) in 100 µl staining buffer for 20 min at RT (**Supplementary Table 2**). A representative gating strategy for TLAT is shown in **Figure 1** (FlowJo® v10 software). To present the expression of all activation markers on all T cell subtypes, tSNE analysis (FCS Express 7, *De Novo* Software) was performed (**Figure 2**).

MAIT cells activation test (MAT)

PBMC treatment and staining

PBMCs were plated at 10⁶ cells/well in 100 µl complete IMDM medium in U-bottom 96-well microplates (Greiner Bio-One, Frickenhausen, Germany) for at least 2 h at 37°C in a 5% CO₂ incubator. In order to specifically activate MAIT cells within PBMCs, *Escherichia coli* K12 MG1655 samples (*E. coli* K12) were prepared as previously described (13) and stored at -80°C until use. Prior experiments determined the optimal bacteria concentration, indicating 10 bacteria per cell (10 BpC) as sufficient to activate MAIT cells (14). PBMCs were stimulated with *E. coli* K12 (10 BpC) in a total volume of 200 µl complete IMDM medium for 6 h. Brefeldin A (10 µg/mL) in 22.5 µl of complete IMDM medium was added for the final 4 h of incubation.

Following 6 h stimulation, PBMCs were transferred to V-bottom 96-well microplates (Thermo Fisher Scientific Waltham, US). To discriminate between viable and dead cells, the samples were stained with 100 µl fixable viability dye-Zombie NIR™ (BioLegend, San Diego, CA, USA) in PBS for 15 min at RT, thereafter stained for surface markers (CD3, CD4, CD8a, CD161, TCRVα7.2) in 100 µl staining buffer for 20 min at RT (**Supplementary Table 3**). After surface staining PBMCs were fixed using FACS™ Lysing Solution (BD Biosciences, San Jose, US) for 10 min, and permeabilized with FACS™ Permeabilizing Solution 2 (BD Biosciences, San Jose, US) for further 10 min. Finally, PBMCs were stained for activation and intracellular markers (CD69, TNF-α, and IFN-γ) in 100 µl staining buffer for 20 min at RT (**Supplementary Table 3**). A representative gating strategy for MAT is shown in **Figure 3** (FlowJo® v10 software).

Basophils activation test (BAT)

Whole blood treatment and cell staining

100 µL of blood were transferred in FACS 5 mL polystyrene round-bottom tubes (Falcon, Corning, New York, US). For this assay, a shorter time for activation was selected due to the shorter half-life of basophils compared to lymphocytes. As negative control, blood exposed to BAT buffer only was used (72.5 µg/ml MgCl₂ (Sigma-Aldrich), 100 µg/ml CaCl₂ (Sigma-Aldrich), 1ng/ml IL-3 in PBS). Basophils were activated through the addition of anti-FcεR1α antibody (0.1 µg/ml, BioLegend) or with N-Formylmethionylleucyl-phenylalanine (fMLP 0.05 µM, Sigma-Aldrich, St. Louis, US) in 50 µl of BAT buffer for 25 min with simultaneous staining with anti-CCR3

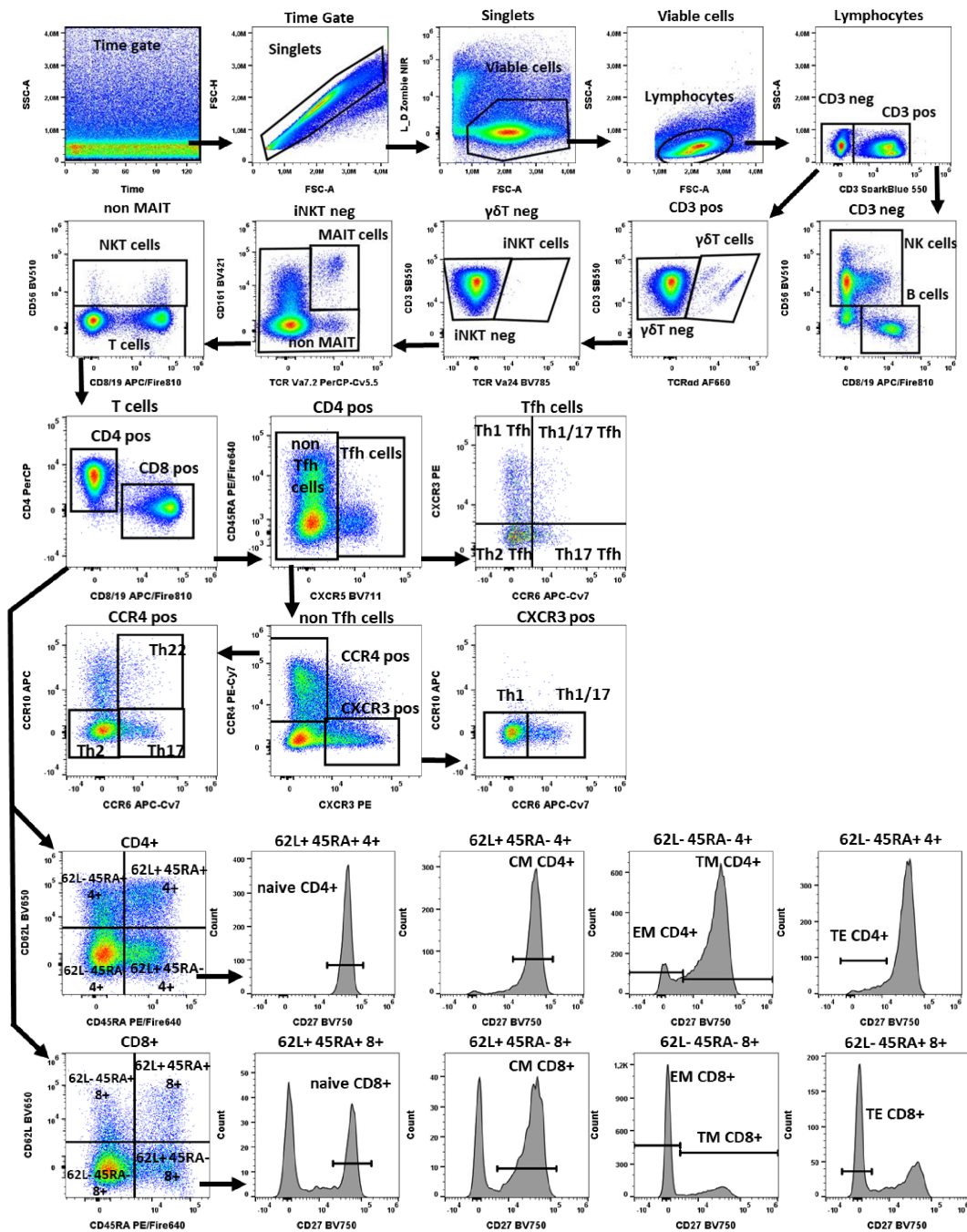


FIGURE 1

Gating strategy in TLAT. We used a time gate to focus on events from stable flow stream. After doublet exclusion, viable cells were selected by using NIR Zombie for dead cell exclusion. Lymphocytes were gated based on FSC-A vs SSC-A. In CD3 neg lymphocytes, B cells were identified by CD19 and NK cells by CD56 expression. In CD3 pos cells $\gamma\delta$ TCR expressing cells were defined as $\gamma\delta$ T cells. Furthermore, in the $\gamma\delta$ T neg population iNKT cells were identified by expression of TCR Va24. Next, in the iNKTneg cells, MAIT cells were selected as double positive for CD161 and TCRVa7.2 expression. In the remaining cells, NKT cells were selected as CD56 expressing cells. Within T cells, conventional T helper (Th) and cytotoxic T (Tc) cells, were identified by the expression of CD4 and CD8 respectively. In both populations, CD45RA, CD62L and CD27 were used to describe: naive T cells (CD45RA+CD62L+CD27+), central memory (CM) (CD45RA-CD62L+CD27+), translational memory (TM) (CD45RA-CD62L-CD27+), effector memory (EM) (CD45RA-CD62L-CD27-), and terminal effector (TE) (CD45RA+CD62L-CD27-) cells. In addition, CD4 pos were subdivided into Tfh (T follicular helper cells) expressing CXCR5+ and non-Tfh cells (CXCR5- cells). Tfh cells were classified according to the expression of CXCR3 and CCR6 into: Th1 Tfh cells (CXCR3+ CCR6-); Th1/17 Tfh (CXCR3+CCR6+); Th17 Tfh (CXCR3-CCR6+) and Th2 Tfh (CXCR3-CCR6-). Non-Tfh cells, were further classified by the expression of CXCR3 and CCR4 as: Th1 (CXCR3+CCR6-); Th1/17 (CXCR3+CCR6+); Th2 (CCR4+CCR6-CCR10-), Th17 (CCR4+CCR6+CCR10-) and Th22 (CCR4+CCR6+CCR10+) cells. A representative color dot plot is shown (n=4). The expression of activation markers on main lymphocyte populations, Th subtypes and T cells maturation subsets is shown in Figure 2 by tSNE analysis and Supplementary Figure 1.

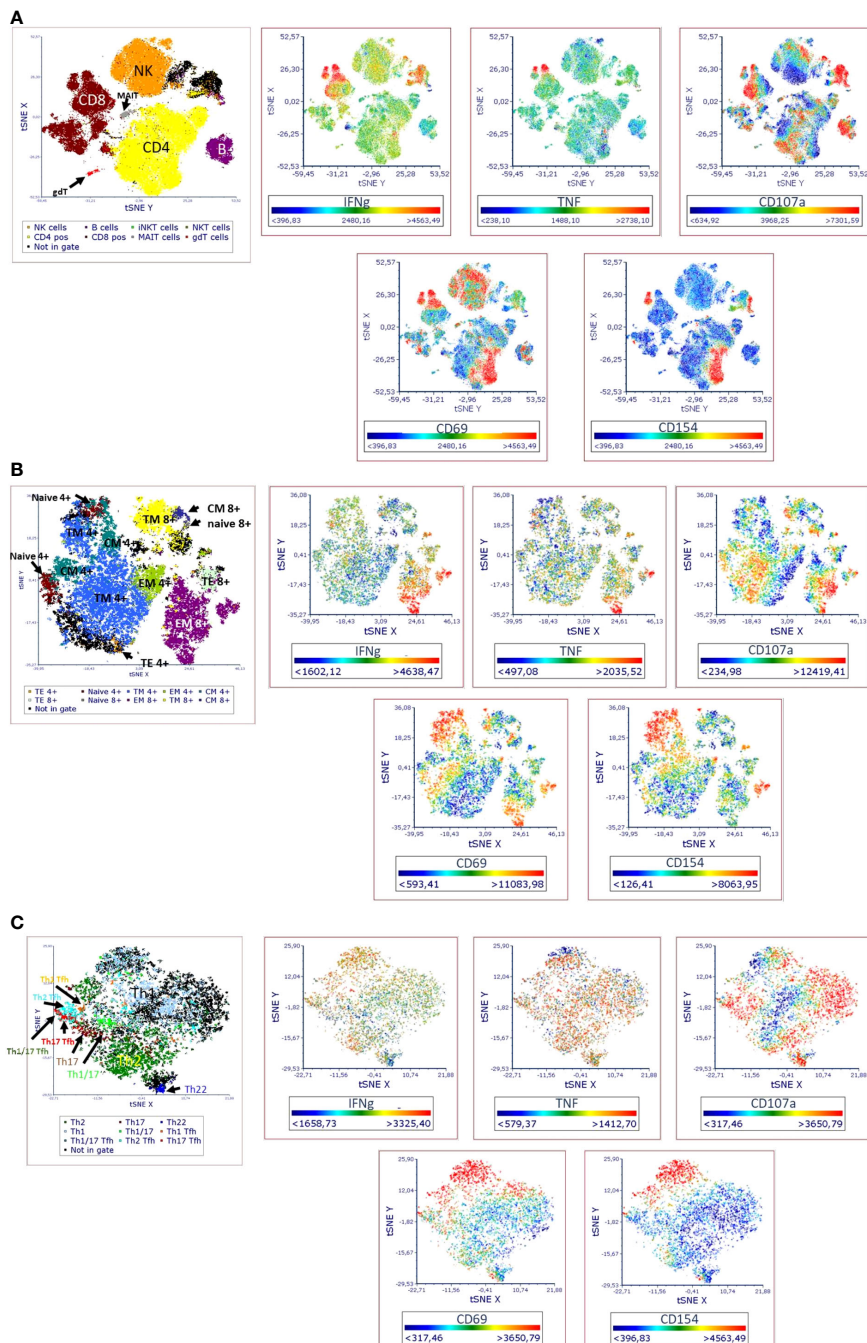


FIGURE 2

Visual distribution of phenotypic and activation markers (t-SNE analysis) in TLAT in (A) lymphocytes (B) maturation subsets of Th and Tc cells (C) cells subsets. t-SNE analysis for a full stained anti-CD3 stimulated PBMC sample was performed in FCS Express 7. Parameters for t-SNE analysis: in (A) sample size of 100,000 total events for lymphocytes, the downsampling was set as interval, with iteration number: 500, perplexity: 50, and approximation: 0.5; in (B) sample size of 10,000 total events for CD3+ cells, the downsampling was set as weighted density with weight: 0 and alpha: 5 with iteration number: 1000, perplexity: 30, and approximation: 0.5; in (C) sample size of 5,000 total events for CD4+ cells, the down-sampling was set as weighted density with weight: 10 and alpha: 5 with iteration number: 1000, perplexity: 50, and approximation: 0.5. Furthermore, in each case the opt-SNE and the estimation for unsampled events were chosen and the Barnes-Hut Approximation was performed. The results were visualized in 2D t-SNE maps. The colors indicate the cell populations which have been identified in t-SNE by backgating. A red color indicates higher expression of a marker and a blue indicates lower/no expression. A representative t-SNE analysis is shown (n=4). Manual gating for each identified cell population and corresponding activation marker is shown in [Supplementary Figure 1](#).

and anti-CD63 antibodies in 50 μ l of BAT buffer ([Supplementary Table 4](#)). After 25 min, the reaction was stopped by adding EDTA 3.8% (Gibco, Thermo Fisher Scientific, Waltham, US). Erythrocytes were then lysed twice using 2 ml erythrocytes lysis buffer (NH_4Cl – Sigma-

Aldrich, NaCO_3 – KMF Laborchemie, Lohmar, Germany, EDTA – Thermo Fisher Scientific) and incubated 10 min at RT. To discriminate between viable and dead cells, 50 μ l of fixable viability dye-eFluorTM 506 (Thermo Fisher Scientific, Waltham, US) in PBS was added and

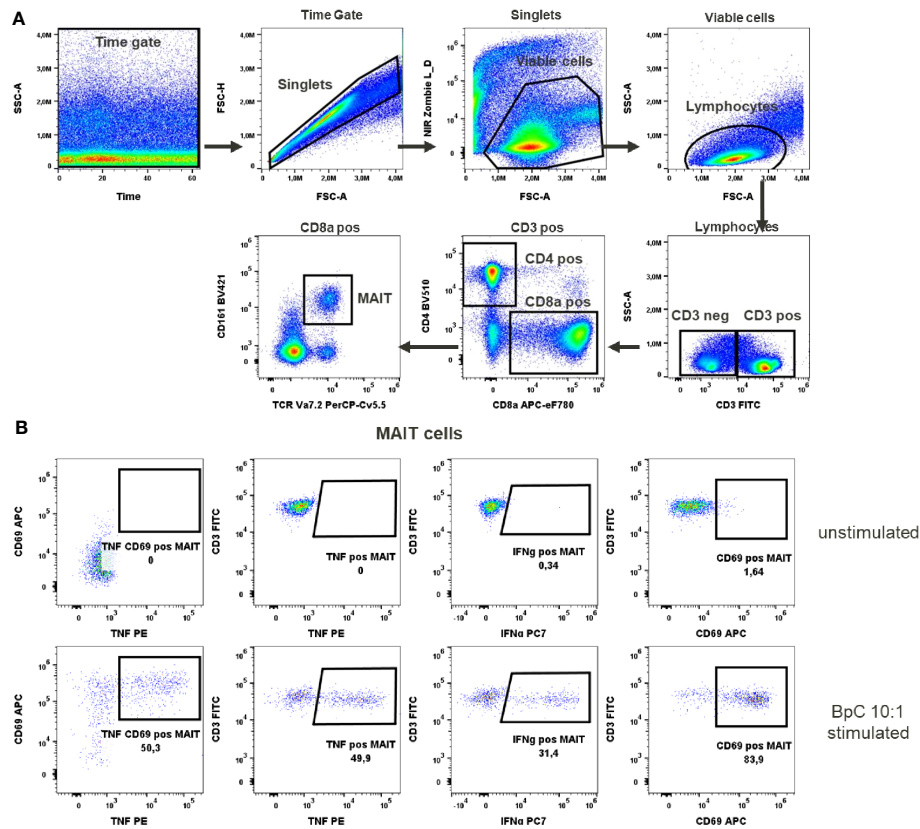


FIGURE 3

MAIT cells activation test. (A) Gating strategy: Time gate was used to focus on events from stable flow stream. After doublet exclusion, viable cells were selected as NIR Zombie negative. Lymphocytes were gated based on FSC-A vs SSC-A. In CD3 positive cells, CD4 and CD8a expressing cells were gated. In CD8a positive cells MAIT cells were identified based on CD161 and TCR Va7.2 expression. (B) Expression of activation markers in unstimulated and *E.coli* stimulated (BpC 10:1) MAIT cells. The numbers shown in the dot plots indicate the percentage of positive events for each marker. A representative color dot plot is shown (n=6).

incubated for 20 min at 4°C. Thereafter, cells were fixed in 200 μ l paraformaldehyde 1% (Sigma-Aldrich) and analyzed by flow cytometry using FACS Canto™ II (BD Biosciences, San Jose, US). A representative gating strategy for BAT is shown in Figure 4 (FlowJo® v10 software).

Cytokines activation test (CAT)

PBMC treatment and staining

PBMCs were plated at 10⁶ cells/well in 100 μ l complete IMDM medium in U-bottom 96-well microplates (Greiner Bio-One, Frickenhausen, Germany) for at least 2 h at 37°C in a 5% CO₂ incubator. In order to specifically stimulate MAIT, NK, NKT and $\gamma\delta$ T cells, PBMC were incubated with IL-12/IL-15/IL-18 (10/25/25 ng/ml) in a total volume of 200 μ l complete IMDM medium for 20 h (Miltenyi/Miltenyi/R&D Systems). Brefeldin A (10 μ g/mL) in 22.5 μ l of complete IMDM medium was added for the final 4 h of incubation.

Following 20h stimulation, PBMCs were transferred to V-bottom 96-well microplates (Thermo Fisher Scientific Waltham, US). To discriminate between viable and dead cells, the samples were stained in 100 μ l fixable viability dye-Zombie NIR™ (BioLegend, San Diego, CA, USA) in PBS for 15 min at RT, thereafter stained for surface

markers (CD3, CD4, CD8, CD56, CD161, TCRgd, TCRV α 7.2) in 100 μ l staining buffer for 20 min at RT (Supplementary Table 5). After surface staining PBMCs were fixed using FACS™ Lysing Solution (BD Biosciences, San Jose, US) for 10 min, and permeabilized with FACS™ Permeabilizing Solution 2 (BD Biosciences, San Jose, US) for further 10 min. Finally, PBMCs were stained for activation and intracellular markers (CD69, CD137, Granzyme B and IFN- γ) in 100 μ l staining buffer for 20 min at RT (Supplementary Table 5). A representative gating strategy for CAT is shown in Figure 5 (FlowJo® v10 software).

B lymphocytes activation test (BLAT)

PBMC treatment and staining

PBMCs were plated at 10⁶ cells/well in 100 μ l of complete IMDM medium in U-bottom 96-well microplates (Greiner Bio-One, Frickenhausen, Germany) for at least 2 h at 37°C in a 5% CO₂ incubator. In order to activate B lymphocytes specifically, PBMCs were stimulated with 0.1 μ M CpG ODN2006 (Miltenyi Biotec, Bergisch-Gladbach, German), 0.25 μ g/ml goat anti-IgM/IgG serum (BioLegend, San Diego, CA, USA), 0.5 μ g/ml R848 (Sigma-Aldrich, St. Louis, US) or 1 μ g/ml anti-CD40 antibodies (BioLegend, San

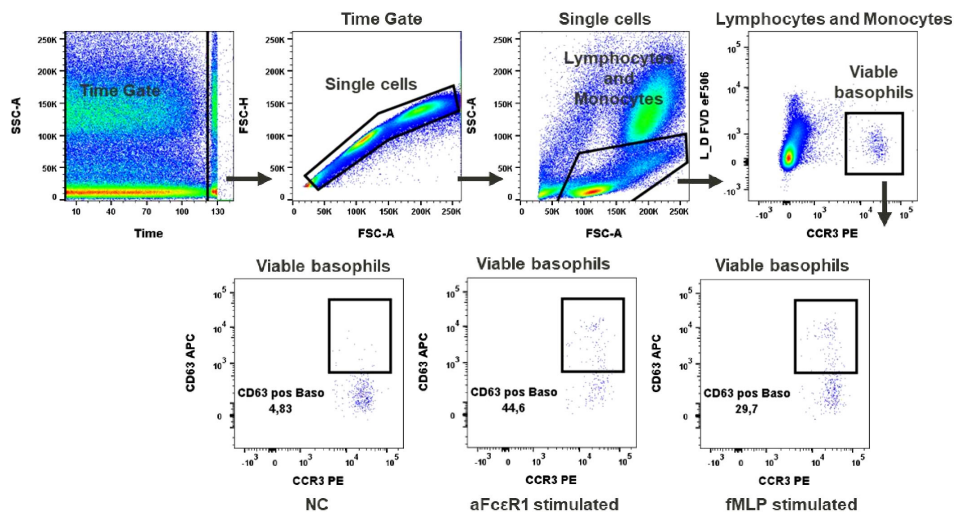


FIGURE 4

Basophils activation test. Gating strategy: Time gate was used to focus on events from stable flow stream. Doublets were excluded in the FSC-A vs FSC-H plot. Lymphocytes/monocytes were gated in FSC-A vs SSC-A. Viable basophils were identified as FVD eF506 negative and CCR3 positive cells. Percentage of CD63 positive events shows activation of basophils upon stimulation with fMLP or anti-FceR1 antibodies, NC (negative control). A representative color dot plot is shown (n=8).

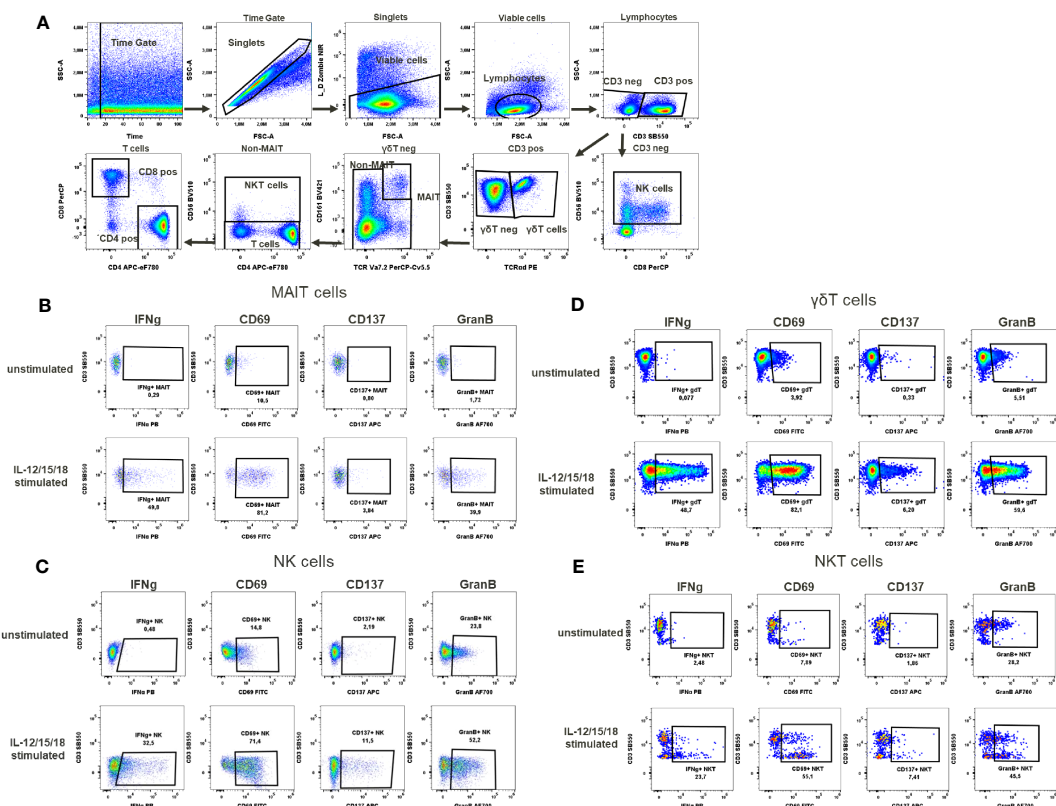


FIGURE 5

Cytokines activation test. (A) Gating strategy: Time gate was used to focus on events from stable flow stream. After doublet exclusion, viable cells were selected as NIR Zombie negative. Lymphocytes were gated based on FSC-A vs SSC-A. In CD3 negative lymphocytes, NK cells were identified by CD56 expression. In CD3 positive cells, $\gamma\delta$ T cells were defined by the expression of TCR $\gamma\delta$. In the non-MAIT population, NKT cells were identified by CD56 expression and remaining cells were defined as T cells expressing CD4 or CD8. Expression of activation markers (IFNg, CD69, CD137, GranB) after IL-12/15/18 stimulation or without stimulation on (B) MAIT cells (C) NK cells (D) $\gamma\delta$ T cells (E) NKT cells. The percentage of positive events is shown below each gate. A representative color dot plot is shown (n=4).

Diego, CA, USA) in a total volume of 200 μ l complete IMDM medium for 4h.

Following 4h stimulation, PBMCs were transferred to V-bottom 96-well microplates (Thermo Fisher Scientific Waltham, US). To discriminate between viable and dead cells, the samples were stained with 100 μ l fixable viability dye-Zombie NIRTM (BioLegend, San Diego, Ca, USA) for 15 min at RT, thereafter stained for surface markers (CD3, CD19, CD20, CD27, IgD) and activation markers (CD69, CD83) in 100 μ l staining buffer for 20 min at RT (Supplementary Table 6). A

representative gating strategy for BLAT is shown in Figure 6 (FlowJo[®] v10 software).

NK cells activation test (NKAT)

PBMC treatment and staining

PBMCs were plated at 250K cells/well in 100 μ l complete IMDM medium in U-bottom 96-well microplates (Greiner BioOne, Frickenhausen, Germany) overnight at 37°C in a 5% CO₂

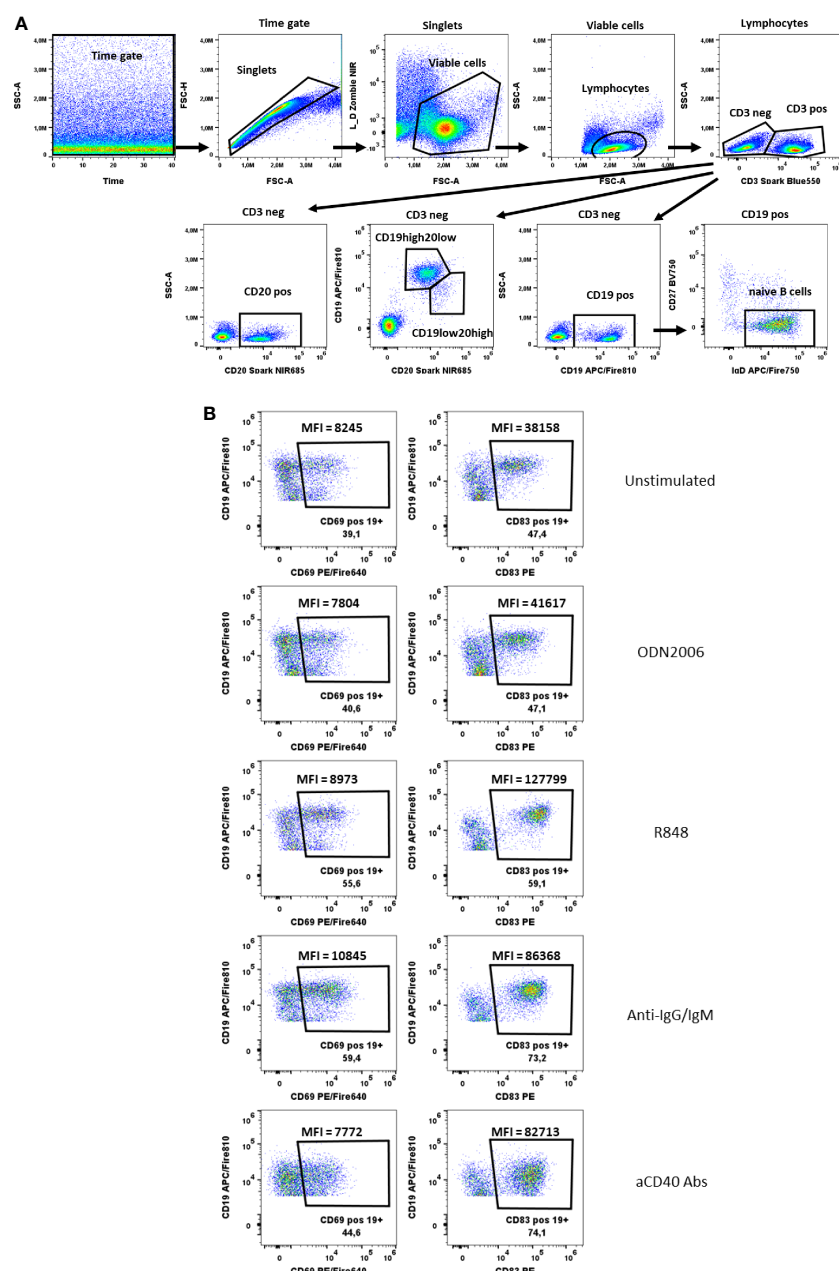


FIGURE 6

B cells activation test. (A) Gating strategy: Time gate was used to focus on events from stable flow stream. After doublets exclusion, viable cells were selected as NIR Zombie negative. Lymphocytes were gated based on FSC-A vs SSC-A. In CD3 negative cells, CD19+ cells, CD20+ cells or CD19+/CD20+ cells were shown. For CD19+ cells, cells negative for CD27 and positive for IgD were defined as naive B cells. (B) Expression of activation markers (CD69, CD83) on CD19+ cells after stimulation with ODN2006 (0.1 μ M), R848 (0.5 μ g/ml), anti-IgG-IgM serum (0.25 μ g/ml), anti-CD40 Abs (0.25 μ g/ml). MFI values indicate the intensity of activation marker expression. A representative color dot plot is shown (n=4).

incubator. To provide NK-specific stimulus K562 cells (human erythroleukemia cells) were used. K562 cells were cultured in RPMI1640 medium supplemented with 10% FBS 1X Penicillin-Streptomycin (Gibco, Thermo Fisher Scientific, Waltham, US), and 50 μ M β -mercaptoethanol. PBMCs were co-exposed to K562 cells at ratios effector (NK) – target (K562): 25:1; 12.5: 1; 6.25:1 in a total 200 μ l of complete IMDM medium for 6h. Brefeldin A (10 μ g/ml), monensin (1 μ M) and anti-CD107a antibodies were added in 22.5 μ l complete IMDM medium for the final 4h incubation.

Following 6h stimulation, PBMCs were transferred to V-bottom 96-well microplates (Thermo Fisher Scientific Waltham, US). To discriminate between viable and dead cells, the samples were stained with fixable viability dye-Zombie NIRTM (BioLegend, San Diego, CA, USA) in PBS for 15 min at RT, thereafter stained for surface markers (CD3, CD16, CD56, HLA-DR) in 100 μ l staining buffer for 20 min at RT (Supplementary Table 7). After surface

staining PBMCs were fixed using FACSTM Lysing Solution (BD Biosciences, San Jose, US) for 10 min, and permeabilized with FACSTM Permeabilizing Solution 2 (BD Biosciences, San Jose, US) for further 10 min. Finally, PBMCs were stained for activation marker (CD137) in 100 μ l staining buffer for 20 min at RT (Supplementary Table 7). A representative gating strategy for NKAT is shown in Figure 7 (FlowJo[®] v10 software).

Proof of concept with immunomodulatory substances

To simulate immunomodulation in our established assays, we performed the TLAT, MAT, CAT, BLAT and NKAT assays with known immunomodulatory substances, i.e. lipopolysaccharide (LPS), rapamycin (RAPA) and cyclosporin A (CsA). Stimulation

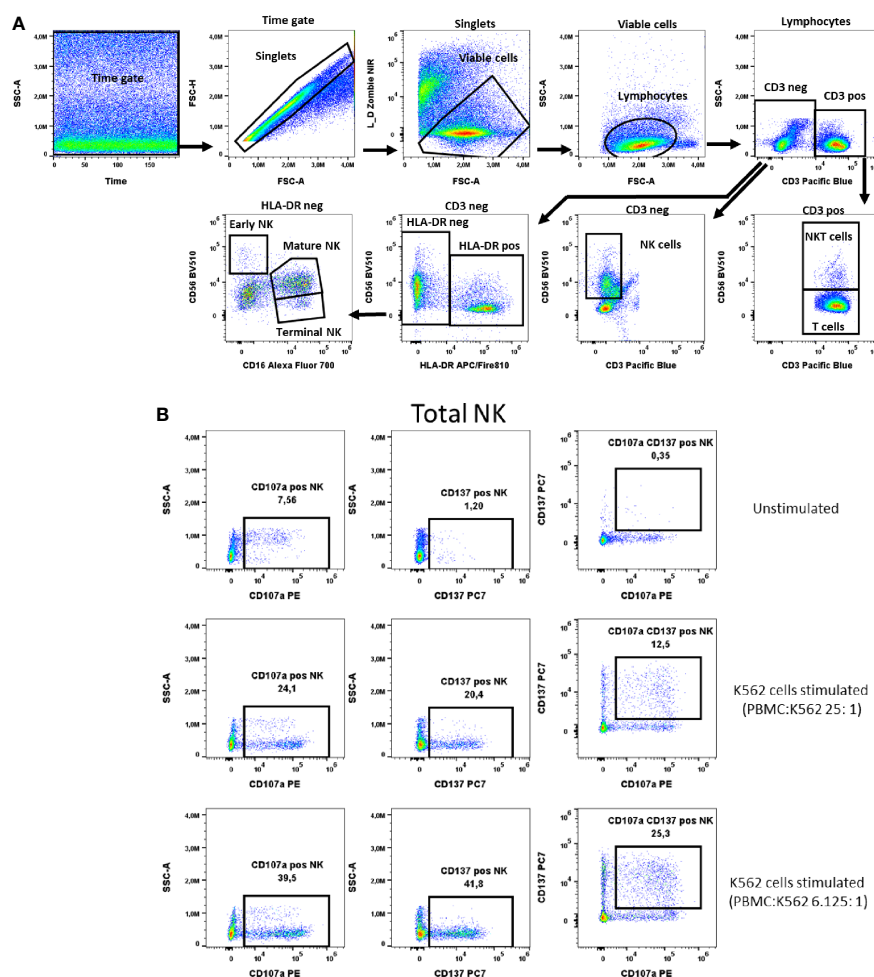


FIGURE 7

NK cells activation test. (A) Gating strategy: Time gate was used to focus on events from stable flow stream. After doublet exclusion, live cells were selected as NIR Zombie negative. Lymphocytes were gated based on FSC-A vs. SSC-A. In the CD3 negative population, CD56 expressing cells were defined as NK cells (total NK). In the CD3 positive population, CD56 expressing cells were defined as NKT cells. In CD3neg cells, HLA-DRneg cell population was identified and by expression of CD16 vs CD56 three NK subpopulations were identified: early (CD56highCD16low), mature (CD56lowCD16high) and terminal (CD56negCD16high) NK. (B) Expression of activation markers on total NK cells. PBMCs were stimulated with K562 cells at different ratios. The numbers in the dot plots indicate the percentage of positive events. In plots showing CD137 vs. CD107a expression, only numbers relating to the double positive population are shown. A representative colored dot plot is shown (n=4). The expression of CD137 and CD107a on NK cell subtypes is shown in Supplementary Figure 4.

in the assays was performed as described above. LPS (100 ng/ml), RAPA (50 nM) and CsA (100 ng/ml or 1 μ g/ml) were added at the same time as the corresponding stimulus in the assay and the cells were then incubated for 4h (BLAT) 6h (TLAT, MAT, NKAT) or 20h (CAT), followed by the procedure described above.

Flow cytometric analysis

Excepting BAT assay, which was analyzed on FACS CantoTM II (BD Biosciences, San Jose, US), for all assays flow cytometrical acquisition was performed using the spectral flow cytometer Cytek Aurora (Cytek Biosciences, California, US). The instrument is equipped with 3 lasers (405, 488 and 635 nm) and 38 detectors. Daily QC was performed using SpectroFlo[®] QC beads prior to acquiring samples to ensure that the cytometer was performing optimally. Daily QC assessed the instrument's optical alignment and the system performance drift by measuring %rCVs and gains needed to place the beads at the target locations established for each detector. During the typical QC protocol, Laser delays and area scaling factors were also optimized, and gain settings adjusted to account for day-to-day instrument variability. We used default instrument settings for PBMCs saved in Cytek Assay Setting (CAS) on all Cytek Aurora systems which are suggested by Cytek as the most accurate for proper fluorochrome recognition. The use of daily QC beads control and Cytek Assay Settings ascertains high reproducibility of results for inter-experiments comparison as well as for inter-laboratory data reproducibility for Cytek Aurora Instruments. The instrument configuration and the selected fluorochromes with their peak emission are shown in [Supplementary Table 8](#). Additional information concerning instrument setup including spectral unmixing as well as N-by-N bivariate plots are provided in [Supplementary Figures S11-S16](#). A minimum of 100,000 viable T cells (according to Zombie NIRTM staining) was acquired per sample.

Results

[Supplementary Table 9](#) in the [Supplementary Material](#) shows the individual results and mean \pm SD of the analyzed donors in each assay. Data of the main immune cell populations are presented after stimulation with the corresponding stimulus giving insights into the variability of immune responses of the donors. In addition, we have calculated the sample size for an expected mean reduction of 25% and a reduction of 50% after a putative chemical exposure. It is obvious that in addition to donors the variability also depends on the markers analyzed. Some of them are very robust and give consistent results even with a small sample size (highlighted in grey, [Supplementary Table 9](#)) as for example all markers in the MAT (MAIT cell activation test) or BLAT (B cell activation test), whereas others such as IFNg in CD4 cells or NKT cells are less robust. Unless otherwise noted below, baseline levels of the analyzed activation markers in unstimulated samples were very low and are not shown.

T Lymphocyte activation test (TLAT)

In the TLAT assay we attempted to obtain a broad lymphocytes response with a special focus on subtypes of T lymphocytes ([Figure 1](#)). As shown in [Figure 2](#) and in [Supplementary Figure 1](#) we have selected two activation markers (CD69 and CD154), cytokines (IFN- γ and TNF) and degranulation marker CD107a to be able to estimate the immune response upon anti-CD3 stimulation. The extent of immune response to aCD3 stimulation differs in magnitude and is cell type specific. As shown in tSNE analysis ([Figure 2](#)), the cytokines IFN- γ and TNF are strongest secreted in CD8+ cells whereas CD107a is expressed on many lymphocyte types including B, NK, CD4+ and CD8+ cells. CD69 is also widely distributed on NK, CD4+ and CD8+ cells. CD154 is mostly expressed in activated CD4+ cells and to a minor extend on CD8+ cells ([Figure 2A](#)). Next, we focused on maturation markers and we observed that IFN- γ and TNF are mostly secreted by effector memory (EM) CD8+ cells. CD107a is expressed on EM CD8+ cells, translational memory (TM) CD8+ cells and TM CD4+ cells, and to a lesser extent on naïve CD4+ cells. CD69 is expressed mostly on TM, central memory (CM) and naïve CD4+ cells, and on TM and EM CD8+ cells. CD154 activation marker is expressed on EM, naïve, TM and CM CD4+ cells as well as on TM and EM CD8+ cells ([Figure 2B](#)). In the case of Th subtypes, IFN- γ was less secreted by Th1 cells and to some extend by Th2 cells and by Tfh cells. TNF was also secreted by Th1 cells, by Th2 cells and also detectable in Th22 cells. CD107a was expressed mainly on Th1 cells, highly on Th22 cells, on Tfh cell subtypes (mainly on Th1, Th1/17 and Th17 subtypes) and to a lesser extent on Th2 cells. CD69 was expressed on Th1 cells and Th1/17 Tfh cells and partially also on Th2 cells. CD154 was distributed similarly to CD69 ([Figure 2C](#)). The detailed expression of activation markers is presented in [Supplementary Figure 1](#). As shown in this figure, the level of activation marker expression is different on different cell subtypes, allowing the choice of the marker that best describes the immune response (e.g. CD107a on CD8+ EM or CD154 on CD4+ EM cells). Depending on the cell type and marker, the response to stimulation with anti-CD3 antibodies is up to 40%, e.g. (mean \pm SD) 36.8 \pm 10 for CD107a +CD8+ cells, [Supplementary Table 9](#). It can also be seen that in the case of B and NK cells, there is hardly any change in the analyzed parameters even after 6 hours of stimulation with aCD3 antibodies. This suggests that the markers selected for T-cell analysis are T-cell specific and that this is a correct approach to using anti-CD3 antibodies to target the T-cell response.

MAIT cell activation test (MAT)

To activate MAIT cells we used a stimulus specific for these cells, the bacterial strain *E. coli* K12. Stimulation at 10 bacteria per cell (BpC) has previously been validated ([14](#)) as the correct ratio to give optimal results for IFN- γ and TNF production in these cells. After this stimulation, 48.8% \pm 6.8 of MAIT cells produced TNF and 42.5% \pm 11.2 of MAIT cells produced IFN- γ , [Supplementary Table 9](#). The

percentage of MAIT cells expressing CD69 after this stimulation was very high ($90\% \pm 7.1$). This would not allow the assessment of an increase in the expression of this marker after chemical exposure, indicating that CD69 is not the optimal activation marker in this case. There was no detectable expression of the activation markers in unstimulated cells (representatively shown in [Figure 3](#)).

Basophil activation test (BAT)

In our test, basophil activation was estimated based on the expression of the activation marker CD63. We observed a low baseline expression of CD63 in unstimulated basophils (up to 5%), [Figure 4](#). Activation after aFc ϵ R1 stimulation was induced in about 40% of basophils, [Supplementary Table 9](#). In the case of fMLP stimulation, the induction was seen in $42.3\% \pm 19.8$ of basophils ([Figure 4](#)). Of note is our observation that the responses to the selected stimuli are very donor dependent and can even exceed 80% of activated cells in the case of fMLP and over 50% for aFc ϵ R1 stimulation ([Supplementary Figure 2](#), [Supplementary Table 9](#)). Therefore, we recommend that the concentrations of these stimulants should be tested for each individual donor before performing the immunomodulatory tests with chemicals.

Cytokine activation test (CAT)

In the cytokine activation assay, the cytokines IL-12/15/18, selected to mimic chronic stimulation, induced the activation of several cell types including MAIT cells, $\gamma\delta$ T cells, NKT cells and NK cells ([Figure 5A](#)). The selected markers, the cytokine IFN- γ , the activation markers CD69, CD137 and the degranulation marker Granzyme B showed a cell type specific activation pattern. In MAIT cells, the CD69 expression to cytokine stimulation was the strongest ($68.1\% \pm 18.9$), followed by Granzyme B expression ($26.9\% \pm 12.5$), IFN- γ expression ($30.9\% \pm 12.6$) and, to a lesser extent, CD137 expression ($3.8\% \pm 1.6$) ([Supplementary Table 9](#), [Figure 5B](#)). No background expression of these markers was observed in unstimulated MAIT cells. In the case of NK cells, background expression of Granzyme B was at a high level ($37\% \pm 16.6$) in unstimulated samples, data not shown. However, after cytokine stimulation, Granzyme B expression was induced to a higher level, reaching $51\% \pm 3.3$ activation of NK cells, [Supplementary Table 9](#). This increase in the percentage of activated cells was accompanied by an increase in mean fluorescence intensity (MFI), which could also be used as a readout of NK cell activation, data not shown. In contrast, the expression of CD137 ($6.1\% \pm 4.3$) and IFN- γ ($17.3\% \pm 12.2$) in activated NK cells was low to moderate ([Figure 5C](#), [Supplementary Table 9](#)). In $\gamma\delta$ T cells, Granzyme B expression was also high in unstimulated cells ($15.7\% \pm 10.4$), data not shown. Again, after stimulation, the percentage of these stimulated $\gamma\delta$ T cells increased ($43.9\% \pm 13.6$, [Supplementary Table 9](#)), with a notable MFI shift. Regarding the expression of IFN- γ , CD69 and CD137 in $\gamma\delta$ T cells after stimulation, the percentages of activated cells were

$37.3\% \pm 20.3$, $56\% \pm 20.1$ and $6.2\% \pm 3.2$, respectively ([Supplementary Table 9](#), [Figure 5D](#)). For NKT cells, the number of activated cells expressing Granzyme B could be induced up to $42.1\% \pm 6.2$ by cytokine stimulation. Excepting for Granzyme B, there was no baseline expression of activation markers in NKT cells in the unstimulated samples (data not shown). Cytokine stimulation induced the expression of CD69 in $31.9\% \pm 16.9$, IFN- γ in $12.1\% \pm 9$ and CD137 in $4.9\% \pm 2.4$ of NKT cells ([Supplementary Table 9](#), [Figure 5E](#)).

B lymphocyte activation test (BLAT)

In the B cell activation test, we identified B cells staining for CD19 and CD20 and additionally naïve B cells via IgD and CD27 specific antibodies ([Figure 6A](#)). The activation markers CD69 and CD83 were chosen to measure the activation after B cell-specific stimulation with anti-IgG/IgM, R848, aCD40 and CpG ODN2006. Both, the % of activated cells and the shift in MFI were used to identify CD69 and CD83-expressing B cells ([Figure 6B](#)). Both markers were also expressed on unstimulated B cells. Nevertheless, an increase in CD69 and CD83 expression was observed after stimulation, which was only visible at the MFI level. The MFI of CD83+CD19+ cells increased from 29930 ± 5627 (unstimulated) to 36733 ± 5265 (CpG ODN2006 stimulated), 101992 ± 17398 (R848 stimulated), 66816 ± 13418 (anti-IgG/IgM stimulated) and 50560 ± 22038 (anti-CD40 stimulated), [Supplementary Table 9](#). For CD69, the effects were less pronounced, [Supplementary Table 9](#). CD20 was shown to be more stable expressed on B cells upon stimulation with anti-CD40 antibodies (see shift of CD19 marker upon aCD40 Abs stimulation in [Figure 6B](#)). Cells with high expression of CD20 and lower expression of CD19 were low abundant and responded less to stimulation that is why we did not focus on their activation pattern. Expression of activation markers on CD20 positive and naïve CD19 positive cells is shown in [Supplementary Figure 3](#).

NK cell activation test (NKAT)

NK cells were defined as CD3- and CD56+ cells (total) and further described with the markers HLA-DR and CD16 into early, mature and terminal NK cells as shown in [Figure 7A](#). The K562 cell line was chosen as a specific stimulus for NK cell activation. In total NK cells the two selected activation markers, CD107a and CD137, were highest expressed, $34.8\% \pm 6.1$ and $29.8\% \pm 10.4$ respectively, when PBMCs were stimulated with K562 at a ratio of K562:PBMC (1:6.125), [Figure 7B](#), [Supplementary Table 9](#). A similar percentage of activated cells expressing these markers has been observed in the early, mature and terminal NK cell subpopulations, [Supplementary Figure 4](#). As representatively shown in [Figure 7B](#) the percentage of NK cells double positive for these markers is lower than the percentage of cells expressing only one of the markers, indicating differences in the NK response to K562 cells with respect to the expression of CD107a and CD137 ([Figure 7B](#)).

Effect of immunomodulatory substances

As a proof of concept, the effects of LPS, rapamycin and cyclosporin A were tested for their immunoactivating and -suppressing activity in the TLAT, MAT, CAT, BLAT and NKAT assays (Supplementary Figures 5–10). With cyclosporine A we observed a downregulation of immune responses in CD154+CD4+, IFNg+CD4+ and TNF+CD4+ cells, but not in CD69+CD4+ and CD107a+CD4+ cells (Supplementary Figure 5). With regard to CD8+ cells, cells expressing CD154, IFNg or TNF also responded strongly to CsA, but in addition also CD69-expressing cells (Supplementary Figure 6). We observed that rapamycin and LPS were not suitable modulators in the TLAT assay. In the MAIT cell activation test (MAT), downregulation of activation was stronger with CsA compared to rapamycin (Supplementary Figure 7). LPS did not exceed a stimulatory effect, but rather a downregulatory effect (Supplementary Figure 7). In the cytokine activation test (CAT), rapamycin, but not CsA, downregulated the immune response, especially in IFNg-producing cells (Supplementary Figure 8). In the BLAT assay, a modulatory effect of the substances used was observed at the MFI level. LPS increased the expression of CD69 in all stimulated CD19+ cells (Supplementary Figure 9). As expected, the strongest effect of LPS was observed on NK cells in the NKAT assay. In particular, a modulatory effect of LPS and CsA was observed in CD137+ NK cells (Supplementary Figure 10). CsA specifically inhibited the activation of CD137-expressing cells, but only to a lesser extent the activation of CD107a-expressing cells.

Discussion

In this paper we propose a battery of *in vitro* assays for immunotoxicology to be considered for the safety assessment of new chemicals. The assays have been designed to cover most of the immune cell subpopulations found in human blood. The main advantage of these assays is that they are simple, rapid, sensitive and reproducible. They are based on human primary blood cells and represent the natural proportion of cells found in human blood. The use of flow cytometry allows to study the effects of chemicals at the level of individual cells. We have also chosen to use a range of cell type-specific stimuli to stimulate the target cells (such as CD3 antibodies for T cells or *E. coli* for MAIT cells), which allows us to validate the extent to which the effects on the target cells can be influenced by a tested chemical. If the aim is to assess immunostimulation and suppression simultaneously, titration of the stimulus must be performed *a priori* in order to determine the concentration that allows both an increase and a decrease in the immune response.

T lymphocytes

Here, we attempted to create a multi-color cytometric panel describing the majority of T cell subsets. In this assay we stimulated the cells by CD3 specific antibodies. We applied a wide range of T cell phenotype describing parameters and we used 5 activation parameters including cytokines, activation markers and degranulation molecules.

In a similar assay, but with a simplified multicolor panel and by using CD3/CD28 stimulation we already analyzed the effect of PFAS on lymphocytes (14). The present assay has the advantage of identifying a greater number of T cell subtypes with less stimulatory agents.

There are already some established assays for the analysis of lymphocytes in immunotoxicity assays. These include first of all Mishell-Dutton (MS) assay which originally was designed to measure proliferation of mouse lymphocytes from spleen in response to sheep erythrocytes (15). This assay was further developed for rat PBMCs (16) and finally for human PBMCs with adaptation of a test to influenza antigen-specific T cells response (HuLA – Human Lymphocytes Activation Assay) which involves the proliferation of T and B cells as well as estimation of antibody secretion by B cells (17, 18). Other tests are focusing on peripheral blood mononuclear cells in depth characterization including cell signaling estimation by phosphorylation of some key molecules involved in immune cells cell signaling so called Single Cell Network Profiling (SCNP) (19, 20). Similar to our approach with multiparameter flow cytometry, others attempted to establish complex assays for multiplex immune cell characterization by mass cytometry (MC) (21). This methodology allows for deep immune phenotyping, but has the disadvantage of being more expensive. The methods like SCNP or MC are to laborious and expensive to be used for routine chemical testing and may serve only as a follow-up in depth testing of mechanism of selected chemicals. In addition to the use of primary human immune cells, there are increasing attempts to establish rodent and human cell lines for chemical testing to avoid the use of living donors. For example, Jurkat T cell line has been used for chemical testing in reporter gene assays (22), at the level of gene expression by PCR (23) and for phosphorylation of intracellular proteins (24). However, these malignant cells are not the true equivalents of primary cells, neither in their phenotypic markers nor in their functionality. Further, immune cells interact within networks and require contact to other immune cell subpopulations to exert their function, a feature that cannot always be mimicked *in vitro*. Activation of T lymphocytes has also been analyzed based on cytokine secretion in supernatant from PBMCs or direct from the cells in the whole blood by using ELISA (25, 26). Also human lymphoblastoid cell line was used to assess cytokine production for assessment of four immunotoxic compounds; tributyltin chloride, cyclosporine A, benzo(a)pyrene and verapamil hydrochloride (27). This however was performed by ELISA and the cells were unspecifically stimulated with PMA/ionomycin. These assays involving cytokines present in the supernatants greatly differs from the established TLAT assay reported here where each immune cell type can be analyzed separately based on profound cell immunophenotyping.

The proposed T lymphocyte activation test covers also Th subsets and maturation stages of T cells (28) which help to identify the T cell subtypes which are affected by chemicals upon T cell specific stimulation. Furthermore, in the cytokine activation test, we focused on characterization of NK cells and innate-like T cells: NKT and MAIT, $\gamma\delta$ T cells in response to cytokines IL-12/15/18. All these cells act in innate immune response and the selected cytokines mimic chronic exposure during immune response (29, 30) which leads to other cytokines release (like IFN- γ or TNF) which takes place at tissue side and may lead to organ failure (31).

In addition, our assay is fast and easy to perform, compared to others which last from 2 days (cytokine release), 4 days for Th cells differentiation up to 7d for cell proliferation (32).

NK cells

NK cells are representatives of innate immune response and numerous *in vitro* tests have been already established to analyze their activity. These methods employ K562 (human erythroleukemia cell line) cells which are either a target of NK cells lytic activity (33, 34) or may be used as stimulators to induce NK response which is evaluated by appearance of degranulation marker CD107a (35, 36). Also proliferation of NK cells was used by others for chemical testing (37). In the NK cell activation assay introduced here, we combined the use of K562 cells as stimulators and two NK cell activation markers, CD107a and CD137. The latter in particular was found to be highly expressed on activated NK cells. The use of both activation markers proved to be very sensitive and led to the description of CD107a only expressing NK cells, CD137 only expressing and double positive for both markers NK cells. In our cytokine activation assay, NK cell activation was assessed by IFN- γ secretion and expression of CD69, CD137 and Granzyme B. As NK cells express high baseline levels of Granzyme B, this marker was not found to be suitable for assessing NK cell activation.

MAIT cells

MAIT cells are the cells orchestrating the immune response to pathogens on the mucosal cell surface (38). They respond to bacterial metabolites of vitamin B origin upon activation of TCR receptor via antigens presented by the MR1 molecule with the subsequent induction of proinflammatory cytokines like TNF or IFN- γ (39). The method described here can be used for the evaluation of MAIT cell responses upon stimulation with *E.coli*. We already used a similar method for the evaluation of chemical effects on these cells for bisphenols, PFAS and samples from wastewater treatment plants (WWTP) (13, 14, 40). The other assay we propose, the cytokine activation of MAIT cells via mixture of IL-12/15/18, serves as surrogate for antigen-independent MAIT cells activation which mimics innate/adaptive immune response leading to chronic activation (41). In the mentioned cytokine activation assay we proved not only that MAIT cells are able to respond to this cytokine cocktail but also that NK, NKT and $\gamma\delta$ T cells do it too, hence more cell types are targeted highlighting the strength and suitability of the proposed flow cytometry assay for multi-parameter marker selection.

B cells

Characterization of the B lymphocyte response can now be measured on the basis of cell proliferation (17), antibody production, cytokine secretion or at the level of surface marker expression (42). There are also attempts to employ B cell lines like

Namalwa B cells for immunotoxicity testing which was shown for PFAS (43). In general there is a high correlation between B cell specific responses (like immunoglobulin secretion and cytokine production) and surface marker expression upon stimulation (42, 44). Here, we attempted to characterize B cell responses by analyzing surface activation markers in PBMC after stimulation with specific agents. We have selected CD69 and CD83 as the most sensitive activation markers. When establishing the tests presented here, we also tested other activation markers like CD70, CD80, CD86 but found them not to be suitable for the characterization of B cell activation (data not shown). Regarding the selected stimuli, by choosing R848 and CpG ODN2006 we were able to determine the innate immune response induced via TLR7/8 and TLR9, respectively. On the other side, by selecting anti-CD40 and anti-IgG/IgM antibodies, we were able to induce the adaptive response of B cells via CD40 and BCR receptor, respectively (42). Hence, by selecting different stimuli, we are able to estimate the effects of chemicals by modulation of innate and adaptive B cells response.

Basophils

Basophils are known to be involved in allergy through the release of IL-4 and their ability to drive antibody responses. These cells play a central role in the regulation of the immune response, which is why their dysregulation by chronic or acute chemical exposure can lead to abnormalities in the immune response (45, 46). Especially their location on mucosal tissues and in the skin make these cells the key responders toward chemical exposure (47). We have selected basophils as proxy for innate immune response. In our assay, whole blood samples are stimulated in different ways to highlight the innate or the adaptive basophil response. We used fMLP, a chemotactic peptide being released by bacteria exerting innate immunity and anti-Fc ϵ R1 α which target the IgE receptor being involved in adaptive immune response. Thus, by selection of the stimulus we are able to discriminate between putative chemical effects on early and late immune responses. By application of our BAT assay we aim to estimate the effects of chemicals on hypersensitivity reactions (48, 49). We selected CD63 as basophil-specific activation marker (50) which correlates with the release of basophil mediators like cytokines and histamine (51). A similar approach for the evaluation of basophil activation in response to quinolones was proposed by Aranda et al. (52). The basophil assay presented has already been validated by us for PFAS, where we found a differential response of basophils to a PFAS mixture depending on the stimulus used (14).

Limitations

The set of immunoassays presented for the testing of chemicals has its own limitations due to the nature of the human biological material, which, although obtained from healthy donors, may contribute to the variability of the response. The variability also depends on the marker analyzed. To overcome the variability, we recommend that the data following chemical stimulation be

normalized for each marker to the values obtained with the activation stimulus only, as each donor may respond differently to the immune cell activation stimulus. The chemical effects are expressed as fold change relative to the corresponding control. This allows the focus to be on the modulation of this stimulation by the chemical exposure, rather than the individual variability of the response to the stimulant (14, 40). It is also a limitation that important immunomodulatory cytokines such as IL-10, IL-17 and TGF- β were not included in our tests because they are barely expressed after the short incubation times we used. Therefore, long-term tests will need to be established to account for chemical effects on these cytokines. We are aware that LPS is an innate, but not the right control to directly assess adaptive immune responses. In this respect, it may act more indirectly by stimulating innate immune responses. Thus, optimal activation and downregulation controls for each immune cell population remain to be evaluated and will be the subject of future research and method development. Another limitation may be that important immune cell subpopulations such as dendritic cells, monocytes or granulocytes were not considered. However, our aim in the present study was to provide fast immunological test systems. In the case of dendritic cells, complex culture conditions would be required as they need few days to differentiate from monocytes (53, 54). In the case of monocytes, the main limiting factor is that they tend to bind to the plastic surfaces, making it difficult to use these cells in flow cytometry. In this case, instead of using human blood monocytes, it is much more advisable to use monocytic cell lines such as THP-1 or U937 for chemical testing (55). Neutrophils could be added to the test portfolio and the effect of chemicals could be measured by the induction of reactive oxygen species after activation of these cells with fMLP or bacteria. However, caution must be exercised as the usability of this test is greatly affected by the rapid degradation of neutrophils, leading to unreliable results (56).

In addition, it is important to consider sex differences as they may influence the assay sensitivity. For example, endocrine disruptors may affect immune cells in a sex-specific manner due to differences in the expression of hormone receptors. The fact that we did not take the sex of the donors into account is a limitation of the present study. However, others have suggested using male donors for the initial testing and then confirming the effects in women at a similar stage of the menstrual cycle (57, 58). It is also possible that *in vitro* testing of chemicals may not reflect the real situation *in vivo*, where the chemicals are subject to metabolism that may either activate or inactivate them, depending on the mode of action (59). Taking all these limitations into account, data should be interpreted with caution and any potential effect of a chemical on the immune response can be verified by other available *in vitro* tests and, to a limited extent, by *in vivo* tests for selected chemicals to explain the mechanism of action.

Conclusions

By selecting PBMC and whole blood as the biological material and addressing the analysis at the multicellular level, we have

established a versatile test system for chemical effect testing. Our assays include T cells, NK cells, B cells, basophils and innate like T cells such as $\gamma\delta$ T, MAIT and NKT cells. By selecting specific stimuli and activation markers, the assays are suitable for identifying chemical effects on certain immune cell subtypes.

Data availability statement

The original contributions presented in the study are included in the article/[Supplementary Material](#). Further inquiries can be directed to the corresponding authors.

Ethics statement

The studies involving humans were approved by Ethics Committees of the University of Leipzig. The studies were conducted in accordance with the local legislation and institutional requirements. The participants provided their written informed consent to participate in this study.

Author contributions

GH: Conceptualization, Supervision, Writing – review & editing. AP: Conceptualization, Data curation, Investigation, Methodology, Visualization, Writing – original draft, Writing – review & editing. AZ: Funding acquisition, Resources, Writing – review & editing.

Funding

The author(s) declare financial support was received for the research, authorship, and/or publication of this article. This work was carried out in the framework of the European Partnership for the Assessment of Risks from Chemicals (PARC) and has received funding from the European Union's Horizon Europe research and innovation programme under Grant Agreement No 101057014.

Conflict of interest

The authors declare that the research was conducted in the absence of any commercial or financial relationships that could be construed as a potential conflict of interest.

Publisher's note

All claims expressed in this article are solely those of the authors and do not necessarily represent those of their affiliated organizations, or those of the publisher, the editors and the reviewers. Any product that may be evaluated in this article, or

claim that may be made by its manufacturer, is not guaranteed or endorsed by the publisher.

Author disclaimer

Views and opinions expressed are however those of the author(s) only and do not necessarily reflect those of the European Union or the Health and Digital Executive Agency. Neither the

European Union nor the granting authority can be held responsible for them.

Supplementary material

The Supplementary Material for this article can be found online at: <https://www.frontiersin.org/articles/10.3389/fimmu.2023.1327960/full#supplementary-material>

References

1. Casas M, Gascon M. Prenatal exposure to endocrine-disrupting chemicals and asthma and allergic diseases. *J Investig Allergol Clin Immunol* (2020) 30:215–28. doi: 10.18176/jiaci.0580
2. Kharrazian D. Exposure to environmental toxins and autoimmune conditions. *Integ Med (Encinitas)* (2021) 20:20–4.
3. Marino M, Mele E, Viggiano A, Nori SL, Meccariello R, Santoro A. Pleiotropic outcomes of glyphosate exposure: from organ damage to effects on inflammation, cancer, reproduction and development. *Int J Mol Sci* (2021) 22:12606. doi: 10.3390/ijms22212606
4. Maddalon A, Iulini M, Melzi G, Corsini E, Galbiati V. New approach methodologies in immunotoxicology: challenges and opportunities. *Endocr Metab Immune Disord Drug Targets* (2023) 23(14):1681–98. doi: 10.2174/187153032366230413081128
5. Ramirez T, Stein N, Aumann A, Remus T, Edwards A, Norman KG, et al. Intra- and inter-laboratory reproducibility and accuracy of the LuSens assay: A reporter gene-cell line to detect keratinocyte activation by skin sensitizers. *Toxicol In Vitro* (2016) 30:278–86. doi: 10.1016/j.tiv.2016.01.004
6. Iulini M, Maddalon A, Galbiati V, Corsini E. The modified THP-1 activation assay for the *in vitro* identification of drug-inducing systemic hypersensitivity. *Front Toxicol* (2022) 4:814050. doi: 10.3389/ftox.2022.814050
7. Kimura Y, Fujimura C, Ito Y, Takahashi T, Terui H, Aiba S. Profiling the immunotoxicity of chemicals based on *in vitro* evaluation by a combination of the Multi-ImmunoTox assay and the IL-8 Luc assay. *Arch Toxicol* (2018) 92:2043–54. doi: 10.1007/s00204-018-2199-7
8. Stolevik SB, Nygaard UC, Namork E, Granum B, Pellerud A, van Leeuwen DM, et al. *In vitro* cytokine release from human peripheral blood mononuclear cells in the assessment of the immunotoxic potential of chemicals. *Toxicol In Vitro* (2011) 25:555–62. doi: 10.1016/j.tiv.2010.11.021
9. Langezaal I, Hoffmann S, Hartung T, Coecke S. Evaluation and prevalidation of an immunotoxicity test based on human whole-blood cytokine release. *Altern Lab Anim* (2002) 30:581–95. doi: 10.1177/026119290203000605
10. Pierzchalski A, Zenclussen AC, Herberth G. OMIP-94: Twenty-four-color (thirty-marker) panel for deep immunophenotyping of immune cells in human peripheral blood. *Cytometry A* (2023) 103:695–702. doi: 10.1002/cyto.a.24766
11. Wang X, Li N, Ma M, Han Y, Rao K. Immunotoxicity *in vitro* assays for environmental pollutants under paradigm shift in toxicity tests. *Int J Environ Res Public Health* (2022) 20:273. doi: 10.3390/ijerph20010273
12. Covey TM, Cesano A, Parkinson DR. Single-cell network profiling (SCNP) by flow cytometry in autoimmune disease. *Autoimmunity* (2010) 43:550–9. doi: 10.3109/08916931003674774
13. Krause JL, Engelmann B, Nunes da Rocha U, Pierzchalski A, Chang HD, Zenclussen AC, et al. MAIT cell activation is reduced by direct and microbiota-mediated exposure to bisphenols. *Environ Int* (2022) 158:106985. doi: 10.1016/j.envint.2021.106985
14. Maddalon A, Pierzchalski A, Kretschmer T, Bauer M, Zenclussen AC, Marinovich M, et al. Mixtures of per- and poly-fluoroalkyl substances (PFAS) reduce the *in vitro* activation of human T cells and basophils. *Chemosphere* (2023) 336:139204. doi: 10.1016/j.chemosphere.2023.139204
15. Mishell RI, Dutton RW. Immunization of dissociated spleen cell cultures from normal mice. *J Exp Med* (1967) 126:423–42. doi: 10.1084/jem.126.3.423
16. Fischer A, Koeper LM, Vohr H-W. Specific antibody responses of primary cells from different cell sources are able to predict immunotoxicity. *in vitro*. *Toxicol In Vitro* (2011) 25:1966–73. doi: 10.1016/j.tiv.2011.06.020
17. Collinge M, Cole SH, Schneider PA, Donovan CB, Kamperschroer C, Kawabata TT. Human lymphocyte activation assay: an *in vitro* method for predictive immunotoxicity testing. *J Immunotoxicol* (2010) 7:357–66. doi: 10.3109/1547691X.2010.523881
18. Collinge M, Schneider P, Li D, Parish S, Dumont C, Freebern W, et al. Cross-company evaluation of the human lymphocyte activation assay. *J Immunotoxicol* (2020) 17:51–8. doi: 10.1080/1547691X.2020.1725694
19. Longo DM, Louie B, Putta S, Evensen E, Ptacek J, Cordeiro J, et al. Single-cell network profiling of peripheral blood mononuclear cells from healthy donors reveals age- and race-associated differences in immune signaling pathway activation. *J Immunol* (2012) 188:1717–25. doi: 10.4049/jimmunol.1102514
20. Hawtin RE, Cesano A. Immune monitoring technology primer: Single Cell Network Profiling (SCNP). *J Immunother Cancer* (2015) 3:34. doi: 10.1186/s40425-015-0075-z
21. Mei HE, Leipold MD, Schulz AR, Chester C, Maecker HT. Barcoding of live human peripheral blood mononuclear cells for multiplexed mass cytometry. *J Immunol* (2015) 194:2022–31. doi: 10.4049/jimmunol.1402661
22. Kimura Y, Yasuno R, Watanabe M, Kobayashi M, Iwaki T, Fujimura C, et al. An international validation study of the IL-2 Luc assay for evaluating the potential immunotoxic effects of chemicals on T cells and a proposal for reference data for immunotoxic chemicals. *Toxicol In Vitro* (2020) 66:104832. doi: 10.1016/j.tiv.2020.104832
23. Schmeits PCJ, Shao J, van der Krieken DA, Volger OL, van Loveren H, Peijnenburg AACM, et al. Successful validation of genomic biomarkers for human immunotoxicity in Jurkat T cells *in vitro*. *J Appl Toxicol* (2015) 35:831–41. doi: 10.1002/jat.3079
24. Shao J, Stout I, Hendriksen PJM, van Loveren H, Peijnenburg AACM, Volger OL. Protein phosphorylation profiling identifies potential mechanisms for direct immunotoxicity. *J Immunotoxicol* (2016) 13:97–107. doi: 10.3109/1547691X.2015.1016635
25. Carfi' M, Gennari A, Malerba I, Corsini E, Pallardy M, Pieters R, et al. *In vitro* tests to evaluate immunotoxicity: a preliminary study. *Toxicology* (2007) 229:11–22. doi: 10.1016/j.tox.2006.09.003
26. Kooijman R, Devos S, Hooghe-Peters E. Inhibition of *in vitro* cytokine production by human peripheral blood mononuclear cells treated with xenobiotics: implications for the prediction of general toxicity and immunotoxicity. *Toxicol In Vitro* (2010) 24:1782–9. doi: 10.1016/j.tiv.2010.07.007
27. Marković T, Gobec M, Gurwitz D, Mlinarić-Raščan I. Characterization of human lymphoblastoid cell lines as a novel *in vitro* test system to predict the immunotoxicity of xenobiotics. *Toxicol Lett* (2015) 233:8–15. doi: 10.1016/j.toxlet.2014.12.013
28. Mousset CM, Hobo W, Woestenenk R, Preijers F, Dolstra H, van der Waart AB. Comprehensive phenotyping of T cells using flow cytometry. *Cytometry Part A* (2019) 95:647–54. doi: 10.1002/cyto.a.23724
29. Piskin G, Tursen U, Sylva-Steenland RMR, Bos JD, Teunissen MBM. Clinical improvement in chronic plaque-type psoriasis lesions after narrow-band UVB therapy is accompanied by a decrease in the expression of IFN-gamma inducers – IL-12, IL-18 and IL-23. *Exp Dermatol* (2004) 13:764–72. doi: 10.1111/j.0906-6705.2004.00246.x
30. Dalbeth N, Gundle R, Davies RJO, Lee YCG, McMichael AJ, Callan MFC. CD56bright NK cells are enriched at inflammatory sites and can engage with monocytes in a reciprocal program of activation. *J Immunol* (2004) 173:6418–26. doi: 10.4049/jimmunol.173.10.6418
31. Pananastasatou M, Verykokakis M. Innate-like T lymphocytes in chronic liver disease. *Front Immunol* (2023) 14:1114605. doi: 10.3389/fimmu.2023.1114605
32. Corsini E, Roggen EL. Immunotoxicology: opportunities for non-animal test development. *Altern Lab Anim* (2009) 37:387–97. doi: 10.1177/026119290903700409
33. Chung HJ, Park CJ, Lim JH, Jang S, Chi HS, Im HJ, et al. Establishment of a reference interval for natural killer cell activity through flow cytometry and its clinical application in the diagnosis of hemophagocytic lymphohistiocytosis. *Int J Lab Hematol* (2010) 32:239–47. doi: 10.1111/j.1751-553X.2009.01177.x
34. Zhang J, Wang Y, Wu L, Wang J, Tang R, Li S, et al. Application of an improved flow cytometry-based NK cell activity assay in adult hemophagocytic lymphohistiocytosis. *Int J Hematol* (2017) 105:828–34. doi: 10.1007/s12185-017-2195-3
35. Alter G, Malenfant JM, Altfeld M. CD107a as a functional marker for the identification of natural killer cell activity. *J Immunol Methods* (2004) 294:15–22. doi: 10.1016/j.jim.2004.08.008

36. Kim J, Phan M-TT, Kweon S, Yu H, Park J, Kim K-H, et al. A flow cytometry-based whole blood natural killer cell cytotoxicity assay using overnight cytokine activation. *Front Immunol* (2020) 11:1851. doi: 10.3389/fimmu.2020.01851

37. Terrén I, Orrantia A, Vitalé J, Zenarruzabeitia O, Borrego F. CFSE dilution to study human T and NK cell proliferation in vitro. *Methods Enzymol* (2020) 631:239–55. doi: 10.1016/bs.mie.2019.05.020

38. Hinks TSC, Zhang X-W. MAIT cell activation and functions. *Front Immunol* (2020) 11:1014. doi: 10.3389/fimmu.2020.01014

39. Godfrey DI, Koay H-F, McCluskey J, Gherardin NA. The biology and functional importance of MAIT cells. *Nat Immunol* (2019) 20:1110–28. doi: 10.1038/s41590-019-0444-8

40. Maddalon A, Pierzchalski A, Krause JL, Bauer M, Finckh S, Brack W, et al. Impact of chemical mixtures from wastewater treatment plant effluents on human immune cell activation: An effect-based analysis. *Sci Total Environ* (2023) 906:167495. doi: 10.1016/j.scitotenv.2023.167495

41. van Wilgenburg B, Scherwitzl I, Hutchinson EC, Leng T, Kurioka A, Kulicke C, et al. MAIT cells are activated during human viral infections. *Nat Commun* (2016) 7:11653. doi: 10.1038/ncomms11653

42. Van Belle K, Herman J, Boon L, Waer M, Sprangers B, Louat T. Comparative in vitro immune stimulation analysis of primary human B cells and B cell lines. *J Immunol Res* (2016) 2016:5281823. doi: 10.1155/2016/5281823

43. Janssen AWF, Louisse J, Rijkers D, Pinckaers NET, Hoekstra SA, Hoogenboom RLAP, et al. Perfluoroalkyl substances (PFASs) decrease the expression of recombination-activating genes (RAG1 and RAG2) in human B lymphoma Namalwa cells. *Arch Toxicol* (2022) 97:457–68. doi: 10.1007/s00204-022-03405-z

44. Lu H, Crawford RB, North CM, Kaplan BLF, Kaminski NE. Establishment of an immunoglobulin m antibody-forming cell response model for characterizing immunotoxicity in primary human B cells. *Toxicol Sci* (2009) 112:363–73. doi: 10.1093/toxsci/kfp224

45. Sokol CL, Medzhitov R. Emerging functions of basophils in protective and allergic immune responses. *Mucosal Immunol* (2010) 3:129–37. doi: 10.1038/mi.2009.137

46. Schwartz C, Voehringer D. Basophils: important emerging players in allergic and anti-parasite responses. *Bioessays* (2011) 33:423–6. doi: 10.1002/bies.201100028

47. Weisse K, Lehmann I, Heroux D, Kohajda T, Herberth G, Röder S, et al. The LINA cohort: indoor chemical exposure, circulating eosinophil/basophil (Eo/B) progenitors and early life skin manifestations. *Clin Exp Allergy* (2012) 42:1337–46. doi: 10.1111/j.1365-2222.2012.04024.x

48. Ariza A, Fernandez TD, Doña I, Aranda A, Blanca-Lopez N, Melendez L, et al. Basophil activation after nonsteroidal anti-inflammatory drugs stimulation in patients with immediate hypersensitivity reactions to these drugs. *Cytometry A* (2014) 85:400–7. doi: 10.1002/cyto.a.22443

49. Chirumbolo S. Major pitfalls in BAT performance may be caused by gating protocols and CD63% cut off evaluation. *Cytometry A* (2014) 85:382–5. doi: 10.1002/cyto.a.22466

50. Bridts CH, Sabato V, Mertens C, Hagendorens MM, De Clerck LS, Ebo DG. Flow cytometric allergy diagnosis: basophil activation techniques. *Methods Mol Biol* (2020) 2163:183–95. doi: 10.1007/978-1-0716-0696-4_15

51. Gamboa PM, Sanz ML, Caballero MR, Antepara I, Urrutia I, Jáuregui I, et al. Use of CD63 expression as a marker of in vitro basophil activation and leukotriene determination in metamizol allergic patients. *Allergy* (2003) 58:312–7. doi: 10.1034/j.1398-9995.2003.00096.x

52. Aranda A, Mayorga C, Ariza A, Doña I, Rosado A, Blanca-Lopez N, et al. In vitro evaluation of IgE-mediated hypersensitivity reactions to quinolones. *Allergy* (2011) 66:247–54. doi: 10.1111/j.1398-9995.2010.02460.x

53. Dauer M, Schad K, Herten J, Junkmann J, Bauer C, Kiefl R, et al. FastDC derived from human monocytes within 48 h effectively prime tumor antigen-specific cytotoxic T cells. *J Immunol Methods* (2005) 302:145–55. doi: 10.1016/j.jim.2005.05.010

54. Martinuzzi E, Afonso G, Gagnerault M-C, Naselli G, Mittag D, Combadière B, et al. acDCs enhance human antigen-specific T-cell responses. *Blood* (2011) 118:2128–37. doi: 10.1182/blood-2010-12-326231

55. Ashikaga T, Yoshida Y, Hirota M, Yoneyama K, Itagaki H, Sakaguchi H, et al. Development of an in vitro skin sensitization test using human cell lines: the human Cell Line Activation Test (h-CLAT). I. Optimization of the h-CLAT protocol. *Toxicol In Vitro* (2006) 20:767–73. doi: 10.1016/j.tiv.2005.10.012

56. Quach A, Glowik S, Putty T, Ferrante A. Delayed blood processing leads to rapid deterioration in the measurement of the neutrophil respiratory burst by the dihydrorhodamine-123 reduction assay. *Cytometry B Clin Cytom* (2019) 96:389–96. doi: 10.1002/cyto.b.21767

57. Maddalon A, Cari L, Iulini M, Alhosseini MN, Galbiati V, Marinovich M, et al. Impact of endocrine disruptors on peripheral blood mononuclear cells in vitro: role of gender. *Arch Toxicol* (2023) 97(12):3129–50. doi: 10.1007/s00204-023-03592-3

58. Klein SL, Flanagan KL. Sex differences in immune responses. *Nat Rev Immunol* (2016) 16:626–38. doi: 10.1038/nri.2016.90

59. Baskett DA, Gerberick GF. Skin sensitization testing: the ascendancy of non-animal methods. *Cosmetics* (2022) 9:38. doi: 10.3390/cosmetics9020038



OPEN ACCESS

EDITED BY

Jeffrey John Bajramovic,
Utrecht University, Netherlands

REVIEWED BY

Nichole Danzl,
Bristol Myers Squibb (United States),
United States
Abdulkader Azouz,
Université libre de Bruxelles,
Belgium

*CORRESPONDENCE

Weiwei Gao
✉ gaoweiwu123@hotmail.com
Yuzhang Wu
✉ wuyuzhang@iiciq.vip

[†]These authors have contributed equally to
this work

RECEIVED 16 October 2023

ACCEPTED 03 January 2024

PUBLISHED 22 January 2024

CITATION

Yang X, Chen X, Wang W, Qu S, Lai B, Zhang J, Chen J, Han C, Tian Y, Xiao Y, Gao W and Wu Y (2024) Transcriptional profile of human thymus reveals IGFBP5 is correlated with age-related thymic involution. *Front. Immunol.* 15:1322214.
doi: 10.3389/fimmu.2024.1322214

COPYRIGHT

© 2024 Yang, Chen, Wang, Qu, Lai, Zhang, Chen, Han, Tian, Xiao, Gao and Wu. This is an open-access article distributed under the terms of the [Creative Commons Attribution License \(CC BY\)](#). The use, distribution or reproduction in other forums is permitted, provided the original author(s) and the copyright owner(s) are credited and that the original publication in this journal is cited, in accordance with accepted academic practice. No use, distribution or reproduction is permitted which does not comply with these terms.

Transcriptional profile of human thymus reveals IGFBP5 is correlated with age-related thymic involution

Xiaojing Yang^{1†}, Xichan Chen^{2†}, Wei Wang³, Siming Qu⁴, Binbin Lai⁵, Ji Zhang², Jian Chen², Chao Han², Yi Tian², Yingbin Xiao³, Weiwei Gao^{2*} and Yuzhang Wu^{1,2*}

¹College of Bioengineering, Chongqing University, Chongqing, China, ²Institute of Immunology People's Liberation Army (PLA) & Department of Immunology, College of Basic Medicine, Army Medical University (Third Military Medical University), Chongqing, China, ³Department of Cardiovascular Surgery, the Second Affiliated Hospital, Army Medical University, Chongqing, China, ⁴Organ Transplantation Center, the First Affiliated Hospital of Kunming Medical University, Kunming, Yunnan, China, ⁵Institute of Medical Technology, Peking University Health Science Center, Beijing, China

Thymus is the main immune organ which is responsible for the production of self-tolerant and functional T cells, but it shrinks rapidly with age after birth. Although studies have researched thymus development and involution in mouse, the critical regulators that arise with age in human thymus remain unclear. We collected public human single-cell transcriptomic sequencing (scRNA-seq) datasets containing 350,678 cells from 36 samples, integrated them as a cell atlas of human thymus. Clinical samples were collected and experiments were performed for validation. We found early thymocyte-specific signaling and regulons which played roles in thymocyte migration, proliferation, apoptosis and differentiation. Nevertheless, signaling patterns including number, strength and path completely changed during aging. Transcription factors (FOXC1, MXI1, KLF9, NFIL3) and their target gene, IGFBP5, were resolved and up-regulated in aging thymus and involved in promoting epithelial-mesenchymal transition (EMT), responding to steroid and adipogenesis process of thymic epithelial cell (TECs). Furthermore, we validated that IGFBP5 protein increased at TECs and Hassall's corpuscle in both human and mouse aging thymus and knockdown of IGFBP5 significantly increased the expression of proliferation-related genes in thymocytes. Collectively, we systematically explored cell-cell communications and regulons of early thymocytes as well as age-related differences in human thymus by using both bioinformatic and experimental verification, indicating IGFBP5 as a functional marker of thymic involution and providing new insights into the mechanisms of thymus involution.

KEYWORDS

IGFBP5, thymus involution, single-cell RNA sequencing, thymic epithelial cell, thymocyte

1 Introduction

Thymus is a major lymphoid organ that is essential for building self-tolerance and functional adaptive immune system (1, 2). Thymic epithelial cells (TECs) closely interact with developing thymocytes to provide a suitable environment for lineage induction and thymocyte selection. In turn, developing thymocytes provide essential signals for TECs maturation. The interaction between TECs and thymocytes, known as “thymic crosstalk”, defines the unique ability of the thymic microenvironment to coordinate T cell development (3, 4). However, the organ degenerates shortly after birth termed as age-related thymic involution which is remarkable in human but not in mouse. Age-related thymic involution leads to immune dysfunction in elder humans which is associated with age-related incidences of cancer, infection, and autoimmunity (5). Yet, the process of thymic degeneration has not been well studied due to the lack of thymic involution models. Therefore, it is urgently needed to study the mechanism of human thymus changes with aging.

Thymus seeding progenitors (TSPs) seed at thymus and begin the following T cell specification and commitment in a series of stages that are precisely coordinated by multiple signaling and transcriptional networks (6). For example, NOTCH signaling drives TSP entering a T cell development trajectory and IL7 signaling boosts early T lineage progenitors' expansion (7, 8). To date, genetic and molecular evidences have identified many of these regulators, but mainly in late stages after T cell commitment and in mouse models (9). There are limited data reporting how immature T cells of human at early stages were regulated. Fortunately, Le et al. provided a high-resolution cellular atlas of the early stages of human immature T cells which motivated us to systematically explore the signaling and regulators of immature T cells by integrating Le et al. data with other available datasets (10). Thymus undergo age-related degenerations with TEC reduction, fibroblast and adipocyte expansion and increasing evidences suggest that thymic involution is mainly caused by thymic stromal cell degeneration, particularly TECs degeneration. For example, gradual loss of FOXN1, which primarily regulates TEC differentiation and homeostasis, has been shown to be associated with age-related thymic involution (11). While, Foxn1-overexpressed embryonic fibroblasts could rejuvenate aged thymic architecture and function in mice (12). However, the mechanistic changes in the aging TECs remain largely unknown. Thanks to Bautista et al. and Park et al. reports which they provided another two high quality and quantity cellular atlas of thymus stroma

Abbreviations: scRNA-seq, single-cell transcriptomic sequencing; EMT, epithelial-mesenchymal transition; TEC, thymic epithelial cell; mTEC, medulla thymic epithelial cell; cTEC, cortex thymic epithelial cell; GEO, Gene Expression Omnibus; HVG, high variable genes; PCA, Principal Component Analysis; UMAP, Uniform Approximation and Projection; GO, Gene ontology; GSVA, Gene Set Variation Analysis; MSigDB, molecular signature database; dbEMT, Epithelial-Mesenchymal Transition gene database; BSA, Bovine serum albumin; DAB, Diaminobenzidine; IgG, Immunoglobulin G; UMI, unique molecular identifiers; DN, double negative; NK, natural killer; DCs, dendritic cells; RSS, regulator specificity score; GCs, glucocorticoids.

including TECs (3, 13), we can data-mine the signals and regulators of TECs during aging. The present work aimed to construct a cell atlas of human thymus and study what signals and transcription factors to be involved in aging thymus.

2 Materials and methods

2.1 Clinical and mouse tissue collection

Human thymic tissues were obtained from patients undergoing cardiac surgery with protocols approved by the Medical Ethics Committee of the Second Affiliated Hospital, Army Medical University following guidelines of the Declaration of Helsinki. Written informed consent was obtained from patients or patient's guardians. C57BL/6J mice were purchased from Chongqing Tengxin Bio-Technology. Mice experiments were performed according to the guidelines of Laboratory Animal Welfare and Ethics Committee of the Third Military Medical University and the study was carried out in compliance with the ARRIVE guidelines.

2.2 Data collection

To obtain single-cell data on human early thymocytes, dataset GSE139042 were acquired from the Gene Expression Omnibus (GEO) database. Dataset GSE147520 was downloaded to obtain enriched human thymic stroma. The dataset downloaded from the Zenodo repository provided most of the thymic immune cells. All data generated or analyzed during this study are freely available in previous publications or in the public domain. All three datasets are raw count matrix. Among them, except for dataset GSE139042, which contains some data from the inDrop platform, the other datasets are all generated by the 10X Genomics platform sequencing. The homogeneity of the datasets was checked to ensure that they can be combined (Supplementary Table 1). The sequencing results from 10X Genomics show a high degree of similarity across the board, with only slight variations observed in the data obtained from inDrop. However, we can integrate them using a specialized algorithm.

2.3 ScRNA-seq analysis in Python

Single-cell data analysis was performed using Python package Scanpy (version 1.9.1) (14). Quality control and data correction for single-cell samples based on the number of genes detected, the number of molecules detected, and the percentage of mitochondria in each single-cell sample. Cells with fewer than 2000 detected molecules and 500 detected genes were removed from the dataset. Cells with more than 7000 detected genes were considered as potential doublets and removed from the dataset. For the percentage of mitochondria, samples using 10X Genomics platform with more than 10% mitochondria genes were removed, and samples using inDrop platform with more than 20% mitochondrial genes were removed. Scrublet (15) algorithm was

applied to calculate scrublet-predicted doublet score to exclude doublets from scRNA-seq data. After data filtration, the concat function was first used to merge data from two different platforms provided by Le et al. and then merged it with data from Park et al. and B et al. to produce a combined dataset. Cell cycle scores were calculated using the score_genes_cell_cycle function. Normalize_per_cell was used to normalize the combined dataset (counts_per_cell_after = 10,000). The top 2,000 high variable genes (HVG) defined by highly_variable_genes were used for principal component analysis (PCA). Cell cycle-dependent changes in gene expression and variation caused by mitochondrial gene expression were regressed out using the regress_out function. BBKNN (16), an integration algorithm, was applied to correct batch effects caused by multiple samples and platforms. Clustering was performed using the Leiden algorithm with a resolution of 1.5. Clustering and visualization results were realized by Uniform Approximation and Projection method (UMAP). The rank_genes_groups (method = t-test) function was used to identify markers for each cluster. Cluster cell identity was named by manual annotation using differentially expressed genes and known marker genes.

2.4 ScRNA-seq analysis in R

Some sub-clustering was further subdivided using Seurat (version 4.2.0) (17) to achieve a high-resolution annotation. The re-analysis of all subpopulations was performed using similar methods. After extracting the original count matrix of the target subpopulation, we adopted the method of re-dimensionality reduction clustering to obtain more diverse cell types. The same cell filtration conditions as in the Scanpy analysis were taken. The NormalizeData function was used to normalize the data, and the CellCycleScoring function was applied to calculate cell cycle related scores. After the top 2000 HVG were obtained, the ScaleData function was used to remove cell cycle effects and PCA was performed. The RunHarmony function in Harmony (18) was then executed to remove the batch effect and 1-40 PCs were used for UMAP dimensionality reduction. The FindallMarkers function was used to identify markers for each cluster. Cell clusters were annotated by differentially expressed genes and markers that had been reported.

2.5 Cell-cell communication analysis

CellChat (version 1.4.0) (19), an algorithm for analyzing the intercellular communication networks at single-cell level, contains ligand-receptor interaction databases for human and mouse. The global intercellular communication network under 19w, 10m and 25y conditions were quantified and compared. To observe trends in cell-cell communication, compareInteractions function was used to compare the total number of interactions and interaction strength or compare them among different cell populations. Comparing the major sources and targets in 2D space to identify the cell populations with obvious changes in sending or receiving signals. To identify the conserved and context-specific signaling pathways, the overall information flow for each signaling pathway were

calculated and compared. Those signaling pathways greatly altered were picked up for specific analysis. Comparing the communication probabilities mediated by ligand-receptor pairs from some clusters to other clusters by setting comparison in the function netVisual_bubble.

2.6 Gene-regulatory networks

SCENIC (version 1.2.4) (20) is a tool to simultaneously reconstruct gene regulatory networks and identify steady cell states from scRNA-seq data. The pySCENIC package (version 0.11.2) (21), a Python-based implementation of the SCENIC pipeline, has a faster analytical speed. The analysis section was run in pySCENIC. The input to pySCENIC was the scRNA-seq expression matrix. The result was printed in loom file format and imported into SCENIC for visualization. R and Cytoscape were used to visualize the results (22).

2.7 Gene ontology (GO) and gene set variation analysis (GSVA)

ClusterProfiler (version 4.2.2) was applied to analyze the enrichment of certain genes (23). Functional enrichment analysis based on the GO database was performed on each cell to explore their possible biological functions. We considered only gene sets with p-value <0.05 were significantly enriched. In addition, 200 hallmark signatures associated with epithelial-mesenchymal transition (EMT) were collected from the molecular signature database (MSigDB) and 1167 genes associated with EMT were downloaded from the Epithelial-Mesenchymal Transition gene database (dbEMT) (24). Gene set variation analysis (GSVA) was performed to calculate the enrichment scores for these TEC clusters.

2.8 Immunohistochemical staining

Thymus tissue was fixed in 4% paraformaldehyde (biosharp life science, BL539A), embedded in paraffin, and sectioned to 4 μ m thickness. Antigen retrieval was performed by boiling sections in Improved Citrate Antigen Retrieval Solution (Beyotime, P0083). Sections were blocked for 1 hour at room temperature using 5% BSA (Solarbio life sciences, SW3015), followed by incubation with IGFBP5 antibody (Abclonal, A12451) overnight at 4 °C. Staining with HRP Donkey Anti-Rabbit IgG (H+L) (Abclonal, AS038) was performed for 1 h at room temperature. Slides were developed using DAB (Beyotime, P0202) and counterstained with hematoxylin (Beyotime, C0107). All slides were scanned by PreciPoint M8 and analyzed with ViewPoint BETA v 0.8.2.7.

2.9 Cell culture and siRNA transfection

Immortalized TECs (iTECs) were cultured in Dulbecco's modified Eagle's medium (DMEM, Gibco, USA) supplemented

with fetal bovine serum (10%, FBS, Gibco, USA) and Penicillin-Streptomycin Solution (1%, PS, Biosharp, China). Cells were maintained in a humidified incubator with 5% CO₂ at 37 °C. siRNAs were synthesized by Sangon Biotech (Shanghai, China). siRNAs transfection was carried out by LipofectamineTM 3000 (InvitrogenTM, LipofectamineTM 3000, USA) according to the manufacturer's instructions. Total RNA was harvested by RNAiso Plus (Takara, Japan) and protein was collected by RIPA Lysis Buffer (Beyotime, China) with Phosphatase and Protease Inhibitor Cocktails (Roche, USA) after 48h and 72h, respectively, then stored at -80°C. The siRNA sequences utilized are shown in **Supplementary Table 2**. C57BL/6J mice were sacrificed and thymocytes were purified and co-culture with iTECs cells for 24 h using 24-well Transwell plates (8-μm pore size; Millipore, USA).

2.10 Cell proliferation assay and flow cytometry

Cell proliferation was assessed by CCK8 incorporation assay (Beyotime, China) as previously described (25). Single-cell suspensions of thymocytes and iTECs from the experiments were used for flow cytometry with a FACSCanto II (BD Biosciences). The surface staining was performed in FACS buffer, the anti-CD4 (RM4-5), anti-CD8 (53-5.8) were obtained from Biolegend. The staining of Ki67(Invitrogen) was performed with a Cytofix/Cytoperm Fixation/Permeabilization Kit (554714, BD Biosciences) according to the manufacturer's instructions after surface staining. Data were analyzed by FlowJo (Treestar).

2.11 Reverse-transcription quantitative PCR (RT-qPCR)

Total RNA was isolated from iTECs cell with RNAiso Plus via Phenol chloroform extraction. gDNA removing and DNA synthesis were implemented by ABScript III RT Master Mix for qPCR with gDNA remover (ABclonal, China) according to the manufacturer's instructions. Real-time PCR was performed (Novogene&Kubo, Quantagene q225, China) with SYBR Green qPCR Master Mix (MedChemExpress, China). The relative mRNA level was calculated by the 2- $\Delta\Delta Ct$ method and normalized to β-actin. RT-PCR primers were synthesized by Sangon Biotech (Shanghai, China) and listed in **Supplementary Table 3**.

2.12 Western blot

Total protein was separated by 4-20% Tris-HCl/SDS-polyacrylamide gels (Beyotime, BeyoGelTM Plus PAGE, China) and transferred to PVDF membranes. Then, the membranes were incubated with blocking buffer (Beyotime, QuickBlockTM Western, China) for 1h, with primary antibodies (IGFBP5 (1:1000, A12451, ABclonal), β-actin (1:5000, ab8226, Abcam)) overnight at 4 °C and with secondary antibody (1:5000, HRP Donkey Anti-Rabbit

IgG (H+L) (AS038), ABclonal) for 1h at room temperature. Membranes were imaged by ChemiDocTM Touch (ChemiDoc Touch 1708370, Bio-red, USA).

2.13 Statistical analysis

Statistical analysis and graphics were generated using GraphPad Prism version 5.0 (GraphPad Software, La Jolla, CA, USA; www.graphpad.com). All statistical analyses were performed using a paired two-sided t test. A difference was considered to be statistically significant at *P< 0.05, **P< 0.01 and ***P< 0.001, and not significant (NS) when P> 0.05.

3 Results

3.1 Integration of cell atlas of human thymus

To gain insight into the mechanisms of development and degeneration of thymus at different ages, we downloaded three recently published scRNA-seq datasets of human thymus to generate an integrated cell atlas (3, 10, 13) (**Figure 1A**). After strict quality control, a total of 350,678 cells from 36 samples were retained for downstream analysis. Cell cycle effects were viewed and regressed out. BBKNN was used to exclude the batch effects across the combined dataset (**Figure S1A**) and datasets were well integrated (**Figure 1B**). After clustering and visualization, we annotated the dataset into 19 different cell types (**Figure 1C**), which can be clearly identified by specific marker genes (**Figure 1D**; **Supplementary Figure 1B**). We divided differentiating T cells into CD34⁺ double negative (CD34⁺ DN), CD34⁻ double negative (CD34⁻ DN), double positive (DP), αβT (entry), CD8⁺ single positive (CD8⁺ T), CD4⁺ single positive (CD4⁺ T), CD80α⁺, FOXP3⁺ regulatory (Treg) and γδT cells. We also identified other immune cells including natural killer (NK) cells, B cells, macrophages & monocytes (Mono&Mac), and DCs. Finally, the integrated human thymus atlas benefited us for the following analysis.

3.2 Cell–Cell communication of early thymocytes

A systematical overview of the intercellular communications of human early thymocytes remained incomplete and we thus investigated intercellular signaling to resolve what and how the signaling impacted development of early thymocytes. CD34⁺ early thymocytes, TECs and thymic stroma were enriched and analyzed (**Supplementary Figure 2A**). We annotated TECs subcluster as cTEC^{hi}, cTEC^{lo}, immature TEC, mTEC^{lo}, mTEC^{hi}, corneocyte-like mTECs, neuroendocrine, muscle-like myoid, and myelin⁺ epithelial cells. The immune cells were further divided into Thy1, CD123⁺ Thy2, Thy2a, Thy2b, Thy2c and Thy3 using accepted

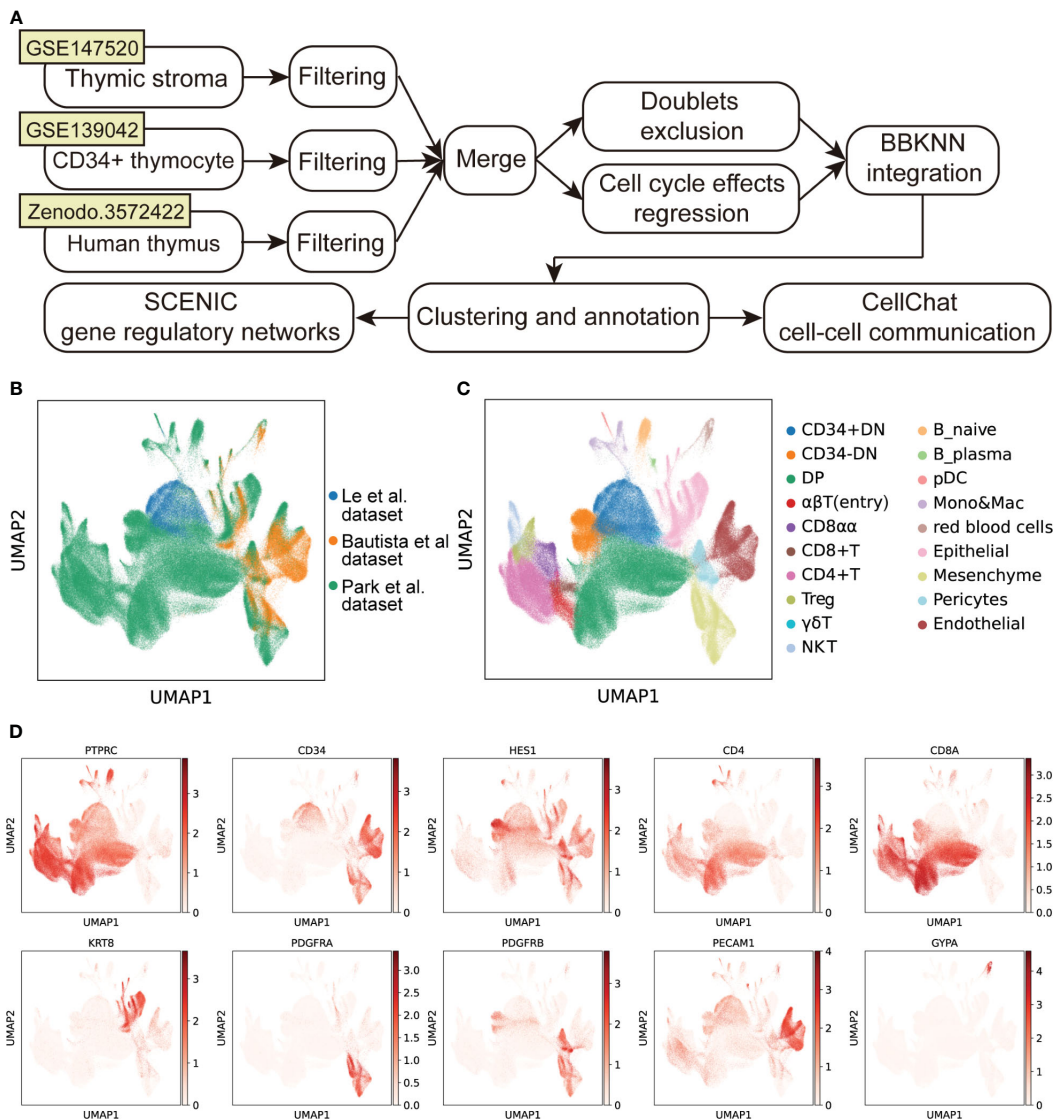


FIGURE 1

Integration of scRNA-seq datasets of human thymus. **(A)** Schematic flowchart showing the processing, integration, and analysis of the cell atlas of human thymus. **(B)** UMAP visualization of human thymus colored by data source. **(C)** UMAP visualization of the cellular composition of human thymus colored by cell type (DN, double-negative T cells; DP, double-positive T cells; pDC, plasmacytoid dendritic cells; Mono, monocyte; Mac, macrophage). **(D)** UMAP visualization of the expression of well-known marker genes used for cell cluster identification.

markers (3, 10, 26). CellChat was performed to predict the ligand-receptor pairs among early thymocytes and other cells (Supplementary Figure 2B; Supplementary Table 4). The number and strength of interactions were shown, indicating that there was extensive “thymic crosstalk” not only between TECs and thymocyte but also between stroma cells and thymocytes (Figure 2A). Ligand-receptor pairs were then divided into 21 signaling pathways. Among them, MK, MIF, PTN, CXCL and GALECTIN signaling were mainly involved in the incoming signaling pattern between early thymocytes and other cells (Figure 2B, bottom panel), while the outgoing signaling pattern mainly included MIF and PARs signaling (Figure 2B, top panel).

We further characterized and visualized specific ligand-receptor pairs. Chemokines were reported to be essential for early

thymocytes seeding and migration in thymus and our following analysis was in accordance with these reports (27). CCL25-CCR9 was illustrated to communicate between TECs and Thy1 (Figure 2C). While, CXCL12 is emitted by nonimmune cells (mainly stroma cells) and received by early thymocytes (Figure 2D, Left panel). As early thymocytes developed, the interaction mediated by this signaling was stronger and CXCR4 expression was also higher (Figure 2D, Right panel). These, together with previous literature descriptions, suggested that CCL25-CCR9 and CXCL12-CXCR4 signaling were involved in early thymocytes migration and development (28). Thymocyte proliferation is also important for thymus maturation, we found VEGF/IGF signals were involved. Specifically, VEGF signal emitting from Thy2 cells (identified as DN2 in mice) may facilitate the growth of endothelial

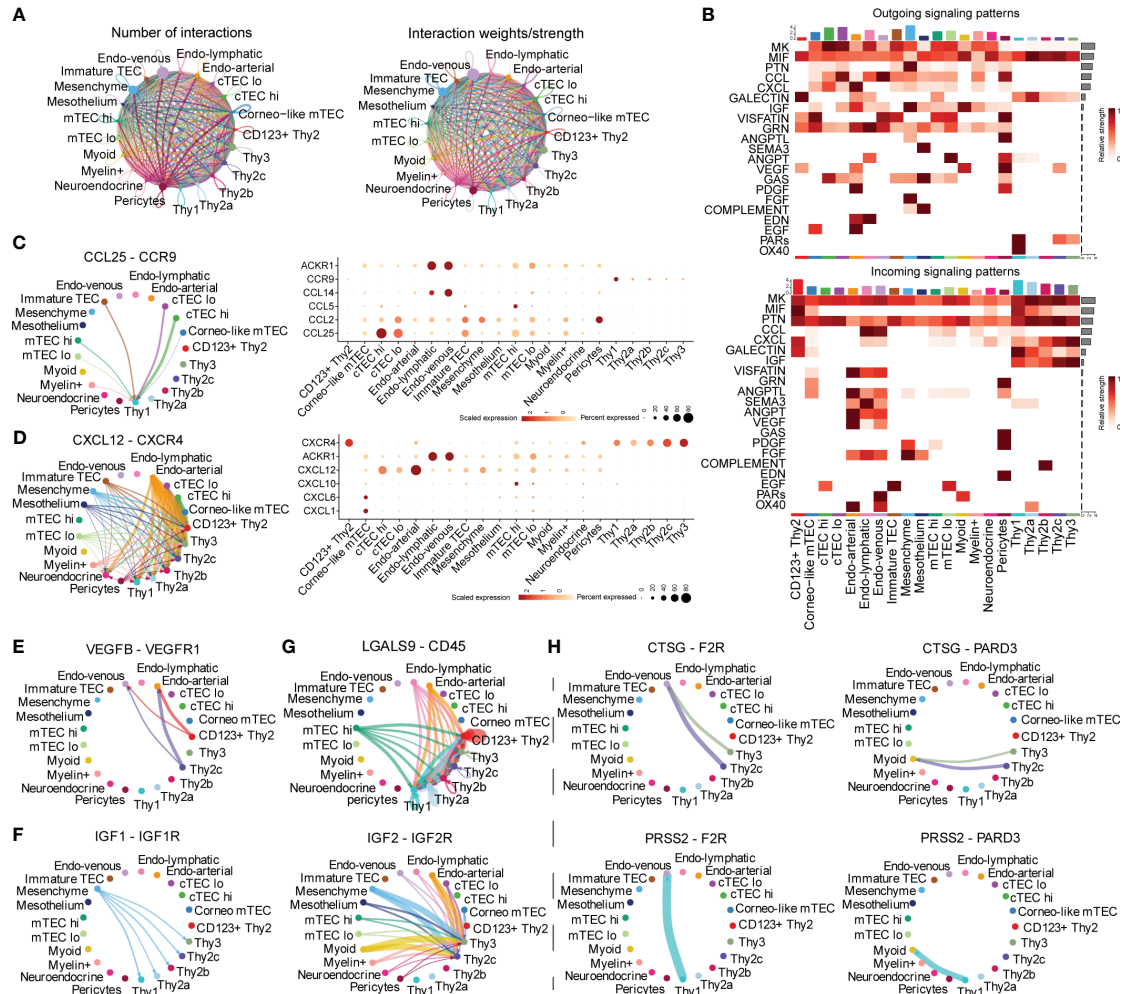


FIGURE 2

FIGURE 2
 Inference of Cell–Cell communications by CellChat of early thymocytes. **(A)** Circle plots of the interaction quantity and interaction strength among cell types. Here and in later figures, dot represents a cell type, line represents the interaction, and color encodes the number of ligand-receptor pairs **(B)** Heatmaps of outgoing and incoming signaling flows of each cell population mediated by individual signaling axes. Here and in later figures, color represents maximum normalized mean strength. **(C, D)** Circle plot show cell–cell communication mediated by CCL/CXCL (Left panel). Dot plot of ligand receptor pair expression of CCL/CXCL (Right panel). **(E)** Circle plots show cell–cell communication mediated by VEGF **(E)**, GALECTIN **(F)**, IGF **(G)**, PARs **(H)**.

cells (Figure 2E). IGF signaling existed between mesenchymal cells and early thymocytes except CD123⁺ Thy2 indicating early T cells also needs IGF proliferating signaling consistent with other's reports in mouse models (Figure 2F) (27, 29). LGALS9 was reported to regulate apoptosis of thymocyte and our analysis revealed that most endothelial cells and mTEC^{hi} expressed the ligand of galectin-9 (LGALS9) and all early thymocytes expressed its receptor (Figure 2G) (30). On the other side, thymocytes can also emit signals such as the proteases, including Cathepsin G (CTSG) and PRSS2 (Figure 2H). CTSG is an endo-protease that plays an important role in regulating chemotaxis with the ability to degrade CXCL12 (31). So, CTSG and PRSS2 may also affect the migration of Thy2c and Thy3 cells. In short, our analysis revealed that the TECs and stroma cells provided various signals for early thymocyte migration, proliferation, and apoptosis.

3.3 Transcriptional regulatory networks of early thymocytes

The development of lymphocytes was precisely regulated by critical transcriptional factors (TF) (8). To obtain an accurate process of early thymocyte specification, we analyzed CD34⁺ thymocytes exclusively (Supplementary Figures 3A, B). To systematically predict cell-type-specific transcriptional regulatory networks, we identified TF regulators based on co-expression and motif enrichment by using SCENIC (21). Regulon modules were identified based on the Connection Specificity Index (CSI) (32). We identified seven TF regulon modules that were active in a cell-type-specific manner (Figures 3A, B). Then, representative TF regulons across different cell types were presented based on regulon activity scores (Figure 3C). MEIS1 and HOXA5 were enriched in Thy1 cells

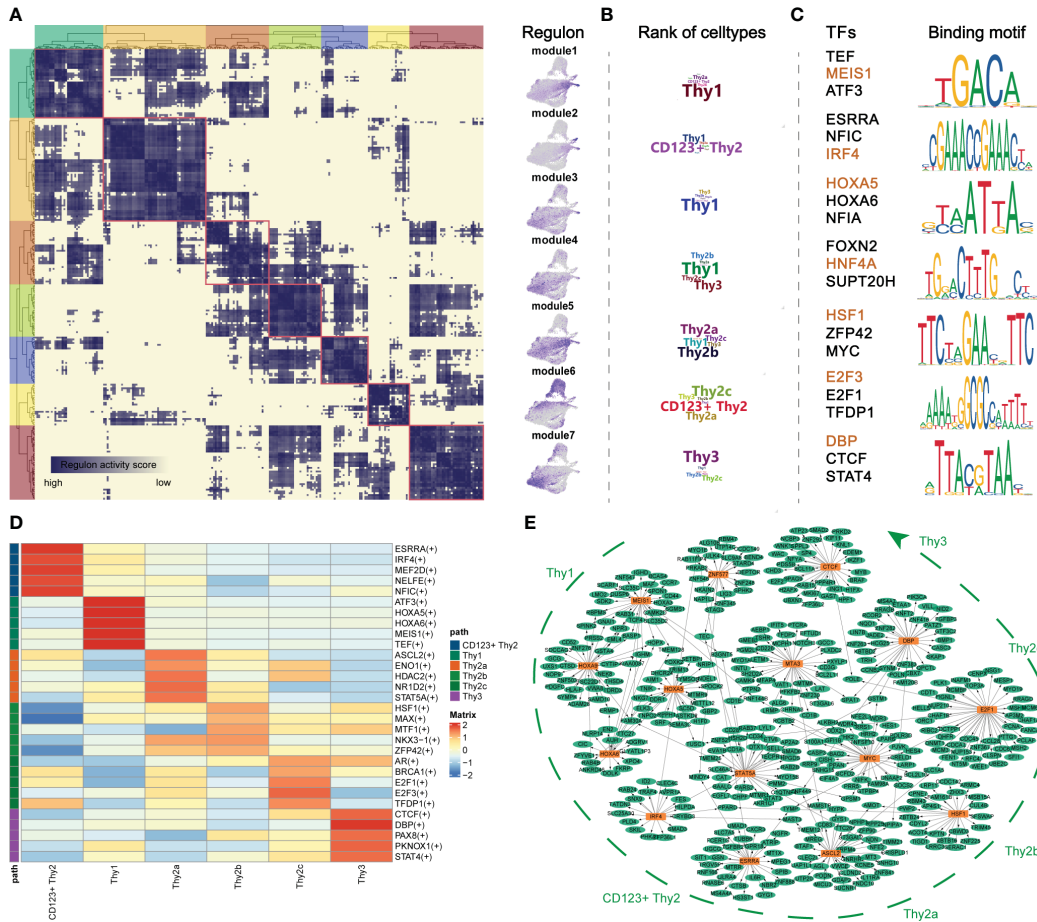


FIGURE 3

Transcriptional regulatory networks of early thymocytes. (A) Identification of regulon modules using SCENIC. Heatmap shows the similarity of different regulons based on the AUCell score (Left panel). UMAPs illustrate the average AUCell score distribution for different regulon modules (Right panel). (B) Wordcloud plots showing enrichment of celltypes in regulon modules. (C) Representative TFs and corresponding TF binding motifs in different regulon modules. (D) Heatmap showing TFs enriched in different celltypes. The level of regulon expression is represented by color depth. (E) Integrated gene-regulatory networks of the regulons. The symbol "+" means that the Spearman correlation between the TF and the potential target is positive (positive-correlated targets).

and may maintain the stemness of T precursor cells as the upregulation of them were reported in acute lymphocytic leukemias (33). IRF4 was highly expressed in module 2 corresponding to CD123⁺ Thy2 and may regulate the fate choice between T progenitor and myeloid lineage in accordance with previous reports (34). For CD123⁻ Thy2 cells, the representative TFs HSF1, MYC and E2F family proteins, acted on mitosis, cell cycle regulation and DNA replication, and they may collaboratively promote cell proliferation of Thy2 which is needed for the following T cell β -selection (35). Interestingly, we noticed that the CTCF, a critical chromatin organizer, was presented in Thy3 cells and we speculated that a chromatin barrier is establishing in Thy3 cells to lock cell fate into the T lineages (36). Besides, we also identified cell-type-specific TFs according to their expression level as shown in Figure 3D. And these cell-type-specific TFs were highly consistent to the TF regulons in the 7 modules above. Furthermore, the representative TF regulons and their associated target genes were organized into gene regulatory networks with cell differentiation trajectory (Figure 3E). In summary, we resolved major TFs and

transcriptional regulatory network at different stages of early T cells development.

3.4 Alterations in Cell–Cell Communications in TECs at different ages

Signaling from degenerated TECs may initiate thymic involution (2). Therefore, we further focused on TECs from different age groups using the CellChat package to gain insight into the signaling changes during thymic involution (Figure 4A; Supplementary Figure 4A). On one side, the total number and strength of cell-cell communication from different ages were illustrated and there were more and stronger signaling after postnatal compared to prenatal stage, while with aging in the adult stage, there was a dramatic decrease in both the number and strength of signaling compared to the postnatal stage (Figure 4B). On the other side, by comparing the outgoing and incoming signaling strength between different ages, we discovered

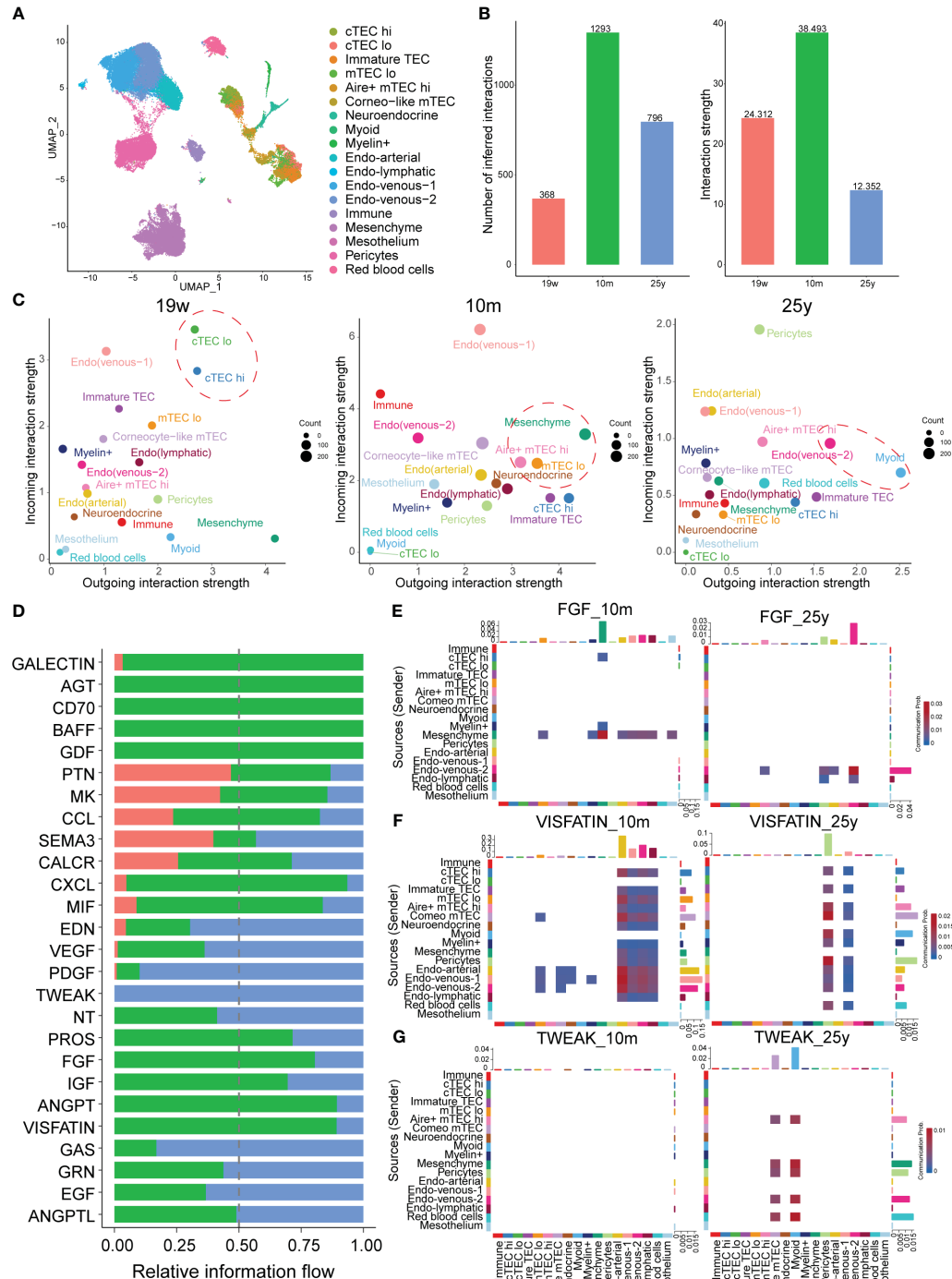


FIGURE 4

Alterations in Cell-Cell Communications in TECs at different ages. **(A)** UMAP visualization of thymic stroma colored by cell types. **(B)** Bar plots of the interaction quantity and interaction strength among different age groups. (Thymus with 19-week, 10-month and 25-year) **(C)** Scatter plots compare the outgoing and incoming interaction strength in 2D space, color represents maximum normalized strength. **(D)** Bar plots of the ranking of signaling axes by overall information flow differences among different age groups. Red-colored labels, 19w; green-colored, 10m; blue-colored, 25y. Heatmaps show outgoing and incoming of FGF signaling **(E)**, VISFATIN **(F)**, TWEAK **(G)** associated with each cell population at different ages.

that the signaling pattern significantly changed with aging. In detail, mature mesenchyme, mTECs including Aire⁺ mTEC^{hi}, Neuroendocrine mTECs dominated the incoming and outgoing signaling in postnatal thymus compared to the prenatal thymus

while the signaling path switched to the endothelial cells, Myoid mTECs in adult thymus (Figure 4C). Furthermore, information flow analysis indicated that signaling contents were also significantly changed among the prenatal, postnatal and adult

thymus (Figure 4D). For example, FGF signaling (FGF7:FGFR1), produced by mesenchymal cells and involved in the proliferation and differentiation of TECs, was reduced in adult thymus (Figure 4E) (27). And GALECTIN signaling (LGALS9:CD45), above analysis of LGALS9 acting on endothelial cells and early thymocytes, wasn't detected in adult thymus (Supplementary Figure 4B). Notably, ANGPT, CXCL and VISFATIN (NAMPT) signaling were drastically decreased in adult thymus (Figure 4F; Supplementary Figures 4C, D). In contrast, TWEAK (TNFSF12:TNFRSF12A) signaling was acting in only adult thymus (Figure 4G). Taken above analysis together, our data suggested that critical signals for thymic function were altered to varied degrees in aging thymus.

3.5 Alterations in gene regulatory networks in TECs with aging

Considering that signaling pattern of TECs were significantly impaired during aging, we therefore further analyzed the regulon changes of TECs with aging. TECs were extracted for following analysis (Figure 5A). We performed GRN inference using computational algorithms implemented in pySCENIC and 443 regulators involving a total of 14,428 genes were chosen for further exploration. We next defined a regulator specificity score (RSS) for each regulon in each cell type based on activity scores (37) (Supplementary Table 5) and determined regulons with the highest RSS values as primary regulators for corresponding aging identity. Notably, our RSS analysis revealed that the most specific regulons of aging thymus TECs included Forkhead box C1 (FOXC1), KLF9 (Kruppel Like Factor 9), MXI1 (MAX Interactor 1), NFIL3 (Nuclear Factor, Interleukin 3 Regulated) and ZBTB14 (Zinc Finger and BTB Domain Containing 14) (Figure 5B). FOXC1 induced EMT reported in epithelial tumor cells and suppression of FOXC1 can partially reverse the EMT process (38). While, knockdown of KLF9 in zebrafish embryos impaired T lymphopoiesis, MXI1 were reported to correlate with cell proliferation and migration and NFIL3 has been reported as a glucocorticoid-regulated gene (39–41). To further specify the roles of regulons of aging TECs, we performed Gene Ontology (GO) enrichment, gene set variation analysis (GSVA) and cytoscape analysis. In accordance, the enriched GO pathways mainly included fat cell differentiation and response to steroid, glucocorticoid, corticosteroid and EGF/VEGF signaling (Figure 5C). Transdifferentiation of TECs into adipocytes with age in mice has been reported and a recent study indicated that EMT process in TECs were through the CD147/p-Smad2/FoxC2 signaling pathway in mouse models (42). We further surveyed whether EMT involved in human TECs. Indeed, GSVA examined that EMT process was enriched in aging TECs and mTEC^{lo} subpopulation had the highest correlation, indicating that mTEC^{lo} subpopulation may initiate the dedifferentiation of TECs to adipocytes (Figure 5D). Interestingly, cytoscape analysis indicated IGFBP5 (insulin-like growth factor binding protein 5) was their main target of the above regulons (Figures 5E, F). Furthermore, the expression levels of FOXC1, KLF9, MXI1 and their target IGFBP5 were significantly increased in a variety of adult

TEC subclusters (Figure 5G). But only IGFBP5 displayed gradually increased-to-highest expression in elder (35y) TECs (Figure 5H). This is consistent with what was reported in Bautista et al. 's study. IGFBP5 has also been reported to increase cell invasion and inhibit cell proliferation by EMT in the human glioma tissues (43). Taken the above analysis data together, we thus speculated that upregulated regulons of aging TECs promoted thymic involution via EMT process.

3.6 IGFBP5 is a maker of thymic involution

Our above analysis provided hints that IGFBP5, the target gene of critical TFs, may be a marker correlating to thymic involution. To validate whether IGFBP5 increases with aging in thymic tissue, clinical samples with a wide range of ages (4/5/10/15/18/44/50/54/59/66) were collected for IHC staining (Supplementary Table 6). The IHC images confirmed that aged thymus displays obvious TEC reduction, fibroblast/adipocyte expansion and strong IGFBP5 staining (Figure 6A). Surprisingly, we also noticed that a strong anti-IGFBP5 positive staining appeared in Hassall's corpuscle, which was used to be regarded as a microstructure deriving from involuted TECs and associated with ageing of thymus (44). IGFBP5 staining was also captured in forming and fusing Hassall's corpuscle (Figures 6B, C). Besides, mTECs adjacent to Hassall's corpuscle also showed strong staining of IGFBP5, forming a satellite-like microstructure in thymus (Figure 6D). Besides, there is also a moderate staining on cortical thymic epithelial cells (Figure 6E). Interestingly, similar feature could be also found in aging c57BL/6 mouse thymus (Figures 6F, G). Thus, the IHC result was perfectly identical to mRNA expression pattern of single-cell data, implying that potentially predictive and functional value of IGFBP5 in aging thymus.

3.7 IGFBP5 inhibits thymocyte proliferation-related genes expression

To verify the role of IGFBP5 in thymus, we transfected small interfering RNA targeting at IGFBP5 (siIGFBP5) or non-specific mock (siNS) in mouse iTEC lines and co-cultured them with primary mouse thymocytes (Figure 7A). To firstly quantify the effect of knockdown, we examined relative IGFBP5 mRNA levels by RT-qPCR and protein level by Western blot, and the results showed that IGFBP5 indeed decreased significantly (Figure 7B). We then tested cell proliferation rate of thymocytes and iTECs in siIGFBP5 and siNS groups, and CCK8 results showed that proliferation rate of iTECs didn't change, while, the silencing of IGFBP5 markedly and significantly promoted proliferation of thymocytes (Figure 7C). To resolve which cell type of thymocytes were affected by knockdown of IGFBP5, we further used flow cytometry to distinguish thymocytes into DN (CD4⁻CD8⁻), CD4⁺SP (CD4⁺CD8⁻), CD8⁺SP (CD4⁻CD8⁺) and DP (CD4⁺CD8⁺) (Figure 7D). The number of thymocytes subsets changed little between the two groups (Figure 7E). Consistent with CCK8 assay, the proliferation levels of all of thymocytes subsets, indicated by Ki67 MFI level, increased

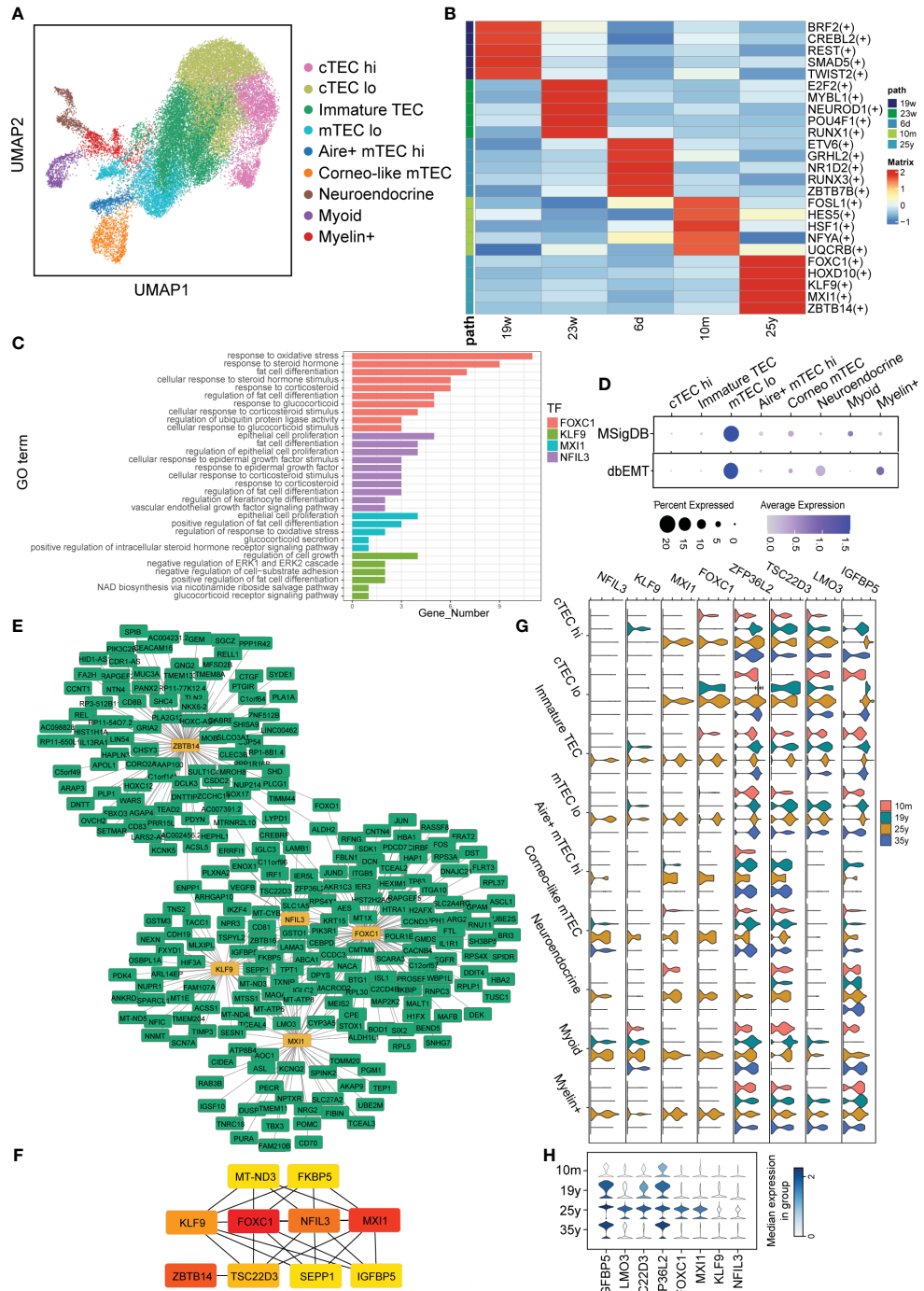


FIGURE 5

Alterations in Gene Regulatory Networks in TECs with aging. **(A)** UMAP visualization of TECs colored by cell types. **(B)** Heatmap showing TFs enriched in TECs with aging. The level of RSS is represented by color depth. **(C)** GO analysis of regulons of aging TECs. **(D)** Dot plots of enrichment of EMT-associated gene sets from MSigDB (Top panel) and dbEMT (Bottom panel) in aging TECs by GSVA. **(E, F)** Integrated gene-regulatory networks of the regulons in aging TECs. **(G)** Violin plots of regulon (IGFBP5, TSC22D3, LMO3, ZFP36L2, NFI3L, KLF9, MXI1 and FOXC1) expression in different TECs subset. **(H)** Violin plots of genes (IGFBP5, TSC22D3, LMO3, ZFP36L2) expression in all TECs with aging. The symbol “(+)” means that the Spearman correlation between the TF and the potential target is positive (positive-correlated targets).

in siIGFBP5 group (Figure 7F). But Ki67 positive percentage of DN and CD4⁺SP cells were mostly increased while DP and CD4⁺SP cells were comparable between siIGFBP5 and siNS group (Figure 7G). We speculated that IGF receptors may only be expressed in DN and CD4⁺SP cells. We thus examined the expression level of IGF family

and its receptors using our single-cell dataset. In accordance, IGF1R and IGF2R expressions in DN cells were significantly higher than others (Supplementary Figure 5). In summary, our results suggested that IGFBP5 derived from TECs can effectively inhibit thymocytes proliferation-related genes expression via IGF signaling.

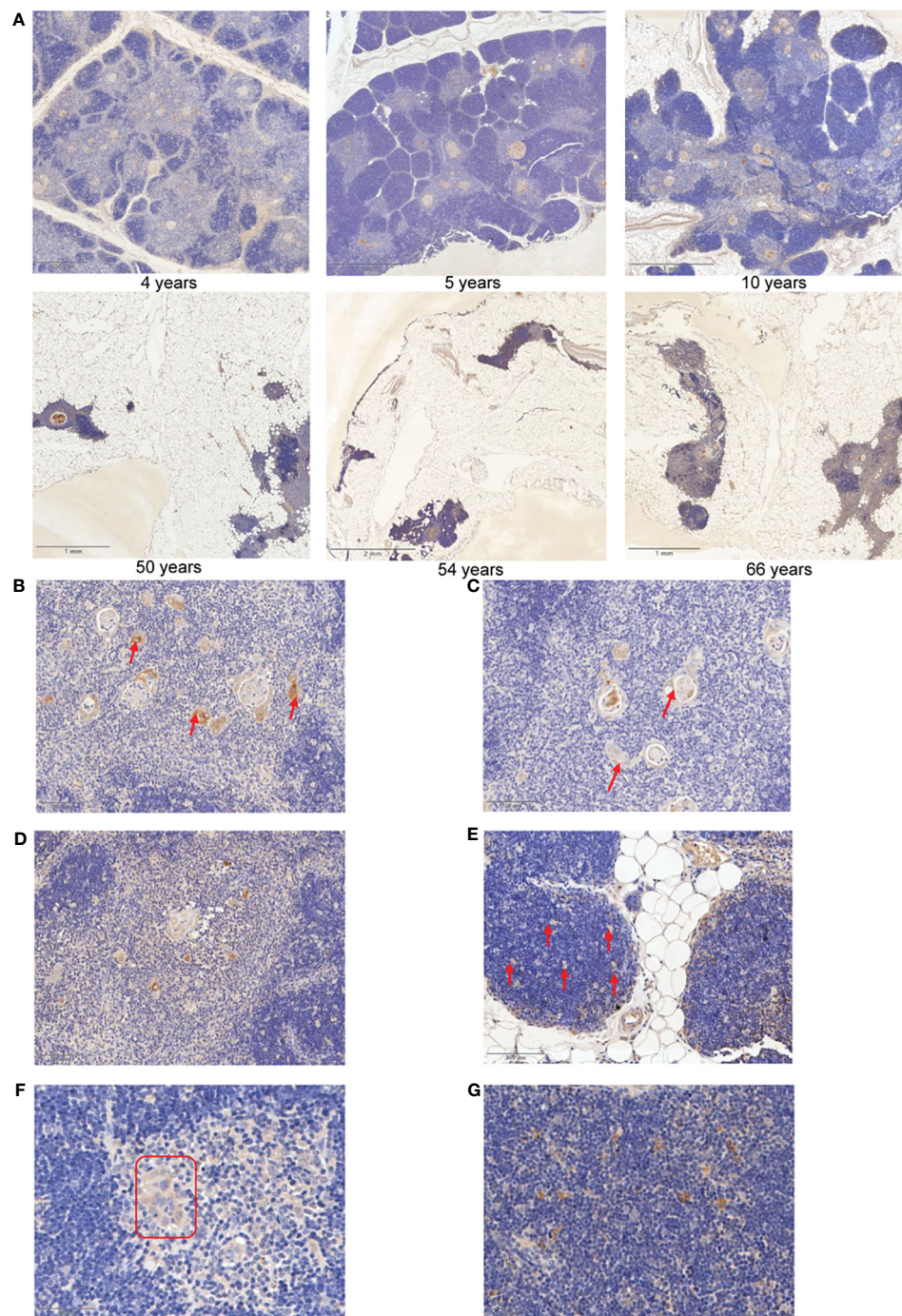


FIGURE 6

IGFBP5 is a marker of thymic involution. **(A)** Representative IHC images of IGFBP5 at different ages in human thymus. **(B, C)** Representative IHC staining showing IGFBP5 in existed and forming Hassall's corpuscle. **(D)** IHC images showing IGFBP5 at peri- Hassall's corpuscle. **(E)** IGFBP5 staining in cortex of human thymus. **(F, G)** Staining of IGFBP5 in cortex and medulla of mouse thymus. The position indicated by the red arrows and red triangle is where IGFBP5 staining is evident.

4 Discussion

Thymus is one of the first organs to experience age-related functional decline during which TECs are diminished and fat tissue replace thymus stroma, together resulting in the decline of mature T cell output. However, limited information of this process are available and effective interventions to rejuvenate

thymus functions are currently lacking (27). Single-cell analysis technologies have improved our understanding of the cellular compositions and functions in a systematic manner. Here, we data-mined published scRNA datasets of human thymus, uncovered critical regulators of both early thymocyte and TECs, and provided new target and mechanism of thymus involution.

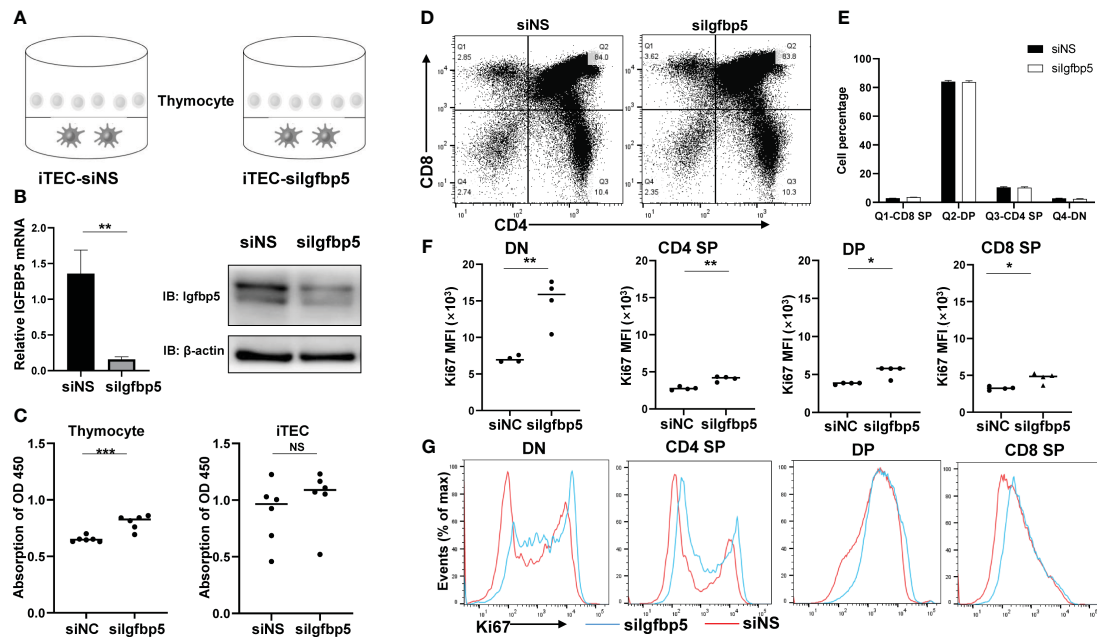


FIGURE 7
IGFBP5 inhibits thymocyte proliferation-related genes expression. **(A)** Co-culture system of IGFBP5 knockdown iTEC cell line and mouse thymocytes. **(B)** IGFBP5 knockdown efficiency in iTECs. Left panel, mRNA expression of IGFBP5 was detected by RT-qPCR. Right panel, the protein level of IGFBP5 detected by WB. **(C)** CCK8 assays detected cell proliferation in thymocytes and iTECs (**p < 0.001). NS is not significant. **(D)** Percentage of CD8⁺SP, DP, CD4⁺SP, DN via Flow cytometry visualized by dot plot and statistic result **(E)**. **(F)** Expression level of Ki67 in DN, CD4⁺SP, DP, CD8⁺SP. MFI, mean fluorescence intensity (*p < 0.05 and **p < 0.01). **(G)** Ki67 positive events in DN, CD4⁺SP, DP, CD8⁺SP cells.

Seeding and developing of TSPs are dependent on thymic stroma which provides signaling. We found chemokines including CCL25/CXCL12 and proteases including CTSG/PRSS2 play roles in early thymocyte homing and migration. Interestingly, Zuklys et al. previously reported that direct targets of Foxn1 in TECs (by chromatin immunoprecipitation sequencing) are chemokines and proteases, including CCL25, CXCL12 and PRSS16 (45) consistent with our finding. Besides, our results also revealed that CCL25/PRSS2 signals were received by only Thy1 cells, while, CXCL12/CTSG signals by Thy1-3 cells. We speculated that CCL25/PRSS2 support the recruitment of thymocyte progenitors while CXCL12/CTSG provide directional cues for migration of thymocytes. In human, transcriptional events of early thymocytes are largely unknown because of their small numbers and therefore, we also inferred a trajectory from Thy1 to Thy3. Our analysis indicated that, consistent with their murine counterparts of DN1-3 cells, Thy1 cells maintain multilineage differentiation ability, CD123⁺ Thy2 cells were potential for myeloid lineage, CD123⁻ Thy2 cells were expanding and Thy3 cells finally commit to T lineage (36). However, further biochemistry and genetic study is needed to clarify the detailed development of human early thymocytes.

Signaling path and contents are substantially altered in the adult thymus compared to early life. TECs couldn't provide enough signals and instead endothelial cells dominate the signaling pattern in aging thymus. This is probably due to functional TECs loss and vascular remodeling in aging thymus. Besides, critical signals for normal thymic function such as FGF, GALECTIN, ANGPT, CXCL and VISFATIN signaling decrease in aging thymus compared to early life. Instead, TWEAK signaling is increasing in the adult thymus and

studies have demonstrated that TWEAK can promote EMT in human bronchial epithelial cells (46). We assumed that TWEAK is either essential or partially involved in EMT of aging thymus. Indeed, EMT of TECs during thymic degeneration has been increasingly approved (42). Our analysis indicated that aging TECs enriched EMT pathway and the identified regulons (FOXC1, KLF9, MXI1, NFIL3, IGFBP5) of aging TECs were reported to be involved in EMT process of other tissues (47, 48). Thus, these results together suggest that TECs undergo EMT during age-related involution which can be impacted by several important regulators.

Our data verified that IGFBP5 is significantly upregulated at TECs and Hassall's corpuscle in the aging thymus, and the expression of proliferation-related genes in thymocytes was significantly different when IGFBP5 was knocked down or not. However, there was no significant change in the number of thymocytes. IGFBP proteins are secreted into microenvironment and known to have the ability to form complexes with IGF (49). Consistent with this notion, our data showed that downregulation of IGFBP5 in thymocyte-TEC co-culture system promoted the expression of proliferation-related genes in thymocytes, especially in the DN cells. And DN cells expressed the highest level of IGF receptors. We speculated that in the aging thymus, IGFBP5 deprived from aging TECs may bind most of the IGF and function as the IGF sponges, resulting in the lack of IGF growth signals to thymocytes, which in turn degenerates the TECs by "thymic crosstalk" (50). At present, we conclude that IGFBP5 can be used as a significant marker indicating the degree of thymic involution and may have a function in regulating thymocyte proliferation. However, further study is needed to validate its function of the regulation of thymus involution *in vivo*.

Collectively, we report here data to show important factors including IGFBP5 that induce EMT of TECs and adipogenesis processes in thymic involution. These factors may provide potential targets for preventing age-related thymic regression and a framework for optimizing thymus reconstitution in T-cell-deficient patients.

Data availability statement

The original contributions presented in the study are included in the article/[Supplementary Material](#). Further inquiries can be directed to the corresponding author.

Ethics statement

The studies involving humans were approved by Medical Ethics Committee of the Second Affiliated Hospital, Army Medical University. The studies were conducted in accordance with the local legislation and institutional requirements. Written informed consent for participation in this study was provided by the participants' legal guardians/next of kin. The animal study was approved by Laboratory Animal Welfare and Ethics Committee of the Third Military Medical University. The study was conducted in accordance with the local legislation and institutional requirements.

Author contributions

XY: Investigation, Software, Writing – original draft. XC: Methodology, Visualization, Writing – original draft. WW: Investigation, Project administration, Validation, Writing – review & editing. SQ: Funding acquisition, Investigation, Writing – review & editing. BL: Data curation, Formal analysis, Writing – original draft. JZ: Funding acquisition, Resources, Writing – review & editing. JC: Investigation, Project administration, Writing – review & editing. CH: Project administration, Writing – review & editing. YT: Investigation, Writing – review & editing. YX: Investigation, Writing – review & editing. WG: Supervision, Writing – review & editing. YW: Supervision, Writing – review & editing.

References

1. Handel AE, Irani SR, Hollander GA. The role of thymic tolerance in CNS autoimmune disease. *Nat Rev Neurol* (2018) 14(12):723–34. doi: 10.1038/s41582-018-0095-7
2. Liang Z, Dong X, Zhang Z, Zhang Q, Zhao Y. Age-related thymic involution: mechanisms and functional impact. *Aging Cell* (2022) 21(8):e13671. doi: 10.1111/ace.13671
3. Bautista JL, Cramer NT, Miller CN, Chavez J, Berrios DI, Byrnes LE, et al. Single-cell transcriptional profiling of human thymic stroma uncovers novel cellular heterogeneity in the thymic medulla. *Nat Commun* (2021) 12(1):1096. doi: 10.1038/s41467-021-21346-6
4. Takahama Y, Ohigashi I, Baik S, Anderson G. Generation of diversity in thymic epithelial cells. *Nat Rev Immunol* (2017) 17(5):295–305. doi: 10.1038/nri.2017.12
5. Chaudhry MS, Velardi E, Dudakov JA, van den Brink MR. Thymus: the next (Re) Generation. *Immunol Rev* (2016) 271(1):56–71. doi: 10.1111/imr.12418
6. Deng Y, Chen H, Zeng Y, Wang K, Zhang H, Hu H. Leaving no one behind: tracing every human thymocyte by single-cell RNA-sequencing. *Semin Immunopathol* (2021) 43(1):29–43. doi: 10.1007/s00281-020-00834-9
7. Paiva RA, Ramos CV, Leiria G, Martins VC. IL-7 receptor drives early T lineage progenitor expansion. *J Immunol* (2022) 209(10):1942–9. doi: 10.4049/jimmunol.2101046
8. Hosokawa H, Rothenberg EV. How transcription factors drive choice of the T cell fate. *Nat Rev Immunol* (2021) 21(3):162–76. doi: 10.1038/s41577-020-00426-6
9. Liu C, Lan Y, Liu B, Zhang H, Hu H. T cell development: old tales retold by single-cell RNA sequencing. *Trends Immunol* (2021) 42(2):165–75. doi: 10.1016/j.it.2020.12.004
10. Le J, Park JE, Ha VL, Luong A, Branciamore S, Rodin AS, et al. Single-cell RNA-seq mapping of human thymopoiesis reveals lineage specification trajectories and a commitment spectrum in T cell development. *Immunity* (2020) 52(6):1105–18 e9. doi: 10.1016/j.jimmuni.2020.05.010

Funding

The author(s) declare financial support was received for the research, authorship, and/or publication of this article. This work was supported by grants from the National Natural Science Foundation of China (No.82200679, 82002586 and 32270987), Young Elite Scientists Sponsorship Program by CAST (No. 2019QNRC001), Science and Technology Innovation Enhancement Project of Army Medical University (No. 2020XQN02) and the Chongqing International Institute for Immunology (2020YJC09).

Acknowledgments

We thank Prof. Jian-li Gao from Zhejiang Chinese Medical University for the generous gift of the iTEC cell line in this study.

Conflict of interest

The authors declare that the research was conducted in the absence of any commercial or financial relationships that could be construed as a potential conflict of interest.

Publisher's note

All claims expressed in this article are solely those of the authors and do not necessarily represent those of their affiliated organizations, or those of the publisher, the editors and the reviewers. Any product that may be evaluated in this article, or claim that may be made by its manufacturer, is not guaranteed or endorsed by the publisher.

Supplementary material

The Supplementary Material for this article can be found online at: <https://www.frontiersin.org/articles/10.3389/fimmu.2024.1322214/full#supplementary-material>.

11. Sun L, Guo J, Brown R, Amagai T, Zhao Y, Su DM. Declining expression of a single epithelial cell-autonomous gene accelerates age-related thymic involution. *Aging Cell* (2010) 9(3):347–57. doi: 10.1111/j.1474-9726.2010.00559.x
12. Oh J, Wang W, Thomas R, Su DM. Thymic rejuvenation via foxn1-reprogrammed embryonic fibroblasts (Frefs) to counteract age-related inflammation. *JCI Insight* (2020) 5(18):e140313. doi: 10.1172/jci.insight.140313
13. Park JE, Botting RA, Dominguez Conde C, Popescu DM, Lavaert M, Kunz DJ, et al. A cell atlas of human thymic development defines T cell repertoire formation. *Science* (2020) 367(6480):eaa3224. doi: 10.1126/science.aaay3224
14. Wolf FA, Angerer P, Theis FJ. Scanpy: large-scale single-cell gene expression data analysis. *Genome Biol* (2018) 19(1):15. doi: 10.1186/s13059-017-1382-0
15. Wolock SL, Lopez R, Klein AM. Scrublet: computational identification of cell doublets in single-cell transcriptomic data. *Cell Syst* (2019) 8(4):281–91 e9. doi: 10.1016/j.cels.2018.11.005
16. Polanski K, Young MD, Miao ZC, Meyer KB, Teichmann SA, Park JE. Bbknn: fast batch alignment of single cell transcriptomes. *Bioinformatics* (2020) 36(3):964–5. doi: 10.1093/bioinformatics/btz625
17. Butler A, Hoffman P, Smibert P, Papalex E, Satija R. Integrating single-cell transcriptomic data across different conditions, technologies, and species. *Nat Biotechnol* (2018) 36(5):411–+. doi: 10.1038/nbt.4096
18. Korsunsky I, Millard N, Fan J, Slowikowski K, Zhang F, Wei K, et al. Fast, sensitive and accurate integration of single-cell data with harmony. *Nat Methods* (2019) 16(12):1289–+. doi: 10.1038/s41592-019-0619-0
19. Jin SQ, Guerrero-Juarez CF, Zhang LH, Chang I, Ramos R, Kuan CH, et al. Inference and analysis of cell-cell communication using cellchat. *Nat Commun* (2021) 12(1):1088. doi: 10.1038/s41467-021-21246-9
20. Aibar S, González-Blas CB, Moerman T, Van AHT, Imrichova H, Hulselmans G, et al. Scenic: single-cell regulatory network inference and clustering. *Nat Methods* (2017) 14(11):1083–+. doi: 10.1038/Nmeth.4463
21. Kumar N, Mishra B, Athar M, Mukhtar S. Inference of gene regulatory network from single-cell transcriptomic data using pycenic. *Methods Mol Biol* (2021) 2328:171–82. doi: 10.1007/978-1-0716-1534-8_10
22. Shannon P, Markiel A, Ozier O, Baliga NS, Wang JT, Ramage D, et al. Cytoscape: A software environment for integrated models of biomolecular interaction networks. *Genome Res* (2003) 13(11):2498–504. doi: 10.1101/gr.123930
23. Wu T, Hu E, Xu S, Chen M, Guo P, Dai Z, et al. Clusterprofiler 4.0: A universal enrichment tool for interpreting omics data. *Innovation (Camb)* (2021) 2(3):100141. doi: 10.1016/j.xinn.2021.100141
24. Zhao M, Kong L, Liu Y, Qu H. Dbemt: an epithelial-mesenchymal transition associated gene resource. *Sci Rep* (2015) 5:11459. doi: 10.1038/srep11459
25. Gao W, Jia Z, Tian Y, Yang P, Sun H, Wang C, et al. Hbx protein contributes to liver carcinogenesis by H3k4me3 modification through stabilizing Wd repeat domain 5 protein. *Hepatology* (2020) 71(5):1678–95. doi: 10.1002/hep.30947
26. Lavaert M, Liang KL, Vandamme N, Park JE, Roels J, Kowalczyk MS, et al. Integrated scRNA-seq identifies human postnatal thymus seeding progenitors and regulatory dynamics of differentiating immature thymocytes. *Immunity* (2020) 52(6):1088–104 e6. doi: 10.1016/j.immuni.2020.03.019
27. Bhalla P, Su DM, van Oers NSC. Thymus functionality needs more than a few tecs. *Front Immunol* (2022) 13:864777. doi: 10.3389/fimmu.2022.864777
28. Kadakia T, Tai X, Kruhlak M, Wisniewski J, Hwang IY, Roy S, et al. E-protein-regulated expression of cxcr4 adheres preselection thymocytes to the thymic cortex. *J Exp Med* (2019) 216(8):1749–61. doi: 10.1084/jem.20182285
29. Zeng Y, Liu C, Gong Y, Bai Z, Hou S, He J, et al. Single-cell RNA sequencing resolves spatiotemporal development of pre-thymic lymphoid progenitors and thymus organogenesis in human embryos. *Immunity* (2019) 51(5):930–48 e6. doi: 10.1016/j.immuni.2019.09.008
30. Wada J, Ota K, Kumar A, Wallner EI, Kanwar YS. Developmental regulation, expression, and apoptotic potential of galectin-9, a beta-galactoside binding lectin. *J Clin Invest* (1997) 99(10):2452–61. doi: 10.1172/JCI119429
31. Burster T, Macmillan H, Hou T, Boehm BO, Mellins ED. Cathepsin G: roles in antigen presentation and beyond. *Mol Immunol* (2010) 47(4):658–65. doi: 10.1016/j.molimm.2009.10.003
32. Fuxman Bass JI, Diallo A, Nelson J, Soto JM, Myers CL, Walhout AJ. Using networks to measure similarity between genes: association index selection. *Nat Methods* (2013) 10(12):1169–76. doi: 10.1038/nmeth.2728
33. Rozovskaia T, Feinstein E, Mor O, Foa R, Blechman J, Nakamura T, et al. Upregulation of meis1 and hoxa9 in acute lymphocytic leukemias with the T(4: 11) abnormality. *Oncogene* (2001) 20(7):874–8. doi: 10.1038/sj.onc.1204174
34. Wang S, He Q, Ma D, Xue Y, Liu F. Irf4 regulates the choice between T lymphoid-primed progenitor and myeloid lineage fates during embryogenesis. *Dev Cell* (2015) 34(6):621–31. doi: 10.1016/j.devcel.2015.07.011
35. Lee YJ, Kim EH, Lee JS, Jeoung D, Bae S, Kwon SH, et al. Hsf1 as a mitotic regulator: phosphorylation of Hsf1 by Plk1 is essential for mitotic progression. *Cancer Res* (2008) 68(18):7550–60. doi: 10.1158/0008-5472.CAN-08-0129
36. Hu G, Cui K, Fang D, Hirose S, Wang X, Wangsa D, et al. Transformation of accessible chromatin and 3D nucleome underlies lineage commitment of early T cells. *Immunity* (2018) 48(2):227–42 e8. doi: 10.1016/j.immuni.2018.01.013
37. Suo S, Zhu Q, Saadatpour A, Fei L, Guo G, Yuan GC. Revealing the critical regulators of cell identity in the mouse cell atlas. *Cell Rep* (2018) 25(6):1436–45 e3. doi: 10.1016/j.celrep.2018.10.045
38. Xia L, Huang W, Tian D, Zhu H, Qi X, Chen Z, et al. Overexpression of forkhead box C1 promotes tumor metastasis and indicates poor prognosis in hepatocellular carcinoma. *Hepatology* (2013) 57(2):610–24. doi: 10.1002/hep.26029
39. Carey KT, Tan KH, Ng J, Liddicoat DR, Godfrey DI, Cole TJ. Nfil3 is a glucocorticoid-regulated gene required for glucocorticoid-induced apoptosis in male murine T cells. *Endocrinology* (2013) 154(4):1540–52. doi: 10.1210/en.2012-1820
40. Zhang Y, Xue Y, Cao C, Huang J, Hong Q, Hai T, et al. Thyroid hormone regulates hematopoiesis via the Tr-Klf9 axis. *Blood* (2017) 130(20):2161–70. doi: 10.1182/blood-2017-05-783043
41. Wechsler DS, Shelly CA, Petroff CA, Dang CV. Mxi1, a putative tumor suppressor gene, suppresses growth of human glioblastoma cells. *Cancer Res* (1997) 57(21):4905–12.
42. Chen R, Wang K, Feng Z, Zhang MY, Wu J, Geng JJ, et al. Cd147 deficiency in T cells prevents thymic involution by inhibiting the Emt process in tecs in the presence of Tgfbeta. *Cell Mol Immunol* (2021) 18(1):171–81. doi: 10.1038/s41423-019-0353-7
43. Dong C, Zhang J, Fang S, Liu F. Igfbp5 increases cell invasion and inhibits cell proliferation by Emt and Akt signaling pathway in glioblastoma multiforme cells. *Cell Div* (2020) 15:4. doi: 10.1186/s13008-020-00061-6
44. Marinova TT, Spassov LD, Vlassov VI, Pashev VV, Markova MD, Ganey VS, et al. Aged human thymus hassall's corpuscles are immunoreactive for Igf-I and Igf-I receptor. *Anat Rec* (2009) 292(7):960–5. doi: 10.1002/ar.20920
45. Zuklys S, Handel A, Zhanybekova S, Govani F, Keller M, Maio S, et al. Foxn1 regulates key target genes essential for T cell development in postnatal thymic epithelial cells. *Nat Immunol* (2016) 17(10):1206–15. doi: 10.1038/ni.3537
46. Itoigawa Y, Harada N, Harada S, Katsura Y, Makino F, Ito J, et al. Tweak enhances Tgf-beta-induced epithelial-mesenchymal transition in human bronchial epithelial cells. *Respir Res* (2015) 16(1):48. doi: 10.1186/s12931-015-0207-5
47. Yu M, Bardia A, Wittner BS, Stott SL, Smas ME, Ting DT, et al. Circulating breast tumor cells exhibit dynamic changes in epithelial and mesenchymal composition. *Science* (2013) 339(6119):580–4. doi: 10.1126/science.1228522
48. Huang S, Wang C, Yi Y, Sun X, Luo M, Zhou Z, et al. Kruppel-like factor 9 inhibits glioma cell proliferation and tumorigenicity via downregulation of mir-21. *Cancer Lett* (2015) 356(2 Pt B):547–55. doi: 10.1016/j.canlet.2014.10.007
49. Neuzillet Y, Chapeaublanc E, Krucker C, De Koning L, Lebret T, Radvanyi F, et al. Igf1r activation and the *in vitro* antiproliferative efficacy of Igf1r inhibitor are inversely correlated with Igfbp5 expression in bladder cancer. *BMC Cancer* (2017) 17(1):636. doi: 10.1186/s12885-017-3618-5
50. Duan C, Allard JB. Insulin-like growth factor binding protein-5 in physiology and disease. *Front Endocrinol (Lausanne)* (2020) 11:100. doi: 10.3389/fendo.2020.00100



OPEN ACCESS

EDITED BY

Jeffrey John Bajramovic,
Utrecht University, Netherlands

REVIEWED BY

Stefano Casarin,
Houston Methodist Research Institute,
United States
Alexander Y. Mitrophanov,
National Cancer Institute at Frederick (NIH),
United States

*CORRESPONDENCE

H. Ibrahim Korkmaz
✉ h.korkmaz@amsterdamumc.nl

[†]These authors have contributed
equally to this work and share
first authorship

RECEIVED 28 September 2023

ACCEPTED 03 January 2024

PUBLISHED 29 January 2024

CITATION

Korkmaz HI, Sheraton VM, Bumbuc RV, Li M, Pijpe A, Mulder PPG, Boekema BKHL, de Jong E, Papendorp SGF, Brands R, Middelkoop E, Sloot PMA and van Zuijlen PPM (2024) An *in silico* modeling approach to understanding the dynamics of the post-burn immune response. *Front. Immunol.* 15:1303776. doi: 10.3389/fimmu.2024.1303776

COPYRIGHT

© 2024 Korkmaz, Sheraton, Bumbuc, Li, Pijpe, Mulder, Boekema, de Jong, Papendorp, Brands, Middelkoop, Sloot and van Zuijlen. This is an open-access article distributed under the terms of the [Creative Commons Attribution License \(CC BY\)](#). The use, distribution or reproduction in other forums is permitted, provided the original author(s) and the copyright owner(s) are credited and that the original publication in this journal is cited, in accordance with accepted academic practice. No use, distribution or reproduction is permitted which does not comply with these terms.

An *in silico* modeling approach to understanding the dynamics of the post-burn immune response

H. Ibrahim Korkmaz^{1,2,3,4*†}, Vivek M. Sheraton^{5,6,7†},
Roland V. Bumbuc^{1,2,5,6,7}, Meifang Li⁵, Anouk Pijpe^{1,3},
Patrick P. G. Mulder^{4,8}, Bouke K. H. L. Boekema^{1,4},
Evelien de Jong⁹, Stephan G. F. Papendorp⁹,
Ruud Brands^{10,11}, Esther Middelkoop^{1,3,4},
Peter M. A. Sloot⁵ and Paul P. M. van Zuijlen^{1,3,4,12}

¹Department of Plastic, Reconstructive and Hand Surgery, Amsterdam Movement Sciences (AMS) Institute, Amsterdam University Medical Center (UMC), Location VUmc, Amsterdam, Netherlands

²Department of Molecular Cell Biology and Immunology, Amsterdam Infection and Immunity (All) Institute, Amsterdam University Medical Center (UMC), Location VUmc, Amsterdam, Netherlands

³Burn Center and Department of Plastic and Reconstructive Surgery, Red Cross Hospital, Beverwijk, Netherlands, ⁴Preclinical Research, Association of Dutch Burn Centres (ADBC), Beverwijk, Netherlands, ⁵Computational Science Lab, Informatics Institute, University of Amsterdam, UvA - LAB42, Amsterdam, Netherlands, ⁶Center for Experimental and Molecular Medicine (CEMM), Amsterdam University Medical Center (UMC), Amsterdam, Netherlands, ⁷Laboratory for Experimental Oncology and Radiobiology, ONCODE, Amsterdam University Medical Center (UMC), Location AMC, Amsterdam, Netherlands, ⁸Laboratory of Medical Immunology, Department of Laboratory Medicine, Radboud University Medical Center, Nijmegen, Netherlands, ⁹Department of Intensive Care, Red Cross Hospital, Beverwijk, Netherlands, ¹⁰Complexity Institute, Nanyang Technological University, Singapore, Singapore, ¹¹Allcksys Life Sciences BV, Wageningen, Netherlands, ¹²Paediatric Surgical Centre, Emma Children's Hospital, Amsterdam University Medical Center (UMC), Location AMC, Amsterdam, Netherlands

Introduction: Burns are characterized by a massive and prolonged acute inflammation, which persists for up to months after the initial trauma. Due to the complexity of the inflammatory process, Predicting the dynamics of wound healing process can be challenging for burn injuries. The aim of this study was to develop simulation models for the post-burn immune response based on (pre) clinical data.

Methods: The simulation domain was separated into blood and tissue compartments. Each of these compartments contained solutes and cell agents. Solutes comprise pro-inflammatory cytokines, anti-inflammatory cytokines and inflammation triggering factors. The solutes diffuse around the domain based on their concentration profiles. The cells include mast cells, neutrophils, and macrophages, and were modeled as independent agents. The cells are motile and exhibit chemotaxis based on concentrations gradients of the solutes. In addition, the cells secrete various solutes that in turn alter the dynamics and responses of the burn wound system.

Results: We developed an Glazier-Graner-Hogeweg method-based model (GGH) to capture the complexities associated with the dynamics of inflammation after burn injuries, including changes in cell counts and cytokine levels. Through simulations from day 0 – 4 post-burn, we successfully identified

key factors influencing the acute inflammatory response, i.e., the initial number of endothelial cells, the chemotaxis threshold, and the level of chemoattractants.

Conclusion: Our findings highlight the pivotal role of the initial endothelial cell count as a key parameter for intensity of inflammation and progression of acute inflammation, 0 – 4 days post-burn.

KEYWORDS

burns, wound healing, inflammation, immune response, computational modeling

1 Introduction

Burns are a significant problem worldwide, having a high mortality and morbidity rate. Especially severe burns generally induce a massive long-term inflammatory response both systemically and locally (1–5).

Even though the inflammatory response is initially indispensable during wound healing, a massive persistent inflammatory response not only negatively affects the wound healing but may also result in multiple organ dysfunction (5). Despite significant progress in unravelling cellular and molecular processes involved in burn wound healing and the post-burn inflammatory response, the pathophysiology of burns and how, in this regard, burns differ from other non-burn wounds is far from fully understood.

The immune system is a key factor in wound healing and tissue regeneration. In the case of severe burns, the post-burn immune response is complex and involves intricate interactions between various cellular and molecular components (6, 7). It is essential to understand the dynamics of the immune response in burn wounds for the development of effective therapeutic interventions to improve patient outcomes (8–10). At the macroscopic level (i.e. patient level), the long-term inflammation that follows burn wounds often leads to deformities that affect the quality of life from burn patients. In severe cases, delayed wound closure (11), abnormal scarring (12), increased fibrosis (13), increased vascular proliferation (14) and excessive extracellular matrix deposition (12) can be caused by intense local and systemic inflammatory reactions.

From a cell biology point of view, the number of inflammatory cells such as neutrophils, monocytes, macrophages, and level of pro-inflammatory cytokines are important at the acute inflammation stage of post-burn wound healing (4–6, 15, 16). During the acute inflammatory phase, between 24 and 72 hours, damage-associated molecular patterns (DAMP) and pathogen-associated molecular patterns (PAMP) trigger the immune response. This is accompanied by the release of interleukin (IL)-8, IL-6, tumor necrosis factor (TNF) α , IL-1 β and IL-10, this process is summarized in Figure 1C. After 72 hours, macrophages are attracted to the wound site and differentiate into pro-inflammatory (M1) or “pro-healing” (M2) phenotypes. Fibroblasts migrate to the wound site, where angiogenesis takes place, with the help of endothelial cells. The

processes that follow over the next days include reepithelialization, revascularization, peripheral nerve repair, collagen fiber organization, reducing the number of macrophages and fibroblasts. Both decreased inflammation (i.e. normalization of the acute inflammatory mediators such as IL-6 and IL-8) and decreased angiogenesis will lead to limited scar formation (17). Endothelial cells play a crucial role in balancing the level of angiogenesis (18), helping to facilitate the inflammatory response and wound healing (19). After a burn injury, endothelial cells are among the first responders at the site of tissue damage. Among their main functions, they initiate the inflammatory response during the inflammation phase by expressing adhesion molecules and chemokines (20), facilitating the recruitment of immune cells such as neutrophils and monocytes to the wound area (21). Since endothelial cells are crucial during the acute inflammatory phase post-burn, we hypothesized that the endothelial cell count is one of the crucial parameters in burn wound healing and the acute immune response as shown in Figure 1C. Another key parameter is the time frame in wound healing.

Until now, both experimental and clinical approaches have been used to gain insight into the post-burn wound healing and specifically the immune response. However, due to the complexity of the involved processes, cellular and molecular pathways, these approaches have limitations such as the ability to sufficiently understand the underlying mechanisms to predict the system's behavior. In some cases, it may not be possible to extract details on a finer-scale, such as spatial concentrations of cytokines at microscale level through animal experiments. Moreover, there are discrepancies in translating knowledge on cellular/molecular level for development of effective therapies for burn patients. To bridge this knowledge gap, computational modeling approaches have been developed as powerful tools to better understand complex biological processes (22–24). Recently, black box approaches such as machine learning and neural networks have been developed in context of burn wound healing process (25). Most of black box models in literature focus on wound healing prediction via image analysis and often overlook the underlying mechanisms driving the healing process. Burn wound healing, in general, wound healing, could benefit vastly from mechanistic computational models focusing on different aspects of the healing process. Turley et al. provide a comprehensive overview of how mathematical model techniques

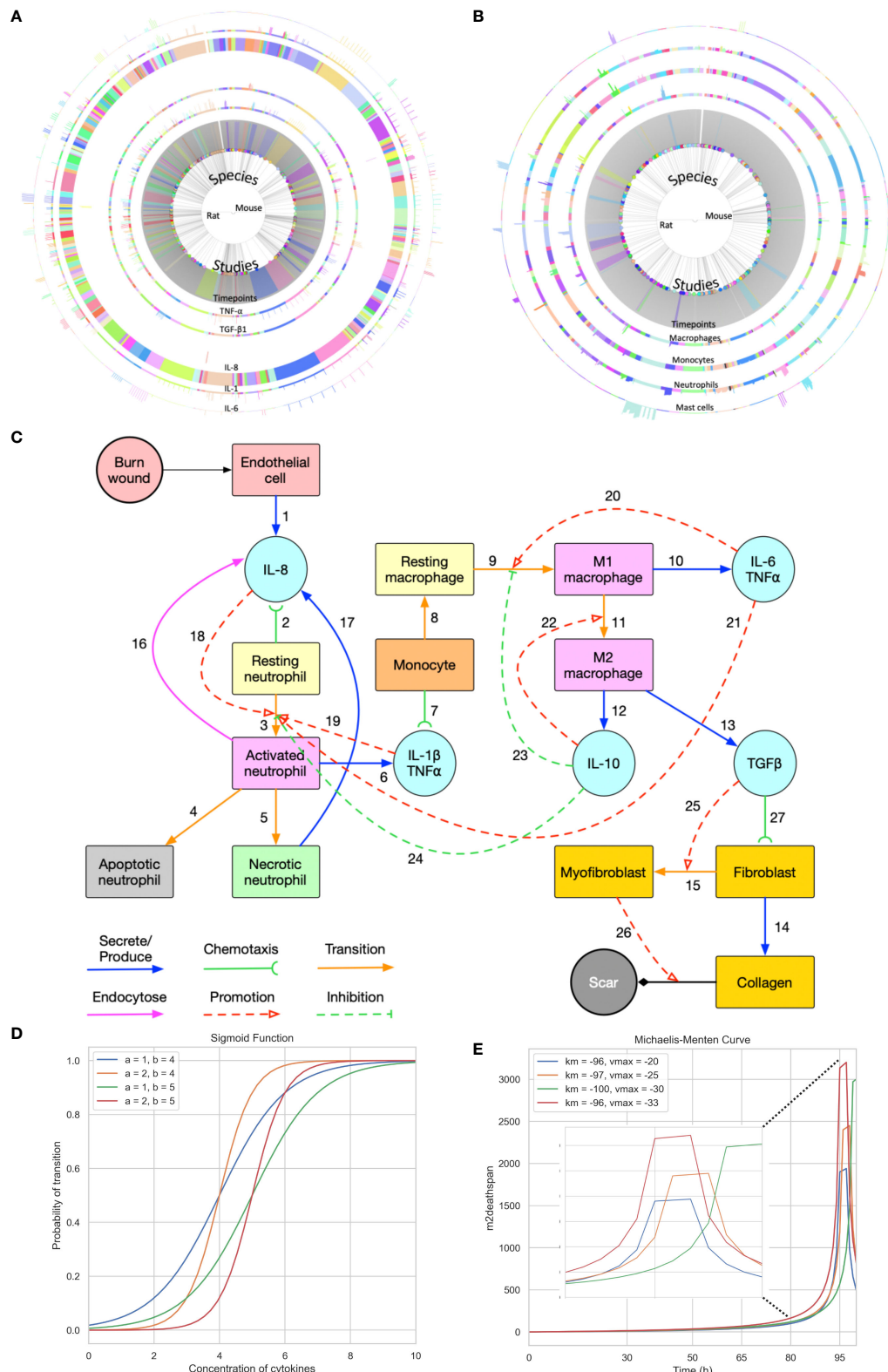


FIGURE 1

Summary of the data used for validation, conceptual model of the modelling approach, and sigmoid function and Michaelis-Menten function with different parameters. **(A)** Cell data relating different species to their respective cell characteristics pre-burn and after burn essay over time series by different studies. **(B)** Cytokine data relating different species to their respective cell characteristics pre-burn and after burn essay over time series by different studies. **(A, B)** Each arc represents different histogram data related to the main characteristic in study, note that this data has been obtained experimentally *in vivo*. **(C)** Conceptual model of the modelling approach. Each stock contains the variable in question and each link represents its relationship between variables (Created with [BioRender.com](https://biorender.com)). **(D, E)** Sigmoid function and Michaelis-Menten function with different parameters, respectively. Each value was randomized to show how different inflection points output different curves.

could play a role in exploring various aspects of wound healing including inflammation, closure and angiogenesis (26). Nagaraja et al. developed mechanistic models to understand the prolonged effects of inflammation (chronic inflammation) on the healing process and to test possible intervention strategies computationally (27, 28). These models were further expanded to identify biomarkers of pathological scarring in skin tissues (29). Though the above models are not specific to burn injuries, they showcase the usefulness of mathematical models in exploration and mechanism driven predictions of wound healing. In this study, we introduce an *in silico* mechanistic modeling approach to investigate the dynamics of the post-burn immune response. Agent-based modeling (ABM) techniques, specifically the Glazier-Graner-Hogeweg (GGH) model (30), is used to simulate the behavior of inflammatory agents and the dynamics of entities involved in burn wound inflammation (31, 32). By combining relevant experimental knowledge, data from existing experimental animal burn models, and mathematical principles (33, 34), our approach provides a comprehensive framework for studying the intricate dynamics of the (acute) immune response in burn wounds. Further, in this study, we hypothesize that endothelial cells act as one of the key players in determining the extent and duration of post-burn inflammation response. To verify this hypothesis, we use the developed spatio-temporal model to numerically simulate, analyze and qualitatively validate post-burn immune responses during the acute inflammation phase.

2 Methods

2.1 Data description, analysis, and processing

The dataset provided by Mulder et al. (2), encompasses a collection of cytokine levels and immune cell counts of 14 different cell types from 247 studies involving rats and mice (Figures 1A, B). These measurements were taken across various animal characteristics (age, sex, species), burn wound characteristics (% total burn surface area, thickness and depth),

sample source (in the skin), repeated samples, baseline comparison used, relative burn wound area, wound status (contraction, re-epithelialization, or overall burn area), anesthetic type used, and animal outcomes (healthy or not). Additionally, cytokine data specifically includes details on the analysis methods and the different cytokines measured, while cell count data specifies the method of inference and measurement. Both types of data are longitudinal follow-ups for some of the animals, which means that cell counts, and concentration of cytokines are accompanied by timeseries.

Notably, the dataset exhibits significant gaps, missing cytokine concentration or cell count reports for a notable amount of time frames, challenging the preprocess of data from a mechanistic standpoint. To address this issue, certain assumptions had to be made to enable specific validation points within the analysis. Table 1 is the result of the raw data analysis on cell count change over time without any assumptions. These assumptions were made while considering the overall integrity and scientific validity of the data. Going forward, the model parameters were adjusted accordingly to fit the values provided by the data.

2.2 Modeling approach

ABM is a computational modeling technique that enables the simulation of complex systems by representing individual agents and their interactions within a defined environment. ABM has gained increasing popularity in immunology (35, 36) because of its ability to capture the spatial heterogeneity and emergent behaviors observed in biological systems.

The GGH model, also known as the Cellular Potts Model (CPM), is a versatile computational method that enables the representation of non-uniform cell shapes as agents in multi-cell systems. It is a widely adopted ABM framework that has been successfully applied to simulate various biological phenomena, including cell migration (37), chemotaxis (38), and cell-cell interactions (39). This model is particularly suitable for studying the complex dynamics of the immune response, as it allows the

TABLE 1 Cell count transitions 0 – 4 days post-burn.

Cell type	0h	T	24h	T	48h	T	72h	T	96h	T
Resting Neutrophils (RN)	-	↗	-	↘	-	↓	-	-	-	-
Monocytes (M)	-	-	-	↑	-	↘	-	-	-	-
Fibroblasts (F)	-	-	-	-	-	-	-	↑	-	-
Activated neutrophils (AN)	-	↑	-	↘	-	↓	-	-	-	-
Necrotic neutrophils (NN)	-	-	-	-	-	-	-	-	-	-
Resting Macrophages (RM)	-	-	-	-	-	-	-	-	-	-
Macrophages type I (M1)	-	-	-	-	-	↑	-	↘	-	-
Macrophages type II (M2)	-	-	-	-	-	-	-	↗	↗	↑
Myofibroblasts (My)	-	-	-	-	-	-	-	-	-	↗

The symbols - , ↗, ↘, ↑, and ↓ indicate unknowns, growth, decline, increase, and decrease respectively, offering an intricate portrayal of cellular dynamics. T represents the transition between timepoints. Assumptions made based on data supplied by Mulder et al. (2).

representation of multiple cell types, the diffusion of soluble factors and the integration of experimental data extracted from existing *in vivo* animal burn models (rats and mice) (2) into the simulation framework (Figures 1A, B). With this integration, we expect to be able to find a good estimate for the parameters used to simulate the post-burn effects on cytokines, cells, and two-dimensional development of the wound. Our condensed two-dimensional simulation of the wound development implements the free energy mechanisms previously proposed using CompuCell3D (40, 41), an open-source GGH implementation.

2.2.1 Simulation dynamics

The burn wound site is created in a 2D 5*5 cm square domain that includes two main components: the central 4*4 cm square represents the tissue component whereas the surrounding area of the central square is treated as the blood component (concept shown in Figure 1C). Because inflammation after burns intensifies during the first three to four days, the whole simulation will perform 1,000,001 Monte Carlo steps (MCS) with each 10,000 MCS representing one hour so that one simulation is treated as 100 hours in real time. The cells used in the simulation environment follow the rules of the conceptual model of Figure 1C, explained by following the links. Resting neutrophils and monocytes circulate commonly in the blood when there is no injury. If a burn occurs, the endothelial cells of the tissue component will secrete IL-8 [Link 1] to trigger the inflammatory response. Resting neutrophils are recruited from blood to tissue by chemotaxis to IL-8 [Link 2] and are activated by IL-8 [Links 3 and 18] when entering the tissue layer. Subsequently, activated neutrophils secrete pro-inflammatory cytokines IL-1 β and TNF- α [Link 6] and these pro-inflammatory cytokines contribute to neutrophil activation [Link 19] and enhance the inflammatory response. Activated neutrophils can also endocytose IL-8 [Link 16] to neutralize inflammation to some extent. Meanwhile, activated neutrophils are short-lived, so they will enter apoptosis [Link 4] during inflammation. If inflammation persists, some activated neutrophils will turn into necrotic neutrophils [Link 5], triggering the release of additional IL-8 in the tissue [Link 17].

Attracted from blood to tissue, monocytes migrate toward IL-1 β and TNF- α , secreted by activated neutrophils [Link 7], and then turn into resting macrophages, also called resting monocytes, in the tissue compartment in the presence of IL-6 [Link 8]. The resting macrophages are then transformed into activated macrophages [Link 9], commonly known as M1 macrophages, promoted by IL-6 and TNF- α . The macrophages of the M1 phenotype can secrete pro-inflammatory cytokines IL-6 and TNF- α [Link 10], which promote the activation of neutrophils and macrophages [Links 20 and 21]. M1 macrophages transition to M2 macrophages [Link 11] is promoted by the anti-inflammatory cytokine IL-10. M2 macrophages secrete IL-10 [Link 12] and TGF- β 1 [Link 13]. In the current conceptual model, we only consider activated TGF- β 1 (no latent), and IL-10 inhibits neutrophil and macrophage activation [Links 23 and 24]. Fibroblasts migrate towards TGF- β 1 [Link 27] and can differentiate into myofibroblasts in the presence of (activated) TGF- β 1 [Links 15 and 25]. Fibroblasts are responsible for collagen production [Link

14] and myofibroblasts cooperate with fibroblasts to form a collagen matrix [Link 26].

2.2.2 Cell distribution, movement, and transitions

In our modeling system, each cell is depicted as a point arranged on a lattice. To introduce randomness and fairness to the position of the cells, we allowed the exchange of lattice sites between adjacent cells at their boundaries. To ensure that each lattice site has an equal chance of undergoing potential exchange during the simulation, we evaluated each potential exchange in random order. This constitutes a Monte Carlo step (MCS) which serves as the unit of time in our simulation. We selected a square grid for the simulations for two main reasons, 1. easier coupling between the cell field and the cytokine field concentrations, solved using finite volume solver (FiPy) and 2. to reduce computational complexity and resource usage if a hexagonal grid were to be considered for the simulation.

All cell types involved in the simulation will move due to chemotaxis and their initial number on the lattice is fixed, except for endothelial cells (as shown in Supplementary Table 1 estimated from experimental data (2)). The Chemotaxis plugin in CC3D calculates the change of energy associated with the movement of the pixels, with the parameter λ controlling the strength of chemotaxis. λ is specified for each type of cell, representing the response speed to a certain chemical. The energy formula is modified with a saturation coefficient, a , to include saturation terms (Equation 1, where $c(x_{\text{destination}})$ and $c(x_{\text{source}})$ denote the chemical concentration in the source pixel and the destination pixel, respectively). The minimum chemical concentration for the initialization condition is defined by a , which is used as an indicator of potential resistance to chemotaxis. Resting neutrophils are attracted by IL-8, monocytes by IL-1 β and TNF- α and fibroblasts by TGF- β 1. We assume that a burn injury occurs on a non-delicate area of the human body and the skin surface is uniform. The starting point of the implemented model are the remaining endothelial cells after the burn injury. Therefore, we assume that these do not move, and their number is limited and does not change during the simulation. We also assume that no cell can move across the boundaries so they will disappear if they reach the boundaries. However, in order to keep the number of cells constant in the simulation, we implement periodic boundary conditions, where every time a cell reaches a boundary, the cell reappears on the other end of the boundary, hence keeping the count of the cells in the simulation constant.

$$\Delta E_{\text{chem}} = \lambda \left[\frac{c(x_{\text{source}})}{a + c(x_{\text{source}})} - \frac{c(x_{\text{destination}})}{a + c(x_{\text{destination}})} \right] \quad (1)$$

When it comes to cell transitions, all the details and effects of the cytokines involved can be found in Table 2. As outlined in the conceptual model, each cell is treated as an agent in the simulation, so there is a chance that this cell will transform into another cell type. To address this probability, we used the sigmoid function (42) (Table 3, also known as the logistic function; Figure 1D). This function can take any real value as input and output value in the range (0, 1), which is necessary to randomly assign a transition probability. The first point of inflection(a) and the second point of

TABLE 2 Cell type transition and the influence of cytokines used in simulations.

Cell type (from)	Cell type (to)	Promotion cytokines	Inhibition cytokines
Resting neutrophil (N_R)	Activated neutrophil (N_A)	$IL - 8, IL - 6, IL - 1\beta, TNF_\alpha$	$IL - 10$
Monocyte (M_o)	Resting macrophage (M_R)	$IL - 6$	—
Resting macrophage (M_R)	M1 macrophage (M_1)	$TNF_\alpha, IL - 6$	$IL - 10$
M1 macrophage (M_1)	M2 macrophage (M_2)	$IL - 10$	—
Fibroblast (fi)	Myofibroblast ($myofi$)	$TGF\beta_1$	—

inflection(b) can be adjusted to the specific needs of the cell transition. Since the sigmoid function is used to simulate the probability of a single factor, all the cytokines of promotion and inhibition should be incorporated to calculate the final transition probability. Based on [Equation 2](#), the final probability that the resting neutrophils become activated consisted of five sigmoid functions, each of which will give a result between 0 and 1 depending on the concentration of each kind of cytokine.

The coefficients w_1, w_2, w_3, w_4 must sum to 1 for the final probability to remain between 0 and 1, and w_5 must not exceed 1. Similarly, w_7, w_8 and w_9 must not exceed 1 in [Equation 4](#). Additionally, w_6, w_{10}, w_{11} must not exceed 1 since there is only one term in [Equations 3, 6](#) respectively. A base probability of 0.1 is given in [Equations 3, 5, 6](#) in the event that there is no IL-6 and IL-10 present, as macrophages M1 and M2 do not exist in that situation. The only remaining cell transition is for activated neutrophils to become necrotic. Since there is no simple method in the literature that can detect neutrophils undergoing necrosis ([43](#)), activated neutrophils are assumed to be necrotic with a random probability (e.g., 0.1) in simulation.

The concentration of cytokines in each grid will be determined by solving the solute diffusion equations, and the cell transition will be based on probability equations. The parameters for the sigmoid function can be found in [Table 3](#). Additionally, the order of magnitude of the cytokine concentration is essential to guarantee the accuracy of the calculations. Multiple pre-simulations were

performed to determine the order of magnitude of the cytokine concentrations, which can be seen in [Supplementary Table 2](#).

$$P_{(N_R-N_A)} = w_1 \sigma_{IL-8} + w_2 \sigma_{IL-1\beta} + w_3 \sigma_{IL-6} + w_4 \sigma_{TNF\alpha} - w_5 \sigma_{IL-10} \quad (2)$$

$$P_{(M_o-M_r)} = P_{base} + w_6 \sigma_{IL-6} \quad (3)$$

$$P_{(M_R-M_1)} = P_{base} + w_7 \sigma_{IL-6} + w_8 \sigma_{TNF\alpha} - w_9 \sigma_{IL-10} \quad (4)$$

$$P_{(M_1-M_2)} = P_{base} + w_{10} \sigma_{IL-10} \quad (5)$$

$$P_{(fi-myofi)} = w_{11} \sigma_{TGF-\beta 1} \quad (6)$$

Some cells, such as resting neutrophils and monocytes, have a predetermined lifespan that is determined by biology (see [Supplementary Table 1 in the Supplementary Material](#)). On the contrary, the lifespan of other cells, such as fibroblasts and macrophages, is more difficult to measure due to the variability between individuals. However, certain assumptions had to be made to calculate changes in cell count during the healing process. For example, if in timepoint A the solute concentration or cell number is increased, and in timepoint B, the solute concentration or cell number is decreased (assuming A < B), then between these two points, the solute concentration or cell count is decreasing. By examining the data presented in [Figures 1A, B](#), we can establish these assumptions ([Table 1](#)) and fit a Michaelis-Menten curve ([44](#)) specifically for macrophages type 2, which are of great importance in the immune response ([45](#)). Type 2 macrophages live beyond day 4 of simulation, however these cells have a significant impact on the downstream of burn wound healing. Assuming these are immortal, does not replicate the behavior in [Table 1](#). Therefore, we assume that their immortality is not constant and tested different parameters and functions that can make sure the dynamics are replicated. The parameters and functions used are shown in [Table 3](#).

2.2.3 Model assumptions

In this model we simulate the burn wound microenvironment after it has occurred, therefore at the initial point ($t=0$), we assume the start of the process of healing after burn injury. Owing to the two dimensional nature of the model, it does not include the depth or proliferation within the wound. To model accurately this wound patch of burn injury, we assume that the burn wound is located on a non-delicate area of the human skin, therefore the injury has not

TABLE 3 Function types and values used in the simulations. $y[x-1]$ means the previously calculated value is used. Inflection points obtained experimentally.

Function	1 st Inflection point	2 nd Inflection point	Equation
Sigmoid	$a = 1$	$b = 4$	$y = \frac{1}{1 + e^{-a(x-b)}}$
Michaelis-Menten	$K_m = -963211.7$	$V_{max} = -17.79826$	$y = \begin{cases} \frac{ V_{max} - x }{ K_m + x }, & \text{if } V_{max} \neq K_m + x \\ y[x-1], & \text{otherwise} \end{cases}$

occurred on the face, genitals, or fingertips, for example. We consider a limited supply of cells in circulation and in the wound patch simulated (16cm^2). This assumption could be replaced with experimentally or clinically observed vessel density metrics from the wound area in future studies. The exchange of cells and solute between the wound area and the blood supply is possible, and this is driven by the interactions described in [Figure 1C](#). The blood supply is limited only by the amount of circulating solute concentration or cells around the wound patch, therefore it implies that more cells can still be recruited. We allow cells to die by either transitioning into necrotic or apoptotic (only in neutrophils) or disappearing from the wound when reaching certain volume. A comprehensive data availability on cell count from the burn wound tissue and blood sample would help side step the above assumption in future models. In the current model, whenever a cell disappears, a new one takes its place, keeping the cell count homogenous across simulations. The severity of the wound is dictated by the concentration of pro-inflammatory cytokines vs anti-inflammatory cytokines given a certain timespan. Finally, we take into consideration only the presence of Fibroblasts and Myofibroblasts, and not collagen or scar formation ([Figure 1C](#)), since we limit the model to the effects on the wound path post-burn injury.

2.2.4 Differential equations

There are six main solute molecules described in the conceptual model. The diffusion of IL-8 ([Equation 7](#)), IL-1 β ([Equation 8](#)), IL-6 ([Equation 9](#)), IL-10 ([Equation 10](#)), ([Equation 11](#)) and TGF- β 1 ([Equation 12](#)) with respect to time. All equations contain one diffusion term (D_{cytokine}), one or two secretion terms (K_{cytokine}), and one decay term (μ_{cytokine}). The values of diffusion coefficient, decay rate, secretion rate, and endocytosis rate (θ_{cytokine}) are found in the literature and adapted to suit the same order of magnitude in the model. All these diffusion equations are solved within each MCS during the simulation. Fixed gradient boundary conditions (Neumann) are specified in the top, right, bottom and left corners of the whole lattice, meaning that the derivative at a boundary is zero or a constant. The cell number parameters in the equations, such as the number of endothelial cells (EC), necrotic neutrophils (N_N), and activated neutrophils (N_A), macrophages type 1 (M_1), macrophages type 2 (M_2) at time t , depend on the presence of the cells in the location where the cytokine is being expressed and the initial values for each can be found in [Supplementary Table 3](#).

$$\frac{\partial \phi_{IL-8}}{\partial t} = D_{IL-8} \nabla^2 \phi_{IL-8} - \mu_{IL-8} \phi_{IL-8} + K_{EC|IL-8} EC + K_{NN|IL-8} N_N - \theta_{N_A|IL-8} N_A \quad (7)$$

$$\frac{\partial \phi_{IL-1\beta}}{\partial t} = D_{IL-1\beta} \nabla^2 \phi_{IL-1\beta} - \mu_{IL-1\beta} \phi_{IL-1\beta} + K_{N_A|IL-1\beta} N_A \quad (8)$$

$$\frac{\partial \phi_{IL-6}}{\partial t} = D_{IL-6} \nabla^2 \phi_{IL-6} - \mu_{IL-6} \phi_{IL-6} + K_{M_1|IL-6} M_1 \quad (9)$$

$$\frac{\partial \phi_{IL-10}}{\partial t} = D_{IL-10} \nabla^2 \phi_{IL-10} - \mu_{IL-10} \phi_{IL-10} + K_{M_2|IL-10} M_1 \quad (10)$$

$$\begin{aligned} \frac{\partial \phi_{TNF\alpha}}{\partial t} = & D_{TNF\alpha} \nabla^2 \phi_{TNF\alpha} - \mu_{TNF\alpha} \phi_{TNF\alpha} + K_{N_A|TNF\alpha} N_A \\ & + K_{M_1|TNF\alpha} M_1 \end{aligned} \quad (11)$$

$$\frac{\partial \phi_{TGF\beta 1}}{\partial t} = D_{TGF\beta 1} \nabla^2 \phi_{TGF\beta 1} - \mu_{TGF\beta 1} \phi_{TGF\beta 1} + K_{M_2|TGF\beta 1} M_2 \quad (12)$$

2.3 Statistical analysis

We employed the Z-score from the *SciPy* package due to its key benefits ([46](#)). This approach offers scale independence, making data unit-independent and allowing comparison between variables with different units. The Z-score also provides interpretability, with each score indicating how many standard deviations (SD) a data point is from the mean. Moreover, the original distribution of the data is preserved. By using this method, we can guarantee that the data are on a common scale, which facilitates meaningful comparisons and statistical analyses. Mathematically, Z-scores (Z) are calculated by subtracting the mean (μ) from the data (X) and dividing by the standard deviation (σ), resulting in [Equation 13](#).

$$Z = \frac{X - \mu}{\sigma} \quad (13)$$

The suitability of this method with wide-ranged data made it an ideal choice for our research context.

2.4 Parameters

Firstly, a parameter scan (i.e. evaluation of possible parameters for the validation assumptions/data) was run thoroughly to verify the sensibility of the Saturation Coefficient and λ parameters. Followed by the experimental design, described in [Table 4](#), for the variable in question, the endothelial cell count.

TABLE 4 Experimental design: Endothelial cell count in 8 groups.

Experiment	S_1	S_2	S_3	S_4	S_5	S_6	S_7	S_8
Endothelial count	10	100	500	1000	2000	3000	4000	5000
Lambda				2000				
Saturation coefficient					10^{-11}			

2.5 Code, plugins, configurations and hardware used

The simulation code, configuration files, and additional results used in our study can be found in this *repository*. Programming was done in Python 3.10. All simulations were performed using CompuCell3D software (version 4.4.1) on Macbook Pro 2019 with a 2,3 GHz 8-Core Intel Core i9 processor.

The chemical field used to simulate chemotaxis is incorporated with *Fipy* and the partial differential equations were solved by using the *LinearGMRESSolver()* function.

Additional modules in the CompuCell3D environments used in our simulations and their function are described in *Supplementary Table 1B*.

3 Results

3.1 Cell count transition 0 – 4 days post-burn

Table 1 presents cell count transitions based on available data from the rat and mouse burn studies (2) in a time frame from 0 – 4 days post-burn. According to this, a lot of data points were unknown. Based on available data, resting neutrophils growth increased immediately (0h) after burn (increased Z-score), and resting neutrophil growth declined 24h post-burn (decreased Z-score). Monocytes number increased after 24h, and monocyte growth declined after 48h post-burn. Fibroblasts number increased after 72h post-burn. Activated neutrophils number increased immediately (0h) post-burn, activated neutrophils growth declined after 24h, and activated neutrophil number decreased after 48h post-burn. Macrophages type I (M1) number increased after 48h, M1 growth decreased after 72h post-burn. Macrophages type II (M2) growth increased after 72h up to 96h, and M2 number increased after 96h post-burn. Myofibroblasts growth increased after 96h post-burn.

3.2 Increasing endothelial cell count leads to opposite correlations between IL-8 and TGF- β 1

After running the experimental design outlined in Section 2, we compared the cell percentages between simulations (Figure 2A). The percentage of necrotic neutrophils was very small compared to other cell types and almost indistinguishable. With increasing number of endothelial cell count, all cell types except necrotic neutrophils were decreased (due to the immortality of endothelial cells) in percentage (Figure 2A). We took snapshots at different time intervals for all cytokines, for different simulations (Figures 2B, C), with only the snapshots from the 100th hour (\pm 4 days post-burn) shown. With higher endothelial cell count, the diffusion of IL-8 towards the center, the site that corresponds with the burn wound, increased and the diffusion of TGF- β 1 towards the center decreased. This caused the relationship between IL-8 and TGF- β 1 to become opposite in all simulations (Figure 2D). Specifically, the

concentration of IL-8 increased from simulation 1 to 8 and TGF- β 1 concentration decreased from simulation 1 to 8, compared in the same order of magnitude (taking highest concentration as comparison), over time.

3.3 Higher endothelial cell count results in higher IL-8 concentrations

IL-8, unlike TGF- β 1, doubles in concentration with increasing endothelial cell count, reaching double the order of magnitude (Figure 2D). Evidently, for IL-8, a higher endothelial cell count leads to a faster equilibrium convergence around the 10^{-8} order of magnitude of concentration, since S6 and S7 slowly converge to the concentration value achieved by S8.

3.4 Higher endothelial cell count resulted in increased cytokine response and cell activation

In the first 24 hours, a lower concentration of IL-8 led to delayed activated neutrophil recruitment, whereas a higher concentration led to a more rapid growth. TGF- β 1 had the opposite reaction at higher concentrations. All simulations showed a similar average number of cells across simulations, suggesting an incoming decrease if the availability of cells is high, and an increase if the cells are needed in early stage (supplied by the blood compartment), evidenced by the high SD (Figure 2E 0-24 hours column).

After 24h, a higher endothelial cell count leads to increased cytokine response and cell activation for tissue repair. The diffusion of TGF- β 1 increased, which was aided by the higher number of M1, and an increase in fibroblast number (Figure 2E 24-48 hours column). Consequently, activated neutrophils also decreased in cell count. Higher endothelial cell count also resulted in decreased cell count of monocytes.

Between 48 and 72 hours (Figure 2E 48-72 hours column), cytokine levels generally decreased as they reached equilibrium and began to influence cell responses. However, myofibroblast counts increased due to the increased presence of TGF- β 1, transitioning from fibroblasts. M2 cell counts also increased.

In the last hours of the simulation, 72 – 96h (Figure 2E 72 – 96 hours column), endothelial cell count resulted in increased M2 cell count.

3.5 The physical and physiological reflection of endothelial cell count difference

We chose a control simulation that showed similar dynamics to the indicated in **Table 1**. We then used the difference in cell count and cytokine concentration for analysis. Figures 3A, B show the Z-scored difference in cell counts and cytokine levels(respectively) between S8 and S4 (control) for different time frames. This provides a more detailed view of the effect of endothelial cell count.

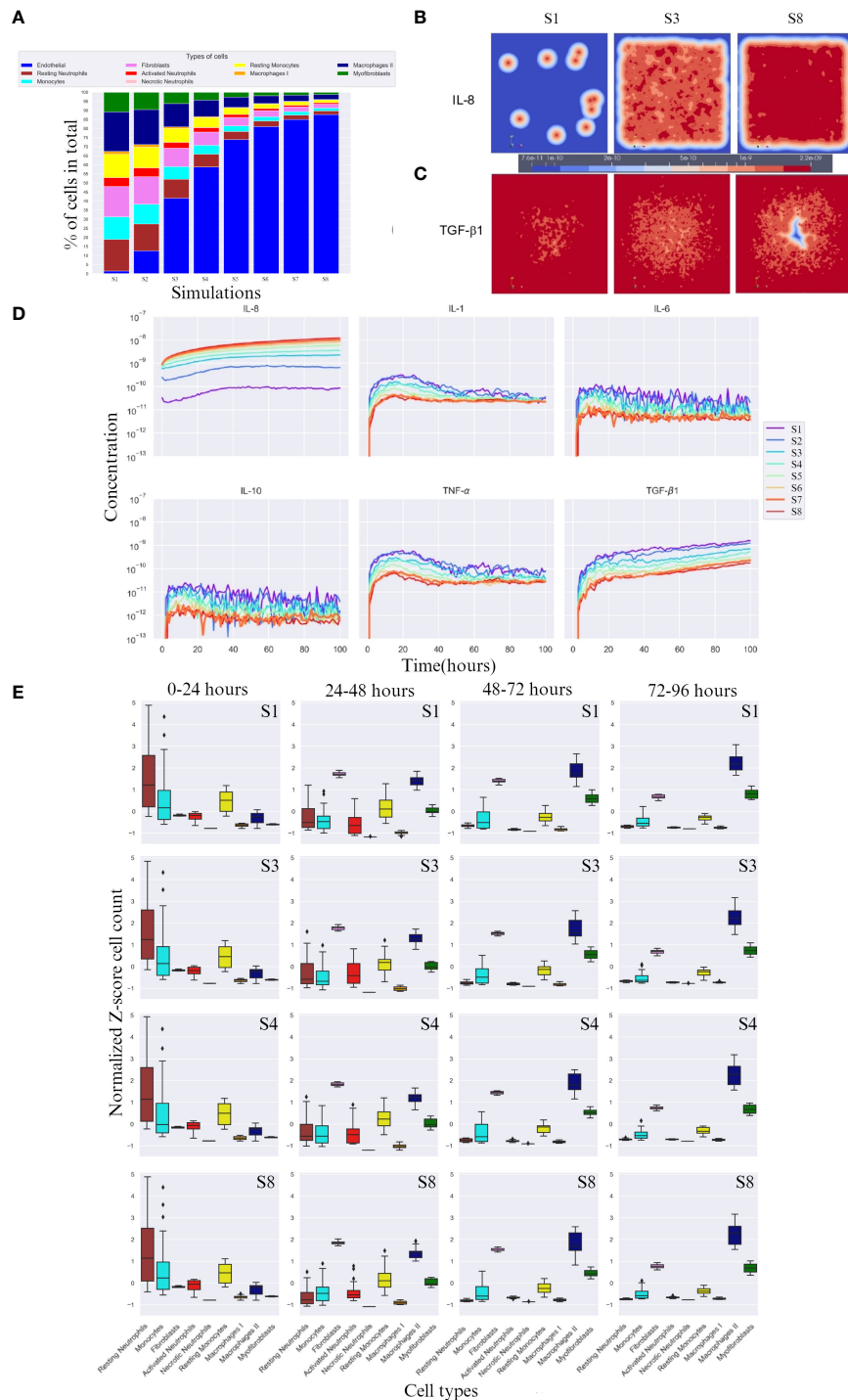
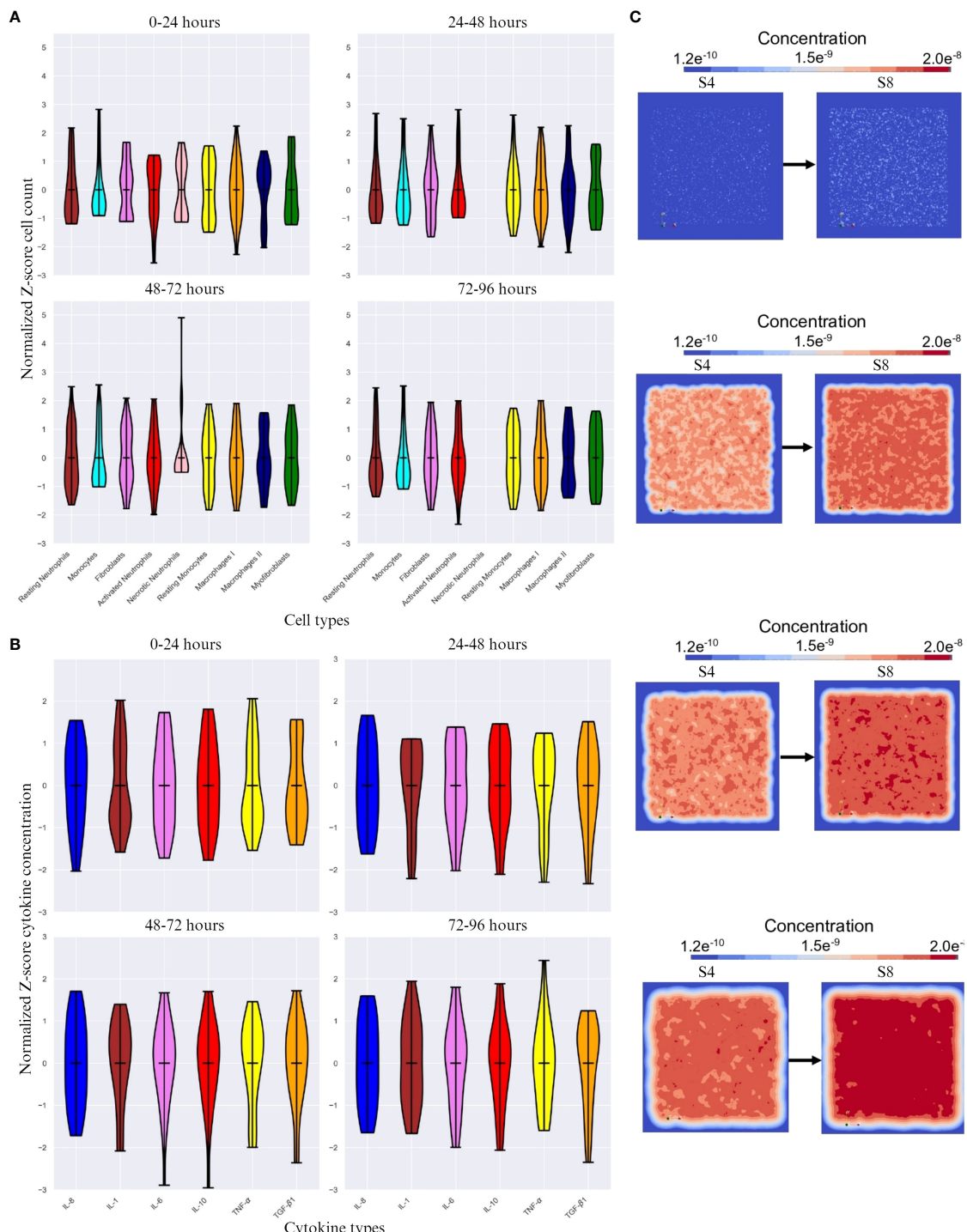


FIGURE 2

Overall cell type percentage per simulation, diffusion of IL-8 and TGF- β , and cytokine concentration and cell count over time. (A) Overall cell type percentage per S (simulation), note that endothelial cell count increases every S. (B, C) Graphic visualization of the diffusion of IL-8 and TGF- β in the 100th hour of simulation, respectively (scale for reference, values range within the same order of magnitude). (D) Cytokine concentration over time (in hours) per (S) simulation on a logarithmic scale (order of magnitude). (E) Breakdown of Z-score normalized cell count over four time frames between hours 0 and 96 for S1, S3, S4 and S8. Only most significant simulations are shown, i.e. where the change in cell count is more evident. For each box plot, the mean is plotted as a black line inside the box and the standard deviation located in each side of the box (at 95% CI), outliers shown as rhombus points. Note that the calculations for Z-score were done with respect to mean of each cell count/cytokine concentration. The score here indicates how many standard deviations an observation is from the mean.

**FIGURE 3**

The difference in cell count and cytokine concentration over different time intervals. **(A)** Z-score normalized difference in cell count(y-axis) over different time intervals between simulation 8 (S8) and simulation 4 (S4 - control) for different cell types(x-axis). **(B)** Z-score normalized difference in cytokine concentration(y-axis) over different time frames. **(C)** Initial, 48 hour, 72 hour and 96 hour change in positional diffusion for TGF- β 1 (from top to bottom) by comparing S4 (control, on the left) and S8 (on the right). Note that the calculations for Z-score were done with respect to mean of each cell count/cytokine concentration. The score here indicates how many standard deviations an observation is from the mean.

3.5.1 Significance of timing in the simulation environment

The cell count is expected to be highly variable, which is reflected in the high SD change for all cell types across time

frames except necrotic neutrophils and myofibroblasts (Figure 3A), which either are not shown (24 – 48 and 72 – 96 timespans for necrotic neutrophils) or vary in Z-score very actively. With increasing endothelial cells, the cell types with the highest SD

change are resting neutrophils, monocytes, resting monocytes, M1 and M2. The most significant difference was seen in the first 24 hours and the last 48 hours of the simulation, with M2 standing out as the most variable cell type across time intervals.

3.5.2 Faster inflammation resolution is caused by the difference in endothelial cell count

A higher endothelial cell count led to faster resolution of inflammation, restricting the duration of the inflammatory phase (Figures 3B, C). Pro-inflammatory cytokines were the most active cytokines, whereas the other cytokines remained relatively stable, with minimal difference in TGF- β 1 concentration. Despite this encounter, TGF- β 1 as an anti-inflammatory cytokine, had most changes in SD during the last 48 hours (Figure 3B) showing inflammatory resolution spatially (Figure 3C).

4 Discussions

In previous studies, we and others have demonstrated that the (acute) immune response is disrupted, i.e., “over-active” and prolonged, in burn patients, which negatively affects the wound healing and can cause further significant complications systemically (1–5).

In this article, we proposed a comprehensive framework to study the intricate cellular and molecular dynamics of the immune response in burn wounds by using relevant biological knowledge, experimental data from existing animal burn models, and mathematical principles.

After burn, endothelial cells play a crucial role in the inflammation phase of the wound healing. Specifically, during the acute phase, endothelial cells facilitate the movement of circulating inflammatory cells into the tissue at the site of burn injury (47). Therefore, we hypothesized that the endothelial cell count is one of the crucial parameters in burn wound healing and the acute immune response. The conceptual model initiates post-burn at $t = 0$; meaning that this is the moment that the simulation starts after burn. Within the model, the cells can move (except endothelial cells), are randomly located (mimicking the real burn wound injury circumstances), secrete cytokines, and differentiate. The burn surface area is limited to 5 by 5 cm area.

With these assumptions we demonstrated that our model can simulate the temporal evolution of the cell counts of the various cell types involved in the wound healing process (e.g., endothelial cells, neutrophils, monocytes/macrophages), and the diffusion of cytokines was simulated over a period of 0 – 4 days post-burn. The resulting simulations were tested and validated by experimental data.

Based on available data from rat and mouse burn studies (2), we identified the cell count transitions 0 – 4 days post-burn. Although, data points at different time frames were missing (unknown); we had to make assumptions for the time points in between, based on known data points we were able to simulate the cell count transitions over time. This is a limitation of the model, but in reality, it is not experimentally feasible to get complete timeseries for cell count (and growth) for each cell type.

Our findings revealed a key role for endothelial cells count in the acute immune response, higher endothelial count led to increased cytokine response and cell activation. Since endothelial

cells play a crucial role in the regulation of inflammation during the early stages of wound healing by facilitating the movement of inflammatory cells into the tissue, it can be expected that higher counts results in higher inflammatory reaction (e.g. increased cytokines and inflammatory cell activation) (48).

4.1 Simulation period 0–24 hours

In the first 24h of simulation, we found already a high number activated neutrophils, where lower concentration of IL-8 led to delayed activated neutrophil recruitment, and TGF- β 1 had the opposite reaction (Figures 2D, E). These findings correlates well with findings in *in vivo* studies. Namely, in the first 24h post-burn, there is an enhanced neutrophil migration activity (49), IL-8 plays a causative role in the recruitment and activation of neutrophils (50), and TGF- β 1 desensitize neutrophils to chemotactic stimulation (48).

4.2 Simulation period 24 – 72 hours

24 – 48h of simulation we found that both resting and activated neutrophil numbers decreased, and monocytes number increased. After 48h, monocyte numbers decreased, activated neutrophil number decreased further, and macrophage type I number increased (Figures 2D, E). The increase of monocyte numbers after 24h are in line with what was found in studies with burn patients (3, 51, 52). From 48 – 72h after burn monocytes are expected to decrease since they differentiate into macrophages (53). However, neutrophils *in vivo* normally increase in count for a longer period after burn (50); especially burn wounds are characterized by a prolonged local acute inflammatory response of innate immune cells (3, 52). This can be explained by the fact that the supply of cells *in vivo* is higher than in the *in silico* setting, since the supply in the model indicates an exchange from the blood compartment to the tissue compartment, where we assume a limited number of cells in both compartments. This means that there is no “unlimited” supply of cells when e.g. neutrophils die by necrosis (apoptosis is not implemented yet into the model either).

4.3 Simulation period 72–96 hours

72 – 96h of simulation, macrophage type I number decreased, while macrophage type II number increased, and both fibroblasts and myofibroblasts numbers increased. Moreover, these phenomena were positively affected by TGF- β 1 concentrations (Figures 2D, E). With higher endothelial cell count, the diffusion of IL-8 towards the center, the site that corresponds with the burn wound, increased and the diffusion of TGF- β 1 towards the center decreased (Figure 3). These findings are in line with the proliferation/remodeling phase during wound repair and scar formation *in vivo*. The macrophage phenotype changes as the wound heals, progressing from the macrophage type I (pro-inflammatory) to the macrophage type II (anti-inflammatory) (54). Fibroblasts first proliferate, and thereafter differentiate into

myofibroblasts, which contract and participate in healing by reducing the size of wound and secreting ECM proteins (55). Regarding this phase of wound repair, processes such as collagen production, wound closure, scar formation, contraction, are not implemented in the conceptual model yet. The current model simulates the cells that are mainly intervening in the (acute) inflammatory phase. And also for these cell types the supply of cells *in vivo* is higher than in the *in silico* setting.

The time frame in (burn) wound healing is another important parameter. In the current simulation this is limited by the 0 – 4 day time frame used to initially simulate the acute inflammatory phase of the post-burn immune response. Furthermore, in our model, we focused on the role of endothelial cells count. In addition to endothelial cells, e.g., thrombocytes play an important role in the inflammation phase of wound healing too (56). Thrombocytes provide high levels of platelet-derived growth factor (PDGF), which stimulates chemotaxis of monocytes/macrophages and proliferation of fibroblasts, both crucial during wound healing (56). However, thrombocytes are not included in the conceptual model yet, to simplify the modelling approach.

With regards to the limitations associated with the current model, most appear to arise from the biological proxies used in the model. For instance, some cell types are assumed to be immortal, this is practical considering the smaller duration of the total simulation period (4 days). However, in reality, some of these cells may die and release ITMs (Inflammation Triggering Moieties). These ITMs could further prolong the local inflammation duration at the wound sites. The extent of inflammation from such events could only be calculated from accurate experimental data of cell counts at different time periods. We assume that wound is in a non-sensitive area. In extensive burns, this may not be the case, thus new players not considered in the model could play a crucial role in the healing and wound closure processes. Finally, to lower computational complexity we have considered only innate immune system (cytokines and cells), the effect of adaptive system is not included, which may reduce the personalization aspect of the current model.

5 Conclusions

In this work, we provided a different perspective of the post-burn transition between cell types and the dynamics of the life span of cells that are difficult to measure experimentally. Although the availability of certain biological factors (data) was at some point limited, our model can simulate events that take place during the post-burn wound healing process can correlate with biological data with appreciable accuracy. The model simulation results are qualitatively verified against relevant studies in the literature. In a way, this is also one of the major limitation of the current model. A complete quantitative verification against experimental or clinical data is currently not possible either due to lack of complete longitudinal data or practical limitations in acquiring some datapoints (such as spatial cytokine concentrations) experimentally. The next step of model development is to investigate the relation with wound healing parameters, i.e., wound closure, re-epithelialization, and scar

formation, and patient specific characteristics; and identify processes on long-term (after 4 days post-burn). This approach would provide a comprehensive quantitative validation against clinical data. Since the current model is developed as a conceptual dynamic model, which will be continuously fed by new (generated) data from micro- to macroscale, we expect it will be a continuous learning model for the cellular and molecular processes during the immune response after burn. We have focused on developing a spatio-temporal model to simulate the inflammatory phase of burn wound in this study. In future studies, we plan to computationally model and validate other aspects and timelines of burn wound healing including acute inflammation, collagen production and scar formation. Such individual yet standardized models would provide a platform to combine them later to simulate the whole process of wound healing. In addition, the open-source nature of the developed GGH models and simulation techniques, other research including omics studies and machine learning techniques could be integrated to the mechanistic approach with little computational effort. Eventually, this will enable to prediction of systems behaviors and clinical outcomes in the burn wound healing process.

Data availability statement

The original contributions presented in the study are included in the article/[Supplementary Material](#), requests to access these datasets should be directed to BB, bboekema@burns.nl.

Ethics statement

Ethical approval was not required for the study involving animals in accordance with the local legislation and institutional requirements because we made use of published data from animal studies to validate our simulation models.

Author contributions

HK: Conceptualization, Data curation, Formal analysis, Investigation, Methodology, Resources, Supervision, Writing – original draft, Writing – review & editing. VS: Conceptualization, Data curation, Formal analysis, Investigation, Methodology, Resources, Software, Supervision, Writing – original draft, Writing – review & editing. RVB: Data curation, Investigation, Methodology, Writing – original draft. ML: Data curation, Investigation, Methodology, Writing – review & editing. AP: Conceptualization, Writing – review & editing. PM: Conceptualization, Writing – review & editing. BB: Conceptualization, Writing – review & editing. EJ: Conceptualization, Writing – review & editing. SP: Conceptualization, Writing – review & editing. RB: Conceptualization, Writing – review & editing. EM: Conceptualization, Writing – review & editing. PS: Conceptualization, Supervision, Writing – review & editing. PZ: Conceptualization, Supervision, Writing – review & editing.

Funding

The author(s) declare financial support was received for the research, authorship, and/or publication of this article. This research was funded by the Dutch Burns Foundation (DBF), Beverwijk, project 22.113; Health Holland, Den Haag, project LSHM18069; DBF, Beverwijk, project PPS 18.01.

Conflict of interest

RB was employed by company Allokys Life Sciences BV.

The remaining authors declare that the research was conducted in the absence of any commercial or financial relationships that could be construed as a potential conflict of interest.

References

1. Korkmaz HI, Ulrich MMW, van Wieringen WN, Vlijg M, Emmens RW, Meyer KW, et al. The local and systemic inflammatory response in a pig burn wound model with a pivotal role for complement. *J Burn Care Res* (2017) 38(5):e796–806. doi: 10.1097/BCR.0000000000000486

2. Mulder PPG, Koenen H, Vlijg M, Joosten I, de Vries RBM, Bockema B. Burn-induced local and systemic immune response: systematic review and meta-analysis of animal studies. *J Invest Dermatol* (2022) 142(11):3093–109.e15. doi: 10.1016/j.jid.2022.05.004

3. Mulder PPG, Vlijg M, Fasse E, Stoop MM, Pijpe A, van Zuijlen PPM, et al. Burn-injured skin is marked by a prolonged local acute inflammatory response of innate immune cells and pro-inflammatory cytokines. *Front Immunol* (2022) 13:1034420. doi: 10.3389/fimmu.2022.1034420

4. Bergquist M, Hästbacka J, Glaumann C, Freden F, Huss F, Lipcsey M. The time-course of the inflammatory response to major burn injury and its relation to organ failure and outcome. *Burns* (2019) 45(2):354–63. doi: 10.1016/j.burns.2018.09.001

5. Jeschke MG, van Baar ME, Choudhry MA, Chung KK, Gibran NS, Logsetty S. Burn injury. *Nat Rev Dis Primers* (2020) 6(1):11. doi: 10.1038/s41572-020-0145-5

6. Martin P, Nunan R. Cellular and molecular mechanisms of repair in acute and chronic wound healing. *Br J Dermatol* (2015) 173(2):370–8. doi: 10.1111/bjd.13954

7. Wilkinson HN, Hardman MJ. Wound healing: cellular mechanisms and pathological outcomes. *Open Biol* (2020) 10(9):200223. doi: 10.1098/rsob.200223

8. Korkmaz HI, Flokstra G, Waasdorp M, Pijpe A, Papendorp SG, de Jong E, et al. The complexity of the post-burn immune response: an overview of the associated local and systemic complications. *Cells* (2023) 12(3):345–65. doi: 10.3390/cells12030345

9. Presbitero A, Mancini E, Brands R, Krzhizhanovskaya VV, Sloot PMA. Supplemented alkaline phosphatase supports the immune response in patients undergoing cardiac surgery: clinical and computational evidence. *Front Immunol* (2018) 9:2342. doi: 10.3389/fimmu.2018.02342

10. van Zuijlen PPM, Korkmaz HI, Sheraton VM, Haanstra TM, Pijpe A, de Vries A, et al. The future of burn care from a complexity science perspective. *J Burn Care Res* (2022) 43(6):1312–21. doi: 10.1093/jbcr/irac029

11. Wu JC, Rose LF, Christy RJ, Leung KP, Chan RK. Full-thickness thermal injury delays wound closure in a murine model. *Adv Wound Care (New Rochelle)* (2015) 4(2):83–91. doi: 10.1089/wound.2014.0570

12. Maquart FX, Monboisse JC. Extracellular matrix and wound healing. *Pathol Biol (Paris)*. (2014) 62(2):91–5. doi: 10.1016/j.patbio.2014.02.007

13. Gabbiani G, Ryan GB, Majne G. Presence of modified fibroblasts in granulation tissue and their possible role in wound contraction. *Experientia* (1971) 27(5):549–50. doi: 10.1007/BF02147594

14. Wang N, Liang H, Zen K. Molecular mechanisms that influence the macrophage m1-m2 polarization balance. *Front Immunol* (2014) 5:614. doi: 10.3389/fimmu.2014.00614

15. Jeschke MG, Gauglitz GG, Kulp GA, Finnerty CC, Williams FN, Kraft R, et al. Long-term persistence of the pathophysiological response to severe burn injury. *PLoS One* (2011) 6(7):e21245. doi: 10.1371/journal.pone.0021245

16. van de Goot F, Krijnen PA, Begieneman MP, Ulrich MM, Middelkoop E, Niessen HW. Acute inflammation is persistent locally in burn wounds: a pivotal role for complement and C-reactive protein. *J Burn Care Res* (2009) 30(2):274–80. doi: 10.1097/BCR.0b013e318198a252

17. DiPietro LA. Angiogenesis and wound repair: when enough is enough. *J Leukoc Biol* (2016) 100(5):979–84. doi: 10.1189/jlb.4MR0316-102R

18. Sorrell JM, Caplan AI. Topical delivery of mesenchymal stem cells and their function in wounds. *Stem Cell Res Ther* (2010) 1(4):30. doi: 10.1186/scrt30

19. Velnar T, Gradišnik L. Tissue augmentation in wound healing: the role of endothelial and epithelial cells. *Med Arch* (2018) 72(6):444–8. doi: 10.5455/medarh.2018.72.444-448

20. Ley K. The microcirculation in inflammation. In: Tuma RFD, W. N, Ley K, editors. *Handbook of physiology: microcirculation*. San Diego: Academic Press (2011). p. 387–448.

21. Mai J, Virtue A, Shen J, Wang H, Yang XF. An evolving new paradigm: endothelial cells–conditional innate immune cells. *J Hematol Oncol* (2013) 6:61. doi: 10.1186/1756-8722-6-61

22. Bumbuc RV, Yildirim V, Sheraton MV. Modelling the interplay between chronic stress and type 2 diabetes on-set. *Int Conf Comput Sci* 2023 (2023) 14074:330–338. doi: 10.1007/978-3-031-36021-3_34

23. Sheraton MV, Chiew GGY, Melnikov V, Tan EY, Luo KQ, Verma N, et al. Emergence of spatio-temporal variations in chemotherapeutic drug efficacy: *in-vitro* and *in-Silico* 3D tumour spheroid studies. *BMC Cancer* (2020) 20(1):1201. doi: 10.1186/s12885-020-07677-5

24. Sheraton MVS, P. M. Parallel performance analysis of bacterial biofilm simulation models. *Computational Science-ICCS 2018: 18th International Conference*; Wuxi, China. *Comput Science-ICCS 2018: 18th Int Conf* (2018) 10860:496–505. doi: 10.1007/978-3-319-93698-7_38

25. Huang S, Dang J, Shekter CC, Yenikomishian HA, Gillenwater J. A systematic review of machine learning and automation in burn wound evaluation: A promising but developing frontier. *Burns* (2021) 47(8):1691–704. doi: 10.1016/j.burns.2021.07.007

26. Turley J, Chenchiah IV, Liverpool TB, Weavers H, Martin P. What good is maths in studies of wound healing? *iScience* (2022) 25(8):104778. doi: 10.1016/j.isci.2022.104778

27. Nagaraja S, Reifman J, Mitrophanov AY. Computational identification of mechanistic factors that determine the timing and intensity of the inflammatory response. *PLoS Comput Biol* (2015) 11(12):e1004460. doi: 10.1371/journal.pcbi.1004460

28. Nagaraja S, Chen L, Zhou J, Zhao Y, Fine D, DiPietro LA, et al. Predictive analysis of mechanistic triggers and mitigation strategies for pathological scarring in skin wounds. *J Immunol* (2017) 198(2):832–41. doi: 10.4049/jimmunol.1601273

29. Nagaraja S, Chen L, DiPietro LA, Reifman J, Mitrophanov AY. Computational analysis identifies putative prognostic biomarkers of pathological scarring in skin wounds. *J Transl Med* (2018) 16(1):32. doi: 10.1186/s12967-018-1406-x

30. Glazier JA, Graner F. Simulation of the differential adhesion driven rearrangement of biological cells. *Phys Rev E Stat Phys Plasmas Fluids Relat Interdiscip Topics* (1993) 47(3):2128–54. doi: 10.1103/PhysRevE.47.2128

31. Andasari V, Lü D, Swat M, Feng S, Spill F, Chen L, et al. Computational model of wound healing: EGF secreted by fibroblasts promotes delayed re-epithelialization of epithelial keratinocytes. *Integr Biol (Camb)* (2018) 10(10):605–34. doi: 10.1039/C8IB00048D

32. Tepole AB. Constitutive modelling of wound healing. In: Limbert G, editor. *Skin biophysics: from experimental characterisation to advanced modelling*. Cham: Springer (2019). p. 101–33.

Publisher's note

All claims expressed in this article are solely those of the authors and do not necessarily represent those of their affiliated organizations, or those of the publisher, the editors and the reviewers. Any product that may be evaluated in this article, or claim that may be made by its manufacturer, is not guaranteed or endorsed by the publisher.

Supplementary material

The Supplementary Material for this article can be found online at: <https://www.frontiersin.org/articles/10.3389/fimmu.2024.1303776/full#supplementary-material>

33. Korkmaz HI, Niessen FB, Pijpe A, Sheraton VM, Vermolen FJ, Krijnen PA, et al. Scar formation from the perspective of complexity science: a new look at the biological system as a whole. *J Wound Care* (2022) 31(2):178–84. doi: 10.12968/jowc.2022.31.2.178

34. van der Wal MB, Tuinebreijer WE, Bloemen MC, Verhaegen PD, Middelkoop E, van Zuijlen PP. Rasch analysis of the Patient and Observer Scar Assessment Scale (POSAS) in burn scars. *Qual Life Res* (2012) 21(1):13–23. doi: 10.1007/s11136-011-9924-5

35. Figueiredo G, Aickelin U, Siebers P-O. Systems dynamics or agent-based modelling for immune simulation? *SSRN Electronic J* (2011) 6825:81–94. doi: 10.2139/ssrn.2829280

36. Norton KA, Gong C, Jamalian S, Popel AS. Multiscale agent-based and hybrid modeling of the tumor immune microenvironment. *Processes (Basel)* (2019) 7(1):37–63. doi: 10.3390/pr7010037

37. Balter A, Merks R, Popławski NJ, Swat M, Glazier J, Rejniak KA, et al. The Glazier–Graner–Hogeweg Model: Extensions, future directions, and opportunities for further study. *Single-Cell-Based Models Biol Med* (2007) 151–67. doi: 10.1007/978-3-7643-8123-3_7

38. Merks RM, Perryn ED, Shirinifard A, Glazier JA. Contact-inhibited chemotaxis in *de novo* and sprouting blood-vessel growth. *PloS Comput Biol* (2008) 4(9):e1000163. doi: 10.1371/journal.pcbi.1000163

39. Andasari V, Roper RT, Swat MH, Chaplain MA. Integrating intracellular dynamics using CompuCell3D and Bionetsolver: applications to multiscale modelling of cancer cell growth and invasion. *PloS One* (2012) 7(3):e33726. doi: 10.1371/journal.pone.0033726

40. Izaguirre JA, Chaturvedi R, Huang C, Cickovski T, Coffland J, Thomas G, et al. CompuCell, a multi-model framework for simulation of morphogenesis. *Bioinformatics* (2004) 20(7):1129–37. doi: 10.1093/bioinformatics/bth050

41. Swat MH, Hester SD, Balter AI, Heiland RW, Zaitlen BL, Glazier JA. Multicell simulations of development and disease using the CompuCell3D simulation environment. *Methods Mol Biol* (2009) 500:361–428. doi: 10.1007/978-1-59745-525-1_13

42. Yuen B, Hoang MT, Dong X, Lu T. Universal activation function for machine learning. *Sci Rep* (2021) 11(1):18757. doi: 10.1038/s41598-021-96723-8

43. Iba T, Hashiguchi N, Nagaoka I, Tabe Y, Murai M. Neutrophil cell death in response to infection and its relation to coagulation. *J Intensive Care* (2013) 1(1):13. doi: 10.1186/2052-0492-1-13

44. Islam MA, Getz M, Macklin P, Versypt ANF. An agent-based modeling approach for lung fibrosis in response to COVID-19. *bioRxiv* (2023). doi: 10.1101/2022.10.03.510677

45. Strudwick XL, Adams DH, Pyne NT, Samuel MS, Murray RZ, Cowin AJ. Systemic delivery of anti-integrin α L antibodies reduces early macrophage recruitment, inflammation, and scar formation in murine burn wounds. *Adv Wound Care (New Rochelle)* (2020) 9(12):637–48. doi: 10.1089/wound.2019.1035

46. Cheadle C, Vawter MP, Freed WJ, Becker KG. Analysis of microarray data using Z score transformation. *J Mol Diagn* (2003) 5(2):73–81. doi: 10.1016/S1525-1578(10)60455-2

47. Johnson KE, Wilgus TA. Vascular endothelial growth factor and angiogenesis in the regulation of cutaneous wound repair. *Adv Wound Care (New Rochelle)* (2014) 3 (10):647–61. doi: 10.1089/wound.2013.0517

48. Ottolenghi L, Ghio M, Contini P, Bertolotto M, Bianchi G, Montecucco F, et al. Nonleukoreduced red blood cell transfusion induces a sustained inhibition of neutrophil chemotaxis by stimulating *in vivo* production of transforming growth factor-beta1 by neutrophils: role of the immunoglobulinlike transcript 1, sFasL, and sHLA-I. *Transfusion* (2007) 47(8):1395–404. doi: 10.1111/j.1537-2995.2007.01268.x

49. de Oliveira S, Rosowski EE, Huttenlocher A. Neutrophil migration in infection and wound repair: going forward in reverse. *Nat Rev Immunol* (2016) 16(6):378–91. doi: 10.1038/nri.2016.49

50. Harada A, Sekido N, Akahoshi T, Wada T, Mukaida N, Matsushima K. Essential involvement of interleukin-8 (IL-8) in acute inflammation. *J Leukoc Biol* (1994) 56 (5):559–64. doi: 10.1002/jlb.56.5.559

51. Moins-Teisserenc H, Cordeiro DJ, Audigier V, Ressaire Q, Benyamina M, Lambert J, et al. Severe altered immune status after burn injury is associated with bacterial infection and septic shock. *Front Immunol* (2021) 12:586195. doi: 10.3389/fimmu.2021.586195

52. Mulder PPG, Vlijg M, Boekema B, Stoop MM, Pijpe A, van Zuijlen PPM, et al. Persistent systemic inflammation in patients with severe burn injury is accompanied by influx of immature neutrophils and shifts in T cell subsets and cytokine profiles. *Front Immunol* (2020) 11:62122. doi: 10.3389/fimmu.2020.62122

53. Wang G, Xia Z. Monocyte subsets and their differentiation tendency after burn injury. *Front Med* (2013) 7(4):397–400. doi: 10.1007/s11684-013-0298-7

54. Kotwal GJ, Chien S. Macrophage differentiation in normal and accelerated wound healing. *Results Probl Cell Differ* (2017) 62:353–64. doi: 10.1007/978-3-319-54090-0_14

55. Darby IA, Laverdet B, Bonté F, Desmoulière A. Fibroblasts and myofibroblasts in wound healing. *Clin Cosmet Investig Dermatol* (2014) 7:301–11. doi: 10.2147/CCID.S50046

56. Pierce GF, Mustoe TA, Altrock BW, Deuel TF, Thomason A. Role of platelet-derived growth factor in wound healing. *J Cell Biochem* (1991) 45(4):319–26. doi: 10.1002/jcb.240450403



OPEN ACCESS

EDITED BY

Thomas Hartung,
Johns Hopkins University, United States

REVIEWED BY

Junping Wang,
Tianjin University of Science and
Technology, China
Steve Taylor,
University of Nebraska-Lincoln, United States

*CORRESPONDENCE

Liming Li
✉ 15083902334@163.com
Shengfa He
✉ heshengfa11@hotmail.com

RECEIVED 18 October 2023

ACCEPTED 05 February 2024

PUBLISHED 19 February 2024

CITATION

Yan Y, Li L, Long C, Dong Y, Li J, Shen C, Zhao Y, Zhao J, Wang J, Xiong A, Li X, Chen H and He S (2024) A novel IgE epitope-specific antibodies-based sandwich ELISA for sensitive measurement of immunoreactivity changes of peanut allergen Ara h 2 in processed foods.

Front. Nutr. 11:1323553.

doi: 10.3389/fnut.2024.1323553

COPYRIGHT

© 2024 Yan, Li, Long, Dong, Li, Shen, Zhao, Zhao, Wang, Xiong, Li, Chen and He. This is an open-access article distributed under the terms of the [Creative Commons Attribution License \(CC BY\)](#). The use, distribution or reproduction in other forums is permitted, provided the original author(s) and the copyright owner(s) are credited and that the original publication in this journal is cited, in accordance with accepted academic practice. No use, distribution or reproduction is permitted which does not comply with these terms.

A novel IgE epitope-specific antibodies-based sandwich ELISA for sensitive measurement of immunoreactivity changes of peanut allergen Ara h 2 in processed foods

Yan Yan¹, Liming Li^{2*}, Caiyun Long³, Yaping Dong¹, Jinyu Li², Caiyi Shen¹, Yiqian Zhao¹, Jiangqiang Zhao¹, Jianbin Wang¹, Anqi Xiong¹, Xin Li⁴, Hongbing Chen⁴ and Shengfa He^{1,5*}

¹School of Public Health and Health Management, Gannan Medical University, Ganzhou, China

²Department of Dermatology, First Affiliated Hospital of Gannan Medical University, Ganzhou, China

³Department of Laboratory, Ganzhou Center for Disease Control and Prevention, Ganzhou, China

⁴State Key Laboratory of Food Science and Resources, Nanchang University, Nanchang, China, ⁵Key Laboratory of Environment and Health of Ganzhou, Gannan Medical University, Ganzhou, China

Background: Peanut is an important source of dietary protein for human beings, but it is also recognized as one of the eight major food allergens. Binding of IgE antibodies to specific epitopes in peanut allergens plays important roles in initiating peanut-allergic reactions, and Ara h 2 is widely considered as the most potent peanut allergen and the best predictor of peanut allergy. Therefore, Ara h 2 IgE epitopes can serve as useful biomarkers for prediction of IgE-binding variations of Ara h 2 and peanut in foods. This study aimed to develop and validate an IgE epitope-specific antibodies (IgE-EsAbs)-based sandwich ELISA (sELISA) for detection of Ara h 2 and measurement of Ara h 2 IgE-immunoreactivity changes in foods.

Methods: DEAE-Sepharose Fast Flow anion-exchange chromatography combining with SDS-PAGE gel extraction were applied to purify Ara h 2 from raw peanut. Hybridoma and epitope vaccine techniques were employed to generate a monoclonal antibody against a major IgE epitope of Ara h 2 and a polyclonal antibody against 12 IgE epitopes of Ara h 2, respectively. ELISA was carried out to evaluate the target binding and specificity of the generated IgE-EsAbs. Subsequently, IgE-EsAbs-based sELISA was developed to detect Ara h 2 and its allergenic residues in food samples. The IgE-binding capacity of Ara h 2 and peanut in foods was determined by competitive ELISA. The dose-effect relationship between the Ara h 2 IgE epitope content and Ara h 2 (or peanut) IgE-binding ability was further established to validate the reliability of the developed sELISA in measuring IgE-binding variations of Ara h 2 and peanut in foods.

Results: The obtained Ara h 2 had a purity of 94.44%. Antibody characterization revealed that the IgE-EsAbs recognized the target IgE epitope(s) of Ara h 2 and exhibited high specificity. Accordingly, an IgE-EsAbs-based sELISA using these antibodies was able to detect Ara h 2 and its allergenic residues in food samples, with high sensitivity (a limit of detection of 0.98 ng/mL), accuracy (a mean bias of 0.88%), precision (relative standard deviation < 16.50%), specificity, and recovery (an average recovery of 98.28%). Moreover, the developed sELISA could predict IgE-binding variations of Ara h 2 and peanut in foods, as verified by using sera IgE derived from peanut-allergic individuals.

Conclusion: This novel immunoassay could be a user-friendly method to monitor low level of Ara h 2 and to preliminary predict *in vitro* potential allergenicity of Ara h 2 and peanut in processed foods.

KEYWORDS

peanut allergen, Ara h 2, IgE epitope-specific antibodies, sandwich ELISA, IgE-binding

1 Introduction

Food allergy is a growing global health concern, affecting up to 10% of the general population (1). One of the most common and severe food allergies is peanut (*Arachis hypogaea*) allergy, an immunoglobulin E (IgE)-mediated food allergy with a prevalence of 1%–3% in developed countries (2). Peanut allergy tends to be lifelong and sub-milligram levels of peanut protein can elicit objective reactions in the most sensitive patients (3). Since there is currently no approved curative treatment for this condition, complete avoidance of peanut proteins is the standard of care. This, however, is often difficult to achieve given the widespread use of peanut as food ingredient and maybe absence of detectable peanut in foods labeled with precautionary (advisory) allergen labeling statements for peanut (4, 5). In addition, peanut allergenicity mainly depends on its IgE epitopes. In the last decade, food processing is increasingly recognized as a method to enhance food tolerance, but the effect of food processing on the structure and allergenicity of peanut proteins is highly variable and therefore difficult to predict (6). Therefore, reliable methods to detect peanut allergenic epitopes and measure changes in IgE-binding ability of peanut in processed foods are warranted.

Analytical methods currently used to detect peanut allergens, such as real-time polymerase chain reaction (7), reversed-phase high-performance liquid chromatography (RP-HPLC) (8), liquid chromatography coupled mass spectrometry (9), enzyme-linked immunosorbent assay (ELISA) (10–12), and lateral flow immunoassay (10), lack the ability to specifically detect allergenic epitopes of the allergens. Traditionally, the method for measurement of IgE-binding capacity variations of peanut allergens is based on patients' IgE antibodies (13–15). However, the limited and variable sera from peanut-allergic patients makes the standardization of the detection method very difficult for commercial purposes. Hence, there is a need for more efficient and simplistic analytical methods that detect minute traces of peanut allergens and reveal changes in the IgE-immunoreactivity of peanut allergens in foods.

One of the analytical methods that can be used for allergen detection and is characterized by high specificity and sensitivity, low cost, and simplicity is ELISA. Recently, an ELISA based on IgE epitope-specific antibodies (IgE-EsAbs) was successfully used for the prediction of IgE-immunoreactivity variations of milk in food samples (16). This technique aims to detect specific IgE epitopes in the allergen, which play vital roles in triggering the allergic cascade and hence may be used to preliminary predict *in vitro* food potential allergenicity (17, 18). One of the most widely characterized allergens in peanut is Ara h 2, which is shown to be the most potent allergen and the best predictor of peanut

allergy (19, 20). Therefore, IgE epitopes in Ara h 2 could serve as reliable biomarkers for measurement of potential changes in IgE-immunoreactivity of Ara h 2 in foods. Based on this, we hypothesized that an ELISA based on IgE-EsAbs directed against Ara h 2 could be used to accurately detect the IgE epitope content of Ara h 2, thereby revealing the IgE-binding changes of Ara h 2 and peanut in processed foods in a cost-efficient and simplistic manner (18).

In this study, our objective was to develop an IgE-EsAbs-based sandwich ELISA (sELISA) for detecting allergenic residues of Ara h 2 and evidencing changes in the IgE-immunoreactivity of Ara h 2 in foods (Figure 1). Briefly, a monoclonal antibody against the major IgE epitope of Ara h 2 and a polyclonal antibody against twelve IgE epitopes of Ara h 2 were generated for use as capture and detection antibodies in the assay (Figures 1A, B). Next, the IgE-EsAbs-based sELISA was used to detect Ara h 2 and its allergenic residues in food samples, and results were compared to those obtained using sera IgE derived from peanut-allergic individuals (Figures 1C, D).

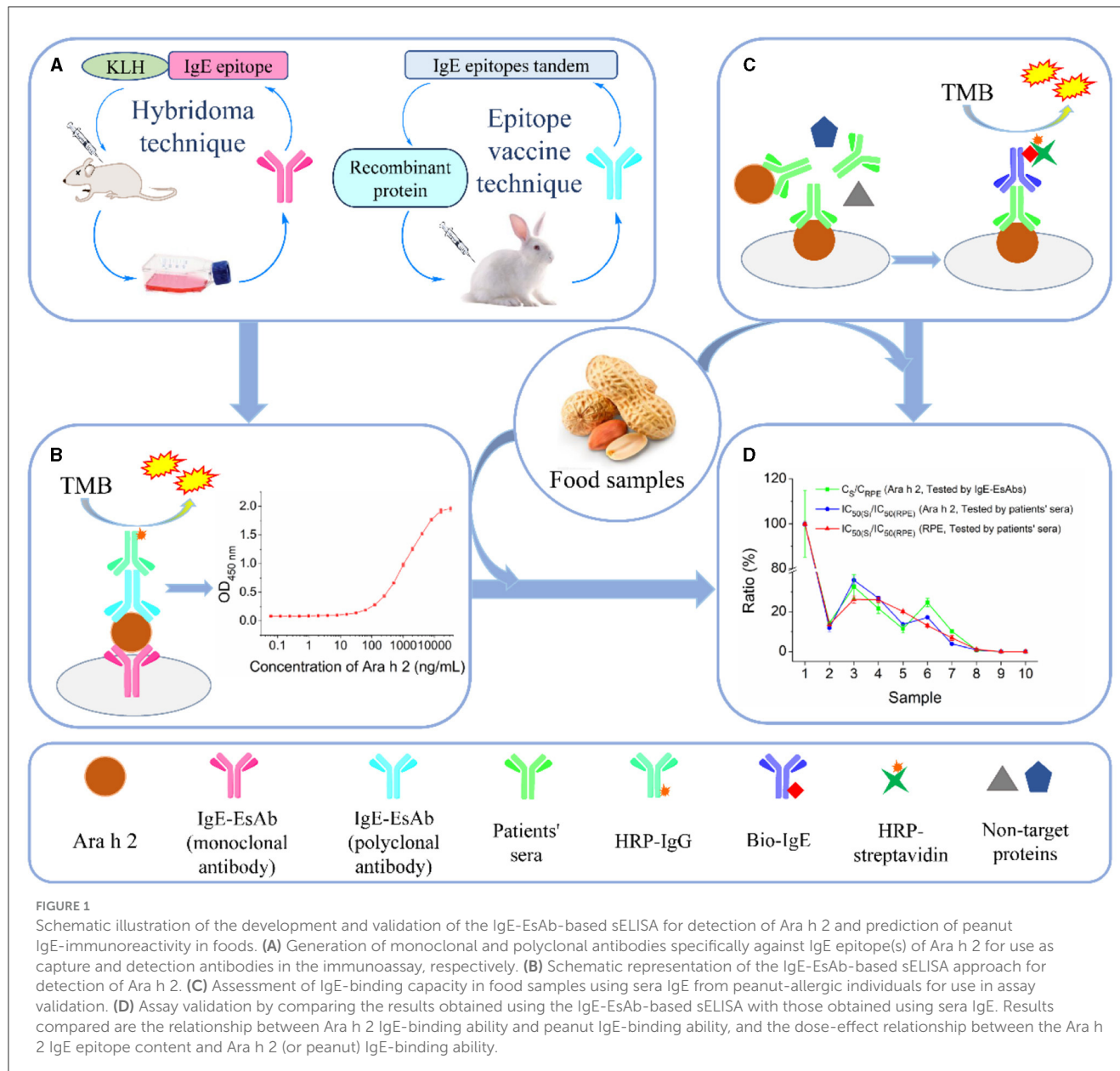
2 Materials and methods

2.1 Materials and reagents

DEAE Sepharose Fast Flow, HistrapTM HP affinity column (1 mL), and HiTrapTM Protein A HP affinity column (1 mL) were purchased from GE Healthcare (Uppsala, Sweden). Prestained protein marker and 3,3';5,5'-Tetramethylbenzidine (TMB) were obtained from Thermo Fisher Scientific (Rockford, USA). Complete Freund's adjuvant, incomplete Freund's adjuvant, gelatin from cold water fish, α -lactalbumin, β -lactoglobulin, casein, goat anti-rabbit HRP-IgG, rabbit anti-mouse HRP-IgG, and biotin-labeled goat anti-human IgE (Bio-IgE) were purchased from Sigma (St. Louis, USA). IgE epitope peptides (purity \geq 95%, RP-HPLC) were synthesized by GL Biochem (Shanghai, China). Food samples were purchased from local supermarkets. Peanut allergy patients' sera were provided by the First Affiliated Hospital of Gannan Medical University and approved by Gannan Medical University Research Ethics Committee (Reference number 2021105, 8/March/2021), details of which are shown in Supplementary Table S1. All reagents were analytical grade and solutions were prepared using ultra-pure water throughout the experiments.

2.2 Purification of peanut allergen Ara h 2

Ara h 2 was isolated from raw peanut protein extract according to the methods described in Hu et al. (21), with minor



modifications. Briefly, raw peanut seeds were ground into peanut butter and defatted three times with acetone containing 0.07% β -mercaptoethanol at a 1:5 (w/v) ratio while being stirred at 25°C for 2 h. After centrifugation (12,000 \times g for 10 min at 4°C), the precipitate was collected and air-dried. Next, the protein from the defatted powder (20.0 g) was extracted by addition of 100 mL Tris-HCl buffer (50 mmol/L, pH 7.2), followed by incubation at 25°C for 2 h while stirring. After centrifugation, the supernatant (peanut protein extract) was collected and Ara h 2 was subsequently isolated from the supernatant by DEAE Sepharose Fast Flow anion exchange chromatography followed by sodium dodecyl sulfate polyacrylamide gel electrophoresis (SDS-PAGE). Shortly, the chromatographic column (1.6 cm \times 50 cm) was equilibrated with Tris-HCl (50 mmol/L, pH 7.2) and subsequently loaded with 10 mL peanut protein extract, after which the loaded column was washed with equilibrating buffer containing 0.04 mol/L NaCl. The

proteins were further eluted using 600 mL of 0.04–0.2 mol/L NaCl gradient in equilibrating buffer. After dialysis and lyophilization of the collected eluates, the eluates were subjected to SDS-PAGE and the Ara h 2 fraction was excised from the SDS-PAGE gel. The purity of Ara h 2 was analyzed by ImageJ software.

2.3 Generation of a monoclonal antibody against IgE epitope of Ara h 2

A mouse monoclonal antibody (mAb, 2K9-1) against the peptide sequence NH₂-DRRCQSQLER-COOH (B3), selected based on the sequence of the most dominant IgE epitope of Ara h 2 (22, 23), was prepared by Abmart (Shanghai, China) and used as a capture antibody in the IgE-EsAb-based sELISA.

2.4 Generation of a polyclonal antibody against IgE epitopes of Ara h 2

IgE-EsAbs for use as detection antibody in the IgE-EsAb-based sELISA were obtained following inoculation of rabbits with a multiepitope-based vaccine (a recombinant protein), comprising of a T cell epitope, IgE epitopes, and linkers, as detailed below.

2.4.1 Construction of an expression system for recombinant tAra h 2

A tandem containing twelve IgE-binding epitopes of Ara h 2 (tAra h 2) was designed as described previously (24). In short, twelve IgE epitopes of Ara h 2 (B1-B12) were selected as part of the tandem based on Stanley et al. (22) and Shreffler et al. (25) epitope mapping results, and one dominant T cell epitope (AA94–113) of Ara h 2 was selected (26–28). The epitope sequences are shown in Supplementary Table S2. To construct the tAra h 2, the T cell epitope and B1–B12 were situated on the N-terminal and C-terminal respectively, and four glycines (GGGG) were inserted as a linker between two adjacent epitopes. Next, the gene sequence of tAra h 2 was custom-synthesized and cloned into the pET-28a(+) expression plasmid. Following confirmation of successful cloning by DNA sequencing, the plasmids were transformed into *E. coli* BL21 (DE3) pLysS cells by Chinapeptides (Shanghai, China).

2.4.2 Expression and purification of recombinant tAra h 2

Expression of recombinant tAra h 2 by *E. coli* BL21 (DE3) pLysS cells was induced by incubating the cells with 0.6 mmol/L isopropyl-β-d-thiogalactoside (IPTG) at OD_{600 nm} ~0.6 at 26°C for 4 h. After centrifugation (12,000 × g for 10 min at 4°C), the cell pellet was resuspended in 10 mmol/L phosphate buffer saline (PBS, pH 7.2) and cells were subsequently lysed by ultrasonication. After centrifuging again, the recombinant tAra h 2 in the supernatant was purified by HisTrap™ HP according to the manufacturer's instructions, and the purity of recombinant tAra h 2 was analyzed by ImageJ software.

2.4.3 Production and purification of a tAra h 2-specific polyclonal antibody

The animal study was approved by Gannan Medical University Animal Care Committee, under the guidelines of China Council for Animal Care (SYXK-Gan 2018-0004, China). Two 8-week-old male New Zealand white rabbits were purchased from the Ganzhou Institute of Animal Husbandry (SCXK-Gan 2018-0009, China). After collecting the negative serum from auricular vein, the rabbits were subcutaneously immunized with 1 mg recombinant tAra h 2 (2 mg/mL) emulsified with complete Freund's adjuvant in a total volume of 1 mL as a priming dose. Subsequently, the rabbits received three 1 mL booster injections containing the same dose of antigen emulsified in incomplete Freund's adjuvant in 2-week intervals for the production of tAra h 2-specific polyclonal antibody (pAb-tAra h 2). One week after the last immunization, blood samples were taken from the carotid artery and were clotted overnight at 4°C. The serum was isolated by centrifugation at 4,500

× g for 10 min at 4°C. Then, the IgG (pAb-tAra h 2) was purified by HiTrap™ Protein A HP according to the manufacturer's instructions, and the obtained pAb-tAra h 2 was stored at –80°C until use.

2.5 Characterization of the generated monoclonal and polyclonal antibodies

Target binding and specificity of the generated monoclonal and polyclonal antibodies for use in the IgE-EsAb-based sELISA were evaluated as detailed below.

2.5.1 Analysis of affinity constant of monoclonal antibody

The affinity constant (K_{aff}) of 2K9-1 to Ara h 2 was analyzed with indirect ELISA as described previously (29). Briefly, a microliter plate was pre-coated overnight at 4°C with three different concentrations of Ara h 2 (0.5 μg/mL, 1 μg/mL, and 2 μg/mL), after which wells were washed three times with PBS containing 0.05% Tween-20 (PBST). Next, wells were blocked with 3% gelatin in PBS for 1 h at 37°C. After washing, serial concentrations (2,000 ng/mL, 1,000 ng/mL, 500 ng/mL, 250 ng/mL, 125 ng/mL, 62.5 ng/mL, 31.25 ng/mL, and 15.625 ng/mL) of 2K9-1 was added and incubated for 1 h at 37°C. The wells were washed and subsequently incubated with 100 μL of rabbit anti-mouse HRP-IgG (diluted 1:10,000 in PBS) for 1 h at 37°C. After washing again, 100 μL of TMB substrate for HRP was added and incubated for 15 min at 37°C, followed by addition of 50 μL of 2 mol/L sulfuric acid and immediate measurement of optical density at 450 nm (OD_{450nm}) using a microplate reader (Varioskan LUX; Thermo Fisher Scientific, USA). The K_{aff} of 2K9-1 was calculated as follows: $K_{aff} = (n - 1)/2(n[Ab']t - [Ab]t)$, where $n = [Ag]/[Ag']$, [Ag] and [Ag'] are two different coating concentrations of Ara h 2, and [Ab]t and [Ab']t are the concentrations (in mol/L) of 2K9-1 at which 50% of the maximum OD_{450nm} values were obtained for plates coated with [Ag] and [Ag'], respectively.

2.5.2 Analysis of the titer of polyclonal antibody

The titers of tAra h 2-specific antibodies in the collected rabbit serum were determined by indirect ELISA. Microplates were coated with 100 μL of recombinant tAra h 2 (1 μg/mL) overnight at 4°C. After washing three times with PBST, each well was blocked with 250 μL of 3% gelatin in PBS for 1 h at 37°C. After washing, a dilution series of rabbit serum (100 μL/well) was added and incubated for 1 h at 37°C. Next, wells were washed and subsequently incubated with 100 μL of goat anti-rabbit HRP-IgG (diluted 1:5,000 in PBS) for 1 h at 37°C. After washing, wells were incubated with 100 μL of TMB solution for 15 min at 37°C, after which 50 μL of sulfuric acid (2 mol/L) was added to stop the color development and the OD_{450nm} was measured using a microplate reader.

The serum antibody titer was defined as the maximum dilution factor that yielded P/N > 2.1, and P > 0.2 ($n = 3$), in which P and N represent the OD_{450nm} of positive and negative serum, respectively.

2.5.3 Evaluation of antibody binding to IgE epitope(s) of Ara h 2

Binding of 2K9-1 and pAb-tAra h 2 to the target IgE epitope(s) of Ara h 2 was assessed by competitive ELISA (cELISA), as described previously (30). In short, the plates were coated with 100 μ L of purified Ara h 2 (0.25 μ g/mL) overnight at 4°C. After washing and blocking, wells were incubated with 50 μ L of varying concentrations of IgE epitope peptide (0.25, 0.5, or 1 μ g/mL for 2K9-1; 0.25, 1, or 4 μ g/mL for pAb-tAra h 2) and 50 μ L of a fixed concentration of antibody (31.25 ng/mL for 2K9-1; 2 μ g/mL for pAb-tAra h 2) for 1 h at 37°C. After washing, wells were incubated with 100 μ L of rabbit anti-mouse HRP-IgG (diluted 1:10,000 in PBS, for 2K9-1) or goat anti-rabbit HRP-IgG (diluted 1:5,000 in PBS, for pAb-tAra h 2) for 1 h at 37°C, and subsequently washed again. Next, wells were incubated with 100 μ L TMB solution for 15 min at 37°C, followed by addition of 50 μ L of 2 mol/L sulfuric acid and immediate measurement of optical density as detailed above.

2.5.4 Evaluation of antibody specificity

The cross-reactivity (CR) of 2K9-1 and pAb-tAra h 2 with various allergens was analyzed by cELISA. First, protein as a source of allergens was extracted from different foods. Protein from egg, soybean, oat, and wheat were extracted as our previously reported method (29). Protein from cashew, macadamia, pistachio, chestnut, almond, sesame, and walnut were first powdered and subsequently defatted using acetone (1:10, w/v). Proteins were then extracted from 1 g defatted powder addition of 20 mL Tris-HCl (50 mmol/L, pH 8.0, containing 2% Tween-20) and subsequent incubation for 4 h at 25°C while stirring. After centrifugation (12,000 \times g for 10 min at 4°C), the supernatant was collected for use in the cELISA.

The competitive concentrations of Ara h 2 and inhibitors (protein extracts) were 2-fold serially diluted from 16 μ g/mL to 0.125 μ g/mL and 128 μ g/mL to 32 μ g/mL, respectively. The ELISA procedures were in accordance with the cELISA described above. The 50% inhibition concentration (IC_{50}) was used to determine the CR as follows: CR (%) = $[IC_{50}(\text{Ara h 2})/IC_{50}(\text{inhibitor})] \times 100\%$.

2.6 Development of the IgE-EsAbs-based sELISA for Ara h 2 detection

The microtiter plate was coated with 100 μ L of 2K9-1 (capture antibody, 1 μ g/mL) and incubated overnight at 4°C. After washing three times with PBS containing 0.2% Tween-20 (PBST), the wells were blocked with 250 μ L of 3% gelatin in PBST and incubated for 1 h at 37°C. The wells were washed and 100 μ L of Ara h 2 (or food samples and blocking buffer as control) was added, followed by incubation for 2 h at 37°C. After washing again, 100 μ L of pAb-tAra h 2 (detection antibody, 4 μ g/mL) was added and incubated for 1 h at 37°C. After removal of unbound pAb-tAra h 2 by washing, 100 μ L of goat anti-rabbit HRP-IgG (diluted 1:5,000) was added to the wells and incubated for 0.5 h at 37°C. After washing, 100 μ L of TMB substrate solution was added and color was developed for 20 min at 37°C. Color development was terminated using 50 μ L of 2 mol/L sulfuric acid, after which the OD_{450nm} was measured using

a microplate reader. To reduce non-specific adsorption, the Ara h 2, food samples, pAb-tAra h 2, and goat anti-rabbit HRP-IgG were diluted with a blocking solution (3% gelatin in PBST).

2.7 Evaluation of the sensitivity, accuracy, precision, and specificity of the IgE-EsAbs-based sELISA for Ara h 2 detection

The limit of detection (LOD) and quantitation (LOQ), accuracy, and precision of the developed IgE-EsAbs-based sELISA were estimated using the Eurachem Guidance on validating analytical methods (31). LOD and LOQ were computed as the concentration of Ara h 2 corresponding to the mean of ten blank values plus three or ten standard deviations (SD), respectively. The accuracy was checked by analyzing the bias (%), which was defined as the difference (%) between the Ara h 2 concentration detected by the developed sELISA and the actual concentration of Ara h 2. The precision of the proposed sELISA was assessed by testing the relative SD of repeatability (RSD_r, intra-day) and reproducibility (RSD_r, inter-day) at a series of Ara h 2 concentrations. Repeatability and reproducibility were determined by analyzing Ara h 2 at different concentrations in 1 day ($n = 5$) and in five different days ($n = 3$), respectively. Results were computed as follows: RSD_r or RSD_r (%) = SD/mean \times 100%.

The specificity of the developed sELISA was evaluated with various proteins (i.e., α -lactalbumin, β -lactoglobulin, casein, and proteins extracted from egg, soybean, wheat, oat, cashew, macadamia, pistachio, chestnut, almond, sesame, and walnut) for CR at 0.125 μ g/mL, 0.5 μ g/mL, 2.0 μ g/mL, and 8.0 μ g/mL.

2.8 Evaluation of applicability of the IgE-EsAbs-based sELISA

A spike/recovery experiment was performed to investigate the capacity of the IgE-EsAbs-based sELISA to accurately detect Ara h 2 in samples with complex matrices. First, proteins were extracted from different foods. Proteins from boiled peanut, roasted peanut, and fried peanut were extracted as described above for raw peanut. Proteins from cookie, bread, and dry baked cake were extracted by first powdering the food, followed by addition of 20 mL Tris-HCl (50 mmol/L, pH 8.0, containing 2% Tween-20) to the powder (1 g) and agitation for 4 h at 25°C. Samples were then centrifuged (12,000 \times g for 10 min at 4°C) and supernatants were collected. Protein extracts from beverages were obtained by centrifugation, followed by collection of supernatants. Protein extracts of peanuts and beverages were spiked with 0, 0.25, or 2.0 mg/mL Ara h 2, and those of cookie, bread, and dry baked cake were spiked with 0, 0.25, or 2.0 mg/g Ara h 2. Samples were analyzed using IgE-EsAbs-based sELISA, and the recovery was calculated as follows: Recovery (%) = $(A_2 - A_0)/A_1 \times 100\%$, where A_0 represents the detected concentration of a sample without spiked Ara h 2, A_1 the concentration of Ara h 2 used for spiking, and A_2 the detected concentration of a sample spiked with Ara h 2.

2.9 Assessment of IgE-binding capacity of food samples

The IgE-binding capacity of Ara h 2 and peanut in food samples was determined by cELISA. The microplate was coated with 100 μ L of Ara h 2 or raw peanut extract (RPE) at 2 μ g/mL and incubated overnight at 4°C. After washing three times with PBS containing 0.1% Tween-20 (PBST), the wells were blocked with 3% gelatin in PBST and incubated for 1 h at 37°C. After washing, equal volume (50 μ L) of food samples and pooled sera (diluted 1:10 for Ara h 2; diluted 1:30 for RPE) were added and incubated for 1 h at 37°C. After washing thrice, 100 μ L of Bio-IgE (diluted 1:2500) was added and incubated for 1 h at 37°C. After washing again, 100 μ L of HRP-streptavidin (diluted 1:60) was added and incubated for 1 h at 37°C. The subsequent procedures were in accordance with the cELISA described above. To reduce non-specific adsorption, food samples, pooled sera, Bio-IgE, and HRP-streptavidin were diluted in blocking solution (3% gelatin in PBST).

2.10 Statistical analysis

Data are reported as mean \pm SD. Statistical analyses were performed using SPSS 17.0 (SPSS Inc., Chicago, USA) and statistical significance was assessed using Tukey's pairwise comparisons of ANOVA. Differences were considered significant when $^*p < 0.05$ and $^{**}p < 0.01$.

3 Results and discussion

3.1 Purification of Ara h 2

The raw peanut protein extract was fractionated into three major peaks (a, b, and c) using anion exchange chromatography under linear gradient elution (Figure 2A). Then, the eluted fractions were analyzed by SDS-PAGE (Figure 2B). The eluates of peak "b" contained two distinct bands with molecular masses ranging from 18 to 20 kDa (Figure 2B, lanes 3–8), which are corresponding to Ara h 2.01 and Ara h 2.02, respectively (21). The purity of Ara h 2 in the eluates, however, was only between 46.61% and 80.95% (Figure 2B, lanes 4–7) as a result of co-elution of Ara h 6 (15 kDa), which has a high homology with Ara h 2 and therefore has similar physical and chemical properties (20, 32). To improve the purity of Ara h 2, the eluates between positions "4" and "7" in Figure 2A were collected, dialyzed, lyophilized, and subsequently subjected to SDS-PAGE. Ara h 2 protein extracted from the SDS-PAGE gel showed a purity of 94.44% (Figure 2C), and the obtained Ara h 2 was identified by mass spectrometry (Supplementary Figure S1). These results indicate that high purity Ara h 2 was obtained by the employed two-step purification method.

3.2 Expression and purification of recombinant tAra h 2

The amino acid and gene sequences of the designed tAra h 2 are shown in Supplementary Figure S2. Sequencing revealed

that the constructed expression plasmid pET28a(+)·tAra h 2 contained the full gene sequence of tAra h 2 in expression strain *E. coli* BL21 (DE3) pLysS (Supplementary Figure S3, located 225–725 bp), indicating that the expression strain was successfully constructed.

To test whether recombinant tAra h 2 could be expressed by the expression strain, cells were incubated with 0.6 mmol/L IPTG at 26°C to induce expression. Following induction, a major band with an apparent molecular weight slightly below 25 kDa was observed, particularly after 4 h of induction (Figure 3A). The band presumably corresponding to recombinant tAra h 2 appeared at a greater molecular weight than the expected molecular mass (~18.03 kDa). This phenomenon is consistent with other reported His-tag fusion proteins (33–35). Thus, these results indicate that the recombinant tAra h 2 was successfully expressed.

Following induction of expression by incubation with 0.6 mmol/L IPTG at 26°C for 4 h, the cells were harvested by centrifugation. The pellet was sonicated, and the recombinant tAra h 2 in the supernatant was purified by HistrapTM HP. As shown in Figure 3B, most of the recombinant tAra h 2 was bound to the column after loading the supernatant (lanes 1 and 2), and there was no protein after non-specific elution (lane 3). The His-tagged protein bound to the HistrapTM HP column was eluted using different concentrations of imidazole (Figure 3B, lanes 4–7), and recombinant tAra h 2 was obtained at a purity of 88.56% (Figure 3B, lane 6).

3.3 Production and characterization of Ara h 2-specific antibodies for use in the IgE-EsAbs-based sELISA

3.3.1 Immunological characterization of capture antibody 2K9-1

The K_{aff} of mouse monoclonal antibody 2K9-1 against Ara h 2 was analyzed by indirect ELISA. The concentration of 2K9-1 at half of the maximum absorbance in the plate coated with 2, 1, and 0.5 μ g/mL of Ara h 2 were 36.37, 37.85, and 43.44 ng/mL, respectively. Consequently, the average K_{aff} was calculated as 1.69×10^9 L/mol (Figure 4A).

The ability of 2K9-1 to bind to its target IgE epitope (B3) of Ara h 2 was assessed by cELISA. The results show that the inhibition increased with increasing peptide concentration (Figure 4B), indicating that 2K9-1 binds its target IgE epitope of Ara h 2. In addition, the epitope B3 can be recognized by sera IgE from most peanut-allergic patients, and has been identified as the most dominant IgE epitope of Ara h 2 (22, 23). This suggests that this epitope remains stable after processing and gastrointestinal digestion. As a result, this epitope can work as a dependable biomarker, and the prepared 2K9-1 can serve as an efficient tool for detecting Ara h 2 and measuring its IgE-binding changes in foods.

The specificity of 2K9-1 for Ara h 2 was additionally determined by cELISA (Figure 4C). The IC_{50} of Ara h 2 was 4.58 μ g/mL. The 2K9-1 showed no binding to cow's milk proteins (α -lactalbumin, β -lactoglobulin, and casein) or to proteins from sesame, pistachio, almond, macadamia, cashew, soybean, wheat,

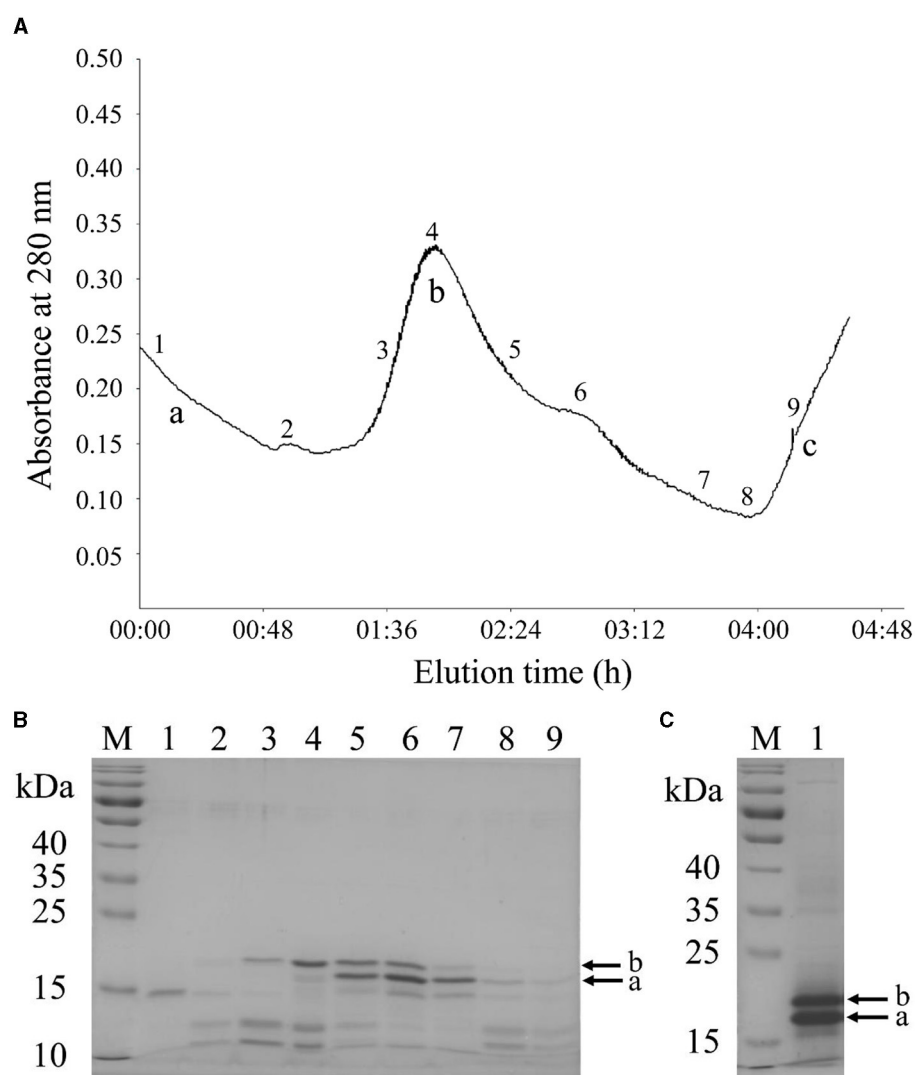


FIGURE 2

Purification of Ara h 2 by two-step method. **(A)** Chromatogram of raw peanut protein extract using DEAE-Sepharose Fast Flow anion-exchange chromatography. **(B)** SDS-PAGE patterns of Ara h 2 purified by anion-exchange chromatography. M: markers; lanes 1 to 9: fractions of 1 to 9 in anion-exchange chromatography profile. **(C)** SDS-PAGE patterns of isolated Ara h 2 from the SDS-PAGE gel. M: markers; lane 1: purified protein from the gel. The bands of Ara h 2.01 (a) and Ara h 2.02 (b) are indicated by arrows. Letters a–c: three major peaks.

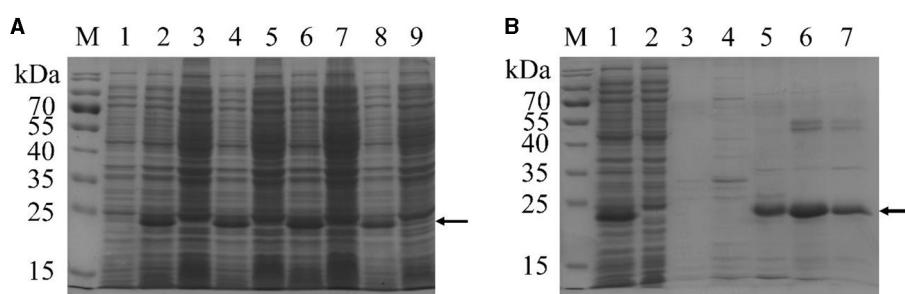


FIGURE 3

SDS-PAGE analysis of recombinant tAra h 2. **(A)** Expression of recombinant tAra h 2 under different induction conditions. M: markers; lanes 1, 3, 5, 7, and 9: incubation without IPTG for 0 h, 2 h, 3 h, 4 h, and 5 h, respectively; lanes 2, 4, 6, and 8: induction with 0.6 mmol/L IPTG for 2 h, 3 h, 4 h, and 5 h, respectively. **(B)** Purification of recombinant tAra h 2 by Histrap™ HP. M: markers; lane 1: supernatant of *E. coli* lysates after centrifugation; lane 2: flow-through protein of the column; lane 3: non-specific elution with 10 column volumes of 20 mmol/L imidazole in PBS (10 mmol/L, containing 0.5 mol/L NaCl, pH 7.2); lanes 4–7: specific elution with 5 column volumes of 25, 50, 100, and 200 mmol/L imidazole in PBS, respectively. The recombinant tAra h 2 is indicated by arrows.

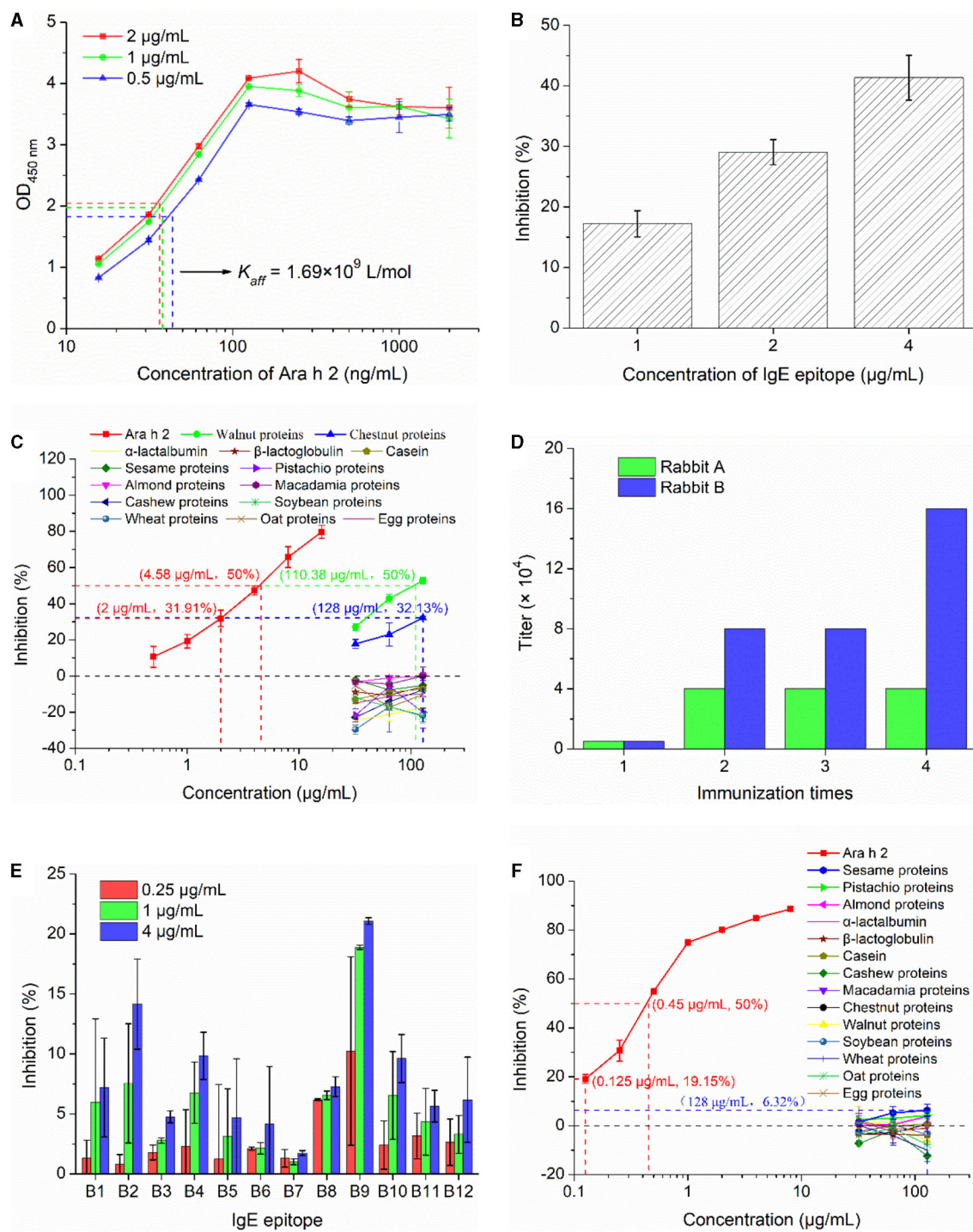


FIGURE 4

Immunological characterization of mAb 2K9-1 and pAb-tAra h 2. **(A)** Affinity constant of 2K9-1 to Ara h 2. The dash lines are the concentrations of 2K9-1 at 50% of the largest absorbance in the plate coated with different concentrations of Ara h 2. **(B)** Binding ability of 2K9-1 to IgE epitope. **(C)** Cross-reactivity of 2K9-1 with food allergens. **(D)** The titers of antisera against recombinant tAra h 2. **(E)** Binding ability of pAb-tAra h 2 to IgE epitopes (B1-B12). **(F)** Cross-reactivity of pAb-tAra h 2 with food allergens. Data are presented as mean \pm SD ($n = 3$).

oat, and egg when these proteins at a concentration of 128 µg/mL. However, slight CR was observed with walnut proteins and chestnut proteins. The IC₅₀ of walnut proteins was 110.38 µg/mL, corresponding to a CR of 4.15%. For chestnut proteins, an

inhibition rate of 32.13% was observed at a concentration of 128 µg/mL. This inhibition rate is similar to that of Ara h 2 at 2 µg/mL (31.91%). Hence, it can be speculated that the CR with chestnut proteins was \sim 1.56%. These might be due to Ara h 2

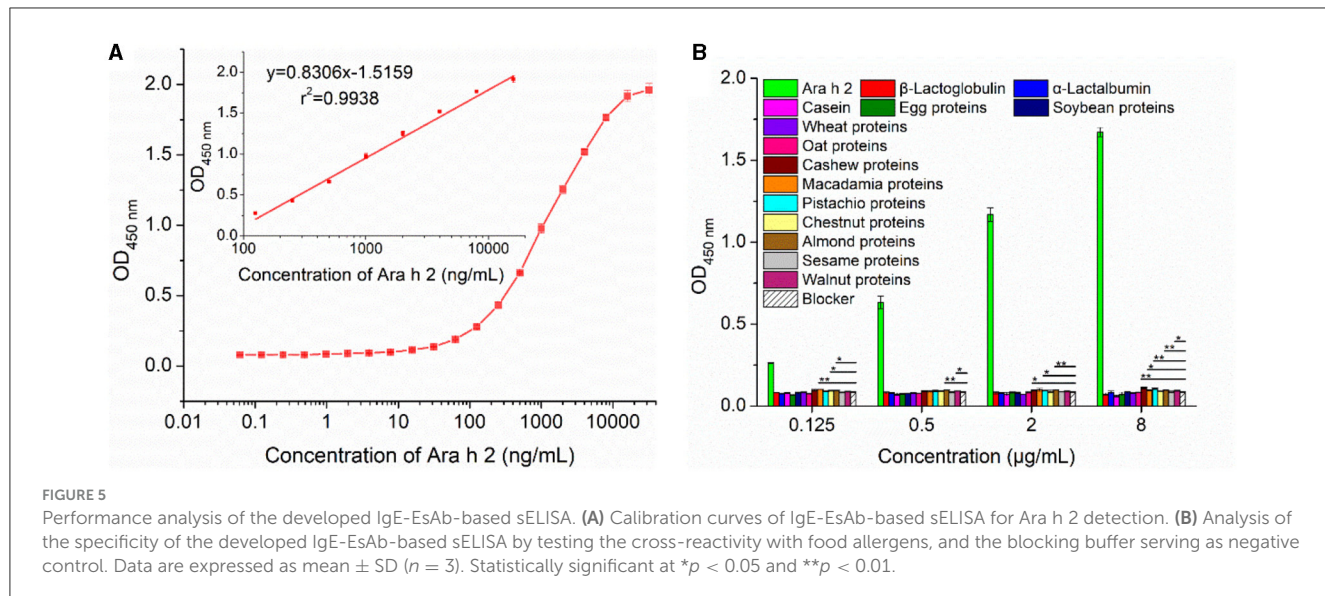


FIGURE 5

Performance analysis of the developed IgE-EsAb-based sELISA. (A) Calibration curves of IgE-EsAb-based sELISA for Ara h 2 detection. (B) Analysis of the specificity of the developed IgE-EsAb-based sELISA by testing the cross-reactivity with food allergens, and the blocking buffer serving as negative control. Data are expressed as mean \pm SD ($n = 3$). Statistically significant at $*p < 0.05$ and $**p < 0.01$.

sharing a similar IgE-reactive epitope with walnut (Jug r 2) and chestnut allergen (36). These results indicate that the 2K9-1 is highly specific.

3.3.2 Immunological characterization of detection antibody pAb-tAra h 2

For the production of polyclonal antibodies against recombinant tAra h 2 (pAb-tAra h 2), rabbits were inoculated with the purified recombinant tAra h 2 four times. Following inoculation, the titer values of antisera were determined as 40,000 and 160,000 for rabbits A and B (Figure 4D), respectively. Therefore, the serum from rabbit B was selected for the purification of pAb-tAra h 2 using the HiTrapTM Protein A HP column.

As recognition of IgE epitopes of native Ara h 2 by pAb-tAra h 2 is critical for successfully detecting Ara h 2 allergenic residues and measuring potential changes in IgE-immunoreactivity of Ara h 2 in foods (18, 30), the binding of the purified pAb-tAra h 2 to twelve selected IgE epitopes of Ara h 2 was analyzed by cELISA (Figure 4E). The results show that the pAb-tAra h 2 recognized all selected IgE epitopes, and the inhibition increased with increasing epitope peptide concentration. These findings suggest that the content of Ara h 2 IgE epitopes in foods can be detected by pAb-tAra h 2.

The specificity of pAb-tAra h 2 for Ara h 2 were determined by cELISA. The IC₅₀ of Ara h 2 was 0.45 μg/mL (Figure 4F). The pAb-tAra h 2 did not show binding to proteins from cow's milk (α-lactalbumin, β-lactoglobulin, and casein), cashew, macadamia, chestnut, walnut, soybean, wheat, oat, and egg at any of the tested protein concentrations (32–128 μg/mL). However, slight inhibition ratio was observed when protein extracted from sesame (6.32%), pistachio (4.26%), and almond (3.82%) at 128 μg/mL. This might be due to Ara h 2 sharing common IgE-binding epitopes with sesame, pistachio, and almond allergens (37, 38). These inhibition rates were significantly ($p < 0.01$) lower than 19.16% when the concentration of Ara h 2 was 0.125 μg/mL, thereby indicating that the CR with sesame, pistachio, and almond was lower than 0.098%. These findings suggest that the pAb-tAra h 2 is highly specific.

3.4 Performance evaluation of the IgE-EsAbs-based sELISA

Using the abovementioned Ara h 2-specific capture and detection antibodies, an IgE-EsAbs-based sELISA for Ara h 2 detection was set up and tested for sensitivity, accuracy, precision, and specificity as detailed below.

3.4.1 Sensitivity evaluation and comparative analysis of the IgE-EsAbs-based sELISA

The sensitivity of the developed IgE-EsAbs-based sELISA was evaluated by assessment of the lowest detectable Ara h 2 concentration. The assay showed a LOD and LOQ of 0.98 ng/mL (0.98 ppb) and 3.91 ng/mL (3.91 ppb), respectively. Generation of a calibration curve (Figure 5A) further revealed a linear working range of 0.125–16 μg/mL ($r^2 = 0.9938$).

Comparative analysis showed that the IgE-EsAbs-based sELISA has a lower LOD than most other analytical methods used for Ara h 2 detection (Supplementary Table S3). Most importantly, our IgE-EsAbs-based sELISA can specifically recognize IgE epitopes of Ara h 2, which makes it able to detect Ara h 2 allergenic residues and with the potential to measure Ara h 2 IgE-binding variations in processed foods (18, 30). As shown in Supplementary Table S3, the only analytical method that detects Ara h 2 IgE epitopes and with a significantly lower LOD is the rat basophilic leukemia (RBL-2H3) immune cell-based biosensing platform, with a LOD of 0.1 fmol/L (~ 0.002 ppb) (39). However, given that this sensor-based analytical technique requires cells culture, IgE antibodies to trigger an immunoreaction, and specialized knowledge, the IgE-EsAbs-based sELISA may be a more suitable method when lower costs and less complexity are desired.

3.4.2 The accuracy, precision, and specificity of the IgE-EsAbs-based sELISA

Assay accuracy and precision were evaluated by assessment of intra-assay and inter-assay variation, using five replicates of Ara h 2 varying in concentration from 0.125 μg/mL to

TABLE 1 Detection and recovery analysis of Ara h 2 concentrations in (spiked) food samples ($n = 3$).

Food sample	Ara h 2 spike concentration (mg/mL ^c or mg/g ^d)	Detected concentration (mg/mL ^c or mg/g ^d)	Recovery (%)
Raw peanut extract ^a	0	1.71 ± 0.26	
	0.25	1.95 ± 0.01	96.25 ± 3.29
	2	4.12 ± 0.09	120.78 ± 4.52
Boiled peanut extract ^a	0	0.25 ± 0.01	
	0.25	0.53 ± 0.05	111.38 ± 20.99
	2	2.24 ± 0.40	99.55 ± 20.13
Roasted peanut-1 extract ^a	0	0.56 ± 0.10	
	0.25	0.78 ± 0.05	89.94 ± 18.78
	2	2.61 ± 0.24	102.72 ± 12.13
Roasted peanut-2 extract ^a	0	0.37 ± 0.05	
	0.25	0.57 ± 0.01	79.00 ± 3.07
	2	2.60 ± 0.19	111.44 ± 9.73
Fried peanut extract ^a	0	0.19 ± 0.03	
	0.25	0.46 ± 0.01	104.40 ± 2.05
	2	2.14 ± 0.15	97.46 ± 7.64
Beverage-1 ^b	0	0.42 ± 0.04	
	0.25	0.64 ± 0.05	88.43 ± 21.09
	2	2.39 ± 0.45	98.59 ± 22.73
Beverage-2 ^b	0	0.18 ± 0.01	
	0.25	0.38 ± 0.06	81.28 ± 23.53
	2	2.13 ± 0.30	97.75 ± 14.86
Cookie ^b	0	0.25 ± 0.02	
	0.25	0.47 ± 0.04	90.87 ± 14.28
	2	2.25 ± 0.03	100.26 ± 1.32
Bread ^b	0	Not detected	
	0.25	0.25 ± 0.02	98.25 ± 7.91
	2	2.11 ± 0.31	105.61 ± 15.70

(Continued)

TABLE 1 (Continued)

Food sample	Ara h 2 spike concentration (mg/mL ^c or mg/g ^d)	Detected concentration (mg/mL ^c or mg/g ^d)	Recovery (%)
Dry baked cake ^b	0	Not detected	
	0.25	0.23 ± 0.04	93.37 ± 16.75
	2	1.97 ± 0.27	98.26 ± 13.70

^aThese extracts contain protein exclusively sourced from peanut, at concentrations of 18.20 mg/mL for raw peanut extract, 2.72 mg/mL for boiled peanut extract, 4.32 mg/mL for roasted peanut-1 extract, 4.00 mg/mL for roasted peanut-2 extract, and 7.68 mg/mL for fried peanut extract. ^bThese extracts contain proteins from different sources, i.e., peanut and milk for beverage-1; peanut, oat, almond, hazelnut, and walnut for beverage-2; wheat, peanut, egg, almond, milk, and soybean for cookie; wheat, egg, and milk for bread; wheat and egg for dry baked cake. Concentrations of peanut protein in these extracts were not determined.

^cApplicable to peanut extracts and beverages. ^dApplicable to cookie, bread, and dry baked cake.

16 µg/mL. The average bias of the intra-assay was 0.88%, and the mean RSD_r and RSD_{DR} were 8.02% (4.13%–12.56%) and 10.68% (3.35%–16.50%), respectively (Supplementary Table S4). These results suggest that the IgE-EsAbs-based sELISA has high accuracy and precision.

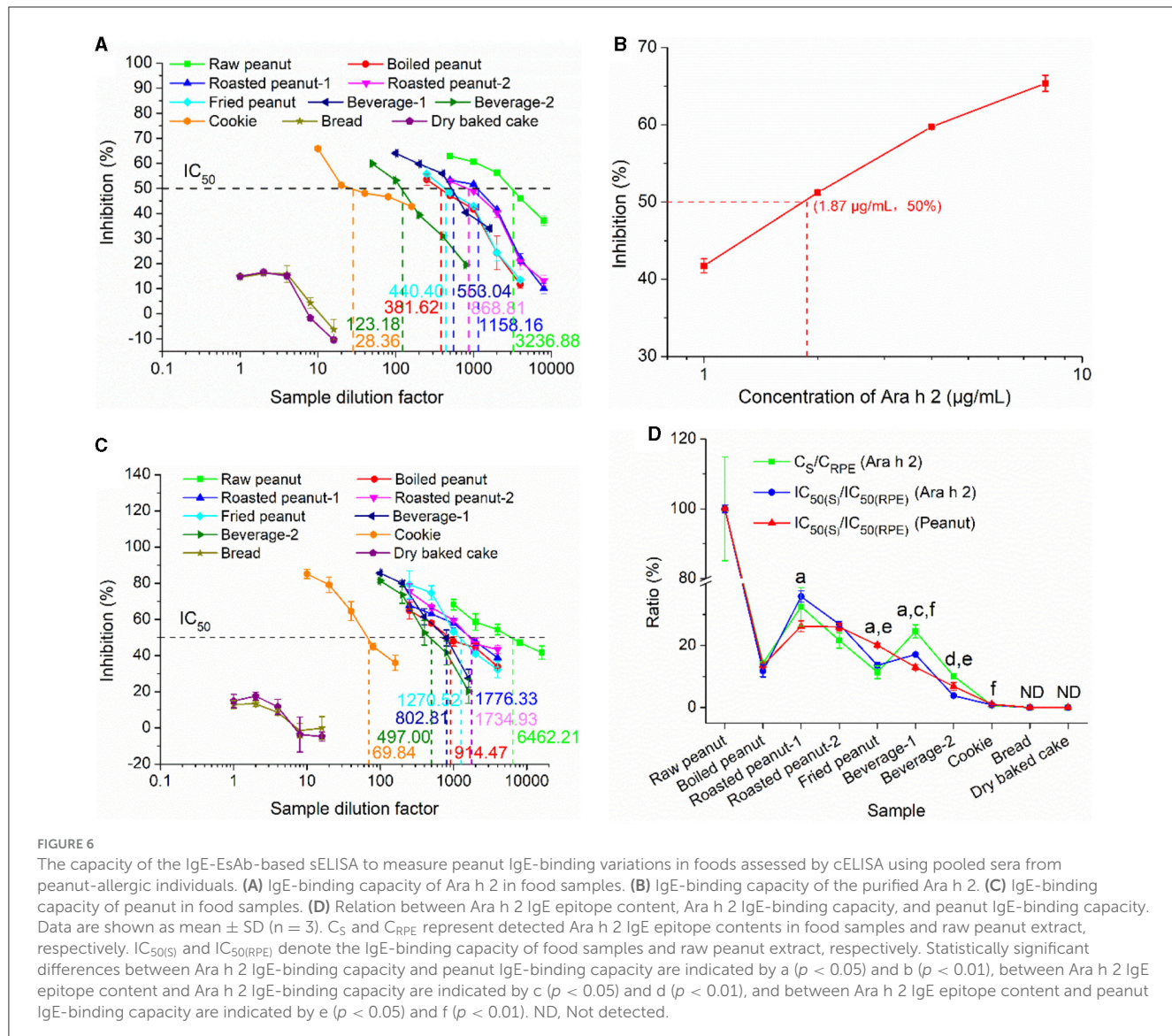
Assay specificity was evaluated by analyzing the CR with various food allergens at an allergen concentration ranging from 0.125 µg/mL to 8 µg/mL. A minor CR was observed for proteins of cashew, macadamia, pistachio, almond, and walnut, but not for any of the other nine food allergens (Figure 5B). These results indicate that the IgE-EsAbs-based sELISA is applicable for Ara h 2 detection with high specificity.

3.5 The applicability of the IgE-EsAbs-based sELISA for Ara h 2 detection in food samples

To assess the suitability of the IgE-EsAbs-based sELISA for detection of Ara h 2 in samples with a complex matrix, recovery experiments were conducted using samples extracted from various foods. As shown in Table 1, Ara h 2 was detected in all tested peanut-containing food samples. Analysis of spiked food samples demonstrated recoveries ranging from 79.00% to 120.78%. These results suggest that the developed immunoassay is a suitable method for the detection of Ara h 2 in food samples.

3.6 Validation of the IgE-EsAbs-based sELISA for measurement of Ara h 2 IgE-binding variations in food samples

The IgE-EsAbs-based sELISA was tested for its capability to measure potential changes in IgE-immunoreactivity of Ara h 2 and peanut in various processed foods using sera IgE. The IgE-binding ability was quantified by competitive ELISA using pooled sera from peanut-allergic individuals. Ara h 2 immunoreactivity variations in different foods are illustrated in Figure 6A, the IC₅₀ of RPE, boiled



peanut extract, roasted peanut-1 extract, roasted peanut-2 extract, and fried peanut extract were found at dilution factors of 3236.88 (5.62 μ g/mL protein), 381.62 (7.13 μ g/mL protein), 1158.16 (3.73 μ g/mL protein), 868.81 (4.60 μ g/mL protein), and 440.40 (17.44 μ g/mL protein), respectively. Taking into account that Ara h 2 comprises about 10% of total peanut proteins (40), the IC_{50} of Ara h 2 in these extracts corresponds to ~ 0.56 μ g/mL, 0.71 μ g/mL, 0.37 μ g/mL, 0.46 μ g/mL, and 1.74 μ g/mL, respectively, which is lower than the IC_{50} of the purified Ara h 2 (1.87 μ g/mL, Figure 6B). This deviation might be due to the presence of Ara h 6 and Ara h 7 in these extracts, which have a high homology with Ara h 2 (20), and may thus cross-react with patients' sera, resulting in lower IC_{50} . Compared with the IC_{50} of RPE, the IC_{50} of roasted peanut-1 extract and roasted peanut-2 extract were lower, while the IC_{50} of boiled peanut extract and fried peanut extract were higher. This indicates that roasting enhances Ara h 2 IgE-immunoreactivity, while boiling/frying reduces it, which is consistent with other reports (6, 13, 41). The IC_{50} of beverage-1, beverage-2, and cookie were at dilution factors of 553.04, 123.18, and 28.36, respectively, indicating that the Ara h 2 IgE-immunoreactivity in these sample

extracts was different. Finally, for bread and dry baked cake, slight inhibition was observed at dilution factors lower than 4, despite these foods being labeled to contain no peanuts. This slight inhibition may be explained by the possibility that the pooled sera used to assess the inhibition contained serum of an individual that was allergic to other food allergens alongside peanut, leading to a cross-reaction at low sample dilutions (42). Alternatively, this may be explained by the relatively high concentration (i.e., 2%) of Tween-20 present in the buffer used for protein extraction, which can suppress the antigen-antibody reaction (43).

The IgE-binding variations of peanut in different food samples as measured using sera IgE from peanut-allergic patients is shown in Figure 6C. The IC_{50} of RPE, boiled peanut extract, roasted peanut-1 extract, roasted peanut-2 extract, and fried peanut extract were observed at dilution factors of 6462.21 (2.82 μ g/mL protein), 914.47 (2.97 μ g/mL protein), 1776.33 (2.43 μ g/mL protein), 1734.93 (2.31 μ g/mL protein), and 1270.52 (6.04 μ g/mL protein), respectively. These findings indicate that roasting enhances human IgE-immunoreactivity of peanut, while boiling/frying reduces

it, which is consistent with the findings on Ara h 2 IgE-immunoreactivity described above and to those of previous reports (40, 44, 45), suggesting that Ara h 2 could serve as a useful biomarker for predicting IgE-binding changes of peanut. The IC_{50} of beverage-1, beverage-2, and cookie were observed at dilution factors of 802.81, 4497.0, and 69.84 respectively, indicating that the IgE-binding ability of peanut in these sample extracts was different. Finally, similar to the observations on Ara h 2 IgE-immunoreactivity described above, slight inhibition was observed for samples of bread and dry baked cake at low dilution factors (4 or lower; **Figures 6A, C**).

To validate the reliability of our developed sELISA in measuring IgE-binding variations of Ara h 2 and peanut in foods, the relationship between Ara h 2 IgE-binding ability and peanut IgE-binding ability, and the dose-effect relationship between the Ara h 2 IgE epitope content and Ara h 2 (or peanut) IgE-binding ability were established (**Figure 6D**). The detected Ara h 2 concentration (C_{RPE}) and the IgE-binding ability of RPE [$IC_{50}(RPE)$] were used as positive controls. Regarding the relationship between Ara h 2 IgE-binding ability (**Figure 6D**, blue line) and peanut IgE-binding ability (**Figure 6D**, red line), although significant differences were observed between the ratios of $IC_{50}(\text{roasted peanut-1, fried peanut, and beverage-1})$ to $IC_{50}(RPE)$ (Ara h 2) and the ratios of $IC_{50}(\text{roasted peanut-1, fried peanut, and beverage-1})$ to $IC_{50}(RPE)$ (peanut), they had the similar trend, except for beverage-1. These results further indicate that Ara h 2 can serve as a reliable marker for predicting peanut IgE-binding capacity. In addition, as indicated in the dose-effect relationship between the Ara h 2 IgE epitope content (**Figure 6D**, green line) and Ara h 2 (or peanut) IgE-binding ability (**Figure 6D**, blue or red line), only fried peanut, beverages, and cookie showed significant difference, but they had the similar trend, except for beverage-1. Therefore, these findings highlight that there is a good dose-effect relationship between the Ara h 2 IgE epitope content and Ara h 2 (or peanut) IgE-binding ability, indicating that the developed immunoassay can reliably reveal and measure potential changes in immunoreactivity of Ara h 2 and peanut in food samples and overcome the shortcomings of the IgE-binding capacity test, which depends heavily on the sera IgE (limited and variable) from peanut allergy patients (6, 13, 41).

In addition, the allergenicity of peanut allergens in food products can be established by basophils/mast cells degranulation and skin prick testing. Studies have shown that the results of IgE-binding experiments are usually in good agreement with these results obtained by basophils/mast cells degranulation assays or skin prick testing (13, 45, 46), which indicate that the IgE-binding capacity has the ability to preliminary predict potential peanut allergenicity (18). Therefore, the good dose-effect relationships obtained in this study suggest that our developed IgE-EsAbs-based sELISA could be used as a preliminary test to predict *in vitro* Ara h 2 and peanut potential allergenicity in processed foods. Also, a more complete validation should be performed in further study.

4 Conclusion

This study describes the development and validation of a novel IgE-EsAbs-based sELISA for detection of Ara h 2 and measurement of its immunoreactivity variations in foods. First, it was demonstrated that the monoclonal and polyclonal antibodies

generated for use as capture and detection antibodies in the assay, respectively, could specifically recognize the target IgE epitope(s) of Ara h 2. Using these antibodies, the IgE-EsAbs-based sELISA exhibited high sensitivity ($LOD = 0.98 \text{ ng/mL}$), specificity, and recovery (79.00%–120.78%) for Ara h 2 in food samples. Moreover, immunoreactivity changes of Ara h 2 in various food samples as tested by the IgE-EsAbs-based sELISA was consistent with that evaluated using sera IgE derived from peanut-allergic individuals. Together, these findings indicate that the developed immunoassay could serve as a sensitive, accurate, and relatively simplistic method for detecting Ara h 2 and measuring IgE-binding changes of Ara h 2 and peanut in food samples.

Data availability statement

The original contributions presented in the study are included in the article/[Supplementary material](#), further inquiries can be directed to the corresponding authors.

Ethics statement

The studies involving humans were approved by the Peanut allergy patients' sera were provided by the First Affiliated Hospital of Gannan Medical University and approved by Gannan Medical University Research Ethics Committee (Reference number 2021105, 8/March/2021). Informed consent was obtained from all subjects involved in this study. The studies were conducted in accordance with the local legislation and institutional requirements. Written informed consent for participation in this study was provided by the participants' legal guardians/next of kin. The animal study was approved by the Gannan Medical University Animal Care Committee, under the guidelines of China Council for Animal Care (SYXK-Gan 2018-0004, China). The study was conducted in accordance with the local legislation and institutional requirements.

Author contributions

YY: Data curation, Methodology, Writing—original draft. LL: Conceptualization, Resources, Supervision, Writing—review & editing. CL: Conceptualization, Writing—review & editing. YD: Methodology, Writing—review & editing. JL: Validation, Writing—review & editing. CS: Investigation, Writing—review & editing. YZ: Software, Writing—review & editing. JZ: Validation, Writing—review & editing. JW: Formal analysis, Writing—review & editing. AX: Visualization, Writing—review & editing. XL: Writing—review & editing. HC: Writing—review & editing. SH: Conceptualization, Data curation, Project administration, Supervision, Writing—review & editing.

Funding

The author(s) declare financial support was received for the research, authorship, and/or publication of this article. This research was funded by the National Natural Science Foundation of China (no. 32160606), the Natural Science Foundation of

Jiangxi Province (no. 20202BAB215013), the Research Fund of Gannan Medical University (no. QD201809), and the Open Project Program of State Key Laboratory of Food Science and Resources, Nanchang University (no. SKLF-KF-202003).

Conflict of interest

The authors declare that the research was conducted in the absence of any commercial or financial relationships that could be construed as a potential conflict of interest.

The reviewer ST declared a shared committee *Ad hoc* Joint FAO/WHO Expert Consultation on Risk Assessment of Food Allergens with the author(s) HC to the handling Editor.

Publisher's note

All claims expressed in this article are solely those of the authors and do not necessarily represent those of their affiliated organizations, or those of the publisher, the editors and the reviewers. Any product that may be evaluated in this article, or claim that may be made by its manufacturer, is not guaranteed or endorsed by the publisher.

References

1. Sicherer SH, Sampson HA. Food allergy: a review and update on epidemiology, pathogenesis, diagnosis, prevention, and management. *J. Allergy Clin Immunol.* (2018) 141:41–58. doi: 10.1016/j.jaci.2017.11.003
2. Fisher HR, Keet CA, Lack G, du Toit G. Preventing peanut allergy: Where are we now? *J Allergy Clin Immunol Pract.* (2019) 7:367–73. doi: 10.1016/j.jaip.2018.11.005
3. Remington BC, Westerhout J, Meima MY, Marty Blom W, Kruizinga AG, Wheeler MW, et al. Updated population minimal eliciting dose distributions for use in risk assessment of 14 priority food allergens. *Food Chem Toxicol.* (2020) 139:111259. doi: 10.1016/j.fct.2020.111259
4. Blom WM, Michelsen-Huisman AD, van Os-Medendorp H, van Duijn G, de Zeeuw-Brouwer ML, Versluis A. Accidental food allergy reactions: products and undeclared ingredients. *J Allergy Clin Immunol.* (2018) 142:865–75. doi: 10.1016/j.jaci.2018.04.041
5. Hefle SL, Furlong TJ, Niemann L, Lemon-Mule H, Sicherer S, Taylor SL. Consumer attitudes and risks associated with packaged foods having advisory labeling regarding the presence of peanuts. *J Allergy Clin Immunol.* (2007) 120:171–6. doi: 10.1016/j.jaci.2007.04.013
6. Shah F, Shi A, Ashley J, Kronfel C, Wang Q, Maleki SJ, et al. Peanut allergy: Characteristics and approaches for mitigation. *Compr Rev Food Sci Food Saf.* (2019) 18:1361–87. doi: 10.1111/1541-4337.12472
7. Sanchiz A, Sánchez-Enciso P, Cuadrado C, Linacero R. Detection of peanut allergen by real-time PCR: looking for a suitable detection marker as affected by processin. *Foods.* (2021) 10:1421. doi: 10.3390/foods10061421
8. Singh H, Cantoria MJ, Malave P, Saputra D, Maleki S. Standardization of RP-HPLC methods for the detection of the major peanut allergens Ara h 1, Ara h 2 and Ara h 3. *Food Chem.* (2016) 194:383–90. doi: 10.1016/j.foodchem.2015.08.024
9. Nelis JLD, Broadbent JA, Bose U, Anderson A, Colgrave ML. Targeted proteomics for rapid and robust peanut allergen quantification. *Food Chem.* (2022) 383:132592. doi: 10.1016/j.foodchem.2022.132592
10. Hnasko RM, Lin AV, Mcgarvey JA, Mattison CP. Sensitive and selective detection of peanut allergen Ara h 1 by ELISA and lateral flow immunoassay. *Food Chem.* (2022) 396:133657. doi: 10.1016/j.foodchem.2022.133657
11. Pandey AK, Varshney RK, Sudini HK, Pandey MK. An improved enzyme-linked immunosorbent assay (ELISA) based protocol using seeds for detection of five major peanut allergens Ara h 1, Ara h 2, Ara h 3, Ara h 6, and Ara h 8. *Front Nutr.* (2019) 29:32–8. doi: 10.3389/fnut.2019.00068
12. Schocker F, Scharf A, Kull S, Jappe U. Detection of the peanut allergens Ara h 2 and Ara h 6 in human breast milk: development of 2 sensitive and specific sandwich ELISA assays. *Int Arch Allergy Immunol.* (2017) 174:17–25. doi: 10.1159/000479388
13. Chang X, Zhou X, Tang Y, Zhang Y, Yuan J, Li X, et al. Effect of processing on the structure and allergenicity of peanut allergen Ara h 2 roasted in a matrix. *J Agric Food Chem.* (2022) 70:626–33. doi: 10.1021/acs.jafc.1c06828
14. Zhou X, Ren L, Zhang Y, Zhang J, Li X, Yang A, et al. Effect of structural targeted modifications on the potential allergenicity of peanut allergen Ara h 2. *J Agric Food Chem.* (2023) 71:836–45. doi: 10.1021/acs.jafc.2c06395
15. Min J, Keswani T, LaHood NA, Lytle IR, Marini-Rapoport O, Andrieux L, et al. Design of an Ara h 2 hypoallergen from conformational epitopes. *Clin Exp Allergy.* (2024) 54:46–55. doi: 10.1111/cea.14433
16. He S, Xiong M, Li L, Yan Y, Li J, Feng Z, et al. One-step purification of IgE epitope-specific antibody using immunomagnetic beads and highly sensitive detection of bovine β -lactoglobulin for the prediction of milk allergenicity in foods. *J Agric Food Chem.* (2023) 71:14068–78. doi: 10.1021/acs.jafc.3c03461
17. Shade KC, Conroy ME, Washburn N, Kitaoka M, Huynh DJ, Laprise E, et al. Sialylation of immunoglobulin E is a determinant of allergic pathogenicity. *Nature.* (2020) 582:265–70. doi: 10.1038/s41586-020-2311-z
18. Orcajo J, Lavilla M, Martinez-De-Maranon I. Specific and sensitive ELISA for measurement of IgE-binding variations of milk allergen beta-lactoglobulin in processed foods. *Anal Chim Acta.* (2019) 1052:163–9. doi: 10.1016/j.aca.2018.11.048
19. Rajput S, Sharma V, Hughes SM, Ewing CI, Arkwright PD. Allergy testing in predicting outcome of open food challenge to peanut. *J Allergy Clin Immunol.* (2018) 141:457–8. doi: 10.1016/j.jaci.2017.05.001
20. Palladino C, Breiteneder H. Peanut allergens. *Mol Immunol.* (2018) 100:58–70. doi: 10.1016/j.molimm.2018.04.005
21. Hu C, Chen H, Gao J, Luo C, Ma X, Tong, P. High-pressure microfluidisation-induced changes in the antigenicity and conformation of allergen Ara h 2 purified from Chinese peanut. *J Sci Food Agric.* (2011) 91:1304–9. doi: 10.1002/jsfa.4318
22. Stanley JS, King N, Burks AW, Huang SK, Sampson H, Cockrell G, et al. Identification and mutational analysis of the immunodominant IgE binding epitopes of the major peanut allergen Ara h 2. *Arch Biochem Biophys.* (1997) 342:244–53. doi: 10.1006/abbi.1997.9998
23. Flinterman AE, Knol EF, Lencer DA, Bardina L, den Hartog Jager CF, Lin J, et al. Peanut epitopes for IgE and IgG4 in peanut-sensitized children in

Supplementary material

The Supplementary Material for this article can be found online at: <https://www.frontiersin.org/articles/10.3389/fnut.2024.1323553/full#supplementary-material>

SUPPLEMENTARY FIGURE S1

Mass spectrometry identification of Ara h 2 (including Ara h 2.01 and Ara h 2.02). (A) The amino acid sequence of Ara h 2.01. (B–H) Mass spectrum of Ara h 2.01. (I) The amino acid sequence of Ara h 2.02. (J–P) Mass spectrum of Ara h 2.02.

SUPPLEMENTARY FIGURE S2

The amino acid sequence (red letters) and gene sequence (black letters) of Ara h 2.

SUPPLEMENTARY FIGURE S3

The sequencing results of vector pET-28a(+)–tAra h 2. The tAra h 2 gene sequence was located between 225 and 725 bp.

SUPPLEMENTARY TABLE S1

Information of patients with peanut allergy.

SUPPLEMENTARY TABLE S2

Amino acid sequences of IgE epitopes and T cell epitope of Ara h 2.

SUPPLEMENTARY TABLE S3

Comparison of analytical methods for detection Ara h 2.

SUPPLEMENTARY TABLE S4

Evaluation of the accuracy and precision of the IgE-EsAb-based sELISA in the detection of Ara h 2.

relation to severity of peanut allergy. *J Allergy Clin Immunol.* (2008) 121:737–43. doi: 10.1016/j.jaci.2007.11.039

24. He S, Li X, Gao J, Tong P, Lu J, Chen H. Preparation, immunological characterization and polyclonal antibody development for recombinant epitope tandem derived from bovine β -lactoglobulin. *Food Agric Immunol.* (2016) 27:806–19. doi: 10.1080/09540105.2016.1183596

25. Shreffler WG, Lencer DA, Bardina L, Sampson HA. IgE and IgG4 epitope mapping by microarray immunoassay reveals the diversity of immune response to the peanut allergen, Ara h 2. *J Allergy Clin Immunol.* (2005) 116:893–9. doi: 10.1016/j.jaci.2005.06.033

26. Prickett SR, Voskamp AL, Dacumos-Hill A, Symons K, Rolland JM, O’Hehir RE. Ara h 2 peptides containing dominant CD4+ T-cell epitopes: candidates for a peanut allergy therapeutic. *J Allergy Clin Immunol.* (2011) 127:608–15. doi: 10.1016/j.jaci.2010.09.027

27. Pascal M, Konstantinou GN, Masilamani M, Lieberman J, Sampson HA. *In silico* prediction of Ara h 2 T cell epitopes in peanut-allergic children. *Clin Exp Allergy.* (2013) 43:116–27. doi: 10.1111/cea.12014

28. King N, Helm R, Stanley JS, Vieths S, Lüttkopf D, Hatahet L, et al. Allergenic characteristics of a modified peanut allergen. *Mol. Nutr. Food Res.* (2005) 49:963–71. doi: 10.1002/mnfr.200500073

29. He S, Li X, Gao J, Tong P, Chen H. Development of a H_2O -sensitive quantum dots-based fluorescent sandwich ELISA for sensitive detection of bovine beta-lactoglobulin by monoclonal antibody. *J Sci Food Agric.* (2018) 98:519–26. doi: 10.1002/jsfa.8489

30. He S, Long C, Li L, Yan Y, Li J, Xiong M, et al. Development of a novel polyclonal antibody against bovine α 1-casein IgE epitopes for prediction of potential allergenicity of milk in foods. *Food Agric Immunol.* (2023) 34:2222932. doi: 10.1080/09540105.2023.2222932

31. Magnusson B, Örnemark U. *Eurachem Guide: The Fitness for Purpose of Analytical Methods – A Laboratory Guide to Method Validation and Related Topics*, 2nd Edn. (2014). Available online at: <http://www.eurachem.org> (accessed October 13, 2023).

32. Mueller GA, Maleki SJ, Pedersen LC. The molecular basis of peanut allergy. *Curr Allergy Asthma Rep.* (2014) 14:429. doi: 10.1007/s11882-014-0429-5

33. Bierig T, Collu G, Blanc A, Poghosyan E, Benoit RM. Design, Expression, purification, and characterization of a YFP-tagged 2019-nCoV spike receptor-binding domain construct. *Front Bioeng Biotechnol.* (2020) 8:618615. doi: 10.3389/fbioe.2020.618615

34. Gul I, Hassan A, Muneeb JM, Akram T, Haq E, Shah RA, et al. multiepitope vaccine candidate against infectious bursal disease virus using immunoinformatics-based reverse vaccinology approach. *Front Vet Sci.* (2023) 9:1116400. doi: 10.3389/fvets.2022.1116400

35. Soleimani M, Mirmohammad-Sadeghi H, Sadeghi-Aliabadi H, Jahanian-Najafabadi A. Expression and purification of toxic anti-breast cancer p28-NRC chimeric protein. *Adv Biomed Res.* (2016) 5:70. doi: 10.4103/2277-9175.180639

36. Maleki SJ, Teuber SS, Cheng H, Chen D, Comstock SS, Ruan S, et al. Computationally predicted IgE epitopes of walnut allergens contribute to cross-reactivity with peanut. *Allergy.* (2011) 66:1522–9. doi: 10.1111/j.1365-9995.2011.02692.x

37. De Leon MP, Drew AC, Glaspole IN, Suphioglu C, O’Hehir RE, Rolland JM. IgE cross-reactivity between the major peanut allergen Ara h 2 and tree nut allergen. *Mol Immunol.* (2007) 44:463–71. doi: 10.1016/j.molimm.2006.02.016

38. Sokol K, Rasooly M, Dempsey C, Lassiter S, Gu WJ, Lumbard K, et al. Prevalence and diagnosis of sesame allergy in children with IgE-mediated food allergy. *Pediatr Allergy Immunol.* (2020) 31:214–8. doi: 10.1111/pai.13143

39. Jeong JY, Kim SO, Bang S, Choi Y, Shin J, Choi D, et al. Adaptive biosensing platform using immune cell-based nanovesicles for food allergen detection. *Biosens Bioelectron.* (2023) 222:114914. doi: 10.1016/j.bios.2022.114914

40. Pi X, Wan Y, Yang Y, Li R, Wu X, Xie M, et al. Research progress in peanut allergens and their allergenicity reduction. *Trends Food Sci Tech.* (2019) 93:212–20. doi: 10.1016/j.tifs.2019.09.014

41. Zhang T, Shi Y, Zhao Y, Wang J, Wang M, Niu B, et al. Different thermal processing effects on peanut allergenicity. *J Sci Food Agric.* (2019) 99:2321–8. doi: 10.1002/jsfa.9430

42. Foo ACY, Nesbit JB, Gipson SAY, DeRose EF, Cheng H, Hurlburt BK, et al. Structure and IgE cross-reactivity among cashew, pistachio, walnut, and peanut vicilin-buried peptides. *J Agric Food Chem.* (2023) 71:2990–8. doi: 10.1021/acs.jafc.2c07061

43. He S, Li X, Gao J, Tong P, Chen H. Development of sandwich ELISA for testing bovine beta-lactoglobulin allergenic residues by specific polyclonal antibody against human IgE binding epitopes. *Food Chem.* (2017) 227:33–40. doi: 10.1016/j.foodchem.2017.01.060

44. Haidar E, Lakkis J, Karam M, Koubaa M, Louka N, Debs E. Peanut allergenicity: an insight into its mitigation using thermomechanical processing. *Foods.* (2023) 12:1253. doi: 10.3390/foods12061253

45. Zhang Y, Wu Z, Li K, Li X, Yang A, Tong P, et al. Allergenicity assessment on thermally processed peanut influenced by extraction and assessment methods. *Food Chem.* (2019) 281:130–9. doi: 10.1016/j.foodchem.2018.12.070

46. Cabanillas B, Cuadrado C, Rodriguez J, Hart J, Burbano C, Crespo JF, et al. Potential changes in the allergenicity of three forms of peanut after thermal processing. *Food Chem.* (2015) 183:18–25. doi: 10.1016/j.foodchem.2015.03.023



OPEN ACCESS

EDITED BY

Jeffrey John Bajramovic,
Utrecht University, Netherlands

REVIEWED BY

Aurobind Vidyarthi,
Yale University, United States
Sudeep Kumar Maurya,
University of Pittsburgh Medical Center,
United States

*CORRESPONDENCE

Jazmina L. Gonzalez Cruz
✉ j.gonzalezcruz@uq.edu.au
Mariusz Skwarczynski
✉ m.skwarczynski@uq.edu.au

RECEIVED 22 September 2023

ACCEPTED 07 February 2024

PUBLISHED 26 February 2024

CITATION

Lu L, Kong WY, Zhang J, Firdaus F, Wells JW, Stephenson RJ, Toth I, Skwarczynski M and Cruz JLG (2024) Utilizing murine dendritic cell line DC2.4 to evaluate the immunogenicity of subunit vaccines *in vitro*. *Front. Immunol.* 15:1298721.
doi: 10.3389/fimmu.2024.1298721

COPYRIGHT

© 2024 Lu, Kong, Zhang, Firdaus, Wells, Stephenson, Toth, Skwarczynski and Cruz. This is an open-access article distributed under the terms of the [Creative Commons Attribution License \(CC BY\)](#). The use, distribution or reproduction in other forums is permitted, provided the original author(s) and the copyright owner(s) are credited and that the original publication in this journal is cited, in accordance with accepted academic practice. No use, distribution or reproduction is permitted which does not comply with these terms.

Utilizing murine dendritic cell line DC2.4 to evaluate the immunogenicity of subunit vaccines *in vitro*

Lantian Lu^{1,2}, Wei Yang Kong², Jiahui Zhang^{1,2},
Farrhana Firdaus¹, James W. Wells², Rachel J. Stephenson¹,
Istvan Toth^{1,3,4}, Mariusz Skwarczynski^{1*}
and Jazmina L. Gonzalez Cruz^{2*}

¹School of Chemistry and Molecular Biosciences, The University of Queensland, St. Lucia, QLD, Australia, ²Faculty of Medicine, Frazer Institute, The University of Queensland, Woolloongabba, QLD, Australia, ³Institute of Molecular Bioscience, The University of Queensland, St. Lucia, QLD, Australia, ⁴School of Pharmacy, The University of Queensland, Woolloongabba, QLD, Australia

Subunit vaccines hold substantial promise in controlling infectious diseases, due to their superior safety profile, specific immunogenicity, simplified manufacturing processes, and well-defined chemical compositions. One of the most important end-targets of vaccines is a subset of lymphocytes originating from the thymus, known as T cells, which possess the ability to mount an antigen-specific immune response. Furthermore, vaccines confer long-term immunity through the generation of memory T cell pools. Dendritic cells are essential for the activation of T cells and the induction of adaptive immunity, making them key for the *in vitro* evaluation of vaccine efficacy. Upon internalization by dendritic cells, vaccine-bearing antigens are processed, and suitable fragments are presented to T cells by major histocompatibility complex (MHC) molecules. In addition, DCs can secrete various cytokines to crosstalk with T cells to coordinate subsequent immune responses. Here, we generated an *in vitro* model using the immortalized murine dendritic cell line, DC2.4, to recapitulate the process of antigen uptake and DC maturation, measured as the elevation of CD40, MHC-II, CD80 and CD86 on the cell surface. The levels of key DC cytokines, tumor necrosis alpha (TNF- α) and interleukin-10 (IL-10) were measured to better define DC activation. This information served as a cost-effective and rapid proxy for assessing the antigen presentation efficacy of various vaccine formulations, demonstrating a strong correlation with previously published *in vivo* study outcomes. Hence, our assay enables the selection of the lead vaccine candidates based on DC activation capacity prior to *in vivo* animal studies.

KEYWORDS

DC2.4, dendritic cell uptake, dendritic cell maturation, *in vitro* assay, subunit vaccine

1 Introduction

Vaccines are critical tools for providing immunity against various pathogens and cancer malignancies (1). In recent years, peptide-based subunit vaccines have gained increasing research interest due to their superior safety profile and specific immunogenicity. However, these vaccines often exhibit lower immunogenicity when compared to conventional whole-pathogen vaccines, necessitating the use of immunopotentiators, such as adjuvants, to enhance the magnitude of the immune response (2). Adjuvants play pivotal roles in cell signaling, stimulating the innate immunity in the preamble to a robust antigen-specific adaptive immunity. Without the presence of an adjuvant, an antigen may induce immune tolerance rather than activating the immune system (3–5). Therefore, it is essential to co-deliver an adjuvant with an antigen to induce a desired immune response.

The assessment of vaccine efficacy is often carried out using *in vivo* models. However, these studies not only require specialized facilities and personnel but also necessitate the use of a significant number of experimental animals and/or human subjects. Consequently, there is a critical imperative to reduce animal usage as much as feasibly possible, to address ethical concerns and to adhere to the 3Rs (Replacement, Reduction, and Refinement) principles governing animal research (6). One strategy to address this issue is to perform *in vitro* evaluations before proceeding to *in vivo* assessments. This helps to reduce the number of experimental animals used by eliminating formulations that fail to demonstrate promise during the *in vitro* evaluation stage, thus precluding their advancement to further *in vivo* testing (7). However, this depends on a proven correlation between the results of *in vitro* and *in vivo* evaluations. Moreover, conducting *in vitro* studies is also important to elucidate the mechanisms that underpin vaccine-mediated protection or failure.

The generation and expansion of antigen-specific T cells is one of the end goals of all vaccines. There are two main T cell lineages: CD4⁺ T cells and CD8⁺ T cells. CD4⁺ T cells, also known as helper T cells, play a crucial role in activating other immune cells, including B cells which are responsible for the initiation of the humoral response, and CD8⁺ T cells which are central to the adaptive immunity cytotoxic response. To activate T cells, professional antigen-presenting cells (APCs), such as dendritic cells (DCs), present fragmented exogenous or endogenous peptide antigens to naïve T cells through MHC molecules. While various DC sources have been used to evaluate the immunogenicity of vaccines or adjuvants in different assays, limited DC-based assays employing a single cell line have been reported for evaluating the efficacy of peptide vaccines (8, 9).

The DC2.4 cell line, derived from C57BL/6 mice, is an immortalized murine DC line generated through retrovirus transduction of oncogenes *myc* and *raf* (10). These cells express DC-specific markers, including MHC class I (MHC-I), MHC-II, B7-1 (CD80), B7-2 (CD86), as well as CD32 and CD54, and possess the ability to present antigens on both MHC-I and -II molecules (11). These properties have made the DC2.4 cell line particularly valuable for assessing the immunogenicity of vaccines *in vitro*.

Herein, we present a detailed step-by-step protocol for the DC uptake and maturation assays utilizing the DC2.4 cell line to facilitate the evaluation of the immunogenicity of peptide-based vaccines. This protocol provides robust and scalable assays with high-throughput potential to identify peptide vaccine candidates with the highest prospects of eliciting humoral/cellular responses *in vivo*.

2 Materials and equipment

2.1 Cells and media

Immortalized DC2.4 cell line (SCC142) was purchased from Merck (Rahway, United States) and cultured in RPMI-1640 medium supplemented with 10% v/v fetal bovine serum (FBS) (Thermo Fisher Scientific, Waltham, United States), 2.5% v/v HEPES (1M) buffer (Thermo Fisher Scientific), 1% v/v L-glutamine (Thermo Fisher Scientific), 1% v/v MEM Non-essential Amino Acids Solution (100X) (NEAA), 1% v/v Penicillin-Streptomycin-Glutamine (100X) (PSG), and 0.00054% v/v 2-mercaptoethanol (Thermo Fisher Scientific, Waltham, United States). Cells for cryopreservation were resuspended in freezing media containing 90% v/v FBS and 10% dimethyl sulfoxide (DMSO; Merck, Rahway, United States). Trypsin-EDTA solution 1X (Merck, Rahway, United States) was used for cell dissociation.

2.2 Antibodies, dyes and beads

The list of antibodies used for flow cytometry is summarized in Table 1. LIVE/DEADTM Fixable Aqua Dead Cell Stain Kit was purchased from BioLegend (San Diego, United States). Anti-rat and Anti-hamster IgG/Negative Control Compensation Beads were purchased from BD Biosciences (Franklin Lakes, United States). Fluorescein isothiocyanate (FITC)-dextran (4 kDa, 25 mg/ml x 5 ml) was purchased from Chondrex (Woodinville, United States).

2.3 Flasks, plates, and tubes

T75 flasks were purchased from Thermo Fisher Scientific (Brisbane, Australia). Corning[®] 50 mL centrifuge tubes, Corning[®] 2 mL Internal Threaded Polypropylene Cryogenic Vials (self-standing with round bottom), Corning[®] Costar[®] TC-treated Multiple Well Plates, Greiner 96-well polypropylene V-bottom plates, and 1.5 mL microcentrifuge tubes were purchased from Merck (Rahway, United States).

2.4 Other reagents

Gibco 1X phosphate buffered saline (1X PBS) pH 7.4, trypan blue solution (0.4%) and lipopolysaccharide solution (500X) were purchased from Thermo Fisher Scientific (Brisbane, Australia).

TABLE 1 The list of antibodies used in this study.

Antibody	Cat number	Manufacturer
Alexa Fluor® 488 anti-mouse langerin	53-2073-80	eBioscience
Alexa Fluor® 700 anti-mouse CD45R/B200	103231	Biolegend
APC anti-mouse H-2Kb	116619	Biolegend
APC-Cy7 anti-mouse I-A/I-E	107628	Biolegend
Brilliant Violet 421™ anti-mouse CD80	104725	Biolegend
Brilliant Violet 421™ anti-mouse CD86	105031	Biolegend
Brilliant Violet 605™ anti-mouse CD8a	100744	Biolegend
Brilliant Violet 650™ anti-mouse CD11b	101239	Biolegend
Brilliant Violet 711™ anti-mouse F4/80	123147	Biolegend
Brilliant Violet 785™ anti-mouse CD86	105043	Biolegend
Brilliant Violet 785™ anti-mouse TNF- α	506341	Biolegend
FITC anti-mouse CD80	104705	Biolegend
PE anti-mouse CD40	124609	Biolegend
PE anti-mouse IL-10	505008	Biolegend
PE/Cyanine7 anti-mouse CD11c	117317	Biolegend
PerCP/Cyanine5.5 anti-mouse CD317 (BST2, PDCA-1)	127021	Biolegend
TruStain FcX™ (anti-mouse CD16/32)	101320	Biolegend

Paraformaldehyde aqueous solution (16% PFA) was purchased from Emgrid Australia (Gulfview Heights, Australia) and diluted to 4% using 1X PBS. Albumin from chicken egg white (OVA) was purchased from Merck (Rahway, United States). Recombinant murine interferon-gamma (IFN- γ) was purchased from Peprotech (Cranbury, United States). Pam₂CSK₄ (trifluoroacetate salt) was purchased from Sapphire Bioscience Pty Limited (Redfern, Australia).

2.5 Equipment

- BD LSRFortessa™ X-20 Cell Analyzer (BD Biosciences, Franklin Lakes, United States).
- TC20 Automated Cell Counter (Bio-Rad, Hercules, United States).
- Mr. Frosty™ Freezing Container (Thermo Fisher Scientific, Waltham, United States).
- CO₂ Incubator (Panasonic, Kadoma, Japan).
- CKX31 Inverted Microscope (Olympus Life Science, Waltham, United States).
- ESCO Biological Safety Cabinet (ESCO Lifesciences, Upper Changi, Singapore).

2.6 Software

- FlowJo (version 10.8.1, BD Biosciences, Franklin Lakes, USA).
- GraphPad Prism (version 9.0, GraphPad, San Diego, USA).

3 Methods

3.1 Synthesis and purification of vaccine candidates

All peptides used for maturation assays were synthesized using butyloxycarbonyl (Boc) solid-phase peptide synthesis (12, 13). Boc-protected L-amino acids were assembled on p-methyl-benzhydrylamine hydrochloride (pMBHA·HCl) resin at 0.2 mmol scale, following the previously reported method (12, 13).

In brief, the resin was weighed and swelled in *N,N*-dimethylformamide (DMF) and *N,N*-diisopropylethylamine (DIPEA) (6.2 eq.) overnight. The coupling cycle for Boc synthesis included deprotection of the Boc group (1 min treatment with TFA, twice at ambient conditions), DMF wash, addition of activated amino acids (0.84 mmol/g, 4.2 eq.) by 0.5 M hexafluorophosphate azabenzotriazole tetramethyl uranium (HATU) (1.6 mL, 4.0 eq.) and DIPEA (0.26 mL, 6.2 eq.), and coupling (10 min and 20 min at RT, respectively). After coupling, the liquid content was aspirated, and the abovementioned steps were repeated until the desired peptide sequence was achieved. For Boc-Gln (Xan)-OH, dichloromethane (DCM) was used to wash between the two trifluoroacetic acid (TFA) deprotection steps to avoid glutamine cyclization. Acetylation was performed after the last amino acid was coupled using acetylation solution (5% DIPEA and 5% acetic anhydride in DMF). The formyl group from tryptophan was removed using 20% piperidine in DMF solution (5 min and 10 min, respectively). The resin was then washed with DMF (3X), followed by DCM (3X), and methanol (1X) before transferring the resin-peptide to a desiccator overnight.

The peptides were cleaved from the resin using anhydrous hydrogen fluoride (HF) with *p*-cresol and/or *p*-thiocresol as scavengers (14). Upon evaporation of HF, the cleaved peptides were washed with cold diethyl ether and/or mixture of diethyl ether and *n*-hexane (1:1). The precipitated compounds were dissolved in mixture of solvent A (100% Milli-Q water containing 0.1% TFA) and solvent B (90% acetonitrile and 10% Milli-Q water containing 0.1% TFA) depending on the hydrophobicity of the peptide. After filtration, the peptide was purified using a Shimadzu preparative reversed-phase HPLC (RP-HPLC; Kyoto, Japan) instrument (LC-20AP x 2, CBM-20A, SPD-20A, FRC-10A) with a 20.0 mL/min flow rate on a C18 (218TP1022; 10 μ m, 22 \times 250 mm) or C4 (214TP1022; 10 μ m, 22 \times 250 mm) column depending on the hydrophobicity of the compound. Once purified, the purity of all peptides was determined using an analytical RP-HPLC on a C18 (218TP54; 5 μ m, 4.6 \times 250 mm) or C4 (214TP54; 5 μ m, 4.6 \times 250 mm).

mm) Vydac column, with a 0 – 100% gradient of solvent B for 40 min at 214 nm. ESI-MS was performed on a LCMS-2020 Shimadzu (Kyoto, Japan) instrument (DGU-20A3, LC-20Ad x 2, SIL-20AHT, STO-20A) and Analyst 1.4 software (Applied Biosystems/MDS Sciex, Toronto, Canada) (Perkin-Elmer-Sciex API3000) to validate the molecular weight of the compound.

PADRE-J8 (AFKVAAWTLKAAA-QAEDKVKQSREAKKQVEKALKQLEDKVQ). Yield: 30%. Molecular weight: 4653.42 g/mol. ESI-MS $[M + 3H]^{3+}$ m/z 1552.7 (calc. 1552.1), ESI-MS $[M + 4H]^{4+}$ m/z 1164.5 (calc. 1164.4), $[M + 5H]^{5+}$ m/z 932.1 (calc. 931.7), $[M + 6H]^{6+}$ m/z 776.8 (calc. 776.6), $[M + 7H]^{7+}$ m/z 666.0 (calc. 665.8). $t_R = 24.5$ min (0 to 100% solvent B; C18 column); purity $\geq 99\%$.

L_{15} -PADRE-J8 (LLLLLLLLLLLLL- AFKVAAWTLKAAA-QAEDKVKQSREAKKQVEKALKQLEDKVQ). Yield: 3%. Molecular weight: 6350.82 g/mol. ESI-MS $[M + 4H]^{4+}$ m/z 1588.3 (calc. 1588.7), $[M + 5H]^{5+}$ m/z 1272.0 (calc. 1271.2), $[M + 6H]^{6+}$ m/z 1060.3 (calc. 1059.5), $[M + 7H]^{7+}$ m/z 908.0 (calc. 908.3), $[M + 8H]^{8+}$ m/z 794 (calc. 794.9), $[M + 9H]^{9+}$ m/z 705.5 (calc. 706.6). $t_R = 39.0$ min (0 to 100% solvent B; C4 column); purity $\geq 99\%$.

J8-K(V_{10})-PADRE (QAEDKVKQSREAKKQVEKALKQLEDKVQ-K(VVVVVVVVVV)- AFKVAAWTLKAAA). Yield: 23%. Molecular Weight: 5814.96. ESI-MS $[M + 3H]^{3+}$ m/z 1938.6 (calc. 1939.3), $[M + 4H]^{4+}$ m/z 1455.0 (calc. 1454.7), $[M + 5H]^{5+}$ m/z 1164.0 (calc. 1164.0), $[M + 6H]^{6+}$ m/z 969.9 (calc. 970.1), $[M + 7H]^{7+}$ m/z 831.5 (calc. 831.7), $[M + 8H]^{8+}$ m/z 728.0 (calc. 727.9). $t_R = 24.1$ min (0 to 100% solvent B; C4 column); purity $\geq 99\%$.

J8-K(F_{10})-PADRE (QAEDKVKQSREAKKQVEKALKQLEDKVQ-K(FFFFFFFFF)- AFKVAAWTLKAAA). Yield: 28%. Molecular weight: 6295.40. ESI-MS $[M + 4H]^{4+}$ m/z 1574.7 (calc. 1574.9), $[M + 5H]^{5+}$ m/z 1260.0 (calc. 1260.0), $[M + 6H]^{6+}$ m/z 1050.3 (calc. 1050.2), $[M + 7H]^{7+}$ m/z 900.4 (calc. 900.3), $[M + 8H]^{8+}$ m/z 788.0 (calc. 787.9), $[M + 9H]^{9+}$ m/z 700.7 (calc. 700.5). $t_R = 24.5$ min (0 to 100% solvent B; C4 column); purity $\geq 99\%$.

J8-K(L_{10})-PADRE (QAEDKVKQSREAKKQVEKALKQLEDKVQ-K(LLLLLLL)- AFKVAAWTLKAAA). Yield: 28%. Molecular weight: 5955.23. ESI-MS $[M + 3H]^{3+}$ m/z 1985.2 (calc. 1986.1), $[M + 4H]^{4+}$ m/z 1489.6 (calc. 1489.8), $[M + 5H]^{5+}$ m/z 1192.0 (calc. 1192.0), $[M + 6H]^{6+}$ m/z 993.5 (calc. 993.5), $[M + 7H]^{7+}$ m/z 851.8 (calc. 851.7), $[M + 8H]^{8+}$ m/z 745.4 (calc. 745.4). $t_R = 25.6$ min (0 to 100% solvent B; C4 column); purity $\geq 99\%$.

J8-K(L_{15})-PADRE (QAEDKVKQSREAKKQVEKALKQLEDKVQ-K(LLLLLLL)- AFKVAAWTLKAAA). Yield: 26%. Molecular weight: 6521.03. ESI-MS $[M + 4H]^{4+}$ m/z 1631.8 (calc. 1631.3), $[M + 5H]^{5+}$ m/z 1305.6 (calc. 1305.2), $[M + 6H]^{6+}$ m/z 1088.0 (calc. 1087.8), $[M + 7H]^{7+}$ m/z 932.9 (calc. 932.6), $[M + 8H]^{8+}$ m/z 816.3 (calc. 816.1), $[M + 9H]^{9+}$ m/z 725.6 (calc. 725.6). $t_R = 30.9$ min (0 to 100% solvent B; C4 column); purity $\geq 99\%$.

3.2 DC2.4 cells culturing protocol

3.2.1 Prepare culture media by supplementing RPMI-1640 media with the following components: 10% v/v FBS, 2.5% v/v HEPES buffer, 1% v/v L-glutamine, 1% v/v NEAA, 1% v/v PSG, and 0.00054% v/v 2-mercaptopethanol, as described in **Section 2.1**.

3.2.2 Thaw cryopreserved DC2.4 cells by placing the cryotube in a 37 °C water bath. Swirl the tube gently until only a small piece of ice remains. Add the cells dropwise using a serological pipette to 20 mL of pre-warmed (37 °C) media. Spin down the cells using a benchtop centrifuge at RT at 1,200 rpm (288 rcf) for 10 min and resuspend in 10 mL of media.

3.2.3 Load 10 μ L of the cell suspension and 10 μ L of 0.4% trypan blue solution into a TC20™ cell counting slide and use a TC20 Automated Cell Counter to determine cell density. Seed 1x – 3x 10^6 cells in a T75 flask for passaging and top up to 30 mL with culturing media. Transfer the flask to an incubator supplemented with 5% CO₂ at 37 °C for cell culturing.

3.2.4 Refresh the culture media every 24 hrs after cell seeding. Harvest the cells when the confluence reaches 60 – 80% (~2 – 4 days post-seeding).

3.2.5 Remove the media using a serological pipette and add 5 mL of trypsin-EDTA 1X. Gently shake the flask at RT or incubate at 37 °C for 5 min until more than 80% of the cells can be seen detached under the microscope. Neutralize trypsin by adding double the volume (10 mL) of media and pipette up and down to help remove undetached cells. Collect the cells in a 50 mL Falcon tube and spin down at 1,200 rpm (288 rcf) at RT for 10 min. Remove the supernatant and suspend the pellet with 20 mL of media. Measure the cell density as described in **Step 3.2.3**.

3.2.6 Seed the cells onto a 48-well plate at the required densities for uptake or maturation studies, as described in **Section 3.4** and **3.5**. Either spin the remaining cells down and resuspend in freezing media containing 90% FBS and 10% DMSO at 1 – 3 million cells/mL for cryopreservation, or passage the cells as described in **Step 3.2.3**.

3.3 DC characterization

3.3.1 Prepare 2 x 10^5 cells per sample for flow cytometry phenotyping of DC2.4 cells. Prepare whole panel-stained samples, as well as unstained, live/dead, and fluorescent minus one (FMO) controls as detailed in the following steps. For the live/dead control, add 50 μ L of 80% ethanol and incubate for 5 min at RT.

3.3.2 Wash the cells with 150 μ L of PBS and spin down at 1,700 rpm (271 rcf) using a microcentrifuge for 5 min. Resuspend the cells in 100 μ L of Zombie Aqua™ Live/Dead solution (1:200 diluted in 1X PBS) on ice in the dark for 10 min.

3.3.3 Wash the cells once with PBS and resuspend the pellet in 100 μ L of TruStain FcX™ solution (1:200 diluted in 1X PBS). Incubate on ice for 15 min, then spin down at 1,700 rpm (271 rcf) for 5 min.

3.3.4 Prepare a cocktail containing all the antibodies listed in **Table 2** using FACs buffer. Add 100 μ L to the cells, and resuspend the cells, label the sample as fully stained samples. For FMO controls, prepare 100 μ L of antibody master mix excluding one of the antibodies in **Table 2**. Prepare a total of five FMOs, including CD11c-PE/Cy7 FMO, CD40-PE FMO, CD80-BV421 FMO, CD86-BV785 FMO, and MHC-I-APC FMO. Stain these samples mentioned in **Step 3.3.4** for 25 min on ice in the dark, followed by washing with 200 μ L of 1X PBS to

TABLE 2 Antibody panel for DC2.4 characterization by flow cytometry.

Antibody	Dilution
MHC-II-APC/Cy7	1:800
B220-AF700	1:600
CD11b-BV650	1:400
CD40-PE	1:400
MHC-I-APC	1:400
CD317-PerCP/Cy5.5	1:200
CD8 α -BV605	1:200
CD80-BV421	1:200
CD86-BV785	1:200
F4/80-BV711	1:200

remove excess antibodies. Centrifuge the samples at 1,700 rpm (271 rcf) for 5 min and discard the supernatant.

3.3.5 Wash the cells once with PBS and resuspend them in 100 μ L of 4% PFA (diluted with 1X PBS) for 15 min at RT to fix the cells.

3.3.6 Wash the fixed cells with PBS once, and resuspend them in 200 μ L of PBS, then transfer them to a FACS tube for flow cytometry analysis.

3.3.7 Before flow analysis, add a small aliquot of fixed untreated live cells to the live/dead control.

3.4 DC uptake protocol

3.4.1 Prepare a 48-well plate and seed 9×10^4 cells in each well with 1.0 mL of cell culturing media.

3.4.2 Incubate the plate in an incubator supplemented with 5% CO₂ at 37°C overnight (~18 hr). Afterwards, remove the media from each well and add 180 μ L of fresh media.

3.4.3 Add 20 μ L of fluorescently labeled compounds (FITC-dextran or fluorescently labeled compounds of choice) to each well, resulting in a final concentration of 0.1 – 1 μ M. Prepare single stain controls following the same steps as the experimental groups by treating the cells with fluorescently labeled compounds at a higher concentration (5~10X). Exclude the staining by Aqua zombie Live/Dead solution specified in **Step 3.4.8** for single stained controls. For unstained control or live/dead control cells, add 20 μ L of culturing media to each well. Prepare all experimental groups in triplicates, except for flow compensation groups.

3.4.4 Carefully remove the media from each well after incubation at 37°C for 4 hr. Wash the cells once with 200 μ L of PBS, and then add 100 μ L of trypsin to each well. Allow trypsinization at 37°C for 5 min until most of the cells detach. Neutralize trypsin activity by adding 100 μ L of media to each well.

3.4.5 Gently pipette the cells up and down in each well and transfer them to either a 96-well V-bottom plate or 1.5 mL microcentrifuge tubes. Spin down the cells at 1,700 rpm (271 rcf) for tubes using a microcentrifuge, or 1,700 rpm (578 rcf) for plates using a benchtop centrifuge for 5 min [Note 1].

3.4.6 Remove the supernatant and add 200 μ L of PBS. Spin down the cells again at 1,700 rpm for 5 min and remove the supernatant.

3.4.7 For unstained control and single stained control, continue from **Step 3.4.10** onwards. For the live/dead control, add 50 μ L of 80% ethanol and incubate at RT for 5 min. Add 150 μ L of PBS, spin down the cells, and remove the supernatant. Proceed with steps from **Step 3.4.8** for the live/dead control and experimental groups. Add a small aliquot of fixed unstained cells to the fixed live/dead control before flow analysis.

3.4.8 Add 100 μ L of Aqua zombie Live/Dead solution (1:200 diluted in 1X PBS) to each well on the plate or each tube to resuspend the pellets. Keep the cells on ice in the dark for 20 min, then spin down at 1,700 rpm for 5 min.

3.4.9 Remove the supernatant, add 200 μ L of PBS, and spin down the cells at 1,700 rpm for 5 min. Remove the supernatant.

3.4.10 Resuspend the cell pellets in 100 μ L of 4% PFA and allow fixation at RT for 15 min. Spin down the cells at 1,700 rpm for 5 min.

3.4.11 Remove the supernatant, add 200 μ L of PBS, and spin down the cells at 1,700 rpm for 5 min. Remove the supernatant, add 200 μ L of PBS for resuspension, and transfer the cell suspension to a FACS tube for flow cytometry analysis.

Note 1: The maximum volume loaded for a well on a 96-well V-bottom plate should be less than 200 μ L for optimal working efficiency. If a plate instead of a tube is used for cell collection, add 100 μ L media to neutralize trypsin.

3.5 DC maturation protocol

3.5.1 Seed 4.5×10^4 cells in each well of a 48-well plate, followed by topping up with culturing media to 1.0 mL.

3.5.2 Remove the media after incubation in an incubator supplemented with 5% CO₂ at 37 °C overnight (~18 hr), followed by adding 900 μ L media to each well.

3.5.3 Dissolve 100 μ L peptide vaccines in 1X PBS and add it to each well to make a final antigen concentration of 10 μ M in 1 mL media [Note 2]. In addition, use 20 ng IFN- γ , 1.0 μ g lipopolysaccharide (LPS) or 1.0 μ g Pam₂CSK₄ per well in certain groups to serve as positive controls [Note 3]. For cells used as unstained, live/dead, or FMO controls, add 100 μ L PBS instead of antigen solution in each well. Perform triplicates for all groups. Allow the cells to be activated by the vaccines for 24 hr in the incubator at 37 °C.

3.5.4 Remove the media, and wash the cells with 200 μ L PBS once, then add 100 μ L trypsin to each well. Allow trypsinization for 5 min in an incubator at 37 °C, then add 100 μ L media to neutralize trypsin activity in each well. Mix the cells in each well by pipetting up and down gently, and then transfer the cell suspensions to a 96-well V-bottom plate or 1.5 mL microcentrifuge tubes, followed by spinning down the cells using a benchtop centrifuge for plates at 1,700 rpm (578 rcf), or a microcentrifuge for tubes at 1,700 rpm (271 rcf) for 5 min. Remove the supernatant and resuspend the cells in 200 μ L of sterile PBS. Spin down the cells at 1,700 rpm for 5 min, then remove the supernatant.

3.5.5 For unstained control, perform **Step 3.5.10**; for live/dead control, add 50 μ L of 80% ethanol and incubate it for 5 min at RT, and add 150 μ L PBS, then spin down the cells and aspirate the supernatant. Re-suspend the cells of live/dead control in 100 μ L Aqua zombie dye (1:200 diluted in 1X PBS) for incubation on ice in the dark for 20 min. For live/dead control, perform **Step 3.5.9** onwards to fix live/dead control after washing the cells once. Add a small aliquot of fixed untreated live cells to fixed live/dead control before flow analysis.

3.5.6 Re-suspend all experimental groups except for the abovementioned groups in **Step 3.5.5** (unstained and live/dead control) in 100 μ L TruStain FcXTM solution (1:200 diluted in 1X PBS) [Note 4]. Allow incubation on ice in the dark for 25 min. Spin down the cells at 1,700 rpm for 5 min, and then remove the supernatant.

3.5.7 Wash the cells by adding 200 μ L PBS. Spin down the cells at 1,700 rpm for 5 min, and discard the supernatant, then re-suspend the cells in 100 μ L Aqua zombie Live/Dead (1:200 diluted in PBS) [Note 4]. Allow incubation on ice in the dark for 20 min. **3.5.8** Wash the cells by adding 200 μ L PBS. Spin down the cells at 1,700 rpm for 5 min, and discard the supernatant. Re-suspend the cells designated for experimental groups in 100 μ L antibody cocktail consisting of PE anti-mouse CD40 (anti-CD40), APC-Cy7 anti-mouse I-A/I-E (anti-MHC-II), FITC anti-mouse CD80 (anti-CD80) and BV421 anti-mouse CD86 (anti-CD86) (all 1:200 diluted in PBS) [Note 4]. Re-suspend cells designated to be FMO1 in 100 μ L FMO1 (CD40 FMO) cocktail consisting of anti-MHC-II, anti-CD80 and anti-CD86 (1:200 diluted in PBS); re-suspend cells designated to be FMO2 in 100 μ L FMO2 (MHC-II FMO) cocktail consisting of anti-CD40, anti-CD80 and anti-CD86 (1:200 diluted in PBS); re-suspend cells designated to be FMO3 in 100 μ L FMO3 (CD80 FMO) cocktail consisting of anti-CD40, anti-MHC-II and anti-CD86 (1:200 diluted in PBS); re-suspend cells designated to be FMO4 in 100 μ L FMO4 (1:200 diluted in PBS) cocktail [Note 3]. Allow incubation on ice in the dark for 25 min.

Meanwhile, prepare single stained bead controls by mixing 1.0 μ L anti-CD40, anti-MHC-II, anti-CD80, or anti-CD86 with a drop of positive bead and a drop of negative bead from the Ig κ bead kit. Allow incubation at RT in the dark for 15 min.

3.5.9 Spin down the cells or beads at 1,700 rpm for 5 min, remove the supernatant, then add 200 μ L of PBS. Repeat the washing step once before the next step.

3.5.10 Re-suspend the cells or beads in 100 μ L 4% PFA for fixation at RT for 15 min [Note 4] [Note 5], and then spin down at 300 g for 5 min. Wash the cells or beads with 200 μ L PBS once before re-suspension in 200 μ L PBS, and then transfer them into a FACS tube for flow cytometry analysis.

Note 2: The compound concentration is subject to change depending on the inherent properties of compounds to be tested. This is crucial as a high concentration of certain compounds may lead to cell toxicity or signal saturation, potentially skewing the experimental results. In cases where signal saturation is observed, particularly when analyzed by frequency (the percentage of cells exhibiting a specific fluorochrome signal), it is advised to use the median fluorescence intensity (MFI) as an

alternative measure. MFI provides a more accurate representation of the signal intensity per cell.

Note 3: To maintain the integrity of reagents and compound solutions, it is imperative to minimize freeze-thaw cycles. For compounds exhibiting limited aqueous solubility, the utilization of dimethyl sulfoxide (DMSO) is recommended at a low concentration. For instance, a 4% (v/v) concentration of DMSO has been demonstrated to be sufficient for dissolving hydrophobic compounds in stock solutions used in this study. Compounds should be first be dissolved in the predetermined volume of DMSO, followed by dilution with PBS. Additionally, if DMSO is employed in any experimental group, it is crucial to include an equivalent concentration of DMSO in every other group to ensure experimental consistency.

Note 4: The volume of reagents used as indicated is tied to the number of cells being treated. For example, if cells from two separate wells are to be combined for a staining procedure, it is important to double the volume of reagents used in the procedure.

Note 5: Fixation can be waived if cells will be analyzed by flow shortly after staining. Fixed cells should be kept in a refrigerator at 4° C in the dark for short-term storage. It is also important to note that beads should also be fixed if cells are fixed.

3.6 Flow cytometry analysis

The acquisition of flow cytometry events was carried out using BD LSRFortessaTM X-20 Cell Analyzer with BD FACSDiva software (BD Biosciences). The compensation set-up was conducted by using the compensation beads stained with single-colored fluorescent-conjugated antibodies. After the compensation set-up, the events for full stained samples and FMO samples were acquired. At least 10,000 events were recorded for each of the samples. Finally, the data were exported as FCS files and analyzed using FlowJoTM v10.8 software (BD Life Sciences).

4 Results

4.1 Characterization of the surface marker expression of DC2.4 cells

The expression of markers including CD11c, CD11b, F4/80, MHC-I, MHC-II, CD8 α , CD317, B220, CD80, CD86, and CD40, were analyzed by flow cytometry (Figure 1A; Supplementary Figure S1). The analysis of these surface markers revealed a distinct expression profile on DC2.4 cells, characterized by high levels of CD11c, CD11b, F4/80, MHC-I, CD80, CD86, moderate expression of CD8 α and CD317, and low to no expression of MHC-II, B220 and CD40. This expression pattern is consistent with previous studies (10), which have suggested that the DC2.4 cell line exhibits a semi-mature phenotype in its resting state, characterized by high expression of MHC-I, CD80, and CD86. Notably, while these cells inherently express high levels of CD80

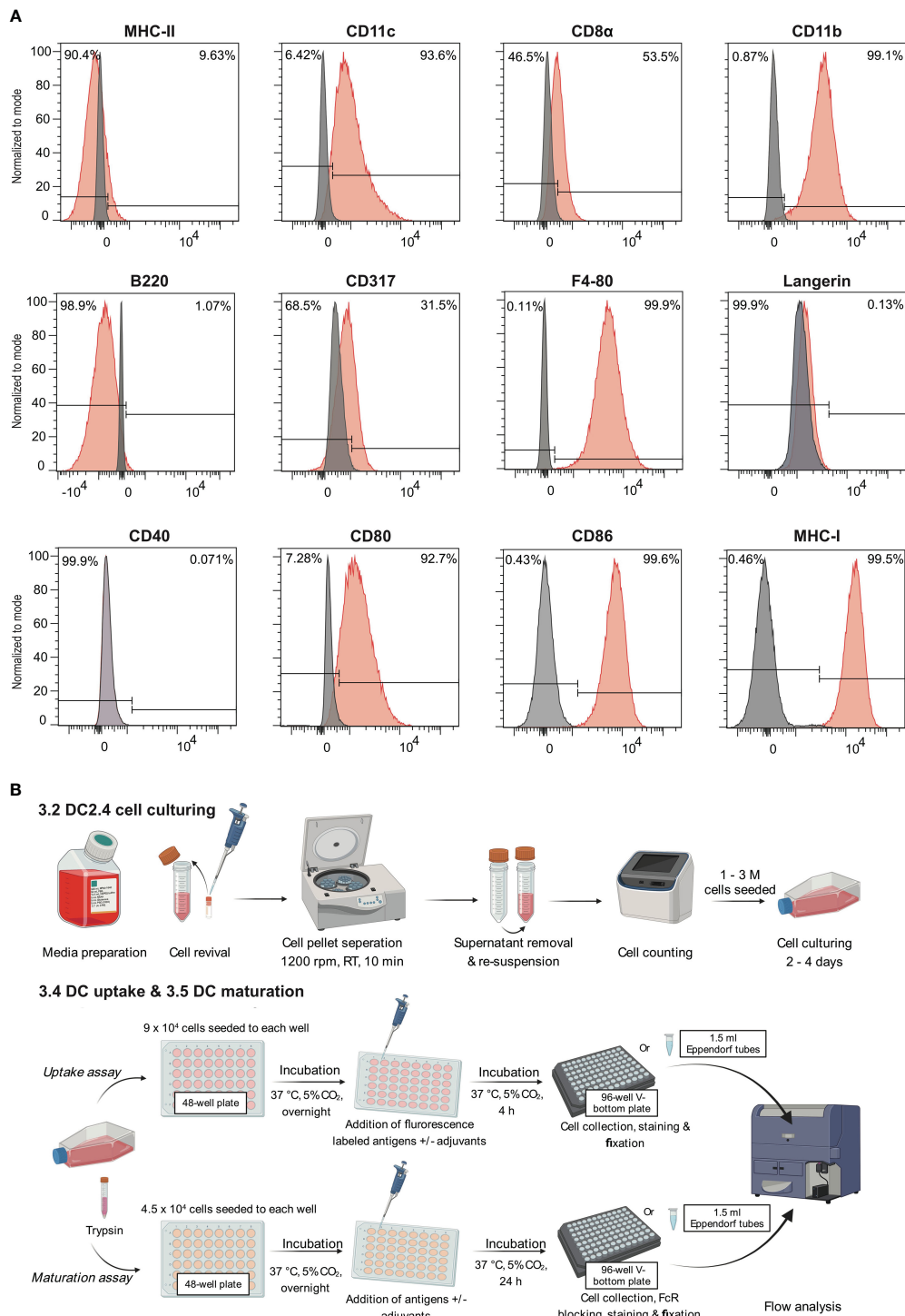


FIGURE 1

Leveraging the semi-mature state of DC2.4 cells to evaluate the efficacy of adjuvants. **(A)** Characterization of cell surface markers on DC2.4 cell line by flow cytometry. The grey histogram represents the fluorescence signal of the control samples (FMO control), and the red histogram represents the fluorescence of a given marker in the sample. **(B)** Schematics of *in vitro* DC2.4 cell uptake and maturation assays.

and CD86 (15), their expression can be further amplified upon activation with certain stimulants (16). Consequently, CD80 and CD86 serve as pivotal markers for assessing the maturation status of DC2.4 cells. This assessment is complemented by tracking markers such as CD40 and MHC-II, which exhibit low to negligible expression in the absence of stimulation.

4.2 DC2.4 cell FITC-dextran uptake assay

In the context of vaccine development, the efficacy of a vaccine is largely dependent on the successful presentation of antigens by DCs to T cells. Adjuvants that enhance antigen uptake by DCs have the potential to substantially increase the likelihood of antigens

being presented. Considering this, we evaluated the capacity of DC2.4 cells to uptake fluorescent dextran (FITC-tagged) via pinocytosis (17) by flow cytometry (Figure 2). The results demonstrated that DC2.4 cells displayed concentration-dependent uptake of FITC-dextran. To prevent signal saturation in future uptake assays, a concentration range of 0.1 – 0.5 μ M was identified as suitable (Figures 2A, B). Using confocal microscopy, we confirmed the presence of FITC-dextran mainly cytoplasmatic granules following a 4-hour incubation with DC2.4 cells (Figure 2C, top). This localization became even more pronounced when FITC-dextran was administered at a concentration ten times higher (5 μ M) to DC2.4 cells (Figure 2C, bottom).

Furthermore, we synthesized a cyanine5.5-tagged peptide antigen (Cy5.5-PADRE-J8) and assessed its uptake by DC2.4 cells at a concentration of 1 μ M (Supplementary Information). Flow cytometry analysis demonstrated a robust Cy5.5 signal intensity, indicating effective internalization of Cy5.5-PADRE-J8 in DC2.4

cells. It's essential to ensure a distinct difference in signal intensity between unadjuvanted antigens and those with adjuvants for accurate observations. Therefore, conducting compound titration is always imperative (Supplementary Figure 2).

4.3 DC maturation and cytokine production

After the evaluation of key DC markers, we selected CD40, MHC-II, CD80 and CD86 to evaluate the maturation status of DC2.4 cells in our assay (Figure 1A). Informed by the literature, LPS and a mixture of OVA and IFN- γ were employed as the positive controls to activate DC2.4 cells (18, 19). The inclusion of IFN- γ was substantiated by its well-established role as a CD40 inducer (20). We also used a robust toll-like receptor (TLR) 2/6 agonist, Pam₂CSK₄ as a positive treatment control. Furthermore, the

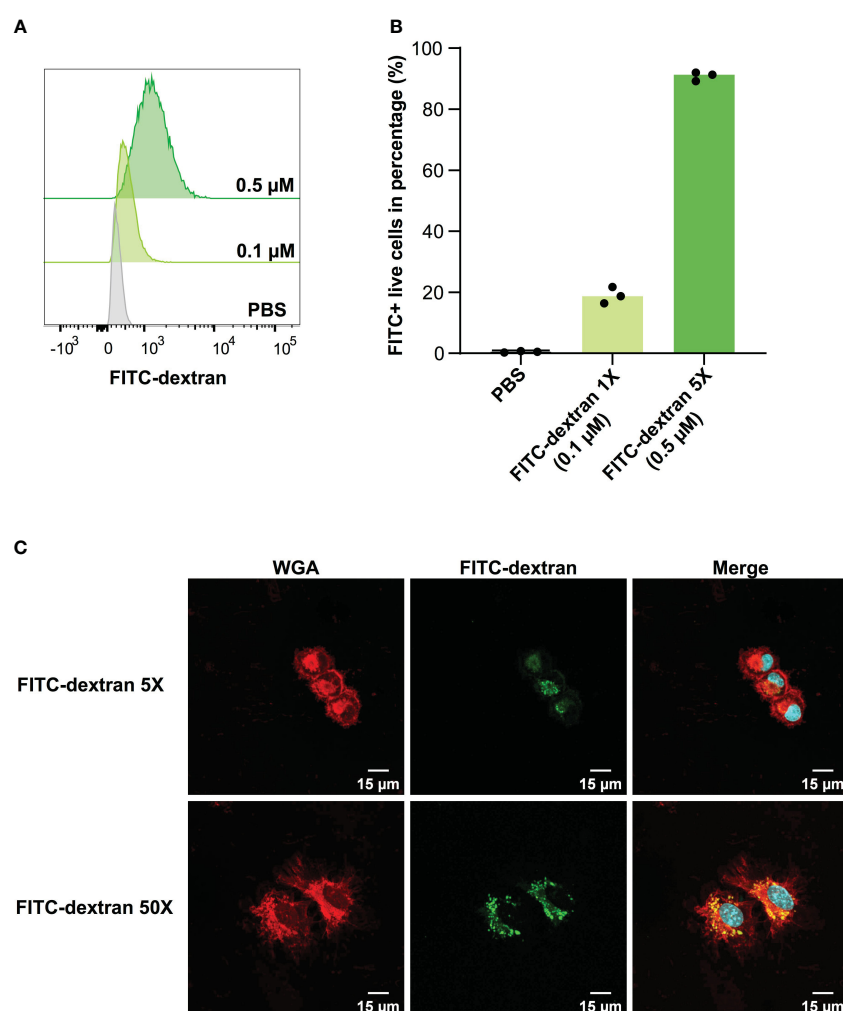


FIGURE 2

Concentration-dependent uptake of FITC-dextran by DC2.4 cells. (A) Mean fluorescent Intensity of the uptake of 0.1 and 0.5 μ M FITC-dextran by DC2.4 cells. (B) Percentage of dextran positive DC2.4 cells post uptake of 0.1 and 0.5 μ M FITC-dextran by DC2.4 cells. (C) Confocal microscopy images of DC2.4 cells after co-incubation with 0.5 (top) or 5 (bottom) μ M FITC-dextran for 4 h (20X objective). Red channel: wheat germ agglutinin (WGA) labeling cell membrane; Blue channel: 4',6-diamidino-2-phenylindole (DAPI) labeling nucleus; Green channel: FITC labeling dextran internalized by DC2.4.

potential of peptide antigens conjugated to peptide-based adjuvants (specially L₁₅-PADRE-J8, J8-K(L₁₅)-PADRE, J8-K(L₁₀)-PADRE, J8-K(F₁₀)-PADRE, and J8-K(V₁₀)-PADRE) in upregulating the selected markers was evaluated. This potential was then compared with that of naked antigens, namely J8, which acts as a B-cell epitope, and PADRE-J8, where PADRE (pan HLA-DR epitope) functions as a T helper epitope (Figures 3A–D; Supplementary Figure 7).

The expression of CD40 was significantly increased in all groups except for cells treated with PBS, J8, PADRE-J8 and IFN- γ (Figure 3A). Notably, the lead candidate, L₁₅-PADRE-J8, which showed the most promising results in animal studies by eliciting the highest antigen-specific IgG titers, also significantly upregulated CD40 expression, surpassing even that induced by LPS. Akin to PBS, J8, PADRE-J8 and IFN- γ , J8-K(L₁₀)-PADRE and J8-K(V₁₀)-PADRE failed to upregulate the expression of MHC-II (Figure 3B). Not surprisingly, L₁₅-PADRE-J8 induced the highest level of MHC-II expression, followed by J8-K(L₁₅)-PADRE. This outcome aligned well with our previous animal studies, where both L₁₅-PADRE-J8 and J8-K(L₁₅)-PADRE demonstrated exceptional promises. In those studies, these two compounds effectively stimulated the production of protective sera against the targeted bacterium (13, 21). In addition to CD40 and MHC-II, L₁₅-PADRE-J8 significantly increased the expression of CD80 on the surface of DC2.4 cells. Interestingly, the remaining groups, except J8-K(F₁₀)-PADRE and J8-K(L₁₅)-PADRE, did not exhibit notable upregulation of CD80 (Figure 3C). However, L₁₅-PADRE-J8 failed to upregulate CD86 expression, whereas LPS, Pam₂CSK₄ and other poly(hydrophobic amino acids) derivatives (J8-K(V₁₀)-PADRE, J8-K(F₁₀)-PADRE, and J8-K(L₁₅)-PADRE) significantly increased it (Figure 3D). The difference in CD80/86 expression patterns amongst groups indicated different maturation statuses of cells stimulated by different compounds. L₁₅-PADRE-J8 may have led to a more advanced maturation status in DC2.4 cells. No significant differences were observed among groups when analyzing the frequency of CD86 expression in DC2.4 cells (Supplementary Figure 4).

To discern between different levels of maturation, we conducted unbiased clustering of all treatment groups using FlowJo's tools, Phenograph and Cluster Explorer (Figures 3E, F). This clustering was based on the physical parameter Side-scatter (SSC), which serves as a proxy for cell granularity, and the median intensity of CD40, MHC-II, CD80 and CD86 expression. In this analysis, we identified a total of thirty-five distinct clusters across the various treatment groups (Figure 3E). Cells treated with the lead compound, L₁₅-PADRE-J8, were mainly clustered in clusters 6, 9 and 17 (Figure 3F). The SSC and the expression of CD40, MHC-II and CD80 of cluster 9 were significantly higher than other clusters, suggesting a distinctive marker signature of cells treated with L₁₅-PADRE-J8. Cells treated with PBS, J8, PADRE-J8 and IFN- γ exhibited similar cluster distribution. These clusters (3, 4, 11, 23, 14, 15, 20, 22, 24, 29, 32 and 35) all showed low expression of CD40, MHC-II and CD80. Interestingly, cells treated with OVA or OVA +IFN- γ , LPS or Pam₂CSK₄, J8-K(L₁₀)-PADRE or J8-K(V₁₀)-PADRE, and J8-K(F₁₀)-PADRE or J8-K(L₁₅)-PADRE showed similar cluster distribution, respectively.

Since DCs secrete cytokines to crosstalk with T cells to regulate downstream immune responses, we measured the intracellular accumulation of two key cytokines, a pro-inflammatory cytokine, tumor necrosis α (TNF- α), and an anti-inflammatory cytokine, interleukin-10 (IL-10) (Supplementary Information, Supplementary Figure S5). As expected, L15-PADRE-J8 elicited robust production of both TNF- α and IL-10, surpassing the response induced by LPS (Figures 4A, B). This suggests a potent inflammatory reaction, potentially counterbalanced by an anti-inflammatory response to maintain homeostasis. Conversely, J8-K (L₁₀)-PADRE only weakly induced the production of TNF- α . To elucidate the relationship between the expression patterns of CD40, MHC-II, CD80, or CD86 and that of TNF- α or IL-10 during DC activation, linear regression models were used (Figures 4C–H). The analysis revealed a high correlation between the expression of TNF- α and CD40, TNF- α and MHC-II, or IL-10 and CD40, with R² values of 0.9856, 0.8377, and 0.9744, respectively (Figures 4C, D, F). Furthermore, a moderate correlation was observed between the expression of TNF- α and CD80, IL-10 and MHC-II, or IL-10 and CD80, with R² values of 0.7266, 0.6566, and 0.5160 (Figures 4E, G, H). However, no linear correlation was found between the expression of TNF- α and CD86, or IL-10 and CD86 (Supplementary Figure S6).

5 Discussion

In vaccine development, the implementation of both *in vivo* and *in vitro* studies is essential. *In vivo* studies provide direct data on the safety and efficacy of vaccines, while *in vitro* studies aim to elucidate the mechanisms of vaccine effectiveness. Employing predictive *in vitro* assays before *in vivo* studies aids in the optimization of vaccine development by identifying preparations that are likely to elicit robust immune responses, thus reducing the utilization of ineffective vaccines in animal experimentation. Both DCs and macrophage cell lines, including RAW264.7 and J774 (22), have been extensively utilized as APCs in research. Here, we present a DC-based assay that has the potential to predict the efficacy of peptide-based vaccines in subsequent *in vivo* studies.

We employed an experimental design where subunit vaccines were directly internalized by DC2.4 cells. We conducted two experiments to evaluate the internalization of candidate subunit vaccines by DCs, and their ability to upregulate DC maturation markers. At first, we investigated DC uptake, employing a quantitative method to analyze internalization using fluorescein-tagged peptide antigens. It is important to note that the use of different fluorescein tags on the same antigen may result in varying levels of DC uptake, even at identical concentrations; namely, the fluorescent tag of choice can influence uptake (23).

DC2.4 cells (*Merck repository*) naturally showed relatively high expression of CD86 and MHC-I at the resting state, but low expression of CD40 and MHC-II. Therefore, we selected MHC-II and several co-stimulatory markers including CD40, CD80, and CD86 to elucidate the potential of vaccine candidates to induce DC2.4 cell maturation. Although IFN- γ is a known CD40 inducer, the addition of IFN- γ (20 ng/mL) did not upregulate CD40

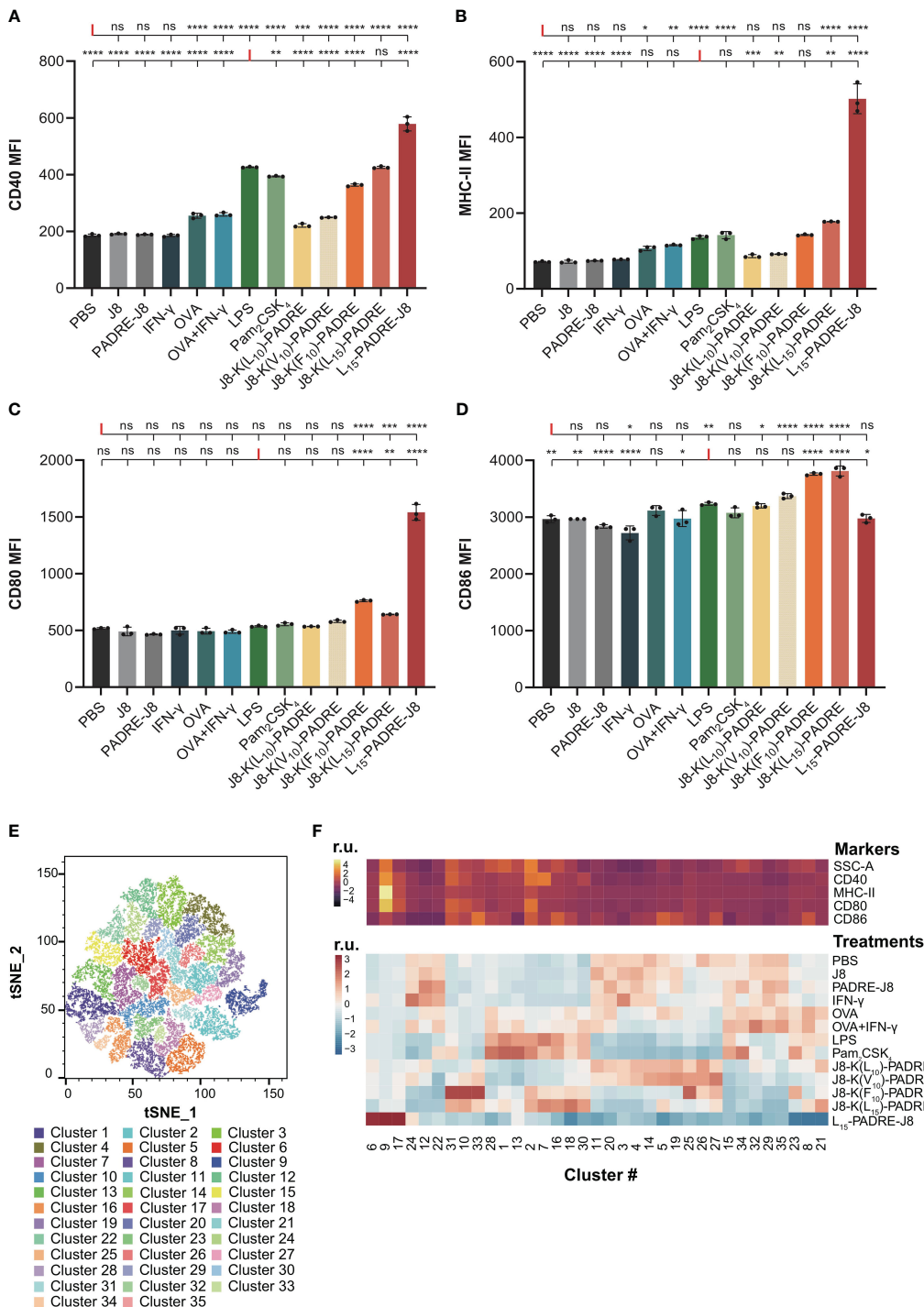


FIGURE 3

Maturation of DC2.4 cells by peptide vaccines. (A) MFI of MHC-II expression in live DC2.4 cell population post-vaccine treatment. (B) MFI of CD40 expression in live DC2.4 cell population post-vaccine treatment. (C) MFI of CD80 expression in live DC2.4 cell population post-vaccine treatment. (D) MFI of CD86 expression in live DC2.4 cell population post-vaccine treatment. (E) Clustering of different vaccines-treated DC2.4 cells by SSC, and expression of CD40, MHC-II, CD80 and CD86. (F) Top heatmap depicting the relative SSC, and expression of CD40, MHC-II, CD80 or CD86, measured in median fluorescent intensity. Bottom heatmap represents the percentage distribution of cells treated with different groups within each cluster. r.u. relative units. *: p-value < 0.05; **: p-value < 0.01; ***: p-value < 0.001; ****: p-value < 0.0001; "ns" means 'not significant'.

expression in DC2.4 cells (Figure 3A). This could be attributed to a different maturation state of our cells purchased from Merck. Several peptide vaccine constructs, previously shown to induce different magnitudes of humoral responses *in vivo*, were

employed to stimulate DC2.4 cells. J8-K(V₁₀)-PADRE, J8-K(F₁₀)-PADRE, and J8-K(L₁₀)-PADRE, which were previously reported to be less immunogenic (13, 21), stimulated DC2.4 cells to a less extent compared to stronger peptide vaccine constructs, J8-K(L₁₅)-

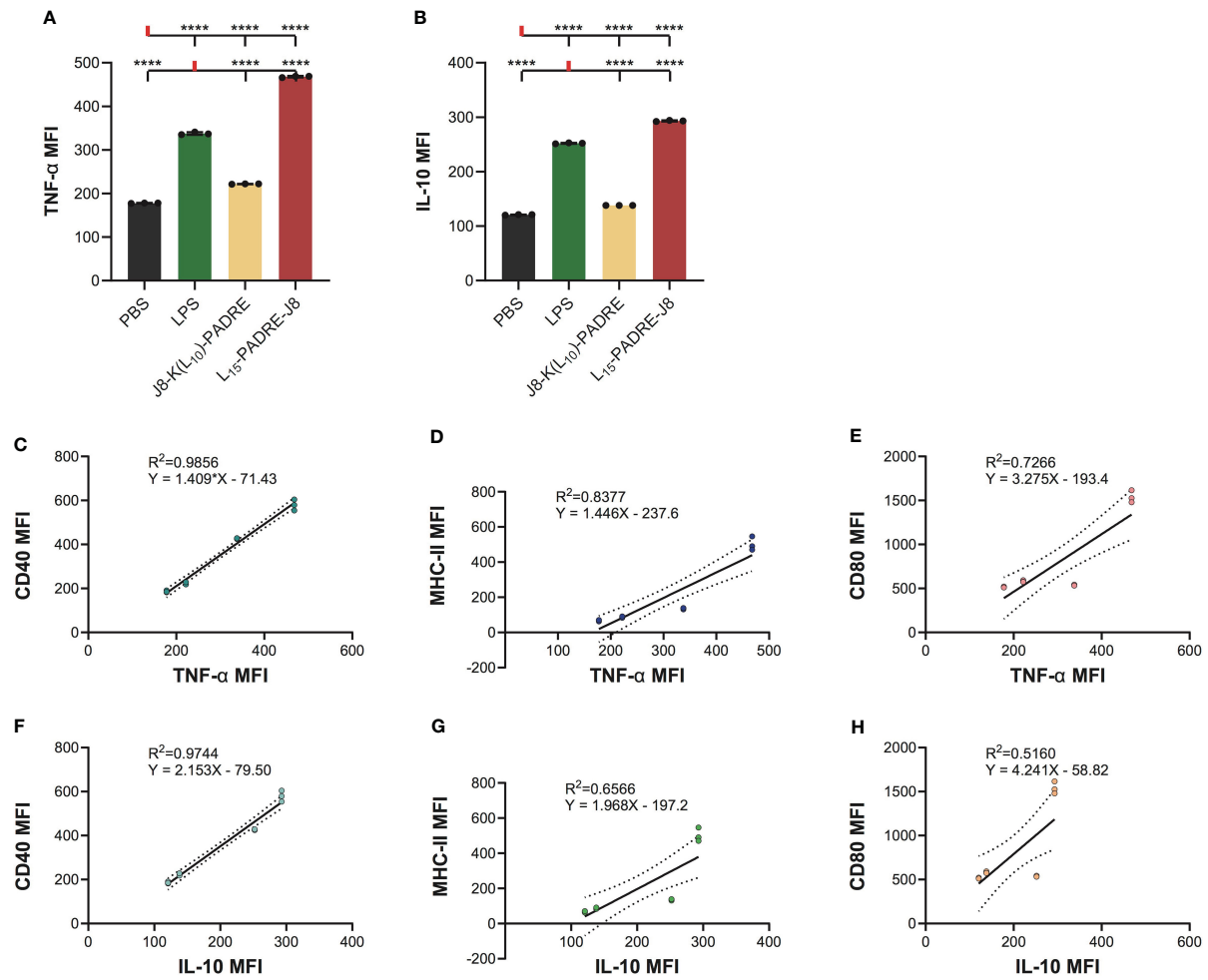


FIGURE 4

Intracellular cytokine staining of cells treated with PBS, LPS, J8-K(L₁₀)-PADRE, and L₁₅-PADRE-J8. (A) TNF- α MFI of cells treated with PBS (shown in black), LPS (shown in green), J8-K(L₁₀)-PADRE, and L₁₅-PADRE-J8 (shown in red). (B) IL-10 MFI of cells treated with PBS (shown in black), LPS (shown in green), J8-K(L₁₀)-PADRE, and L₁₅-PADRE-J8 (shown in red). (C) Linear regression model of TNF- α MFI and CD40 MFI. (D) Linear regression model of TNF- α MFI and MHC-II MFI. (E) Linear regression model of TNF- α MFI and CD80 MFI. (F) Linear regression model of IL-10 MFI and CD40 MFI. (G) Linear regression model of IL-10 MFI and MHC-II MFI. (H) Linear regression model of IL-10 MFI and CD80 MFI. ****: p-value < 0.0001.

PADRE and L₁₅-PADRE-J8. Lower CD40, MHC-II, and CD80 expression was found in cells treated with J8-K(V₁₀)-PADRE, J8-K(F₁₀)-PADRE, or J8-K(L₁₀)-PADRE compared with cells treated with J8-K(L₁₅)-PADRE or L₁₅-PADRE-J8. Interestingly, all poly(hydrophobic amino acid)-adjuvanted antigens (J8-K(V₁₀)-PADRE, J8-K(F₁₀)-PADRE, J8-K(L₁₀)-PADRE, and J8-K(L₁₅)-PADRE) except for L₁₅-PADRE-J8 upregulated CD86 expression compared to PBS, indicating a different maturation state of cells treated with L₁₅-PADRE-J8. Studies have shown that dendritic cells express both CD80 (B7.1) and CD86 (B7.2) upon activation. CD86 is recognized as a marker for early maturation, whereas CD80 expression typically increases only in fully mature DCs (24). In fact, CD80 has a higher monomeric affinity for CD80/86's ligands, CD28 or CTLA-4, than CD86 (25). While we cannot disregard the potential impact of DC-trafficking and interactions with other cells that take place *in vivo*, the notable strong correlation observed between our *in vitro* assay and *in vivo* studies bolsters

the validity of our model as a valuable preliminary screening tool before animal experimentation.

The subsequent cytokine profiling indicated that J8-K(L₁₀)-PADRE was weaker in generating pro-inflammatory responses than L₁₅-PADRE-J8. Interestingly, we found that L₁₅-PADRE-J8 not only strongly induced the production of pro-inflammatory cytokine, TNF- α , but also anti-inflammatory cytokine, IL-10. This intricate balance facilitated by TNF- α and IL-10 highlights a sophisticated feedback loop within dendritic cells, essential for modulating the immune system's response to ensure an equilibrium between pro-inflammatory and anti-inflammatory signals (26). In our linear regression models, we found that the correlation between CD40 and TNF- α or IL-10 expression was particularly strong ($R^2 = 0.9856$ and 0.9744 , respectively). This implies that CD40 may serve as a reliable marker for indicating the production levels of TNF- α and IL-10. As previously reported, all poly(hydrophobic amino acids)-containing vaccine formulations

(J8-K(V₁₀)-PADRE, J8-K(F₁₀)-PADRE, J8-K(L₁₀)-PADRE, J8-K(L₁₅)-PADRE, and L₁₅-PADRE-J8) self-assemble into nanoparticles (13, 21, 27, 28), which facilitate their recognition by APCs, including DCs, thereby enhancing the internalization of vaccine components and further accelerating the processing of antigens and presentations by DCs. This was in line with our findings that naked antigen (J8, or PADRE-J8) without a nanoparticulate delivery system could not upregulate CD40, MHC-II, CD80 or CD86 expression on DC2.4 cells.

The method proposed here offers a simplified approach for swiftly and affordably screening vaccine formulations, facilitating subsequent validation steps. To confirm the successful induction of antigen-specific T cells, our method can be complemented with tetramer staining. This allows for the detection of antigen-specific T cells following the exposure of vaccine-activated dendritic cells. In the presented method, we have optimized different variables related to DC2.4 culturing and passaging to ensure both high reproducibility and straightforward applicability. For instance, we optimized the seeding density and increased the frequency of media changes to once per day. These modifications resulted in accelerated cell growth and consistently high cell viability, exceeding 97% at the time of collection. Moreover, for uptake and maturation studies, we determined that the appropriate cell confluence was 80% to prevent over-confluence and cell death. Both LPS and OVA were suitable positive controls for maturation.

Additionally, we recommend the use of V-bottom plates as they minimize cell loss during washing steps. We meticulously optimized compound concentrations to prevent signal saturation, providing a guideline for future experiments that will avoid signal saturation and ensure differentiation between experimental groups. Of note, antibody titration should be performed when determining the most appropriate concentration of antibodies for staining, which is subject to change when activation compounds perform differently in upregulating certain markers.

It is important to underscore the versatility of the presented assay, as it enables the evaluation of not only peptide-based vaccines but also protein-based vaccines or standalone adjuvants upon careful titration of antigen/adjuvant concentrations.

6 Conclusion

Here, we present a refined protocol to test the capacity of synthetic vaccines to induce DC maturation *in vitro*. Our comprehensive methods offer essential insights into the ideal seed cell density, compound concentration, incubation duration, and staining protocols. These details are instrumental in achieving a reproducible, efficient, and high-throughput assessment of subunit vaccine candidates.

Data availability statement

The original contributions presented in the study are included in the article/[Supplementary Material](#). Further inquiries can be directed to the corresponding authors.

Ethics statement

Ethical approval was not required for the studies on animals in accordance with the local legislation and institutional requirements because only commercially available established cell lines were used.

Author contributions

LL: Data curation, Formal analysis, Investigation, Methodology, Validation, Visualization, Writing – original draft, Writing – review & editing. WK: Data curation, Formal analysis, Investigation, Methodology, Software, Validation, Visualization, Writing – review & editing. JZ: Data curation, Investigation, Methodology, Validation, Writing – review & editing. FF: Data curation, Investigation, Methodology, Writing – review & editing. JW: Resources, Supervision, Writing – review & editing. RS: Resources, Supervision, Writing – review & editing. IT: Funding acquisition, Resources, Supervision, Writing – review & editing. MS: Conceptualization, Funding acquisition, Methodology, Project administration, Resources, Supervision, Writing – review & editing. JC: Conceptualization, Data curation, Formal analysis, Funding acquisition, Investigation, Methodology, Project administration, Resources, Software, Supervision, Validation, Visualization, Writing – original draft, Writing – review & editing.

Funding

The author(s) declare financial support was received for the research, authorship, and/or publication of this article. This research was funded by the Garnett Passe and Rodney Williams Memorial Foundation Cojoint Perry-Cruz 2019 grant, the Princess Alexandra Research Foundation 2021 Research Award, and the ARC Discovery Project DP21010280.

Acknowledgments

We acknowledge all authors' contributions to this work.

Conflict of interest

The authors declare that the research was conducted in the absence of any commercial or financial relationships that could be construed as a potential conflict of interest.

The author(s) declared that they were an editorial board member of Frontiers, at the time of submission. This had no impact on the peer review process and the final decision.

Publisher's note

All claims expressed in this article are solely those of the authors and do not necessarily represent those of their affiliated

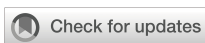
organizations, or those of the publisher, the editors and the reviewers. Any product that may be evaluated in this article, or claim that may be made by its manufacturer, is not guaranteed or endorsed by the publisher.

References

- Pollard AJ, Bijker EM. A guide to vaccinology: from basic principles to new developments. *Nat Rev Immunol.* (2021) 21:83–100. doi: 10.1038/s41577-020-00479-7.
- Skwarczynski M, Toth I. Peptide-based synthetic vaccines. *Chem Sci.* (2016) 7:842–54. doi: 10.1039/C5SC03892H.
- Hochweller K, Sweeney CH, Anderton SM. Immunological tolerance using synthetic peptides—basic mechanisms and clinical application. *Curr Mol Med.* (2006) 6:631–43. doi: 10.2174/156652406778194982.
- Wikstrom ME, Batanero E, Smith M, Thomas JA, von Garnier C, Holt PG, et al. Influence of mucosal adjuvants on antigen passage and CD4+ T cell activation during the primary response to airborne allergen. *J Immunol.* (2006) 177:913–24. doi: 10.4049/jimmunol.177.2.913.
- Timothy AA, Tokanovic A, Snibson KJ, Edwards SJ, Pearse MJ, Scheerlinck JP, et al. ISCOMATRIX™ adjuvant reduces mucosal tolerance for effective pulmonary vaccination against influenza. *Hum Vaccines Immunotherapeutics.* (2015) 11:377–85. doi: 10.4161/21645515.2014.990859.
- Hubrecht RC, Carter E. The 3Rs and humane experimental technique: implementing change. *Anim (Basel).* (2019) 9:754–63. doi: 10.3390/ani9100754.
- Vandebril R, Hoefnagel MM. Dendritic cell-based *in vitro* assays for vaccine immunogenicity. *Hum Vaccines Immunotherapeutics.* (2012) 8:1323–5. doi: 10.4161/hvi.21350.
- Scheffel F, Knuschke T, Otto L, Kollenda S, Sokolova V, Cosmovici C, et al. Effective activation of human antigen-presenting cells and cytotoxic CD8+ T Cells by a calcium phosphate-based nanoparticle vaccine delivery system. *Vaccines (Basel).* (2020) 8:110–24. doi: 10.3390/vaccines8010110.
- Tang J, Yang Y, Qu J, Ban W, Song H, Gu Z, et al. Mesoporous sodium four-coordinate aluminosilicate nanoparticles modulate dendritic cell pyroptosis and activate innate and adaptive immunity. *Chem Sci.* (2022) 13:8507–17. doi: 10.1039/D1SC05319A.
- Hargadon KM. Murine and human model systems for the study of dendritic cell immunobiology. *Int Rev Immunol.* (2016) 35:85–115. doi: 10.3109/08830185.2014.952413.
- Shen Z, Reznikoff G, Dranoff G, Rock KL. Cloned dendritic cells can present exogenous antigens on both MHC class I and class II molecules. *J Immunol.* (1997) 158:2723–30. doi: 10.4049/jimmunol.158.6.2723.
- Yang J, Firdaus F, Azuar A, Khalil ZG, Marasini N, Capon RJ, et al. Cell-penetrating peptides-based liposomal delivery system enhanced immunogenicity of peptide-based vaccine against Group A Streptococcus. *Vaccines (Basel).* (2021) 9:499–516. doi: 10.3390/vaccines9050499.
- Azuar A, Li Z, Shibu MA, Zhao L, Luo Y, Shalash AO, et al. Poly(hydrophobic amino acid)-Based Self-Adjuvanting Nanoparticles for Group A Streptococcus Vaccine Delivery. *J Med Chem.* (2021) 64:2648–58. doi: 10.1021/acs.jmedchem.0c01660.
- JadHAV KB, Woolcock KJ, Muttenthaler M. Anhydrous hydrogen fluoride cleavage in Boc solid phase peptide synthesis. *Methods Mol Biol.* (2020) 2103:41–57. doi: 10.1007/978-1-0716-0227-0_4.
- Gong YB, Huang YF, Li Y, Han GC, Li YR, Wang DJ, et al. Experimental study of the mechanism of tolerance induction in dexamethasone-treated dendritic cells. *Med Sci Monit.* (2011) 17:Br125–31. doi: 10.12659/MSM.881758.
- Vangasseri DP, Cui Z, Chen W, Hokey DA, Falo LD Jr., Huang L. Immunostimulation of dendritic cells by cationic liposomes. *Mol Membrane Biol.* (2006) 23:385–95. doi: 10.1080/09687860600790537.
- Aung KT, Yoshioka K, Aki S, Ishimaru K, Takuwa N, Takuwa Y. The class II phosphoinositide 3-kinases PI3K-C2 α and PI3K-C2 β differentially regulate clathrin-dependent pinocytosis in human vascular endothelial cells. *J Physiol Sci.* (2019) 69:263–80. doi: 10.1007/s12576-018-0644-2.
- He T, Tang C, Xu S, Moyana T, Xiang J. Interferon gamma stimulates cellular maturation of dendritic cell line DC2.4 leading to induction of efficient cytotoxic T cell responses and antitumor immunity. *Cell Mol Immunol.* (2007) 4:105–11.
- Fu RH, Hran HJ, Chu CL, Huang CM, Liu SP, Wang YC, et al. Lipopolysaccharide-stimulated activation of murine DC2.4 cells is attenuated by n-butylidenephthalide through suppression of the NF- κ B pathway. *Biotechnol Lett.* (2011) 33:903–10. doi: 10.1007/s10529-011-0528-5.
- Nguyen VT, Benveniste EN. IL-4-activated STAT-6 inhibits IFN-gamma-induced CD40 gene expression in macrophages/microglia. *J Immunol.* (2000) 165:6235–43. doi: 10.4049/jimmunol.165.11.6235.
- Skwarczynski M, Zhao G, Boer JC, Ozberk V, Azuar A, Cruz JG, et al. Poly (amino acids) as a potent self-adjuvanting delivery system for peptide-based nanovaccines. *Sci Adv.* (2020) 6:eaax2285–2295. doi: 10.1126/sciadv.aax2285.
- Marohn ME, Barry EM. Live attenuated tularemia vaccines: recent developments and future goals. *Vaccine.* (2013) 31:3485–91. doi: 10.1016/j.vaccine.2013.05.096.
- Takakura H, Sato H, Nakajima K, Suzuki M, Ogawa M. *In vitro* and *in vivo* cell uptake of a cell-penetrating peptide conjugated with fluorescent dyes having different chemical properties. *Cancers (Basel).* (2021) 13:2245–56. doi: 10.3390/cancers13092245.
- AI-Ashmawy GMZ. Dendritic Cell Subsets, Maturation and Function. In: Chapoval SP, editor. *Dendritic Cells*. London, UK: IntechOpen (2018). p. 11–24.
- Kennedy A, Waters E, Rowshanravan B, Hinze C, Williams C, Janman D, et al. Differences in CD80 and CD86 transendocytosis reveal CD86 as a key target for CTLA-4 immune regulation. *Nat Immunol.* (2022) 23:1365–78. doi: 10.1038/s41590-022-01289-w.
- Hirata N, Yanagawa Y, Ogura H, Satoh M, Noguchi M, Matsumoto M, et al. The role of tumor necrosis factor- α for interleukin-10 production by murine dendritic cells. *Cell Immunol.* (2011) 266:165–71. doi: 10.1016/j.cellimm.2010.09.012.
- Azuar A, Madge HYR, Boer JC, Gonzalez Cruz JL, Wang J, Khalil ZG, et al. Poly (hydrophobic amino acids) and liposomes for delivery of vaccine against Group A Streptococcus. *Vaccines (Basel).* (2022) 10:1212–24. doi: 10.3390/vaccines10081212.
- Shalash AO, Becker L, Yang J, Giacomin P, Pearson M, Hussein WM, et al. Oral peptide vaccine against hookworm infection: correlation of antibody titers with protective efficacy. *Vaccines (Basel).* (2021) 9:1034–49. doi: 10.3390/vaccines9091034.

Supplementary material

The Supplementary Material for this article can be found online at: <https://www.frontiersin.org/articles/10.3389/fimmu.2024.1298721/full#supplementary-material>



OPEN ACCESS

EDITED BY

Thomas Hartung,
Johns Hopkins University, United States

REVIEWED BY

Maria Ramos,
University of Minho, Portugal
Yashwant Kumar,
Post Graduate Institute of Medical Education
and Research (PGIMER), India

*CORRESPONDENCE

Alina Volkova
alina.volкова@msdecisions.tech

RECEIVED 16 January 2024

ACCEPTED 29 February 2024

PUBLISHED 14 March 2024

CITATION

Ugolkov Y, Nikitich A, Leon C, Helmlinger G, Peskov K, Sokolov V and Volkova A (2024) Mathematical modeling in autoimmune diseases: from theory to clinical application. *Front. Immunol.* 15:1371620. doi: 10.3389/fimmu.2024.1371620

COPYRIGHT

© 2024 Ugolkov, Nikitich, Leon, Helmlinger, Peskov, Sokolov and Volkova. This is an open-access article distributed under the terms of the [Creative Commons Attribution License \(CC BY\)](#). The use, distribution or reproduction in other forums is permitted, provided the original author(s) and the copyright owner(s) are credited and that the original publication in this journal is cited, in accordance with accepted academic practice. No use, distribution or reproduction is permitted which does not comply with these terms.

Mathematical modeling in autoimmune diseases: from theory to clinical application

Yaroslav Ugolkov^{1,2}, Antonina Nikitich^{1,2}, Cristina Leon³,
Gabriel Helmlinger⁴, Kirill Peskov^{1,2,3,5}, Victor Sokolov^{2,3}
and Alina Volkova^{2,3*}

¹Research Center of Model-Informed Drug Development, Ivan Mikhaylovich (I.M.) Sechenov First Moscow State Medical University, Moscow, Russia, ²Marchuk Institute of Numerical Mathematics of the Russian Academy of Sciences (RAS), Moscow, Russia, ³Modeling and Simulation Decisions FZ - LLC, Dubai, United Arab Emirates, ⁴Biorchestra Co., Ltd., Cambridge, MA, United States, ⁵Sirius University of Science and Technology, Sirius, Russia

The research & development (R&D) of novel therapeutic agents for the treatment of autoimmune diseases is challenged by highly complex pathogenesis and multiple etiologies of these conditions. The number of targeted therapies available on the market is limited, whereas the prevalence of autoimmune conditions in the global population continues to rise. Mathematical modeling of biological systems is an essential tool which may be applied in support of decision-making across R&D drug programs to improve the probability of success in the development of novel medicines. Over the past decades, multiple models of autoimmune diseases have been developed. Models differ in the spectra of quantitative data used in their development and mathematical methods, as well as in the level of "mechanistic granularity" chosen to describe the underlying biology. Yet, all models strive towards the same goal: to quantitatively describe various aspects of the immune response. The aim of this review was to conduct a systematic review and analysis of mathematical models of autoimmune diseases focused on the mechanistic description of the immune system, to consolidate existing quantitative knowledge on autoimmune processes, and to outline potential directions of interest for future model-based analyses. Following a systematic literature review, 38 models describing the onset, progression, and/or the effect of treatment in 13 systemic and organ-specific autoimmune conditions were identified, most models developed for inflammatory bowel disease, multiple sclerosis, and lupus (5 models each). $\geq 70\%$ of the models were developed as nonlinear systems of ordinary differential equations, others – as partial differential equations, integro-differential equations, Boolean networks, or probabilistic models. Despite covering a relatively wide range of diseases, most models described the same components of the immune system, such as T-cell response, cytokine influence, or the involvement of macrophages in autoimmune processes. All models were thoroughly analyzed with an emphasis on assumptions, limitations, and their potential applications in the development of novel medicines.

KEYWORDS

autoimmune diseases, mathematical modeling, quantitative systems pharmacology, model-informed drug development, immune system modeling

1 Introduction

Autoimmune diseases (ADs) are a group of diverse disorders that occur widely and affect approximately 12.5% of the global population, with a greater prevalence among childbearing women (1). A landmark feature in ADs can be found in immune disturbances causing autoreactivity of lymphocytes against normal cells of the organism (2). Even though all ADs share a common pathophysiological basis of development, their clinical manifestations could vary from mild abnormalities in laboratory measurements to life-threatening conditions such as organ failure following serious tissue damage (3). Depending on the origin of their manifestation, ADs could be restricted to a single organ (organ-specific ADs) such as the thyroid gland in Hashimoto's thyroiditis (HT) or the pancreas in type 1 diabetes mellitus (T1DM) or, on the other hand, affect multiple organs and tissues within the body, such as systemic lupus erythematosus (SLE) or rheumatoid arthritis (RA). Both types of ADs may exhibit a wide range of symptoms and can be challenging to diagnose and treat (4).

The exact causes of autoimmunity are not fully understood. Despite the presence of known genetic and epigenetic predisposing factors, environmental factors are believed to be an essential trigger of autoimmune response (5). The most well-studied example of such an external stimulus are pathogenic microorganisms or dysbiosis in commensal organisms, initiating either a non-specific immune response, or an immune response specific to self-antigens through molecular mimicry, like in the cases of the Epstein–Barr virus (6) or the group A streptococcus (7). Other well-known environmental factors leading to autoimmunity include smoking, diet, and drug administration (e.g., immune checkpoint inhibitors therapy); and more such factors remain to be defined (3, 8).

ADs exhibit multi-phase dynamics and complex pathogenesis, including dysregulation in both adaptive and innate immune systems (9). At preclinical stages of the disease, autoantibodies – the hallmark of ADs – are expressed, in the absence of clinical signs

Abbreviations: Ab, Antibody; AD, Autoimmune disease; APC, Antigen-presenting cells; BAFF, B-cell activating factor; CD, Crohn's disease; CNS, Central nervous system; CRP, C-reactive protein; DC, Dendritic cells; EASI, Eczema Area and Severity Index; EAU, Experimental autoimmune uveitis; EC, Epithelial cells; GI, Gastrointestinal; GM-CSF, Granulocyte-macrophage colony-stimulating factor; HT, Hashimoto's thyroiditis; IBD, Inflammatory bowel disease; IC, Immune complex; IFN, Interferon; IL, Interleukin; IL-6R, IL-6 receptor; IPF, Idiopathic pulmonary fibrosis; JAK, Janus kinase; LN, Lupus nephritis; MMP, Matrix metalloproteinase; MS, Multiple sclerosis; Mφ, Macrophages; NK, Natural killer; ODE, Ordinary differential equation; OSC, Organ-specific cells; PD, Pharmacodynamics; PDE, Partial differential equation; PDGF, Platelet-derived growth factor; PK, Pharmacokinetics; PPMS, Primarily progressive multiple sclerosis; QSP, Quantitative systems pharmacology; R&D, Research & development; RA, Rheumatoid arthritis; RRMS, Relapsing-remitting multiple sclerosis; SLE, Systemic lupus erythematosus; SPMS, Secondary progressive multiple sclerosis; T1DM, Type 1 diabetes mellitus; Tcon, Conventional T-cells; Teff, Effector T-cells; TGF, Transforming growth factor; Th, T-helper cells; TIMP, Tissue inhibitor of metalloproteinases; TNF- α , Tumor necrosis factor- α ; Treg, Regulatory T-cells; UC, Ulcerative colitis; uMCP-1, Urine monocyte chemotactic protein-1.

and symptoms of autoimmune disorders such as fever, rash, and fatigue (10). A gradual involvement of functional elements of the immune system over time, such as aberrant B- and T-cells, leads to an eventual diversification of clinical phenotypes. However, despite the evolving understanding of the autoimmunity mechanisms, there are still numerous gaps in our knowledge regarding the role of specific immune components within a tangled network with multiple feedback loops in the pathophysiology of ADs, further complicating the management of disease progression (11).

The first-line therapy to control ADs include conventional immunosuppressive or anti-inflammatory therapies, such as corticosteroids and methotrexate, which dampen the overactivated immune system (12, 13). However, non-selective immunomodulators do not always provide sufficient benefit in a heterogeneous population of patients; also, their long-term administration leads to the appearance of side effects, the most common ones being an increased risk of infections and malignancies (14). Eventually, the accumulated knowledge on the pathophysiology of ADs has contributed to the development of targeted drugs with notably higher benefit-risk ratios. These selective immunotherapies are designed to suppress major pro-inflammatory signaling pathways by blocking inflammatory cytokines (e.g., anti-interleukin (IL)-17 in psoriasis), target immune cells (e.g., anti-B-cell activating factor (BAFF) in SLE), or intracellular kinases (e.g., Janus kinase (JAK) inhibitors in RA). Despite the tremendous success of targeted therapies in ADs, unmet medical needs remain, in terms of long-term safety as well as overall efficacy, since many patients do not achieve disease remission (15). A deeper understanding of mechanisms and of their corresponding heterogeneity in the development of ADs would provide opportunities to overcome these limitations, ultimately leading to a more personalized and, therefore, a more efficient approach to treatment.

Mechanistic, physiologically-based mathematical modeling is widely accepted as a supportive tool for better understanding and interrogating diseases pathophysiology, given its ability to integrate biological and pharmacological knowledge with a quantitative description of the underlying processes, therefore making such modeling essential in enhancing decision-making at all stages of drug development (16, 17). For example, by reconstructing biochemical or signaling cascades *in silico*, a researcher may formulate and challenge theoretical hypotheses regarding the contribution of certain signaling components, to support the rational identification and validation of new drug targets (18, 19). Mechanistic modeling can also be employed to explore the impact of patient-specific factors, such as demographic characteristics and comorbidities, on drug action, potentially explaining the heterogeneity in treatment responses and providing options for adjustments or changes in treatment strategies. Modeling may further help in rationalizing the selection and application of drug combinations, in optimizing dosing schedule, and more (16). In summary, mechanistic mathematical modeling represents a tool to support the targeting of the right molecular pathway in a given disease context, with the right dose, and in the right patient population or phenotype (20).

The aim of this work was to conduct a systematic review and analysis of mathematical models of ADs focused on the mechanistic

description of the immune system, to shape and consolidate the current landscape of quantitative knowledge on autoimmune processes, to outline most promising directions for further model developments, and to perform model-informed analyses aimed at supporting drug discovery and development against autoimmune pathologies.

2 Methods

A systematic literature search was performed in the PubMed database, to identify all mechanistic mathematical models with relevance to ADs. The search query consisted of two semantic components. The first one involved keywords related to autoimmunity, specifically, 184 disease-specific terms from the list of ADs (21) and general descriptors of autoimmune-related processes (e.g., “autoimmune disease”, “autoinflammatory”, etc.). The second one was used to seek out studies on mechanistic, physiologically-based, or quantitative systems pharmacology (QSP) models. Additional search conditions were implemented, to eliminate records in non-English language and those focused on clinical trial results, reviews, or meta-analyses. To derive and compare the number of publications available in the PubMed database on mechanistic models *versus* empirical ones, another search was performed, with the second semantic component replaced with terms related to pharmacokinetics (PK) and pharmacodynamics (PD) analyses. The exact queries used are listed in the [Supplementary Methods](#).

The search resulted in 500 potentially relevant publications (last accessed: 20 October 2023). Two authors (Y.U., A.V.) independently screened the articles for duplication and eligibility. Disagreements were resolved through discussion with independent reviewers (V.S., K.P.). A prerequisite for transferring an article into further analysis was the description of autoimmune-related processes at any level of generalization and organization (e.g., molecular, cellular, tissue-level), including antigen presentation, cytokine production, immune complex (IC) formation, etc., using a mathematical framework such as ordinary differential equations (ODEs), partial differential equations (PDEs), and others. A model with any number of variables or parameters was considered mechanism-based as long as it included more than one of the above-mentioned components. In addition, articles featuring minor modifications vs. previously published models within a single AD were grouped and analyzed together.

Several classifications were used to categorize the models: by target organ or system, by indication, by mathematical method, and by associated data. The following criteria were applied to define the latter: if only clinical vs. preclinical data were used for calibration, fine-tuning of parameters, or model validation, the model was tagged to the respective group (*i.e.*, “Clinical” or “Preclinical”). If both types of data, preclinical and clinical, were used, or the parametrization was not within the scope of the research, “Combined” or “Not specified” tags were assigned.

Visualization and statistical analyses of the gathered data were carried out using reproducible scripts in the R Statistics software (version 4.0.2), using the R “tidyverse” package (version 1.3.0) (22). A network diagram of immune components was prepared using the R “igraph” package (version 1.2.7) (23).

3 Results

To illustrate the growing body of publications related to mathematical modeling in ADs, the numbers of articles appearing in the PubMed database following the search queries for either PK/PD models or mechanistic models were visualized against years of publication (Figure 1A). According to the search results, the first papers matching the specifications date back to the 1970s. Since then, the number of relevant articles increased exponentially, reaching more than 200 publications per year by 2024. The ratio of studies appearing in the search for mechanistic models vs. empirical ones was small (~1-to-5).

Following a detailed investigation of these 500 publications potentially associated with mechanistic models, 47 studies were identified, which described the development, analysis, and application of 38 unique physiologically-based models. These 38 models were categorized according to 13 related AD indications, including alopecia areata, atopic dermatitis, autoimmune myocarditis, experimental autoimmune uveitis (EAU), celiac disease, HT, idiopathic pulmonary fibrosis (IPF), inflammatory bowel disease (IBD), multiple sclerosis (MS), pulmonary sarcoidosis, RA, SLE, T1DM, or classified into “Autoimmune processes” category if the model investigated autoimmunity in a more generic context rather than according to a specific AD (Figure 1B). The most frequently featured pathologies were IBD, MS, and lupus (5 models per disease), followed by RA (4 models), atopic dermatitis and T1DM (2 models each).

These models predominantly employed nonlinear systems of ODEs (71%) (Figure 1C). Some models were built using PDEs (15.8%); others featured integro-differential equations, Boolean networks, or Markov jump processes (13.2%). The models were developed primarily based on clinical data (39.4%); a small proportion of models made use of preclinical data only (5.3%), while 26.3% of model used a combination of clinical and preclinical data; 28.9% of models did not rely on quantitative data (Figure 1D).

Given the multitude of ramifications found in the immune system, the mechanistic models we evaluated typically focused on specific aspects of autoimmune conditions and the related pathophysiology, and often at various levels of “mechanistic granularity”. To identify those components and interactions which occurred most frequently in the mathematical systems, we extracted all variables from the modeling papers – except for the Boolean network models – *i.e.*, 214 variables from 36 models; we then unified these variables into 60 terms and counted the incidence of terms occurring simultaneously within a single model (Supplementary Material; Table 1). If a term was encountered together with another term for at least 3 times, the corresponding interaction was added to the network diagram (Figure 2). The 31

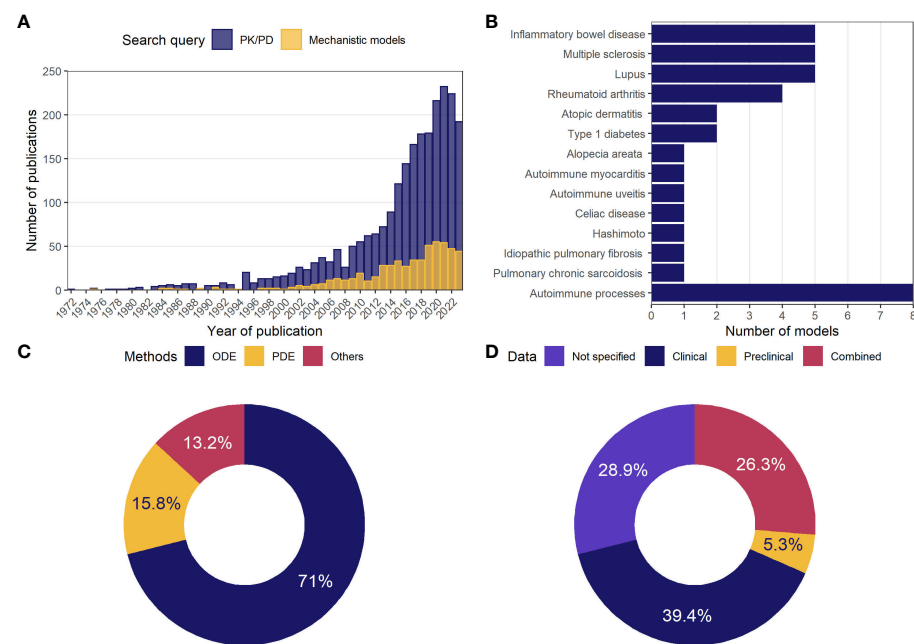


FIGURE 1

General statistics on model-based analyses in autoimmune diseases. **(A)** Number of publications in the PubMed database per year, following a search for mechanistic or PK/PD models of ADs; **(B)** number of mechanistic models identified through a systematic review and classified by indication; **(C)** percentage of mechanistic models using the described methodology; **(D)** percentage of mechanistic models by type of data used in model development or validation. AD, autoimmune disease; ODE, ordinary differential equations; PD, pharmacodynamics; PDE, partial differential equations; PK, pharmacokinetics.

TABLE 1 Summary of mechanistic models of autoimmune diseases.

Reference	Indication	Description	Application	Key limitations
Systemic autoimmune diseases				
Lupus				
Ruiz-Cerdá et al. (24)	Systemic lupus erythematosus	A Boolean network model of antigen presentation	Identification of promising biological targets (including their combinations) as well as conditions defining the treatment response.	1. Qualitative nature of the Boolean network models. 2. The scope of the system is limited to the antigen presentation.
Yazdani et al. (25)	Systemic lupus erythematosus	Mechanistic ODE-based model of SLE at different stages of the disease progression	Model-based assessment of immune system condition at different stages of SLE (e.g., tolerance breach, occurrence of flares, etc.) and the effect of mesenchymal stem cell therapy.	1. Qualitative rather than quantitative approach to model parametrization. 2. Utilization of generic variables not directly associated with laboratory measurements.
Budu-Grajdeanu et al. (26)	Lupus nephritis	Generic 4-ODE system describing the dynamics of ICs, anti- and pro-inflammatory mediators, and tissue damage	Exploration of intersubject variability associated with the treatment benefit.	1. Utilization of generic variables not directly associated with laboratory measurements. 2. The model was calibrated using the data on 4 subjects.
Hao et al. (27) Karagiannis et al. (28)	Lupus nephritis	A system of convection-diffusion equations describing the progression of renal fibrosis	Identification of promising biological targets for the treatment of renal fibrosis.	Limited application of clinical data for model development.
Gao et al. (29)	Systemic lupus erythematosus	The effect of exogenous IL-2 on the ratio between conventional T-cells and Tregs described using ODE framework	1. Defining therapeutic window for IL-2 in patients with SLE. 2. Search for covariates and predictive biomarkers associated with the IL-2 treatment.	The scope of the model is focused on the clinical issues specific to the IL-2 therapy.

(Continued)

TABLE 1 Continued

Reference	Indication	Description	Application	Key limitations
Rheumatoid arthritis				
Rullmann et al. (30)	Rheumatoid arthritis	Application of the Entelos® RA PhysioLab® platform	1. Validation of potential biological targets. 2. Prediction of the effect of hypothetical anti-IL-15 and anti-IL-12 treatment on synovial cell density and cartilage degradation rate.	Source code is not available.
Moise et al. (31)	Rheumatoid arthritis	A system of PDEs describing rheumatic joint (cartilage, synovial membrane, synovial fluid compartments) in the chronic state of RA	1. Mathematical evaluation of the disease state. 2. Evaluation of the effect of conventional therapies (methotrexate, infliximab, tofacitinib), and hypothetical ones (anti-IL-23 and anti-IL-17), including their combinations.	1. Simplified geometry of the joint. 2. Focus on the behavior of the mathematical system without direct association with the clinical data (e.g., model validation or parameter calibration against the observed data).
Nakada et al. (32)	Rheumatoid arthritis	Five target engagement models of cytokines and respective antagonists in ODEs, linked with the CRP dynamics	A robust quantitative model calibrated and validated using data from multiple clinical trials and applied to explain interpatient variability in support of dosing strategy optimization for the considered compounds.	Limited roster of biological entities (e.g., immune cells not included) and associated therapies.
Meyer-Hermann et al. (33)	Rheumatoid arthritis	A system of ODEs quantifying circadian variations of cortisol, noradrenaline, and TNF- α in healthy subjects and patients with RA	1. Evaluation of the cortisol and noradrenaline response under anti-TNF- α treatment. 2. Optimization of the clock time of drug administration.	Immune response is represented only by TNF- α .
Organ-specific autoimmune diseases				
Gastrointestinal tract				
Wendelsdorf et al. (34)	Inflammatory bowel disease	An ODE model that describes innate and adaptive immune response to bacteria stimuli in IBD across gut lumen, lamina propria, and mesenteric lymph node	1. Testing different rescue strategies (e.g., targeting M ϕ or Treg) for IBD <i>in silico</i> . 2. Explaining the mechanisms behind PPAR γ -mediated IBD prevention.	1. Relatively high-level description (i.e., using generic variables) of the biological mechanisms. 2. The model was developed and validated using preclinical data.
Lo et al. (35, 36) Park et al. (37)	Inflammatory bowel disease	An ODE model of T-cell polarization in IBD	1. Exploration of the cytokine and transcription factor balance associated with proper and pathological T-cell immune response. 2. Evaluation of the treatment effect of anti-cytokine therapies across 4 sub-groups of IBD patients defined by the ratio of Th1 and Th2 transcription factors.	1. The quantities of T-cells are represented by transcription factors. 2. Part of the model parameters were derived from the models of other diseases.
Dwivedi et al. (38)	Inflammatory bowel disease	Mechanistic model of IL-6 signaling adapted for IBD	Benchmarking different targets for IL-6 signaling disruption based on CRP concentrations as a marker of inflammation.	The focus of the modeling is only on the IL-6 pathway.
Rogers et al. (39, 40)	Inflammatory bowel disease	Comprehensive mechanistic model that includes detailed description of innate and adaptive immune response in IBD developed in ODEs	1. Explaining the mechanisms behind IL-17 inhibition-mediated disease worsening. 2. Utilizing virtual population approach to predict the number of responders to different treatment options, including the combination of anti-TNF- α and anti-IL-12p40 compounds.	Large scale of the model (116 reactions and 334 parameters) which makes it hard to adapt and qualify.
Balbas-Martinez et al. (41, 42)	Inflammatory bowel disease	Boolean network model with 43 nodes spread across lymph node, blood, lymph circulatory system, and gut lumen compartments, subsequently expanded with an ODE sub-module	1. General description of the IBD condition and the effect of several therapeutic interventions using Boolean network approach. 2. Predicting the effect of recombinant human IL-10 administration on other cytokines in the system.	Qualitative nature of the Boolean network models.
Demin et al. (43)	Celiac disease	A mechanistic model in ODEs attempting to describe immune response in lamina propria provoked by the consumption and deamidation of gluten	Benchmarking potential biological targets, including transglutaminase-2 inhibitors, for the treatment of celiac disease.	Limited clinical data available for model validation.

(Continued)

TABLE 1 Continued

Reference	Indication	Description	Application	Key limitations
Nervous system and eyes				
Nicholson et al. (44)	Autoimmune uveitis	A 10-ODE model that describes the processes of antigen presentation and T-cell activation on both sides of the blood-retina barrier	Evaluation of the impact of blood-retina barrier permeability and other factors (<i>i.e.</i> , APC production) on the disease state.	Biological mechanisms represented in the model are simplified and limited to several generic variables.
Moise et al. (45)	Multiple Sclerosis	A 27-PDE model describing immune and inflammatory interactions within the focal plaque	Quantifying the impact of stand-alone treatment and combinations of IFN- β , glatiramer acetate, natalizumab, and dimethyl fumarate on plaque growth	1. Simplified geometry of the plaque. 2. Limited application of clinical data for model development.
Vélez de Mendizábal et al. (46)	Multiple Sclerosis	A generic model of the cross-regulation between regulatory and effector T-cell in MS in ODEs	Exploring the mechanisms behind different MS phenotypes.	1. Limited number of immune response components considered in the model. 2. Focus on the behavior of the mathematical system with limited application of the clinical data.
Kannan et al. (47)	Multiple Sclerosis	A generic 4-ODE model of inflammatory and anti-inflammatory components, demyelination, and neuronal death	Exploring the mechanisms behind different MS phenotypes.	1. Focus on the behavior of the mathematical system with limited application of the clinical data. 2. Utilization of generic variables not directly associated with laboratory measurements.
Gross et al. (48)	Multiple Sclerosis	A probabilistic model describing transmigration and differentiation of lymphocytes in the CNS	Assessing the effectiveness of immune-modulating therapies without the need for lumbar punctures.	Limited clinical data available for model validation.
Broome et al. (49)	Multiple Sclerosis	An ODE systems model describing the interactions between reactive oxygen and nitrogen species, the permeability transition pore, apoptotic factors, and eventual cell death in oligodendrocytes	Identification of the promising biological targets for the treatment of MS.	Limited number of immune response components considered in the model due to the biochemical scope of the model.
Skin				
Dobreva et al. (50, 51)	Alopecia areata	An ODE model describing hair follicles dystrophy as a function of several immune components, including autoreactive T-cells, IFN- γ , MHC-I and immune privilege guardians	Exploring hypotheses on disease pathogenesis <i>via</i> mathematical description of the alopecia areata progression.	1. The model was developed using preclinical data. 2. Focus on the behavior of the mathematical system with limited application of the clinical data. 3. Limited number of immune response components considered in the model.
Tanaka et al. (52) Domínguez-Hüttiger et al. (53) Christodoulides et al. (54)	Atopic dermatitis	An ODE-based system describing the four phenotypes typical for atopic dermatitis patients as a function of pathogen load, immune response, and the strength of skin barrier	Optimization of treatment schedule and combinatory effect of antibiotics, emollients, and corticosteroids in terms of transition between pathogenic and healthy phenotypes.	1. No clinical data was used in model development. 2. Lack of temporal components in drug PK and several major factors affecting disease phenotype.
Miyano et al. (55)	Atopic dermatitis	Modeling of the EASI efficacy score as a function of pathogen load, cytokine concentration, and skin barrier integrity using ODE framework	1. Indirect comparison of efficacy across 9 anti-cytokine drugs. 2. Optimization of therapeutic strategy for dupilumab-resistant patients and search for predictive biomarkers associated with the dupilumab treatment-mediated response.	1. Covariance in model parameters was not considered when generating virtual patient population. 2. Each cytokine independently affects skin barrier integrity and infiltration by pathogens. 3. PK/PD relationship was not explored was only maximum dose of investigated compounds was considered.

(Continued)

TABLE 1 Continued

Reference	Indication	Description	Application	Key limitations
Endocrine system				
Magomedzze et al. (56)	Type 1 diabetes mellitus	A 6-ODE model capturing changes over time in β -cells, effector T-cells, Tregs, Mφ (resting and activated), and autoantigen	Exploring the mixture of factors causing the onset and progression of T1DM, particularly the impact of Tregs on the suppression of autolytic T-cells.	1. Limited number of immune response components considered in the model. 2. Focus on the behavior of the mathematical system with limited application of the clinical data.
Jaber-Douraki et al. (57)	Type 1 diabetes mellitus	A concise model of integro-differential equations reflecting the interplay between β -cell, effector T-cells and Tregs along with antigen and IL-2	Describing the onset and progression of T1DM and categorizing individuals based on the balance between effector T-cells and Tregs, and T-cells avidity.	1. Limited number of immune response components considered in the model. 2. Focus on the behavior of the mathematical system with limited application of the clinical data.
Salazar-Viedma et al. (58)	Hashimoto's thyroiditis	A 4-ODE model representing Th1, Th17, thyrocytes and gut microbiome dynamics	Identifying the scenarios in Th and intestinal microbiota imbalance causing the development and progression of HT.	1. Limited number of immune response components considered in the model. 2. Focus on the behavior of the mathematical system with limited application of the clinical data.
Lungs				
Aguda et al. (59) Hao et al. (60)	Pulmonary chronic sarcoidosis	A system of convection-diffusion equations describing cells dispersion and cytokine diffusion within granuloma	Benchmarking the effect of cytokine-targeting drugs (anti-TNF- α , anti-IL-12, anti-IFN- γ , TGF- β enhancement) on the size of sarcoid granulomas.	1. Limited application of clinical data for model development. 2. Simplistic geometrical representation of the granuloma as a sphere with uniform distribution of Mφ, Th1, Th17 and Treg.
Hao et al. (61)	Idiopathic pulmonary fibrosis	A system of convection-diffusion equations describing the progression of pulmonary fibrosis	Benchmarking the effect of cytokine-targeting drugs (anti-TNF- α , anti-PDGF, anti-IL-13, anti-TGF- β) on pulmonary fibrosis progression.	1. Limited application of clinical data for model development. 2. Simplistic geometrical representation of the lung tissue.
Cardiovascular				
van der Vegt et al. (62)	Autoimmune myocarditis	A 4-ODE model capturing the development of autoimmune myocarditis under treatment with immune checkpoints inhibitors	Establishing individual patient characteristics reflected in the values of several key model parameters leading to the development of autoimmune myocarditis under treatment with nivolumab or ipilimumab.	1. Biological mechanisms represented in the model are simplified and limited to several generic variables. 2. Focus on the behavior of the mathematical system with limited application of the clinical data.
General autoimmune reactions				
Head et al. (63)	Autoimmune processes	A systems model describing IC formation, opsonization and clearance	Evaluation of mathematical conditions resulting in an increased production ICs to identify the states associated with the high risk of the development of IC-mediated autoimmune disease.	Focus on the behavior of the mathematical system with limited application of the clinical data.
Arazi et al. (64)	Autoimmune processes	A generic 3-ODE model reflecting the quantities of autoreactive B-cells, autoantigen, and ICs	Establishing how initial conditions affect the degree of IC-mediated inflammation and which processes contribute the most to it.	1. Focus on the behavior of the mathematical system with limited application of the clinical data. 2. Limited number of immune response components considered in the model.
Iwami et al. (65)	Autoimmune processes	A 3-ODE model of immune cells, target cells, and damaged cells	Exploring different functional relationships and parameter spaces explaining different states of immune tolerance/dormancy and repeated flare-ups in AD.	1. Focus on the behavior of the mathematical system with limited application of the

(Continued)

TABLE 1 Continued

Reference	Indication	Description	Application	Key limitations
General autoimmune reactions				
				clinical data. 2. Utilization of generic variables not directly associated with laboratory measurements.
Khailaie et al. (66)	Autoimmune processes	A mechanistic model of the interplay between conventional and Treg	Delineating three regimes of immune activation (complete lack of response, the first peak following by complete clearance of the antigen and chronic persistence of the antigen) primarily through the differences in the renewal rate of naïve T-cells and resting Tregs and antigen-stimulation thresholds.	1. Focus on the behavior of the mathematical system with limited application of the clinical data. 2. Limited number of immune response components considered in the model.
Louzoun et al. (67)	Autoimmune processes	A model representing the dynamics of Th1, Th2, Mφ their cytokines, as well as naïve T-cells and pooled Teff and Treg	Characterizing the progression of Th1-type autoimmune diseases from Th1 to Th2 steady-state	1. Focus on the behavior of the mathematical system with limited application of the clinical data. 2. Utilization of generic variables not directly associated with laboratory measurements.
Hara et al. (68)	Autoimmune processes	A 4-ODE model describing the interplay between Th (reactive to self-antigen or viral infection), virus, and memory T cells	Identifying the conditions that trigger autoimmunity in response to viral infection	1. Focus on the behavior of the mathematical system with limited application of the clinical data. 2. Utilization of generic variables not directly associated with laboratory measurements.
Ramos et al. (69)	Autoimmune processes	A system of integro-differential equations and ODE describing the interaction of self-APC, self-reactive T cells and immunosuppressive cells	Exploring of mathematical conditions resulting in the regulatory effect of immunosuppressive cells on the proliferation and activation of self-reactive T cells in an autoimmune reaction.	1. Focus on the behavior of the mathematical system with limited application of the clinical data. 2. Limited number of immune response components considered in the model.
Valeyev et al. (70)	Autoimmune processes	An ODE model representing two exemplar immune cell populations and their mutual regulation through cytokine signalling	Defining mathematical conditions leading to the oscillating or trigger-based pathological disease phenotype.	1. Focus on the behavior of the mathematical system with limited application of the clinical data. 2. Utilization of generic variables not directly associated with laboratory measurements.

CNS, central nervous system; CRP, C-reactive protein; HT, Hashimoto's thyroiditis; IBD, inflammatory bowel disease; IC, immune complex; IFN, interferon; IL, interleukin; MHC, major histocompatibility complex; MS, multiple sclerosis; Mφ, macrophages; ODE, ordinary differential equation; PDE, partial differential equation; PK, pharmacokinetics; RA, rheumatoid arthritis; SLE, systemic lupus erythematosus; T1DM, type 1 diabetes mellitus; Th, T-helper cells; TNF- α , tumor necrosis factor- α ; Treg, regulatory T-cells.

nodes which appeared on the diagram were next divided into 3 categories, by biological origin (*i.e.*, cellular, or molecular) or effect (*e.g.*, fibrosis, inflammation, tissue damage). The most frequently occurring terms were antigen and regulatory T-cells (Treg) (12 cases), followed by interferon (IFN)- γ and macrophages (Mφ) (9 cases each), tumor necrosis factor- α (TNF- α), T-helper cells (Th) and Th1, (8 cases each), and Th17, inflammation, fibrosis (7 cases each). Consequently, most frequent interactions (at least 5 per edge) were observed between T-cells (Tregs, Th1, Th17) and related cytokines (IFN- γ , IL-2, IL-4, IL-6, IL-17).

Next, the 30 models associated with specific diseases (see Figure 1B) were categorized into 2 groups: systemic- and organ-specific. The latter category was, in turn, separated into 6 subgroups: endocrine, lungs, skin, nervous system and eyes, cardiovascular, and

gastrointestinal (GI) tract (Figure 3). Mathematical systems describing autoimmune processes in a more generic sense (8 models) were kept in a separate category. All 38 models were subjected to a comprehensive evaluation encompassing their description, applications, and limitations, summarized in Table 1 and in the text below.

3.1 Lupus

Lupus is a chronic systemic AD with heterogeneous clinical manifestations, ranging from mild joint and skin abnormalities to life-threatening kidney, cardiac, or central nervous system (CNS)

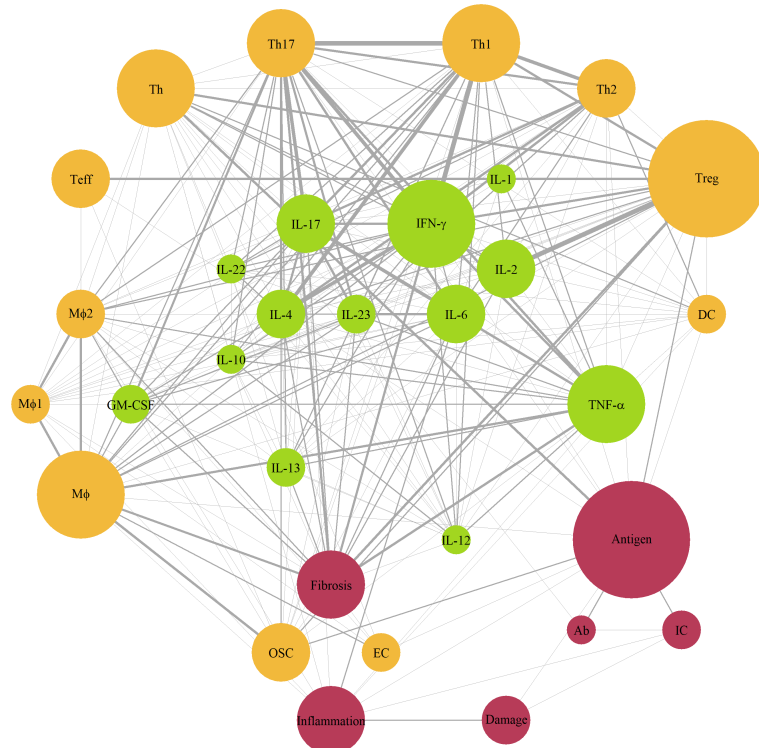


FIGURE 2

Network diagram of immune components represented in mechanistic models of autoimmune diseases. Green color – cytokines; yellow color – cells; red color – other components; size of a node – number of models with the component (3 to 11); edge width – number of interaction (3 to 6). Ab, antibody; APC, antigen-presenting cells; DC, dendritic cells; EC, epithelial cells; GM-CSF, granulocyte-macrophage colony-stimulating factor; IC, immune complex; IFN, interferon; IL, interleukin; Mφ, macrophages; OSC, organ-specific cells; Teff, effector T-cells; Th, T-helper cells; TNF- α , tumor necrosis factor- α ; Treg, regulatory T-cells.

impairment (71). The etiology and pathophysiology of this AD is complex and is still poorly understood. Multiple genetic, immunological, and environmental factors may influence the loss of immunological tolerance against self-antigens, leading to the activation of autoreactive T- and B-cells. Dysregulation in T-cell response results in an imbalance in cytokine production, attracting an increasing number of immune cells to the affected tissue and provoking further inflammation. Moreover, pathological B-cells produce autoantibodies that cause organ damage by IC deposition and complement system activation (72, 73).

The first endeavor in providing a comprehensive depiction of systemic inflammation in SLE was a Boolean network model developed by Ruiz-Cerdá and colleagues (24). This model employed 52 nodes, to represent components of antigen presentation by antigen-presenting cells (APC) to T-cells, with 254 interactions describing activation, inhibition, upregulation, or downregulation processes between nodes. By knocking out or overstimulating isolated nodes, the authors identified and classified perturbations leading to a “lupus-like” phenotype in a virtual subject.

A recent example of another self-contained SLE model, built upon ODEs, is the work by Yazdani et al. (25). These authors created a system that delineates various stages of SLE progression, encompassing the entire immune response in 13 variables: 8 of these are generic (e.g., “proinflammatory mediators”, “damaged

tissue”), and the other 5 reflect specific immune response components: autoantibodies, antigens, IC, and mesenchymal stem cells, as a potential approach for SLE treatment. Model parameters were manually tuned to reproduce key immunological patterns at different phases of SLE, such as tolerance breach, the onset of systemic inflammation, the development of clinical signs, and the occurrence of flares and remissions.

Subsequently, this model underwent modifications through the incorporation of a tissue inflammation submodule, which, in turn, was adopted from another model developed by Budu-Grajdeanu and colleagues for lupus nephritis (LN) (26). This model describes changes over time for 4 variables: IC, anti-inflammatory mediators, pro-inflammatory mediators, and damaged tissue. The first two variables are generic (*i.e.*, not associated with specific biological entities), whereas the last two variables represent urine biomarkers measured in routine clinical practice: urine monocyte chemotactic protein-1 (uMCP-1) and urine protein-to-urine creatinine ratio, respectively. 4 sets of individual parameters were derived from the model calibration procedure, based on individual data from 4 subjects with SLE – a first step towards the quantification of inter-individual variability.

The pathophysiology of LN, specifically in relation to the progression of renal fibrosis, is also the focus of another series of articles published by Hao and colleagues (27, 28). The

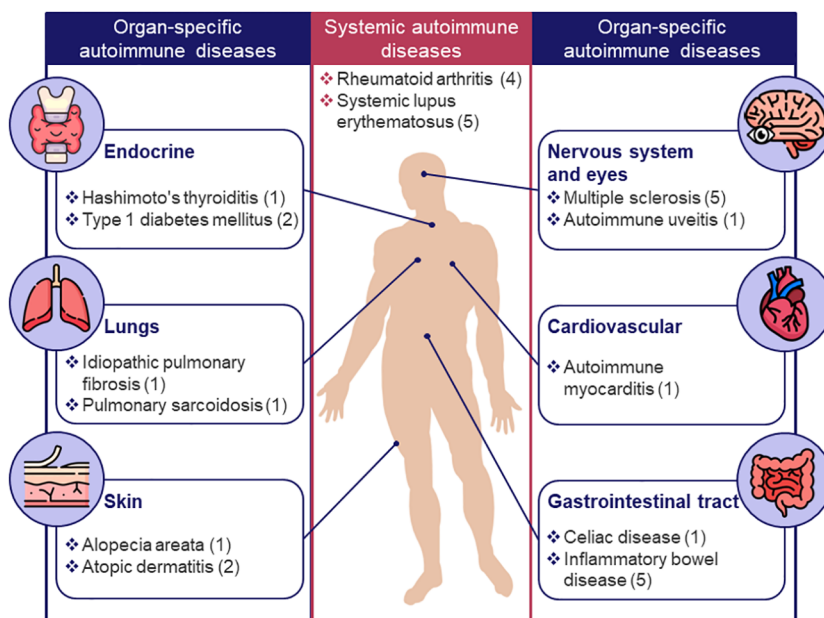


FIGURE 3

Classification of existing models for autoimmune diseases by target organ or system. Only diseases for which mechanistic models were identified are shown; the number of models for a given disease is indicated in brackets.

publications describe the system as a set of 11 PDEs depicting the dispersion of various types of cells involved in fibrosis, across rectangular cross-section of the renal cortex, and regulated by a network of cytokines and growth factors, including uMCP-1, platelet-derived growth factor (PDGF), transforming growth factor-beta (TGF- β), matrix metalloproteinase (MMP), and tissue inhibitor of metalloproteinases (TIMP). Through a sensitivity analysis, two parameters were identified as most influential for the formation of interstitial fibrosis and were estimated based on uMCP-1 time profiles measured in 84 subjects. Between-subject variability was taken into account by dividing the subjects according to their severity of fibrosis (low, intermediate, or high). The estimated two parameters affect the production of TGF- β by tubular epithelial cells (EC) and uMCP-1 synthesis by M ϕ ; modulating these has been shown to provide a potentially beneficial therapeutic strategy for mitigating renal fibrosis.

As opposed to a rather qualitative assessment of drug effects in the aforementioned models, another model considered in this section was specifically designed to quantify the treatment effect of exogenous IL-2 therapy in patients with SLE (29). The model by Gao et al. consists of 10 ODEs and focuses on a limited number of immune components directly associated with the therapeutic effect of IL-2, including conventional T-cells (Tcon), Treg, and natural killer (NK) cells – also taking into account differences in IL-2 receptor densities on each cell type and the formation of receptor-ligand complexes. The model was applied to select an effective range of IL-2 concentrations for treating SLE patients based on their Tcon/Treg ratio. Furthermore, factors affecting the exposure-response relationship were identified, and a new prognostic

biomarker (Treg/CD4+ T-cells ratio) was proposed to separate responders and non-responders prior to treatment initiation.

3.2 Rheumatoid arthritis

RA is a chronic, systemic AD characterized by joint inflammation, synovial hyperplasia, and the progressive destruction of cartilage and bone, leading to disability and impaired quality of life. The disease pathophysiology is complex and involves a wide array of elements of the innate and adaptive immune responses, including M ϕ , dendritic cells (DC), NK cells, T- and B-cells, fibroblast-like synoviocytes, as well as cytokines such as TNF- α and IL-6, along with others: IL-7, IL-15, IL-17, IL-21, IL-23, and granulocyte-macrophage colony-stimulating factor (GM-CSF) (74–77). Similarly to other ADs, the heterogeneity in RA pathophysiology represents a major confounding factor for the development of targeted RA therapies. Despite several drugs available on the market, including anti-TNF- α (infliximab, etanercept), anti-IL-6 (tocilizumab), anti-JAK (tofacitinib), and anti-CD20 (rituximab), their effectiveness is limited to subgroups of patients, while their administration is associated with serious side effects such as ulcers, fatigue, reduced immunity to infections, and osteoporosis (78, 79).

In our search, we identified 4 diverse examples of mechanistic models applied to study RA disease and associated treatments. The first study by Rullmann, published in 2005, describes the application of the Entelos® (80) RA PhysioLab® platform to validate potential biological targets as well as to predict the effect of hypothetical anti-IL-15 and anti-IL-12 treatments on synovial cell density and cartilage degradation rate (30). The model consists

of ODEs, is claimed to include several dozens of soluble factors, cell surface molecules, and numerous types of cells in rheumatoid joint, and can simulate virtual patients with various properties; the lack of the source code, however, prevents a further detailed evaluation.

In 2018, Moise and Friedman developed their own model of a rheumatic joint in a chronic RA state, using PDEs (31). The system describes the dynamics, distribution, and cross-influence of Th17 cells, fibroblasts, Mφ, and associated cytokines and chemokines (e.g., IL-17, GM-CSF, IL-6, fibroblast growth factors, TNF- α , etc.) across cartilage, synovial membrane, and synovial fluid compartments. In addition to an evaluation of model behavior over time without treatment (i.e., disease progression), the model was used to test theoretical effects of conventional therapies (methotrexate, infliximab, tofacitinib), and hypothetical ones (anti-IL-23 and anti-IL-17), including their combinations. Cartilage degradation was used as a surrogate measure of disease status.

One of the more recent works published by Nakada and Mager (2022) describes a mechanistic ODE model focused on the interplay between several key cytokines associated with RA pathophysiology: IL-6, IL-17, TNF- α and IL-1 – complemented with the PK of therapeutic agents such as tofacitinib, secukinumab, infliximab, canakinumab, and anakinra (32). The dynamics of each cytokine and respective antagonist(s) were described by a target-mediated drug disposition module. Modules were connected through a network of feedback mechanisms, with, at the top, C-reactive protein (CRP) turnover as a marker of inflammation. The model is highly quantitative, being informed by data from multiple clinical trials based on the above-mentioned compounds and validated using external datasets not used for model calibration. From a drug development perspective, the model was applied to identify covariates (primarily baseline cytokine concentrations) explaining inter-patient variability in anti-inflammatory effects of the considered anti-cytokine therapies.

The fourth and final model in this section does not focus on inflammatory components but rather on circadian variations of cortisol, noradrenaline, and TNF- α as key players, respectively, of the endocrine, nervous, and immune system, in healthy subjects and patients with RA (33). As such, the characterization of daily oscillations of these markers under anti-TNF- α treatment can be considered as the main output of this model-based research. In addition, the authors demonstrated, *via* simulations, that glucocorticoid treatment between midnight and 2:00 AM would result in the strongest inhibitory effect on TNF- α secretion.

3.3 Gastrointestinal tract

The GI tract is a chain of interconnected organs that consists of the oral cavity, pharynx, esophagus, stomach, small intestine, large intestine, and anal canal. It is a system constantly exposed to the elements of the environment, simultaneously providing an organism with nutrition while keeping numerous pathogens at bay. Multiple ADs (e.g., autoimmune hepatitis, autoimmune pancreatitis, SLE) exhibit symptoms associated with the GI tract

(81), while others are directly caused by abnormal immune reactions within the organ system. Most common examples of the latter are IBD, which includes Crohn's disease (CD) and ulcerative colitis (UC), and celiac disease (82). A large volume of empirical knowledge has accumulated over the years, allowing us to define the pathogenesis of these conditions with relative certainty. Firstly, the right balance between a proper immune response to disease agents and the lack of such for food-related antigens can be challenged by an increased permeability in the gut and a loss of immune tolerance to self-antigens (83). Secondly, inflammation may be provoked by the dysregulation of Th processes, e.g., an increased activation of Th1/Th17 or deactivation of the Th2/Treg pathway (84).

One of the first mechanistic models of IBD by Wendelsdorf and colleagues attempts to quantify these processes across three physiological compartments: the lumen, the lamina propria, and the mesenteric lymph node (34). The model describes the amplification of innate and adaptive immune responses in response to bacteria stimuli which may cause depletion of the epithelial lining. The model operates with 30 variables which can be roughly divided between Mφ (M0, M1, M2), DC, and T-cells (both pro- and anti-inflammatory), as well as cytokines (activating and deactivating). The model allows for a comprehensive sensitivity analysis and a high-level hypothesis evaluation related to general interactions between immune cells. For example, the model was applied to propose rescue strategies that remove M1 from the site of infection, which explains the mechanisms of proliferator-activated receptor- γ -mediated IBD prevention; the model also describes effects of chemokine and cytokine deprivation that allow for Mφ to remain activated. However, the price for the large scale of the model is a rather abstract description of mechanisms, a limitation which has been partially compensated for by subsequent modeling research.

For example, Lo and colleagues focused on aspects of T-cell polarization during the initial steps of the inflammatory processes in IBD, by modeling Th1, Th2 and Treg population densities as a function of concentrations of transcription factors (T-bet, Gata3 and Foxp3) and four cytokines (IFN- γ , IL-4, TGF- β and IL-2) (35). The system was explored primarily along two scenarios: bacterial infection and protozoan infection – under normal and abnormal immune responses, through the modulation of model parameters. It provides a better understanding of the delicate balance between cytokine and transcription factors required for proper T-cell immune response in the gut and the consequences of its disruption. At the same time, the model lacks several essential mechanistic components, including the polarizing effect of cytokines produced by activated Mφ. This limitation was addressed in subsequent work by the same authors, where they expanded on the developed model and added several additional immune components, including Th17, M1 and M2 Mφ, along with IL-6, IL-10, IL-12, IL-21 and TNF- α (36). The model was applied to characterize 4 subgroups of patients with CD, as defined by the ratio of Th1 and Th2 transcription factors, relative to values in healthy volunteers, based on biopsy data. A hypothetical anti-TNF- α therapy was then tested in each subgroup, to find the population most sensitive to the treatment. The article by Park et al. capitalizes

on the work by Lo and colleagues and explores the effect of anti-IL-12 and pro-IL-10 treatment along with TNF- α suppression in the same system, with 4 cohorts of patients differing in their quantities of Th1 and Th2 (37).

The model by Dwivedi et al. is another example of a systems model focused on cytokine effects, IL-6 in particular (38), which contribute to Th17 differentiation (85). This network of ODEs is based on a previously developed model of IL-6-mediated immune signaling, includes 3 compartments (liver, GI tract and circulation), and describes IL-6 binding with its IL-6 receptor (IL-6R) and gp130. The model was validated based on tofacitinib (an anti-IL-6R antibody) data and used to benchmark different targets for IL-6 signaling disruption using circulating levels of CRP, a well-established marker of inflammation, as the primary pharmacodynamic measurement.

The most ambitious attempt to quantify and integrate all pathways and processes described above and beyond can be attributed to a series of papers by Rogers and colleagues, who describe a model with 116 reactions and 334 parameters (39, 40). This model includes multiple cell types associated with innate (DC, Mφ, NK cells, and neutrophils) and adaptive immunity (Th1, Th2, Th17, and Tregs), more than 10 cytokines, CRP and fecal calprotectin as dependent variables, and was parameterized for three types of subjects (healthy, CD, UC), using a technique proposed by Allen et al. (86) to generate virtual populations with baseline biomarker levels corresponding to actual observations. Moreover, the model includes PK models of anti-TNF- α (infliximab), anti-IL-12p40 (ustekinumab), anti-IL-23 (risankizumab and brazikumab), and anti-IL-6 (PF-04236921) compounds. In the first part of their work, the authors performed a sensitivity analysis to identify key mechanisms affecting fecal calprotectin and CRP; they then applied the model to understand mechanisms underlying the worsening of CD, in the case of IL-17 inhibition. In the second part, the model was thoroughly validated against data on multiple existing compounds and was used to predict responder rates based on biomarker cutoffs as well as the effect of combined anti-TNF- α and anti-IL-12p40 treatments.

Another example of a comprehensive, yet qualitative model of IBD is based on a Boolean network, rather than ODEs, created by Balbas-Martines et al. (41). It consists of 43 nodes spread across lymph node, blood, lymph circulatory system, and gut lumen, with MMP being the main marker of tissue damage in the system. The model was shown to correctly reflect the lack of response in MMPs under IL-10 overexpression, IL-17 or IFN- γ knockout and, in turn, demonstrates marked improvement in disease condition mediated by TNF- α suppression or granulocyte and monocyte apheresis. Subsequently the system was ameliorated to a hybrid model of ODEs and Boolean processes, to allow for the characterization of the magnitude and dynamics of IL response, to predict the effect of recombinant human IL-10 administration on 14 cytokines involved in CD pathogenesis (42).

Aside from IBD, which holds the central place as the subject of multiple model-based research, other GI tract-related ADs, such as celiac disease, have been represented by a single model (43). It is similar in principle to the model by Wendelsdorf et al. (34) and

attempts to describe the dynamics of several key immune components and disease progression elements, including gluten deamidation, antigen presentation, T-cell activation, and the formation of auto-antibodies, in the lamina propria. The model was applied to evaluate potential targets for the treatment of celiac disease, among which gluten-peptide analogues showed the strongest effect on antibodies and the villous area, although the clinical efficacy of DQ2 or DQ8 gene analogues remains, to date, unknown (87).

3.4 Nervous system and eyes

Various ADs, including RA, SLE, and MS, might have devastating effects on vision (88–90). However, the eyes themselves can be the target of an autoimmune condition such as, for example, EAU, which has been explored via the means of mathematical modeling by Nicholson et al. (44). Similarly to many other organ-specific autoimmune disorders, EAU is caused by an abnormal influx of effector cells into the target organ. A distinctive feature of EAU, however, is the presence of the blood-retina barrier. Thus, Nicholson et al. developed a minimalistic model of 10 ODEs that describes essential processes of antigen presentation and T-cell activation on both sides of the blood-retina barrier, with corresponding transitions. This allowed the authors to evaluate the impact of permeability on disease state and highlight other factors (*i.e.*, APC production) which may contribute significantly to abnormal inflammation.

The nervous system, comprised of the CNS and the peripheral nervous system, regulates the functionality of organs through the processing of internal and external information conveyed via electrical impulses along an extensive network of nerve endings. MS, a prevalent autoimmune neurological disorder, manifests itself as demyelinating lesions in the CNS (91, 92). From a clinical perspective, MS displays notable heterogeneity, divided among a primarily progressive multiple sclerosis (PPMS) type, which is characterized by a gradual accumulation of clinical disabilities, and a relapsing-remitting multiple sclerosis (RRMS) type, which is characterized by disease exacerbations followed by periods of remission – although often switching to a secondary progressive multiple sclerosis (SPMS) type in the long-term (93, 94). The immune pathophysiology of MS involves bidirectional interactions among peripheral immune cells (T-cells, B-cells, myeloid cells) and resident CNS cells (microglia, astrocytes). For the RRMS type, focal inflammatory demyelination caused by peripheral immune cells infiltrating the CNS is believed to be the cause of relapses, whereas for the progressive type, diffuse tissue damage of white and gray matter is predominant (95).

In their model, Moise and Friedman focused on delineating immune and inflammatory interactions within the focal plaque, quantifying their impact on plaque growth (45). The authors proposed a model based on 23 PDEs encompassing the dynamics of Th, cytotoxic T-cells, Mφ, astrocytes, oligodendrocytes, chemokines, and 8 pro- and anti-inflammatory cytokines. Additionally, 4 PDEs defined the PK of immunomodulators such

as IFN- β , glatiramer acetate, natalizumab, and dimethyl fumarate, which have all been evaluated in the treatment of MS. The authors used the model to explore the effects of these drugs and their combinations; the combination of the first three aforementioned drugs resulted in a decrease in initial plaque volume under specific dose combinations, emphasizing the potential efficacy of drug combinations in MS treatment.

Other modeling studies have adopted a more generalized approach to immune response dynamics (46–48). Vélez de Mendizabal et al., using a system of 6 ODEs, postulated that recurrent dynamics in autoimmunity could arise from failures in cross-regulation mechanisms between regulatory and effector T-cells (Teff), alongside stochastic events triggering the immune response (46). Their model incorporated concepts such as cross-regulation between regulatory and Teff and tissue damage. By introducing reversible and irreversible tissue damage, the model aimed at linking autoimmune activity with clinical relapses in MS patients. Simulations suggested that weakened negative feedback between effector and Treg enabled the immune system to generate characteristic RRMS dynamics without additional environmental triggers.

Another example of a generalized model has been proposed by Kannan et al. (47). It includes 4 ODEs, reflecting inflammatory and anti-inflammatory components, demyelination, and neuronal death in MS. By embedding complex control mechanisms into the equations, the authors were able to identify two key thresholds – one in the immune components and another one in the CNS – that separate distinct dynamical behaviors in the model, classifying disease subtypes *in silico* as RRMS or progressive SPMS/PPMS, based on these thresholds, once exceeded.

Expanding the ways in using mathematical tools to model detailed biological processes, Gross et al. proposed a probabilistic model to predict the differentiation and migration of lymphocyte subsets in the CNS under homeostatic and neuroinflammatory conditions (48). The 7-equation model aimed at reproducing the acquired data on the location and differentiation states of lymphocyte subsets, to provide quantitative assessments of differentiation and transmigration rates and to predict the qualitative behavior of immune-modulating therapies – thereby enabling simulation-based predictions of lymphocyte subset distributions. Validated based on data from patients with somatoform disorders, RRMS patients, and patients undergoing specific treatments, the model demonstrated accuracy in predicting differentiation stages and distribution of lymphocyte subsets under both steady-state conditions and neuroinflammatory diseases such as MS.

Finally, Broome and colleagues attempted to describe MS pathophysiology from a biochemical perspective, using a complex model capable of predicting: interactions between reactive oxygen and nitrogen species; the permeability transition pore; apoptotic factors; and eventual cell death in oligodendrocytes (49). Immune components within the model were represented only at a high level by Mφ, T-cells and several cytokines (IFN- γ , TNF- α , and IL-1), while the main focus of the model was on intracellular molecular processes. The system reflects healthy, diseased, and treated states,

and allows for the identification of trigger points for disease onset and the exploration of potential drug therapies.

3.5 Skin

The skin is an organ constantly exposed to external factors such as injuries and infections that can disrupt the barrier function and initiate a dysregulated immune response, which may, in turn, cause chronic inflammation and autoimmunity. Despite the prevalence of autoimmune skin diseases, only two of them – alopecia areata and atopic dermatitis – have been studied using mechanistic mathematical models (50–55). Although the autoimmune nature of the latter is a matter of debate, the well-known association with multiple ADs and the presence of autoreactive T-cells and autoantibodies provide sufficient evidence for including this atopic dermatitis disorder to this review (96–99).

Atopic dermatitis (also known as eczema) is a chronic disease affecting the upper level of the skin and characterized by persistent skin inflammation. The pathogenesis of dermatitis involves epidermal barriers abnormalities, leading to heterogeneous immunological dysregulations predominantly in type 2 immunity (Th2, IL-4, IL-13, IL-31), but also including varying degrees of upregulation of the Th1 (IFN- γ), Th17 (IL-17), and Th22 axes (IL-22) (100). Tanaka and colleagues published several articles focused on the interplay between the pathogen load, immune response, and the degree of skin barrier integrity to describe recurrent dermatitis flares associated with pathogen levels surpassing certain thresholds (52–55). The model reproduces 4 types of dynamical phenotypes typically observed in patients – recovery, chronic damage, oscillations, and bistability – mirroring different stages of dermatitis severity. The model was applied to evaluate the effects of first-line nonspecific therapies (topical antibiotics, emollients, corticosteroids) on the transition from pathologic to healthy state. The model gradually evolved over time, for example, by introducing multiple subtypes of Th and their effector ILs (IL-4, IL-13, etc.) (55). Another significant augmentation of the modified model was the inclusion of clinical efficacy endpoints – eczema area and severity index (EASI) – which enabled a comparison of the efficacy of multiple anti-IL drugs.

Alopecia areata is an AD that causes the formation of distinct hairless patterns on the scalp or other parts of the body. According to a widely accepted hypothesis, hair loss occurs due to the collapse of the immune privilege of hair follicles under environmental factors, with subsequent migration of autoreactive lymphocytes into the hair bulb (101). A set of modeling studies by Atanaska Dobreva et al. describes the dynamics of autoreactive CD4+ and CD8+ T-cells, immune privilege guardians and IFN- γ involved in the development of alopecia, and the hair follicle growth cycles (50, 51). The developed model succeeds in capturing healthy and pathological states of a subject, highlighting the key role of IFN- γ and immune privilege guardians in disease progression. However, the uniqueness of the triggers and localness of the disease challenges the applicability of this model to other autoimmune disorders.

3.6 Endocrine diseases

The endocrine system is a vital regulator of biological processes, responsible for the development of the nervous system, growth, reproductive function, metabolism, and more (102). As such, autoimmune conditions associated with it usually lead to severe health complications (103).

T1DM is one such disease known from ancient times and considered fatal until the invention of recombinant insulin in the early XXth century (104). The autoimmune response in T1DM is directed primarily towards β -cells in the islets of Langerhans in the pancreas, thereby depriving the organism of insulin hormone, which in turn regulates glucose uptake by tissues. Since recombinant insulin is the primary method of controlling the disease, the majority of mathematical models for this indication are focused on short- and long-term glycemic controls (105, 106). However, two models stand out, in terms of characterizing autoimmune processes relevant for the disease, and beyond insulin-glucose cross-talks (56, 57). Both models contain 5 to 6 ODEs of a highly theoretical nature, which capture the quantities of β -cells, Teff, Tregs, antigen, and other components (either Mφ or IL-2), and they allow for the exploration of the fundamental systems behavior rather than addressing questions specific to drug development. Jaber-Douraki and colleagues highlight the impact of T-cell avidity on disease outcomes in T1DM, whereas Magomedbeze et al. emphasize the crucial role of the balance between Treg and auto-reactive T-cells in diabetes progression.

HT is another example of a relatively common chronic autoimmune condition, affecting the thyroid gland through an infiltration of T- and B-cells (107). Excessively stimulated Th1 cells, Th17 cells, and Tregs play important roles in the pathogenesis of HT (108). Thus, in their work, Salazar-Viedma et al. investigated the immune response mediated by Th1 and Th17 on thyrocytes (3 ODEs) (58). Interestingly, the authors also included gut microbiota into the model (a 4th ODE), thereby linking autoimmunity with the function of the microbiome. Results of the modeling suggest that an imbalance in the intestinal microbiota could lead to an increase in Th17 lymphocyte activity, contributing to the development of HT.

3.7 Lungs

There are two mechanistic models describing autoimmune-related lung diseases, namely pulmonary sarcoidosis and IPF (59–61). It should be noted that the etiology and role of autoimmunity in the development and progression of these diseases are still unknown. However, genetic predisposition and external triggers such as infection, inorganic materials, and environmental factors are likely to lead to the development of an autoimmune response (109–112). Mφ and lymphocytes are key players involved in the initiation of the immune response in the lung, in both indications: Mφ, serving as scavenger cells, ingesting and degrading the inhaled antigenic load, initiate a typical Th1 immune response. Interestingly, both diseases are characterized by a shift from the

M1 (pro-inflammatory) to the M2 (anti-inflammatory) Mφ phenotype, which is considered responsible for the progression from inflammation to interstitial fibrosis in IPF and formation of granulomas in sarcoidosis.

The first model by Hao et al. considers the progression of sarcoidosis in terms of a granuloma radius represented as a conglomerate of Mφ, Th1, Treg and Th17 cells, which affect each other through a network of cytokines and chemokines (IL-2, IL-10, IL-12, IL-13, chemokine ligand 20, IFN- γ , TNF- α and TGF- β) (59, 60). The model shows the beneficial effect of infliximab (anti-TNF- α) and other potential anti-cytokine therapies on the granuloma radius. In subsequent work, the authors investigated the progression of fibrosis in IPF by adding features unique to pulmonary tissue fibrosis, based on their previous model of kidney fibrosis (27, 61). This second model includes two Mφ phenotypes and takes into account the complex geometry of lungs through a system of PDEs, to calculate the effective interactions among model species: Mφ, epithelial and mesenchymal cells, extracellular matrix and molecular profibrotic mediators (TNF- α , TGF- β , PDGF, TIMP). The authors explored the efficacy of four therapies (anti-TNF- α , anti-PDGF, anti-IL13, anti-TGF- β) and showed that only targeting TGF- β should result in a beneficial effect on pulmonary fibrosis.

3.8 Cardiovascular

The heart muscle, just like any other part of the body, is no exception in terms of self-stimulated inflammation and tissue damage. While rare, autoimmune myocarditis can be caused as a side effect incurred by treatment using immune checkpoint inhibitors – a large and effective class of anti-cancer therapies (113, 114). Building up on the historical research of the immune system, Van der Vegt and colleagues pioneered the modeling of checkpoint-induced autoimmune reaction, in an effort to provide an instrument that helps in balancing the benefits and risks of this type of treatment (62). The core of the developed system consists of 4 ODEs, complemented with the pharmacodynamic effects of PD-1 and CTLA-4 inhibitors as explicit functions. The model was subjected to stability and sensitivity analyses. Most importantly, model evaluation results demonstrate that the development of autoimmune myocarditis under treatment with high doses of nivolumab or ipilimumab is practically inevitable, depending on individual patient characteristics reflected in the values of several key model parameters.

3.9 Generalized models of autoimmune processes

Mathematical modeling, by implication, is a transformation of empirical knowledge into a system of cause-consequence relationships using the universal language of mathematics, theoretically applicable to any object or phenomenon. As such, not all models are necessarily associated with specific diseases but

rather focus on the general behavior of immune response components potentially leading to autoimmune disorders. Although mostly qualitative, inferences derived from these models significantly broaden our understanding of interactions within the system of interest and provide a companion tool for further experimental research.

A notable early example of such a mathematical system is the ICMODEL developed by Martha Head et al. (63). This model represents a theoretical interpretation of a mechanism for IC formation, opsonization, and clearance. It consists of 3 sub-modules: (1) production of antibodies and their interaction with antigen (*i.e.*, IC formation); (2) opsonization and clearance of IC; (3) tissue damage and antigen release. The model was explored for consistency with the known behavior of the immune system, evaluated for stability, and then applied to identify processes leading to a substantial rise or oscillations in pathogenic IC concentrations (*e.g.*, impaired antigen efflux, Fc- γ -mediated phagocytosis, complement synthesis). Such a model may be beneficial in understanding the cyclical course of various autoimmune disorders.

Later, Arazi and Neumann developed a more parsimonious model focused on the same spectrum of processes as the ICMODEL; it consists of 3 ODEs reflecting the quantities of autoreactive B-cells, autoantigen, and IC (64). Thorough steady-state, hysteresis, and parameter sensitivity analyses, as well as an evaluation of the different functional relationships was performed, to demonstrate that a positive feedback loop between IC and tissue damage would not be sufficient to drive the system to a pathological state - thereby confirming that the clearance rates of ICs and self-antigens are one of the key factors triggering a clinically impactful autoimmune response.

Another example, similar in principle to the work by Arazi and Neumann, is a minimalistic ODE model by Iwami and colleagues that includes 3 dependent variables: population size of target cells, damaged cells, and immune cells (65). The authors proposed several functional relationships (linear and non-linear) of target cell growth and immune response followed by a stability analysis, to describe mathematically different states of immune tolerance/dormancy and repeated flare-ups.

Further modeling work can be found in a generalized model by Khailaie et al., in a series of studies dedicated to the investigation of T-cell activation (66). However, this paper is centered around disturbances in the delicate balance between Tcon and Tregs leading to autoimmunity. The authors methodically tested different models, starting from the simplest structure with 2 ODEs describing the dynamics of activated T-cells and IL-2 and ending with pathways of Tregs and Tcon renewal rates, activation, proliferation, and reciprocal influences. They derived an antigen-stimulation threshold (*i.e.*, the proliferation rate of activated T-cells depending on the avidity to an antigen) that defines three scenarios of immune response: a complete lack of a response; a first peak followed by complete clearance of the antigen; or the failure of such, which would result in chronic persistence of the antigen, and is primarily defined by the renewal rate of naïve T-cells and resting Tregs.

The balance of T-cells, although Th1 and Th2 instead of Tcon and Tregs, is the subject of another model-based analysis, performed by Louzoun et al. (67). This work, published in 2001, thoroughly explores mathematical system that includes 5 cell types (Th1, Th2, Mφ, naïve T-cells, and pooled Teff and Treg) and 3 types of cytokines, aggregated by associated cells (Th1, Th2, or Mφ), to characterize the transition from healthy condition (designated as Th2 steady-state) to autoimmunity (designated as Th1 steady-state). Although the rationale behind the model is based on the preclinical observations (*i.e.*, insulin-dependent diabetes and experimental autoimmune encephalomyelitis mouse models), proposed model is positioned as qualitative investigation of Th1-mediated autoimmune diseases.

Another aspect of autoimmune disease onset, namely immune response to self-antigen caused by cross-reactivity to viral antigen, was investigated by Hara and Iwasa using a model in 4 ODEs, which reflects the kinetics of Th-cells (reactive to self-antigen or viral infection), viral antigen, and memory T-cells (68). As in the case of previous qualitative model, characterization of general patterns in the dynamics of the system through sensitivity analysis, including the evaluation of autoimmune response relative to the different modes of cross-immunity, rather than qualitative predictions of the treatment-related effects was the focus of this research.

Continuing the thread of qualitative models, the study by Machado Ramos et al. considers three cell populations associated with autoimmune response – self-APCs, self-reactive T-cells, and immunosuppressive cells (69). The model was developed using a combination of integro-differential equations and ODEs to track the total number of cells within each population and their respective functional states and tested for robustness. Sensitivity analysis of the model highlights the critical roles of proliferation of immunosuppressive cell, destruction of self-APC and self-reactive T-cell, and the tolerance of self-reactive T-cells to self-antigens in regulating autoimmune responses effectively.

The last piece of modeling work evaluated in this section is devoted to the mathematical description of two generic, inter-dependent immune cell populations, mutually regulating one another *via* cytokine production (70). The interactions between the two cytokine production profiles reflect the point of a synergistic balance, where both cell populations reach equilibrium. An exhaustive screening of possible parameter values revealed that an AD may occur when the alteration of the feedback between immune cells results in hyper-induced homeostasis or a loss of stability in the system, leading to oscillations or trigger-based inflammatory disease phenotypes.

4 Discussion

Mathematical modeling in drug development is an essential tool necessary to transform heterogeneous experimental data from numerous sources into a system of quantitative knowledge, with an ultimate goal of facilitating the delivery of innovative therapies to patients. The indispensability of this tool is especially noticeable in therapeutic areas such as ADs, with non-trivial diversity in

pathogenesis, etiology, manifestations, and the associated plethora of unanswered questions related to drug development. Among modeling methods, empirical PK/PD models first introduced in the 1970s and focused on the direct assessment of the dose-concentration-effect relationship can be considered as the most established and frequently used models (115, 116). In ADs, this type of research has been pioneered by Brooks et al., with a model-based investigation of the clinical effects of concomitant use of indomethacin and furosemide in RA patients (117). Since then, the number of publications that could be attributed towards PK/PD modeling in ADs grew almost exponentially (Figure 1A). However, the utility of empirical models can be limited by their simplicity, whereas multiple drug R&D questions, such as target selection, animal-to-human translation, and others, require an in-depth analysis of the underlying biological mechanisms (16, 17).

This is where mechanistic models may come into play. These models represent a slice of knowledge in selected disease areas, and, therefore, first understanding the scope of a given endeavor in this field is important, to focus the efforts of subsequent research – which is the main purpose of this review. In our systematic search and curation, we identified 38 mechanistic models of ADs across 47 publications. While it is challenging to define the fine line between mechanistic and non-mechanistic models, in this paper, we attributed models to the former category if they contained a description of autoimmune processes at any level of generalization, regardless of the mathematical method used or the number of equations featured. It is worth noting that the majority of the identified models (>70%) are expressed as ODEs, similarly to most systems pharmacology models, with a minimum of 3 equations being featured in their structure (Figure 1C) (118). In addition to ODE models, two groups of models featuring PDEs were found, with a distinct focus on tissue remodeling: a set of publications by Wenrui Hao and colleagues (27, 28, 60, 61), examining kidney and lung fibrosis, and models of plaque growth in MS and cartilage degradation in RA, by Moise and Friedman (31, 45). A Boolean model was developed by Ruiz-Cerdá and colleagues, to describe the antigen presentation process in lupus (24), and another Boolean model with subsequent ODE extensions, by Balbas-Martinez et al., was identified for IBD (41, 42). Finally, a unique probabilistic (Markov jump processes) model by Catharina Gross and colleagues was developed, to capture the differentiation and migration of lymphocyte subsets to CNS (48).

The number of publications related to mechanistic modeling is overall markedly smaller as compared to PK/PD modeling studies, with a slower and shallower increase over time (Figure 1A), which could be explained by the time and efforts, as well as the high expertise in immunology required, to build such models. Interestingly, while the search contained more than 180 terms for different ADs (see **Supplementary Materials**), only models for 13 disease-specific were identified by the search, with models for 2 systemic conditions (SLE and RA) and 11 for organ-specific indications (Figure 1B). Hence, the mechanisms for more than 150 other ADs, such as psoriasis, systemic sclerosis, involvement of the urinary system and Sjogren's syndrome, are not covered by the currently available mathematical modeling literature, and thus

present a high opportunity for further research. However, the biological entities embedded in the identified models are all linked to the immune response and are thus expected to overlap in these other ADs. Indeed, the analysis of variables and their interactions among currently available models revealed several common clusters (Figure 2).

Approximately 1/3 of the models included antigens, in a broad sense (e.g., pathogen load, commensal bacteria, damaged tissue), as a dependent variable, which is not surprising considering ADs are characterized by responses to self-antigen or may be triggered *via* external microorganisms. A similar frequency of occurrence in the models was observed for Tregs, important gatekeepers of the immune system that inhibit the activation and expansion of Th, cytotoxic T-cells and B-cells. Their role has been extensively described in SLE, RA and MS (119). Overall, most of the models explored T-cell-mediated immune response with an emphasis on Th, with a different degree of generalization (*i.e.*, either by pooling different subtypes of cells into generic variables or by considering them individually). In contrast, autoreactive cytotoxic T lymphocytes characterized by cytolytic activities against target cells are under-represented in the models and are often lumped together into effector T-cell variables. Other types of lymphocytes are modeled only in isolated cases, even in ADs classified as B-cell-mediated or antibody-driven pathologies, such as SLE (120).

In addition to featuring immune cells, the models cover a wide range of pro- and anti-inflammatory ILs as a critical part of cross-regulation, proliferation, and polarization of Th subtypes. For example, 6 out of 36 models incorporate the connection between IL-2 and Tregs, as well as IFN- γ and Th1. Furthermore, cytokines with well-established roles in AD progression (e.g., TNF- α , IL-6, IL-23, etc.) and respective therapeutic interventions are also frequently included in the models. Despite this, none of them contain type I IFN (e.g., IFN- α or IFN- β), although its substantial role has been highlighted in several ADs, including SLE, where multiple approved or developing therapies are designed to block the type I IFN-inducible pathway of inflammation.

Lastly, tissue damage or fibrosis is also frequently modeled, as a final outcome of AD progression. In Figure 2, tissue scarring is associated with a cluster of M ϕ , GM-CSF, and a lumped term “fibrosis” that includes MMPs, elements of the extracellular matrix, fibroblasts, and several growth factors (e.g., TGF- β , PFG, PDGF). Tissue damage is either modeled as a generic variable or through a number of organ-specific cells, *e.g.*, thyrocytes in HT. It is worth noting that the main mechanisms of tissue damage, consisting of cytotoxic activity of autoreactive CD8+ T-cells and IC-related activation of complement system, are missing in these models, with few exceptions that link IC to cell death.

While mathematical modeling is an essential tool to support decision-making, the practical value of a particular model for drug development is defined by the adherence to good modeling practices and is inherently limited by the underlying assumptions (121). The latter is directly tied to the data used for model development and calibration. About 40% of the identified models were built around clinical data only, whereas practically 29% of models additionally involved animal data, when information in

human was lacking or scarce (Figure 1D). Mixing such different types of data may be a sensitive subject to perform model inference, and it calls for further verification of the similarities in immune mechanisms across species, as a distinct direction for future analyses (122, 123). Among good modeling practices, several key components could be named, *e.g.*, extensive model calibration and evaluation, including identifiability analyses, external validation, sensitivity analyses, and more (124). Several models, *e.g.*, the works of Gao et al. (29), Nakada and Mager (32), Rogers et al. (39, 40), and Miyano et al. (55) feature a broad array of these technical model-based analyses. Furthermore, these models attempt to incorporate subject inter-individual variability through the means of generating realistic virtual populations; they also consider realistic PK models of the compounds, driving the effects, which greatly expands the applicability of such models to real-world scenarios. These models may be considered as an exception, since the remaining models discussed here do not rely on parameter identifiability, extensive model diagnostics or advanced simulations. In fact, nearly a quarter of all models considered in this review operate as a system without a direct link to the observed time series of laboratory measurements (Figure 1D) and do not make use of external validation techniques (Table 1). This may be explained by differences in the relevant questions that motivate the development of such models. For example, modeling studies classified as describing general autoimmune reactions as well as several others are built to explore mathematical systems with specific behaviors, through an analysis of stability and phase portraits (*e.g.*, to describe periodical nature of flares) (64, 66). Likewise, many models are primarily developed to perform a sensitivity analysis, with parameter values assumed or fine-tuned manually (65, 70). As a result, the potential impact of such models can be limited to mechanistic hypothesis generation and target validation. Because of that reason, our search was restricted to the PubMed database, which specifically indexes biomedical and life sciences journals. As such, it should be mentioned that the total number of published model-based analyses of autoimmune processes exceeds those discussed in detail in this review *e.g.*, (125–131). However, the focus of these studies lies primarily in the analysis of specific patterns of mathematical systems, their phase trajectories, steady-states, etc., rarely informed by the large quantities of clinical data and thereby, while providing important insights into theoretical behavior of the immune system, have limited practical applicability in model-informed drug development.

In summary, the applicability of current mechanistic models of ADs in drug development could be limited by several factors. Firstly, the lack of evaluation of model performance against the observed clinical data, including the assessment of uncertainty in model parameters and the validation against independent data, results in qualitative predictions of system behavior rather than quantitative ones. Secondly, most existing models do not incorporate PK submodules to describe drug exposure in target compartments over time. Furthermore, some components of the immune system are under-represented or simply are lacking in the available models. For instance, current treatment options for SLE

are focused primarily in three areas: disrupting type I IFN-mediated inflammation, targeting B-cell response, and inhibiting intracellular signaling; none of which are among the modeled immune components (15). Finally, to provide insight into an actual clinical benefit, the models should strive to incorporate clinical endpoints. Currently available models are built upon inferences around surrogate biomarkers or generic variables (*e.g.*, tissue damage or fibrosis), with a single exception by Miyano et al. (55), where the EASI endpoint was described as a function of skin barrier integrity and infiltrated pathogens.

This analysis follows the requirements of a robust systematic review, with documented sources and search queries, and, to our knowledge, is a unique venture to comprehensively identify and categorize existing mechanistic models of ADs. It should not be viewed as an objective effort to qualify the formidable effort that each of the analyzed models represents, as the value of modeling is always relative to its aim. Rather, it is an attempt to draw a landscape of the ever-evolving quantitative knowledge on ADs in the form of mathematical models to define the most desirable paths of moving forward in relation to drug development. In this context, the amount of robust QSP models, with extensive model calibration and evaluation and built on clinical data, while maintaining a delicate balance between the available data and model complexity, is significantly lacking in the considered disease domain. This gap is further broadened by the emergence of new therapeutic modalities (*e.g.*, chimeric antigen receptor T-cell), not yet covered by these existing models (132). Taken together, these results highlight the necessity and aspiration to enhance proactiveness and efforts in mechanistic quantitative analyses in the intricate therapeutic area of ADs, to facilitate the development of novel therapeutics.

Author contributions

YU: Data curation, Formal Analysis, Investigation, Methodology, Software, Visualization, Writing – original draft. AN: Formal Analysis, Investigation, Writing – original draft. CL: Formal Analysis, Investigation, Methodology, Visualization, Writing – original draft. GH: Writing – review & editing. KP: Funding acquisition, Resources, Writing – review & editing. VS: Conceptualization, Methodology, Project administration, Supervision, Writing – review & editing. AV: Conceptualization, Funding acquisition, Methodology, Project administration, Supervision, Validation, Writing – original draft, Writing – review & editing.

Funding

The author(s) declare financial support was received for the research, authorship, and/or publication of this article. This work was supported by the Academic leadership program Priority 2030 proposed by the Federal State Autonomous Educational Institution of Higher Education I.M. Sechenov First Moscow State Medical

University of the Ministry of Health of the Russian Federation (Sechenov University), the Ministry of Science and Higher Education of the Russian Federation (Agreement 075-10-2021-093, Project MMD-RND-2266), Russian Science Foundation (Grant Number 23-71-10051) and Modeling & Simulation Decisions FZ -LLC, Dubai, UAE.

Conflict of interest

Author GH was employed by the company Biorchestra Co., Ltd. Authors CL, KP, VS, and AV were employed by the company Modeling and Simulation Decisions FZ-LLC.

The remaining authors declare that the research was conducted in the absence of any commercial or financial relationships that could be construed as a potential conflict of interest.

References

1. Lerner A, Jeremias P, Matthias T. The world incidence and prevalence of autoimmune diseases is increasing. *Int J Celiac Dis.* (2015) 3:151–5. doi: 10.12691/ijcd-3-4-8
2. Pisetsky DS. Pathogenesis of autoimmune disease. *Nat Rev Nephrol.* (2023) 19:509–24. doi: 10.1038/s41581-023-00720-1
3. Wang L, Wang F-S, Gershwin ME. Human autoimmune diseases: a comprehensive update. *J Intern Med.* (2015) 278:369–95. doi: 10.1111/joim.12395
4. Fugger L, Jensen LT, Rossjohn J. Challenges, progress, and prospects of developing therapies to treat autoimmune diseases. *Cell.* (2020) 181:63–80. doi: 10.1016/j.cell.2020.03.007
5. Villalta D, Tozzoli R, Tonutti E, Bizzaro N. The laboratory approach to the diagnosis of autoimmune diseases: is it time to change? *Autoimmun Rev.* (2007) 6:359–65. doi: 10.1016/j.autrev.2007.01.009
6. Ascherio A, Munger KL. EBV and autoimmunity. *Curr Top Microbiol Immunol.* (2015) 390:365–85. doi: 10.1007/978-3-319-22822-8_15
7. Cunningham MW. Molecular mimicry, autoimmunity, and infection: the cross-reactive antigens of group A streptococci and their sequelae. *Microbiol Spectr.* (2019) 7 (4). doi: 10.1128/microbiolspec.GPP3-0045-2018
8. Trier NH, Houen G. Antibody cross-reactivity in auto-immune diseases. *Int J Mol Sci.* (2023) 24:13609. doi: 10.3390/ijms241713609
9. Lang KS, Burow A, Kurrer M, Lang PA, Recher M. The role of the innate immune response in autoimmune disease. *J Autoimmun.* (2007) 29:206–12. doi: 10.1016/j.jaut.2007.07.018
10. Deane KD. Preclinical rheumatoid arthritis (Autoantibodies): an updated review. *Curr Rheumatol Rep.* (2014) 16:419. doi: 10.1007/s11926-014-0419-6
11. Rosenblum MD, Remedios KA, Abbas AK. Mechanisms of human autoimmunity. *J Clin Invest.* (2015) 125:2228–33. doi: 10.1172/JCI78088
12. Bach JF. Immunosuppressive therapy of autoimmune diseases. *Immunol Today.* (1993) 14:322–6. doi: 10.1016/0167-5699(93)90053-N
13. Cipriani P, Ruscitti P, Carubbi F, Liakouli V, Giacomelli R. Methotrexate: an old new drug in autoimmune disease. *Expert Rev Clin Immunol.* (2014) 10:1519–30. doi: 10.1586/1744666X.2014.962996
14. Dropulic LK, Lederman HM. Overview of infections in the immunocompromised host. *Microbiol Spectr.* (2016) 4(4). doi: 10.1128/microbiolspec.dmh2-0026-2016
15. Jung SM, Kim W-U. Targeted immunotherapy for autoimmune disease. *Immune Netw.* (2022) 22:e9. doi: 10.4110/in.2022.22.e9
16. Bradshaw EL, Spilker ME, Zang R, Bansal L, He H, Jones RDO, et al. Applications of quantitative systems pharmacology in model-informed drug discovery: perspective on impact and opportunities. *CPT Pharmacomet Syst Pharmacol.* (2019) 8:777–91. doi: 10.1002/psp4.12463
17. Felmlee MA, Morris ME, Mager DE. Mechanism-based pharmacodynamic modeling. *Methods Mol Biol Clifton NJ.* (2012) 929:583–600. doi: 10.1007/978-1-62703-050-2_21
18. Zhang L, Pfister M, Meibohm B. Concepts and challenges in quantitative pharmacology and model-based drug development. *AAPS J.* (2008) 10:552–9. doi: 10.1208/s12248-008-9062-3
19. Madabushi R, Seo P, Zhao L, Tegenge M, Zhu H. Review: role of model-informed drug development approaches in the lifecycle of drug development and regulatory decision-making. *Pharm Res.* (2022) 39:1669–80. doi: 10.1007/s11095-022-03288-w
20. Morgan P, Brown DG, Lennard S, Anderton MJ, Barrett JC, Eriksson U, et al. Impact of a five-dimensional framework on R&D productivity at AstraZeneca. *Nat Rev Drug Discovery.* (2018) 17:167–81. doi: 10.1038/nrd.2017.244
21. Autoimmune Disease List. *Glob Autoimmune Inst.* Available online at: <https://www.autoimmuneinstitute.org/resources/autoimmune-disease-list/> (Accessed December 13, 2023).
22. R: The R Project for Statistical Computing. Available online at: <https://www.r-project.org/> (Accessed December 13, 2023).
23. igraph – Network analysis software. Available online at: <https://igraph.org/> (Accessed December 25, 2023).
24. Ruiz-Cerdá ML, Irurzun-Arana I, González-García I, Hu C, Zhou H, Vermeulen A, et al. Towards patient stratification and treatment in the autoimmune disease lupus erythematosus using a systems pharmacology approach. *Eur J Pharm Sci Off J Eur Fed Pharm Sci.* (2016) 94:46–58. doi: 10.1016/j.ejps.2016.04.010
25. Yazdani A, Bahrami F, Pourgholamnejad A, Moghadasli R. A biological and a mathematical model of SLE treated by mesenchymal stem cells covering all the stages of the disease. *Theory Biosci Theor Den Biowissenschaften.* (2023) 142:167–79. doi: 10.1007/s12064-023-00390-4
26. Budu-Grădeanu P, Schugart RC, Friedman A, Birmingham DJ, Rovin BH. Mathematical framework for human SLE Nephritis: disease dynamics and urine biomarkers. *Theor Biol Med Model.* (2010) 7:14. doi: 10.1186/1742-4682-7-14
27. Hao W, Rovin BH, Friedman A. Mathematical model of renal interstitial fibrosis. *Proc Natl Acad Sci.* (2014) 111:14193–8. doi: 10.1073/pnas.1413970111
28. Karagiannis G, Hao W, Lin G. Calibrations and validations of biological models with an application on the renal fibrosis. *Int J Numer Methods BioMed Eng.* (2020) 36: e3329. doi: 10.1002/cnm.3329
29. Gao X, He J, Sun X, Li F. Dynamically modeling the effective range of IL-2 dosage in the treatment of systemic lupus erythematosus. *iScience.* (2022) 25:104911. doi: 10.1016/j.isci.2022.104911
30. Rullmann J a C, Struemper H, Defranoux NA, Ramanujan S, Meeuwisse CML, van Elsas A. Systems biology for battling rheumatoid arthritis: application of the Entelos PhysioLab platform. *Syst Biol.* (2005) 152:256–62. doi: 10.1049/ip-syb:20050053
31. Moise N, Friedman A. Rheumatoid arthritis - a mathematical model. *J Theor Biol.* (2019) 461:17–33. doi: 10.1016/j.jtbi.2018.10.039
32. Nakada T, Mager DE. Systems model identifies baseline cytokine concentrations as potential predictors of rheumatoid arthritis inflammatory response to biologics. *Br J Pharmacol.* (2022) 179:4063–77. doi: 10.1111/bph.15845
33. Meyer-Hermann M, Figge MT, Straub RH. Mathematical modeling of the circadian rhythm of key neuroendocrine-immune system players in rheumatoid arthritis: a systems biology approach. *Arthritis Rheum.* (2009) 60:2585–94. doi: 10.1002/art.24797
34. Wendelsdorf K, Bassaganya-Riera J, Hontecillas R, Eubank S. Model of colonic inflammation: immune modulatory mechanisms in inflammatory bowel disease. *J Theor Biol.* (2010) 264:1225–39. doi: 10.1016/j.jtbi.2010.03.027

Publisher's note

All claims expressed in this article are solely those of the authors and do not necessarily represent those of their affiliated organizations, or those of the publisher, the editors and the reviewers. Any product that may be evaluated in this article, or claim that may be made by its manufacturer, is not guaranteed or endorsed by the publisher.

Supplementary material

The Supplementary Material for this article can be found online at: <https://www.frontiersin.org/articles/10.3389/fimmu.2024.1371620/full#supplementary-material>

35. Lo W-C, Arsenescu RI, Friedman A. Mathematical model of the roles of T cells in inflammatory bowel disease. *Bull Math Biol.* (2013) 75:1417–33. doi: 10.1007/s11538-013-9853-2

36. Lo W-C, Arsenescu V, Arsenescu RI, Friedman A. Inflammatory bowel disease: how effective is TNF- α Suppression? *PLoS One.* (2016) 11:e0165782. doi: 10.1371/journal.pone.0165782

37. Park A, Kim S, Jung IH, Byun JH. An immune therapy model for effective treatment on inflammatory bowel disease. *PLoS One.* (2020) 15:e0238918. doi: 10.1371/journal.pone.0238918

38. Dwivedi G, Fitz L, Hegen M, Martin SW, Harrold J, Heatherington A, et al. A multiscale model of interleukin-6-mediated immune regulation in Crohn's disease and its application in drug discovery and development. *CPT Pharmacomet Syst Pharmacol.* (2014) 3:e89. doi: 10.1038/psp.2013.64

39. Rogers KV, Martin SW, Bhattacharya I, Singh RSP, Nayak S. A dynamic quantitative systems pharmacology model of inflammatory bowel disease: part 1 - model framework. *Clin Transl Sci.* (2021) 14:239–48. doi: 10.1111/cts.12849

40. Rogers KV, Martin SW, Bhattacharya I, Singh RSP, Nayak S. A dynamic quantitative systems pharmacology model of inflammatory bowel disease: part 2 - application to current therapies in crohn's disease. *Clin Transl Sci.* (2021) 14:249–59. doi: 10.1111/cts.12850

41. Balbas-Martinez V, Ruiz-Cerdá L, Irurzun-Arana I, González-García I, Vermeulen A, Gómez-Mantilla JD, et al. A systems pharmacology model for inflammatory bowel disease. *PLoS One.* (2018) 13:e0192949. doi: 10.1371/journal.pone.0192949

42. Balbas-Martinez V, Asin-Prieto E, Parra-Guillen ZP, Troconiz IF. A quantitative systems pharmacology model for the key interleukins involved in crohn's disease. *J Pharmacol Exp Ther.* (2020) 372:299–307. doi: 10.1124/jpet.119.260539

43. Demin OO, Smirnov SV, Sokolov VV, Cucurull-Sánchez L, Pichardo-Almarza C, Flores MV, et al. Modeling of celiac disease immune response and the therapeutic effect of potential drugs. *BMC Syst Biol.* (2013) 7:56. doi: 10.1186/1752-0509-7-56

44. Nicholson D, Kerr EC, Jepps OG, Nicholson LB. Modelling experimental uveitis: barrier effects in autoimmune disease. *Inflammation Res Off J Eur Histamine Res Soc Al.* (2012) 61:759–73. doi: 10.1007/s00011-012-0469-z

45. Moise N, Friedman A. A mathematical model of the multiple sclerosis plaque. *J Theor Biol.* (2021) 512:110532. doi: 10.1016/j.jtbi.2020.110532

46. Vélez de Mendizábal N, Carneiro J, Solé RV, Goñi J, Bragard J, Martínez-Forero I, et al. Modeling the effector - regulatory T cell cross-regulation reveals the intrinsic character of relapses in Multiple Sclerosis. *BMC Syst Biol.* (2011) 5:114. doi: 10.1186/1752-0509-5-114

47. Kannan V, Kiani NA, Piehl F, Tegnér J. A minimal unified model of disease trajectories captures hallmarks of multiple sclerosis. *Math Biosci.* (2017) 289:1–8. doi: 10.1016/j.mbs.2017.03.006

48. Gross CC, Pawlitzki M, Schulte-Mecklenbeck A, Rolfes L, Ruck T, Hundehege P, et al. Generation of a model to predict differentiation and migration of lymphocyte subsets under homeostatic and CNS autoinflammatory conditions. *Int J Mol Sci.* (2020) 21:2046. doi: 10.3390/ijms21062046

49. Broome TM, Coleman RA. A mathematical model of cell death in multiple sclerosis. *J Neurosci Methods.* (2011) 201:420–5. doi: 10.1016/j.jneumeth.2011.08.008

50. Dobreva A, Paus R, Cogan NG. Mathematical model for alopecia areata. *J Theor Biol.* (2015) 380:332–45. doi: 10.1016/j.jtbi.2015.05.033

51. Dobreva A, Paus R, Cogan NG. Analysing the dynamics of a model for alopecia areata as an autoimmune disorder of hair follicle cycling. *Math Med Biol JMA.* (2018) 35:387–407. doi: 10.1093/imammb/dqx009

52. Tanaka G, Domínguez-Hüttlinger E, Christodoulides P, Aihara K, Tanaka RJ. Bifurcation analysis of a mathematical model of atopic dermatitis to determine patient-specific effects of treatments on dynamic phenotypes. *J Theor Biol.* (2018) 448:66–79. doi: 10.1016/j.jtbi.2018.04.002

53. Domínguez-Hüttlinger E, Christodoulides P, Miyauchi K, Irvine AD, Okada-Hatakeyama M, Kubo M, et al. Mathematical modeling of atopic dermatitis reveals “double-switch” mechanisms underlying 4 common disease phenotypes. *J Allergy Clin Immunol.* (2017) 139:1861–1872.e7. doi: 10.1016/j.jaci.2016.10.026

54. Christodoulides P, Hirata Y, Domínguez-Hüttlinger E, Danby SG, Cork MJ, Williams HC, et al. Computational design of treatment strategies for proactive therapy on atopic dermatitis using optimal control theory. *Philos Transact A Math Phys Eng Sci.* (2017) 375:20160285. doi: 10.1098/rsta.2016.0285

55. Miyano T, Irvine AD, Tanaka RJ. A mathematical model to identify optimal combinations of drug targets for dupilumab poor responders in atopic dermatitis. *Allergy.* (2022) 77:582–94. doi: 10.1111/all.14870

56. Magomedzade G, Nduru P, Bhunu CP, Mushayabasa S. Mathematical modelling of immune regulation of type 1 diabetes. *Biosystems.* (2010) 102:88–98. doi: 10.1016/j.biosystems.2010.07.018

57. Jaber-Douraki M, Pietropaolo M, Khadra A. Continuum model of T-cell avidity: Understanding autoreactive and regulatory T-cell responses in type 1 diabetes. *J Theor Biol.* (2015) 383:93–105. doi: 10.1016/j.jtbi.2015.07.032

58. Salazar-Viedma M, Vergaño-Salazar JG, Pastenes L, D'Afonseca V. Simulation model for hashimoto autoimmune thyroiditis disease. *Endocrinology.* (2021) 162: bqb190. doi: 10.1210/endcr/bqb190

59. Aguda BD, Marsh CB, Thacker M, Crouser ED. An in silico modeling approach to understanding the dynamics of sarcoidosis. *PLoS One.* (2011) 6:e19544. doi: 10.1371/journal.pone.0019544

60. Hao W, Crouser ED, Friedman A. Mathematical model of sarcoidosis. *Proc Natl Acad Sci U.S.A.* (2014) 111:16065–70. doi: 10.1073/pnas.1417789111

61. Hao W, Marsh C, Friedman A. A mathematical model of idiopathic pulmonary fibrosis. *PLoS One.* (2015) 10:e0135097. doi: 10.1371/journal.pone.0135097

62. van der Vegt SA, Polonchuk L, Wang K, Waters SL, Baker RE. Mathematical modelling of autoimmune myocarditis and the effects of immune checkpoint inhibitors. *J Theor Biol.* (2022) 537:111002. doi: 10.1016/j.jtbi.2021.111002

63. Head M, Meryhew N, Runquist O. Mechanism and computer simulation of immune complex formation, opsonization, and clearance. *J Lab Clin Med.* (1996) 128:61–74. doi: 10.1016/s0022-2143(96)90114-6

64. Arazi A, Neumann AU. Modeling immune complex-mediated autoimmune inflammation. *J Theor Biol.* (2010) 267:426–36. doi: 10.1016/j.jtbi.2010.08.033

65. Iwami S, Takeuchi Y, Miura Y, Sasaki T, Kajiwara T. Dynamical properties of autoimmune disease models: tolerance, flare-up, dormancy. *J Theor Biol.* (2007) 246:646–59. doi: 10.1016/j.jtbi.2007.01.020

66. Khailaie S, Bahrami F, Janahmadi M, Milanez-Almeida P, Huehn J, Meyer-Hermann M. A mathematical model of immune activation with a unified self-nonself concept. *Front Immunol.* (2013) 4:474. doi: 10.3389/fimmu.2013.00474

67. Louzoun Y, Atlan H, Cohen IR. Modeling the influence of TH1- and TH2-type cells in autoimmune diseases. *J Autoimmun.* (2001) 17:311–21. doi: 10.1006/jaut.2001.0508

68. Hara A, Iwasa Y. Autoimmune diseases initiated by pathogen infection: Mathematical modeling. *J Theor Biol.* (2020) 498:110296. doi: 10.1016/j.jtbi.2020.110296

69. Ramos MPM, Ribeiro C, Soares AJ. A kinetic model of T cell autoreactivity in autoimmune diseases. *J Math Biol.* (2019) 79:2005–31. doi: 10.1007/s00285-019-01418-4

70. Valeev NV, Hundhausen C, Umezawa Y, Kotov NV, Williams G, Clop A, et al. A systems model for immune cell interactions unravels the mechanism of inflammation in human skin. *PLoS Comput Biol.* (2010) 6:e1001024. doi: 10.1371/journal.pcbi.1001024

71. Lisnevskaya L, Murphy G, Isenberg D. Systemic lupus erythematosus. *Lancet Lond Engl.* (2014) 384:1878–88. doi: 10.1016/S0140-6736(14)60128-8

72. Tsokos GC. Systemic lupus erythematosus. *N Engl J Med.* (2011) 365:2110–21. doi: 10.1056/NEJMra1100359

73. Mok CC, Lau CS. Pathogenesis of systemic lupus erythematosus. *J Clin Pathol.* (2003) 56:481–90. doi: 10.1136/jcp.56.7.481

74. Smolen JS, Aletaha D, McInnes IB. Rheumatoid arthritis. *Lancet Lond Engl.* (2016) 388:2023–38. doi: 10.1016/S0140-6736(16)30173-8

75. Angelotti F, Parma A, Cafaro G, Capecci R, Alunno A, Puxeddu I. One year in review 2017: pathogenesis of rheumatoid arthritis. *Clin Exp Rheumatol.* (2017) 35:368–78.

76. Edilova MI, Akram A, Abdul-Sater AA. Innate immunity drives pathogenesis of rheumatoid arthritis. *BioMed J.* (2021) 44:172–82. doi: 10.1016/j.bj.2020.06.010

77. Kondo N, Kuroda T, Kobayashi D. Cytokine networks in the pathogenesis of rheumatoid arthritis. *Int J Mol Sci.* (2021) 22:10922. doi: 10.3390/ijms222010922

78. Ben Mrid R, Bouchmaa N, Ainani H, El Fatimy R, Malka G, Mazini L. Anti-rheumatoid drugs advancements: New insights into the molecular treatment of rheumatoid arthritis. *BioMed Pharmacother.* (2022) 151:113126. doi: 10.1016/j.biopharm.2022.113126

79. Polmar SH. New drugs for rheumatoid arthritis: The industry point of view. *Reumatol Clinica.* (2010) 6:3–4. doi: 10.1016/j.reuma.2009.10.002

80. Entelos Inc. - CMOCRO. Domain Name . Available online at: <http://www.cmocro.com/> (Accessed December 25, 2023)

81. Cojocaru M, Cojocaru IM, Silosi I, Vrabie CD. Gastrointestinal manifestations in systemic autoimmune diseases. *Mædica.* (2011) 6:45–51.

82. Kunovský L, Dite P, Jabandziev P, Kala Z, Vaculova J, Andrasina T, et al. Autoimmune diseases of digestive organs—A multidisciplinary challenge: A focus on hepatopancreatobiliary manifestation. *J Clin Med.* (2021) 10:5796. doi: 10.3390/jcm10245796

83. An J, Liu Y, Wang Y, Fan R, Hu X, Zhang F, et al. The role of intestinal mucosal barrier in autoimmune disease: A potential target. *Front Immunol.* (2022) 13:871713. doi: 10.3389/fimmu.2022.871713

84. Xu X-R, Liu C-Q, Feng B-S, Liu Z-J. Dysregulation of mucosal immune response in pathogenesis of inflammatory bowel disease. *World J Gastroenterol.* (2014) 20:3255–64. doi: 10.3748/wjg.v20.i12.3255

85. Shahini A, Shahini A. Role of interleukin-6-mediated inflammation in the pathogenesis of inflammatory bowel disease: focus on the available therapeutic approaches and gut microbiome. *J Cell Commun Signal.* (2023) 17:55–74. doi: 10.1007/s12079-022-00695-x

86. Allen RJ, Rieger TR, Musante CJ. Efficient generation and selection of virtual populations in quantitative systems pharmacology models. *CPT Pharmacomet Syst Pharmacol.* (2016) 5:140–6. doi: 10.1002/psp.412063

87. Alhassan E, Yadav A, Kelly CP, Mukherjee R. Novel nondietary therapies for celiac disease. *Cell Mol Gastroenterol Hepatol.* (2019) 8:335–45. doi: 10.1016/j.jcmgh.2019.04.017

88. Petzold A, Balcer LJ, Calabresi PA, Costello F, Frohman TC, Frohman EM, et al. Retinal layer segmentation in multiple sclerosis: a systematic review and meta-analysis. *Lancet Neurol.* (2017) 16:797–812. doi: 10.1016/S1474-4422(17)30278-8

89. Conigliaro P, Cesareo M, Chimenti MS, Triggiani P, Canofari C, Barbato C, et al. Take a look at the eyes in Systemic Lupus Erythematosus: A novel point of view. *Autoimmun Rev.* (2019) 18:247–54. doi: 10.1016/j.autrev.2018.09.011

90. Reddy AK, Kolfenbach JR, Palestine AG. Ocular manifestations of rheumatoid arthritis. *Curr Opin Ophthalmol.* (2022) 33:551–6. doi: 10.1097/ICU.0000000000000890

91. Compston A, Coles A. Multiple sclerosis. *Lancet.* (2008) 372:1502–17. doi: 10.1016/S0140-6736(08)61620-7

92. Barkhane Z, Elmadi J, Satish Kumar L, Pugalenti LS, Ahmad M, Reddy S. Multiple sclerosis and autoimmunity: A veiled relationship. *Cureus.* (2022) 14:e24294. doi: 10.7759/cureus.24294

93. Filippi M, Bar-Or A, Piehl F, Preziosa P, Solari A, Vukusic S, et al. Multiple sclerosis. *Nat Rev Dis Primer.* (2018) 4:43. doi: 10.1038/s41572-018-0041-4

94. Bennett JL, Stüve O. Update on inflammation, neurodegeneration, and immunoregulation in multiple sclerosis: therapeutic implications. *Clin Neuropharmacol.* (2009) 32:121–32. doi: 10.1097/WNF.0b013e3181880359

95. Greiner T, Kipp M. What guides peripheral immune cells into the central nervous system? *Cells.* (2021) 10:2041. doi: 10.3390/cells10082041

96. Mothes N, Niggemann B, Jenneck C, Hagemann T, Weidinger S, Bieber T, et al. The cradle of IgE autoreactivity in atopic eczema lies in early infancy. *J Allergy Clin Immunol.* (2005) 116:706–9. doi: 10.1016/j.jaci.2005.06.025

97. Roesner LM, Werfel T. Autoimmunity (or not) in atopic dermatitis. *Front Immunol.* (2019) 10:2128. doi: 10.3389/fimmu.2019.02128

98. Tang TS, Bieber T, Williams HC. Does “autoimmunity” play a role in atopic dermatitis? *J Allergy Clin Immunol.* (2012) 129:1209–1215.e2. doi: 10.1016/j.jaci.2012.02.002

99. Badloe FMS, De Vries S, Coolens K, Schmidt-Weber CB, Ring J, Gutermuth J, et al. IgE autoantibodies and autoreactive T cells and their role in children and adults with atopic dermatitis: at the origin of the problem. *Clin Transl Allergy.* (2020) 10:34. doi: 10.1186/s13601-020-00338-7

100. Orciani M, Campanati A, Caffarini M, Ganzetti G, Consales V, Lucarini G, et al. T helper (Th)1, Th17 and Th2 imbalance in mesenchymal stem cells of adult patients with atopic dermatitis: at the origin of the problem. *Br J Dermatol.* (2017) 176:1569–76. doi: 10.1111/bj.15078

101. Bertolini M, McElwee K, Gilhar A, Bulfone-Paus S, Paus R. Hair follicle immune privilege and its collapse in alopecia areata. *Exp Dermatol.* (2020) 29:703–25. doi: 10.1111/exd.14155

102. Hiller-Sturmholz S, Bartke A. The endocrine system. *Alcohol Health Res World.* (1998) 22:153–64.

103. Baker JR. Autoimmune endocrine disease. *JAMA.* (1997) 278:1931–7. doi: 10.1001/jama.278.22.1931

104. Polonsky KS. The past 200 years in diabetes. *N Engl J Med.* (2012) 367:1332–40. doi: 10.1056/NEJMra1110560

105. Ajmera I, Swat M, Laibe C, Le Novère N, Chelliah V. The impact of mathematical modeling on the understanding of diabetes and related complications. *CPT Pharmacomet Syst Pharmacol.* (2013) 2:e54. doi: 10.1038/psp.2013.30

106. Fritzen K, Heinemann L, Schnell O. Modeling of diabetes and its clinical impact. *J Diabetes Sci Technol.* (2018) 12:976–84. doi: 10.1177/1932296818785642

107. Ralli M, Angeletti D, Fiore M, D’Aguanno V, Lambiase A, Artico M, et al. Hashimoto’s thyroiditis: An update on pathogenic mechanisms, diagnostic protocols, therapeutic strategies, and potential Malignant transformation. *Autoimmun Rev.* (2020) 19:102649. doi: 10.1016/j.autrev.2020.102649

108. Pyzik A, Grywalska E, Matyjaszek-Matuszek B, Roliński J. Immune disorders in Hashimoto’s thyroiditis: what do we know so far? *J Immunol Res.* (2015) 2015:979167. doi: 10.1155/2015/979167

109. Kaiser Y, Eklund A, Grunewald J. Moving target: shifting the focus to pulmonary sarcoidosis as an autoimmune spectrum disorder. *Eur Respir J.* (2019) 54:1802153. doi: 10.1183/13993003.021532018

110. Starshinova AA, Malkova AM, Basantsova NY, Zinchenko YS, Kudryavtsev IV, Ershov GA, et al. Sarcoidosis as an autoimmune disease. *Front Immunol.* (2019) 10:2933. doi: 10.3389/fimmu.2019.02933

111. Koether K, Besnard V, Sandig H, Carruthers A, Miranda E, Grootenhoefer-Mignot S, et al. Autoantibodies are associated with disease progression in idiopathic pulmonary fibrosis. *Eur Respir J.* (2023) 61:2102381. doi: 10.1183/13993003.02381-2021

112. Leuschner G, Semenova A, Mayr CH, Kapellos TS, Ansari M, Seeliger B, et al. Mass spectrometry-based autoimmune profiling reveals predictive autoantigens in idiopathic pulmonary fibrosis. *iScience.* (2023) 26:108345. doi: 10.1016/j.isci.2023.108345

113. Bracamonte-Baran W, Čiháková D. Cardiac autoimmunity: myocarditis. *Adv Exp Med Biol.* (2017) 1003:187–221. doi: 10.1007/978-3-319-57613-8_10

114. Tsuruoka K, Wakabayashi S, Morihara H, Matsunaga N, Fujisaka Y, Goto I, et al. Exacerbation of autoimmune myocarditis by an immune checkpoint inhibitor is dependent on its time of administration in mice. *Int J Cardiol.* (2020) 313:67–75. doi: 10.1016/j.ijcard.2020.04.033

115. Sheiner LB, Stanski DR, Vozeh S, Miller RD, Ham J. Simultaneous modeling of pharmacokinetics and pharmacodynamics: application to d-tubocurarine. *Clin Pharmacol Ther.* (1979) 25:358–71. doi: 10.1002/cpt1979253358

116. Holford NH, Sheiner LB. Understanding the dose-effect relationship: clinical application of pharmacokinetic-pharmacodynamic models. *Clin Pharmacokinet.* (1981) 6:429–53. doi: 10.2165/00003088-198106060-00002

117. Brooks PM, Bell MA, Lee P, Rooney PJ, Dick WC. THE EFFECT OF FRUSEMIDE ON INDOMETHACIN PLASMA LEVELS. *Br J Clin Pharmacol.* (1974) 1:485–9. doi: 10.1111/j.1365-2125.1974.tb01698.x

118. Nijssen MJMA, Wu F, Bansal L, Bradshaw-Pierce E, Chan JR, Liederer BM, et al. Preclinical QSP modeling in the pharmaceutical industry: an IQ consortium survey examining the current landscape: preclinical QSP in pharmaceutical industry. *CPT Pharmacomet Syst Pharmacol.* (2018) 7:135–46. doi: 10.1002/psp.4.12282

119. Zhang X-M, Liu C-Y, Shao Z-H. Advances in the role of helper T cells in autoimmune diseases. *Chin Med J (Engl).* (2020) 133:968–74. doi: 10.1097/CM9.00000000000000748

120. Foreman AL, Van de Water J, Gougeon M-L, Gershwin ME. B cells in autoimmune diseases: Insights from analyses of immunoglobulin variable (Ig V) gene usage. *Autoimmun Rev.* (2007) 6:387–401. doi: 10.1016/j.autrev.2006.12.005

121. Mould DR, Upton RN. Basic concepts in population modeling, simulation, and model-based drug development. *CPT Pharmacomet Syst Pharmacol.* (2012) 1:e6. doi: 10.1038/psp.2012.4

122. Bolton C. The translation of drug efficacy from *in vivo* models to human disease with special reference to experimental autoimmune encephalomyelitis and multiple sclerosis. *Inflammopharmacology.* (2007) 15:183–7. doi: 10.1007/s10787-007-1607-z

123. Zhu AZ. Quantitative translational modeling to facilitate preclinical to clinical efficacy & toxicity translation in oncology. *Future Sci OA.* (2018) 4:5. doi: 10.4155/fsoa-2017-0152

124. Caro JJ, Briggs AH, Siebert U, Kuntz KMISPOR-SMDM Modeling Good Research Practices Task Force. Modeling good research practices—overview: a report of the ISPOR-SMDM Modeling Good Research Practices Task Force-1. *Med Decis Mak Int J Soc Med Decis Mak.* (2012) 32:667–77. doi: 10.1177/0272989X12454577

125. Delitala M, Dianzani U, Lorenzi T, Melensi M. A mathematical model for immune and autoimmune response mediated by T cells. *Comput Math Appl.* (2013) 66:1010–23. doi: 10.1016/j.camwa.2013.06.026

126. Zhang W, Wahl LM, Yu P. Modeling and analysis of recurrent autoimmune disease. *SIAM J Appl Math.* (2014) 74:1998–2025. doi: 10.1137/140955823

127. Zhang W, Yu P. Hopf and generalized hopf bifurcations in a recurrent autoimmune disease model. *Int J Bifurc Chaos.* (2016) 26:1650079. doi: 10.1142/S021827416500796

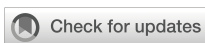
128. Zhang W, Yu P. Revealing the role of the effector-regulatory t cell loop on autoimmune disease symptoms *via* nonlinear analysis. *Commun Nonlinear Sci Numer Simul.* (2021) 93:105529. doi: 10.1016/j.cnsns.2020.105529

129. Kolev M. Mathematical modeling of autoimmune diseases. *Symmetry.* (2020) 12:1457. doi: 10.3390/sym12091457

130. Costa MFP, Ramos MP, Ribeiro C, Soares AJ. Optimal control model of immunotherapy for autoimmune diseases. *Math Methods Appl Sci.* (2021) 44:8883–902. doi: 10.1002/mma.8229

131. Della Marca R, MaChado Ramos M da P, Ribeiro C, Soares AJ. Mathematical modelling of oscillating patterns for chronic autoimmune diseases. *Math Methods Appl Sci.* (2022) 45:7144–61. doi: 10.1002/mma.8229

132. Mackensen A, Müller F, Mougiakakos D, Böltz S, Wilhelm A, Aigner M, et al. Anti-CD19 CAR T cell therapy for refractory systemic lupus erythematosus. *Nat Med.* (2022) 28:2124–32. doi: 10.1038/s41591-022-02017-5



OPEN ACCESS

EDITED BY

Thomas Hartung,
Johns Hopkins University, United States

REVIEWED BY

Lin Shang,
VU Amsterdam, Netherlands
Tarek A. Ahmad,
Bibliotheca Alexandrina, Egypt

*CORRESPONDENCE

Arjen Sloots
✉ arjen.sloots@intravacc.nl

RECEIVED 19 January 2024

ACCEPTED 19 March 2024

PUBLISHED 05 April 2024

CITATION

Hoonakker M, Zariri A, de Brouwer L, David D, Borgman A and Sloots A (2024) An *in vitro* assay for toxicity testing of *Clostridium perfringens* type C β -toxin. *Front. Immunol.* 15:1373411. doi: 10.3389/fimmu.2024.1373411

COPYRIGHT

© 2024 Hoonakker, Zariri, de Brouwer, David, Borgman and Sloots. This is an open-access article distributed under the terms of the [Creative Commons Attribution License \(CC BY\)](#). The use, distribution or reproduction in other forums is permitted, provided the original author(s) and the copyright owner(s) are credited and that the original publication in this journal is cited, in accordance with accepted academic practice. No use, distribution or reproduction is permitted which does not comply with these terms.

An *in vitro* assay for toxicity testing of *Clostridium perfringens* type C β -toxin

Marieke Hoonakker, Afshin Zariri, Lisette de Brouwer, Dionne David, Anouska Borgman and Arjen Sloots*

Department of Product Characterization and Formulation, Intravacc B.V., Bilthoven, Netherlands

Introduction: Veterinary vaccines against *Clostridium perfringens* type C need to be tested for absence of toxicity, as mandated by pharmacopoeias worldwide. This toxicity testing is required at multiple manufacturing steps and relies on outdated mouse tests that involve severe animal suffering. *Clostridium perfringens* type C produces several toxins of which the β -toxin is the primary component responsible for causing disease. Here, we describe the successful development of a new cell-based *in vitro* assay that can address the specific toxicity of the β -toxin.

Methods: Development of the cell-based assay followed the principle of *in vitro* testing developed for *Cl. septicum* vaccines, which is based on Vero cells. We screened four cell lines and selected the THP-1 cell line, which was shown to be the most specific and sensitive for β -toxin activity, in combination with a commercially available method to determine cell viability (MTS assay) as a readout.

Results: The current animal test is estimated to detect 100 – 1000-fold dilutions of the *Cl. perfringens* type C non-inactivated antigen. When tested with an active *Cl. perfringens* type C antigen preparation, derived from a commercial vaccine manufacturing process, our THP-1 cell-based assay was able to detect toxin activity from undiluted to over 10000-fold dilution, showing a linear range between approximately 1000- and 10000-fold dilutions. Assay specificity for the β -toxin was confirmed with neutralizing antibodies and lack of reaction to *Cl. perfringens* culture medium. In addition, assay parameters demonstrated good repeatability.

Conclusions: Here, we have shown proof of concept for a THP-1 cell-based assay for toxicity testing of veterinary *Cl. perfringens* type C vaccines that is suitable for all vaccine production steps. This result represents a significant step towards the replacement of animal-based toxicity testing of this veterinary clostridial antigen. As a next step, assessment of the assay's sensitivity and repeatability and validation of the method will have to be performed in a commercial manufacturing context in order to formally implement the assay in vaccine quality control.

KEYWORDS

Cl. perfringens type C β toxin, *in vitro*, cell-based assay, alternatives, 3R

Introduction

Clostridium perfringens type C is a Gram-positive, spore-forming bacterium that can be found as a normal component of soil or decaying vegetation and it is a common bacterium in the intestinal tract of humans and other domestic animals. It is a well-known cause of food poisoning as a result of poor preparation or conservation. The spores formed by the bacterium can withstand cooking temperature which can result in the formation of infective colonies. *C. perfringens* type C isolates produce among others α -toxin, β -toxin, perfringolysin O (1) and enterotoxin (2). The bacterium causes necrotic enteritis mainly in piglets and sheep and food-borne *C. perfringens* type C can also cause necrotic enterocolitis in humans. Several lines of evidence demonstrate that the β -toxin is the major pathogenic component of the bacterium (1).

The β -toxin is a monomeric pore-forming protein of 34,861 Da (3), that is highly sensitive to thiol group reagents and proteases and can easily change into a non-toxic form (4). β -toxin is extremely toxic to porcine and human endothelial cells and causes acute cell death (5, 6). The toxin is considered to form cationic selective oligomer pores in cell membranes resulting in influx of Ca^{2+} , Na^+ and Cl^- , causing swelling and lysis of cells (7). The β -toxin can bind to the P2X₇ receptor (8), though recent evidence also suggest the involvement of pannexin (9) and CD31 (10) in β -toxin mediated cell lysis. THP-1 cells express both the P2X₇ receptor (7) and CD31 (11) and die as a result of exposure to *C. perfringens* type C β -toxin (8, 11).

Administration of inactivated *C. perfringens* type C preparations containing β -toxin has been shown to dramatically reduce the frequency of necrotic enterocolitis in humans (12, 13). For livestock, vaccines based on inactivated, so-called toxoided, β -toxin are successfully used (14) and were shown to induce protective antibody responses (15). β -toxoid vaccines are often mixed with antigens of various other *Clostridium* species to form multivalent clostridial vaccines for veterinary use. Quality control testing of the β -toxoid vaccines starts directly after bacterial cultivation and is performed at several steps until the blending and filling of the final product (16). The testing always addresses the toxicity of the toxin itself, but fulfills different purposes, *i.e.* quantification of toxin activity before inactivation or testing for absence of toxicity after inactivation. Depending on the purpose and the manufacturing stage the toxicity tests may have different names. Due to the historic implementation of toxicity testing before 1950 and its codification in pharmacopoeias in many regions, a broad variety of names are used globally. The common denominator is that toxicity testing heavily relies on mouse-based tests, that use many animals and can inflict severe suffering to the animals involved. The potency of the final product is often quantified by the induction of antibodies in rabbits, with the neutralizing capacities of the induced antibodies assessed in naïve mice. All these tests all have lethal endpoints, for which the β -toxin is responsible (17), except for the rabbits, and inflict severe suffering.

In the tests described above for *C. perfringens* type C, the mice primarily serve as indicators for the presence of active toxin, similar to the tests used for quality control of other *Clostridium*-based

vaccines. For example, vaccines containing *C. septicum* also require mouse tests for both toxicity and potency. This principle of using an indicator to detect the presence of active toxin can be used to replace the animal testing with alternative methodologies. In 2012, Redhead *et al.* (16) developed an *in vitro* cell-based assay as an alternative for the toxicity and antigenicity tests for *C. septicum*, using the Vero cell line as indicator for toxin activity. This assay has undergone a large series of formal and regulatory steps including a Biological Standardisation Programme (BSP) study (BSP130) run by the European Directorate for the Quality of Medicines & HealthCare (EDQM) in order to prepare its implementation in a GMP production environment. The Vero cell assay is the official method in the European monograph 07/2022:0364 on *C. septicum* vaccine for veterinary use from July 2022.

Here, we applied a similar strategy of utilizing a cell line as indicator for *C. perfringens* type C β -toxin activity in a non-inactivated antigen preparation. This term describes the filtrated culture supernatant derived from an industrial vaccine manufacturing process, containing the active β -toxin. Whereas the simple presence of β -toxin can be addressed by PCR or Western blotting, these methods cannot distinguish between the active and inactivated forms of the toxin. However, as β -toxin is a pore-forming toxin, mammalian cells are well suited for assessment of its toxic effects and could, therefore, serve as an alternative toxicity indicator to the mouse. The susceptibility of a wide range of cells, among others Vero cells and various immune cell lines including THP-1 and U937 has been evaluated elsewhere (7, 18). The β -toxin had no effect on the Vero cells but affected all immune cell lines of which the THP-1 and the U937 cell line were the most sensitive. More recently, these results were confirmed by a different research group that also identified endothelial cells as β -toxin sensitive (10).

In the present study, from a panel of four tested cell lines, we identified two cell lines (THP-1 and A10) that were sensitive to the *C. perfringens* type C non-inactivated antigen, evaluated a selection of readout methods and selected the THP-1 cell line in combination with the MTS method as the most appropriate for our purposes. We determined the sensitivity of the resulting assay for *C. perfringens* type C non-inactivated antigen and its specificity for β -toxin, using a neutralizing monoclonal antibody and an antitoxin preparation directed against *C. perfringens* type C β -toxin. Importantly, we also demonstrated the compatibility of our THP-1 cell-based assay with an inactivated β -toxoid preparation. Together, our results show proof of principle for a new *in vitro* cell-based assay allowing detection of β -toxin activity. Upon validation, the assay has the potential to replace all mouse-based toxicity testing performed during production of *C. perfringens* type C vaccines.

Materials and methods

Cell lines and culture conditions

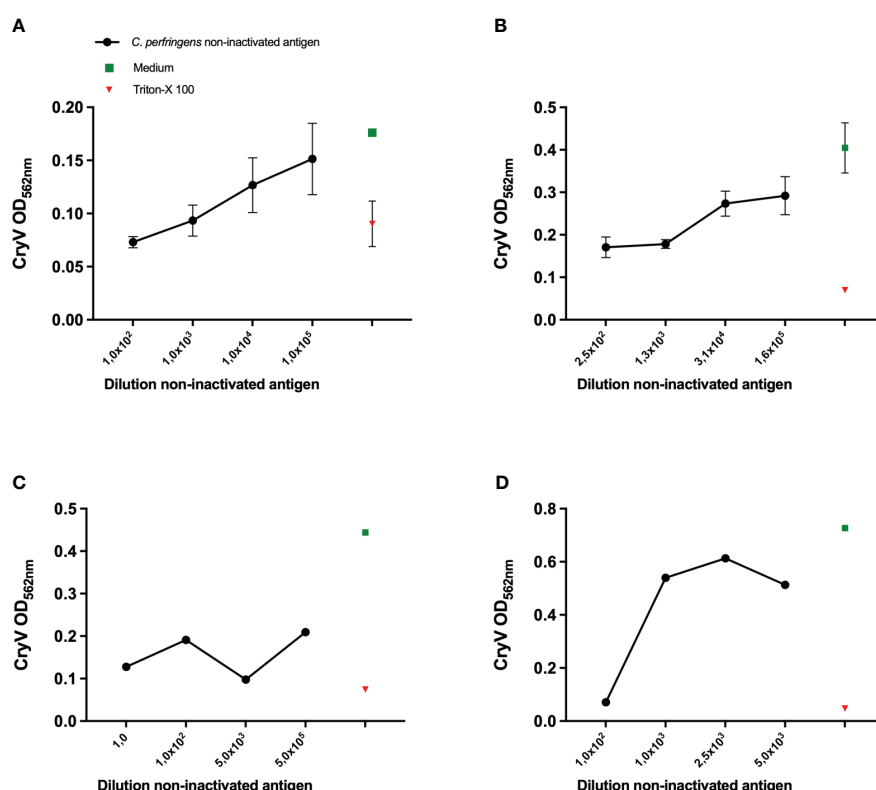
J774.1 cells (ATCC; TIB-67) were cultured in DMEM medium supplemented with 100 U/ml penicillin, 100 $\mu\text{g}/\text{ml}$ streptomycin, 0.3 mg/ml L-glutamine (Gibco), and 10% FBS (Gibco). A10 cells were purchased at ATCC (CRL-1476) and were cultured in DMEM

medium supplemented with 1 mM pyruvate (Gibco), 100 U/ml penicillin, 100 µg/ml streptomycin, 0.3 mg/ml L-glutamine (Gibco) and 10% FBS (Gibco). Vero cells were obtained from WHO (10-87) (originally derived from ATCC (CCL-81)) and were cultured in VP-SFM medium (Gibco), supplemented with 2 mM L-Glutamine (Gibco). THP-1 cells used in **Figures 1, 2, 3A–C, 4A, Supplementary Figures S1, and S2** were obtained from an in-house stock. To confirm results obtained with this stock, subsequent experiments were performed with THP-1 cells from a stock derived from a vial purchased at ATCC (TIB-202) (**Figures 3D, 4B–D, 5, 6, Supplementary Figures S3–S5**). THP-1 cells were maintained in RPMI medium (Gibco), supplemented with 50 µM β-mercaptoethanol, 100 U/ml penicillin, 100 µg/ml streptomycin, 0.3 mg/ml L-glutamine (Gibco) and 10% FBS (Gibco). All cell lines were cultivated at 37°C in a humidified atmosphere of 5% CO₂.

Cell seeding, exposure to *Cl. perfringens* type C non-inactivated antigen and readout methods

THP-1 cells were seeded at 25000 cells/well in a 96-well flat bottom plates (Greiner Bio One) and differentiated with 300 ng/mL PMA (Sigma), unless mentioned otherwise. A10 cells, J774.1 and Vero cells were seeded at 100000, 25000 and 25000 cells/well in 96-

well flat bottom plates. For all cell types, viable cells were counted following staining with a 0.4% trypan blue solution and only cell populations with a minimal viability of 70% were used for seeding. After seeding, cells were incubated over night at 37°C in a humidified 5% CO₂ incubator. Subsequently, the cells were exposed to various dilutions of the *Cl. perfringens* type C non-inactivated antigen preparation, containing active β-toxin (kindly provided by a pharmaceutical company that was part of the VAC2VAC consortium (<http://www.vac2vac.eu>), hereafter referred to as company B), medium or Triton-X-100 (Merck) for 16-24 hours. Cell viability was verified either by staining with 1) Crystal Violet (Sigma) - which stains living cells; 2) by addition of MTS (MTS assay, Promega) - a substance (3-(4,5-dimethylthiazol-2-yl)-5-(3-carboxymethoxyphenyl)-2-(4-sulfophenyl)-2H-tetrazolium) that is converted into colored formazan by living cells or 3) the LDH assay (Promega) performed on the culture supernatant, measuring the conversion of tetrazolium salt (iodonitrotetrazolium violet) into a red formazan product by cellular lactate dehydrogenase (LDH) released into the supernatant upon cell death. The MTS and LDH assay were performed according to the manufacturer's protocol and the quantity of formazan product as measured after 3.5-4.5 hours for the MTS assay and 30 minutes for the LDH assay at 490 nm. Crystal Violet (Sigma) staining was also performed according to manufacturer's protocol and was measured at 562 nm.



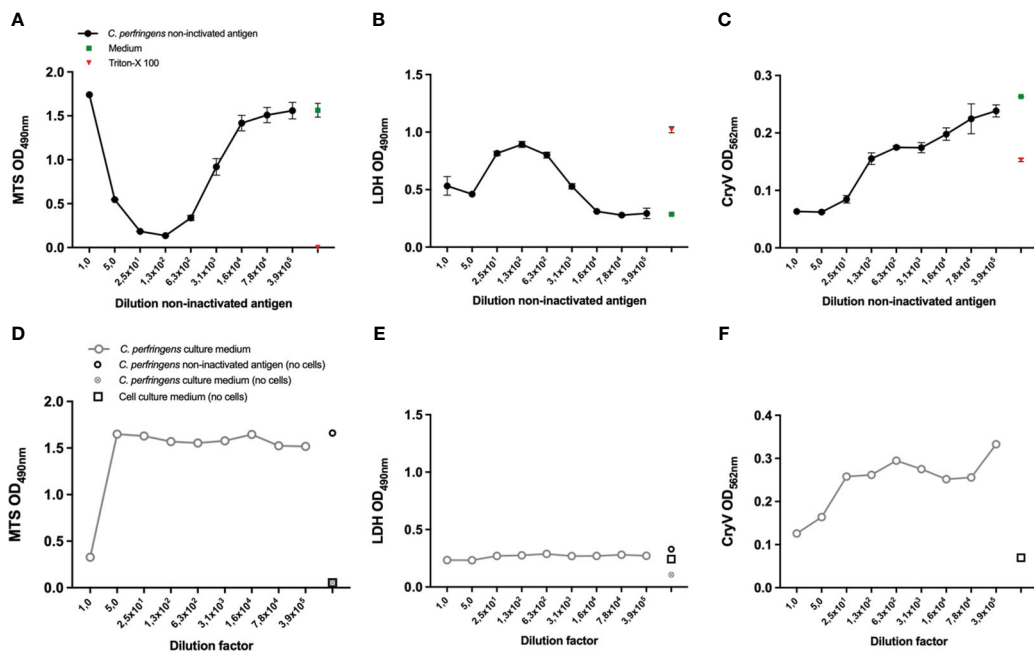


FIGURE 2

Selection of a suitable readout parameter for THP-1 and A10 cells and the effect of *Cl. perfringens* type C culture medium. THP-1 cells (PMA differentiated, **(A, B, D, E)**) and A10 cells (**(C, F)**) were exposed to the indicated dilutions of the *Cl. perfringens* type C non-inactivated antigen preparation, *Cl. perfringens* type C culture medium, cell culture medium or Triton-X-100 for 16–24 hours. Cell viability was measured with the MTS assay (**A, D**) and the LDH assay (**B, E**). The loss of cells as a result of toxicity was measured by staining the remaining cells with Crystal Violet (CryV) (**C, F**). Data are expressed as mean values \pm SD of triplicates (**A–C**) or shown as single measurements (**D–F**). Shown is one of three representative experiments (**A, C**), one out of two representative experiments (**B, D, E**) and data from a single experiment (**F**).

Preparations of non-inactivated antigen and antibody-antigen mixtures

Cl. perfringens type C non-inactivated antigen samples were prepared in medium containing 10% FCS (unless mentioned otherwise) at the indicated dilutions within one hour before addition to the cells. To determine the specificity for β -toxin, the *Cl. perfringens* type C non-inactivated antigen samples were pre-incubated for 30 min incubation at 2–8°C on an orbital shaker (250 rpm) with dilutions of a neutralizing monoclonal antibody (clone 10A2 purchased from the USDA; concentration unknown, produced either in mice (referred to as ‘Ascites’) or in a bioreactor (referred to as ‘Bioreactor’) or an international antitoxin standard (2CPBETAAT from NIBSC; 4770 IU of antitoxin, reconstituted in 1 mL PBS, referred to as ‘Antitoxin’).

Cl. perfringens type C β -toxoid and β -toxoid spiked with β -toxin

Cl. perfringens type C toxoid (kindly provided by company B) samples were prepared in medium containing 0.5% FCS at the indicated dilutions within one hour before addition to the cells. To neutralize the effect of residual formaldehyde (CH_2O) present in the

inactivated toxoid preparation, the undiluted β -toxoid and toxin preparations were incubated with 25% acetoacetamide ($\text{C}_4\text{H}_7\text{NO}_2$) for 30 minutes at room temperature or dialyzed against PBS overnight at 2–8°C. 0.5 g/L formaldehyde served as a control. If indicated, dialyzed samples were passed through a 0.22 μm filter before being added to the cells. For the spiking experiment, the undiluted toxoid preparation was treated with a 1/54 dilution of the *Cl. perfringens* type C non-inactivated antigen or left untreated. The toxoid or toxin samples were prepared on the day of the experiment or incubated overnight as indicated.

Statistical analysis

As the dose-response curves of β -toxin dilutions (x-axis) versus the OD at 490 nm (y-axis) follow a symmetrical sigmoidal shape, 4-parameter curve fitting (GraphPad Prism version 10.1.2) was used to mathematically describe the curves that were based on triplicate measurements (Figures 3D, Supplementary Figure S5D) and the curves shown in Figure 5 (duplicate measurements and one single measurement). The linear part of Figure 5 was analyzed using simple linear regression on the average values of duplicate measurements and one single measurement. The results are shown in Supplementary Figure S4.

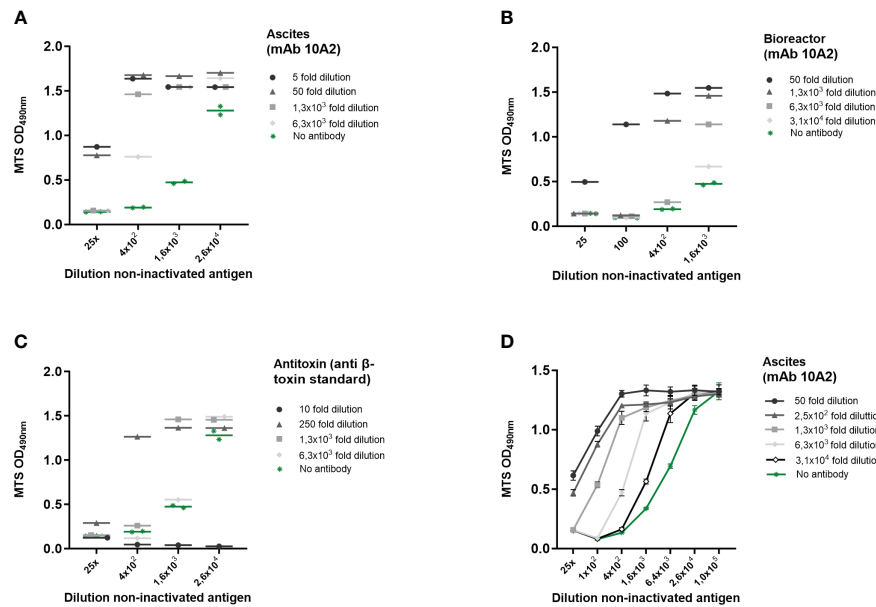


FIGURE 3

β-toxin specific induction of cell death on THP-1 cells. *Cl. perfringens* type C non-inactivated antigen preparation dilutions were incubated with the indicated dilutions of ascites-derived mAb 10A2 (A, D) and bioreactor-derived mAb 10A2 (B) and an international anti-β-toxin standard (2CPBETAAT) (C). THP-1 cells (PMA differentiated) were exposed to the antibody-β-toxin mixtures for 16–24 hours. Cell viability was measured with the MTS assay. Data are expressed as single or duplicate measurements (A–C), or as mean values \pm SD of triplicates (D). Shown is one of four experiments (A) and one experiment (B–D).

Results

Sensitivity of cell lines to *Cl. Perfringens* type C non-inactivated antigen preparation

Inspired by the *in vitro* assay based on the Vero cell line in combination with Crystal Violet staining, which proved to be suitable for assessment of toxicity of *Cl. septicum* vaccines and intermediate products (16), we aimed at using this strategy as the readout for the current *Cl. perfringens* type C toxicity test, as well. From a wider range of cell lines that was evaluated elsewhere (7, 10, 18), we selected THP-1 cells as one of our candidate cell lines, along with the β-toxin sensitive cell line A10 and the P2X₇ expressing murine J774A.1 cell line (19). Vero cells were included as a control. Both THP-1 and A10 cells (Figures 1A, B) were sensitive to *Cl. perfringens* type C non-inactivated antigen in a concentration-dependent manner, though the measured ODs were relatively low. The measured ODs for the Crystal Violet staining of J774A.1 (Figure 1C) were also very low and not concentration-dependent. Whereas the ODs for the Crystal Violet staining were higher for Vero cells (Figure 1D), toxicity was only observed for a 100-fold dilution of the *Cl. perfringens* type C non-inactivated antigen preparation or less diluted, suggesting this cell line has a lower sensitivity compared to the THP-1 and A10 cell lines. THP-1 cells and A10 cells were therefore selected for subsequent experiments.

Selection of a suitable readout parameter to assess either cell death or viability

In Figure 1, the remaining cells after *Cl. perfringens* type C non-inactivated antigen exposure were visualized by staining with Crystal Violet as a readout for viability, like the Vero-cell based test for veterinary *Cl. septicum* vaccines. However, since the measured ODs were relatively low the MTS and the LDH assays were evaluated as alternative methods to estimate cell viability. The MTS assay measures the conversion of the MTS tetrazolium compound into formazan by living cells. The assay is therefore directly proportional to the number of living cells. The LDH assay measures the activity of lactate dehydrogenase, a stable enzyme that is released upon cell lysis. Released LDH converts the tetrazolium salt into formazan and is therefore proportional to the number of dying cells. Exposure of THP-1 cells to *Cl. perfringens* type C non-inactivated antigen in a dilution range between 25 to 3.9x10⁵ fold resulted in a concentration dependent increase of the MTS signal (Figure 2A) and decrease of the LDH signal (Figure 2B). The range of the ODs was acceptable for both readout parameters and substantially higher than the Crystal Violet readout (Figure 1A) with the dynamic range (highest OD/lowest OD) being 12-fold for MTS and 3.2-fold for LDH (Figures 2A, B). Exposure of THP-1 cells to a one- or five-fold dilution of the *Cl. perfringens* type C non-inactivated antigen preparation resulted in a higher signal of the

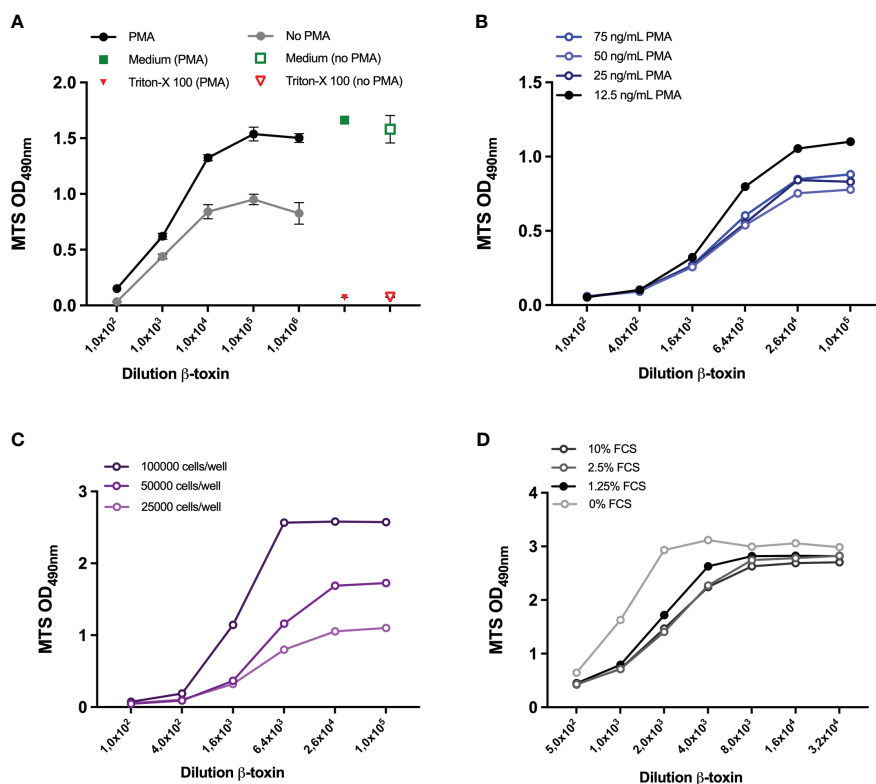


FIGURE 4

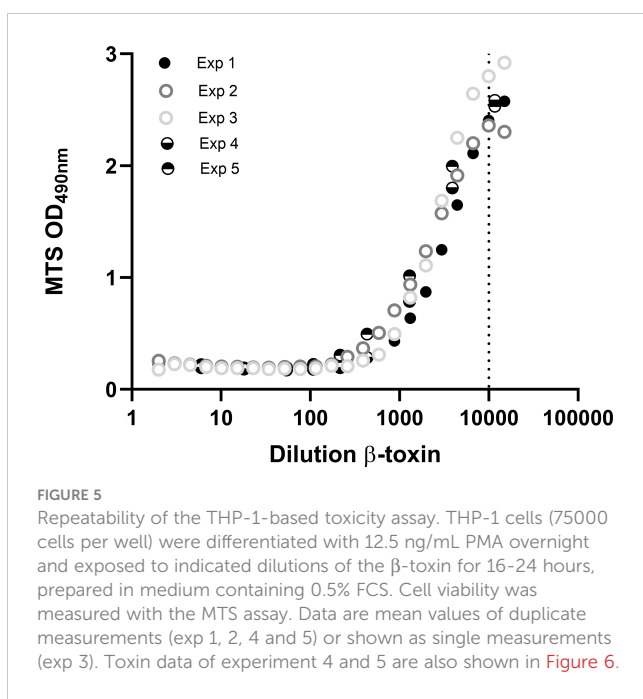
Optimization of cell density and PMA and FCS concentration. THP-1 cells (25000 cells/well) were either left untreated or differentiated with 300 ng/ml PMA (A) or 12.5, 25, 50, 75 ng/ml PMA (B) overnight. THP-1 cells at a density of 25000, 50000, 100000 (C) or 75000 (D) were seeded and differentiated with 12.5 ng/ml PMA overnight. Subsequently, all cells were exposed to the indicated dilutions of the β -toxin sample for 16–24 hours, either prepared in medium with 10% FCS (A–C) or FCS concentrations ranging between 0–10%. Subsequently, cell viability was assessed by MTS assay. Data are expressed as mean values \pm SD of triplicates (A) or duplicate measurements (B–D). Shown is one experiment for each condition examined.

MTS assay as compared to the 25-fold dilution (Figure 2A), which most likely is the result of a direct reaction between the *Cl. perfringens* type C non-inactivated antigen preparation and the MTS reagent (Figure 2D). Remarkably, exposure of THP-1 cells to the one- and five-fold dilutions of the *Cl. perfringens* type C non-inactivated antigen preparation was associated with a lower LDH signal as compared to the 25-fold dilution, which cannot be attributed to the *Cl. perfringens* culture medium or a reaction of the preparation with the LDH reagent (Figure 2E), but nonetheless should be taken into account. More importantly, the absence of an effect of the *Cl. perfringens* culture medium (5–3.9 \times 10⁵ fold dilution) on THP-1 viability indicates that the effect of the *Cl. perfringens* type C non-inactivated antigen can be specifically attributed to the β -toxin or other (toxic) components in the preparation. Exposure of A10 cells to the *Cl. perfringens* type C non-inactivated antigen preparation in the range of 10–3.9 \times 10⁵ fold dilution resulted in a very slight concentration dependent increase in MTS signal with a dynamic range of 1.5-fold (Supplementary Figure S1A). The level of LDH released by A10 cells was only affected by a 10-fold dilution of the non-inactivated antigen preparation to the point of total cell death (Triton-X-100 control), while all other dilutions (50–3.9 \times 10⁵) resulted in the release of LDH at a level of the medium control (Supplementary Figure S1B). In contrast the Crystal Violet staining does suggest a toxin concentration dependent effect with a dynamic

range of 3.8 (Figure 2C), however the effect is not specific since the *Cl. perfringens* type C culture medium has a similar effect (Figure 2F). Consequently, the THP-1 cells in combination with the MTS assay were selected as most promising for further assay development.

Determination of assay specificity using antibodies

To further determine whether the toxicity can be specifically attributed to β -toxin activity, experiments were performed where THP-1 cells were exposed to serially diluted *Cl. perfringens* type C non-inactivated antigen in the presence of serial dilutions of three different sources of β -toxin specific antibody preparations (ascites-derived and bioreactor-derived monoclonal antibody 10A2, and an international anti- β -toxin standard (2CPBETAAT)). All antibody preparations neutralized the effect of the *Cl. perfringens* type C non-inactivated antigen preparation, which is reflected in an increase in THP-1 viability (Figures 3A–D). The strength of neutralization differed between the three antibody preparations. Whereas mAb 10A2 from ascites had the highest neutralizing capacity, the international antitoxin clearly had the lowest neutralizing capability (Supplementary Figure S2A, Figure 3D). Furthermore,



cell viability was not affected by any of the included dilutions of mAb 10A2 (both from ascites or bioreactor sources), while the international antitoxin at a one- and ten-fold dilution did negatively affect cell viability (Supplementary Figure S2B). Taken together, the results clearly show that the toxicity on THP-1 cells induced by the *Cl. perfringens* type C non-inactivated antigen can be specifically attributed to the β -toxin. Therefore, effects will subsequently be indicated as being β -toxin dependent.

Optimization of several assay parameters

The experimental setup thus far consisted of 25000 cells per well, 300 ng/ml PMA and 10% FCS. Initial optimization experiments with and without PMA (Figure 4A) and with different concentrations of PMA (data not shown), confirmed the necessity of PMA-differentiation of the THP-1 cells for the assay and demonstrated that lower PMA concentrations (75 ng/mL) are associated with a higher maximum OD at 490 nm. Lowering the PMA concentration down to 12.5 ng/mL further increased the OD and the dynamic range to 21-fold (Figure 4B). Using a PMA concentration of 12.5 ng/mL, the OD at 490 nm also increased when the number of cells was increased up to 50000 and 100000 cells per well (Figure 4C), though the latter cell densities did change the shape of the curve. In a subsequent experiment, a cell density of 50000 and 75000 cell per well (in combination with a PMA concentration of 12.5 ng/ml and 10% FCS, Supplementary Figure S3) was examined and a density of 75000 cells per well resulted in the highest OD, with a 11-fold dynamic range (Supplementary Figure S3B). After determination of the optimal cell density (75000) and PMA concentration (12.5 ng/ml), several concentrations of FCS were compared to the 10% used thus far. Lowering the FCS

concentrations only had a slight effect (Figure 4D), 0% FCS being associated with the highest OD but also with a higher background. 0% FCS also changed the shape of the curve and slightly decreased dynamic range to 9.1-fold (Supplementary Figure S3B). Based on these results and personal communication with company B, 0.5% was chosen as the most optimal FCS concentration and used for sample preparation in subsequent experiments, while cell culturing was still performed in 10% FCS.

Repeatability and sensitivity

Repeatability is an important aspect of toxicity tests and quality control tests in general and was evaluated here based on five individual experiments in which very similar dilution ranges of β -toxin were used (Figure 5). There is only a very small variability between the five experiments regarding the absolute maximal OD at 490 nm. The fold change between total toxicity (lowest OD) and no toxicity (highest OD) for all experiments was between 12 and 16 fold and the lowest dilution still affecting cell viability, indicating the assay's sensitivity, was around 10000-fold dilution of the toxin in this R&D setting. Analysis of the data of the five experiments shown in Figure 5 revealed that all adequately fit a four parameter logistic curve with similar r^2 (0.98–0.99) and a slight range in EC₅₀ (2163–3843 fold dilution) (Supplementary Figure S4A). The results were confirmed by fitting the data of Figure 3D and Supplementary Figure S5D (EC₅₀ of 7086 and 1343 and r^2 of 0.99 and 0.99, respectively) (Supplementary Figures S4B, C). Simple linear regression analysis was performed on a part of the curve (875–6650 fold dilution) and revealed that the r^2 was 0.87 (Supplementary Figure S4D). Whereas sensitivity of the assay was sufficient in all of these experiments, the range in EC₅₀ highlights the needed for dedicated experiments to examine the linear range of the curve in more detail. These experiments should be a part of a (pre-)validation study.

Suitability of the assay for (spiked) *Cl. perfringens* type C toxoid samples

The assay developed so far allows detection of *Cl. perfringens* type C β -toxin activity in a specific and sensitive manner. In addition to the evaluation of β -toxin activity, detection of β -toxin in the context of a toxoided antigen preparation is of key importance because it would allow the assay to be used for non-toxicity testing of inactivated *Cl. perfringens* type C vaccine intermediate and end-products. We therefore determined the compatibility of the assay with a toxoided *Cl. perfringens* type C antigen preparation (Figures 6A–C) and its ability to detect β -toxin in the presence of this toxoid preparation by spiking with a fixed concentration of toxin (1/54 dilution) (Figure 6D). One of the obstacles is the residual free formaldehyde in commercial toxoid preparations. The toxoid itself negatively affects cell viability and a 220x dilution is required to negate this effect (Figure 6A), an effect that can primarily be attributed to residual formaldehyde present in the toxoid preparation (Supplementary Figure S5A). Various

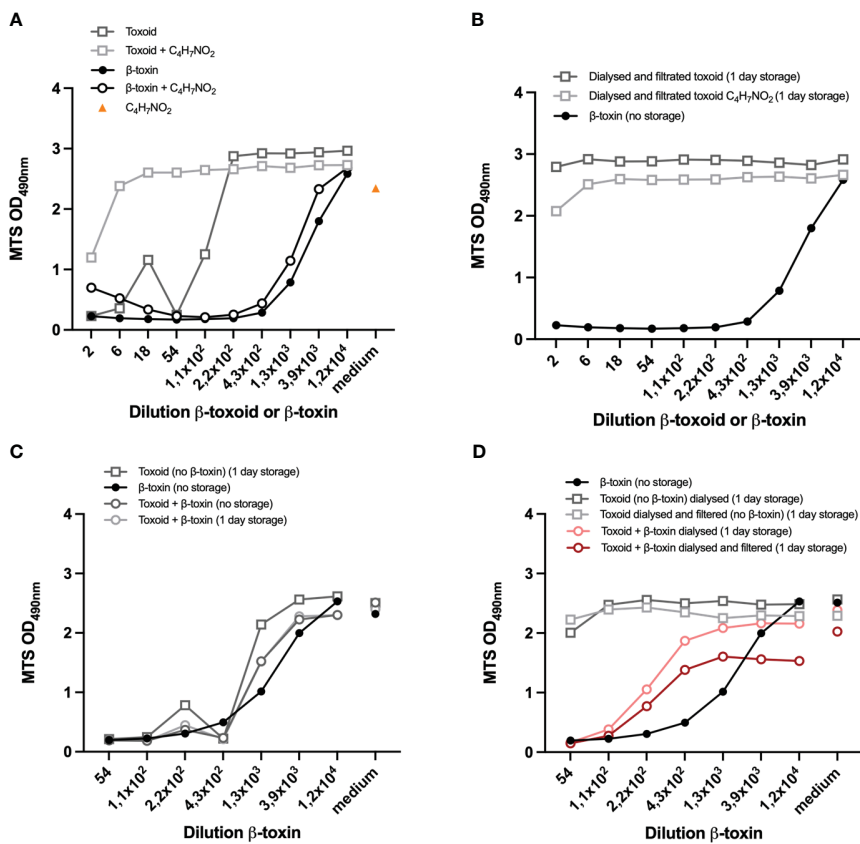


FIGURE 6

Compatibility of the assay with (spiked) β -toxoid. Preparations of toxoid and β -toxin were incubated with 25% acetoacetamide ($C_4H_7NO_2$) (A) or dialyzed and filtrated (overnight) and incubated with 25% $C_4H_7NO_2$ or left untreated (B). Controls are shown in [Supplementary Figure S5A](#). Toxoid (undiluted) was spiked with 1/54 dilution of the β -toxin or left untreated. Samples were prepared on the day of the experiment (no storage) or incubated overnight (1 day storage) as indicated (B-D). Toxoid (undiluted) and non-inactivated antigen (1/54 dilution)-spiked toxoid samples were prepared and dialyzed overnight and filtrated as indicated (B, D). Representative β -toxin and β -toxin-spiked toxoid samples were prepared on the day of the experiment (B-D). THP-1 cells (75.000 cell per well) were differentiated with 12.5 ng/mL PMA overnight and subsequently exposed to the indicated samples for 16–24 hours, prepared in medium containing 0.5% FCS. In A and B the toxoid or β -toxin dilutions are indicated, while in C and D the β -toxin dilution is indicated and the corresponding toxoid concentrations are shown in [Supplementary Figures S5B](#), C. Control measurements of cells incubated with medium with $C_4H_7NO_2$ (A) or medium only (C, D) are indicated by "medium" on the x-axis. Cell viability was measured with the MTS assay. Datapoints are mean values of duplicate measurements from one experiment. A direct comparison between the two experiments shown in this figure is shown in [Supplementary Figure S5C](#).

substances were tested for their ability to neutralize this effect ($NaHSO_3$, Bovine Serum Albumin, Tris, glycine), but only acetoacetamide and dialysis ([Figures 6A, B](#)) against PBS effectively neutralized the formaldehyde effect. Acetoacetamide has a slight effect on cell viability ([Figure 6A](#)), but a one in six dilution is sufficient to negate this effect. Dialysis increased the sample volume from 1 to 1.5 mL, which was reflected in the protein content that decreased from 1407 μ g/ml to 1092 μ g/ml, while filtration had a negligible effect (1086 μ g/ml), suggesting a minimal loss of material. This was confirmed by spiking toxoid with a 1/54 dilution of the non-inactivated antigen. Without any treatment, a pilot experiment demonstrated that the effect of the toxoid with a 1/54 dilution of the non-inactivated antigen is similar to the effect of the β -toxin itself and a discrimination between the negative effect of the toxoid and β -toxin is therefore impossible ([Figure 6C](#)). However, dialyzed spiked toxoid preparations (with and without filtration) caused cell death ([Figure 6D](#)), though to a smaller extent than the toxin itself. This is most likely due to a loss in β -toxin

activity overnight, as storage for one day had no effect on the activity of the toxin ([Supplementary Figure S5D](#)). More importantly, the experiment demonstrates that dialysis of the toxoid is a treatment that allows for the detection of β -toxin in the context of a β -toxoid preparation.

Discussion

There is a strong incentive to replace the use of animals for batch release testing of biological medicinal products, especially vaccines. Replacing *in vivo* quality control tests for vaccine batch release is particularly appealing where the *in vivo* test is merely used as a readout for toxicity and where a laboratory rather than the target species is used. The multiple mouse tests performed throughout the production process of *C. perfringens* type C vaccines are a typical example of tests in which animals function as a readout for toxicity. These mouse tests are performed for testing

of toxin activity and quantity before inactivation, for absence of toxicity after inactivation and to measure the neutralization capacities of antibodies induced in rabbits to assess the presence of crucial epitopes on the toxoided antigen (20). Although various cell lines have been described as susceptible to *Cl. perfringens* type C β -toxin (18), their suitability for development of a cell-based alternative *in vitro* method had not been explored to date.

The current mouse tests for inactivated *Cl. perfringens* type C antigen based-vaccines allow for quantification of β -toxin activity. Any alternative assay should therefore be quantitative and allow for validation according to the VICH guidelines for the “Validation of analytical procedures: Definition and Terminology” (21) and “Validation of analytical procedures: Methodology” (22). These guidelines require determination of the specificity, accuracy, precision, linearity, range and limit of quantitation. In this study, the THP-1 cell line was selected as the most β -toxin sensitive cell line as compared to A10, J774A.1 and Vero cells (Figure 1). In combination with the MTS assay, PMA differentiated THP-1 cells allow for the detection of up to 1:10000 dilution of the β -toxin preparation with a linear range between a 1000-fold and a 10000-fold dilution making this assay approach more sensitive than the currently performed *in vivo* test which have an estimated sensitivity range of 100 – 1000-fold dilutions of the *Cl. perfringens* type C non-inactivated antigen (VAC2VAC industry partners, personal communication). This sensitivity was confirmed in five repetitive experiments (Figure 5), which also documented the assay repeatability. Nevertheless, formal assessment of the assay’s sensitivity and repeatability needs to be addressed in a subsequent validation study or directly by manufacturers.

The specificity is the ability to unequivocally assess an analyte (here β -toxin) in the presence of components which may be present in the sample under study. Here, we used the *Cl. perfringens* type C non-inactivated antigen preparation of a commercial manufacturer, cleared from *Cl. perfringens* type C bacteria using a 0.2 μ m filter. Apart from β -toxin and culture medium, *Cl. perfringens* type C also produces α -toxin, perfringolysin O and enterotoxin (1, 2). The *Cl. perfringens* type C culture medium had no effect on THP-1 cell viability and a monoclonal antibody as well as an international antitoxin standard specific for β -toxin substantially reduced the detrimental effect of the *Cl. perfringens* type C non-inactivated antigen preparation on cell viability (Figure 3). The ascites-derived mAb 10A2 was the most potent of the three tested antitoxin preparations and at a dilution of 1:100 of the *Cl. perfringens* type C non-inactivated antigen preparation, the pre-incubation with ascites-derived mAb 10A2 resulted in complete neutralization. Based on these results, we conclude that the assay is specific for *Cl. perfringens* type C β -toxin.

Our *in vitro* assay should not only allow for testing of β -toxin activity in the non-inactivated antigen preparation, it should also allow for testing of traces of toxin in inactivated (*i.e.* toxoided) antigen preparations. To achieve inactivation of *Cl. perfringens* type C preparations, formaldehyde is usually added in sufficient quantities before filtration (23), to ensure the reliable and complete killing of the bacteria and quantitative inactivation of the toxins. This, however, results in the presence of residual formaldehyde in β -toxoid preparations, which is most likely the cause of the negative effect of low toxoid dilutions on cell viability (Figures 6A, S5A and S5C). A 220-

fold dilution of the toxoid preparation was required to minimize this detrimental effect. Fortunately, both incubation with acetoacetamide and exchange of the solvent in toxoid preparations with PBS by dialysis are methods that can overcome the impact of residual formaldehyde. Spiking of the toxoid preparation with a 1/54 dilution of the β -toxin in combination with dialysis, proved a suitable method to determine β -toxin activity in the presence of a representative concentration of toxoid (Figure 6D), though to a lesser extent than the toxin itself. The cause of this slight loss of toxin activity is unknown and needs further investigation. The results, however, provide an indication for the assay’s specificity for β -toxin in the presence of toxoid, although additional studies are required to confirm these results.

Here, we provide proof of principle for a THP-1 cell-based assay as a suitable and reliable *in vitro* alternative for assessing β -toxin activity in *Cl. perfringens* type C non-inactivated antigen and toxoided vaccines. The study shows that the assay is sensitive and specific, but requires validation before it can serve as a replacement for current mouse testing performed during *Cl. perfringens* type C vaccine production and batch release. Such validation studies should include evaluation of parameters specified by the VICH, among others by using blinded spiked samples. The studies performed by Redhead *et al.* (16) might serve as an example, involving a side-by-side evaluation of the new THP-1 cell-based assay and the historic *in vivo* methods. Hence, the THP-1 cell-based assay described in this study offers great potential as a convenient quantitative *in vitro* alternative to the mouse tests performed throughout *Cl. perfringens* type C vaccine production. Following validation, its implementation is expected to reduce costs, speed up the vaccine release process and avoid unnecessary animal suffering.

Data availability statement

The raw data supporting the conclusions of this article will be made available by the authors, without undue reservation.

Ethics statement

Ethical approval was not required for the studies on humans in accordance with the local legislation and institutional requirements because only commercially available established cell lines were used. Ethical approval was not required for the studies on animals in accordance with the local legislation and institutional requirements because only commercially available established cell lines were used.

Author contributions

MH: Data curation, Investigation, Methodology, Supervision, Writing – original draft, Writing – review & editing, Formal analysis, Visualization. AZ: Data curation, Formal analysis, Investigation, Methodology, Supervision, Writing – original draft, Writing – review & editing. LB: Investigation, Methodology, Writing – original draft, Writing – review & editing. DD: Investigation, Methodology, Writing – original draft, Writing –

review & editing. AB: Investigation, Methodology, Writing – original draft, Writing – review & editing. AS: Investigation, Methodology, Writing – original draft, Writing – review & editing, Conceptualization, Data curation, Supervision.

Funding

The author(s) declare that financial support was received for the research, authorship, and/or publication of this article. This project has received funding from the Innovative Medicines Initiative 2 Joint Undertaking under grant agreement no. 115924 (VAC2VAC). This joint undertaking receives support from the European Union's Horizon 2020 research and innovation program and EFPIA.

Acknowledgments

The authors thank Elisabeth Kamphuis (new name after marriage: Elisabeth Ruzin), Mohammad Daas, Silvia Fragoeiro, Anne Thomas and Catrina Stirling for reviewing the manuscript.

Conflict of interest

All authors were employed by company Intravacc B.V.

Publisher's note

All claims expressed in this article are solely those of the authors and do not necessarily represent those of their affiliated organizations, or those of the publisher, the editors and the reviewers. Any product that may be evaluated in this article, or claim that may be made by its manufacturer, is not guaranteed or endorsed by the publisher.

Supplementary material

The Supplementary Material for this article can be found online at: <https://www.frontiersin.org/articles/10.3389/fimmu.2024.1373411/full#supplementary-material>

References

- McClane B. Clostridium perfringens type C isolates rapidly upregulate their toxin production upon contact with host cells: new insights into virulence? *Virulence*. (2010) 1:97–100. doi: 10.4161/viru.1.2.10679
- Holanda Cavalcanti MT, Porto T, Figueiredo Porto AL, Viana Brandi I, de Lima Filho JL, Pessoa A. Large scale purification of Clostridium perfringens toxins: a review. *Braz J Pharm Sci.* (2004) 40:151–64. doi: 10.1590/S1516-93322004000200004
- Tweten RK. Clostridium perfringens beta toxin and Clostridium septicum alpha toxin: their mechanisms and possible role in pathogenesis. *Vet Microbiol.* (2001) 82:1–9. doi: 10.1016/S0378-1135(01)00372-8
- Nagahama M, Ochi S, Oda M, Miyamoto K, Takehara M, Kobayashi K. Recent insights into Clostridium perfringens beta-toxin. *Toxins (Basel)*. (2015) 7:396–406. doi: 10.3390/toxins7020396
- Popescu F, Wyder M, Gurtner C, Frey J, Cooke RA, Greenhill AR, et al. Susceptibility of primary human endothelial cells to C. perfringens beta-toxin suggesting similar pathogenesis in human and porcine necrotizing enteritis. *Vet Microbiol.* (2011) 153:173–7. doi: 10.1016/j.vetmic.2011.02.017
- Gurtner C, Popescu F, Wyder M, Sutter E, Zeeh F, Frey J, et al. Rapid cytopathic effects of Clostridium perfringens beta-toxin on porcine endothelial cells. *Infect Immun.* (2010) 78:2966–73. doi: 10.1128/IAI.01284-09

SUPPLEMENTARY FIGURE S1

Selection of a suitable readout parameter for A10 cells. A10 cells (**A, B**) were exposed to the indicated dilutions of the *Clostridium perfringens* non-inactivated antigen sample, medium or Triton-X-100 for 16–24 hours. Cell viability was measured with the MTS assay (**A**) and the LDH assay (**B**). Shown is data from one experiment (**A, B**).

SUPPLEMENTARY FIGURE S2

Specificity of the assay for β -toxin. Dilutions of the *Clostridium perfringens* type C non-inactivated antigen preparation were incubated with the indicated dilutions of ascites and bioreactor-derived mAb 10A2 and antitoxin 2CPBETAAT (**A**). THP-1 cells (PMA differentiated) were exposed to the antibody-antigen mixtures (**A**) or only the antibodies from three different sources (**B**) for 16–24 hours and cell viability was measured with the MTS assay. The effects of the antibodies on the MTS reagent (no cells) were also measured for the highest concentrations of the antibodies (**B**). Data are expressed as single measurements (**A, B**) in a single experiment (**A, B**).

SUPPLEMENTARY FIGURE S3

Optimization of cell density and FCS concentration. THP-1 cells at a concentration of 50.000 (**A**) or 75.000 (**B**) per well were seeded and differentiated with 12,5 ng/ml PMA overnight. Subsequently, all cells were exposed to the indicated dilutions of the β -toxin sample for 16–24 hours, prepared in medium with FCS concentrations ranging between 2,5–10%. Subsequently, cell viability was assessed by MTS assay. Data are expressed as mean values of duplicate measurements from a single experiment (**A, B**).

SUPPLEMENTARY FIGURE S4

Four parameter curve fitting and linear regression analysis of dose-response relationship. Statistical analysis was performed on the data of (**A**), (**B, C**) and (**D**) as described in the materials and methods section.

SUPPLEMENTARY FIGURE S5

The effect of toxoid and formaldehyde (CH_2O) on cell viability of neighboring wells, the effect of toxin-spiked toxoid preparations, a comparison between two experiments that included toxoid and the effect of one day storage on β -toxin activity. (**A**) 0.5g/L CH_2O was diluted as indicated in medium containing 0,5% FCS. (**B**) Toxoid (undiluted) was spiked with 1/54 dilution of the β -toxin or left untreated, β -toxin preparations were prepared starting with a 1/54 dilution. Samples were prepared on the day of the experiment or incubated overnight as indicated. (**C**) Toxoid (starting at a 1/2 dilution) and toxin (starting at a 1/54 dilution) were prepared and dialyzed or dialyzed overnight and filtrated as indicated for two experiments. (**D**) Toxin samples were prepared at the indicated dilutions one day before the experiment (indicated as "1 day storage") or on the day of the experiment (indicated as "no storage"). THP-1 cells (75.000 cell per well) were differentiated with 12,5 ng/mL PMA overnight and subsequently exposed to the indicated samples for 16–24 hours, prepared in medium containing 0,5% FCS. In **A** the dilution of CH_2O is shown, while in **B** and **C** the toxoid dilutions are shown, the corresponding β -toxin dilutions are shown in Figure 6C. Cell viability was measured with the MTS assay. Data are mean values of duplicates for one experiment (**A–C**) or triplicates \pm SD (**D**).

7. Nagahama M, Hayashi S, Morimitsu S, Sakurai J. Biological activities and pore formation of *Clostridium perfringens* beta toxin in HL 60 cells. *J Biol Chem.* (2003) 278:36934–41. doi: 10.1074/jbc.M306562200

8. Nagahama M, Seike S, Shirai H, Takagishi T, Kobayashi K, Takehara M, et al. Role of P2X7 receptor in *Clostridium perfringens* beta-toxin-mediated cellular injury. *Biochim Biophys Acta.* (2015) 1850:2159–67. doi: 10.1016/j.bbagen.2015.08.011

9. Seike S, Takehara M, Kobayashi K, Nagahama M. Role of pannexin 1 in *Clostridium perfringens* beta-toxin-caused cell death. *Biochim Biophys Acta.* (2016) 1858:3150–6. doi: 10.1016/j.bbamem.2016.10.003

10. Bruggisser J, Tarek B, Wyder M, Muller P, von Ballmoos C, Witz G, et al. CD31 (PECAM-1) Serves as the Endothelial Cell-Specific Receptor of *Clostridium perfringens* beta-Toxin. *Cell Host Microbe.* (2020) 28:69–78 e6. doi: 10.1016/j.chom.2020.05.003

11. Tarek B, Bruggisser J, Cattalani F, Posthaus H. Platelet endothelial cell adhesion molecule 1 (CD31) is essential for *Clostridium perfringens* beta-toxin mediated cytotoxicity in human endothelial and monocytic cells. *Toxins (Basel).* (2021) 13. doi: 10.3390/toxins13120893

12. Lawrence G, Shann F, Freestone DS, Walker PD. Prevention of necrotising enteritis in Papua New Guinea by active immunisation. *Lancet.* (1979) 1:227–30. doi: 10.1016/S0140-6736(79)90764-5

13. Davis M, Lawrence G, Shann F, Walker PD. Longevity of protection by active immunization against necrotising enteritis in Papua New Guinea. *Lancet.* (1982) 2:389–90. doi: 10.1016/S0140-6736(82)90582-7

14. Songer JG. Clostridial enteric diseases of domestic animals. *Clin Microbiol Rev.* (1996) 9:216–34. doi: 10.1128/CMR.9.2.216

15. Milach A, de los Santos JR, Turnes CG, Moreira AN, de Assis RA, Salvarani FM, et al. Production and characterization of *Clostridium perfringens* recombinant beta toxoid. *Anaerobe.* (2012) 18:363–5. doi: 10.1016/j.anaerobe.2012.01.004

16. Redhead K, Wood K, Jackson K. Testing of veterinary clostridial vaccines: from mouse to microtitre plate. *Dev Biol (Basel).* (2012) 134:45–50.

17. Knight PA, Queminet J, Blanchard JH, Tilleray JH. *In vitro* tests for the measurement of clostridial toxins, toxoids and antisera. II. Titration of *Clostridium perfringens* toxins and antitoxins in cell culture. *Biologicals.* (1990) 18:263–70. doi: 10.1016/1045-1056(90)90028-X

18. Nagahama M, Shibutani M, Seike S, Yonezaki M, Takagishi T, Oda M, et al. The p38 MAPK and JNK pathways protect host cells against *Clostridium perfringens* beta-toxin. *Infect Immun.* (2013) 81:3703–8. doi: 10.1128/IAI.00579-13

19. Bartlett R, Yerbury JJ, Sluyter R. P2X7 receptor activation induces reactive oxygen species formation and cell death in murine EOC13 microglia. *Mediators Inflamm.* (2013) 2013:271813. doi: 10.1155/2013/271813

20. Pharmacopoeia E. *Clostridium novyi* (type B) vaccine for veterinary use, 8th edition. (2013). pp. 952–3.

21. Products TEAftEoM. Validation of analytical procedures: Definition and Terminology (1998). Available online at: https://www.ema.europa.eu/en/documents/scientific-guideline/vich-gl1-validation-analytical-procedures-definition-terminology-step-7-consensus-guideline_en.pdf.

22. Products TEAftEoM. Validation of analytical procedures: Methodology (1998). Available online at: https://www.ema.europa.eu/en/documents/scientific-guideline/vich-gl2-validation-analytical-procedures-methodology-step-7-consensus-guideline_en.pdf.

23. Saad MJ, Sa'adeh IJ, Dababneh MF, Almaaytah AM, Bayan MF. Production, immunogenicity, stability, and safety of a vaccine against *Clostridium perfringens* beta toxins. *Vet World.* (2020) 13:1517–23. doi: 10.14202/vetworld



OPEN ACCESS

EDITED BY

Grazisa Rossetti,
IFOM - The FIRC Institute of Molecular
Oncology, Italy

REVIEWED BY

Noo Li Jeon,
Seoul National University, Republic of Korea
Yaqing Wang,
University of Science and Technology of
China, China

*CORRESPONDENCE

Jasper J. Koning
✉ jj.koning@amsterdamumc.nl

RECEIVED 19 January 2024

ACCEPTED 30 April 2024

PUBLISHED 21 May 2024

CITATION

Morrison AI, Sjoerds MJ, Vonk LA, Gibbs S and Koning JJ (2024) *In vitro* immunity: an overview of immunocompetent organ-on-chip models. *Front. Immunol.* 15:1373186. doi: 10.3389/fimmu.2024.1373186

COPYRIGHT

© 2024 Morrison, Sjoerds, Vonk, Gibbs and Koning. This is an open-access article distributed under the terms of the [Creative Commons Attribution License \(CC BY\)](#). The use, distribution or reproduction in other forums is permitted, provided the original author(s) and the copyright owner(s) are credited and that the original publication in this journal is cited, in accordance with accepted academic practice. No use, distribution or reproduction is permitted which does not comply with these terms.

In vitro immunity: an overview of immunocompetent organ-on-chip models

Andrew I. Morrison ^{1,2}, Mirthe J. Sjoerds ¹,
Leander A. Vonk ¹, Susan Gibbs ^{1,2,3}
and Jasper J. Koning ^{1,2*}

¹Molecular Cell Biology and Immunology, Amsterdam UMC Location Vrije Universiteit Amsterdam, Amsterdam, Netherlands, ²Amsterdam Institute for Infection and Immunity, Inflammatory Diseases, Amsterdam, Netherlands, ³Department of Oral Cell Biology, Academic Centre for Dentistry Amsterdam (ACTA), University of Amsterdam and Vrije Universiteit, Amsterdam, Netherlands

Impressive advances have been made to replicate human physiology *in vitro* over the last few years due to the growth of the organ-on-chip (OoC) field in both industrial and academic settings. OoCs are a type of microphysiological system (MPS) that imitates functional and dynamic aspects of native human organ biology on a microfluidic device. Organoids and organotypic models, ranging in their complexity from simple single-cell to complex multi-cell type constructs, are being incorporated into OoC microfluidic devices to better mimic human physiology. OoC technology has now progressed to the stage at which it has received official recognition by the Food and Drug Administration (FDA) for use as an alternative to standard procedures in drug development, such as animal studies and traditional *in vitro* assays. However, an area that is still lagging behind is the incorporation of the immune system, which is a critical element required to investigate human health and disease. In this review, we summarise the progress made to integrate human immunology into various OoC systems, specifically focusing on models related to organ barriers and lymphoid organs. These models utilise microfluidic devices that are either commercially available or custom-made. This review explores the difference between the use of innate and adaptive immune cells and their role for modelling organ-specific diseases in OoCs. Immunocompetent multi-OoC models are also highlighted and the extent to which they recapitulate systemic physiology is discussed. Together, the aim of this review is to describe the current state of immune-OoCs, the limitations and the future perspectives needed to improve the field.

KEYWORDS

human immunology, organ-on-chip (OoC), organotypic models, microfluidics, immune cells (ICs)

Abbreviations: 3D, Three-dimensional; BBB, Blood-brain barrier; DC, Dendritic cell; EC, Endothelial cell; ECM, Extracellular matrix; FDA, Food and Drug Administration; FRC, Fibroblastic reticular cells; HLA, Human leukocyte antigen; HUVEC, Human umbilical vein endothelial cells; IL, Interleukin; LC, Langerhans cell; LPS, Lipopolysaccharide; MPS, Microphysiological systems; OoC, Organ-on-chip; NK, Natural Killer; PBMC, Peripheral blood mononuclear cells; PDMS, Polydimethylsiloxane; RhS, Reconstructed human skin; TCR, T cell receptor; TNF α , Tumour necrosis factor alpha.

1 Introduction

Disease is a major burden on society; economically, socially, physically and psychologically. Worldwide, over 7.6 million people die annually from transferable diseases, like influenza and COVID-19, and over 40 million people from non-transferable diseases, such as cancer and cardiovascular diseases (1). Over the past decades, progress at healthcare organisations and pharmaceutical industries has advanced to such a level that many diseases can be prevented, controlled or even cured. Significant improvements have been made, with key driving factors including vaccination programs, innovative research on disease pathophysiology, discovery of new drug targets and advancements in toxicity screenings (2, 3).

Given the complexity of human physiology and ethical considerations, many human diseases have been investigated using animal models or *in vitro* cultures of human cells (4). Animal studies have traditionally been the gold standard in the drug development process preceding clinical trials. While they have been recognised as a necessity for evaluating drug metabolism, toxicity and efficacy, they do have several drawbacks. These include poor translatability to humans, low reproducibility rates, high costs and a time-consuming nature (5). Together, this results in around 90% of drug trials that are pre-screened in animals failing in humans due to differences with drug efficacy and toxicity effects (6). In addition to *in vivo* models, conventional *in vitro* assays have been widely used for predictive drug testing. These make use of human cells derived from either fresh human tissues/organs, or immortalised cell lines cultured under static conditions (7). However, such cultures generally lack the intricate three-dimensional (3D) multicellular organisation of a human organ, including vascularisation, which is complex to recreate in a static model. As such, this has led to the birth of MPS; a more realistic human physiological microenvironment represented in an *in vitro* setting.

1.1 Microphysiological systems and organ-on-chip platforms

MPS is a hypernym for *in vitro* models capable of replicating features of human physiology on a micro-scale that is biologically suitable for their intended function (8). OoCs are a type of MPS platform in a microfluidic device that can control and allow the imitation of native tissue/organ functions such as dynamic, organisational and physiological responses. An OoC microfluidic device can act as a small scale bioreactor to maintain fresh human biopsies or reconstructed organotypic tissues/organoids for extended periods of time (9). These microfluidic devices can enable additional mechanical parameters like flow rate, stretch and pressure, which are traditionally lacking in static two-dimensional (2D) and 3D cultures (10). Such parameters allow constant supply of oxygen and nutrients to the organ models, as well as removal of toxic metabolites, while also facilitating cell migration and multi-organ crosstalk. The design of the microfluidic device varies based on the requirements for culturing single or multiple organ types within the device and the biological questions

that need addressing (11, 12). Examples of such microfluidic OoC platforms can be seen in Figure 1. Typically, microfluidic devices are made from cell culture-compatible materials, namely polydimethylsiloxane (PDMS), and feature micro-channels for media flow and culture compartments that can be filled with cells, ECM-like gels, organotypic models or biopsies (13). OoCs have been made in academic bioengineering laboratories and are also commercially available from industrial companies. Both sectors have generated promising results in terms of modelling true human representative organ functions-on-chip. This includes toxicity screens performed during drug development and disease mechanisms that can be further understood to a deeper level than what is currently possible in animal models (14). The more accurate portrayal of human physiology *in vitro* has led to official acknowledgement by the United States (US) FDA, who has authorised the “use of certain alternatives to animal testing” that includes OoC models to investigate the safety and effectiveness of a drug (15, 16).

1.2 The necessity to incorporate the immune system

Although encouraging advancements have been made in OoC innovation, the inclusion of the immune system is still significantly lacking and is crucial for these models to reflect more optimally human physiology and disease (17–20). The human immune system has a major underlying role in the pathophysiology of almost every disease, whether that be cancer (21), metabolic disease (22), infection (23) or autoimmunity (24). The process by which the human body reacts to external or internal threat is called inflammation, and this can be an acute reaction, where unwanted pathogens, wound debris or toxins are swiftly removed, or chronic where the response persists for weeks or even years (25). Inflammation in itself is an umbrella term for a cascade of events that result in the recruitment and activation of immune cells via release of pro- or anti-inflammatory mediators, such as lipids, cytokines and enzymes (26). The landscape of these inflammatory mediators varies throughout different organs, resulting in organ-specific immune responses.

Immune cells develop within primary lymphoid organs and can then migrate through complicated blood and lymphatic vascular networks to secondary lymphoid organs and tissues. Lymphoid organs systemically co-operate with innate and adaptive immune cells, who can be migratory or tissue-resident (27). Innate immunity is the first line of defence and includes cells such as dendritic cells (DC), macrophages, monocytes, neutrophils and mast cells from myeloid origin, and nature killer (NK) cells. These innate cells sense danger via pattern recognition receptors (PRRs) (28) and offer a quick immune response upon pathogenic challenge, such as phagocytosis and secretion of inflammatory cytokines. In contrast, T and B cells are the main subsets in adaptive immunity, which exhibit memory capabilities and are specific in their immune response. T cells become activated after the T cell receptor (TCR) recognises its cognate antigen in the lymph nodes via presentation by DCs using human leukocyte antigen class II

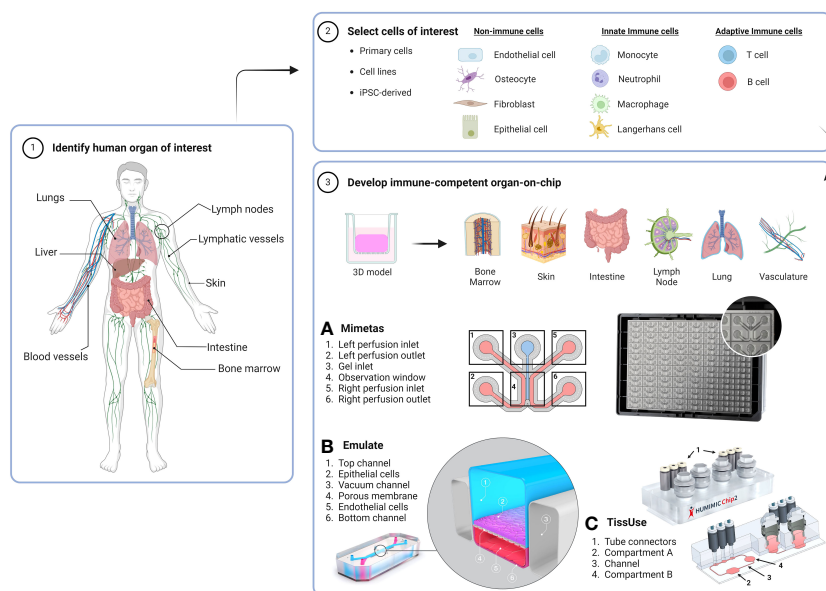


FIGURE 1

Workflow for generating an immunocompetent OoC. The human organ of interest (1) is modelled by using cells derived from either primary tissues or organs, cell lines or iPSCs (2) to make a 3D organotypic model that can be incorporated or built directly into an OoC microfluidic device (3). Dependent on organ anatomy and chip layout, single-OoCs are possible with various commercial chips companies, e.g. (A) Mimetas have a high-throughput 3-lane channel OrganoPlate® with 64-chips per plate, and (B) Emulate have a design that features a single chip with two channels separated by a porous membrane. (C) multi-OoCs are achievable through connection of multiple single-OoCs or within one microfluidic device, e.g. the setup of the TissUse HUMIMIC Chip2 where two (shown) or up to four compartments can house organotypic models or media reservoirs. Compartments can be connected by a channel, forming a continuous circuit with up to two separate circuits per chip. Chip images are courtesy of MIMETAS US Inc., Emulate Inc., and TissUse GmbH. Created with BioRender.com.

(HLA) molecules. These molecules are composed of different subtypes, termed HLA-DR, -DP, -DQ. T cell activation also depends on co-stimulatory molecules, such as CD27 from T cells bound to CD80/CD86 on antigen presenting cells (APCs). Once T cells are activated, they can either stimulate other lymphocytes to respond to potential threat or directly eliminate the target through the release of cytotoxic proteins, like granzymes. B cells also become activated after stimulation from T-helper cells or via antigen recognition directly, and can produce antibodies to neutralise the pathogen and/or facilitate opsonisation; a specific type of directed phagocytosis.

Until now, innate immunity has been predominantly simulated in OoC platforms. Unlike adaptive immune cells, innate immune cells do not rely on HLA molecules for their activation. Complexity greatly increases when adaptive immune cells are to be used due to their associated HLA-molecules, which may result in immune cell activation when other HLA-mismatched cell types are also present in the platform. This undesirable effect, mirrors the phenomenon known as graft *versus* host disease (GVHD) which leads to organ rejection by the adaptive immune system (29). In order to avoid cytotoxicity initiated by HLA-mismatch in OoC when investigating adaptive immune responses, all cell types should be derived from the same individual or at least be HLA-matched, introducing a major limitation of cell sourcing for current models. While efforts have been made by researchers to integrate immune cells into OoCs (30), development of human immunocompetent-organ models is needed to help us further understand how immune cells interact

with organs during health and disease. This is particularly important for understanding how drugs can influence these interactions (e.g. localised immunotherapies for treating autoimmune disorders or cancer).

Therefore, the aim of this review is to provide a comprehensive overview describing the extent in which the human immune system, specifically innate and adaptive immune cells, has been incorporated into both single- (Table 1) and multi-OoC (Table 2) models, and to discuss their current limitations and future perspectives. The focus is mainly on the body barriers (lung, skin, intestine and liver) and lymphoid organs.

2 Organ barriers

Tissue barriers (e.g. lung, skin and intestine) play a vital role in maintaining systemic homeostasis by protecting internal organs from direct environmental assault, such as pathogens. In this way, the tissue barriers preserve organ functions and provide a robust defence against immunological challenges. Additionally, although the human liver is not directly connected and exposed to the external environment, it is an immune-rich tissue that acts as a checkpoint for the clearance of foreign intestine-derived antigens before they can enter the systemic blood stream (105). Therefore, characteristics of single organ barriers-on-chip with an immune component, including the liver, are summarised in Table 1 and are further described in the following text below.

TABLE 1 Overview of immunocompetent single-organ-on-chip models.

Organ	Simulated feature(s)	Cell types	Microfluidic device and readouts
Lung	Inflammation (31–34)	IC: (P) PBMCs (31, 32, 35), macrophages (36, 37), neutrophils (33, 38, 39), T cells (40, 41)	MD: commercial OoC (Emulate) (32, 34, 36–43) and in-house (31, 33, 35), unidirectional open systems
	Cell crosstalk (37, 38, 40–42)	SC: (P) alveolar epithelial cells (32, 34–38, 40–42), microvascular ECs (31, 34, 36, 37, 39–42), lung fibroblasts (33), HUVECs (31, 33), airway epithelial cells (33, 39)	R: IC migration and adhesion, cytokine secretion, gene and protein expression, barrier permeability, metabolomics and proteomics
	SARS-CoV-2 (35–37, 39, 43)		
Skin	Barrier function (44)	IC: (P) PBMCs (45), macrophages (46), T cells (47), neutrophils (47) (CL) U937-monocytes (44), HL-60 cells (48)	MD: in-house (44–49), dynamic open/closed systems
	Wound healing (46)		
	Inflammation (47–49)	SC: (P) keratinocytes (44, 49), fibroblasts (46, 48, 49), HUVECs (46), ECs (45) (CL) HaCaT cells (46–48)	R: barrier function (microscopy, electrical resistance and fluorescent tracers), inflammation (cytokine secretion), viability, cell-cell interactions, IC phenotype and migration
	Adipose (45)		
Intestine	Host immune-microbiome interactions (50–53)	IC: (P) PBMCs (52), monocyte/macrophages (54, 55), moDCs (56), neutrophils (57) (CL) THP-1 cells (57–59), MUTZ-3-DC precursors (58), U937 cells	MD: in-house (53, 54, 56, 59) and commercial OoC (Emulate (43, 50, 51), ChipShop (52), and Mimetas (55, 57, 58, 60)), unidirectional/bidirectional/dynamic open/closed systems
	Barrier function (57)	SC: (P) HUVECs (54, 59), microvascular ECs (41, 52), organoids/iPSC (43, 55, 56, 59, 60)	
	IC migration (56)	(CL) epithelial cells (Caco-2), HT-29-MTX-12 cells (58),	
	Inflammation (41, 54, 55, 58–60)		R: barrier function (permeability), cell viability, bacterial activity, gene and protein expression, cytokine secretion, transcriptomics
Liver	Inflammation (61–66)	IC: (P) PBMC-isolated macrophages (61), Kupffer cells SC: (P) Hepatocytes, HUVECs (61)	MD: in-house (64), commercial OoC (CNbio (65, 66), Emulate (63), Mimetas (62), ChipShop (61)), unidirectional/bidirectional/dynamic open/closed systems
	IC infiltration (61)	(CL) stellate cells LX-2 (61, 63), HepaRG (66)	R: IC migration, cell-cell interactions, gene and protein expression, cytokine secretion, metabolomics, cell viability
Bone Marrow	Haematopoiesis and niche formation (67–69)	IC: (P) HSPCs, BMNCs (70), CD34 ⁺ progenitors (70, 71) (CL) SUP-B15 (72)	MD: in-house (67, 68, 71, 72) and commercial (TissUse (69) and Emulate (70)) OoC, dynamic/unidirectional closed/open systems
	Bone marrow and cancer cell interactions (71, 72)	SC: (P) BMSCs, MSCs, HUVECs (71), osteoblasts (71)	R: cell survival and phenotype, cell-cell/matrix interactions, gene and protein expression, cytokine secretion, oxygen consumption
	Shwachman–Diamond syndrome (70)		
Lymph Node	IC interaction and trafficking (73–75)	IC: (P) PBMCs (73, 76–78), DCs (75), moDCs (77), T cells (75), (CL) MUTZ-3 cells (73), THP-1 cells (79, 80), Jurkat cells (74, 79)	MD: in-house (73–76, 79, 80) and commercial (Emulate (78), TissUse (77)) OoC, unidirectional/dynamic open/closed systems
	Cellular organisation (78, 79)	SC: (CL) fibroblasts (75)	
	Antigen-antibody		R: DC maturation and migration, T cell activation, cell adhesion, antigen-specific antibody secretion, cytokine production and permeability

(Continued)

TABLE 1 Continued

Organ	Simulated feature(s)	Cell types	Microfluidic device and readouts
	responses (76, 77)		
	Cancer metastasis (80)		
Spleen	Blood filtration (81, 82)	IC: (CL) THP-1 cells (83) Other: RBCs	MD: in-house (81–83) R: cell viability, morphology, metabolomics, mechanical parameters, microscopy
	Sickle-cell disease (83)		
Vasculature	Blood and lymph vessel-IC interaction (84, 85)	IC: (P) PBMCs (86), T cells (84, 85, 87–89), neutrophils (90–92), moDCs (93), (CL) THP-1 cells (87)	MD: in-house (86–89, 91–93) and commercial [Mimetas (84, 85, 90)] OoC, dynamic/bidirectional open systems R: DC maturation and migration, T cell activation, Cell adhesion, antigen-specific antibody secretion, cytokine production and permeability
	IC migration and infiltration (88–90, 93)	SC: (P) HUVECs (84, 87, 89, 90), (CL) HMEC-1 ECs (85)	
	Cancer metastasis (87, 91, 92, 94–97)	Cancer cells: (CL) melanoma A375 cells (85), breast cancer cells (87)	

P, primary; CL, cell line; IC, immune cell; SC, stromal cells; MD, microfluidic device; R, readout.

2.1 Lung

The first OoC model to be established, which represented a more complex human micro-physiology, compared to what could be achieved in static models, was a model of the lung (10). The airways are prone to infection and inflammation and therefore have numerous mechanisms for protection such as; mucus surfactant for trapping foreign particles, epithelial cell barriers and resident immune cell populations, where the most prevalent are the alveolar macrophages (106).

The lung-on-chip mirrors human physiology by replicating essential tissue characteristics, including dynamic airway movements, surfactant release, the alveolar-capillary interface, airway inflammation and incorporation of blood vessels (42). Such chip models contain an air-liquid interface (ALI) and are generally constructed in two-channel microfluidic devices. These channels can house primary lung alveolar epithelial cells and pulmonary microvascular endothelial cells (ECs) on either side to simulate an epithelial barrier, separated by a porous membrane. A standard configuration of a lung-on-chip is illustrated in Figure 1, which shows a design associated with the Emulate lung-on-chip system.

Incorporation of immune cells into existing lung-on-chips has been used mainly for disease models, namely that of the lung's response to SARS-CoV-2 from the COVID-19 global pandemic, but also inflammatory diseases like asthma (38). The most common approach to introduce immunity involves the use of peripheral blood mononuclear cells (PBMCs) obtained from buffy coats, which consist predominantly of T cells and different proportions of B cells, NK cells, monocytes and DCs. PBMCs can be administered into the vascular endothelial lined channels of the chip, simulating the circulation of immune cells from blood. In the context of a lung-on-

chip exposure to SARS-CoV-2, PBMC-derived macrophages were found to contribute towards a SARS-CoV-2 induced interferon β (IFN β) inflammatory response. The use of an inhibitor targeting the type 1 IFN intracellular pathway demonstrated the capability to alleviate the inflammation-on-chip, bringing the IFN β levels down to those observed in an uninfected chip (36). Additionally, macrophages were recorded to have the ability to phagocytose SARS-CoV-2 damaged ECs (35). Furthermore, a severe immune overreaction, known as a cytokine storm, was modelled when SARS-CoV-2 infected patient samples were tested on a lung-on-chip, where the high cytokine levels were suppressed after monoclonal antibody treatment (37). In addition, clinically relevant SARS-CoV-2 treatments demonstrated drug efficacy by reducing viral load and inflammation on a lung-on-chip when PBMCs were present, indicating a benefit for the use of immune cells (43).

While most disease-related inflammatory lung-on-chip models focus on SARS-CoV-2, other viral infections have also been studied. PBMCs in a lung-on-chip model of rare acute respiratory distress syndrome (ARDS) displayed extravasation from one chip channel to another that was dependent on the presence of an endothelial barrier, ECM density/stiffness, and the flow profile (31). Bidirectional flow delayed the extravasation of immune cells compared to unidirectional flow, highlighting the importance of organ-specific dynamic flow conditions. Another study focusing on influenza virus-induced endothelial inflammation found that the number of PBMCs adhering to the lung-on-chip's endothelium was 100 times higher compared to uninfected chips (32), demonstrating their capability to react to pathogenic challenges.

In addition to PBMCs, single immune cell populations have also been brought into lung-on-chips. For instance, neutrophils, a major component of the lung's innate immune system (42), have

TABLE 2 Overview of all immunocompetent multi-organ-on-chip models.

Organ	Simulated feature(s)	Cell types	Microfluidic device and readouts
Gut/ Skin (98)	Gut inflammation and lipid uptake on skin	IC: (P) macrophages SC: (P) dermal fibroblasts, keratinocytes (CL) Caco-2 cells	MD: in-house R: cell viability, metabolite production, cytokine/chemokine secretion, permeability and immunofluorescence
Liver/ Gut (99, 100)	Inflammation mediated modulation of drug disposition.	IC: (P) Kupffer cells, DCs, T cells (100) SC: (P) hepatocytes (CL) Caco-2 cells and HT29-MTX (99)	MD: in-house R: cytokine/chemokine secretion and gene expression
Skin/ Gingiva (101)	Nickel induced inflammation	IC: (CL) LCs SC: (P) keratinocytes, fibroblasts	MD: commercial HUMIMIC multi-OoC (TissUse), dynamic system
Lung/ BBB (102)	Lung cancer metastasis to the brain	IC: (CL) THP-1 monocytes SC: (CL) lung cancer cells, fibroblast, ECs, epithelial cells, astrocytes, ECs	MD: in-house R: barrier integrity and permeability, immunofluorescence and cytokine/chemokine secretion and gene expression
Lung/ Liver/ Heart (103)	Drug toxicity screening	IC: (P) Kupffer cells SC: (P) hepatic stellate cells, hepatocytes, iPSC-derived cardiomyocytes, cardiac fibroblasts, ECs, stromal mesenchymal cells, bronchial epithelial cells	MD: in-house R: barrier function (microscopy, electrical resistance and fluorescent tracers), inflammation (cytokine secretion), viability, metabolite secretion
Gut/ Liver/ Kidney/ Bone Marrow (104)	First pass metabolism, PK and toxicity.	IC: (P) CD34+ progenitor cells	MD: in-house R: viability and cell tracking by immunofluorescence

P, primary; CL, cell line; IC, immune cell; SC, stromal cell; MD, microfluidic device; R, readout.

displayed migratory chemotactic properties across the EC barrier to epithelial cells upon Influenza A exposure in lung-on-chips (39), as well as in fibrotic lung-chips (33). Next to this, T cells are the predominant adaptive immune cell present in the airways and consist of mainly tissue resident memory T cells. When applied to lung-on-chips in a pool of PBMCs, activated T cells also had a migratory capacity towards epithelial cells upon inflammation using different viruses (39). Since T cells have a prominent role in recognising infected cells or cancer cells, effort has been made to increase their killing capability via multiple mechanisms, including the generation of bi-specific antibodies (40). The safety efficacy of a bi-specific antibody coupling CD3⁺ T cells to tumour antigens has been evaluated using an alveolus-on-chip, highlighting the practical use of such a model in the toxicology field (41). T cells also have a

pathophysiological role in asthma, and while T cells have not yet been used in asthma-on-chip, interleukin (IL)-13 was used to represent a T-helper cell type 2 suited microenvironment in a microfluidic device that replicated clinical data in terms of mucociliary clearance and increased mucus secretion (34).

In summary, immunocompetent lung-on-chips have rapidly evolved, heightened by the COVID-19 pandemic, and have started to characterise the role of immune cells in viral and bacterial infections and their effect on epithelial and ECs. There is still a need for further representation of the innate and adaptive immune system in these chips, particularly for more inflammatory diseases such as respiratory allergies to elucidate the role of allergen-related immune cells i.e., mast cells, and for understanding drug mechanisms.

2.2 Skin

The skin is another protective barrier against external pathogens, chemicals and physical stimuli. It consists of two main layers; the epidermis and the dermis. The epidermis is composed of highly specialised keratinocytes, melanocytes and immune cells, such as Langerhans cells (LCs). The dermis is a fibroblast-populated ECM compartment containing the vasculature and immune cells such as dermal DCs, T cells and macrophages (107). These skin immune cells exist in either resident or migratory populations, where upon tissue damage the APCs (LCs and DCs) become activated and migrate towards the skin-draining lymph nodes through the lymphatic vasculature.

A major characteristic of *in vitro* human organotypic skin models is their exposure to the air from the epidermis side, known as the ALI, which promotes spontaneous epidermal differentiation and stratification. Nutrients are supplied via culture medium in contact with the basal layer of the epidermis in reconstructed human epidermal (RhE) models or via the dermis side in full-thickness reconstructed human skin (RhS) models. RhS are typically bi-layered structures with keratinocytes seeded on top of a fibroblast-populated collagen-based 3D matrix (108). This design offers several advantages over *ex vivo* skin biopsies, e.g. prolonged culture duration with defined cell types present and can be readily used for safety/risk assessment, wound healing, drug delivery and allergen induced inflammation/disease. However, immunocompetent skin-on-chip models are still in their infancy and relatively simple in terms of their cellular setup.

One of the first reported immunocompetent skin-on-chip models was developed using epidermal keratinocytes, cultured together with the U937 monocyte-like cell line under dynamic flow. The model showed improved keratinocyte tight junction formation and general long term cell survival (44). Such immunocompetent skin-on-chips have evolved further by the addition of dermal fibroblasts with PBMC-derived T cells (47) or human umbilical vein endothelial cells (HUEVCs) with macrophages (46) to simulate a vascular channel. These immune cell additions facilitate the study of tissue infiltration, cytokine production and dynamic cell-cell interactions that more closely resemble normal native skin processes. In addition, vascularised

skin-on-chip models have demonstrated neutrophil migration from endothelium to dermis upon ultraviolet (UV) radiation exposure (48), further showcasing the ability to recapitulate dermatology-based phenomenon. Increased complexity of skin-on-chip has been described to include neopapillae into the dermis hydrogel, which are precursors of the hair follicle (109), but this has yet to include immune cells.

The pathophysiology of numerous skin related-diseases show immune cell involvement. For example, the addition of an adipocyte layer to RhS model has displayed an essential role in stabilising the metabolic properties of the skin (110), and as such, obesity has been mimicked with immune cell incorporation into a white adipose tissue (WAT)-on-chip (45). Adipocytes and ECs were isolated from skin biopsies and co-cultured in a chip with the same patient derived PBMCs, namely CD14⁺ monocytes and T cells. The addition of these immune cells to the model could recapitulate endocrine and immunomodulatory WAT functions. For more inflammatory and allergy-associated skin diseases-on-chip, incorporation of immune cells has yet to be achieved. However, potential does exist to address these disease mechanisms. For example, atopic dermatitis (AD) was modelled on chip using the disease-relevant cytokines IL-4 and IL-13. This resulted in tissue dehydration, keratin exfoliation and suppression of barrier-related genes (49).

In summary, skin-on-chip models have been comprehensively characterised and demonstrate robust properties in comparison to native human skin, albeit still lacking key features such as adipocyte layers, glands, nerves and growth of hair follicles. However, their immune-compatibility is still in its initial phases, primarily relying on the use of innate immune cells.

2.3 Intestine (Gut)

Like the skin and airways, the intestine (gut) is a barrier organ that is constantly in contact with external stimuli, harbouring a microbe dense microenvironment to fine tune a balance between tissue homeostasis and pathogenic infection. Hence, this is why the gut houses an extensive population of resident immune cells in the body. These immune cells can be found in an area of connective tissue called the lamina propria that house a plethora of e.g. macrophages, T cells and DCs (111, 112). The intestinal architecture contains villi, which are small projections of epithelium extending into the lumen to increase the surface area for nutrient uptake. The majority of gut-on-chips have overlapping attributes with lung-on-chips, such as inclusion of vacuum chambers to replicate peristaltic movement and chip-channels separated with a semi-porous membranes or ECM-rich hydrogel to enable culture of human intestine (or colon) epithelial cells and ECs (Figure 1).

Immune cells of myeloid origin have generally been used in multiple gut-on-chip models. Similar to skin-on-chip models, the first immunocompetent gut-on-chip model introduced the monocyte cell line U937, perfused through a two-channel chip containing the epithelial cell line CaCo-2. After lipopolysaccharide

(LPS) or tumour necrosis factor alpha (TNF α) exposure to trigger inflammation, the epithelium increased barrier permeability and induced immune activation (44). To date, gut-on-chip models have become more complex by the addition of HUVECs for the endothelial compartment, and gut commensal microbiome components such as probiotic bacterial strains as detailed below. Gut-on-chip co-cultures with microbial species have included either complete PBMCs or PBMC-isolated macrophages/DCs perfused through endothelial channels to study several different parameters, such as microbe-dependent tissue inflammation, damage and cell differentiation (50–52). Such addition of immune cells in these experiments have displayed protective properties of the endothelium, as the ECs were normally subjected to inflammation-associated tissue damage from the microbial species when immune cells were not present.

The major chronic inflammatory disease associated with the gut is inflammatory bowel disease (IBD), encompassing conditions like ulcerative colitis and Crohn's disease. This condition poses significant challenges for individuals, which is why gut-on-chip models are an appealing choice for IBD disease modelling and testing drug efficacy. When epithelial barriers are damaged, it leads to leaky gut, allowing pathogens to enter the bloodstream. In the context of gut-on-chips, IBD has been recapitulated through combinations of inflammatory cytokines, *E. coli* or LPS, and has involved the use of monocyte-derived DCs, macrophages, and PBMCs (53, 54, 56). More specifically, after cytokine exposure, pro-inflammatory M1 macrophage differentiation occurred via crosstalk with epithelial cells (55) and the monocyte cell lines THP-1 and MUTZ-3 were able to provoke synergistic inflammation through increase in IL-8 secretion in a chip (58). The theme of gut inflammation has extended to the use of neutrophils in an LPS-induced gut-on-chip, which mimics epithelial damage by neutrophil invasion and inflammatory crosstalk between resident and circulating immune cells (57).

Interestingly, there has been limited incorporation of adaptive immune cells in gut-on-chip models. One study has explored the safety and efficacy of T cell bi-specific antibodies targeting tumour antigens, which was conducted in parallel with an alveolus-on-chip model, as previously mentioned (40, 41). Nonetheless, for an incapacitating disease like IBD, the addition of immune cells, such as macrophages, and inflammatory mediators to the intestine-on-chips recapitulates a physiologically-relevant disease setting. This is particularly relevant since IBD patients have a higher abundance of macrophages and inflamed epithelium compared to healthy individuals (113, 114). Notably, models of the human intestine have a well distinguished organoid profile, whether derived from patient samples or induced pluripotent stem cell (iPSCs). Such organoids are now being cultured in gut-on-chip models that have an immune-like environment, such as iPSC-derived gut-like tubules that secrete IL-6 and IL-8 under an inflammatory stimulus (60). Likewise, a vascularised colon organoid demonstrated monocyte adherence to ECs, which then transmigrated towards the epithelium to undergo macrophage differentiation (59).

To summarise these immune gut-on-chip studies, it becomes apparent that they have predominantly featured innate immune cells over adaptive immune cells. This is reasonable given their

prominent involvement in gut-related diseases to a certain extent. However, it is worth noting that the gut contains a substantial population of T cells, which play a foundational role in other gut disorders, like Crohn's and celiac disease. Our intestine is influential to general health, so it would be pivotal to include adaptive immunity into future gut-on-chip models.

2.4 Liver

As stated in the introduction to the organ barriers, the liver is included in this review. The liver directly receives intestine draining-blood from the portal vein and thereby can act as a barrier to systemic infection. Since it is crucial for filtering blood and metabolising drugs and toxins which have bypassed the lymph node and spleen, this makes it an ideal organ for on-chip immunotoxicity testing. The liver is an immune privileged organ, with specialised resident macrophages known as Kupffer cells (115).

Liver-on-chip models normally use primary human hepatocytes, but the inclusion of immune cells at the single-OoC level are still lacking and are in a relative infant state. Such liver-on-chips can be used to study hepatocyte differentiation and culture stability e.g. LPS-induced inflammation with PBMC-derived macrophages resulted in macrophage polarisation to a M2 phenotype and demonstrated their adhesive properties and infiltration into hepatic cell channels on the chip (61). Inclusion of Kupffer cells allow for a more physiological immune model, where their use has been validated in a liver-chip as a hepatotoxic screening platform based on metabolic readouts (62, 63). These Kupffer cells have also been administered to study liver-related diseases on chip, such as advanced stages of non-alcoholic fatty liver disease (NAFLD), where exposure to an overload of long-chain free fatty acids induced pro-inflammatory biomarkers that could then be attenuated with drug application, indicating a proof-of-concept for hepatotoxicity testing of drugs (64). Likewise, in a liver-on-chip model of hepatitis, the Kupffer cells responded to LPS and hepatitis B virus (HBV) infection by secreting pro-inflammatory molecules associated with the disease (65). Additionally, glucocorticoids were assessed on liver-on-chips containing Kupffer cells to evaluate their anti-inflammatory properties (66).

Henceforth, it is clear that so far only innate immunity is partially represented in liver-on-chip models with the use of Kupffer cells. Integration of other innate immune cells to represent liver functioning is still required for future studies.

3 Lymphoid vasculature and organs

Lymphoid organs are a crucial component of the human immune system and distributed throughout the body to regulate and support immune responses. These specialised organs are integral in the production, maturation and activation of various immune cells. This all begins in the primary lymphoid organs and proceeds to the secondary lymphoid organs, which are strategically located to drain interstitial fluid from tissue. These secondary lymphoid organs play a fundamental role in immune surveillance, tissue specific immunity and memory responses.

The trafficking of immune cells between organs and tissues takes place in blood and lymphatic vessels, which serve as a key structural element for systemic immunology e.g. to guide immune cells from the tissue into secondary lymphoid organs and to direct them to the sites of inflammation. Since it is evident that vessel-on-chip has almost unlimited potential for its integration into the OoC field amongst numerous scientific disciplines (116, 117), this review focusses only on literature which includes vessel-on-chip to study immune cell migration. As such, features of lymphoid organs- and immunocompetent vasculature-on-chip are summarised together in Table 1 and discussed in detail below.

3.1 Primary lymphoid organs

In comparison to other organ models, lymphoid organ-on-chip models are distinctive for their abundance of immune cells since they play a primary role in regulating our immune system. The bone marrow and thymus are essential constituents of our immune system. Innate immune cells arise in the bone marrow and mature in tissue. Adaptive immune cells stem from the bone marrow, functionally mature in the thymus and differentiate in the lymph nodes. In this review, we focus on bone marrow-on-chip models for immune cells, as immunocompetent thymus-on-chips are yet to be developed.

The bone marrow is a complex organ that consists of several unique niches with differing microenvironments of ECM structures to perform several functions, namely erythropoiesis, myelopoiesis and lymphopoiesis. The first bone marrow-on-chip model was created by implanting a PDMS device into the bone marrow of mice, loaded with bone marrow-stimulating growth factors. The device was then explanted after 8 weeks of growth and maintained for up to seven days *ex vivo*. The model, albeit using mice in this study, was shown to accurately mimic physiological niches in the bone marrow and was later used in drug toxicity tests (67). Progress without using animal material for bone marrow niches are now widely modelled on chip. Numerous studies have recreated the endosteal niche, located at the surface of the bone for hematopoietic stem and progenitor cell (HSPC) differentiation, on chip to highlight the importance of mesenchymal stromal cell adhesion and cytokine secretion for CD34⁺ HSPCs maintenance and haematopoiesis (68, 70, 71). Currently, one bone marrow-on-chip study has demonstrated the formation of macrophage colonies from HSPCs (69) and, to date, the generation of further immune cell subsets are yet to be recapitulated.

One of the most studied diseases on bone marrow-chips is bone marrow cancer. As the bone marrow is closely situated to the blood supply, cancers that develop in the bone marrow can be prone to metastasis. This proximity provides a route for cancer cells to enter the bloodstream, facilitating their travel to distant organs and the subsequent formation of secondary tumours. This is particularly perilous, as the spread of cancer cells can impact the normal functioning of various organs. Cancer cells have been included in bone marrow-on-chips to study tumour migration, indicating preferential metastasis to different niches (71). Moreover, anti-leukaemia drugs have been screened in bone marrow-on-chips.

Here, the 3D microenvironment was deemed to protect the cancer cells from drug-induced apoptosis compared to 2D cultures (72), highlighting the advantages of chip models for the study of drug efficacy. In addition to bone marrow cancer-on-chip, the genetic disease Shwachman–Diamond syndrome (SDS) was emulated on chip, where mechanisms of the disease pathophysiology were revealed to indicate association with neutrophil maturation impairment (70).

The modelling of bone marrow-on-chip is a complex task since the bone marrow features an intricate organisation of different compartments, each with their own functions. Future improvements could be made by demonstrating haematopoiesis for multiple immune cell subsets and/or the inclusion of lymphoid progenitors. Further development of these models is crucial in our understanding of the bone marrow microenvironment.

3.2 Secondary lymphoid organs

Secondary lymphoid organs are strategically located throughout the body and are inter-connected by a network of lymphatic vessels that transport lymph-fluid drained from the peripheral tissues. These organs include lymph nodes, tonsils, spleen and Peyer's patches. Their key feature is a complex multicellular environment that is organised into special niches by lymph node stromal cells (LNSCs), and this is where the adaptive immune response is orchestrated (118). Due to the involvement of secondary lymphoid organs in the pathophysiology of inflammatory diseases and tumour metastasis, recreating an organotypic lymph node environment that encompasses every biological process is challenging.

While there is a lot of complexity to immunological processes within lymph nodes, the majority of models have used PBMC-derived moDCs, T cells and B cells to investigate immune cell clustering. This research has included dynamic perfusion with adaptive immune readouts such as plasma cell differentiation, antigen-specific antibody formation and cytokine productions (76–78). Furthermore, imitation of immune cell chemotaxis across lymph nodes has extended to include DC maturation and migration in the direction of flow to T cell compartments (73, 79). DC migration could be standardised using the commercially available drug hydroxychloroquine, which induced reactive oxygen species in T cells on the chip (74). Cell-cell interactions have also been explored by investigating adhesion molecules in a subcapsular sinus model (80), although the extent of this cellular characterisation remains somewhat limited.

The spleen is another secondary lymphoid organ which, unlike the lymph node, filters blood. Initial efforts have been made to recapitulate core spleen-functions, such as blood filtration, from perfusion of ex-vivo spleen tissue (81) and spleen-on-chip devices using red blood cells (RBCs) (82). Intriguingly, macrophages were used in a spleen-on-chip model of sickle cell disease that revealed differences in their phagocytic capabilities between sickled red RBCs and non-sickled RBCs, under hypoxia (83). In spite of the fact that robust spleen features have been well-characterised with immune cells-on-chip, the technical developments to advance spleen-on-

chip models are still at an early stage. For example, further studies to recreate immune cell behaviour with spleen-on-chip are required to more accurately portray splenic tissue biology, as well as using such models to better investigate infectious diseases, like visceral leishmaniasis (119).

The challenges of modelling secondary lymphoid organs, the lymph node in particular, lies in their complexity. A vital feature across all lymph node-on-chip models to date is their lack of stromal cells, in contrast to other tissue/organ models-on-chip, which all contained a stromal component, as detailed above. Currently, there is one chip model that has included fibroblast reticular cells (FRCs) from a cell line source (75), which showcased DC and T cell migration towards this FRC compartment. There is clearly an unmet need for incorporation of these FRCs, given their role in not only shaping immune responses within the lymph node (120), but also their importance for immune cell survival and functioning in a 3D environment (121). Considering the abundance of lymph nodes in the human body and their central role in continuous filtration of interstitial fluid containing toxins, metabolites, and immune cells from large organ barriers (such as skin), lymph nodes are an ideal candidate for incorporation into multi-OoCs. Combined with other organ models, this can allow the recreation of a systemic immune response *in vitro*, as depicted in the schematic of Figure 2.

3.3 Vasculature

Blood and lymphatic vessels play an important role in immunological processes by trafficking immune cells between organs, tissue and the lymphatic system. Blood vessels allow for the transport and circulation of a plethora of lymphocytes from primary lymphoid organs into secondary lymphoid organs via high endothelial venules, as well as multiple other organs and tissue types. Lymphatic vessels drain interstitial fluid, which contains waste metabolites, pathogens and activated APCs, from all tissue to secondary lymphoid organs through afferent lymphatic vessels, for filtration and to initiate adaptive immunity. Once primed in secondary lymphoid organs, immune cells leave through efferent lymphatic vessels, and re-join the peripheral circulation. Therefore, without vasculature, it is not possible for a systemic immune response to occur. Vascularisation of organ models within microfluidic devices has become somewhat of a hot topic in the OoC field. This includes the integration of ECs under a single organotypic model and/or the seeding of ECs in vessel-like compartments entering or leaving the organ model. These models can provide insight into significant parameters such as blood and lymphatic vessel permeability of endothelial walls, shear stress, vessel formation and inflammatory responses, such as cytokine production. In addition, immune cell migration and cancer metastasis can also be modelled. Typically, the configurations of vessels-on-chip involve a primary microfluidic channel that can be populated with ECs, allowing immune cells to be administered through this channel. ECs can form lumen-like structures, which are often surrounded by a matrix containing stimulants or even tumour cells.

As such, vascular inflammation-on-chip with immune cell migration revealed that cytokine-stimulated PBMCs could change EC barrier properties, such as affecting EC morphology and upregulation of certain adhesion molecules (84). Similarly, T cells were characterised on their response to chemotactic gradients and shown to interact with ECs through transmigration into ECM hydrogels (85–87). The versatility of T cells was explored in other vascularised OoCs to highlight their functionality against tumour cells (88, 89).

Another immune cell type regularly integrated into vessels-on-chip is the neutrophil. It has been shown that ECM components can dictate their migration capacities (90). Neutrophils were shown to exacerbate tumour cell metastasis in an ovarian cancer-on-chip device, indicating their unique role in cancer progression, which may have been overlooked in standard static cultures (91). A similar result was also observed with LPS-stimulated neutrophils that disrupted EC barriers and enhanced tumour cell extravasation (92). Likewise, APC characteristics could be recapitulated with vessels-on-chip, where DCs exhibited their antigen capturing and presenting ability along a chemotactic gradient (93) and macrophages exhibited phagocytic capacities (94). M1 macrophages were also seen significantly inhibited tumour-induced angiogenesis on chip (95). These cellular functions even extended to NK cells, which underwent trans-endothelial migration and killed tumour cells on chip (96). Further NK cell killing properties were also displayed through trans-endothelial migration into breast cancer spheroids-on-chip (97).

In summary, there are numerous prospects to explore immune cell migration through vessels-on-chip. While it is already at a

promising stage, this could be better accomplished by defining the use of blood ECs (BECs) or lymphatic ECs (LECs) for showing specific immune processes. As such, vessels-on-chip possesses unlimited potential for integration into pre-existing organ models and multi-OoC devices, aiming to truthfully replicate a systemic immune response *in vitro* (Figure 2).

4 Multi-organ-on-chip

The systemic physiological nature of the human immune response ensures a coordinated, total-body defence against a variety of health threats, like infections, cancer and toxic substances. This is why multi-OoCs have been developed. The arrangement of multi-OoCs can either be one microfluidic device that contains multiple interconnected organ models via channels and chambers, or multiple separate single-OoC microfluidic devices that are externally connected through tubing. The goal of such an integrated system, even without immune cells, offers a beneficial predictive value for drug safety and toxicity testing at a more systemic physiological level (123). From an immunology perspective *in vitro*, the potential of multi-OoCs are ideal for replicating dynamic immune cell migration between human organs to initiate tissue-specific immune responses. A comprehensive summary of all multi-OoC attributes with immune cells is displayed in Table 2, visualised in Figures 2, 3, and elaborated upon below.

At a two-organ immunocompetent multi-OoC level, crosstalk between the gut and liver during LPS-induced inflammation was

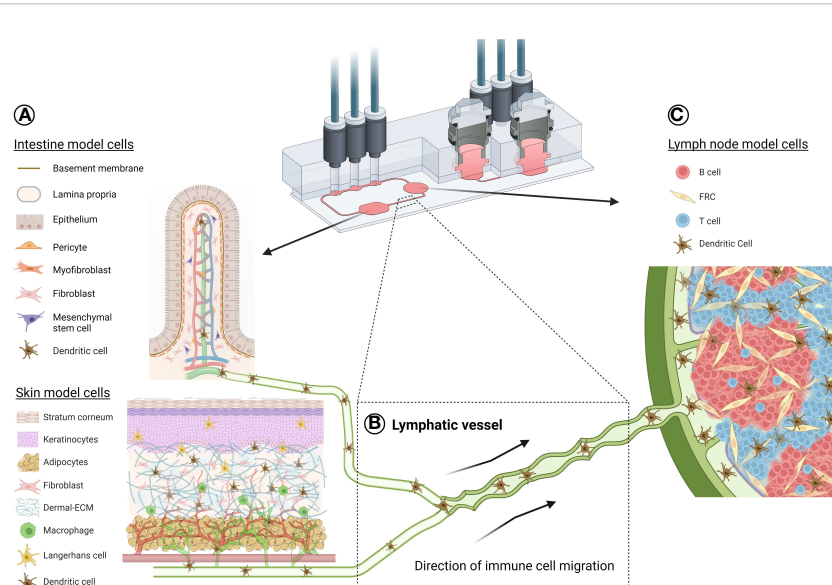


FIGURE 2

Schematic illustration of a potential organ-draining lymph node-on-chip. Exemplar use of a TissUse multi-OoC device to demonstrate immune cell migration between an organotypic skin or intestine model (A) through lymphatic vasculature (B) to an organotypic lymph node model (C). This is representative of a standard immune response, where skin Langerhans cells and skin/intestine dendritic cells can become activated in the epidermis or dermis/lamina propria, respectively, due to either allergen/bacterial exposure, injury or disease. APC migrate into the lymphatic vessels for their journey to the lymph node for antigen presentation to the adaptive immune cells. Such a response can be possible using multi-OoCs, as well as other types of organ-crosstalk models. Chip image is courtesy of TissUse GmbH. Image of intestine model is credited to and adapted from (122). Created with BioRender.com.

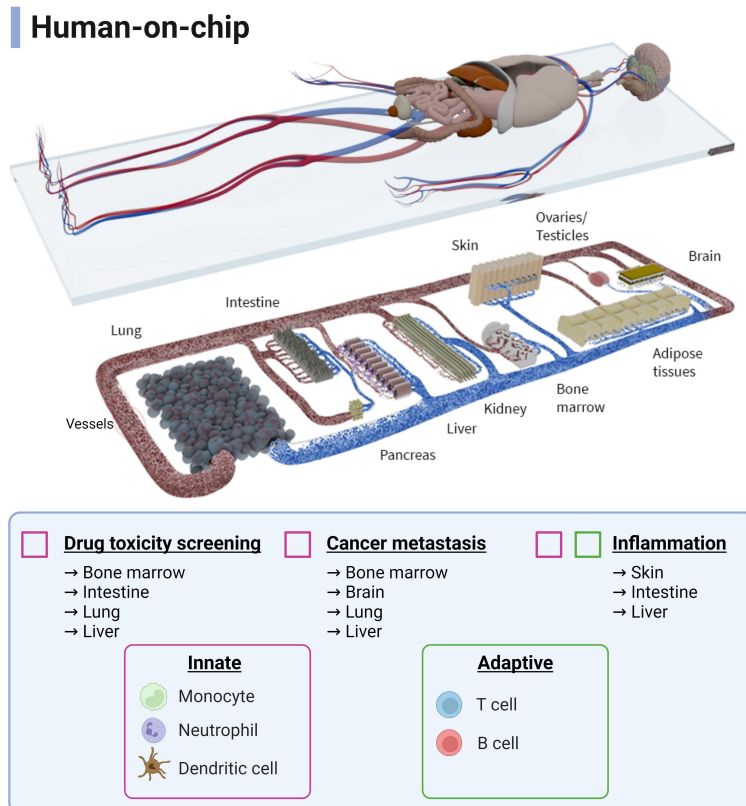


FIGURE 3

Schematic overview of a human-on-chip design from all possible immunocompetent multi-OoCs. Immune cells (innate and adaptive) are colour-coded to show the combinations to which they are currently used in various biological processes and applications. Connecting and expanding such multi-OoCs would create the ability to recapitulate human physiology in an *in vitro* setting, albeit on a more simplified level. Image is courtesy of TissUse GmbH. Created with BioRender.com.

recreated by administering DCs to the gut compartment and Kupffer cells to the liver model. Here, the upregulation of immune pathway genes and pro-inflammatory cytokines was detected when the immune cells were present in each organ compartment (99). In a separate gut-liver axis study, the addition of circulating T cells enhanced IBD-like conditions on the multi-OoC, enhancing its practical use for a disease-based model (100). In another study, the skin was separately combined in two multi-OoCs devices, such as connection to gingiva (101) and the gut (98). The skin-gingiva organotypic model on chip mimicked a clinical case study where topical allergen exposure to the gingiva resulted in activation of a skin immune response, as illustrated by LC migration in the skin model thus representing a systemic inflammatory response. The gut-skin multi-OoC assessed the downstream effect of fatty acid absorption by the gut model on skin inflammation, where macrophages increased nitric oxide uptake, associated with a pro-inflammatory response. Next to this, a lung-blood brain barrier (BBB) multi-OoC was developed containing monocytes to study the epigenetics of non-small cell lung cancer. The outcome was a consistent data profile between mice and patient studies, indicating an accurate proof-of-principle set up that does not require animal models (102).

A singular immunocompetent three-organ multi-OoCs has been developed, where lung-liver-heart organs were connected

through external tubing linking microreactors. Using liver Kupffer cells, cardiotoxicity was to be mediated by pro-inflammatory cytokine secretion after inducing toxicity to the lung model with bleomycin, a chemotherapy antibiotic (103).

Four-organ multi-OoCs have demonstrated crosstalk among organs in both lung-brain-bone-liver and gut-liver-kidney-bone marrow multi-OoCs. The lung-brain-bone-liver multi-OoC showcased immune involvement, where monocytes seeded in the lung tissue differentiated to M2 macrophages after tumour cell introduction. This provoked transmigration of cancer cells into other tissues and inflicted damage on the astrocytes (brain tissue), osteocytes (bone tissue) and hepatocyte (liver tissue) organ compartments (124). The gut-liver-kidney-bone marrow multi-OoC used CD34⁺ progenitor immune cells to represent the bone marrow and study metabolomics with pharmacodynamic and pharmacokinetic parameters. However, such readouts were not immunology-related (104).

In summary, immunocompetent multi-OoCs are still in their initial stages of development, predominantly featuring innate over adaptive immune cells. Multi-OoCs represent the ultimate frontier in replicating systemic immunological processes in an *in vitro* environment. It is evident that progress is being made in the immunotoxicity field, but the path ahead is long and numerous challenges still need to be overcome.

5 Conclusion and perspectives

OoCs are crucial for advances in studying immunity *in vitro*. However, scientists are challenged by the most optimal chip design, fabrication and implementation to address biological questions. Human immunology is complicated on a physiological level and this review has aimed to summarise the extent of which the immune system has been recapitulated into OoC models.

In general, the innate branch of the immune system has most frequently been included into single- and multi-OoC compared to adaptive immune cells. From a logical perspective, these innate cells are the first line of defence against external pathogens, disease and inflammation, and therefore offer an unspecific and diligent response that may be easier to model. Such immune cells are readily available through PBMC-isolation from blood donors or as cell lines, allowing practical universal benefits and a somewhat unlimited source of cells. However, as we learn more about tissue microenvironments, the importance of tissue-specific immune cells becomes apparent and must be considered. This for example includes the liver Kupffer cells or skin LCs, which each exhibit specific environmental profiles that dictate their tissue functioning.

While adaptive immune cells have been employed sparingly in non-lymphoid OoCs, these cells present a genuine assessment of functional specificity due to their long-lasting and memory-like properties representing the adaptive immune response. Once successfully integrated and thoroughly evaluated, this development will mark a significant step towards systemic immunology *in vitro*, further complementing areas such as disease modelling, drug testing and personalised medicine. As OoCs become more and more advanced and complicated, this will allow the opportunity to use tissue-specific cells that can either be obtained from biopsies or more appealingly; iPSCs. The strength of using iPSC-derived immune cells above primary cells or cell lines will be that they will enable donor-matched autologous cell types to be integrated into OoCs, thus bypassing the allogenic responses in a donor HLA-mismatch, a vital hurdle for immune modelling. However, the current limitations with iPSCs include the incomplete maturation status of the differentiated cells, unknown ability to skew towards tissue specificity and, especially in the immunology field, their unknown ability to generate diverse repertoires of T and B cells. The origin of these cell types can naturally raise complex questions concerning whether an individual's sex, age or lifestyle choice might influence their functionality in an OoC, especially considering how our immune system alters over time under the influence of epigenetic factors (125).

As mentioned above, OoCs still lack the inclusion of all organ-specific cells. This is where the organoid field can act as a promising tool for creating models of the immune system for organ-on-chip. Such examples include kidney organoid-on-chip (126) and BBB-on-chip (127), which both feature T cells that demonstrate tumour eradication and adhesion, extravasation, and migration under inflammatory conditions. Additionally, a primary NK cell model has illustrated dynamic extravasation into a physically separated tumour cell niche on a microfluidic device (128), indicating that immune cell migration can be recapitulated without using an actual

organ model on the chip. For immune organs, human tonsil organoids have been established to show early promise for modelling vaccine efficacy (129) and a lymphoma microenvironment (130). However, these tonsil models do not feature or acknowledge stromal cells, which are integral for lymphoid organ functioning as alluded to earlier. In future studies, we anticipate a greater shift towards making these organoid models into more immunology based-on-chip.

The gold standard consideration is to what extent one must delicately balance the complexity and simplicity of the biological and technical OoC design. For example, a liver-on-chip was able to detect close to 90% of drug-induced liver toxicity in patients, a result that went completely under the radar in an animal model (131) (132). While this liver-on-chip did not include immune cells, it is just one initial example of the potential promise that immunocompetent OoCs will have in superiority over animal experiments. Likewise, the very first lung-on-chip, developed by Emulate, mimicked lung pathology to a level that was never observed before in an *in vitro* setting (42). Not to mention, the technical design of such microfluidic devices must be considered for adding an immune element. The 3D environment of tissue models, whether that be built around biological or synthetic scaffolds, need to mimic the correct ECM of the native organ (133), and should be bio-compatible and spatially suitable for bringing into a microfluidic compartment (134). Care must also be taken in regards to the properties of such biomaterials on immune cell sensitivity. For example, hydrogel components like fibrinogen can modulate immune cell behaviour in either a suppressive or supportive manner (135, 136). Other factors such as the mechanical stimuli within the microfluidic device, such as shear stress, flow rate etc., and the type of experimental readouts, such as in-line or end-point sampling, must all be acknowledged when studying human immunology.

How far this work can progress into human immunology-on-chip, rather than multi-OoCs, is somewhat of a paradoxical outstanding question that only time will tell if it will be a tangible possibility or whether it is even needed. The recent approval by the US FDA for OoCs to be used in pre-clinical testing (15) has complemented the progress of this field which works towards efficient standardisation and safe robust use of such chips, as well as incorporating the immune system. This has already seen a benefit from a drug repurposing perspective, as a human lung-on-chip accelerated the discovery of a novel class of RNA-based therapeutics, where a pathological role of receptor found on lung alveolar cells was identified in viral infections (32). Such an avenue is also highly appealing for big pharma, as it has been reported that OoCs could reduce up to 26% of the costs for each drug that is approved (137), therefore applicable companies with the appropriate resources can invest to scale up OoC research, and in turn save finances, accelerate drug development and deliver the promise of personalised medicine in the near future (138, 139).

In conclusion, improvements of immunocompetent single-OoC and multi-OoC models are critical for their utilisation in both the fundamental research and drug development field. The closer these models come to accurately represent physiological systemic processes, the more widely available and applicable they will

become. In this way, they will play a pivotal role in the need to study human diseases in more physiologically relevant models.

Author contributions

AM: Conceptualization, Writing – original draft. MS: Writing – original draft. LV: Writing – original draft. SG: Conceptualization, Funding acquisition, Supervision, Writing – review & editing. JK: Conceptualization, Supervision, Writing – review & editing.

Funding

The author(s) declare that financial support was received for the research, authorship, and/or publication of this article. The presented work was funded by the European Union's Horizon 2020 research and innovation programme under grant agreement No. 847551 ARCAID and NWA-ORC 2019 1292.19.019 of the NWA research program "Research on Routes by Consortia (ORC)," which is funded by the Netherlands Organisation for Scientific Research (NWO).

Acknowledgments

We would like to extend our appreciation to Emulate Inc., MIMETAS US Inc., and TissUse GmbH for granting us permission to use their images in this review.

Conflict of interest

The authors declare that the research was conducted in the absence of any commercial or financial relationships that could be construed as a potential conflict of interest.

Publisher's note

All claims expressed in this article are solely those of the authors and do not necessarily represent those of their affiliated organizations, or those of the publisher, the editors and the reviewers. Any product that may be evaluated in this article, or claim that may be made by its manufacturer, is not guaranteed or endorsed by the publisher.

References

1. World Health O. *WHO methods and data sources for country-level causes of death 2000–2019* (2020). Available online at: <https://www.who.int/data/gho/data/themes/mortality-and-global-health-estimates/ghe-leading-causes-of-death>.
2. Pognan F, Beilmann M, Boonen HCM, Czich A, Dear G, Hewitt P, et al. The evolving role of investigative toxicology in the pharmaceutical industry. *Nat Rev Drug Discovery*. (2023) 22:317–35. doi: 10.1038/s41573-022-00633-x
3. Lindstrand A, Cherian T, Chang-Blanc D, Feikin D, O'Brien KL. The world of immunotoxicology: achievements, challenges, and strategic vision for the next decade. *J Infect Dis.* (2021) 224:S452–S67. doi: 10.1093/infdis/jiab284
4. Weaver RJ, Valentin JP. Today's challenges to de-risk and predict drug safety in human "Mind-the-gap". *Toxicol Sci.* (2019) 167:307–21. doi: 10.1093/toxsci/kfy270
5. Leenaars CHC, Kouwenen C, Stafleu FR, Bleich A, Ritskes-Hoitinga M, De Vries RBM, et al. Animal to human translation: a systematic scoping review of reported concordance rates. *J Transl Med.* (2019) 17:223. doi: 10.1186/s12967-019-1976-2
6. Sun D, Gao W, Hu H, Zhou S. Why 90% of clinical drug development fails and how to improve it? *Acta Pharm Sin B.* (2022) 12(7), 3049–3062.
7. Zhao C. Cell culture: *in vitro* model system and a promising path to *in vivo* applications. *J Histotechnol.* (2023) 46:1–4.
8. Marx U, Akabane T, Andersson TB, Baker E, Beilmann M, Beken S, et al. Biology-inspired microphysiological systems to advance patient benefit and animal welfare in drug development. *ALTEX.* (2020) 37:365–94. doi: 10.14573/altx
9. Langhans SA. Three-dimensional *in vitro* cell culture models in drug discovery and drug repositioning. *Front Pharmacol.* (2018) 9. doi: 10.3389/fphar.2018.00006
10. Huh D, Hamilton GA, Ingber DE. From 3D cell culture to organs-on-chips. *Trends Cell Biol.* (2011) 21:745–54. doi: 10.1016/j.tcb.2011.09.005
11. Leung CM, de Haan P, Ronaldson-Bouchard K, Kim G-A, Ko J, Rho HS, et al. A guide to the organ-on-a-chip. *Nat Rev Methods Primers.* (2022) 2:33. doi: 10.1038/s43586-022-00118-6
12. Cao UMN, Zhang Y, Chen J, Sayson D, Pillai S, Tran SD. Microfluidic organ-on-a-chip: A guide to biomaterial choice and fabrication. *Int J Mol Sci.* (2023) 24. doi: 10.3390/ijms2404323
13. Wu Q, Liu J, Wang X, Feng L, Wu J, Zhu X, et al. Organ-on-a-chip: recent breakthroughs and future prospects. *BioMed Eng OnLine.* (2020). doi: 10.1186/s12938-020-0752-0
14. Sharifi F, Su Htwe S, Righi M, Liu H, Pietralunga A, Yesil-Celiktas O, et al. A foreign body response-on-a-chip platform. *Advanced Healthcare Materials.* (2019) 8:1801425–. doi: 10.1002/adhm.201801425
15. *Federal food, and cosmetics act S.5002 - FDA modernization act 2.0* (2022). Available online at: <https://www.congress.gov/bill/117th-congress/senate-bill/5002>.
16. Han JJ. FDA Modernization Act 2.0 allows for alternatives to animal testing. *Artif Organs.* (2023) 47:449–50. doi: 10.1111/aor.14503
17. Morsink MAJ, Willemen NGA, Leijten J, Bansal R, Shin SR. Immune organs and immune cells on a chip: an overview of biomedical applications. *Micromachines (Basel).* (2020) 11:849. doi: 10.3390/mi11090849
18. Polini A, Del Mercato LL, Barra A, Zhang YS, Calabi F, Gigli G. Towards the development of human immune-system-on-a-chip platforms. *Drug Discovery Today.* (2019) 24:517–25. doi: 10.1016/j.drudis.2018.10.003
19. Maherjan S, Cecen B, Zhang YS. 3D immunocompetent organ-on-a-chip models. *Small Methods.* (2020) 4:2000235–. doi: 10.1002/smtd.202000235
20. Michaels YS, Buchanan CF, Gjorevski N, Moisan A. Bioengineering translational models of lymphoid tissues. *Nat Rev Bioengineering.* (2023) 1:731–48. doi: 10.1038/s44222-023-00101-0
21. Hiam-Galvez KJ, Allen BM, Spitzer MH. Systemic immunity in cancer. *Nat Rev Cancer.* (2021) 21:345–59. doi: 10.1038/s41568-021-00347-z
22. Zmora N, Bashiardes S, Levy M, Elinav E. The role of the immune system in metabolic health and disease. *Cell Metab.* (2017) 25:506–21. doi: 10.1016/j.cmet.2017.02.006
23. Sattler S. The role of the immune system beyond the fight against infection. *Adv Exp Med Biol.* (2017) 1003:3–14. doi: 10.1007/978-3-319-57613-8
24. Saferding V, Blumli S. Innate immunity as the trigger of systemic autoimmune diseases. *J Autoimmun.* (2020) 110:102382. doi: 10.1016/j.jaut.2019.102382
25. Oronsky B, Caroen S, Reid T. What exactly is inflammation (and what is it not)? *Int J Mol Sci.* (2022) 23. doi: 10.3390/ijms232314905
26. Chen L, Deng H, Cui H, Fang J, Zuo Z, Deng J, et al. Inflammatory responses and inflammation-associated diseases in organs. *Oncotarget.* (2018) 9:7204–18. doi: 10.18632/oncotarget.v9i6
27. McDaniel MM, Meibers HE, Pasare C. Innate control of adaptive immunity and adaptive instruction of innate immunity: bi-directional flow of information. *Curr Opin Immunol.* (2021) 73:25–33. doi: 10.1016/j.coi.2021.07.013
28. Janeway CA Jr. Approaching the asymptote? Evolution and revolution in immunology. *Cold Spring Harb Symp Quant Biol* (1989) 54Pt 1:1–13. doi: 10.1101/SQB.1989.054.01.003
29. Magenau J, Runaas L, Reddy P. Advances in understanding the pathogenesis of graft-versus-host disease. *Br J Haematol.* (2016) 173:190–205. doi: 10.1111/bjh.13959
30. Van Os L, Engelhardt B, Guenat OT. Integration of immune cells in organs-on-chips: a tutorial. *Front Bioeng Biotechnol.* (2023) 11:1191104. doi: 10.3389/fbioe.2023.1191104

31. van Os L, Yeoh J, Witz G, Ferrari D, Krebs P, Chandorkar Y, et al. Immune cell extravasation in an organ-on-chip to model lung inflammation. *Eur J Pharm Sci.* (2023) 187:106485. doi: 10.1016/j.ejps.2023.106485

32. Bai H, Si L, Jiang A, Belgur C, Zhai Y, Plebani R, et al. Mechanical control of innate immune responses against viral infection revealed in a human lung alveolus chip. *Nat Commun.* (2022) 13:1–17. doi: 10.1038/s41467-022-29562-4

33. Mejias JC, Nelson MR, Liseth O, Roy K. A 96-well format microvascularized human lung-on-a-chip platform for microphysiological modeling of fibrotic diseases. *Lab Chip.* (2020) 20:3601–11. doi: 10.1039/DOLC00644K

34. Nawroth JC, Lucchesi C, Cheng D, Shukla A, Nguyen J, Shroff T, et al. A microengineered airway lung chip models key features of viral-induced exacerbation of asthma. *Am J Respir Cell Mol Biol.* (2020) 63:591–600. doi: 10.1165/rcmb.2020-0010MA

35. Zhang M, Wang P, Luo R, Wang Y, Li Z, Guo Y, et al. Biomimetic human disease model of SARS-CoV-2-induced lung injury and immune responses on organ chip system. *Advanced Sci.* (2021) 8. doi: 10.1002/advs.202002928

36. Domizio JD, Gulen MF, Saidouni F, Thacker VV, Yatim A, Sharma K, et al. The cGAS-STING pathway drives type I IFN immunopathology in COVID-19. *Nature.* (2022) 603:145–51. doi: 10.1038/s41586-022-04421-w

37. Thacker VV, Sharma K, Dhar N, Mancini G-F, Sordet-Dessimoz J, McKinney JD. Rapid endotheliitis and vascular damage characterize SARS-CoV-2 infection in a human lung-on-a-chip model. *EMBO Rep.* (2021) 22:e52744–e. doi: 10.15252/embr.202152744

38. Benam KH, Villenave R, Lucchesi C, Varone A, Hubeau C, Lee HH, et al. Small airway-on-a-chip enables analysis of human lung inflammation and drug responses in vitro. *Nat Methods.* (2016) 13:151–7. doi: 10.1038/nmeth.3697

39. Si L, Bai H, Rodas M, Cao W, Oh CY, Jiang A, et al. A human-airway-on-a-chip for the rapid identification of candidate antiviral therapeutics and prophylactics. *Nat Biomed Engineering.* (2021) 5:815–29.

40. Kerns SJ, Belgur C, Petropoli D, Kanellias M, Barrile R, Sam J, et al. Human immunocompetent Organ-on-Chip platforms allow safety profiling of tumor-targeted T-cell bispecific antibodies. *eLife.* (2021) 10. doi: 10.7554/eLife.67106

41. Kerns JS, Belgur C, Kanellias M, Manatakis DV, Barrile R, Tien-Street W, et al. Safety profiling of tumor-targeted T cell-bispecific antibodies with alveolus lung- and colon-on-chip. *Bio Protoc.* (2023) 13. doi: 10.21769/BioProtoc.4579

42. Huh D, Matthews BD, Mammoto A, Montoya-Zavala M, Hsin HY, Ingber DE. Reconstituting organ-level lung functions on a chip. *Science.* (2010) 328:1662–8. doi: 10.1126/science.1188302

43. Bein A, Kim S, Goyal G, Cao W, Fadel C, Naziripour A, et al. Enteric coronavirus infection and treatment modeled with an immunocompetent human intestine-on-a-chip. *Front Pharmacol.* (2021) 12. doi: 10.3389/fphar.2021.718484

44. Ramadan Q, Ting FC. *In vitro* micro-physiological immune-competent model of the human skin. *Lab Chip.* (2016) 16:1899–908. doi: 10.1039/C6LC00229C

45. Rogal J, Roosz J, Teufel C, Cipriano M, Xu R, Eisler W, et al. Autologous human immunocompetent white adipose tissue-on-chip. *Adv Sci (Weinh).* (2022) 9:e2104451. doi: 10.1002/advs.202104451

46. Bigliari S, Le TYL, Tan RP, Wise SG, Zambon A, Codolo G, et al. Simulating inflammation in a wound microenvironment using a dermal wound-on-a-chip model. *Adv Healthc Mater.* (2019) 8:e1801307. doi: 10.1002/adhm.201801307

47. Ren X, Getschman AE, Hwang S, Volkman BF, Klonisch T, Levin D, et al. Investigations on T cell transmigration in a human skin-on-chip (SoC) model. *Lab Chip.* (2021) 21:1527–39. doi: 10.1039/DOLC01194K

48. Kwak BS, Jin SP, Kim SJ, Kim EJ, Chung JH, Sung JH. Microfluidic skin chip with vasculature for recapitulating the immune response of the skin tissue. *Biotechnol Bioengineering.* (2020) 117:1853–63. doi: 10.1002/bit.27320

49. Kim K, Kim H, Sung GY. An interleukin-4 and interleukin-13 induced atopic dermatitis human skin equivalent model by a skin-on-a-chip. *Int J Mol Sci.* (2022) 23:2116–. doi: 10.3390/ijms23042116

50. Kim HJ, Ingber DE. Gut-on-a-Chip microenvironment induces human intestinal cells to undergo villus differentiation. *Integr Biol (Camb).* (2013) 5:1130–40. doi: 10.1039/c3ib40126

51. Kim HJ, Li H, Collins JJ, Ingber DE. Contributions of microbiome and mechanical deformation to intestinal bacterial overgrowth and inflammation in a human gut-on-a-chip. *Proc Natl Acad Sci U S A.* (2016) 113:E7–15. doi: 10.1073/pnas.1522193112

52. Maurer M, Gresnigt MS, Last A, Wollny T, Berlinghof F, Pospich R, et al. A three-dimensional immunocompetent intestine-on-chip model as *in vitro* platform for functional and microbial interaction studies. *Biomaterials.* (2019) 220:119396. doi: 10.1016/j.biomaterials.2019.119396

53. Shin W, Kim HJ. Intestinal barrier dysfunction orchestrates the onset of inflammatory host-microbiome cross-talk in a human gut inflammation-on-a-chip. *Proc Natl Acad Sci U S A.* (2018) 115:E10539–E47. doi: 10.1073/pnas.1810819115

54. Jing B, Xia K, Zhang C, Jiao S, Zhu L, Wei J, et al. Chitosan oligosaccharides regulate the occurrence and development of enteritis in a human gut-on-a-chip. *Front Cell Dev Biol.* (2022) 10:877892. doi: 10.3389/fcell.2022.877892

55. Beaurivage C, Kanapekaite A, Loomans C, Erdmann KS, Stallen J, Janssen RAJ. Development of a human primary gut-on-a-chip to model inflammatory processes. *Sci Rep.* (2020) 10:1–16. doi: 10.1038/s41598-020-78359-2

56. Cherne MD, Sidar B, Sebrell TA, Sanchez HS, Heaton K, Kassama FJ, et al. A synthetic hydrogel, vitroGel® ORGANOID-3, improves immune cell-epithelial interactions in a tissue chip co-culture model of human gastric organoids and dendritic cells. *Front Pharmacol.* (2021) 12:707891–. doi: 10.3389/fphar.2021.707891

57. Gjorevski N, Avignon B, Gerard R, Cabon L, Roth AB, Bscheider M, et al. Neutrophilic infiltration in organ-on-a-chip model of tissue inflammation. *Lab Chip.* (2020) 20:3365–74. doi: 10.1039/DOLC00417K

58. Gijzen L, Marescotti D, Raineri E, Nicolas A, Lanz HL, Guerrera D, et al. An intestine-on-a-chip model of plug-and-play modularity to study inflammatory processes. *SLAS Technol.* (2020) 25:585–97. doi: 10.1177/2472630320924999

59. Rajasekar S, Lin DSY, Abdul L, Liu A, Sotra A, Zhang F, et al. iFlowPlate-A customized 384-well plate for the culture of perfusable vascularized colon organoids. *Adv Mater.* (2020) 32:e2002974. doi: 10.1002/adma.202002974

60. Naumovska E, Aalderink G, Wong Valencia C, Kosim K, Nicolas A, Brown S, et al. Direct on-chip differentiation of intestinal tubules from induced pluripotent stem cells. *Int J Mol Sci.* (2020) 21. doi: 10.3390/ijms21144964

61. Groger M, Rennert K, Giszas B, Weiss E, Dinger J, Funke H, et al. Monocyte-induced recovery of inflammation-associated hepatocellular dysfunction in a biochip-based human liver model. *Sci Rep.* (2016) 6:21868. doi: 10.1038/srep21868

62. Bircsak KM, DeBiasio R, Miedel M, Alsebahi A, Reddinger R, Saleh A, et al. A 3D microfluidic liver model for high throughput compound toxicity screening in the OrganoPlate(R). *Toxicology.* (2021) 450:152667. doi: 10.1016/j.tox.2020.152667

63. Jang KJ, Otinoma MA, Ronxhi J, Lim HK, Ewart L, Kodella KR, et al. Reproducing human and cross-species drug toxicities using a Liver-Chip. *Sci Transl Med.* (2019) 11. doi: 10.1126/scitranslmed.aax5516

64. Freag MS, Namgung B, Reyna Fernandez ME, Gherardi E, Sengupta S, Jang HL. Human nonalcoholic steatohepatitis on a chip. *Hepatol Commun.* (2021) 5:217–33. doi: 10.1002/hep4.1647

65. Ortega-Prieto AM, Skelton JK, Wai SN, Large E, Lussignol M, Vizcay-Barrena G, et al. 3D microfluidic liver cultures as a physiological preclinical tool for hepatitis B virus infection. *Nat Commun.* (2018) 9:1–15. doi: 10.1038/s41467-018-02969-8

66. Sarkar U, Rivera-Burgos D, Large EM, Hughes DJ, Ravindra KC, Dyer RL, et al. Metabolite profiling and pharmacokinetic evaluation of hydrocortisone in a perfused three-dimensional human liver bioreactor. *Drug Metab Dispos.* (2015) 43:1091–9. doi: 10.1124/dmd.115.063495

67. Torigawa YS, Spina CS, Mammoto T, Mammoto A, Weaver JC, Tat T, et al. Bone marrow-on-a-chip replicates hematopoietic niche physiology in vitro. *Nat Methods.* (2014) 11:663–9. doi: 10.1038/nmeth.2938

68. Nelson MR, Ghoshal D, Mejias JC, Rubio DF, Keith E, Roy K. A multi-niche microvascularized human bone marrow (hBM) on-a-chip elucidates key roles of the endosteal niche in hBM physiology. *Biomaterials.* (2021) 270:120683. doi: 10.1016/j.biomaterials.2021.120683

69. Sieber S, Wirth L, Cavak N, Koenigsmark M, Marx U, Lauster R, et al. Bone marrow-on-a-chip: Long-term culture of human haematopoietic stem cells in a three-dimensional microfluidic environment. *J Tissue Eng Regener Med.* (2018) 12:479–89. doi: 10.1002/term.2507

70. Chou DB, Frismantas V, Milton Y, David R, Pop-Damkov P, Ferguson D, et al. On-chip recapitulation of clinical bone marrow toxicities and patient-specific pathophysiology. *Nat Biomed Eng.* (2020) 4:394–406. doi: 10.1038/s41551-019-0495-z

71. Glaser DE, Curtis MB, Sariano PA, Rollins ZA, Shergill BS, Anand A, et al. Organ-on-a-chip model of vascularized human bone marrow niches. *Biomaterials.* (2022) 280:121245. doi: 10.1016/j.biomaterials.2021.121245

72. Bruce A, Evans R, Mezan R, Shi L, Moses BS, Martin KH, et al. Three-dimensional microfluidic tri-culture model of the bone marrow microenvironment for study of acute lymphoblastic leukemia. *PloS One.* (2015) 10:e0140506. doi: 10.1371/journal.pone.0140506

73. Mitra B, Jindal R, Lee S, Xu Dong D, Li L, Sharma N, et al. Microdevice integrating innate and adaptive immune responses associated with antigen presentation by dendritic cells. *RSC Adv.* (2013) 3:16002–10. doi: 10.1039/c3ra41308j

74. Hallfors N, Shanti A, Sapudom J, Teo J, Petroianu G, Lee S, et al. Multi-compartment lymph-node-on-a-chip enables measurement of immune cell motility in response to drugs. *Bioengineering (Basel).* (2021) 8:19. doi: 10.3390/bioengineering8020019

75. Kwee BJ, Akue A, Sung KE. On-chip human lymph node stromal network for evaluating dendritic cell and T-cell trafficking. *bioRxiv.* (2023) 2023:03.21.533042.

76. Giese C, Demmler CD, Ammer R, Hartmann S, Lubitz A, Miller L, et al. A human lymph node *in vitro*-challenges and progress. *Artif Organs.* (2006) 30:803–8. doi: 10.1111/j.1525-1594.2006.00303.x

77. Giese C, Lubitz A, Demmler CD, Reuschel J, Bergner K, Marx U. Immunological substance testing on human lymphatic micro-organoids *in vitro*. *J Biotechnol.* (2010) 148:38–45. doi: 10.1016/j.biote.2010.03.001

78. Goyal G, Prabhala P, Mahajan G, Bausk B, Gilboa T, Xie L, et al. Ectopic lymphoid follicle formation and human seasonal influenza vaccination responses recapitulated in an organ-on-a-chip. *Advanced Science.* (2022) 9:2103241–. doi: 10.1002/advs.202103241

79. Shanti A, Samara B, Abdullah A, Hallfors N, Accoto D, Sapudom J, et al. Multi-compartment 3D-cultured organ-on-a-chip: towards a biomimetic lymph node for drug development. *Pharmaceutics.* (2020) 12:464–. doi: 10.3390/pharmaceutics12050464

80. Birmingham KG, O'Melia MJ, Bordy S, Reyes Aguilar D, El-Reyas B, Lesinski G, et al. Lymph node subcapsular sinus microenvironment-on-A-chip modeling shear flow relevant to lymphatic metastasis and immune cell homing. *iScience*. (2020) 23:101751. doi: 10.1016/j.isci.2020.101751

81. Buffet PA, Milon G, Brousse V, Correas JM, Douisset B, Couvelard A, et al. Ex vivo perfusion of human spleens maintains clearing and processing functions. *Blood*. (2006) 107:3745–52. doi: 10.1182/blood-2005-10-4094

82. Rigat-Brugarolas LG, Elizalde-Torrent A, Bernabeu M, De Niz M, Martin-Jaular L, Fernandez-Becerra C, et al. A functional microengineered model of the human spleon-on-a-chip. *Lab Chip*. (2014) 14:1715–24. doi: 10.1039/C3LC51449H

83. Qiang Y, Sissoko A, Liu ZL, Dong T, Zheng F, Kong F, et al. Microfluidic study of retention and elimination of abnormal red blood cells by human spleen with implications for sickle cell disease. *Proc Natl Acad Sci U S A*. (2023) 120: e2217607120. doi: 10.1073/pnas.2217607120

84. Ehlers H, Nicolas A, Schavemaker F, Heijmans JPM, Bulst M, Trietsch SJ, et al. Vascular inflammation on a chip: A scalable platform for trans-endothelial electrical resistance and immune cell migration. *Front Immunol*. (2023) 14:1118624. doi: 10.3389/fimmu.2023.1118624

85. de Haan L, Suijker J, van Roey R, Berges N, Petrova E, Queiroz K, et al. A microfluidic 3D endothelium-on-a-chip model to study transendothelial migration of T cells in health and disease. *Int J Mol Sci*. (2021) 22. doi: 10.3390/ijms22158234

86. Lin F, Butcher EC. T cell chemotaxis in a simple microfluidic device. *Lab Chip*. (2006) 6:1462–9. doi: 10.1039/B607071

87. Aung A, Kumar V, Theprungsirikul J, Davey SK, Varghese S. An engineered tumor-on-a-chip device with breast cancer-immune cell interactions for assessing T-cell recruitment. *Cancer Res*. (2020) 80:263–75. doi: 10.1158/0008-5472.CAN-19-0342

88. Pavesi A, Tan AT, Koh S, Chia A, Colombo M, Antonecchia E, et al. A 3D microfluidic model for preclinical evaluation of TCR-engineered T cells against solid tumors. *JCI Insight*. (2017) 2. doi: 10.1172/jci.insight.89762

89. Paek J, Park SE, Lu Q, Park KT, Cho M, Oh JM, et al. Microphysiological engineering of self-assembled and perfusable microvascular beds for the production of vascularized three-dimensional human microtissues. *ACS Nano*. (2019) 13:7627–43. doi: 10.1021/acsnano.9b00668

90. Riddle RB, Jennbacken K, Hansson KM, Harper MT. Endothelial inflammation and neutrophil transmigration are modulated by extracellular matrix composition in an inflammation-on-a-chip model. *Sci Rep*. (2022) 12:1–14. doi: 10.1038/s41598-022-10849-x

91. Surendran V, Rutledge D, Colmon R, Chandrasekaran A. A novel tumor-immune microenvironment (TIME)-on-Chip mimics three dimensional neutrophil-tumor dynamics and neutrophil extracellular traps (NETs)-mediated collective tumor invasion. *Biofabrication*. (2021) 13:035029–. doi: 10.1088/1758-5090/abe1cf

92. Chen MB, Hajal C, Benjamin DC, Yu C, Azizgolshani H, Hynes RO, et al. Inflamed neutrophils sequestered at entrapped tumor cells via chemotactic confinement promote tumor cell extravasation. *Proc Natl Acad Sci U S A*. (2018) 115:7022–7. doi: 10.1073/pnas.1715932115

93. Parlato S, De Ninno A, Molfetta R, Toschi E, Salerno D, Mencattini A, et al. 3D Microfluidic model for evaluating immunotherapy efficacy by tracking dendritic cell behaviour toward tumor cells. *Sci Rep*. (2017) 7:1–16. doi: 10.1038/s41598-017-01013-x

94. Boussoumier-Calleja A, Atiyas Y, Haase K, Headley M, Lewis C, Kamm RD. The effects of monocytes on tumor cell extravasation in a 3D vascularized microfluidic model. *Biomaterials*. (2018) 198:180–93. doi: 10.1016/j.biomaterials.2018.03.005

95. Bi Y, Shirure VS, Liu R, Cunningham C, Ding L, Meacham JM, et al. Tumor-on-a-chip platform to interrogate the role of macrophages in tumor progression. *Integr Biol (Camb)*. (2020) 12:221–32. doi: 10.1093/intbio/zyaa017

96. Song J, Choi H, Koh SK, Park D, Yu J, Kang H, et al. High-throughput 3D *in vitro* tumor vasculature model for real-time monitoring of immune cell infiltration and cytotoxicity. *Front Immunol*. (2021) 12:3848–. doi: 10.3389/fimmu.2021.733317

97. Ayuso JM, Truttschel R, Gong MM, Humayun M, Virumbrales-Munoz M, Vitek R, et al. Evaluating natural killer cell cytotoxicity against solid tumors using a microfluidic model. *Oncimmunology*. (2019) 8:1553477. doi: 10.1080/2162402X.2018.1553477

98. Lee HR, Sung JH. Multi-organ-on-a-chip for realization of gut-skin axis. *Biotechnol Bioengineering*. (2022) 119(9):2590–601. doi: 10.1002/bit.28164

99. Chen WLK, Edington C, Suter E, Yu J, Velazquez JJ, Velazquez JG, et al. Integrated gut/liver microphysiological systems elucidates inflammatory inter-tissue crosstalk. *Biotechnol Bioeng*. (2017) 114:2648–59. doi: 10.1002/bit.26370

100. Trapecar M, Communal C, Velazquez J, Maass CA, Huang YJ, Schneider K, et al. Gut-liver physiomics reveal paradoxical modulation of IBD-related inflammation by short-chain fatty acids. *Cell Syst*. (2020) 10:223–39 e9. doi: 10.1016/j.cels.2020.02.008

101. Koning JJ, Rodrigues Neves CT, Schimek K, Thon M, Spiekstra SW, Waaijman T, et al. A multi-organ-on-chip approach to investigate how oral exposure to metals can cause systemic toxicity leading to langerhans cell activation in skin. *Front Toxicology*. (2022) 0:70–. doi: 10.3389/ftox.2021.824825

102. Liu W, Song J, Du X, Zhou Y, Li Y, Li R, et al. AKR1B10 (Aldo-keto reductase family 1 B10) promotes brain metastasis of lung cancer cells in a multi-organ microfluidic chip model. *Acta Biomater*. (2019) 91:195–208. doi: 10.1016/j.actbio.2019.04.053

103. Skardal A, Murphy SV, Devarasetty M, Mead I, Kang HW, Seol YJ, et al. Multi-tissue interactions in an integrated three-tissue organ-on-a-chip platform. *Sci Rep*. (2017) 7:1–16. doi: 10.1038/s41598-017-08879-x

104. Herland A, Maoz BM, Das D, Somayaji MR, Prantil-Baum R, Novak R, et al. Quantitative prediction of human pharmacokinetic responses to drugs *via* fluidically coupled vascularized organ chips. *Nat Biomed Eng*. (2020) 4:421–36. doi: 10.1038/s41551-019-0498-9

105. Stamatakis Z, Swadling L. The liver as an immunological barrier redefined by single-cell analysis. *Immunology*. (2020) 160:157–70. doi: 10.1111/imm.13193

106. Snyder ME, Farber DL. Human lung tissue resident memory T cells in health and disease. *Curr Opin Immunol*. (2019) 59:101–8. doi: 10.1016/j.co.2019.05.011

107. Zhang C, Merana GR, Harris-Tryon T, Scharschmidt TC. Skin immunity: dissecting the complex biology of our body's outer barrier. *Mucosal Immunol*. (2022) 15:551–61. doi: 10.1038/s41385-022-00505-y

108. Rodrigues Neves C, Gibbs S. Progress on reconstructed human skin models for allergy research and identifying contact sensitizers. *Curr Top Microbiol Immunol*. (2021) 430:103–29.

109. Nahavandian A, Thon M, van den Broek LJ, Spiekstra SW, Atac B, Lindner G, et al. Proof-of-concept organ-on-chip study: topical cinnamaldehyde exposure of reconstructed human skin with integrated neopapillae cultured under dynamic flow. *Pharmaceutics*. (2022) 14. doi: 10.3390/pharmaceutics14081529

110. Jager J, Nahavandian A, Thon M, Waaijman T, Spanhaak B, de Kok M, et al. Reconstructed human skin with hypodermis shows essential role of adipose tissue in skin metabolism. *Tissue Eng Regener Med*. (2024) 21:499–511. doi: 10.1007/s13770-023-00621-1

111. Chassaing B, Kumar M, Baker MT, Singh V, Vijay-Kumar M. Mammalian gut immunity. *BioMed J*. (2014) 37:246–58. doi: 10.4103/2319-4170.130922

112. Mowat AM, Agace WW. Regional specialization within the intestinal immune system. *Nat Rev Immunol*. (2014) 14:667–85. doi: 10.1038/nri3738

113. Zhu W, Yu J, Nie Y, Shi X, Liu Y, Li F, et al. Disequilibrium of M1 and M2 macrophages correlates with the development of experimental inflammatory bowel diseases. *Immunol Invest*. (2014) 43:638–52. doi: 10.3109/08820139.2014.909456

114. Lissner D, Schumann M, Batra A, Kredel LI, Kuhl AA, Erben U, et al. Monocyte and M1 macrophage-induced barrier defect contributes to chronic intestinal inflammation in IBD. *Inflammation Bowel Dis*. (2015) 21:1297–305. doi: 10.1097/MIB.0000000000000384

115. Kubes P, Jenne C. Immune responses in the liver. *Annu Rev Immunol*. (2018) 36:247–77. doi: 10.1146/annurev-immunol-051116-052415

116. Moses SR, Adorno JJ, Palmer AF, Song JW. Vessel-on-a-chip models for studying microvascular physiology, transport, and function *in vitro*. *Am J Physiol Cell Physiol*. (2021) 320:C92–C105. doi: 10.1152/ajpcell.00355.2020

117. Pollet A, den Toonder JMJ. Recapitulating the vasculature using organ-on-chip technology. *Bioengineering (Basel)*. (2020) 7. doi: 10.3390/bioengineering7010017

118. Krishnamurty AT, Turley SJ. Lymph node stromal cells: cartographers of the immune system. *Nat Immunol*. (2020) 21:369–80. doi: 10.1038/s41590-020-0635-3

119. de Melo CVB, Hermida MD, Mesquita BR, Fontes JLM, Koning JJ, Solca MDS, et al. Phenotypical characterization of spleen remodeling in murine experimental visceral leishmaniasis. *Front Immunol*. (2020) 11:653. doi: 10.3389/fimmu.2020.00653

120. Grasso C, Pierie C, Mebius RE, van Baarsen LGM. Lymph node stromal cells: subsets and functions in health and disease. *Trends Immunol*. (2021) 42:920–36. doi: 10.1016/j.it.2021.08.009

121. Morrison AI, Mikula AM, Spiekstra SW, de Kok M, Affandi AJ, Roest HP, et al. An organotypic human lymph node model reveals the importance of fibroblastic reticular cells for dendritic cell function. *Tissue Eng Regener Med*. (2023) 21:455–71. doi: 10.1007/s13770-023-00609-x

122. Asal M, Rep M, Bontkes HJ, van Vliet SJ, Mebius RE, Gibbs S. Towards full thickness small intestinal models: incorporation of stromal cells. *Tissue Eng Regener Med*. (2024) 21:369–77. doi: 10.1007/s13770-023-00600-6

123. Sung JH. Multi-organ-on-a-chip for pharmacokinetics and toxicokinetic study of drugs. *Expert Opin Drug Metab Toxicol*. (2021) 17:969–86. doi: 10.1080/17425255.2021.1908996

124. Xu Z, Li E, Guo Z, Yu R, Hao H, Xu Y, et al. Design and construction of a multi-organ microfluidic chip mimicking the *in vivo* microenvironment of lung cancer metastasis. *ACS Appl Mater Interfaces*. (2016) 8:25840–7. doi: 10.1021/acsami.6b08746

125. Cisneros B, Garcia-Aguirre I, Unzueta J, Arrieta-Cruz I, Gonzalez-Morales O, Dominguez-Larrieta JM, et al. Immune system modulation in aging: Molecular mechanisms and therapeutic targets. *Front Immunol*. (2022) 13:1059173. doi: 10.3389/fimmu.2022.1059173

126. Kroll KT, Mata MM, Homan KA, Micallef V, Carpy A, Hiratsuka K, et al. Immune-infiltrated kidney organoid-on-chip model for assessing T cell bispecific antibodies. *Proc Natl Acad Sci U S A*. (2023) 120:e2305322120. doi: 10.1073/pnas.2305322120

127. Nair AL, Groenendijk L, Overdevest R, Fowke TM, Annida R, Mocellin O, et al. Human BBB-on-a-chip reveals barrier disruption, endothelial inflammation, and T cell migration under neuroinflammatory conditions. *Front Mol Neurosci*. (2023) 16. doi: 10.3389/fnmol.2023.1250123

128. Marzagalli M, Pelizzoni G, Fedi A, Vitale C, Fontana F, Bruno S, et al. A multi-organ-on-chip to recapitulate the infiltration and the cytotoxic activity of circulating NK cells in 3D matrix-based tumor model. *Front Bioeng Biotechnol.* (2022) 10:945149. doi: 10.3389/fbioe.2022.945149

129. Wagar LE, Salahudeen A, Constantz CM, Wendel BS, Lyons MM, Mallajosyula V, et al. Modeling human adaptive immune responses with tonsil organoids. *Nat Med.* (2021) 27:125–35. doi: 10.1038/s41591-020-01145-0

130. Kastensmidt JM, Schroers-Martin JG, Swarder BJ, Sureshchandra S, Khodadoust MS, Liu CL, et al. A human lymphoma organoid model for evaluating and targeting the follicular lymphoma tumor immune microenvironment. *Cell Stem Cell.* (2024) 31:410–20 e4. doi: 10.1016/j.stem.2024.01.012

131. Ewart L, Apostolou A, Briggs SA, Carman CV, Chaff JT, Heng AR, et al. Performance assessment and economic analysis of a human Liver-Chip for predictive toxicology. *Commun Med (Lond).* (2022) 2:154. doi: 10.1038/s43856-022-00209-1

132. Nahle Z. A proof-of-concept study poised to remodel the drug development process: Liver-Chip solutions for lead optimization and predictive toxicology. *Front Med Technol.* (2022) 4:1053588. doi: 10.3389/fmedt.2022.1053588

133. Kutluk H, Bastounis EE, Constantinou I. Integration of extracellular matrices into organ-on-chip systems. *Adv Healthc Mater.* (2023) 12:e2203256. doi: 10.1002/adhm.202203256

134. Danku AE, Dulf EH, Braicu C, Jurj A, Berindan-Neagoe I. Organ-on-A-chip: A survey of technical results and problems. *Front Bioeng Biotechnol.* (2022) 10:840674. doi: 10.3389/fbioe.2022.840674

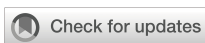
135. Bu W, Wu Y, Ghaemmaghami AM, Sun H, Mata A. Rational design of hydrogels for immunomodulation. *Regener Biomater.* (2022) 9:rbac009. doi: 10.1093/rb/rbac009

136. Pereira RVS, EzEldeen M, Ugarte-Berzal E, Martens E, Malengier-Devlies B, Vandooren J, et al. Physiological fibrin hydrogel modulates immune cells and molecules and accelerates mouse skin wound healing. *Front Immunol.* (2023) 14:1170153. doi: 10.3389/fimmu.2023.1170153

137. Franzen N, van Harten WH, Retel VP, Loskill P, van den Eijnden-van Raaij J, M IJ. Impact of organ-on-a-chip technology on pharmaceutical R&D costs. *Drug Discovery Today.* (2019) 24:1720–4. doi: 10.1016/j.drudis.2019.06.003

138. Sunildutt N, Parihar P, Chethikkattuvelli Salih AR, Lee SH, Choi KH. Revolutionizing drug development: harnessing the potential of organ-on-chip technology for disease modeling and drug discovery. *Front Pharmacol.* (2023) 14:1139229. doi: 10.3389/fphar.2023.1139229

139. Ingber DE. Human organs-on-chips for disease modelling, drug development and personalized medicine. *Nat Rev Genet.* (2022) 23:467–91. doi: 10.1038/s41576-022-00466-9



OPEN ACCESS

EDITED BY

Thomas Hartung,
Johns Hopkins University, United States

REVIEWED BY

Kumar Pavanish,
Singhealth/Duke-NUS Academic Medical
Centre, Singapore
Guillaume Hoeffel,
INSERM U1104 Centre d'immunologie de
Marseille-Luminy (CIML), France

*CORRESPONDENCE

Béatrice Cousin
✉ beatrice.cousin@inserm.fr

RECEIVED 15 December 2023

ACCEPTED 31 May 2024

PUBLISHED 21 June 2024

CITATION

Arlat A, Renoud M-L, Nakhle J, Thomas M, Fontaine J, Arnaud E, Dray C, Authier H, Monsarrat P, Coste A, Casteilla L, Ousset M and Cousin B (2024) Generation of functionally active resident macrophages from adipose tissue by 3D cultures. *Front. Immunol.* 15:1356397. doi: 10.3389/fimmu.2024.1356397

COPYRIGHT

© 2024 Arlat, Renoud, Nakhle, Thomas, Fontaine, Arnaud, Dray, Authier, Monsarrat, Coste, Casteilla, Ousset and Cousin. This is an open-access article distributed under the terms of the [Creative Commons Attribution License \(CC BY\)](#). The use, distribution or reproduction in other forums is permitted, provided the original author(s) and the copyright owner(s) are credited and that the original publication in this journal is cited, in accordance with accepted academic practice. No use, distribution or reproduction is permitted which does not comply with these terms.

Generation of functionally active resident macrophages from adipose tissue by 3D cultures

Adèle Arlat¹, Marie-Laure Renoud¹, Jean Nakhle¹, Miguel Thomas¹, Jessica Fontaine¹, Emmanuelle Arnaud¹, Cédric Dray¹, Hélène Authier¹, Paul Monsarrat^{1,2,3}, Agnès Coste¹, Louis Casteilla¹, Marielle Ousset¹ and Béatrice Cousin^{1*}

¹RESTORE Research Center, Université de Toulouse, INSERM 1301, CNRS 5070, Etablissement Français du Sang (EFS), Ecole Nationale Vétérinaire de Toulouse (ENVT), Toulouse, France, ²Dental Faculty and Hospital of Toulouse – Toulouse Institute of Oral Medicine and Science, CHU de Toulouse, Toulouse, France, ³Artificial and Natural Intelligence Toulouse Institute (ANITI), Toulouse, France

Introduction: Within adipose tissue (AT), different macrophage subsets have been described, which played pivotal and specific roles in upholding tissue homeostasis under both physiological and pathological conditions. Nonetheless, studying resident macrophages *in-vitro* poses challenges, as the isolation process and the culture for extended periods can alter their inherent properties.

Methods: Stroma-vascular cells isolated from murine subcutaneous AT were seeded on ultra-low adherent plates in the presence of macrophage colony-stimulating factor. After 4 days of culture, the cells spontaneously aggregate to form spheroids. A week later, macrophages begin to spread out of the spheroid and adhere to the culture plate.

Results: This innovative three-dimensional (3D) culture method enables the generation of functional mature macrophages that present distinct genic and phenotypic characteristics compared to bone marrow-derived macrophages. They also show specific metabolic activity and polarization in response to stimulation, but similar phagocytic capacity. Additionally, based on single-cell analysis, AT-macrophages generated in 3D culture mirror the phenotypic and functional traits of *in-vivo* AT resident macrophages.

Discussion: Our study describes a 3D *in-vitro* system for generating and culturing functional AT-resident macrophages, without the need for cell sorting. This system thus stands as a valuable resource for exploring the differentiation and function of AT-macrophages *in vitro* in diverse physiological and pathological contexts.

KEYWORDS

resident macrophage, macrophage subpopulation, adipose tissue, bone marrow, 3D culture, metabolism, phagocytosis, unsupervised analysis

1 Introduction

Adipose tissue (AT) is not only a passive storage depot for energy excess but also a vital endocrine and immune organ (1). Indeed, AT communicates with all other organs through an active release of various adipokines and inflammatory factors that significantly influence overall energy balance in the body and metabolic health (2). In addition to mature adipocytes, AT harbors a diverse and plentiful immune cell population, extensively investigated, with macrophages emerging as the predominant cell type (3). Macrophages play a critical role in triggering immune responses by detecting initial insults and releasing an array of inflammatory mediators, including cytokines and chemokines (4). Their biology is intricate and influenced by various factors such as tissue environment, ontogeny, and their inflammatory status within their respective niches (5, 6). Like in most tissues, AT-macrophages form a diverse population, with resident AT-macrophages believed to primarily originate from embryonic yolk-sac precursors under normal conditions, exhibiting the ability to self-renew through proliferation (7, 8). Another subset of AT-macrophages arises after the final differentiation of monocytes [bone marrow (BM)-derived macrophages] (9). In most tissues, resident and BM-derived macrophage subsets can be distinguished using four markers, namely, *Timd4*, *Folr2*, and *Lyve1* for identifying resident macrophages, while *Ccr2* is proposed for identifying BM-derived macrophages (10). A recent analysis of macrophage heterogeneity identified CD206 as a marker of resident macrophages in AT (11) and dermis (12).

Depending on their origin and their environment, macrophages display specific functional characteristics (13). In the physiological state, resident macrophages play a critical role in maintaining tissue homeostasis (14). In the skin, resident dermal macrophages have been described to coordinate defense against infection, to play critical roles in all stages of healing process, or to contribute to stress-induced hair follicle regeneration (15–17). In the AT, macrophages play a critical role in a variety of physiological and pathological processes. In a physiological state, resident AT-macrophages are considered metabolically advantageous. They play crucial roles in maintaining AT homeostasis, tissue expansion, and remodeling (18), as well as tissue regeneration (19). Conversely, BM-derived macrophages can negatively impact AT function by promoting inflammation, insulin resistance, and fibrosis (20, 21). The distinct roles of various AT-macrophages subsets highlight the importance of their imprinting by the cellular niche. This prompts our investigation into their intrinsic properties.

Unfortunately, studying resident macrophages *in vitro* presents a challenge due to the lack of an adequate culture system that can produce enough cells that accurately reflect *in-vivo* characteristics. Furthermore, sorting resident macrophages usually alters their intrinsic properties. Additionally, the preservation of their properties in culture for an extended period while maintaining their characteristics is a challenging task due to the tissue microenvironment's critical role in macrophage imprinting (22). Therefore, an *in-vitro* approach that supports the production of resident macrophages seems essential.

In this study, we adapted an efficient method initially developed for the production of mature and functional AT mastocytes (23) to generate mouse AT resident macrophages. Our research demonstrates that cultivating AT stroma-vascular cells in a three-dimensional (3D) environment generates fully developed and functional AT-macrophages with distinct transcriptomic, phenotypic, metabolic, and functional characteristics compared to BM-derived macrophages *in vitro*. These cultured cells successfully recapitulate the characteristics observed *in vivo* for resident AT-macrophages.

2 Material and methods

2.1 Animals

Experiments were performed on 6- to 8-week-old male C57Bl6/J Hola HSD mice (ENVIGO, Gannat, France). Animals were group-housed in a controlled environment (12h light/dark cycles at 21°C) with unrestricted access to water and a standard chow diet in a pathogen-free animal facility. Mice were killed by cervical dislocation and AT and femur were removed.

The animal study was approved by European Community Guidelines (2010/63/UE)/institutional ethics committee N.122 US006/CREFRE. The study was conducted in accordance with the local legislation and institutional requirements.

2.2 Isolation of adipose derived stromal vascular cells fraction and bone marrow cells

Sub-cutaneous adipose tissues (sc-AT) were collected, and lymph nodes removed. Femurs were collected and immediately flushed with α-MEM medium (Gibco, Thermo Fisher Scientific, Waltham, USA). Sc-AT sustained a mechanical dissociation and enzymatic digestion at 37°C with collagenase (NB4, Sigma-Aldrich, Saint-Louis, USA) for 30 min. After filtration and centrifugation, stroma vascular cells were isolated as described previously (19). A red blood cells lysis (NH4Cl 155 mM, K2HPO4 5.7 mM, EDTA 0.1 mM) was performed on BM and adipose stromal vascular fraction (SVF), and cells were then counted with cell counter (Beckman Coulter, Brea, USA).

2.3 *In vitro* production of adipose tissue macrophages

Adipose SVF cells were seeded on ultra-low adherence 96 wells round bottom plates (COSTAR, Dutcher, Bernolsheim, France) (10^5 cells/well) with Roswell Park Memorial Institute (RPMI, InVitrogen, Thermo Fisher Scientific, Waltham, USA) supplemented with Glutamax medium (Gibco, Thermo Fisher Scientific, Waltham, USA), Heat Inactivated Newborn Calf Serum (hiNBS; Gibco) (10%), a cocktail of amphotericin (Invitrogen, Thermo Fisher Scientific, Waltham, USA), streptomycin, and

penicillin (1%; Life Technologies, Carlsbad, USA) and macrophage colony-stimulating factor (M-CSF) (10 ng/ml; PeproTech, Thermo Fisher Scientific, Waltham, USA). Cells were briefly centrifuged and incubated at 37°C with 5% CO₂. After 4 days of culture, the cells spontaneously aggregate to form spheroids. Starting on day 7, the cells begin to spread out of the spheroid and adhere to the culture plate.

2.4 *In vitro* macrophages culture

BM cells were seeded on non-adherent Petri dishes at a concentration of 2.10⁶ cells in RPMI supplemented with Glutamax medium (Gibco, Thermo Fisher Scientific, Waltham, USA), hiNBSC (Gibco, Thermo Fisher Scientific, Waltham, USA) (10%), a cocktail of amphotericin (Invitrogen, Thermo Fisher Scientific, Waltham, USA), streptomycin, and penicillin (Thermo Fisher Scientific, Waltham, USA) (1%) and M-CSF (Pepro Tech, Thermo Fisher Scientific, Waltham, USA) (10 ng/ml). Cells were then incubated at 37°C with 5% CO₂.

After 13 days in culture, differentiated BM-macrophages and cells harvested from AT-3D cultures were counted and seeded on adherent culture plates with RPMI supplemented with Glutamax medium (Gibco, Thermo Fisher Scientific, Waltham, USA), hiNBSC (Gibco, Thermo Fisher Scientific, Waltham, USA) (10%) and a cocktail of amphotericin, streptomycin, and penicillin (1%) overnight. Macrophages were then treated or not with interleukine-4 (IL-4; PeproTech, Thermo Fisher, Waltham, USA) (10 ng/ml) or interferon-γ (IFN-γ; PeproTech, Thermo Fisher, Waltham, USA) (50 ng/ml) for 4h (gene expression) or 24h (protein expression), or used for flow cytometry analyses or functional assays [phagocytosis and reactive oxygen species (ROS) production].

2.5 Spheroid dissociation

After 7, 13, or 21 days in culture, spheroids were collected and dissociated with NB4 (1.7 U/ml; Sigma-Aldrich, Saint-Louis, USA) and dispase I (2.5 U/ml; Sigma-Aldrich, Saint-Louis, USA) at 37°C for 40 min. Spheroid were then mechanically dissociated with a pipette and cells were centrifuged to complete dissociation.

2.6 Immunohistochemistry and microscopy

After 13 days, cells that had spread around the spheroids were seeded onto adherent culture plates, fixed with paraformaldehyde (PFA; Sigma-Aldrich, Saint-Louis, USA) (2%) and permeabilized with saponin (0.25%) (Sigma-Aldrich). Unspecific binding sites were blocked using fetal bovin serum (Sigma-Aldrich, Saint-Louis, USA) before incubation overnight at 4°C with primary antibody rat anti-mouse F4/80 (Bio-Rad, Hercules, USA). Cells were then washed and stained with a secondary Alexa Fluor 488-coupled donkey anti-rat antibody (Invitrogen, Thermo Fisher Waltham, USA), and 4',6-diamidino-2-phenylindole (DAPI) (Sigma-Aldrich, Saint-Louis, USA). Images were obtained with

Opera Phenix (PerkinElmer, Waltham, USA) and analyzed with Harmony software.

2.7 Flow cytometry analysis and cell sorting

AT- and BM-macrophages, dissociated spheroid cells, and sc-AT SVF cells were incubated with live/dead reagent (Thermo Fisher Scientific, Waltham, USA) and FcR-blocking reagent (BD Pharmigen, Franklin Lakes, USA) (except for CD16/32 staining). Cells were then stained with conjugated rat anti-mouse antibodies and the specificity of each staining was checked using specific isotype controls (Supplementary Table S1). After extracellular staining, cells were washed with MACS buffer (Miltenyi Biotec, Bergisch Gladbach, Germany). For intracellular staining, cells were fixed with 2% PFA (Sigma-Aldrich, Saint Louis, USA) solution and permeabilized with 0.5% Saponin (Sigma Aldrich, Saint Louis, USA) before incubating with coupled intracellular antibodies diluted in 0.5% Saponin for 40 min. Events were acquired on flow cytometer (LSRFortessa, BD Biosciences, Franklin Lakes, USA), and data were analyzed using Kalusa version 1.2 (Beckman Coulter, Brea, USA).

For unsupervised analyses, preprocessing of cytometry data was realized using FlowJo 10.8.1 software (Flow Jo LLC, Becton Dickinson, Franklin Lakes, USA). Arc sinh normalization of concatenated individual flow cytometry standard files and homogenization by downsampling of each sample were performed before gating on alive, CD45⁺. Then we selected F4/80⁺, CD11b⁺ cells. A nonlinear dimensionality reduction [Uniform Manifold Approximation and Projection (UMAP)] and Louvain clustering on Python was performed to segregate populations based on the expression of specific macrophage markers (CD45, F4/80, CD11b, CD206, CD16/32, MHC-II, MerTK, Dectin-1, and CD36).

For macrophage sorting experiments, sc-AT SVF cells were stained with DAPI, CD45, CD11b, and F4/80 antibodies (Supplementary Table S1). DAPI⁻/CD45⁺/CD11b⁺/F4/80⁺ cells were sorted (BD FACS ARIA Fusion III Cell sorter, BD Biosciences, Franklin Lakes, USA) and directly incubated in lysis buffer (Promega, Madison, USA) for subsequent analysis.

2.8 RNA extraction, real-time qPCR, and bulk RNA-seq

RNA was extracted from sorted sc-AT macrophages, AT- and BM-cultured macrophages, and purified using a Promega extraction kit (Relia PreP™ RNA Cell Miniprep, Promega, Madison, USA). For real-time PCR, 250 ng of total RNA were reverse transcribed using the High-Capacity cDNA Reverse Transcription kit (Applied Biosystems, Thermo Fisher Scientific, Waltham, USA). cDNAs were diluted and mixed with FAST SYBR GREEN (Roche Diagnostics, Meylan, France), and primers (Supplementary Table S2) on a LightCycler 480 (Roche Applied Science, Penzberg, Germany). All relative gene expression was determined using a standard curve realized with cDNA dilutions (1/5, 1/10, 1/20, and 1/40) and the ratio with GAPDH reporter gene.

For bulk RNA-seq, RNA quality was assessed using HS RNA Kit on Fragment analyser (Agilent Technologies, Santa Clara, USA). Analysis was performed in triplicate/duplicate of total RNAs from AT- and BM-cultured macrophages and sc-AT-sorted macrophages. cDNA libraries were generated according to Illumina Stranded mRNA Prep kit (Illumina, San Diego, USA) from 100 ng tRNA. cDNA was amplified for 13 cycles and barcoded with IDT® for Illumina® RNA UD Indexes Set A, Ligation (96 indexes, 96 samples). Libraries were tested for quality using HS NGS Fragment kit on Fragment Analyzer (Agilent Technologies, Santa Clara, USA) and concentrations were measured using KAPA qPCR library quantification kit (Roche Diagnostics, Meylan, France). Samples were pooled together to 8 nM concentration and sequenced with an Illumina NovaSeq SP 200 using 2 × 100 bp mode. RNA-seq reads were processed using the Galaxy web-based platform (<https://usegalaxy.eu/>). RNA-seq data were obtained in FASTQ format, reads were trimmed using Trim Galore! (24), and read quality was analyzed by FASTQC (25). Trimmed reads were mapped to the *Mus musculus* genome assembly GRCm39 using HISAT2 (26). Reads were assigned to genes in the custom GTF files and counted using featureCounts (27).

Analysis was performed through R/RStudio. Hierarchical gene clustering was achieved using *multiClust* package. Differential analysis of gene expression between AT and BM was performed using *DESeq2* package with False Discovery Rate at the adjusted *p*-value level of 0.001 to counteract gene expression linked to a culture effect. Using only the previous significant genes, principal components analysis (PCA) was performed on normalized counts for all samples. To functionally group genes weighting for each PCA dimension, Gene Set Enrichment Analysis (GSEA) on biological processes was run using *clusterProfiler* package and the respective contribution of each gene in each PCA dimension as the ranking criteria. Over representation analysis (ORA) was performed through the *goseq* package. Bulk RNA-seq datasets were deposited in the ArrayExpress repository under the following accession numbers E-MTAB-14120.

2.9 Cytokine and NO production analysis

After 24h of treatment (cf. *in-vitro* macrophages culture) supernatants of AT- or BM-macrophage cultures were collected and cytokines, chemokines, or NO production was measured. Cytokine and chemokines production was analyzed with Mouse Macrophage/Microglia LEGENDplex™ fluorescence bead-based immunoassay (BioLegend, San Diego, USA) to probe and quantify the levels of seven soluble factors (CXCL1, TGF- β 1, CCL22, IL-12p70, IL-6, TNF- α , and IL-12p40) following supplier's protocol. Raw data were given as the MFI of phycoerythrin (PE) signal. The concentration (pg/ml) of each soluble factor present in culture supernatants was determined by comparing the PE MFI for each target against seven individual protein standards. Data were analyzed using LEGENDplex™ v.8.1 data analysis software (BioLegend, San Diego, USA). NO production was quantified using Griess reagent. Absorbances were measured in ENVISION (PerkinElmer, Waltham, USA) at 630 nm.

2.10 Metabolic flux analysis

AT- and BM-macrophages were seeded at 20,000 cells/well in a poly-D-lysine-coated Seahorse XFe96 cell culture microplate (Agilent Technologies, Santa Clara, USA) in complete RPMI/ Glutamax medium (Gibco, Thermo Fisher Scientific, Waltham, USA) supplemented with Heat Inactivated Newborn Calf Serum (hiNBSC; Gibco, Thermo Fisher Scientific, Waltham, USA) (10%) and a cocktail of amphotericin (Invitrogen, Thermo Fisher Scientific, Waltham, USA), streptomycin, and penicillin (Life Technologies, Carlsbad, USA) (1%) and incubated overnight at 37°C in 5% CO₂. A minimum of five replicate wells were plated for each condition. Sensor cartridges were hydrated overnight in Seahorse XF calibrant at 37°C without CO₂ supplementation. On the day of the assay, macrophages were thoroughly washed with PBS and the culture medium was replaced with XF DMEM supplemented with glutamine (2 mM; Sigma-Aldrich, Saint-Louis, USA), pyruvate (1 mM; Sigma-Aldrich, Saint-Louis, USA), and glucose (10 mM; Sigma-Aldrich, Saint-Louis, USA) for the Mito Stress Test or without glucose for the Glycolysis Stress Test. The plate was then incubated for 1 h at 37°C without CO₂ supplementation while the Seahorse XFe96 Analyzer was calibrated. Mito stress test consisted of the sequential injection of oligomycin (1 μ M; Sigma-Aldrich, Saint-Louis, USA), FCCP (1 μ M; Sigma-Aldrich, Saint-Louis, USA), and rotenone (1 μ M; Sigma-Aldrich, Saint-Louis, USA) + antimycin A (1 μ M; Sigma-Aldrich, Saint-Louis, USA). Glycolysis stress test was performed using glucose (10 mM), oligomycin (1 μ M), and 2-deoxyglucose (100 mM; Sigma-Aldrich, Saint-Louis, USA). Oxygen consumption rates (OCR) and extracellular acidification rate (ECAR) were measured three times with 6 min intervals at the basal level then after each injection. All measures were normalized to the number of DAPI-stained nuclei per well at the end of the experiment, using the Operetta High Content Imaging System (PerkinElmer, Waltham, USA). Cell density, plate coating and FCCP concentration were determined by a dedicated pilot experiment. Data were analyzed with the Agilent Wave desktop software.

2.11 *In vitro* study of phagocytosis

To evaluate phagocytosis of *E. coli*, AT or BM-macrophages were incubated with pH-rodo *E. coli* Bioparticles (100 μ g/ml) (Invitrogen, Thermo Scientific, Waltham, USA) in S3 IncuCyte (sartorius, Göttingen, Germany). Pictures of bright field and red fluorescence were acquired each 15 min during 48h. Data were analyzed with S3 IncuCyte software measuring red object intensity on cells area. Areas under the curve were then calculated.

Candida albicans strain (isolated from a blood culture of a Toulouse-Rangueil Hospital patient (28)) was seeded on Sabouraud Petri dish 24h before experiment. AT- or BM-macrophages were washed with DMEM medium to remove serum and incubated with *C. albicans* for 30 min at 37°C (ratio 3 yeasts per macrophages). Unbound yeasts were removed by successive washes. Macrophages were then incubated for 4 h at 37°C with 5% CO₂ to evaluate killing of *C. Albicans* or stored at 4°C to evaluate binding of *C. Albicans*.

Cells were then lysed by adding sterile H₂O 5 minutes at room temperature and PBS was added to stop the reaction. Cell lysates were seeded on Sabouraud dextrose agar medium (Bio-Rad, Hercules, USA) and incubated for 24h at 37°C to determine yeast colony forming unit (CFU).

2.12 *In vitro* ROS production

AT- or BM-macrophages ROS production was evaluated by adding 5-amino-2,3-dihydro-1,4-phthalazinedione (Luminol; Sigma-Aldrich, Saint-Louis, USA) on culture dishes. Basal chemiluminescence reflecting ROS production was measured continuously during 30 min at 37°C with luminometer ENVISION (PerkinElmer, Waltham, USA).

2.13 Single-cell RNA-seq analysis

Sc-AT single cell dataset was obtained from Emont et al. (29) (#GSE176171) (GSM5820690_Mm_ING_08-3). An initial quality control filtering was performed. First, we identified potential single-cell doublets using the Doublet Detection Python package. Further low-quality single cells containing < 200 expressed genes and > 0.1% mitochondrial transcripts, as well as less than 2,000 counts and more than 50,000 counts were excluded from the analysis. Following the removal of low quality and doublet cells, bioinformatics processing of the single cell RNA-seq data was performed using Single Cell Analysis in Python (Scanpy) toolkit. Single cells data were log-transformed and normalized. We applied principal components analyses to reduce the dimensionality of the data. The top 100 principal components selected using the Elbow plot method were used for further analyses analysis. We selected macrophages based on Cd45/Ptprc, F4/80/Adgre1 and Cd11b/Itgam and performed an unsupervised agglomerative clustering represented on a UMAP.

2.14 Statistics

Comparisons between groups were made using paired or unpaired t-tests, one sample t-test or one-way ANOVA. Prism v10.1.2 software (GraphPad, Dotmatics, Boston, USA) was used for the statistical analyses. p values < 0.05 were considered statistically significant.

For cytokine production, results were analyzed with principal components analysis (PCA) as an unsupervised dimension reduction method. R software 4.2.3 with the factoextra and factomineR packages.

3 Results

3.1 Generation of AT-macrophages from 3D culture system

We adapted a previously published protocol of 3D culture, used to generate AT-mast cells (23). The cells of stroma vascular fraction

(SVF) derived from the sc-AT were cultured on ultra-low adherent plates with medium supplemented with M-CSF. This resulted in the development of spheroids within 4 days of culture initiation. Spheroids were then maintained for at least 13 days (Figure 1A). The size of the spheroids (Figure 1B), and their cell content (Figure 1C) decreased from 4 to 13 days in culture. Spheroids cell composition was analyzed by flow cytometry after enzymatic dissociation and compared to sc-AT composition. Spheroids contained mainly stromal cells (CD45⁻), and 10% to 20% of immune cells (CD45⁺) (Figures 1D, E). The analysis of the stromal population revealed that the spheroid contained a high percentage (80%) of cells expressing mesenchymal markers (CD90, CD29), including CD24⁺ cells, (Supplementary Figures S1A–D). In contrast, the proportion of endothelial cells identified as CD45⁺/CD31⁺ was significantly lower in the spheroid compared to the SVF, indicating that they were not maintained in the 3D cultures (Supplementary Figures S1E, F).

In addition, based on the phenotypes described in the BM and in the sc-AT (30, 31), hematopoietic stem/progenitor cells were identified in the spheroid over time (Supplementary Figure S2A). Hematopoietic stem/progenitor cells population (LSK: Lin⁻/Sca1⁺/CD117⁺) was enriched in the spheroid compared to uncultured SVF (Supplementary Figure S2B). The proportion of engaged myeloid progenitors including Megakaryocyte-Erythrocyte Progenitor (Lin⁻/CD117⁺/Sca-1⁻/CD16/32⁻/CD34⁻), common myeloid progenitor (Lin⁻/Sca1⁻/CD117⁺/CD16/32⁻/CD34⁺) and Granulocyte-Macrophage Progenitor (Lin⁻/Sca1⁻/CD117⁺/CD16/32⁺/CD34⁺) was less than 1% of the total living cells in the spheroid. These percentages were comparable to those observed in uncultured SVF (Supplementary Figure S2C).

The analysis of the immune mature population showed that the proportion of CD45⁺ cells decreased over time, and was significantly lower than the percentage of immune cells present in the uncultured SVF under homeostatic conditions (Figures 1D, E). Both myeloid (CD45⁺/CD11b⁺) and lymphoid (CD45⁺/CD11b⁻) cells were identified in the spheroid as in the sc-AT SVF (Supplementary Figure S3A). Lymphoid cells accounted for 3%–5% of the SVF or the spheroid (Supplementary Figures S3A, B). In contrast, the percentage of myeloid cells was significantly lower in the spheroid compared to the SVF and decreased over time in culture, suggesting that myeloid cells did not persist within the spheroid (Supplementary Figure S3B). To further analyze the myeloid population, we examined monocytes (CD45⁺/CD11b⁺/F4/80⁻/Ly6C⁺), dendritic cells (CD45⁺/CD11b⁺/F4/80⁻/CD11c⁺) and neutrophils (CD45⁺/CD11b⁺/F4/80⁻/Ly6G⁺), present in the sc-AT SVF. We found that these cell types were almost absent from the spheroid (Supplementary Figures S3C–H). In contrast, macrophages (CD45⁺/CD11b⁺/F4/80⁺/Ly6C⁻) accounted for 50% of the immune population in both the sc-AT SVF and the spheroid at day 7, but this percentage decreased significantly by day 13 of culture (Supplementary Figures S3C, D). This reduction is concomitant to a significant decrease in the percentage of proliferating macrophages contained in the spheroid after 13 days of culture (Supplementary Figure S3I). Overall, spheroids represent a three-dimensional structure composed of various cell populations present in the sc-AT and preserved over time.

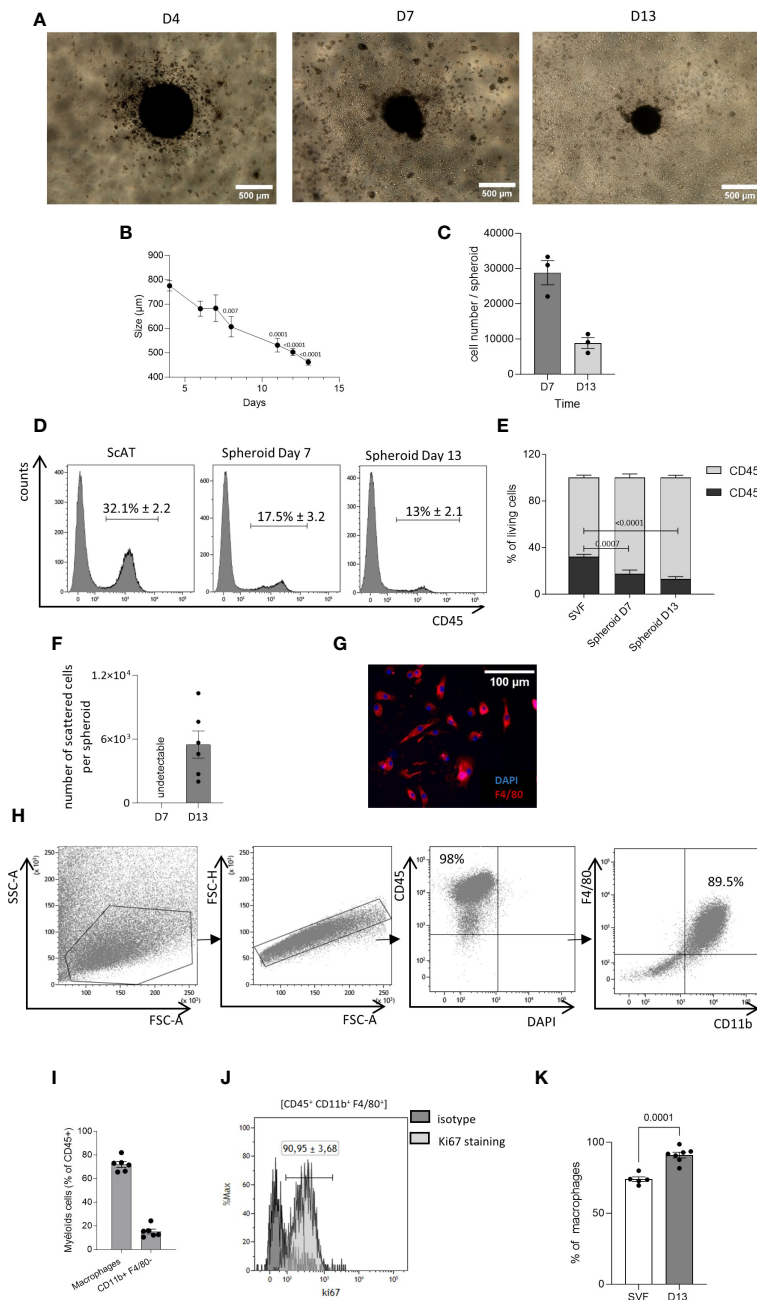


FIGURE 1

Generation of AT-macrophages from 3D culture system. The seeding of the stromal vascular fraction (SVF) cells obtained from the murine sc-adipose tissue (AT) into plates with low adherence leads to the formation of spheroids. **(A)** Representative picture of these spheroids at 4, 7, and 13 days of culture. Acquisition was performed using an inverted Nikon Objective $\times 40$ (scale bar = 500 μ m). **(B)** Kinetic of the spheroid size. *P*-values were obtained by comparing the mean values of each time point with the mean value of day 4. **(C)** Spheroid cell number at days 7 and 13 of culture. **(D, E)** After dissociation, at days 7 and 13 spheroid composition was analyzed by flow cytometry. **(D)** Representative histograms of CD45 expression in dissociated cells from scAT SVF, spheroid day 7 and spheroid day 13, gated on singlets DAPI[−] (4',6-diamidino-2-phenylindole) cells. **(E)** Quantification of hematopoietic (CD45⁺) and non-hematopoietic (CD45[−]) cells in the scAT SVF and within the spheroid, expressed in % of DAPI[−] cells. **(F–K)** Starting at day 10 of culture, dispersed cells migrate outside of the spheroids. **(F)** Number of scattered cells per spheroid obtained after 7 and 13 days in culture. **(G)** Representative picture of cells that have spread out of the spheroid after 13 days in culture (scale bar = 100 μ m). Macrophages were stained with F4/80 (red) and their nuclei stained with DAPI (blue). **(H)** Representative dot plot of flow cytometry showing the expression of macrophage-specific markers on the surface of scattered cells out of the spheroid and selected among singlet DAPI[−] cells. **(I)** Percentage of macrophages (CD45⁺/F4/80⁺/CD11b⁺) and other myeloid cells (CD45⁺/CD11b⁺/F4/80[−]) among CD45⁺ scattered cells surrounding spheroids and quantified by flow cytometry at day 13. **(J)** Representative histogram of flow cytometry showing the expression of Ki67 on AT cultured macrophages outside spheroids. **(K)** Quantification of Ki67 staining in the SVF and AT cultured macrophages outside spheroids. Results are expressed as mean \pm SEM and compared using one-way ANOVA and *t*-test.

Starting from day 10 of culture, dispersed cells emerged surrounding the spheroid and at day 13, up to 5×10^3 cell/spheroid were obtained (Figure 1F). These cells formed a homogeneous immune population mostly expressing the macrophage cell surface markers CD45, CD11b, and F4/80, as shown by flow cytometry and immunohistochemistry (Figures 1G, H). Macrophage purity reached $71.98 \pm 2.42\%$ after 13 days in culture (Figure 1I). The 3D culture system also generated CD11b⁺/F4/80[−] myeloid cells, accounting for $15.21 \pm 2\%$ of the population surrounding the spheroid (Figure 1I). Flow cytometry analyses also showed that the large majority of AT-cultured macrophages expressed Ki67 (Figures 1J, K), suggesting that macrophages were proliferating in these conditions. Hence, this approach generates living tissue macrophages in culture without the need for purification by cell sorting.

3.2 Cultured AT-macrophage population exhibits specific features compared to macrophages derived from medullar monocytes

Macrophages generated from AT spheroids were compared to macrophages obtained through classical medullar monocyte differentiation. To this end, both macrophage populations were harvested and seeded on adherent culture dishes, for 24h before flow cytometry analysis. Singlet and viability gating was performed manually prior to data export for analysis (Figure 2A). Individual flow cytometry standard files of CD45⁺ cells in each type of culture were concatenated to ensure spatial alignment of the same population between samples. A total of 17,409 cells were randomly used per sample to create a final file containing 15,6681 total cells. Then macrophages were selected on the basis of CD11b and F4/80 expression. UMAP dimensional reduction revealed a clear difference between AT- and BM-macrophages (Figure 2B). Protein expression patterns of selected antigens (CD206, CD16/32, MHC-II, MerTK, Dectin-1, and CD36), classically used to characterize macrophage subsets, were superimposed on a UMAP (Figure 2C) and highlighted on a heatmap (Figure 2D), revealing that most of these markers were differentially expressed by AT- and BM-macrophages that thus clustered separately.

The comparison between both populations was then quantified using conventional flow cytometry analysis. The percentage of positive cells (Figure 2E) and the MFI (Figure 2F) were shown for classical core macrophage surface markers. AT-macrophage population was highly homogeneous regarding the content of CD206, CD36, and CD16/32 positive cells, that represented 75%–97% of the population. TIM4 and Lyve-1, 2 cell surface markers specific for resident macrophages, were expressed by 36%–53% of AT-macrophages. CCR2, Dectin, MHC-II, and MerTK were only detected on 9%–20% of the AT-macrophages. The percentage of positive cells for all these cell surface markers was significantly higher in the AT-macrophages than in the BM-macrophages except for CCR2 (Figure 2E). According to the UMAP visualization (Figure 2C), AT-macrophages showed a significantly higher MFI

for all these markers except CCR2 and Lyve 1 in comparison to BM-macrophages (Figure 2F).

In order to evaluate the functional capacity of AT- and BM-macrophages, the production of cytokines was quantified in the cell culture supernatants in unstimulated conditions. We used LEGENDplex bead-based assays to quantify the amount of secreted CXCL1, IL-6, TNF- α , IL12p40, IL12p70, TGF- β , and CCL22 via flow cytometry. AT- and BM-macrophages exhibited specific cytokine production signature (Figure 2G). This clear segregation appears to be due to a higher secretion of CXCL1, IL-6, and CCL22 by AT-macrophages compared to BM-macrophages (Supplementary Figure S4). These results were confirmed through PCA (Figure 2H), which demonstrated a clear distinction in cytokine production profiles between AT- and BM-macrophages. We performed RT-qPCR to assess the expression of *iNOS* and *Arginase-1*, as representative pro- and anti-inflammatory polarization markers respectively (Figure 2I). Unstimulated AT-macrophages expressed *Arginase-1* while BM-macrophages expressed *iNOS*. Consequently, AT-macrophages generated lower levels of NO and ROS than BM-macrophages (Figures 2J, K), indicating that in the absence of stimulation, AT-macrophages exhibit a less pro-inflammatory phenotype than BM-macrophages. Altogether, these results show that AT- and BM-macrophages have distinct phenotypic and functional characteristics, and suggest that these two populations display different metabolic activities.

3.3 Cultured AT-macrophages display high metabolic rate

Specific metabolic pathways are increasingly being recognized as essential hallmarks of macrophage subsets. We thus compared the energetic metabolism of AT- and BM-macrophages using the Seahorse technology. This allows the real-time measurement of ECAR and OCR as indicators of glycolytic function and oxidative phosphorylation, respectively, as readouts of cellular bioenergetic profiles in response to metabolic stressors. Glycolysis stress tests were conducted to evaluate the glycolytic function of macrophages. The ECAR of AT-macrophages was higher than that of BM-macrophages (Figure 3A), leading to a significant increase in key glycolytic function parameters such as glycolysis (3.7-fold), glycolytic capacity (5.9-fold), and glycolytic reserve (300-fold) (Figure 3B). To determine whether BM-macrophages exhibit compensatory mitochondrial metabolism, mitochondrial stress tests were performed. Interestingly, AT-macrophages exhibit higher OCR compared to their BM counterparts (Figure 3C). This was highlighted by a significant increase in basal respiration (2.2-fold), maximal respiration (3.6-fold) and respiration-coupled ATP production (2.4-fold) (Figure 3D). These results indicate that AT-macrophages exhibit a highly energetic metabolic state (high glycolytic capacity and concomitant respiration) compared to BM-macrophages that adopt a relatively low bioenergetic profile, reminiscent of a quiescent state (Figure 3E). Additionally, the increased metabolic activity in AT-macrophages resulted in a

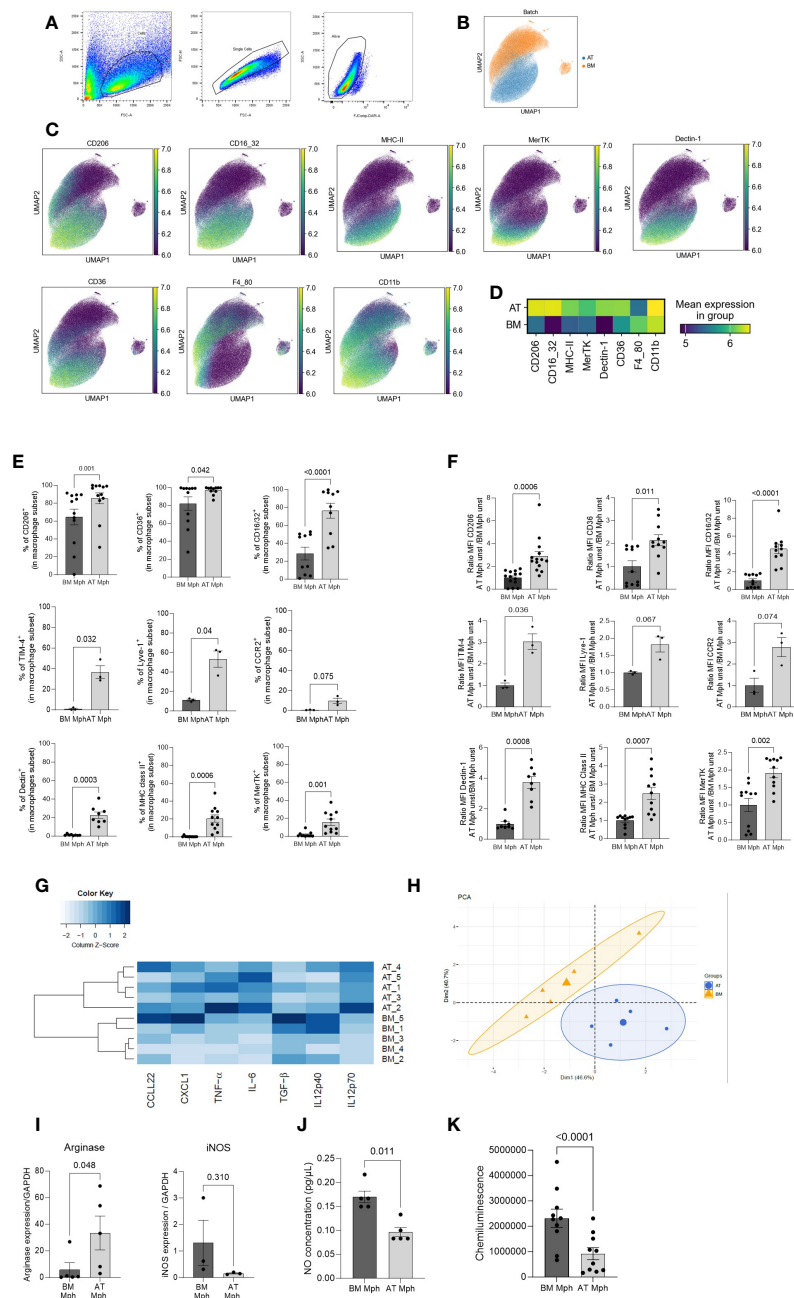


FIGURE 2

AT-macrophages are mature and phenotypically different from BM-macrophages. Macrophages generated from adipose tissue (AT) spheroids or from bone marrow (BM) monocyte differentiation were harvested and then seeded on adherent culture dishes, for 24h. Cells and supernatant were then collected and analyzed by flow cytometry. (A) Gating strategies for AT- and BM-macrophages. (B–D) Unbiased analysis of 5 independent samples of AT- and BM-macrophages realized using Uniform Manifold Approximation and Projection (UMAP) visualization with the signal strength of key phenotypic macrophages markers. (B) Cell clustering of both macrophage populations showing that AT- and BM-macrophages are distinct populations. (C) Protein expression patterns projected of CD206, CD16/32, MHC-II, MerTK, Dectin-1, CD36, F4/80, and CD11b MFI represented on a UMAP and illustrated using blue-green-yellow continuous color scale. (D) Heatmap visualization of surface markers expression on AT- and BM-macrophages. (E) Percentage of AT- and BM-macrophage (CD45⁺/CD11b⁺/F4/80⁺) expressing extracellular markers: CD206, CD36, CD16/32, Dectin-1, MHC-II, MerTK, TIM-4, Lyve-1, CCR2, ($n = 3$ to 14). Results are expressed as percentage of macrophage population and compared using paired t-test. (F) MFI of macrophages markers analyzed by flow cytometry in AT- and BM-macrophages ($n = 3$ to 14). Results are expressed as ratio of values obtained in BM-macrophages and compared using paired t-test. (G) Heatmap performed on the production of seven cytokines (pg/μl) quantified by LEGENDplex in supernatant of AT- and BM-macrophages cultures in unstimulated conditions. The dendrogram performed using complete linkage method was able to cluster BM- and AT-macrophages on the basis of their cytokines production. ($n = 5$). (H) Principal components analysis (PCA) performed on macrophages cytokine production. BM- and AT-macrophages were colored in orange and blue, respectively. (I) Arginase-1 and iNOS mRNA relative expression evaluated by RT-qPCR ($n = 3$ –5). Results are express as a ratio of housekeeper gene expression (GAPDH). (J) Nitric Oxide (NO) production was quantified in the culture medium using Griess Reagent ($n = 5$). Results are expressed in pg/μl. (K) ROS production was followed during 90 min using Luminol and Chemiluminescence was measured ($n = 10$). Results were compared using paired t-test.

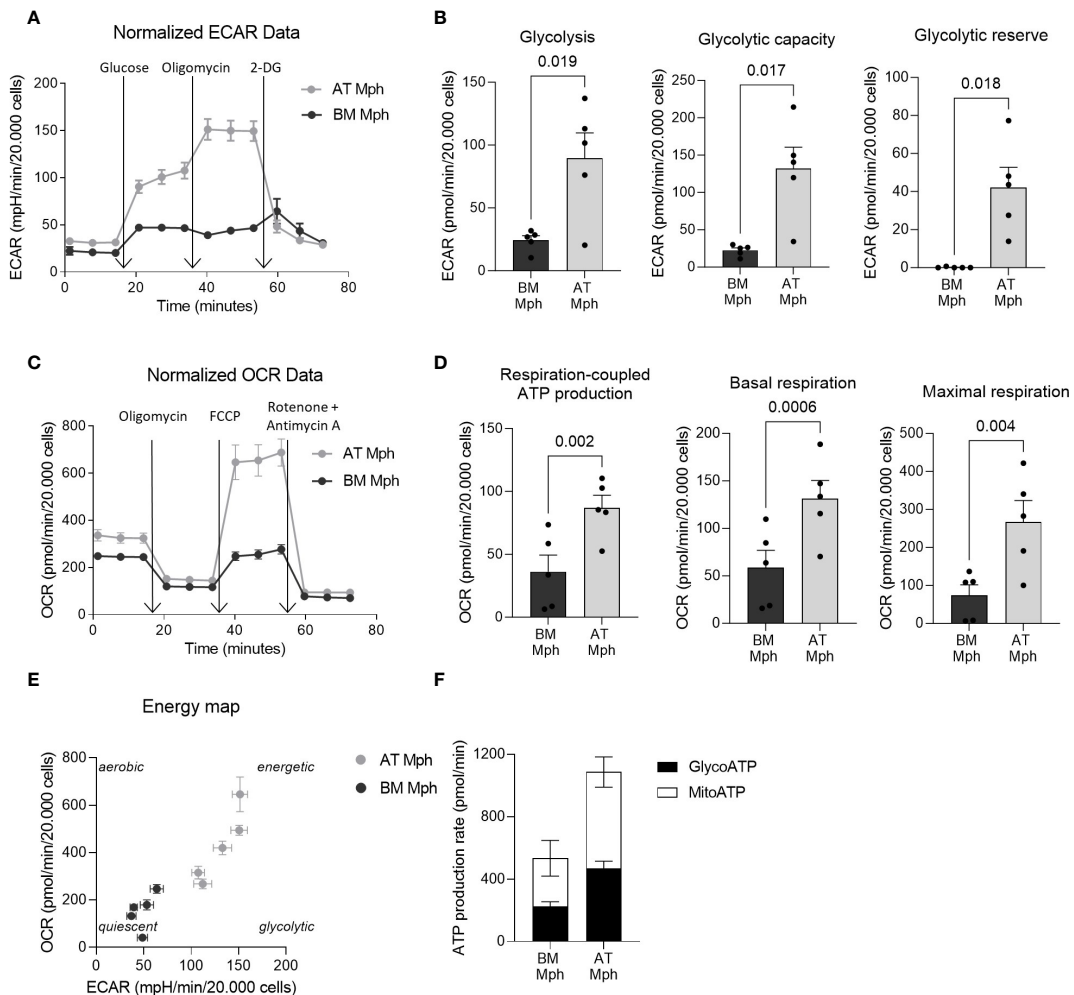


FIGURE 3

AT-macrophages are more metabolically active than BM-macrophages. Macrophages generated from adipose tissue (AT) spheroids or from bone marrow (BM) monocyte differentiation were seeded onto seahorse plates for 24h before to analyze mitochondrial respiration and glycolytic capacity. (A–D) Mitochondrial respiration and glycolytic capacity of AT- and BM-macrophages quantified using Seahorse Agilent Technology 96eXF. Results were normalized to the cell number using DAPI staining after the assay. (A, B) Extracellular acidification rate (ECAR) upon glycolytic stress (injection of glucose, oligomycin, and 2-deoxyglucose) was measured. (A) Representation of real-time measurement of ECAR. (B) Glycolysis, glycolytic capacity and glycolytic reserve were calculated ($n = 5$). (C, D) Oxygen consumption rate (OCR) upon mitochondrial stress (injection of oligomycin, FCCP, rotenone and antimycin A) was measured. (C) Representation of real-time measurement of OCR. (D) Basal respiration, maximal respiration and respiration-coupled ATP production were calculated ($n = 5$). (E) Energy map of maximal respiration versus glycolytic capacity after FCCP injection ($n = 5$). (F) Glyco- and mito-ATP production rates were calculated using the aforementioned ECAR and OCR data ($n = 5$). Results were compared using paired t-test.

higher rate of ATP production, which was twice that of BM-macrophages (Figure 3F).

3.4 Pro/anti-inflammatory polarization induction of cultured AT-macrophages

We compared the polarization abilities of cultured AT- and BM-macrophages in response to IFN- γ and IL-4. Specifically, we assessed the induction of pro- or anti-inflammatory cell surface markers and the production of corresponding cytokines in the cell culture supernatants using flow cytometry, after 24h of stimulation. The AT-macrophages demonstrated a significant increase in both the MFI and positive cell percentage for MHCII in response to IFN-

γ treatment. A comparable response was observed in BM-macrophages although to a lesser extent (Figures 4A, B). This increase in MHC-II was associated with increased secretion of TNF- α , IL-6, and IL-12p40 in both types of macrophages (Figure 4C). Interestingly, only BM-macrophages treated with IFN- γ showed decreased CXCL1 secretion, while IL-12p70 expression remained unchanged (Figure 4C).

IL-4 treatment was used to polarize macrophages towards an anti-inflammatory phenotype. As expected, the treatment resulted in enhanced MFI of CD206, Dectin-1 and CD16/32 in both AT- and BM-macrophages (Figure 4D). Although MerTK MFI level remained unchanged, CD36 was induced specifically in BM-macrophages (Figure 4D). Except for Dectin-1 in BM-macrophages, IL-4 did not elicit any change in the percentage of

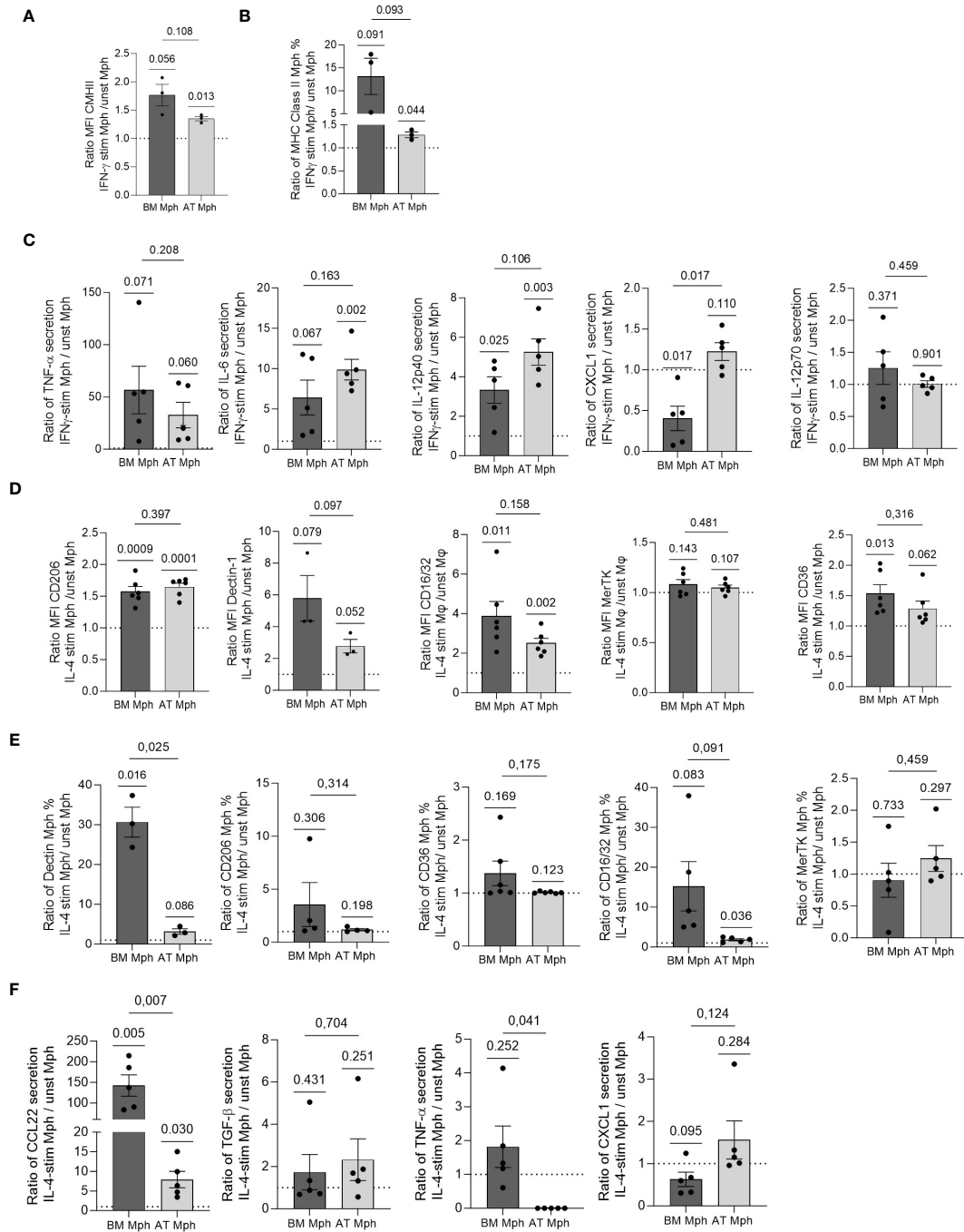


FIGURE 4

AT- and BM-macrophages are differentially polarized by IL-4 or IFN- γ treatment. Macrophages generated from adipose tissue (AT) spheroids or from bone marrow (BM) monocyte differentiation were seeded onto adherent culture dishes for 24h, and treated with IFN- γ (A–C) or IL-4 (D–F) for another 24h. Flow cytometry was used to assess MFI (A, D) and % of positive cells (B, E) for each cell surface marker expressed by macrophages after treatment ($n = 3–6$). (C, F) Supernatants were collected and cytokine production quantified by LEGENDPlex ($n = 5$) in AT- and BM-macrophages. Results were compared using paired t -test. One Sample t -test analysis was used to compare stimulated and unstimulated conditions.

positive cells for each cell surface marker (Figure 4E). IL-4 treatment significantly increased the production of CCL22 in both AT- and BM-macrophages, with a more pronounced effect observed in BM cultures (Figure 4F). While TGF- β secretion was induced to a small extent by IL-4 in AT- and BM-macrophages, the production of TNF- α decreased only in AT-macrophages. Notably,

BM-macrophages treated with IL-4 exhibited a reduction in CXCL1 secretion (Figure 4F).

Overall, these results showed that AT- and BM-macrophages undergo activation toward a pro-inflammatory phenotype when stimulated by IFN- γ , while the stimulation with IL-4 polarizes them towards an anti-inflammatory phenotype. Notably, while IFN- γ

induced comparable changes in AT- and BM-macrophages, AT-macrophages showed less pronounced polarization towards an anti-inflammatory phenotype when stimulated with IL-4, compared to BM-macrophages.

3.5 AT- and BM-macrophages show similar phagocytic activity

The phagocytic capability of AT- and BM-macrophages was then assessed *in vitro* by incubation with bacteria *E. coli* or yeast *C. albicans*. Phagocytosis of *E. coli* is a classical measure for macrophage function. The pH-sensitive Rhodo *E. coli* was used, which produces red fluorescence in acidic pH conditions, thereby indicating the presence of the bacteria within the phagosome (Figure 5A). A rapid and transient increase in red fluorescence was observed in both AT- and BM-macrophages produced *in vitro*, suggesting that all macrophages exhibit rapid phagocytic activity (Figure 5B). The phagocytic efficacy of AT- and BM-macrophages towards *E. coli* was found to be comparable (Figure 5C). The overexpression of CD206 and Dectin-1 (both being receptors for polysaccharides) in AT-macrophage suggests their potential efficiency in yeast phagocytosis. When incubated with *C. albicans*,

AT-macrophages were able to bind and kill the yeasts. Interestingly, AT-macrophages displayed a significantly higher binding capacity than BM-macrophages, although their killing capacity was similar (Figures 5D, E).

3.6 AT-macrophages produced in 3D culture are similar to sc-AT resident macrophages *in vivo*

We then conducted a comparative analysis between the AT-macrophages derived from 3D cultures and *in vivo* sc-AT macrophage populations. To this end, bulk RNA-seq analysis was performed between these two populations, and compared to BM-cultured macrophages. We first removed the culture effect performing a comparative analysis between AT- and BM-cultured macrophages. We identified 6,855 differentially expressed genes (adjusted *p*-value < 0.001) corresponding to specific signatures of AT- and BM- cultured macrophages. To arrange these genes according to the similarity of the gene expression pattern between our three conditions (AT- and BM-cultured macrophages and sc-AT-sorted macrophages), a hierarchical clustering was performed with a beforehand determined optimal number of clusters of 7.

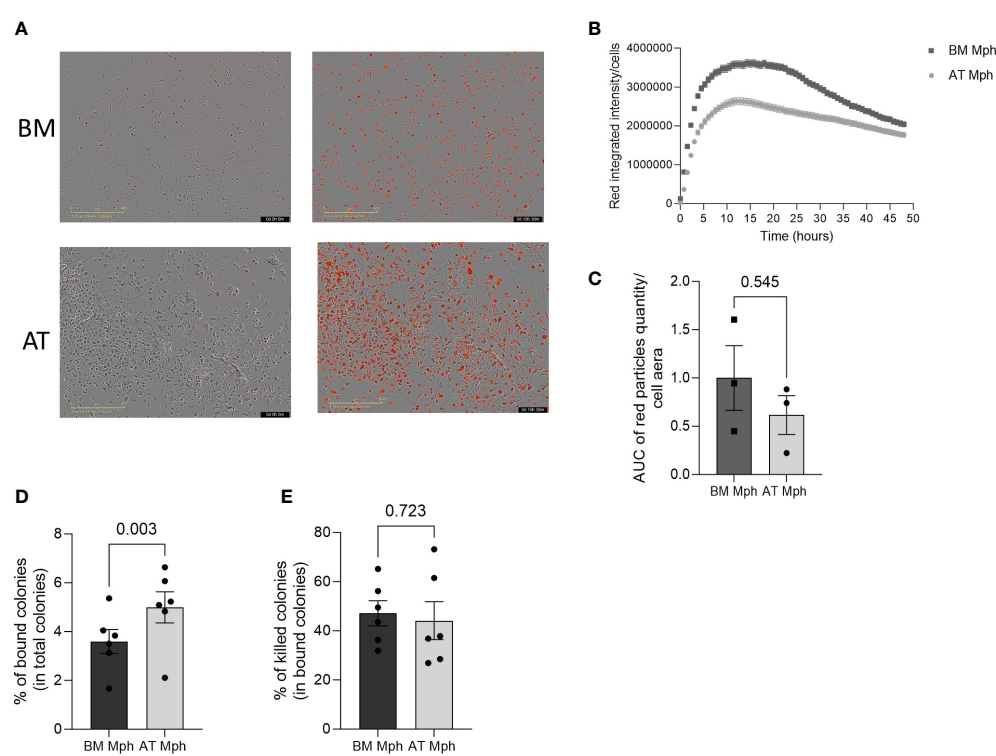


FIGURE 5

AT- and BM-macrophages show similar phagocytic activity. Phagocytic capacity of *E. coli* or *C. Albicans* yeast was assessed in adipose tissue (AT)- and bone marrow (BM)-macrophages generated from AT spheroids or from BM monocyte differentiation. (A–C) pH-Rodo *E. coli* were added to macrophages and phagocytosis (apparition of red particles) was analyzed on IncuCyte during 48h. (A) Representative pictures (IncuCyte) of phagocytose by BM- (up) and AT- (down) macrophages before (left) and after (right) *E. coli* addition. (B) A representative kinetic curve of bacteria phagocytosis by AT- and BM-macrophages. (C) Quantification of *E. coli* phagocytosis. Results are express in AUC of red particles reported to cell area. (*n* = 3). (D, E) *C. Albicans* yeast were added to macrophages for 30 min before assessing binding (D) and killing capacity (E). Macrophages were lysed and the supernatants were plated on Sabouraud Petri dishes. Twenty-four hours later, colonies were counted. Results are express as percent of bound among total colonies or killed colonies among total bound colonies. (*n* = 6) Results were compared using Paired *t*-test.

Figure 6A shows the change in expression of these 6,855 genes between the three conditions, with minimal variations between technical replicates. AT-cultured macrophages and sc-AT sorted macrophages displayed similar pattern of gene expression in three

out of seven clusters (clusters numbers 1, 4, and 5). ORA using Gene Ontology biological processes (GO BP) showed that cluster 1 contained genes involved in regulation of inflammatory response, secretion, and interferon-mediated signaling pathways. Genes

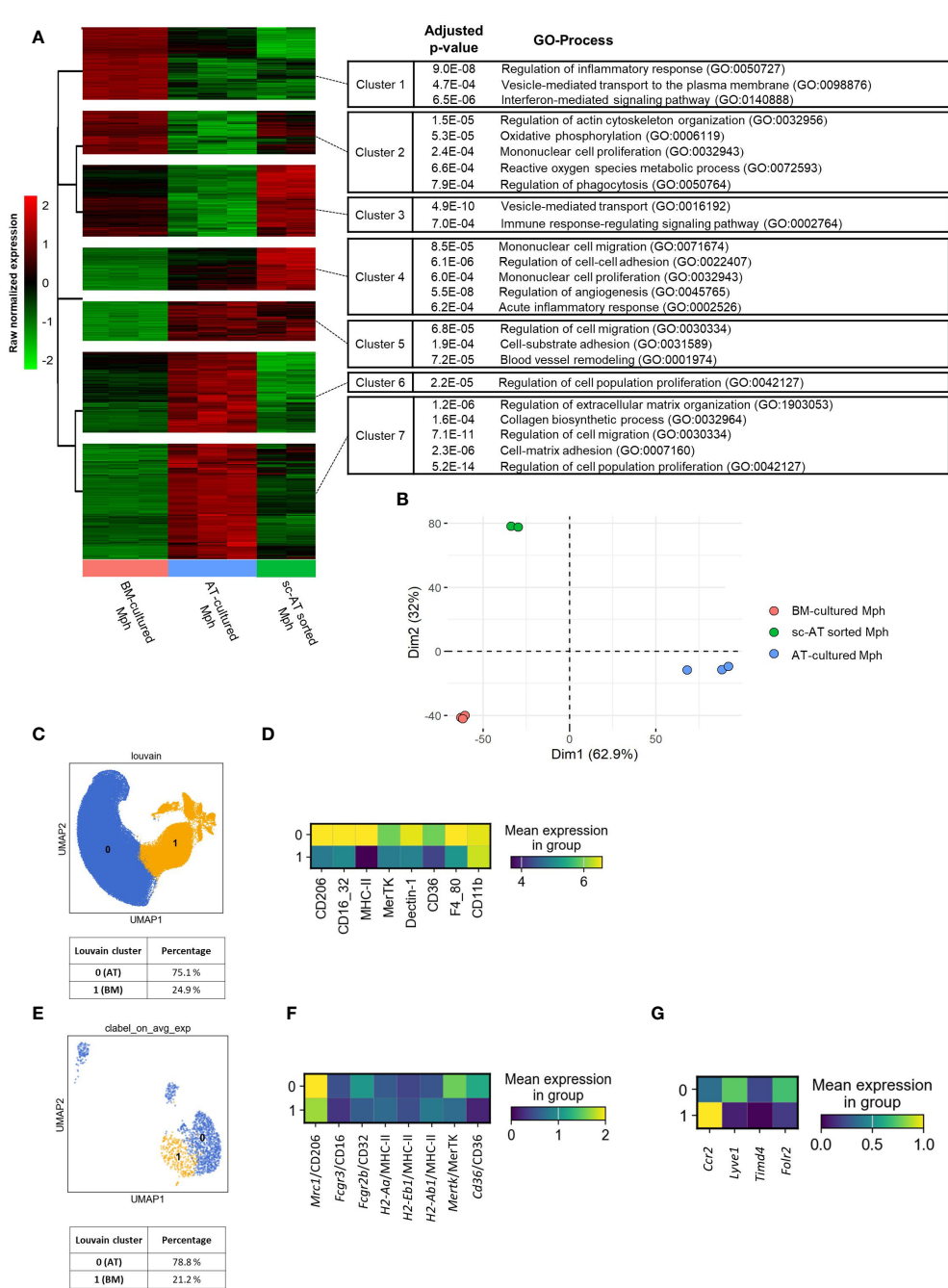


FIGURE 6

3D cultures to generate macrophages that mirror the phenotypic traits of *in-vivo* AT-resident macrophages. (A, B) A bulk RNA-seq analysis was performed on mouse-sorted sc- adipose tissue (AT) macrophages, AT- and bone marrow (BM)-cultured macrophages. (A) Hierarchical clustering of the 6,855 genes differentially expressed between AT- and BM-macrophages, according to their expression pattern across all samples, using multiClust R library. GO processes and adjusted P-values are mentioned. (B) Principal components analysis (PCA) on standardized gene expression of AT- (blue), BM- (orange), and sc-AT sorted (green) macrophages. (C, D) Unbiased analysis of SVF cells obtained from mouse sc-AT was realized by flow cytometry. (C) UMAP showing the clustering (Louvain method) of sc-AT macrophages in two populations and their percentages. (D) Heatmap of specific cell surface markers expression of sc-AT macrophages (clusters 0 and 1) ($n = 7$). (E–G) Single-cell RNA-seq analysis of sc-AT macrophages extracted from Emont et al. dataset (#GSE176171) (GSM5820690_Mm_ING_08-3) (29). (E) UMAP showing agglomerative clustering of macrophage population based on the gene expression. (F) Heatmap visualization of *Mrc1*, *Fcgr3*, *Fcgr2b*, *Mertk*, *H2-Aa*, *H2-Ab1*, and *CD36* gene expression (for clusters 0 and 1). (G) Heatmap visualization of *Ccr2*, *Lyve1*, *Timd4* and *Folr2* (for clusters 0 and 1).

present in clusters 4 and 5 were mainly involved in cell migration, cell–cell, and cell–substrate adhesion and proliferation (Figure 6A). As expected, BM-cultured macrophages also shared similarities with sc-AT sorted macrophages in four out of seven clusters (numbers 2, 3, 6, and 7). These clusters include genes involved in immune response (metabolic process, phagocytosis, secretion, signaling pathway), and cell behavior (proliferation, extracellular matrix organization and biosynthesis, cell migration, and cell–matrix adhesion) (Figure 6A). This analysis also showed that genes associated with inflammatory responses exhibited reduced expression levels, whereas genes involved in cell migration and cell adhesion exhibited elevated expression levels in AT- versus BM-cultured macrophages. Two components of a PCA were sufficient to capture 95% of the variance (Figure 6B; Supplementary Figure S5A). The PCA plot showed a clustering of the conditions, with the first dimension able to discriminate between the AT-cultured macrophage phenotype and the other populations, and the second dimension explaining the BM-cultured macrophage phenotype (Figure 6B; Supplementary Figure S5A). In order to provide a semantic summary of the genes implicated in each dimension, GSEA was performed for each dimension, utilizing the PCA contribution as a ranking function for GO BP exploration. Among the significant BP with $P < 0.001$, extracellular matrix organization and morphogenesis were enriched in the first dimension, and angiogenesis in the second dimension (Supplementary Figure S5B). We then selected the top 5 contributing genes for these 3 BP to plot normalized expression of these genes on an heatmap (Supplementary Figure S5C). Using these five genes in each BP, we confirm that these BP discriminate the different macrophage populations as seen in the PCA.

To go further, sc-AT SVF was analyzed using flow cytometry. The data set was represented on a UMAP, a Louvain clustering grouped cells into two distinct clusters (0 and 1), and the percentage of each population was calculated (Figure 6C). The expression of macrophage surface markers was represented on a heatmap (Figure 6D) and plotted onto a UMAP (Supplementary Figure S6A). The clustering of *in-vivo* sc-AT-macrophages revealed a major population (Cluster 0, 75.1%) that highly expressed most of the cell surface markers and a smaller population (Cluster 1, 24.9%) that also expressed these markers but at a lower level (Figure 6D). Cluster 0 of *in-vivo* sc-AT-macrophages displayed a similar profile to AT-macrophages obtained in culture (Figures 2C, D), as revealed by heatmaps comparison. In contrast, cluster 1 of *in-vivo* sc-AT macrophages resembled BM-macrophages generated in culture (Figures 2C, D). To go further, we explored single-cell gene expression of sc-AT macrophage populations obtained from Emont et al's dataset (29) (Figures 6E–G). Agglomerative clustering revealed two distinct populations: clusters 0 and 1 accounting for 78.8% and 21.2% of the total population, respectively (Figure 6E). Both heatmap and UMAP plots were used to display the expression of genes coding for the cell surface markers (*Mrc1* as CD206; *Fcgr3* and *Fcgr2b* as CD16/32; *Cd36* as CD36; *Merk* as MertK; *H2-Aa*, *H2-Eb1* and *H2-Ab1* as MHC-II) (Figure 6F; Supplementary Figure S6B). In accordance to the flow cytometry results, this analysis showed that cluster 0 displayed

exclusive gene expression compared to cluster 1 (Figure 6F; Supplementary Figure S6B). These results indicated that the AT-macrophages produced in 3D cultures have comparable phenotypic and genotypic characteristics to one of the two macrophage populations described in the sc-AT *in vivo* (cluster 0). Cluster 1, on the other hand, closely resembles BM-macrophages.

Strikingly, in single-cell analysis of the sc-AT *in vivo*, cluster 0 (similar to AT-cultured macrophages) showed high expression of *Lyve1* and *Folr2* and low expression of *Timd4* (Figure 6G; Supplementary Figure S6C) which have been described as a gene signature for resident macrophages (10). Conversely, cluster 1 (resembling BM-macrophages) showed high expression of *Ccr2* (Figure 6G; Supplementary Figure S6C), which is recognized as a signature of monocyte-derived macrophages infiltrating tissue. These findings suggest that macrophages produced in AT-3D cultures mimic the resident macrophage population found *in vivo*.

4 Discussion

AT-macrophages are essential in both regulating AT homeostasis and preventing metabolic diseases (31–36). Our study provides a 3D *in-vitro* system for generating and culturing AT-resident functional macrophages, without the need for cell sorting. This system also paves the way for subsequent functional analyses of these highly specialized cells.

To date, only a limited number of studies have provided a comprehensive description of the isolation and *in-vitro* culture of resident macrophages without modifying their function. Alveolar macrophage-like cells were obtained from BM-monocyte differentiation by adding cytokines in the culture medium (37). Various techniques have been developed to culture resident macrophages, including co-culturing with stromal cells (38, 39). Although these techniques are effective for maintaining and preserving the function of resident macrophages in the long term, they require subsequent separation of the macrophages from the stromal cells for analysis. Unfortunately, this step is often deleterious to the cells. The 3D system we have developed provides an optimal microenvironment for culturing resident macrophages. Indeed, the microenvironment plays a pivotal role in macrophage polarization and survival. Macrophages are continually adapting to their environment in order to effectively eliminate cells, debris, and released molecules and maintain homeostasis (14, 40). All tissues exhibit distinct characteristics and create a unique microenvironment that determines the phenotype and function of the macrophage (41). In this study, spheroids derived from sc-AT SVF preserved cells present in the AT stroma, and mimicked the microenvironment of AT-macrophages. It has to be noted that the spheroids contain native AT-resident macrophages, hematopoietic myeloid precursors, and a few circulating monocytes, all of which may contribute to the generation of macrophages within the 3D culture. Nevertheless, to use this culture system in other contexts or for other tissues is conditioned by the capacity of the cells to form a 3D structure.

The 3D cultures generate cells, which exhibit specific cell surface markers of mature macrophages including CD11b and F4/80. They

also display functional hallmarks of mature macrophages, and are capable of responding to pro- and anti-inflammatory stimulation, through adapting their cell surface and secretory phenotype. In addition, these cells exhibit efficient phagocytosis of various pathogens. When compared, AT- and BM-macrophages display distinct characteristics, primarily attributed to specific gene profile, differential expression of macrophage markers, ROS production, and basal respiration. Overall, the phenotypic and metabolic features of AT- and BM-macrophages obtained *in vitro* indicate different basal state polarization, with AT-macrophages exhibiting a more anti-inflammatory phenotype than BM-macrophages, in line with *in-vivo* data on resident versus monocyte-derived macrophages (3, 25). IL-4 treatment elicits a stronger response in BM-macrophages compared to AT-macrophages potentially due to the high expression of anti-inflammatory phenotypic markers in the basal state in these AT-macrophages. In contrast, IFN- γ has a similar effect on both populations, consistent with the same phagocytic capacity. This has already been described for Kupffer cells, which respond similarly to BM-macrophages to an infectious challenge *in vivo* despite a distinct transcriptomic signature (42). The phenotype and the response to stimulations in BM-macrophages in culture suggest that they are probably less mature than AT-macrophages, potentially due to the absence of microenvironment.

It is proposed that *in-vivo*, anti-inflammatory AT-macrophages exhibit high oxidative rate capacity and mitochondrial function (43). In contrast, inflammatory macrophages are considered to be glycolytic (44). However, a recent study suggests that glycolysis is essential for the anti-inflammatory macrophage polarization (45). AT-macrophages generated in 3D culture exhibit high levels of both OCR (oxidative phosphorylation rate) and ECAR (extracellular acidification rate), indicating significant metabolic activity following stimulation and a high degree of metabolic plasticity. This metabolic signature has been previously observed in activated macrophages in the peritoneum (46), and in obese AT (47, 48). The metabolic profile of macrophages is an indicator of macrophage activation and largely explains their function in maintaining tissue homeostasis. A change in the microenvironment impacts macrophage metabolism. In AT, obesity is associated with an accumulation of lipids and an increase in both oxidative and glycolytic metabolisms of resident macrophages resulting in an increase in pro-inflammatory phenotype markers (47, 49).

AT-macrophages produced in 3D cultures were able to proliferate, as described for resident AT-macrophages in lean mice (50). An unsupervised genic and phenotypic comparison of macrophage populations isolated from sc-AT, 3D culture system, or medullary monocyte differentiation showed that macrophages produced in 3D culture correspond to the fraction of resident macrophages present *in vivo* within the AT. Indeed, AT-cultured macrophages and sc-AT-macrophages shared functional similarities identified in bulk RNA-seq analysis, that appear to be involved in the maintenance of the tissue microenvironment (adhesion, migration, vessel remodeling). In addition, they express markers of resident cells such as TIM4 and Lyve1 (10). Moreover, most of the macrophages generated in 3D culture highly

express the CD206, a cell surface marker defined by Félix et al. as a hallmark of AT-resident macrophages (11). This cell surface marker has also been reported to identify M2-like AT-resident macrophages, which serve as a niche for adipocyte progenitors in AT (51). Furthermore, these macrophages display minimal expression of CCR2, a marker indicative of macrophages that have migrated to AT (21). In physiological conditions, these macrophages are sparsely distributed within AT (52). Maintaining an appropriate balance of these two macrophage subsets is crucial for tissue homeostasis. Indeed, a disruption of this balance with an accumulation of macrophages derived from circulating monocytes within AT is observed in obese individuals (52). The application of this culture method to pathological AT could provide a more comprehensive understanding of the intrinsic defaults in resident macrophage populations.

In summary, our study yields an efficient culture technique that maintains the phenotypic and functional characteristics of resident AT-macrophages. This method stands as a valuable resource for exploring the differentiation and function of AT-macrophages *in vitro* in diverse physiological and pathological contexts.

Data availability statement

The original contributions presented in the study are included in the article/[Supplementary Material](#). Further inquiries can be directed to the corresponding author.

Ethics statement

The animal study was approved by European Community Guidelines (2010/63/UE)/institutional ethics committee N.122 US006/CREFRE. The study was conducted in accordance with the local legislation and institutional requirements.

Author contributions

AA: Conceptualization, Writing – original draft, Writing – review & editing, Formal analysis, Investigation, Methodology. MR: Formal analysis, Investigation, Methodology, Writing – review & editing. JN: Formal analysis, Investigation, Methodology, Writing – review & editing. MT: Formal analysis, Investigation, Methodology, Writing – review & editing. JF: Formal analysis, Investigation, Methodology, Writing – review & editing. EA: Formal analysis, Investigation, Methodology, Writing – review & editing. CD: Resources, Writing – review & editing. HA: Resources, Writing – review & editing. PM: Writing – review & editing, Formal analysis, Investigation, Methodology, Validation. AC: Resources, Writing – review & editing. LC: Resources, Writing – review & editing. MO: Resources, Writing – review & editing, Formal analysis, Investigation, Methodology. BC: Conceptualization, Funding acquisition, Resources, Supervision, Writing – original draft, Writing – review & editing.

Funding

The author(s) declare that no financial support was received for the research, authorship, and/or publication of this article.

Acknowledgments

We thank A. Boissonnas, A. Carriere-Pazat and A. Varin for insightful discussions. The authors also thank the US006/CREFRE INSERM/UT3 (Toulouse, France) and specifically the zootechnical core facility for animal care. We also acknowledge RESTORE-CERT and Genotoul-Tri, members of the national infrastructure France-BioImaging supported by the French National Research Agency (ANR-10-INBS-04). AA was a fellow of the French Ministère de l'Enseignement Supérieur et de la Recherche. We also gratefully acknowledge the Programme d'Investissements d'Avenir and the Agence Nationale pour la Recherche for the support of the national infrastructure “ECELLFrance: Development of mesenchymal stem cell-based therapies” (PIA-ANR-11-INBS-005).

References

1. Kershaw EE, Flier JS. Adipose tissue as an endocrine organ. *J Clin Endocrinol Metab.* (2004) 89:2548–56. doi: 10.1210/jc.2004-0395

2. Wang S, Liu Y, Chen J, He Y, Ma W, Liu X, et al. Effects of multi-organ crosstalk on the physiology and pathology of adipose tissue. *Front Endocrinol.* (2023) 14:1198984. doi: 10.3389/fendo.2023.1198984

3. Ferrante AW. The immune cells in adipose tissue. *Diabetes Obes Metab.* (2013) 15:34–8. doi: 10.1111/dom.12154

4. Medzhitov R. Origin and physiological roles of inflammation. *Nature.* (2008) 454:428–35. doi: 10.1038/nature07201

5. Bouloumié A, Curat CA, Sengeçs C, Lolmède K, Miranville A, Busse R. Role of macrophage tissue infiltration in metabolic diseases. *Curr Opin Clin Nutr Metab Care.* (2005) 8:347–54. doi: 10.1097/01.mco.0000172571.41149.52

6. Wynn TA, Chawla A, Pollard JW. Origins and hallmarks of macrophages: development, homeostasis, and disease. *Nature.* (2013) 496:445–55. doi: 10.1038/nature12034

7. Hashimoto D, Chow A, Noizat C, Teo P, Beasley MB, Leboeuf M, et al. Tissue-resident macrophages self-maintain locally throughout adult life with minimal contribution from circulating monocytes. *Immunity.* (2013) 38:792–804. doi: 10.1016/j.immuni.2013.04.004

8. Hassnain Waqas SF, Noble A, Hoang AC, Ampem G, Popp M, Strauß S, et al. Adipose tissue macrophages develop from bone marrow-independent progenitors in Xenopus laevis and mouse. *J Leukoc Biol.* (2017) 102:845–55. doi: 10.1189/jlb.1A0317-082R

9. Yona S, Kim KW, Wolf Y, Mildner A, Varol D, Breker M, et al. Fate mapping reveals origins and dynamics of monocytes and tissue macrophages under homeostasis. *Immunity.* (2013) 38:79–91. doi: 10.1016/j.immuni.2012.12.001

10. Dick SA, Wong A, Hamidzada H, Nejat S, Nechamitzky R, Vohra S, et al. Three tissue resident macrophage subsets coexist across organs with conserved origins and life cycles. *Sci Immunol.* (2022) 7:eabf7777. doi: 10.1126/sciimmunol.abf7777

11. Félix I, Jokela H, Karhula J, Kotaja N, Savontaus E, Salmi M, et al. Single-cell proteomics reveals the defined heterogeneity of resident macrophages in white adipose tissue. *Front Immunol.* (2021) 12:719979. doi: 10.3389/fimmu.2021.719979

12. Hoeffel G, Debroas G, Roger A, Rossignol R, Gouilly J, Laprie C, et al. Sensory neuron-derived TAFA4 promotes macrophage tissue repair functions. *Nature.* (2021) 594:94–9. doi: 10.1038/s41586-021-03563-7

13. Blériot C, Chakarov S, Ginhoux F. Determinants of resident tissue macrophage identity and function. *Immunity.* (2020) 52:957–70. doi: 10.1016/j.immuni.2020.05.014

14. Guilliams M, Thierry GR, Bonnardel J, Bajenoff M. Establishment and maintenance of the macrophage niche. *Immunity.* (2020) 52:434–51. doi: 10.1016/j.immuni.2020.02.015

15. Feuerstein R, Forde AJ, Lohrmann F, Kolter J, Ramirez NJ, Zimmermann J, et al. Resident macrophages acquire innate immune memory in staphylococcal skin infection. *eLife.* (2020) 9:e55602. doi: 10.7554/eLife.55602

16. Sim SL, Kumari S, Kaur S, Khosrotehrani K. Macrophages in skin wounds: functions and therapeutic potential. *Biomolecules.* (2022) 12:1659. doi: 10.3390/biom12111659

17. Gao Y, Wang J, Zhu DC, Miao Y, Hu ZQ. Dermal macrophage and its potential in inducing hair follicle regeneration. *Mol Immunol.* (2021) 134:25–33. doi: 10.1016/j.molimm.2021.02.021

18. Asterholm IW, Tao C, Morley TS, Wang QA, Delgado-Lopez F, Wang ZV, et al. Adipocyte inflammation is essential for healthy adipose tissue expansion and remodeling. *Cell Metab.* (2014) 20:103–18. doi: 10.1016/j.cmet.2014.05.005

19. Rabiller L, Robert V, Arlat A, Labit E, Ousset M, Salon M, et al. Driving regeneration instead of healing, in adult mammals: the decisive role of resident macrophages through efferocytosis. *NPJ Regener Med.* (2021) 6:41. doi: 10.1038/s41536-021-00151-1

20. Weisberg SP, McCann D, Desai M, Rosenbaum M, Leibel RL, Ferrante AW. Obesity is associated with macrophage accumulation in adipose tissue. *J Clin Invest.* (2003) 112:1796–808. doi: 10.1172/JCI200319246

21. Weisberg SP, Hunter D, Huber R, Lemieux J, Slaymaker S, Vaddi K, et al. CCR2 modulates inflammatory and metabolic effects of high-fat feeding. *J Clin Invest.* (2006) 116:115–24. doi: 10.1172/JCI24335

22. Guilliams M, Scott CL. Does niche competition determine the origin of tissue-resident macrophages? *Nat Rev Immunol.* (2017) 17:451–60. doi: 10.1038/nri.2017.42

23. Paupert J, Espinosa E, Cenac N, Robert V, Laharrague P, Evrard SM, et al. Rapid and efficient production of human functional mast cells through a three-dimensional culture of adipose tissue-derived stromal vascular cells. *J Immunol Baltim Md 1950.* (2018) 201:3815–21. doi: 10.4049/jimmunol.1701751

24. Krueger F. *Trim Galore! a wrapper to automate quality and adapter trimming* (2012). Available online at: https://www.bioinformatics.babraham.ac.uk/projects/trim_galore/

25. Adrews S. *FastQC A Quality Control tool for High Throughput Sequence Data* (2010). Available online at: <https://www.bioinformatics.babraham.ac.uk/projects/fastqc/>

26. Kim D, Langmead B, Salzberg SL. HISAT: a fast spliced aligner with low memory requirements. *Nat Methods.* (2015) 12:357–60. doi: 10.1038/nmeth.3317

27. Liao Y, Smyth GK, Shi W. featureCounts: an efficient general purpose program for assigning sequence reads to genomic features. *Bioinformatics.* (2014) 30:923–30. doi: 10.1093/bioinformatics/btt656

28. Coste A, Dubourdeau M, Linas MD, Cassaing S, Lepert JC, Balard P, et al. PPARgamma promotes mannose receptor gene expression in murine macrophages and contributes to the induction of this receptor by IL-13. *Immunity.* (2003) 19:329–39. doi: 10.1016/S1074-7613(03)00229-2

29. Emont MP, Jacobs C, Essene AL, Pant D, Tenen D, Colleluori G, et al. A single cell atlas of human and mouse white adipose tissue. *Nature.* (2022) 603:926–33. doi: 10.1038/s41586-022-04518-2

Conflict of interest

The authors declare that the research was conducted in the absence of any commercial or financial relationships that could be construed as a potential conflict of interest.

Publisher's note

All claims expressed in this article are solely those of the authors and do not necessarily represent those of their affiliated organizations, or those of the publisher, the editors and the reviewers. Any product that may be evaluated in this article, or claim that may be made by its manufacturer, is not guaranteed or endorsed by the publisher.

Supplementary material

The Supplementary Material for this article can be found online at: <https://www.frontiersin.org/articles/10.3389/fimmu.2024.1356397/full#supplementary-material>

30. Lemus-Conejo A, Medrano M, Lopez S, Millan-Linares MC, Rosillo MA, Perez-Simon JA, et al. MUFAAs in high-fat diets protect against obesity-induced bias of hematopoietic cell lineages. *Mol Nutr Food Res.* (2021) 65:2001203. doi: 10.1002/mnfr.202001203

31. Luche E, Robert V, Cuminetti V, Pomié C, Sastourné-Arrey Q, Waget A, et al. Corrupted adipose tissue endogenous myelopoiesis initiates diet-induced metabolic disease. *eLife.* (2017) 6:e23194. doi: 10.7554/eLife.23194

32. Olefsky JM, Glass CK. Macrophages, inflammation, and insulin resistance. *Annu Rev Physiol.* (2010) 72:219–46. doi: 10.1146/annurev-physiol-021909-135846

33. de Luca C, Olefsky JM. Inflammation and insulin resistance. *FEBS Lett.* (2008) 582:97–105. doi: 10.1016/j.febslet.2007.11.057

34. Heilbronn LK, Campbell LV. Adipose tissue macrophages, low grade inflammation and insulin resistance in human obesity. *Curr Pharm Des.* (2008) 14:1225–30. doi: 10.2174/138161208784246153

35. Suganami T, Ogawa Y. Adipose tissue macrophages: their role in adipose tissue remodeling. *J Leukoc Biol.* (2010) 88:33–9. doi: 10.1189/jlb.0210072

36. Bourlier V, Bouloumié A. Role of macrophage tissue infiltration in obesity and insulin resistance. *Diabetes Metab.* (2009) 35:251–60. doi: 10.1016/j.diabet.2009.05.001

37. Luo M, Lai W, He Z, Wu L. Development of an optimized culture system for generating mouse alveolar macrophage-like cells. *J Immunol.* (2021) 207:1683–93. doi: 10.4049/jimmunol.2100185

38. Ogawa K, Tsurutani M, Hashimoto A, Soeda M. Simple propagation method for resident macrophages by co-culture and subculture, and their isolation from various organs. *BMC Immunol.* (2019) 20:34. doi: 10.1186/s12865-019-0314-z

39. Tsurutani M, Horie H, Ogawa K. Cell properties of lung tissue-resident macrophages propagated by co-culture with lung fibroblastic cells from C57BL/6 and BALB/c mice. *Biomedicines.* (2021) 9:1241. doi: 10.3390/biomedicines9091241

40. Park MD, Silvin A, Ginhoux F, Merad M. Macrophages in health and disease. *Cell.* (2022) 185:4259–79. doi: 10.1016/j.cell.2022.10.007

41. Lee CZW, Ginhoux F. Biology of resident tissue macrophages. *Development.* (2022) 149:dev200270. doi: 10.1242/dev.200270

42. Beattie L, Sawtell A, Mann J, Frame TCM, Teal B, de Labastida Rivera F, et al. Bone marrow-derived and resident liver macrophages display unique transcriptomic signatures but similar biological functions. *J Hepatol.* (2016) 65:758–68. doi: 10.1016/j.jhep.2016.05.037

43. Huang SCC, Everts B, Ivanova Y, O'Sullivan D, Nascimento M, Smith AM, et al. Cell-intrinsic lysosomal lipolysis is essential for alternative activation of macrophages. *Nat Immunol.* (2014) 15:846–55. doi: 10.1038/ni.2956

44. Viola A, Munari F, Sánchez-Rodríguez R, Scolaro T, Castegna A. The metabolic signature of macrophage responses. *Front Immunol.* (2019) 10:1462. doi: 10.3389/fimmu.2019.01462

45. Yu Q, Wang Y, Dong L, He Y, Liu R, Yang Q, et al. Regulations of glycolytic activities on macrophages functions in tumor and infectious inflammation. *Front Cell Infect Microbiol.* (2020) 10:287. doi: 10.3389/fcimb.2020.00287

46. Pavlou S, Wang L, Xu H, Chen M. Higher phagocytic activity of thioglycollate-elicited peritoneal macrophages is related to metabolic status of the cells. *J Inflamm.* (2017) 14:4. doi: 10.1186/s12950-017-0151-x

47. Serbulea V, Upchurch CM, Schapke MS, Voigt P, DeWeese DE, Desai BN, et al. Macrophage phenotype and bioenergetics are controlled by oxidized phospholipids identified in lean and obese adipose tissue. *Proc Natl Acad Sci.* (2018) 115:E6254–63. doi: 10.1073/pnas.1800544115

48. Sharma M, Boytard L, Hadi T, Koelwyn G, Simon R, Ouimet M, et al. Enhanced glycolysis and HIF-1 α activation in adipose tissue macrophages sustains local and systemic interleukin-1 β production in obesity. *Sci Rep.* (2020) 10:5555. doi: 10.1038/s41598-020-62272-9

49. Wculek SK, Dunphy G, Heras-Murillo I, Mastrangelo A, Sancho D. Metabolism of tissue macrophages in homeostasis and pathology. *Cell Mol Immunol.* (2022) 19:384–408. doi: 10.1038/s41423-021-00791-9

50. Li Y, Yun K, Mu R. A review on the biology and properties of adipose tissue macrophages involved in adipose tissue physiological and pathophysiological processes. *Lipids Health Dis.* (2020) 19:164. doi: 10.1186/s12944-020-01342-3

51. Nawaz A, Tobe K. M2-like macrophages serve as a niche for adipocyte progenitors in adipose tissue. *J Diabetes Investig.* (2019) 10:1394–400. doi: 10.1111/jdi.13114

52. Chavakis T, Alexaki VI, Ferrante AW. Macrophage function in adipose tissue homeostasis and metabolic inflammation. *Nat Immunol.* (2023) 24:757–66. doi: 10.1038/s41590-023-01479-0

Frontiers in Immunology

Explores novel approaches and diagnoses to treat immune disorders.

The official journal of the International Union of Immunological Societies (IUIS) and the most cited in its field, leading the way for research across basic, translational and clinical immunology.

Discover the latest Research Topics

[See more →](#)

Frontiers

Avenue du Tribunal-Fédéral 34
1005 Lausanne, Switzerland
frontiersin.org

Contact us

+41 (0)21 510 17 00
frontiersin.org/about/contact



Frontiers in
Immunology

